

**Quantifying physical river habitat
parameters using hyperspatial resolution
UAS imagery and SfM-photogrammetry**

A. S. Woodget

PhD

2015

**Quantifying physical river habitat
parameters using hyperspatial resolution
UAS imagery and SfM-photogrammetry**

A. S. Woodget

A thesis submitted in partial fulfilment of the
University's requirements for the Degree of Doctor
of Philosophy

2015

University of Worcester

Abstract

The quantification of physical river habitat parameters is of fundamental importance for a range of river science and management applications, including investigations of flow hydraulics, sediment dynamics and fluvial habitats. These parameters include elements of the fluvial geomorphology (e.g. topography, substrate size) and hydraulics (e.g. water depth, flow velocity). Traditional methods for sampling these parameters are typically slow and labour intensive and do not meet the requirements of the increasingly recognised ‘riverscape’ paradigm. Methods are needed which are spatially continuous, spatially explicit and objective. Whilst remote sensing based approaches have made some progress here, few have been capable of quantifying simultaneously a number of physical habitat parameters using a single dataset. Recent research using unmanned aerial systems (UAS) and structure-from-motion (SfM) photogrammetric processing offers a new method (termed here as UAS-SfM) for quantifying physical river habitat parameters. However, this approach remains in its infancy, its wider limitations are largely unknown and very limited quantitative validation has been undertaken, especially within fluvial settings.

This research aimed to conduct a rigorous, quantitative assessment of the capabilities of a UAS-SfM approach for quantifying a series of physical river habitat parameters at the mesoscale (defined as channel lengths from a few tens of metres to a few hundred metres), and evaluated the results against existing remote sensing based techniques. The physical habitat parameters (1) topography/flow depth, (2) substrate size and (3) surface flow types (SFTs) (as indicators of hydraulic heterogeneity) were selected for assessment as the hydromorphological elements of greatest importance in determining fluvial habitat quality. The research was conducted at three contrasting river sites; the River Arrow in Warwickshire, UK, Coledale Beck in Cumbria, UK and the San Pedro River in south-central Chile.

The quantification of topography, in both exposed and submerged parts of the fluvial environment, was achieved using high resolution (c. 2cm) digital elevation models (DEMs), produced from the UAS-SfM approach, and validated against an independent topographic survey. DEM quality was found to vary within and between sites and was dependent on vegetation coverage, water depth, the spatial configuration of ground control points (GCPs) and the camera viewing angle. Mean errors were in the range 4-44mm for exposed areas and

17-89mm for submerged areas. A simple refraction correction was found to reduce errors in submerged areas by c. 50%. Additional testing of the approach over a flat sports hall floor revealed a slight doming of the DEM which is thought relate to the self-calibration of the camera lens within the SfM software and the acquisition of imagery predominantly at nadir, highlighting the importance of error assessment.

The quantification of substrate size, in exposed parts of the fluvial environment, was investigated using the dense point clouds produced from the UAS-SfM process. A variety of point cloud roughness metrics were calculated and calibrated against field-measures of substrate size. Point cloud detrending, filtering and smoothing were explored to minimise the effects of local topography and noise on the calibration relationship. Jack knife validation analysis showed that the model is capable of predicting grain sizes with an average residual error of -0.011cm and standard deviation of 1.64cm. An over-prediction of grains less than 5cm in size indicated the lower limit of accurate grain size estimations. Normalised residual errors were found to be considerable and would limit the wider applicability of this approach at present. A comparison against two other remote sensing approaches provided mixed results, with none of the methods emerging as consistently superior.

Surface flow types, as a proxy for hydraulic heterogeneity, were mapped visually from the high resolution (c. 1cm) orthophotos produced from the UAS-SfM process, and validated against traditional bankside mapping and an independent ground truth survey. The results indicated that the overall accuracy of SFT mapping conducted on the UAS-SfM orthophotos can be as good as 75%, but was variable between surveys and was affected by scene illumination, the indistinct nature of SFT boundaries, the vertical camera viewing angle, variable flow level and lack of temporal data. In addition, quantitative outputs from the SfM process (water depth and point cloud roughness) were not found to improve the separability of SFTs when explored using analysis of similarity (ANOSIM) tests. The data presented raises the question of the basic suitability of SFT mapping for inferring hydraulic diversity, which requires further research.

Overall, the UAS-SfM approach was found to offer great potential as a rapid, relatively inexpensive, spatially continuous, spatially explicit method for providing quantitative information concerning physical river habitat parameters at exceptionally high spatial and temporal resolutions. However, the accuracy, precision and reliability of results were variable,

and the ability to produce consistently high quality outputs for all the specified physical river habitat parameters simultaneously has not yet been proven. Critical limitations include the effects of image blurring, the need for favourable weather conditions and systematic errors arising from the SfM processing. It is likely that future improvements to UAS platforms and sensors, in conjunction with further quantitative assessments, will facilitate the development of the approach and permit its application for routine and reliable assessments of river habitat quality.

Acknowledgements

So here is my PhD thesis, the summary of my three years devotion to a small remote control helicopter, to processing millions of points scattered in 3D space and, amongst other things, contemplating my favourite colour ramp. But it's also not just a PhD. For me, it represents my freedom and my choice, and it is no exaggeration to say I have loved (almost!) every minute. What an amazing opportunity it has been.

My very great thanks go to my supervisors - Fleur Visser for providing me with the opportunity to undertake this PhD, giving me the freedom to regain my sense of self and trusting me to get on with it; Ian Maddock for the opportunity to work in some fantastic places with some great people, for the laughs and for the on-going support and encouragement, and; Patrice Carbonneau for crucial technical guidance.

Special thanks also go to –

- Richard Johnson and other colleagues at the University of Bath Spa for collaborating on the fieldwork at Coledale Beck and initial processing of the TLS data.
- Evelyn Habit and colleagues at the University of Concepción for the opportunity to work on the San Pedro, provision of dGPS data and organising our fieldwork in Chile.
- Technician James Atkins for flying assistance, provision of field equipment, general encouragement and many cups of tea.
- Technician Robbie Austrums for in-house code writing, helpful discussions and more cups of tea.
- Martin Wilkes, Jenni Lodwick and William Woodget for fieldwork assistance.
- Daniel Girardeau-Montaut of CloudCompare fame for helpful modifications to his very useful software.
- The RSPSoc Council for the support provided during my time as Wavelength representative and the opportunity to become a part of such a welcoming community.
- Monica Rivas-Casado and others at Cranfield University for joint fieldwork and other collaboration opportunities.
- Finally, to my family and close friends (especially Sally, Mark and William Woodget, Janet Keefe, Hannah Namih and Jenni Lodwick) - I cannot thank you enough for the on-going encouragement and inspiration you provide, as well as the welcome distractions. I hope I can make you proud.

My research was funded by a University of Worcester studentship and I have really valued the opportunity to work within the exceptionally friendly, supportive and inclusive environment which this University provides. Additional financial support for fieldwork and conference attendance was also gratefully received from the Remote Sensing and Photogrammetry Society, the Geological Remote Sensing Group, the British Society for Geomorphology and the British Hydrological Society.

The Journey

Mary Oliver

One day you finally knew
what you had to do, and began,
though the voices around you
kept shouting
their bad advice-
though the whole house
began to tremble
and you felt the old tug
at your ankles.

"Mend my life!"
each voice cried.

But you didn't stop.
You knew what you had to do,
though the wind pried
with its stiff fingers
at the very foundations,
though their melancholy
was terrible.

It was already late
enough, and a wild night,
and the road full of fallen
branches and stones.

But little by little,
as you left their voices behind,
the stars began to burn
through the sheets of clouds,
and there was a new voice
which you slowly
recognised as your own,
that kept you company
as you strode deeper and deeper
into the world,
determined to do
the only thing you could do-
determined to save
the only life you could save.

Table of Contents

Abstract	i-iii
Acknowledgements	iv-v
Table of Contents	vi-x
Glossary	xi
List of Figures	xii-xx
List of Tables	xxi-xxv
Chapter 1 – Introduction	1-37
1.1 Physical river habitat and remote sensing	1
1.1.1 Definition and importance of physical river habitat.....	1-3
1.1.2 Conceptualising river systems.....	3-5
1.1.3 The need for quantifying physical river habitat.....	5-6
1.1.4 The role of remote sensing.....	6-8
1.2 Unmanned aerial systems and structure from motion photogrammetry	8
1.2.1 Development of UAS	8-11
1.2.2 New opportunities provided by UAS.....	11
1.2.3 Challenges of working with UAS.....	11-13
1.2.4 The theory of SfM-photogrammetry	13-15
1.2.5 Application of SfM-photogrammetry.....	15-16
1.3 Aims of this thesis	17
1.3.1 Motivation.....	17
1.3.2 Research aims.....	17-19
1.4 Thesis structure	19-21
1.5 The study sites	21
1.5.1 The River Arrow.....	21-24
1.5.2 Coledale Beck.....	25-28
1.5.3 The San Pedro River.....	28-31
1.5.4 Sports hall floor.....	31
1.6 Summary	32
1.7 References	33-37

Chapter 2 – Methods.....38-68

2.1	The Draganflyer X6 UAS.....	38-41
2.2	Pre-flight camera characterisation.....	42-44
2.3	UAS surveys.....	45-53
2.3.1	Ground control.....	45-49
2.3.2	Image acquisition – sports hall.....	49-50
2.3.3	Image acquisition – field sites.....	50-53
2.4	Image selection.....	53-56
2.4.1	Camera tilt angle.....	54
2.4.2	Visual image quality.....	54-55
2.4.3	Platform roll and pitch angles.....	55-56
2.5	Structure-from-motion processing.....	56-64
2.5.1	Image import.....	56
2.5.2	Image alignment.....	57-58
2.5.3	Geometry building.....	58-60
2.5.4	Texture building.....	60-61
2.5.5	Georeferencing.....	61-62
2.5.6	Optimisation.....	62-63
2.5.7	Model re-building.....	63
2.5.8	Export.....	63-64
2.6	TLS data acquisition and initial processing.....	64-67
2.6.1	Background.....	64
2.6.2	Field set-up.....	65
2.6.3	Data acquisition.....	65-66
2.6.4	Initial data processing.....	66-67
2.7	References.....	68

**Chapter 3 - Quantifying fluvial topography using hyperspatial resolution
UAS imagery and SfM-photogrammetry.....69-147**

3.1	Background and Context.....	70-95
3.1.1	Fluvial topography.....	70-71
3.1.2	The importance of topography and flow depth.....	71
3.1.3	The measurement of topography and depth.....	71-73
3.1.4	Quantifying fluvial topography and flow depth using remote sensing.....	73-93
3.1.5	Summary.....	93-95
3.2	Research Questions.....	95

3.3	Site Locations.....	96-98
3.4	Methods.....	98-104
3.4.1	Independent topographic survey.....	99-101
3.4.2	Refraction correction.....	101-103
3.4.3	Quantitative DEM validations.....	103
3.4.4	Comparison of UAS-SfM and TLS DEMs.....	103-104
3.5	Results and Analysis.....	104-127
3.5.1	Digital elevation models.....	104-110
3.5.2	Exposed areas.....	110-112
3.5.3	Submerged areas.....	113-115
3.5.4	Spatial patterns of DEM error.....	116-121
3.5.5	Comparison with TLS.....	122-127
3.6	Discussion.....	128-140
3.6.1	Accuracy, precision and repeatability.....	128-136
3.6.2	Comparison with TLS.....	136-138
3.6.3	Summary.....	138-140
3.7	Conclusions.....	140-141
3.8	References.....	142-147

Chapter 4 - Quantifying fluvial substrate size using hyperspatial resolution UAS imagery and SfM-photogrammetry.....148-233

4.1	Background and Context.....	149-167
4.1.1	Fluvial substrate size and its importance.....	149-150
4.1.2	Traditional methods of mapping and quantifying substrate size.....	150-152
4.1.3	Quantifying substrate size using remote sensing.....	152-165
4.1.4	Summary.....	166-167
4.2	Research Questions.....	167-168
4.3	Site Locations.....	168
4.4	Methods.....	169-182
4.4.1	Ground truthing of substrate size.....	171-172
4.4.2	Processing of UAS-SfM point cloud.....	172-176
4.4.3	Computing UAS-SfM image texture.....	176-178
4.4.4	Processing of TLS point cloud.....	178-180
4.4.5	Establishing a relationship with substrate size (model calibration).....	180-182
4.4.6	Substrate size model validation.....	182

4.5	Results and Analysis.....	183-211
4.5.1	Ground truth substrate size.....	183
4.5.2	UAS-SfM point cloud roughness.....	184-193
4.5.3	UAS-SfM image texture.....	193-200
4.5.4	TLS point cloud roughness.....	200-207
4.5.5	Comparison of techniques.....	207-211
4.6	Discussion.....	212-226
4.6.1	Quantifying substrate size using UAS-SfM point cloud roughness.....	212-221
4.6.2	Comparison with other techniques.....	221-225
4.6.3	Summary and future work.....	225-226
4.7	Conclusions.....	226-228
4.8	References.....	229-233

***Chapter 5 – Mapping surface flow types using hyperspatial resolution
UAS imagery and SfM-photogrammetry.....234-305***

5.1	Background and Context.....	235-246
5.1.1	Defining surface flow types.....	235-236
5.1.2	The importance of surface flow types.....	236-239
5.1.3	Traditional mapping of surface flow types.....	239-240
5.1.4	Surface flow type mapping using remote sensing.....	240-245
5.1.5	Summary.....	245-246
5.2	Research Questions.....	247
5.3	Site Locations.....	247-249
5.4	Methods.....	250-261
5.4.1	Surface flow type mapping from the bankside.....	250-252
5.4.2	Ground truthing of surface flow types.....	253
5.4.3	Surface flow type mapping from UAS-SfM imagery.....	253
5.4.4	Comparing bankside and UAS-SfM surface flow type mapping.....	254
5.4.5	Accuracy assessment of surface flow type mapping.....	254-256
5.4.6	Deriving quantitative information from UAS-SfM outputs.....	256-258
5.4.7	Differentiating surface flow types.....	258-261
5.5	Results and Analysis.....	261-288
5.5.1	Comparing surface flow type mapping.....	261-268
5.5.2	Accuracy of surface flow type mapping.....	269-271
5.5.3	Differentiating surface flow types using quantitative UAS-SfM outputs.....	271-288
5.6	Discussion.....	289-300
5.6.1	Surface flow type mapping from UAS-SfM orthophotos.....	289-293

5.6.2	Differentiating surface flow types using quantitative UAS-SfM outputs.....	294-300
5.7	Conclusions.....	301-302
5.8	References.....	303-305
 Chapter 6 – Discussion & Conclusion.....		306-327
6.1	Aims of this research.....	306
6.2	Summary of key findings.....	306-310
6.2.1	Fluvial topography.....	307
6.2.2	Substrate size.....	308
6.2.3	Surface flow types.....	308-310
6.3	Evaluation of the UAS-SfM approach.....	310-317
6.3.1	Advantages.....	310-312
6.3.2	Limitations.....	312-315
6.3.3	Applicability to physical river habitat surveying.....	315-317
6.4	Recommendations for future work.....	317-318
6.5	Potential applications.....	318-322
6.6	Final conclusions.....	323-324
6.7	References.....	325-327
 Appendix A (Methods).....		328-346
Appendix B (Topography).....		347
Appendix C (Substrate Size).....		348-366
Appendix D (Surface Flow Types).....		367-379
Appendix E (Discussion & Conclusion).....		380-387

Glossary

ANOSIM	Analysis of similarity (test)
BNUC	Basic National UAS Certificate
BNUC-S	Basic National UAS Certificate for Small UAS
BSW	Broken standing waves (SFT)
CAA	Civil Aviation Authority
DEM	Digital elevation model
dGPS	Differential global positioning system
DSLR	Digital single-lens reflex (camera)
DTM	Digital terrain model
EA	Environment Agency
GCP	Ground control point
GLCM	Grey level co-occurrence matrix
GNSS	Global navigation satellite signal
GPR	Ground penetrating radar
GPS	Global positioning system
INS	Inertial navigation system
LiDAR	Light detection and ranging
LiPo	Lithium polymer (batteries)
LWD	Large woody debris
NC	Non-refraction corrected
NPF	No perceptible flow (SFT)
OSGB	Ordnance Survey Great Britain
PHABSIM	Physical Habitat Simulation System (model)
R	Rippled (SFT)
RC	Refraction corrected
RCC	River Continuum Concept (Vannote et al., 1980)
RGB	Red green blue (true colour imagery)
RHS	River Habitat Survey
RINEX	Receiver Independent Exchange (data interchange format for raw GNSS data)
RMSE	Root mean square error
RPAS	Remotely piloted aircraft systems
RTK	Real time kinematic (GPS set up)
S	Smooth (SFT)
SfM	Structure from motion
SFT	Surface flow type
SIFT	Scale invariant feature transform (algorithm)
TLS	Terrestrial laser scanning/scanner
UAS/UAV	Unmanned aerial system/vehicle
UP	Upwelling (SFT)
USW	Unbroken standing waves (SFT)
UTM	Universal Transverse Mercator
WFD	Water Framework Directive
WGS	World Geodetic System

List of Figures

Chapter 1 Introduction

- Figure 1.1. Physical river habitat determined by the interaction between geomorphology and hydrology (Maddock 1999).
- Figure 1.2. Frissell et al., (1986)'s hierarchical organisation of the river system and habitat subsystems (linear scale is approximate).
- Figure 1.3. Examples of unmanned aerial systems; a) SmartPlanes SmartOne fixed-wing UAS (Smart Planes 2014); b) Mikrokopter Oktokopter rotary-winged UAS (Turner et al., 2012).
- Figure 1.4. Overview of the thesis structure.
- Figure 1.5. The study site at the River Arrow, near Studley (Zone B).
- Figure 1.6. Location map for the River Arrow research site, Warwickshire, UK.
- Figure 1.7. The downstream end of the research site at Coledale Beck, Cumbria.
- Figure 1.8. Location map for the Coledale Beck research site, Cumbria, UK.
- Figure 1.9. Location of the Piedra Blanca research site on the San Pedro River, Chile (Google Maps 2014).
- Figure 1.10. The Piedra Blanca research site on the San Pedro River.
- Figure 1.11. The sports hall floor at the University of Worcester.

Chapter 2 Methods

- Figure 2.1. The Draganflyer X6 UAS platform.
- Figure 2.2. The Draganflyer X6 handheld controller (Source: www.draganfly.com, accessed May 2013).
- Figure 2.3. a) Video goggles capable of displaying real-time imagery from the camera mounted on the Draganflyer X6 during flight (Source: www.dragonfly.com, accessed May 2012), b) Panasonic Lumix DMC-LX3 (Source: www.panasonic.co.uk, accessed March 2013)
- Figure 2.4. Screenshots of the Draganview software showing a) real-time imagery and b) telemetry information (Source: www.draganfly.com, accessed May 2013)
- Figure 2.5. Set-up of the camera characterisation tests, with example artificial target (measuring 20cm x 20cm).
- Figure 2.6. Relationship between distance (i.e. flight altitude) and image pixel size, as determined by characterisation of the Panasonic DMC-LX3 camera.
- Figure 2.7. Relationship between distance (i.e. flight altitude) and image dimensions, as determined by characterisation of the Panasonic DMC-LX3 camera.
- Figure 2.8. The artificial ground control points constructed for use within this research.
- Figure 2.9. Locations of ground control points (GCPs) during the UAS survey of the San Pedro River, May 2012.
- Figure 2.10. Locations of ground control points during the UAS survey of the River Arrow, July 2012.
- Figure 2.11. Locations of ground control points during the UAS surveys of the River Arrow in May, June and August 2013, shown over the June 2013 orthophoto (modified from Woodget et al., 2015)

- Figure 2.12. Locations of ground control points during the UAS survey of Coledale Beck, July 2013 (modified from Woodget et al., 2015).
- Figure 2.13. Arrangement of GCPs used for the sports hall tests
- Figure 2.14. Example images acquired using the Panasonic Lumix DMC-LX3 camera mounted on the Draganflyer X6 at a) The San Pedro River, Chile, May 2012, b) The River Arrow May 2013, c) The River Arrow August 2013 and d) Coledale Beck, July 2013.
- Figure 2.15. Extract from an example log file.
- Figure 2.16. Examples of clear (a - left) and blurred (b - right) imagery.
- Figure 2.17. Established measures of aircraft movement – altitude, roll, pitch and yaw (Source: www.draganfly.com, accessed March 2013).
- Figure 2.18. Overview of the SfM process, as implemented using the Agisoft PhotoScan Pro software.
- Figure 2.19. Leica ScanStation C10 terrestrial laser scanner (left) and Leica reflective targets (right), in use at Coledale Beck, July 2013.
- Figure 2.20. Location of TLS targets and scan station positions at Coledale Beck, July 2013.
- Figure 2.21. Example of a marker established at Coledale Beck and used as TLS reflective target markers and TLS scan station position markers.

Chapter 3 Topography

- Figure 3.1. Radiometric differences between adjacent images, as presented by Lejot et al., 2007.
- Figure 3.2. The relationship between camera location, water surface elevation, apparent water depth (indicated by the initial point) and actual water depth (indicated by the actual point). Not to scale (after Westaway et al., 2001, Woodget et al., 2015).
- Figure 3.3. Schematic diagram to show the typical set-up of an airborne LiDAR system (Mosaic Mapping Systems Inc, 2001).
- Figure 3.4. An example of a GPR-generated cross section for the Skagit River in Washington, USA (Costa et al., 2000).
- Figure 3.5. Validation plot of the fit between the SfM DEM and GPS observed elevations (Fonstad et al., 2013).
- Figure 3.6. Photographs of the sites used for assessing topography and/or flow depth (a) San Pedro River, (b) River Arrow (c) Coledale Beck and (d) Sports hall floor at University of Worcester.
- Figure 3.7. Methods workflow for topography chapter.
- Figure 3.8. Example cross sections demonstrating the effect of refraction correction on DEM elevations in submerged areas a) at the River Arrow and b) at Coledale Beck (Woodget et al., 2015).
- Figure 3.9. Digital elevation model (left) and refraction corrected water depth data (right) computed for the San Pedro River research site.
- Figure 3.10. Digital elevation model (top) and refraction corrected water depth data (bottom) for the River Arrow survey conducted in May 2013.
- Figure 3.11. Digital elevation model (top) and refraction corrected water depth data (bottom) for the River Arrow survey conducted in June 2013.
- Figure 3.12. Digital elevation model (top) and refraction corrected water depth data (bottom) for the River Arrow survey conducted in August 2013.

- Figure 3.13. Digital elevation model (top) and refraction corrected water depth data (bottom) for the Coledale Beck survey conducted in July 2013.
- Figure 3.14. DEM elevations plotted against independent topographic survey data for exposed areas of all field sites (after Woodget et al., 2015).
- Figure 3.15. DEM elevations plotted against independent topographic survey data for submerged areas of all field sites. Black circles and lines represent non-corrected data, and blue triangles and lines represent refraction corrected data (after Woodget et al., 2015).
- Figure 3.16. DEM error values plotted against field measured water depths for all field sites. Black circles and lines represent non-corrected data, and blue triangles and lines represent refraction corrected data (after Woodget et al., 2015).
- Figure 3.17. Digital elevation models for the four tests carried out for the Sports Hall floor. The dashed line indicates the location of the cross sections used to produce the DEM profiles shown in Figure 3.18.
- Figure 3.18. Cross section DEM profiles of the four Sports Hall tests (after Woodget et al., 2015).
- Figure 3.19. DEM errors at the San Pedro River plotted against distance from the central alignment of GCPs.
- Figure 3.20. Spatial distribution of DEM error for the San Pedro River, May 2012.
- Figure 3.21. Spatial distribution of DEM error for the River Arrow, May 2013.
- Figure 3.22. Spatial distribution of DEM error for the River Arrow, June 2013 (after Woodget et al., 2015).
- Figure 3.23. Spatial distribution of DEM error for the River Arrow, August 2013.
- Figure 3.24. Spatial distribution of DEM error for Coledale Beck, July 2013 (after Woodget et al., 2015).
- Figure 3.25. Digital elevation model of the Coledale Beck research site, generated from data collected using a TLS, July 2013.
- Figure 3.26. Spatial distribution of TLS DEM error for Coledale Beck, July 2013.
- Figure 3.27. DEM of difference map showing the difference in elevation between TLS and UAS-SfM DEMs. Yellows through to reds indicate that the TLS DEM has a higher elevation than the UAS-SfM DEM. Greens through to blues indicates that the UAS-SfM DEM has a higher elevation than the TLS DEM.
- Figure 3.28. Spatial distribution of colour-coded residual elevation errors for all ground truth values (Javernick et al., 2014).

Chapter 4 Substrate Size

- Figure 4.1. Comparison of grain axes measured by direct sampling against those using a fully automated photo-sieving approach (method 1A in Butler et al., 2001).
- Figure 4.2. Regression plots showing (a) the calibration relationship between median substrate size (D_{50}) and semivariance for exposed substrate and (b) the validation relationship between predicted and observed median substrate size (Carbonneau et al., 2004).
- Figure 4.3. Regression plots showing (a) the calibration relationship between median substrate size (D_{50}) and semivariance for submerged substrate and (b) the validation relationship between predicted and observed median substrate size for submerged areas (Carbonneau et al., 2005).

- Figure 4.4. Example of the correlation between roughness ($2\sigma_z$) and clast size percentiles for a sample site on a gravel bar on the River South Tyne at Lambley (Heritage and Milan 2009).
- Figure 4.5. Regression plots showing relationship between median substrate size (D_{50}) and standard deviation of local elevation, for both raw and detrended TLS datasets acquired from (a) the River Feshie and (b) with additional data incorporated from the Tan u Bwlch and Rees River (Brasington et al., 2012).
- Figure 4.6. Substrate size mapping of the River Feshie derived from TLS point cloud data (Brasington et al., 2012).
- Figure 4.7. Regression plot for the relationship between median substrate size (D_{50}) determined through photo-sieving and UAS orthomosaic image texture computed using a 1m^2 moving window (Tamminga et al., 2014).
- Figure 4.8. Predicted substrate size (D_{50}) and digitised cover features for the area of interest on the Elbow River (Tamminga et al., 2014).
- Figure 4.9. The Coledale Beck research site (July 2013).
- Figure 4.10. Methods workflow for substrate size chapter.
- Figure 4.11. Location of ground truth sample plots at Coledale Beck, July 2013.
- Figure 4.12. Examples of ground truth sample plots. Photos show plots A7 (left) and B3 (right).
- Figure 4.13. Example of erroneous points above the main UAS-SfM cloud (left – plot C7) and ‘shadows’ of points below the main point cloud within the buffered ground truth sample plots (right – plot C2).
- Figure 4.14. Raw, unprocessed UAS-SfM point cloud for ground truth plot B3 (top), filtered and smoothed (middle) and showing roughness computed using a 30cm kernel size (bottom).
- Figure 4.15. Example ground truth and 50cm buffer plots used for calculating point cloud roughness.
- Figure 4.16. Example TLS point clouds for 50cm buffer areas of plots A4 (left) and A3 (right).
- Figure 4.17. Example of footprints present within ground truth sample plot A1 (Photos: A.Woodget).
- Figure 4.18. Linear regression of UAS-SfM point cloud roughness (no detrending, smoothed and filtered, 20cm roughness kernel size) and ground truth substrate size (D_{84} of B axis). Plots A1 and C1 are not included.
- Figure 4.19. a) Point cloud roughness for the Coledale Beck site, computed using a 20cm kernel size on a non detrended, smoothed and filtered point cloud, b) Predicted substrate size for the Coledale Beck, based on the roughness data shown in map (a). Roughness and predicted substrate size layers are displayed with a 30-50% transparency.
- Figure 4.20. Residual error of predicted substrate size from the UAS-SfM point cloud roughness approach plotted against ground truth substrate size.
- Figure 4.21. Normalised residual error of predicted substrate size from the UAS-SfM point cloud roughness approach plotted against ground truth substrate size.
- Figure 4.22. Observed ground truth substrate size plotted against predicted substrate size using UAS-SfM point cloud roughness.
- Figure 4.23. Linear regression of UAS-SfM maximum image entropy and ground truth substrate size (average of A axis). Plots A1 and C1 are not included.
- Figure 4.24. a) Image entropy for the Coledale Beck site, computed using a c. 41cm kernel size on the UAS-SfM orthophoto, b) Predicted substrate size for Coledale Beck,

- based on the image entropy data shown in map (a). Image entropy and predicted grain size layers are displayed with a 50% transparency.
- Figure 4.25. Residual error of predicted substrate size from the UAS-SfM image texture approach plotted against ground truth substrate size.
- Figure 4.26. Normalised residual error of predicted substrate size from the UAS-SfM image texture approach plotted against ground truth substrate size.
- Figure 4.27. Observed ground truth substrate size plotted against predicted substrate size from the UAS-SfM image texture approach.
- Figure 4.28. Linear regression of TLS point cloud roughness and ground truth substrate size (D_{84} of B axis). Plots A1 and C1 are not included.
- Figure 4.29. a) TLS point cloud roughness for the Coledale Beck site, computed using a 20cm kernel (radius size), b) Predicted substrate size for Coledale Beck, based on the TLS roughness data shown in map (a). Roughness and predicted grain size layers are displayed with a 50% transparency
- Figure 4.30. Residual error of predicted substrate size from the TLS point cloud roughness approach plotted against ground truth substrate size.
- Figure 4.31. Normalised residual error of predicted substrate size from the TLS point cloud roughness approach plotted against ground truth substrate size.
- Figure 4.32. Observed ground truth substrate size plotted against predicted substrate size from the TLS point cloud roughness approach. Plots A1 and C1 are excluded.
- Figure 4.33. Histogram of residual errors, by approach.
- Figure 4.34. Histogram of normalised residual errors, by approach.
- Figure 4.35. Observed ground truth substrate size plotted against predicted substrate size computed using the UAS-SfM point cloud roughness, UAS-SfM image texture and TLS point cloud roughness approaches. P values for all regressions are less than 0.01.
- Figure 4.36. Residual error of predicted substrate sizes (from the UAS-SfM point cloud roughness, UAS-SfM image texture and TLS point cloud roughness approaches) plotted against ground truth substrate size.
- Figure 4.37. Normalised residual error of predicted substrate sizes (from the UAS-SfM point cloud roughness, UAS-SfM image texture and TLS point cloud roughness approaches) plotted against ground truth substrate size.
- Figure 4.38. Vegetation within and near to ground truth sample plot C3 (left) introducing noise and erroneous points to the UAS-SfM point cloud covering this plot (point cloud shown includes the 50cm buffer zone) (right).
- Figure 4.39. Close-up of orthophoto, UAS-SfM point cloud roughness and predicted substrate size, highlighting at points A, B and C the over-prediction of smaller clasts where they are situated in gaps between larger clasts.
- Figure 4.40. Close-up of orthophoto, UAS-SfM point cloud roughness and predicted substrate size, highlighting at point A the underprediction of large, flat grains.

Chapter 5 Surface Flow Types

- Figure 5.1. The proposed continuum of surface flow types, and their relationship with local morpho-hydraulic conditions (Hill 2011).
- Figure 5.2. The River Arrow research site (May 2013).
- Figure 5.3. The Coledale Beck research site (July 2013).
- Figure 5.4. Methods workflow for SFTs chapter.

- Figure 5.5. SFT mapping conducted visually from the bankside (top) and from the UAS-SfM orthophoto (bottom) for the River Arrow July 2012 survey.
- Figure 5.6. SFT mapping conducted visually from the bankside (top) and from the UAS-SfM orthophoto (bottom) for the River Arrow May 2013 survey.
- Figure 5.7. SFT mapping conducted visually from the bankside (top) and from the UAS-SfM orthophoto (bottom) for the River Arrow June 2013 survey.
- Figure 5.8. SFT mapping conducted visually from the bankside (top) and from the UAS-SfM orthophoto (bottom) for the River Arrow August 2013 survey.
- Figure 5.9. SFT mapping conducted from a combination visual mapping from the bankside, mapping from the UAS-SfM orthophoto and ground truth data for Coledale Beck, July 2013.
- Figure 5.10. Stacked bar charts indicating how ground truth SFTs are mapped by the UAS-SfM survey, by SFT and date of survey.
- Figure 5.11. Point cloud roughness data derived from the UAS-SfM process for the River Arrow July 2012 dataset. The SFT units mapped from the orthophoto are shown as polygons, and the SFT 'core' areas as small black circles. Code to SFTs: S (smooth), R (rippled), NPF (no perceptible flow), USW (unbroken standing waves), UP (upwelling).
- Figure 5.12. Refraction corrected water depth and point cloud roughness data derived from the UAS-SfM process for the River Arrow May 2013 dataset. The SFT units mapped from the orthophoto are shown as polygons, and the SFT 'core' areas as small black circles. Code to SFTs: S (smooth), R (rippled), NPF (no perceptible flow), USW (unbroken standing waves), UP (upwelling).
- Figure 5.13. Refraction corrected water depth and point cloud roughness data derived from the UAS-SfM process for the River Arrow June 2013 dataset. The SFT units mapped from the orthophoto are shown as polygons, and the SFT 'core' areas as small black circles. Code to SFTs: S (smooth), R (rippled), NPF (no perceptible flow), USW (unbroken standing waves), UP (upwelling).
- Figure 5.14. Refraction corrected water depth and point cloud roughness data derived from the UAS-SfM process for the River Arrow August 2013 dataset. The SFT units mapped from the orthophoto are shown as polygons, and the SFT 'core' areas as small black circles. Code to SFTs: S (smooth), R (rippled), NPF (no perceptible flow), USW (unbroken standing waves), UP (upwelling). Areas labelled V denote patches of submerged aquatic vegetation.
- Figure 5.15. Refraction corrected water depth and point cloud roughness data derived from the UAS-SfM process for the Coledale Beck July 2013 dataset. The SFT units mapped from the orthophoto are shown as polygons, and the SFT 'core' areas as small black circles. Code to SFTs: S (smooth), R (rippled), NPF (no perceptible flow), USW (unbroken standing waves), UP (upwelling).
- Figure 5.16. Roughness distributions profiles by site and by SFT (for SFT core areas only).
- Figure 5.17. Roughness distributions for the core area of each SFT, by survey. The error bars represent one standard deviation of roughness either side of the mean roughness.
- Figure 5.18. Point cloud roughness from the River Arrow May 2013 survey regressed against field-measured hydraulic variables water depth and mean column velocity.
- Figure 5.19. Point cloud roughness from the River Arrow June 2013 survey regressed against field-measured hydraulic variables water depth and mean column velocity.

- Figure 5.20. Point cloud roughness from the River Arrow August 2013 survey regressed against field-measured hydraulic variables water depth and mean column velocity.
- Figure 5.21. Point cloud roughness from the Coledale Beck July 2013 survey regressed against field-measured hydraulic variables water depth and mean column velocity.
- Figure 5.22. Spatial assessment of SFT mapping accuracy for the River Arrow May 2013 survey. Code to SFTs: S (smooth), R (rippled), NPF (no perceptible flow), USW (unbroken standing waves), UP (upwelling) and LWD indicates a piece of large woody debris.
- Figure 5.23. Spatial assessment of SFT mapping accuracy for the River Arrow June 2013 survey. Code to SFTs: S (smooth), R (rippled), NPF (no perceptible flow), USW (unbroken standing waves), UP (upwelling).
- Figure 5.24. Spatial assessment of SFT mapping accuracy for the River Arrow August 2013 survey. Code to SFTs: S (smooth), R (rippled), NPF (no perceptible flow), USW (unbroken standing waves), UP (upwelling).
- Figure 5.25. Local site observations of the relationship between point cloud roughness and areas of fast flow, deep water or increased water surface roughness.

Chapter 6 Discussion & Conclusion

- Figure 6.1. Overview of the set-up and key findings of this research, with suggestions for future work.
- Figure 6.2. The spatial scales of remote sensing and geospatial technologies for mapping fluvial systems (Brasington 2014).
- Figure 6.3. Habitat distribution for juvenile Salmon, showing areas in white which meet the depth (0.1-0.6m) and particle size (25-250mm for D50) requirements, and areas in black which do not. The river has been reprojected to a rectangular display so the entire river can be displayed (Carbonneau et al., 2012).
- Figure 6.4. Distribution of habitat suitability for (a) adult and (b) juvenile brown trout, based on a composite suitability index (Tamminga et al., 2014).
- Figure 6.5. Geomorphic change between 2010 and 2011, based on the contiguous DEMs created from UAS and mobile TLS data (Flener et al., 2013).

Appendix A

- Figure A1. Orthophoto and DEM for the San Pedro River, May 2012.
- Figure A2. Orthophoto and DEM for the River Arrow, July 2012.
- Figure A3. Orthophoto and DEM for the River Arrow, May 2013.
- Figure A4. Orthophoto and DEM for the River Arrow, June 2013.
- Figure A5. Orthophoto and DEM for the River Arrow, August 2013.
- Figure A6. Orthophoto and DEM for the Coledale Beck, July 2013.

Appendix B

See Woodget et al., (2015)

Appendix C

- Figures C1-25. Plot photos and substrate size distributions for ground truth plots A1 to D5.
Figure C26. Wentworth size class frequencies of the D84 of the B axis for each sample plot.
Figure C27. Wentworth size class frequencies of the D84 of the B axis for all measured clasts.

Appendix D

- Figure D1. Annotated mapping of SFTs, River Arrow, July 2012.
Figure D2. Annotated mapping of SFTs, River Arrow, May 2013
Figure D3. Annotated mapping of SFTs, River Arrow, June 2013.
Figure D4. Annotated mapping of SFTs, River Arrow, August 2013.
Figure D5. Annotated mapping of SFTs, Coledale Beck, July 2013.
Figure D6. Selected field photos of SFTs, River Arrow, July 2012 (Photos by P. Jurga).
Figure D7. Selected field photos of SFTs, River Arrow, May 2013.
Figure D8. Selected field photos of SFTs, River Arrow, June 2013.
Figure D9. Selected field photos of SFTs, River Arrow, August 2013.
Figure D10. Selected field photos of SFTs, Coledale Beck, July 2013.
Figure D11. Percentage agreement between UAS-SfM mapped SFTs and ground truthing by SFT. Values are averages for the surveys conducted at the River Arrow in May, June and August 2013. The green bars indicate where the surveys are in agreement. SFTs are ordered on the x axis according to the continuum of SFTs proposed by Hill 2011 (Figure 5.1 in Chapter 5).
Figure D12. Roughness distributions profiles by site and by SFT (for whole SFT polygons).
Figure D13. Point cloud roughness from the River Arrow May 2013 survey regressed against Froude number (calculated using field-measured water depth and mean column velocity).
Figure D14. Point cloud roughness from the River Arrow June 2013 survey regressed against Froude number (calculated using field-measured water depth and mean column velocity).
Figure D15. Point cloud roughness from the River Arrow August 2013 survey regressed against Froude number (calculated using field-measured water depth and mean column velocity).
Figure D16. Point cloud roughness from Coledale Beck July 2013 survey regressed against Froude number (calculated using field-measured water depth and mean column velocity).

Appendix E

- Figure E1. Geomorphological map for the Piedra Blanca research site on the San Pedro River, mapped visually from the UAS-SfM orthophoto and DEM (May 2012).
Figure E2. Predicted substrate sizes for Coledale Beck, classified according to the Wentworth Scale (Wentworth 1922). The inset frequency chart shows the difference between observed and predicted ground truth sample plot size classes (excluding plots A1 and C1).
Figure E3. Dominant substrate size classes for the Piedra Blanca research site, mapped visually from the UAS-SfM orthophoto.

- Figure E4. Predicted habitat suitability for the adult life stage of native Chilean fish species *Percilia Irwini* at the Piedra Blanca research site, based on water depth and substrate preferences published by Garcia et al., 2011.
- Figure E5. Predicted habitat suitability for the juvenile life stage of native Chilean fish species *Percilia Irwini* at the Piedra Blanca research site, based on water depth and substrate preferences published by Garcia et al., 2011.
- Figure E6. DEM of difference computed using the River Arrow May and August 2013 UAS-SfM DEMs (overlying the August 2013 orthophoto with 30% transparency). Refraction corrected data have not been used in this case, but further work exploring the use of these data should be pursued in future.

List of Tables

Chapter 1 Introduction

- Table 1.1. Typical classification of unmanned aerial systems (Dunford et al., 2009, MacKenzie et al., 2009, Hugenholtz et al., 2012, Watts et al., 2012, Petrie 2013).
- Table 1.2. Use of study sites by chapter.

Chapter 2 Methods

- Table 2.1. Specification of the Panasonic Lumix DMC-LX3 camera.
- Table 2.2. UAS data collection information by survey.*Whilst a c.500m reach of the River Arrow was surveyed in July 2012, only 160m of this reach were used in subsequent analyses. (Some of the data used in this table also appear in Woodget et al., 2015).
- Table 2.3. Time required for UAS data collection and subsequent SfM processing (some of the data in this table also appear in Woodget et al., 2015).
- Table 2.4. Spatial resolution and residual errors associated with the orthophotos and DEMs produced using UAS imagery within the SfM workflow (some of these data also appear in Woodget et al., 2015).

Chapter 3 Topography

- Table 3.1. Assessment of traditional methods for quantifying fluvial topography and depth against the requirements of the 'riverscape' concept (Fausch et al., 2002).
- Table 3.2. Comparison of topographic products obtained using the four most popular remote sensing techniques during field tests. Values for submerged areas are shown in italics (Woodget et al., 2015).
- Table 3.3. Assessment of remote sensing based methods of quantifying fluvial topography and/or water depth against requirements of the 'riverscape' concept (Fausch et al., 2002).
- Table 3.4. Datasets used to address each of the research questions.
- Table 3.5. Overview of methods used within this chapter and where they are described within the thesis.
- Table 3.6. Quantity of independent topographic survey points collected at each site.*Denotes that water depth data not collected at this site.
- Table 3.7. Spatial coverage and resolution of UAS-SfM DEMs by site.
- Table 3.8. Residual errors associated with the UAS-SfM DEM for each survey.
- Table 3.9. Summary of error assessment of UAS-SfM DEMs for each survey. NC denotes non-refraction corrected, and RC denotes refraction corrected dataset (after Woodget et al., 2015).^a [precision: flying height] ratios are calculated by dividing average flying height by mean error, ^b [pixel size: precision] ratios are calculated by dividing mean error by final DEM resolution.
- Table 3.10. Spatial resolution, accuracy and precision results for the four Sports Hall tests.

- Table 3.11. Summary of error assessment of TLS and UAS-SfM DEM for Coledale Beck. NC denotes non-refraction corrected datasets. Refraction corrected results are not shown for the UAS-SfM data because no equivalent procedure was carried out on the TLS data.
- Table 3.12. Comparison of the validation results from recent UAS and SfM approaches. Results from Woodget et al., 2015 are shown in bold and are the same as those reported within this chapter (for the June 2013 survey of the River Arrow). NC and RC denote non-refraction corrected and refraction corrected datasets respectively.

Chapter 4 Substrate Size

- Table 4.1. The Wentworth Scale of particle size definitions (after Wentworth 1922).
- Table 4.2. Assessment of remote sensing based methods of quantifying fluvial substrate size against requirements of the ‘riverscape’ concept (Fausch et al., 2002).
- Table 4.3. Overview of methods used within this chapter and where they are described within the thesis.
- Table 4.4. Overview of ground truth substrate size data per plot.
- Table 4.5. Linear regression results for assessing the impact of detrending. The cells are coloured to show the strength of relationship, with light yellow representing the weaker relationships and dark green representing the stronger. The strongest relationship is highlighted by the black box.
- Table 4.6. Linear regression results for testing smoothing and filtering. The cells are coloured to show the strength of relationship, with light yellow representing the weaker relationships and dark green representing the stronger. The strongest relationship is highlighted by the black box.
- Table 4.7. Model validation results for the UAS-SfM point cloud roughness approach (using grain size in centimetres). The coloured cells highlight positive residual error in blue (i.e. overestimation of grain size) and negative residual error in red (i.e. underestimation). *Normalised residual error is defined as the residual error as a percentage of the ground truth measure of substrate size (D_{84} of B axis).
- Table 4.8. Image entropy statistics computed from the UAS-SfM orthophoto for each ground truth sample plot. Cells have been coloured to highlight those plots showing higher image texture in darker green, and lower image texture in light yellow.
- Table 4.9. Linear regression results for image entropy and substrate size. The cells are coloured to show the strength of relationship, with light yellow representing the weaker relationships and dark green representing the stronger. The strongest relationship is highlighted by the black box.
- Table 4.10. Model validation results for the UAS-SfM image texture approach. The coloured cells highlight positive residual error in blue (i.e. overestimation of grain size) and negative residual error in red (i.e. underestimation). *Normalised residual error is defined as the residual error as a percentage of the ground truth measure of substrate size (D_{84} of B axis).
- Table 4.11. Average TLS point cloud roughness values per ground truth plot. The darker green highlights plots of higher roughness, and the lighter yellow highlights plots of lower roughness.

- Table 4.12. Linear regression results for TLS point cloud roughness (20cm kernel size) and substrate size measures. The cells are coloured to show the strength of relationship, with light yellow representing the weaker relationships and dark green representing the stronger. The strongest relationship is highlighted by the black box.
- Table 4.13. Model validation results for the UAS-SfM image texture approach. The coloured cells highlight positive residual error in blue (i.e. overestimation of grain size) and negative residual error in red (i.e. underestimation). *Normalised residual error is defined as the residual error as a percentage of the ground truth measure of substrate size (D_{84} of B axis).
- Table 4.14. Comparison of key quantitative results for predicting substrate size from different approaches. The cells are coloured to highlight increasingly 'better' results in darker greens (e.g. lowest mean errors, highest observed v. predicted slope, etc).
- Table 4.15. Comparison of different remote sensing methods for grain size estimation. Typical accuracy is defined as the mean of residual errors and typical precision is defined as the standard deviation of residual errors.

Chapter 5 Surface Flow Types

- Table 5.1. Descriptions of surface flow types and associated biotopes (River Habitat Survey 2003, and Newson and Newson 2000).
- Table 5.2. Assessment of traditional SFT mapping against requirements of the 'riverscape' concept (Fausch et al., 2002).
- Table 5.3. Assessment of remote sensing based methods of SFT mapping against requirements of the 'riverscape' concept (Fausch et al., 2002).
- Table 5.4. Datasets used to address each of the research questions.
- Table 5.5. Overview of methods used within this chapter and where they are described within this thesis.
- Table 5.6. Base maps used for SFT mapping in the field, by survey.
- Table 5.7. Number of SFT ground truth points acquired per survey.
- Table 5.8. Summary of notation used in accuracy equations 1-4 (after Liu and Mason, 2009).
- Table 5.9. Multiplier values using for creating zonal histograms.
- Table 5.10. Scenarios used for ANOSIM tests. *With the exception of Coledale, where non-RC depth was used.
- Table 5.11. Level of agreement (%) between bankside and UAS-SfM mapped SFTs by survey and SFT.
- Table 5.12. Quantitative comparison of bankside and UAS-SfM mapped SFTs. Values are in percentages. Rows in **bold** highlight where the two SFT classifications are in agreement (e.g. both smooth), all others indicate where the two SFT classifications do not agree (e.g. smooth and rippled). Cells are colour coded to highlight the magnitude of agreement, with higher levels of agreement shown in the darker greens and lower levels of agreement shown in yellow.
- Table 5.13. Summary of overall SFT mapping accuracy by method and date of survey.
- Table 5.14. Summary of individual SFT user's accuracies by method and date of survey.
- Table 5.15. Global ANOSIM test results by survey and scenario.
- Table 5.16. Pairwise ANOSIM test results for the **River Arrow May 2013** survey, by scenario. Values highlighted in **bold** indicate pairwise combinations where the

- R value is greater than 0.5 **and** the significance level is less than the 5% threshold (i.e. < 0.05).
- Table 5.17. Pairwise ANOSIM test results for the **River Arrow June 2013** survey, by scenario. Values highlighted in **bold** indicate pairwise combinations where the R value is greater than 0.5 **and** the significance level is less than the 5% threshold (i.e. <0.05).
- Table 5.18. Pairwise ANOSIM test results for the **River Arrow August 2013** survey, by scenario. Values highlighted in **bold** indicate pairwise combinations where the R value is greater than 0.5 **and** the significance level is less than the 5% threshold (i.e. <0.05).
- Table 5.19. Pairwise ANOSIM test results for the **Coledale Beck July 2013** survey, by scenario. Values highlighted in **bold** indicate pairwise combinations where the R value is greater than 0.5 **and** the significance level is less than the 5% threshold (i.e. < 0.05).

Chapter 6 Discussion & Conclusion

This chapter does not contain any tables.

Appendix A

- Table A1. TLS error diagnostics, exported from Leica Cyclone (Leica Geosystems Ltd).

Appendix B

See Woodget et al., (*in press*)

Appendix C

- Table C1. Average roughness values per plot computed for different roughness kernel sizes on the non-de-trended UAS-SfM point cloud.
- Table C2. Average roughness values per plot computed for different roughness kernel sizes on the UAS-SfM point cloud which had been de-trended using a 3rd order polynomial function.
- Table C3. Average roughness values per plot computed for different roughness kernel sizes on the UAS-SfM point cloud which had been de-trended using a 4th order polynomial function.
- Table C4. Average roughness values per plot computed for different roughness kernel sizes on the UAS-SfM point cloud which had been de-trended using a 5th order polynomial function.
- Table C5. Average roughness values per plot computed for different roughness kernel sizes on the UAS-SfM point cloud which had not been de-trended and had not been smoothed and filtered according to the methods specified in Chapter 4. Note that some of this data is therefore reproduced from Table C1.

- Table C6. Average roughness values per plot computed for different roughness kernel sizes on the UAS-SfM point cloud which had not been de-trended but had been smoothed and filtered according to the methods specified in Chapter 4.
- Table C7. Model validation results for the UAS-SfM point cloud roughness approach (using phi scale grain sizes shown to 2 d.p.). The coloured cells highlight positive residual error in blue (i.e. overestimation of grain size) and negative residual error in red (i.e. underestimation).
- Table C8. Model validation results for the UAS-SfM point cloud roughness approach (using phi scale grain sizes shown to 2 d.p.). The coloured cells highlight positive residual error in blue (i.e. overestimation of grain size) and negative residual error in red (i.e. underestimation).
- Table C9. Model validation results for the TLS point cloud roughness approach (using phi scale grain sizes shown to 2 d.p.). The coloured cells highlight positive residual error in blue (i.e. overestimation of grain size) and negative residual error in red (i.e. underestimation).

Appendix D

This appendix does not contain any tables.

Appendix E

This appendix does not contain any tables.

Chapter 1

Introduction

Chapter Overview

The overarching aim of this research is to conduct a rigorous, quantitative assessment of the capabilities of a novel approach using unmanned aerial systems (UAS) and structure from motion photogrammetry (SfM) for quantifying a series of physical river habitat parameters at the mesoscale. This introductory chapter describes the importance of physical river habitat assessments and considers the limitations of existing field-based and remote sensing methods for conducting them. It then reviews recent developments in the capabilities of UAS technologies and SfM image processing as an alternative for quantifying physical river habitat parameters. The aims and research questions are stated, an overview of the thesis structure is presented and details of each research site are given.

1.1 Physical river habitat and remote sensing

1.1.1 Definition and importance of physical river habitat

River systems form important habitats for a wide range of fauna and flora. The conditions within river channels play a key role in determining the type, extent and quality of habitat available. These conditions include the quality of the water, the energy budget within the river (e.g. temperature), the vegetation cover, the structure of the channel and banks, and the nature of the flow hydraulics (Maddock 1999). A combination of the latter two variables, that is the fluvial geomorphology and hydrology, create what is known as the river's physical habitat (Figure 1.1). These physical parameters contribute directly to the ecological quality of rivers (Vaughan et al., 2009, Kovalenko et al., 2012) and form the focus of this thesis.

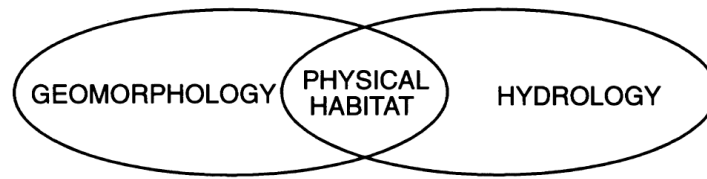


Figure 1.1. Physical river habitat determined by the interaction between geomorphology and hydrology (Maddock 1999).

Fluvial geomorphology comprises the size and shape of the channel, the size and structure of the banks, the size and shape of the material on the channel bed and the inclination or slope angle of the channel with distance downstream (Maddock 1999). These characteristics vary spatially within the four dimensions of river systems (Ward 1989); i.e. the longitudinal (downstream), lateral (across stream) and vertical dimensions of river systems, as well as over time with the processes of erosion, accretion and sediment transport. The hydrology of a river describes the dynamics of river discharge within the system, which are determined by the water depth, the flow velocity and nature of the flow turbulence (Maddock 1999). These characteristics also vary both in space (longitudinally, laterally and vertically) and in time with changes in discharge resulting from climate and weather patterns (e.g. rainfall events) and human impacts (e.g. flow regulations). The channel geomorphology and hydrology are intimately connected, so that a change in one element inevitably influences the other and vice versa. When considered together these variables are often described as the hydromorphology (Orr et al., 2008, Vaughan et al., 2009).

Anthropogenic modifications to river systems typically comprise channel engineering works (i.e. modification to the geomorphology) and/or regulation of river discharge (i.e. modification to the hydrology). These modifications may be undertaken for a number of reasons, including for the operation of reservoirs, water abstraction for irrigation, channel diversions and flood mitigation. Such alterations modify the basic physical template of the river both directly and indirectly and therefore also modify the quality and availability of fluvial habitat (Nilsson and Berggren 2000, Vaughan et al., 2009, Kingsford 2011). For example, Frothingham et al., (2002, p.16) suggest that, *"In fluvial systems modified and controlled by humans, the lack of spatial diversity in geomorphological conditions may be the most critical habitat attribute constraining biological diversity"*. Monitoring of this spatial (and temporal) variation in physical river parameters is therefore of paramount importance for understanding and improving habitat

quality and distribution, especially in light of the potential impacts of climate change (Newson and Large 2006, Kingsford 2011).

Physical habitat monitoring within rivers forms a key aspect of the European Union's (EU) Water Framework Directive (WFD). The WFD legislation demands that the hydromorphological quality of all EU rivers be assessed to ensure they meet the defined criteria of 'good ecological status' (European Commission 2000). These assessments typically consider the condition of the hydrological regime (i.e. the quantity and dynamics of water flow) and the morphological conditions (i.e. river depth and width, channel substrate and vegetation structure). In England, the Environment Agency (EA) conducts River Habitat Surveys, "*...designed to characterise and assess, in broad terms, the physical structure of freshwater streams and rivers...*" in order to meet the WFD requirements (Environment Agency 2003, p.4). This prescribed assessment includes the recording of physical habitat conditions such as channel geomorphology, dominant substrate size, vegetation type and distribution of dominant surface flow types (taken to be indicative of local flow hydraulics). A variety of other applications, including river restoration projects, enhancements to fishery environments and assessments for determining environmental flows as a result of dam construction, may also include detailed assessments of in stream physical habitat conditions (Raven et al., 1998, Maddock 1999, Maddock et al., 2004).

1.1.2 Conceptualising river systems

"...the problem becomes one of understanding these physical patterns across time and space"
(Frissell et al., 1986, p.200)

The need for understanding and monitoring physical river habitat parameters is clear. However, in recent years much discussion surrounding the conceptualisation and understanding of river systems has taken place. These paradigms in turn influence our understanding and choice of an approach for measuring and classification of such systems.

Perhaps the most influential and most cited work has been the 'River Continuum Concept' (RCC) proposed by Vannote et al., (1980). This theory was rooted in ecology and conceptualised the river as a smoothly changing system in which the physical environment and its inhabitant biota varied gradually and predictably in the downstream direction (Vannote et

al., 1980, Ward 1998, Weins 2002, Thorp et al., 2006). Acceptance of this concept allowed for the measurement of physical river habitat parameters at discrete sampling locations, and the subsequent assumption that interpolation between these locations provided an adequate representation of the spatial distribution of physical conditions within the system (Fausch et al., 2002).

A different approach for classifying and understanding fluvial habitats was put forward in a seminal paper by Frissell et al., (1986). A spatially nested, hierarchical classification framework was proposed, for organising our understanding of the spatial and temporal variation within river systems. Within this framework five levels of river systems were identified; stream, segment, reach, pool/riffle and microhabitat, as shown in Figure 1.2. This framework allows for a greater spatial heterogeneity within river systems than the previous RCC. The nature of such a hierarchical classification means that the class of any particular system is partly determined by the class of the higher level system within which it sits. As such, this conceptualisation allows for the integration of different data types at different resolutions and for scientists or managers to choose the level most applicable to their needs (Frissell et al., 1986). Indeed, this paper provides an important framework within which physical river habitat assessments can be set in context and their scale of applicability understood. The issue and importance of scale is also noted elsewhere (Newson and Newson 2000, Frothingham et al., 2002, Dollar et al., 2007, Lapointe 2012).

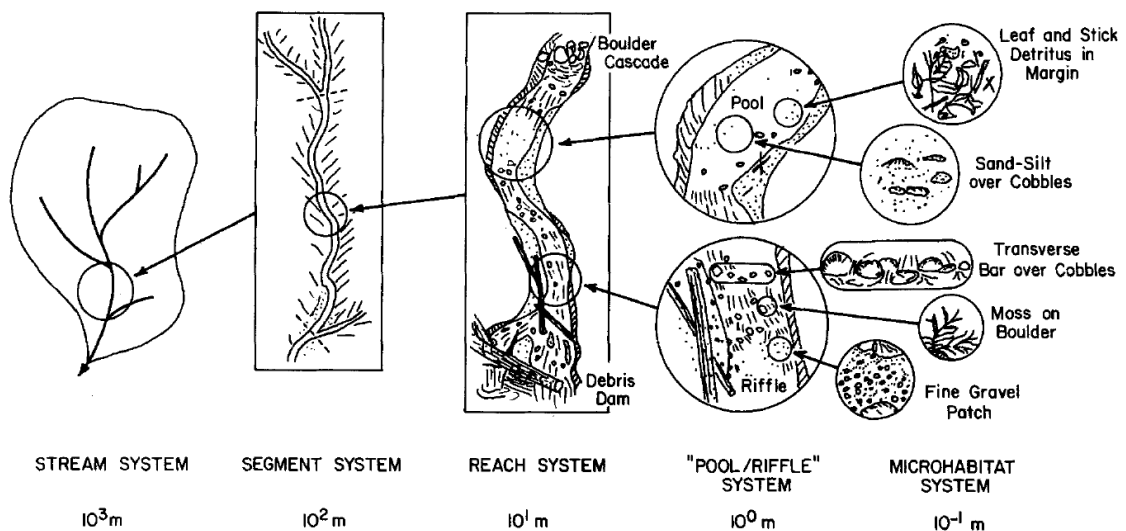


Figure 1.2. Frissell et al., (1986)'s hierarchical organisation of the river system and habitat subsystems (linear scale is approximate).

In more recent years, some of the established theories concerning the conceptualisation of rivers and their ability to provide meaningful data and tools for river management have been questioned (Bergeron and Carbonneau 2012). Of particular note is work by Fausch et al., (2002), Ward et al., (2002) and Wiens (2002), who argue that "*...established research and management concepts often fail to fully recognise the crucial roles played by habitat heterogeneity...*" (Ward et al., 2002, p. 36). They instead advocate a 'riverscape' type approach for understanding and characterising physical river habitat, which shifts our understanding of rivers from gradually changing longitudinal elements of a terrestrial landscape to those characterised by high levels of spatial and temporal heterogeneity. This alternative paradigm takes inspiration from some of the themes of landscape ecology, and aims to view the fluvial system as a landscape (or 'riverscape') in its own right (Wiens 2002). In this way, it is the spatial heterogeneity within the system, beyond simply the longitudinal dimension, which becomes the focus of physical river habitat assessment (Ward 1998, Fausch et al., 2002).

1.1.3 The need for quantifying physical river habitat

"...there is an urgent need to generate data to describe the physical template of rivers on which biotic function depends" (Orr et al., 2008, p.32)

The riverscape paradigm has been gaining increasing support within river science and management arenas in recent years (Fernandez et al., 2011, Bergeron and Carbonneau 2012, Carbonneau et al., 2012). This shift in our understanding of river systems precipitates a need for different ways in which physical habitat is measured and classified. Discrete point or transect sampling are no longer deemed sufficient for characterising the spatial structure of fluvial habitat heterogeneity (Vaughan et al., 2009).

Fausch et al., (2002) suggest that new approaches should involve characterisation of physical river habitat in a way which is both spatially continuous (rather than sampling points or lines) and spatially explicit (i.e. fully georeferenced to absolute or relative co-ordinate systems). This allows the quantification of physical habitat variables and permits an improved understanding of the size, distribution and connectivity of different habitat types (Orr et al., 2008). It also facilitates the integration of multiple spatial datasets, and allows an important consideration of the spatial scale and context of the study. In a recent review of river habitat assessment methods, Fernandez et al., (2011) lent support to this idea. They found that spatially

continuous and spatially explicit studies of physical river habitat parameters provided the most effective methods for understanding these habitats. Such approaches also allow for the establishment of baseline conditions and thus provide the opportunity for exploring temporal variability within physical habitat parameters, which is currently rarely considered.

As argued by Newson and Newson (2000, p.199), "*Real contributions from research to sustainable management of river systems... need to match a sophistication of concepts with a direct practicality (without which applications are unlikely)*". Thus the ideal approach for quantifying physical habitat parameters should be practical, logistically feasible, cost effective as well as objective and repeatable. The challenges associated with such an approach are not to be underestimated, but Newson and Newson (2000, p.199) go on to suggest that studies undertaken at the mesohabitat scale hold potential here; "*A mesoscale approach has obvious potential to act as a fulcrum between scientific detail and applied universality*". The mesoscale is typically defined as the active channel width and channel lengths which are small multiples of channel width (Newson and Newson 2000). Studies over these channel extents comprise both meso- and micro-scale features and typically require data of hyperspatial resolutions (<10cm). The importance of fluvial habitat studies at this scale has also been acknowledged elsewhere (e.g. Frissell et al., 1986, Frothingham et al., 2002).

1.1.4 The role of remote sensing

*"Fluvial remote sensing methods have now reached a stage where remotely sensed data allows
fundamental science questions to be examined within a riverscape framework"*
(Carbonneau et al., 2012, p. 78)

Remote sensing based methods have been advocated for providing such approaches for fulfilling these data collection ideals of the riverscape paradigm (Fausch et al., 2002, Carbonneau et al., 2012). Indeed, there is a growing body of literature demonstrating the use of a variety of remote sensing techniques for characterising physical river habitat parameters. Examples include the use of digital photogrammetry and spectral-depth correlations for quantifying fluvial topography and flow depth (e.g. Westaway et al., 2001, Winterbottom and Gilvear 1997), the computation of image textural variables and roughness of terrestrial laser scanner point clouds for quantifying fluvial substrate size (e.g. Carbonneau et al., 2004,

Heritage and Milan 2009) and the use of multispectral imagery for mapping hydrogeomorphic units (e.g. Wright et al., 2000). These developments have undoubtedly made important contributions to our abilities to map and measure physical river habitat parameters. As discussed at length in subsequent chapters however, few of these approaches are capable of quantifying simultaneously a number of physical habitat parameters (e.g. topography, depth, substrate size and hydraulic variables) using a single dataset, whilst also operating within the ideals of a riverscape approach (i.e. spatially continuous and explicit, objective, repeatable, practical, logistically feasible, cost effective with hyperspatial resolution over a range of spatial scales, including the critical mesoscale). To date, the Geosalar project, described by Bergeron and Carbonneau (2012) and associated work of Carbonneau et al., (2012), perhaps comes closest to meeting these objectives. These works produced high resolution, spatially continuous maps of physical river habitat variables over extended channel lengths using optical digital imagery acquired from a conventional aircraft. They have demonstrated significant potential for mapping Atlantic salmon habitats and quantifying downstream changes in physical river habitat parameters over the length of an entire river in the Scottish Highlands. Given the high (1m) but not hyperspatial resolution (<10cm) mapping of physical habitat parameters and extensive spatial coverage offered by this airborne approach however, it is perhaps better suited to applications at the catchment scale rather than the mesoscale.

Recent developments in the capabilities and availability of small unmanned aerial systems (UAS), alongside parallel advances in a novel approach for processing their imagery means that a relatively new, alternative approach for the remote sensing of rivers is now possible. Interest in UAS platforms for image acquisition and associated so-called Structure-from-Motion (SfM) photogrammetric image processing has seen a dramatic expansion over the last few years, within both academic and commercial arenas. Published studies to date suggest that such approaches are capable of rapid, flexible, bespoke data acquisition which is relatively inexpensive and capable of exceptionally high spatial resolutions (see section 1.2). As such, the combined UAS-SfM approach has been heralded as the route to democratisation of data acquisition and in this capacity might enable the quantification of physical river habitat parameters at the mesoscale within the bounds of the aforementioned riverscape requirements. To date however, very few published works have investigated the application of these new techniques to the fluvial environment and as a result, our understanding of their value for quantifying fluvial habitat parameters remains largely theoretical.

The overarching aim of this thesis is to conduct a rigorous, quantitative assessment of the potential of a UAS-SfM approach for quantifying a series of physical river habitat parameters at the mesoscale, and to compare the results against those from existing remote sensing based techniques. These aims are formally introduced in section 1.3, following a more detailed review of the history and applications of UAS platforms and SfM-photogrammetric processing.

1.2 Unmanned aerial systems and structure from motion photogrammetry

1.2.1 Development of UAS

There has been a dramatic growth in the availability of UAS in recent years, and application within research and commercial settings is increasing. Whilst referred to as UAS within this thesis, elsewhere these platforms are increasingly known as remotely piloted aircraft systems (RPAS), and have previously been referred to as unmanned aerial vehicles (UAVs) or drones (although the latter is usually avoided within the environmental sector due to the link with military applications). The umbrella term of UAS includes a range of platforms including fixed wing planes, rotary-winged systems, motorised paragliders, kites and balloons. Some examples are given in Figure 1.3.

Historically, UAS have been used predominantly for military reconnaissance purposes. As a result, early technological developments in this field were driven largely by defence agendas (Hardin and Jensen 2011, Watts et al., 2012). Research into the environmental applications of UAS was led by NASA from the 1970s onwards. This research included high altitude atmospheric sampling and the major 'Environmental Research Aircraft and Sensor Technology' programme (ERAST) which led to development of platforms such as the NASA Pathfinder UAS (Watts et al., 2012). Since the 1990s, and more so in recent years, new application opportunities have been explored for civilian research and commercial purposes. This has included application in the areas of archaeology (e.g. Eisenbeiss et al., 2005), landslide and hazard mapping (e.g. Niethammer et al., 2012, Bellis et al., 2013), mapping of glacial landforms (e.g. Smith et al., 2009), monitoring of crops and vegetation (e.g. Dunford et al., 2009, Laliberté and Rango 2009, Hunt et al., 2010, Laliberté et al., 2011), geomorphological mapping (e.g.

Hugenholtz et al., 2013), coastal monitoring (e.g. Dugdale 2007) and wildlife conservation (e.g. Vaughan 2013).

Applications of UAS in fluvial settings have been limited to date. The work of Dunford et al., (2009) and Hervouet et al., (2011) assessed the potential of a motorised paraglider for mapping riparian vegetation. Others have demonstrated the use of UAS for tracking woody debris (MacVicar et al., 2009), mapping water depth and topography (Lejot et al., 2007, Flener et al., 2013, Fonstad et al., 2013) and other river habitat features (Tamminga et al., 2014). Further discussion of these papers is provided in Chapters 3-5.

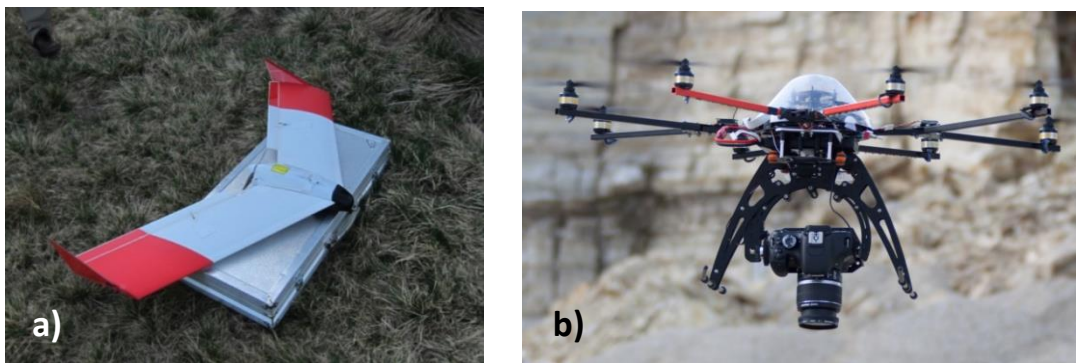






Figure 1.3. Examples of unmanned aerial systems; a) SmartPlanes SmartOne fixed-wing UAS (Smart Planes 2014); b) Mikrokopter Oktokopter rotary-winged UAS (Turner et al., 2012).

Typically, a UAS consists of an aircraft platform mounted with a series of sensors, combined with a ground-based control station from where the UAS is operated. The types of aircraft platform are usually classified into fixed- and rotary-winged systems and by weight and endurance capabilities (Watts et al., 2012, Petrie 2013). Classifications vary within the published literature, but a general overview is provided in Table 1.1, and is largely based on military definitions. The research presented within this thesis is carried out using a mini-UAS known as the Draganflyer X6, and therefore the remainder of this section will focus on UAS of this size (<20kg). Under the UK's Civil Aviation Authority (CAA) classification the Draganflyer X6 is a 'small unmanned aircraft'. Further detail about the Draganflyer X6 platform is provided in Chapter 2.

Table 1.1. Typical classification of unmanned aerial systems (Dunford et al., 2009, MacKenzie et al., 2009, Hugenholtz et al., 2012, Watts et al., 2012, Petrie 2013).

UAS Classification	UAS Description	Example
Micro, Mini, Nano or Lightweight UAS	<ul style="list-style-type: none"> - Very low altitude (<300m) - Small size (fits into a backpack, easily portable by hand) - Weight typically <20kg - Short flight times (< 1 hour) - Flown within line-of-sight - Fixed or rotary winged, may also include kite and balloon based set-ups 	<p style="text-align: center;">Draganflyer X6</p> 
Small UAS	<ul style="list-style-type: none"> - Low altitude (<3km) - Flight times typically a few hours - Weight typically 25-150kg - Usually fixed wings with need for runways 	<p style="text-align: center;">Hawkeye R8-84Z (Hawkeye UAV 2013)</p> 
MALE UAS (medium altitude, long endurance)	<ul style="list-style-type: none"> - Medium altitude (<14km) - Flight times up to 24 hours - Weight up to 1500kg - Usually fixed wings with need for runways 	<p style="text-align: center;">NASA Ikhana (Anderson 2013)</p> 
HALE UAS (high altitude, long endurance)	<ul style="list-style-type: none"> - High altitude (>14km, typically 20km) - Flight times of >24 hours - Largest and most complex UAS - Typically fixed wing requiring proper runways 	<p style="text-align: center;">NASA Global Hawk (USGS 2010)</p> 

The sensors and instruments mounted aboard UAS vary hugely depending on the payload capabilities of the platform and the purpose of use. For mini-UAS there has been an increase in the availability of platforms equipped with global positioning devices (GPS) and inertial measurement units (IMUs) in recent years, allowing more precise and stable flight. Currently, mini-UAS are typically limited to payloads of a few kilograms. This restricts the imaging sensors to those which are small and lightweight, although this is changing rapidly. Many UAS used for environmental research use relatively inexpensive, non-metric, consumer-grade digital

cameras which tend to produce small format images, collected with short exposure times to minimise the effects of motion blur, and high levels of overlap to allow for subsequent image matching (Petrie 2013). The market for provision of mini-UAS for civilian research applications is expanding very rapidly, as is platform and sensor technology (Petrie 2013). As a result, UAS and the reviews which describe them quickly become out-of-date.

1.2.2 New opportunities provided by UAS

In the context of remote sensing research, lightweight UAS offer a unique platform for data collection, capable of providing a number of benefits and opportunities over other remote sensing approaches. Perhaps the greatest benefit is their ability to fly at low altitudes for the collection of very high resolution imagery (e.g. Hervouet et al., 2011, Laliberté et al., 2011, Niethammer et al., 2012, Turner et al., 2012). Typical image resolution is less than 10cm and sometimes less than 1cm, which is not usually obtained from higher flying manned aircraft or space-borne satellites.

Other advantages offered by UAS include; the ability to mobilise quickly and collect imagery on-demand, as frequently as required; the flexibility of use, allowing tailored flight paths and bespoke data collection at a range of scales (Harwin and Lucieer 2012), although this is limited to some extent by regulations and logistics; the relatively inexpensive per-flight costs, making the survey of smaller study sites more feasible and worthwhile, and; the ability to fly below cloud cover, thereby easily obtaining cloud free imagery. Lightweight UAS have therefore opened up the possibilities for low altitude, high spatial and high temporal resolution remote sensing of smaller sites which would otherwise have been impossible or too costly to survey. Furthermore, these platforms place the control of data acquisition with the researcher, thereby making "*...question-driven, high resolution research considerably more feasible than it has been previously*" (Hervouet et al., 2011, p.71).

1.2.3 Challenges of working with UAS

Whilst recent research has shown the successful use of UAS for environmental applications, these studies have also helped to highlight a number of challenges of working with these platforms. The disadvantages include the small size and weight of the platforms, which means they are strongly affected by light winds and are limited in terms of their payload capacity

(Hardin and Hardin 2010). Adverse wind conditions compromise safe flying, and hamper the collection of high quality imagery by increasing platform instability. In certain geographical areas, this presents a significant obstacle to data collection and research progression, as reported by Hardin and Jensen (2011, p.102); "*Having enough good weather days to safely fly our small-scale vehicles has been a recurring challenge for us*". Skilled and experienced UAS pilots are required for adequate data collection, especially where UAS control is not autonomous (Eisenbeiss et al., 2005, Hardin and Hardin 2010).

The distorted and off-nadir imagery acquired under suboptimal conditions has been shown to adversely affect image processing and subsequent analyses, as have datasets with large variations in illumination between images (Dugdale 2007, Lejot et al., 2007, Dunford et al., 2009, Vericat et al., 2009, Hardin and Hardin 2010, Hervouet et al., 2011). This often results in lengthy and laborious data processing chains (Eisenbeiss et al., 2005, Dugdale 2007, Hardin and Jensen 2011, Hervouet et al., 2011, Rosnell and Honkavaara 2012). However, recent advancements in dedicated UAS image processing software are now starting to change this (Turner et al., 2012), as described further in sections 1.2.4/1.2.5.

The payload limitation of lightweight UAS is another well acknowledged challenge for data collection (Hardin and Jensen 2011), with the majority of UAS used in environmental research carrying only low-grade, non-metric cameras with limited spectral resolution. Some have compensated for this lack of more sophisticated sensors by making use of image texture, intensity, hue and saturation information, with success reported in object-based image analysis procedures (Laliberté and Rango 2009). However, there is a growing demand for the miniaturisation of more complex sensors, including laser scanners, multi- and hyper-spectral systems, to enable their use with UAS platforms (Hardin and Jensen 2011, Harwin and Lucieir 2012). In fact, significant progress in sensor development has been made during the course of this research.

Limited battery life is also reported as a restricting factor on UAS remote sensing. Most UAS are powered by electrical batteries, which weigh less and are quieter than the alternative methanol or gasoline powered platforms, but tend to provide shorter flight times. Earlier UAS were limited to 5-15 minutes worth of flight, which is reduced further by windy conditions requiring additional power to maintain position (Eisenbeiss et al., 2005, Hardin and Jensen 2011). Newer systems can reportedly fly for longer (up to 2 hours, S. Lane 2015, *pers. comm.*)

but flight endurance remains an area for development which would enable surveys of much larger areas.

Finally, the regulatory environment within some countries imposes severe restrictions on the use of civilian UAS. In the USA, the Federal Aviation Administration strictly controls the operation of UAS. Researchers must obtain a 'Certificate of Authorization' before flying is permitted, and these are reportedly difficult and costly to obtain and may be valid for short time periods only (Hardin and Jensen 2011). This presents a major barrier to the progression of environmental remote sensing from UAS in the USA (Watts et al., 2012). Fortunately, the regulatory situation in the UK is different. UAS operations are regulated by the CAA as detailed in the UK's Air Navigation Order 2009. Mini-UAS (weights less than 20kg) do not require a permit to fly from the CAA, so long as flight operation adheres to the following conditions (MacKenzie et al., 2009, Petrie 2013, G. Corbett 2014, *pers. comm.*);

- Flight altitude is less than 400 ft (120m).
- Flight range is less than 500m and always within line of sight.
- Flight is not over or within 150m of groups of more than 1000 people.
- Flight is not undertaken over or within 50m of anyone who has not been informed of the flight (reduced to 30m for take-off and landing).
- Flight is not permitted in restricted areas (e.g. near airports).
- Flight is not permitted in congested/urban areas.

For commercial operators, it is also necessary to obtain a certificate of airworthiness for the UAS and pilots must have obtained the appropriate 'Basic National UAS Certificate' (BNUC).

1.2.4 The theory of structure-from-motion photogrammetry (SfM)

In parallel with the rapid development of UAS for civilian research, advances in computer vision and image analysis have also been taking place. This has led to an increased availability of software packages offering image processing chains capable of producing fully orthorectified imagery and rasterised digital elevation models (DEMs) from UAS image sequences. In particular, a method known as 'Structure from Motion' has been gaining popularity in recent years. This technique is not divergent from digital photogrammetry (hence

use of the phrase 'SfM-photogrammetry', which is often abbreviated to SfM within this thesis), however it has a number of key differences.

The SfM approach essentially provides an automated image matching method for generating the relative 3D geometry of a scene from a series of overlapping 2D images, which may then be georeferenced to map co-ordinates. The algorithms used differ from those employed within traditional photogrammetry in that they allow the collinearity equations to be solved and the relative scene geometry to be constructed without prior knowledge of camera positions or the use of ground control points (GCPs – see section 2.3.1) (Lane et al., 1993, Rosnell and Honkavaara 2012, Westoby et al., 2012, Fonstad et al., 2013). The SIFT ('scale invariant feature transform') function developed by Lowe (2004) is one of the image matching algorithms frequently used as part of the SfM process and is a powerful method capable of recognising conjugate (matching) points in overlapping images regardless of changes in image scale, view angle or orientation (Turner et al., 2012, Fonstad et al., 2013). This is performed using patterns of image brightness and colour gradients (i.e. variations in image texture) which can be identified at various different scales, and represents a significant advantage for use with UAS imagery. The kernel- or area-based approaches used in traditional photogrammetry require constant image resolution and the acquisition of imagery at nadir, which is difficult to obtain using the less stable UAS platforms (Rosnell and Honkavaara 2012, Turner et al., 2012, Fonstad et al., 2013).

The SfM process allows the identification of prominent matching points between convergent, overlapping images and successive least squares bundle block adjustments are then used to estimate the camera parameters, relative camera positions, and the scene geometry. This process aligns the separate input images and outputs a model of the scene geometry as a set of sparse data points, known as a 'point cloud' (Neitzel and Klonowski 2011, Harwin and Lucieer 2012). During this phase, automated camera lens calibrations are also conducted. These self-calibrations help to reduce the impact of lens distortion on the resulting model. Following the generation of the sparse point cloud, multi-view stereo techniques are used to revisit the original images and densify the point cloud. This step is particularly memory intensive.

At this stage in the process, camera positions are known only in relative space and the GCPs locations have not yet been specified. As a result, the point cloud is generated in an arbitrary

'image-space' co-ordinate system (Harwin and Lucieer 2012, Turner et al., 2012, Verhoeven 2012, Verhoeven et al., 2012, Westoby et al., 2012), and must be georeferenced to an absolute co-ordinate system to be useful for quantitative geomorphological studies. Georeferencing is typically then performed using one of two approaches:

- Direct georeferencing. This makes use of image acquisition locations collected with the on-board GPS during flight (Neitzel and Klonowski 2011, Harwin and Lucieer 2012, Turner et al., 2012). Such information is not always available, and for imagery collected from UAS often has a relatively low spatial accuracy (in the order of a few metres). As a result, this approach does not always produce the most accurately positioned output (Turner et al., 2012).
- Indirect georeferencing. This approach is carried out using the known positions of GCPs, which are used to perform the three-dimensional, seven-parameter transformation (Verhoeven 2012, Verhoeven et al., 2012, Westoby et al., 2012). GCPs may be fixed features of known position within the imagery, or artificial targets distributed within the area of interest whose position is accurately surveyed (Harwin and Lucieer 2012, Turner et al., 2012, Westoby et al., 2012). A minimum of three GCPs are required for a successful transformation (Verhoeven et al., 2012).

These methods both provide a linear transformation of the point cloud and any errors will be carried through to the final georeferenced output (Fonstad et al., 2013). Once transformed into real-world co-ordinates using one of these methods, the point cloud may be exported as a rasterised DEM or textured using the original imagery to give an orthophoto. Further detail on the SfM process is provided in Chapter 2. SfM-photogrammetry has been integrated into a number of readily available software packages, including the commercial PhotoScan (Agisoft LLC), the free 123D Catch (Autocad Inc.) and the open source VisualSFM (Wu 2015).

1.2.5 Application of SfM-photogrammetry

Research using and assessing the quality of novel SfM techniques has only started to appear within the academic literature since 2011-2012. However, even within this short time interest in SfM has grown rapidly. It is likely that this rapid growth can be attributed to a combination of the following factors;

- SfM processing using both commercially available and open-source software packages is rapid and largely automated and therefore can be easily performed by non-experts.
- Currently available SfM software packages are relatively inexpensive and therefore available to a wide range of users.
- Algorithms within the SfM workflow are capable of processing imagery acquired both at nadir and obliquely, of varying resolutions, with variable levels of overlap, and with unknown interior and exterior orientations. Therefore, it is ideal for use with imagery acquired using low cost, non-metric cameras and/or from unstable UAS platforms. Very recent research has even assessed the potential for using smartphone imagery in an SfM workflow (Micheletti et al., *in press*).
- The process is capable of producing orthophotos and DEMs of high spatial resolution, with point cloud densities becoming comparable to those collected using laser scanning approaches.
- With the adequate use of GCPs, outputs have been shown to be capable of high levels of accuracy (mean errors of 0.02-0.15m).

Applications in the fields of archaeology (e.g. Verhoeven 2012, Verhoeven et al., 2012) and geomorphology have been presented (e.g. James and Robson 2012, Harwin and Lucieer 2012, Westoby et al., 2012, Fonstad et al., 2013, Javernick et al., 2014, Micheletti et al., *in press*) using a variety of different camera and platform set-ups.

1.3 Aims of this thesis

1.3.1 Motivation

Within the last decade or so, the growing recognition of the riverscape paradigm has necessitated a different approach to quantifying fluvial habitats than has previously been provided by traditional, discrete point or transect sampling techniques. Remote sensing has gone some of the way to providing more spatially continuous, objective and repeatable approaches but few of these are capable of quantifying a number of physical habitat parameters simultaneously using a single dataset, whilst also operating within the ideals of a riverscape approach. Novel developments in UAS and SfM processing suggest that these approaches might hold great potential for filling this gap, or at least complementing existing remote sensing methods, in a way which puts the control of data acquisition and processing into the hands of the user. However, despite the recent excitement surrounding the combined use of UAS and SfM, these approaches remain very much in their infancy. The wider limitations of these approaches remain largely unknown and very limited quantitative evaluation has been undertaken, especially within fluvial settings. As a result, there is a need for rigorous and robust testing which compares outputs with conventional techniques. Such assessments will help to establish how these relatively novel methods might contribute to the assessment of physical river habitat for both science and management applications, and form the focus of this thesis.

1.3.2 Research aims

The overarching aim of this research is to conduct a rigorous, quantitative assessment of the capabilities of a UAS-SfM approach for quantifying a series of physical river habitat parameters at the mesoscale, and to evaluate the results against those from existing remote sensing based techniques. The mesoscale is defined as channel lengths from a few tens of metres up to a few hundred metres.

The focus of the work will be on deriving three key physical habitat parameters; (1) fluvial topography/flow depth, (2) substrate size and; (3) surface flow types (as indicators of hydraulic conditions). These three parameters were selected as they represent “*hydromorphological components of most importance to biotic response*” (Newson and Large 2006, p. 1617), as evidenced for example by their place at the foundation of many PHABSIM studies (e.g. Bovee

1996). The investigation of other habitat parameters (e.g. cover, in-stream vegetation and direct measures of velocity) would also be of interest, but was not possible within the time constraints of this study. The thesis structure is presented in section 1.4, and is based around these three key physical river habitat parameters. Within each of these parameter-specific chapters, the following research questions are posed;

(1) Topography/Flow depth (Chapter 3)

- a. How accurate, precise and replicable are the topographic datasets generated using a UAS-SfM approach? Do these measures vary between different river systems?
- b. How does the accuracy and precision of the UAS-SfM DEMs vary between exposed and submerged terrain, and does the application of a simple refraction correction procedure improve the accuracy of topographic products in submerged areas?
- c. How does the DEM obtained using the UAS-SfM approach compare with a DEM obtained using terrestrial laser scanning (TLS)?

(2) Substrate size (Chapter 4)

- a. Can the roughness of the UAS-SfM point cloud be used to quantify fluvial substrate size, and if so, how accurately?
- b. How do the results of the UAS-SfM approach compare with those obtained using existing remote sensing techniques: a) image texture analysis on the UAS imagery and b) the roughness of a TLS point cloud?

(3) Surface flow types (Chapter 5)

- a. How does the spatial extent and classification of surface flow type (SFT) mapping at the mesoscale vary between (i) that conducted by eye from a bankside location in the field and (ii) that mapped directly from the UAS-SfM orthophoto?

- b. How accurate and repeatable is the SFT mapping conducted on the UAS-SfM orthophoto and how does the accuracy vary between different SFTs and different surveys?
- c. Does the use of quantitative information derived from the UAS-SfM process (i.e. refraction corrected water depth and point cloud roughness) help to differentiate between SFTs?

Data collected from three field sites and one indoor setting are used to address some or all of these research questions, as detailed in section 1.5.

1.4 Thesis structure

This thesis comprises six chapters, plus appendices, and is structured according to Figure 1.4. The three key data analysis chapters (3 to 5) each deal with one of the physical river habitat parameters, as listed in section 1.3. These chapters have been structured to facilitate conversion to future scientific papers for publication, and thus each includes an introduction and background section, specific research questions, methods, results, discussion and conclusions. Some of these chapters are lengthy in terms of page count because they include a large number of figures and tables (rather than due to a high word count). It was decided not to place these figures and tables in the Appendices where they would be more difficult to access. The following paragraphs provide an overview of each chapter.

The remainder of this chapter (Chapter 1) describes the nature and significance of the study sites used to conduct the research presented in subsequent chapters.

Chapter 2 provides a description of the key methods which are common to the assessment of some or all of the physical river habitat parameters considered within this thesis. This includes the UAS set-up and image acquisition procedures, the SfM-photogrammetry processing workflow and the TLS data collection.

Within Chapter 3, the use of the UAS-SfM approach for quantifying fluvial topography and water depth is assessed. The focus is on quantifying the accuracy and precision of the results, and comparing these within and between different field sites, and against a comparable TLS survey. The benefits of a simple refraction correction procedure are assessed for improving the

quality of UAS-SfM results in submerged parts of the environment. Finally, the ability of the UAS-SfM process to reproduce a flat, indoor surface is tested and used to highlight systematic errors which may be present within the field data.

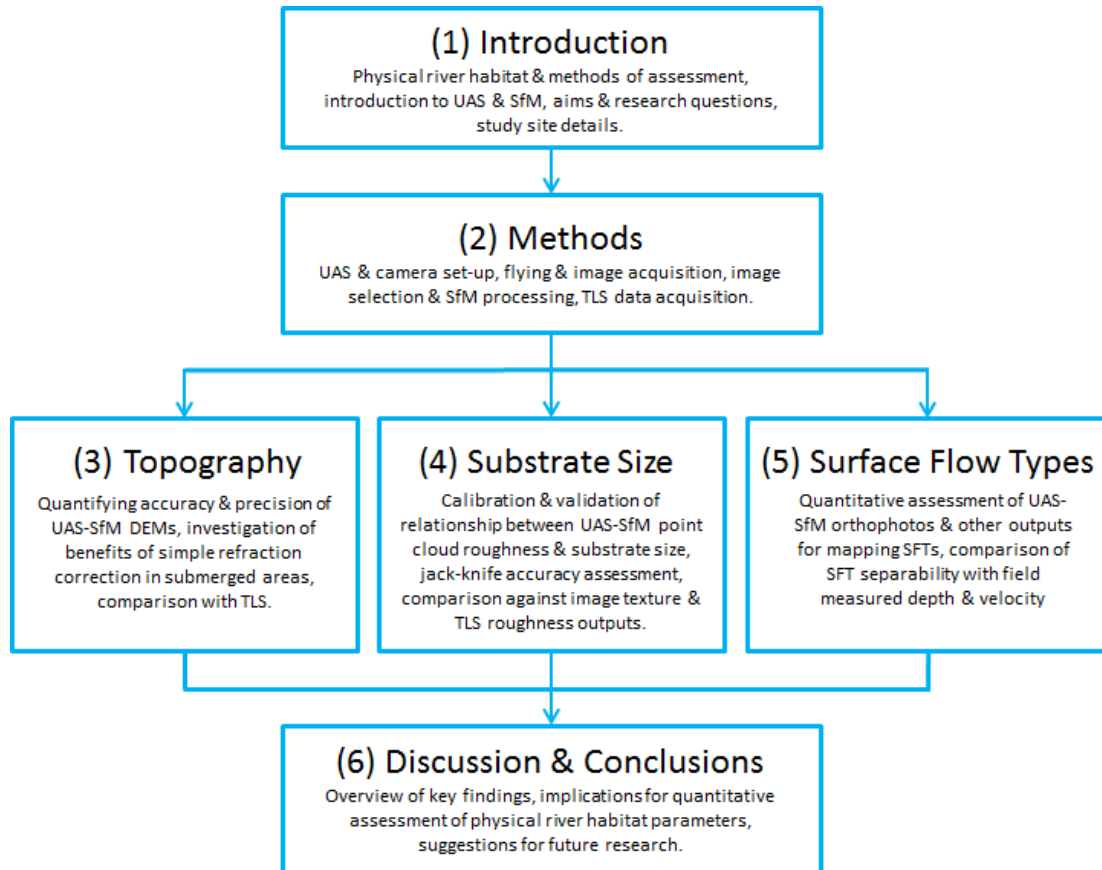


Figure 1.4. Overview of the thesis structure.

Chapter 4 is focussed on assessing the potential of UAS-SfM point clouds for quantifying fluvial substrate size. Measures of point cloud roughness are computed and then correlated against substrate size to develop a predictive relationship. The accuracy and precision of predicted substrate size estimates are explored, and compared against equivalent estimates from two other remote sensing based approaches.

Chapter 5 explores the use of the UAS-SfM orthophotos and other quantitative information derived from this process for mapping surface flow types as a proxy for hydraulic habitat

heterogeneity. The separability of these different mapped classes is assessed quantitatively and compared to field measures of water depth and flow velocity.

Finally, Chapter 6 draws together the major findings from each chapter and critically evaluates how this relatively novel UAS-SfM approach might contribute to the assessment of physical river habitat for science and management applications. This chapter also makes suggestions for further research.

1.5 The study sites

The research presented within this thesis was conducted at three contrasting field study sites; (1) the lowland River Arrow (Warwickshire, UK); (2) the upland Coledale Beck (Cumbria, UK) and; (3) the much larger San Pedro River (south-central Chile). These sites were chosen because they provide a diverse range of physical habitat conditions at the mesoscale, within different landscape settings. All were easily accessible and permission from the landowners was granted for UAS flying. None of the sites have continuous tree coverage, nor are they near major roads or railways, power lines or sensitive areas such as airports, factors which might otherwise prohibit UAS flying. The characteristics and significance of these field sites are described in detail below. In addition, a number of flights were conducted within an indoor setting to further assess the quality of the UAS-SfM data outputs. A summary of where the data from each site are used within this thesis is provided in Table 1.2.

Table 1.2. Use of study sites by chapter.

Study Site	Chapter 3 Topography	Chapter 4 Substrate Size	Chapter 5 Surface Flow Types
San Pedro River	✓		
River Arrow	✓		✓
Coledale Beck	✓	✓	✓
Sports Hall Floor	✓		

1.5.1 The River Arrow

Site overview

The River Arrow (Figure 1.5) is a small (c. 5-12m wide), lowland river which runs through parts of North Worcestershire and Warwickshire (UK) and is a tributary of the River Avon. The reach

of interest is located near Studley in Warwickshire (Grid reference SP 08130 63450, Figure 1.6) and forms a meandering, pool-riffle system. The channel banks are steep and incised, especially on the outer bends of meanders where there is active erosion. Point bars are located on the opposing side of the meander bends and gravels and cobbles accumulate around the margins of vegetated islands. There are some patches of submerged aquatic vegetation within the channel and in places the channel and banks are obscured by overhanging trees and other terrestrial vegetation. The channel bed is composed predominantly of cobbles with some patches of finer substrate. The study site is located within a large grassed field used for the pasture of cattle and sheep, and is located about 600m upstream of Redditch Sewage Treatment Works which discharges its final effluent into the river.

The flow level within this section of the River Arrow is highly variable and sensitive to rainfall events. Environment Agency flow data for the period 1978-2008 reports a typical high stage discharge of 1.75 cumecs (Q10) and a typical low stage discharge of 0.14 cumecs (Q95). However, recent flow gauge data collected between 2007 and 2011 suggests flow levels can be as great as 18 cumecs (C. Wallis 2013, *pers. comm.*).

Surveys

A number of surveys were carried out at the River Arrow in order to assess the repeatability of the UAS-SfM approach. Data collection was conducted for two different reach extents, as shown in Figure 1.6 and labelled as Zone A and Zone B. A survey of the larger zone A was conducted in July 2012 during hot and sunny conditions. This survey followed a period of heavy rainfall, so that flow levels were high at this time. It was found that a survey of this size could not be easily conducted within a day given the available manpower and resources, typical variability in wind conditions during the course of a day, issues relating to the presence of livestock and limited flight times permitted by the UAS batteries. As a consequence, subsequent surveys were carried out over the smaller zone B, which could be reliably surveyed within the bounds of these restrictions. Surveys of zone B were conducted in May, June and August 2013. During the former two surveys, weather conditions were dry, still and sunny. During the August survey, conditions were overcast and slightly misty. Data collected at the site included the following, further details of which are provided in Chapters 2-5;

- UAS hyperspatial image surveys (July 2012, May 2013, June 2013, August 2013)
- Topographic survey using a total station (May 2013, June 2013) or dGPS (August 2013)
- Positioning survey using a differential GPS (to reference total station data, May 2013)
- Visual mapping of surface flow types (July 2012, May 2013, June 2013, August 2013)
- Measurement of flow depth and mean column velocity (May 2013, June 2013, August 2013)

Site significance

The diverse physical habitat conditions and close proximity of the River Arrow site made it ideal for assessing the repeatability of the UAS-SfM approach described within this thesis. It represents a typical lowland stream in the UK and as such it provides an adequate test site for early-stage investigations into the potential of a UAS-SfM approach for quantifying physical river habitat parameters.



Figure 1.5. The study site at the River Arrow, near Studley (Zone B).

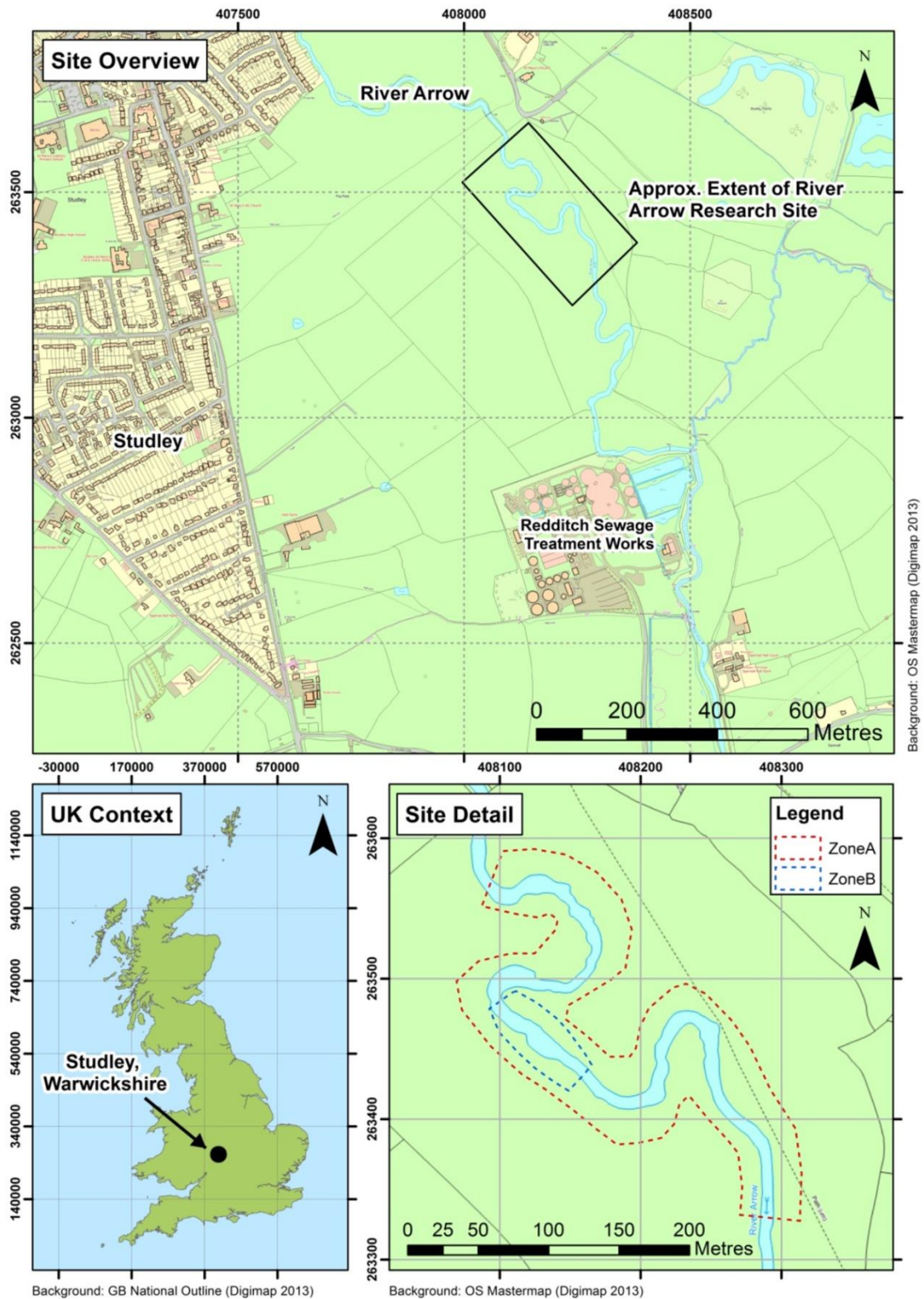


Figure 1.6. Location map for the River Arrow research site, Warwickshire, UK.

1.5.2 Coledale Beck

Site overview

Coledale Beck is a small (c. 3-10m wide), upland river located in the Coledale Valley, below Grisedale Pike in the English Lake District (Grid reference NY 21400 22400). It flows through the village of Braithwaite, joins Newlands Beck which eventually runs into Bassenthwaite Lake. A photo of the site is shown in Figure 1.7 and a location map in Figure 1.8.

A reconnaissance of Coledale Beck between the Force Crag Mine and Braithwaite was conducted in April 2013 to identify a suitable length of channel for this research. A c. 120m length of channel located c. 1.5km downstream of Force Crag Mine was chosen for its topographic diversity, accessibility and suitability for data collection using an unmanned aerial system (UAS) and terrestrial laser scanner (TLS).

The selected reach comprises a series of pools and riffles, and has a bed composed predominantly of cobbles and boulders. The channel is gently meandering and features a number of exposed point bars and opposing steep, undercut banks. These banks are composed of matrix supported gravels, cobbles and boulders. The water clarity is very good and there is an absence of submerged aquatic vegetation.

Surveys

Fieldwork at Coledale Beck was undertaken in conjunction with colleagues from Bath Spa University and Durham University during July 2013 (details on the division of work are provided in Appendix A). Data collected at the site included the following, further details of which are provided in Chapters 2-5;

- UAS hyperspatial image survey
- TLS survey
- Topographic survey using a total station
- Positioning survey using a differential GPS (dGPS)
- Measurement of substrate sizes within a series of sample plots
- Visual mapping of surface flow types
- Measurement of flow depth and mean column velocity



Figure 1.7. The downstream end of the research site at Coledale Beck, Cumbria.

Site significance

Coledale Beck has been the subject of recent research into the sediment and catchment dynamics of Bassenthwaite Lake. The lake is listed as a National Nature Reserve and a Site of Special Scientific Interest, partly due to its rare vendace (*Coregonus vandesius*) fish population. The spawning grounds of this species are particularly sensitive to changes in the quantity and quality of sediment within the lake. Significant declines in vendace have been noted in recent years and it is now thought that this fish no longer occupies Bassenthwaite Lake. It is suggested that this is due to increasing siltation of the lake, as well as pollution and the impacts of invasive species (Orr and Brown 2004).

The Bassenthwaite Lake Restoration Programme (BLRP) was established in 2002 with an aim to improve conditions for vendace. This involved commissioning a geomorphological study of the surrounding catchment (including Coledale Beck) to identify sediment sources. This study identified bank erosion within rivers feeding into Bassenthwaite Lake as having a direct impact on lake conditions, an effect which may be exacerbated following extreme rainfall events. Since 2009, research by Durham University into erosion at Coledale Beck has also been contributing to the BLRP (BLRP 2010, R. Johnson 2013 *pers. comm.*).

Quantifying physical river habitat parameters using hyperspatial resolution
UAS imagery and SfM-photogrammetry

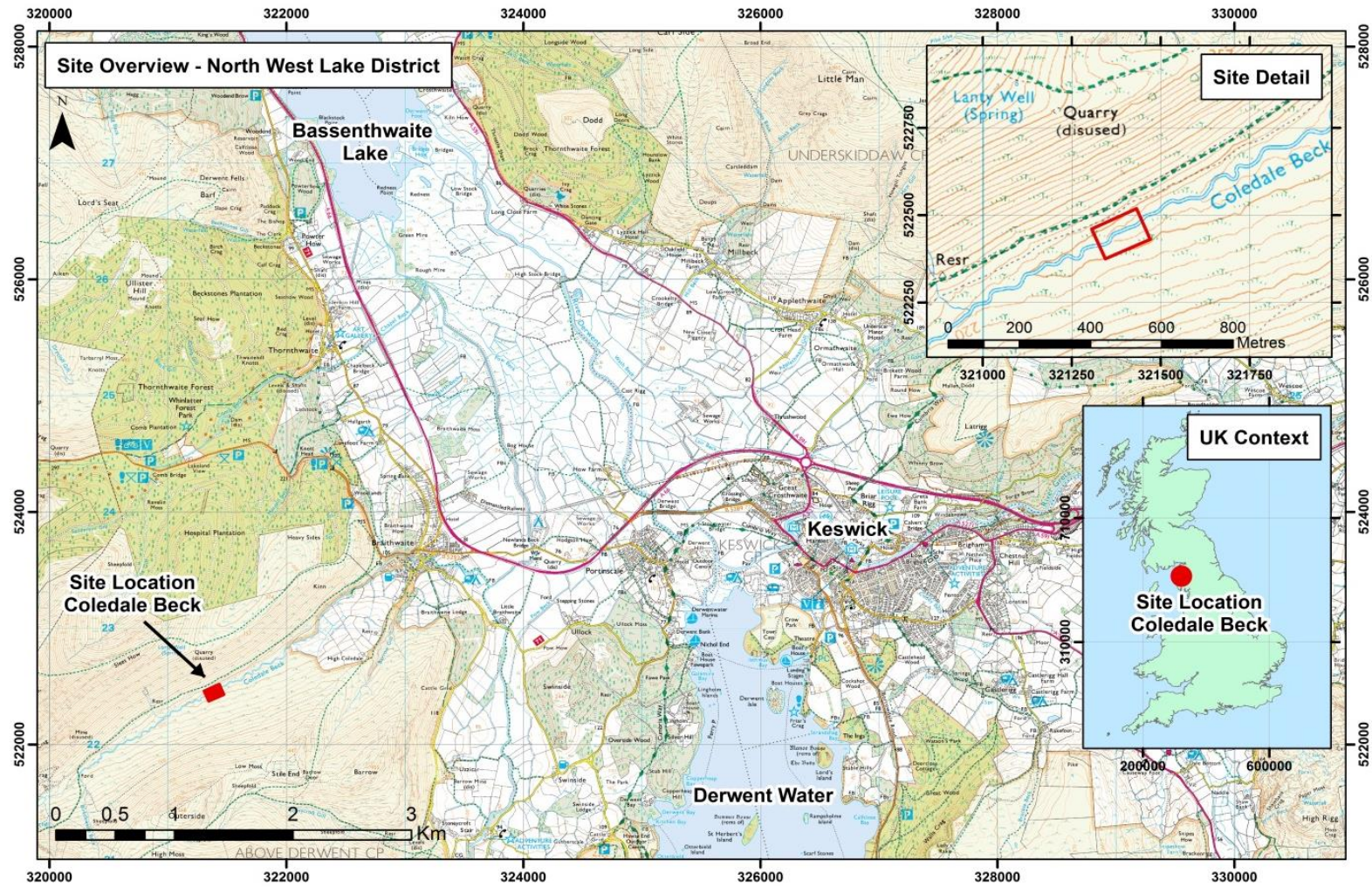


Figure 1.8. Location map for the Coledale Beck research site, Cumbria, UK (maps sourced from OS digimap).

Topographic data in the form of digital terrain models (DTMs) were used as part of the geomorphological study of the Bassenthwaite catchment (Orr and Brown 2004). Repeat surveys of sites such as Coledale Beck using a UAS-SfM approach may have the potential to provide such topographic data with higher spatial resolution and at more frequent time intervals than can currently be achieved using established airborne surveys. Whilst this PhD research is not affiliated with the BLRP, it is hoped that it will highlight the future possibilities of such an approach for providing key information concerning topography and channel erosion to important environmental management and restoration schemes.

1.5.3 The San Pedro River

Site overview

The San Pedro is a large (c. 100m wide), deep (thalweg depth up to c. 25m) river located in the Valdivia region of south-central Chile (39°46'18''S, 72°27'35''W, Figure 1.9). The banks and channel are composed of consolidated clay bedrock, overlain by areas of gravel and cobbles with some boulders and isolated large woody debris. The clay forms a shelf along parts of the river margin, where the water depth is relatively shallow before it drops off sharply to maximum depths of c. 25m in the centre of the channel.

The selected study reach forms part of a different, but associated, on-going research project with colleagues from the University of Concepción, Chile and is known as the 'Piedra Blanca' site (Figure 1.10). This c. 170m reach is downstream of the outlet of Lake Riñihue and comprises a narrow shelf mesohabitat along the right bank of the river, where flow depth is relatively shallow (up to c. 3m). The water is very clear and there is an absence of submerged aquatic vegetation within this area, although some pieces of large woody debris were present.

Surveys

Fieldwork at the Piedra Blanca site was undertaken in conjunction with colleagues from the University of Concepción in May 2012 (a breakdown of the division of work is provided in Appendix A). Data collected at the site included;

- UAS hyperspatial image survey
- Topographic survey using a dGPS

Site significance

The high gradient and powerful hydraulic nature of a number of large rivers in Chile make them well suited for the development of hydroelectric power dams. Currently there is a move to increase the number of such dams in Chile to meet growing energy demands. This has led to significant concerns about the impact of such constructions on natural river habitats (Vince 2010). Hydro-peaking operations and the flow regulations which follow dam construction modify the natural flow and sediment regime, thereby impacting on the physical and chemical conditions of the river downstream (Nilsson and Berggren 2000, Garcia et al., 2011). Such changes have significant implications for habitat availability and biotic communities. Furthermore, the geographical history of this region of Chile has resulted in rivers characterised by unique native fish fauna, such as the *Galaxiidae*. Relatively little is known concerning the habitat requirements of such fish and they are likely to be highly affected by the construction of dams and their subsequent impact on river flow regimes (Habit et al., 2007, Habit and Parra 2012). These species are also currently threatened by the introduction of predatory, non-native fish species associated with growth of the aquaculture industry in Chile (Arismendi et al., 2009, Habit et al., 2010).

On-going research has been aiming to characterise the current fluvial environments within a number of Chilean rivers, prior to dam construction (e.g. Habit and Parra 2012), in order to better understand the requirements of the little studied native fish species. It is hoped that this will help to inform the nature and location of dam construction and the subsequent flow regulations to help maintain suitable fish habitats.

In recent years, a research group based at the Environmental Science Centre (EULA-Chile) at the University of Concepción has been working at the Piedra Blanca site on the San Pedro River, where there are plans for the construction of a large (56m high) hydropower dam further downstream. The on-going research of the EULA Centre has been funded by the hydropower company and is aimed at characterising the migration patterns and spatio-temporal habitat use dynamics of various native fish species (e.g. *Galaxias platei*) within the San Pedro River (E. Habit 2012, *pers. comm.*).

As part of the EULA research, the local topography of the banks and shallow submerged shelf section of the Piedra Blanca site have been mapped. This has been carried out using a dGPS to collect x, y and z data at sampling points every 1-2m. Such an approach is very time

consuming, labour intensive and requires interpolation. Furthermore, given the remote location of this site, high resolution aerial imagery and LiDAR are not available and would incur significant costs to commission. As a result, if sufficient accuracy and precision of UAS-SfM topographic outputs can be proven, then this approach may be capable of providing a cheaper, faster and less laborious solution for providing continuous topographic data in such settings. In turn, this may contribute to our understanding of native fish habitat preferences and facilitate decision making as part of important environmental engineering projects.

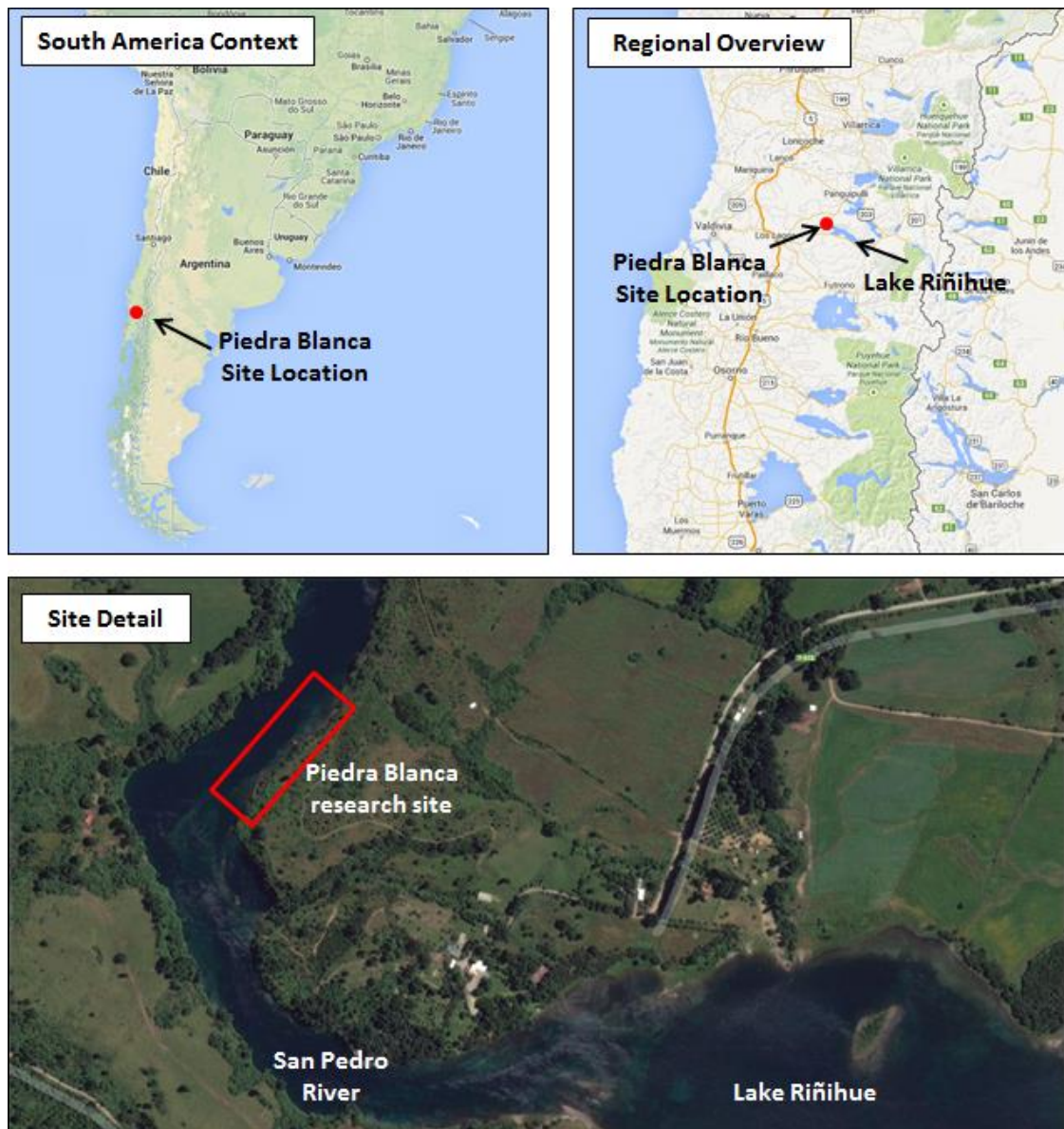


Figure 1.9. Location of the Piedra Blanca research site on the San Pedro River, Chile
(Google Maps 2014).



Figure 1.10. The Piedra Blanca research site on the San Pedro River.

1.5.4 Sports hall floor

Two UAS flights were also conducted over the floor of a large sports hall at the University of Worcester (Figure 1.11) to assess the ability of the UAS-SfM approach to reproduce a flat surface. Some variation in elevation was introduced by the positioning of objects within the scene. This experiment was aimed at exploring the effects of different camera viewing angles and ground control point configurations on the quality of output elevation data. Further detail is provided in Chapters 2 and 3.



Figure 1.11. The sports hall floor at the University of Worcester.

1.6 Summary

This chapter has set the scene for the research presented within this thesis by highlighting the importance of quantifying physical river habitat parameters and reviewing recent developments in UAS and SfM technologies. The key aims and research questions have been identified and the study sites introduced. The methods common to the quantification of the three physical river habitat parameters studied here are presented in Chapter 2, with details of parameter-specific methods following in Chapters 3 to 5 accompanied by subsequent in-depth analyses and discussions.

1.7 References

- Anderson, C. (2013) DIY Drones. Available online: <http://diydrones.com/> (accessed 01.06.2013).
- Arismendi, I., Soto, D., Penaluna, B., Jara, C., Leal, C. and León-Muñoz, J. (2009) Aquaculture, non-native salmonids invasions and associated declines of native fishes in Northern Patagonia lakes. *Freshwater Biology* 54 (5): 1135-1147
- Bassenthwaite Lake Restoration Programme (2010) Achievements Report 2009/10. Available online: <http://www.bassenthwaite-lake.co.uk/> (accessed 23.07.2013).
- Bellis, A., Stockwell, N., Moore, R. and Fish, P. (2013) UAV survey for cliff instability and rockfall hazard and risk assessment. *Remote Sensing from Small UAVs Workshop*, University of Worcester, UK, 4th July 2013.
- Bergeron, N. and Carbonneau, P.E. (2012) Geosalar: Innovative remote sensing methods for spatially continuous mapping of fluvial habitat at riverscape scale. In Carbonneau, P.E. and Piegay, H. (Eds) *Fluvial Remote Sensing for Science and Management*, Wiley-Blackwell, Chichester.
- Bovee, K.D. (1996) Perspectives on two-dimensional river habitat models: the PHABSIM experience. In Le Clerc, M., Capra, H., Valentin, S., Boudreault, A., and Cote, Y. (Eds) *Ecohydraulique 2000: Proceedings of the 2nd IAHR Symposium on Habitat Hydraulics*, Quebec: 150-162.
- Carbonneau, P.E., Lane, S.N. and Bergeron, N. (2004) Catchment-scale mapping of surface grain size in gravel bed rivers using airborne digital imagery. *Water Resources Research* 40, W07202, doi:10.1029/2003WR002759.
- Carbonneau, P.E., Fonstad, M.A., Marcus, W.A. and Dugdale, S.J. (2012) Making riverscapes real. *Geomorphology* 123: 74-86.
- Dollar, E.S.J., James, C.S., Rogers, K.H. and Thoms, M.C. (2007) A framework for interdisciplinary understanding of rivers as ecosystems. *Geomorphology* 89: 147-162.
- Dugdale, S.J. (2007) An evaluation of imagery from an unmanned aerial vehicle (UAV) for the mapping of intertidal macroalgae on Seal Sands, Tees Estuary, UK. Unpublished MSc thesis, Durham University.

Dunford, R., Michel, K., Gagnage, M., Piegay, H. and Tremelo, M-L. (2009) Potential constraints of unmanned aerial vehicle technology for the characterization of Mediterranean riparian forest. *International Journal of Remote Sensing* 30 (19): 4915-4935.

Eisenbeiss, H., Lambers, K., Sauerbier, M. and Li, Z. (2005) Photogrammetric documentation of an archaeological site (Palpa, Peru) using an autonomous model helicopter. *CIPA 2005 XX International Symposium*, 26 September-1 October, Torino, Italy.

Environment Agency (2003) River Habitat Survey in Britain and Ireland: Field Survey Guidance Manual. Available online: https://www.gov.uk/government/uploads/system/uploads/attachment_data/file/311579/LIT_1758.pdf (accessed 11.02.2015).

European Commission (2000) Directive 2000/60/EC of the European Parliament and of the Council of 23rd October 2000: Establishing a framework for Community action in the field of water policy. *Official Journal of the European Communities, Brussels, 22.12.2000, L327*: 1-72.

Fausch, K.D., Torgersen, C.E., Baxter, C.V. and Hiram, L.W. (2002) Landscapes to riverscapes: bridging the gap between research and conservation of stream fishes. *BioScience* 52 (6): 483-498.

Fernandez, D., Barquin, J. and Raven, P.J. (2011) A review of river habitat characterisation methods: indices vs. characterisation protocols. *Limnetica* 30 (2): 217-234.

Flener, C., Vaaja, M., Jaakkola, A., Krooks, A., Kaartinen, H., Kukko, A., Kasvi, E., Hyyppä, H., Hyyppä, J. and Alho, P. (2013) Seamless mapping of river channels at high resolution using mobile LiDAR and UAV-photography. *Remote Sensing* 5: 6382-6407.

Fonstad, M.A., Dietrich, J.T., Courville, B.C., Jensen, J.L. and Carbonneau, P.E. (2013) Topographic structure from motion: a new development in photogrammetric measurement. *Earth Surface Processes and Landforms* 38 (4): 421-430.

Frissell, C.A., Liss, W.J., Warren, C.E. and Hurley, M.D. (1986) A hierarchical framework for stream habitat classification: viewing streams in a watershed context. *Environmental Management* 10 (2): 199-214.

Frothingham, K.M., Rhoads, B.L. and Herricks, E.E. (2002) A multiscale conceptual framework for integrated ecogeomorphological research to support stream naturalisation in the agricultural Midwest. *Environmental Management* 29 (1): 16-33.

Garcia, A., Jorde, K., Habit, E., Caamano, D. and Parra, O. (2011) Downstream environmental effects of dam operations: changes in habitat quality for native fish species. *River Research and Applications* 27: 312-327.

Habit, E., Belk, M.C. and Parra, O. (2007) Response of the riverine fish community to the construction and operation of a diversion hydropower plant in central Chile. *Aquatic Conservation: Marine and Freshwater Ecosystems* 17: 37-49.

Habit, E., Piedra, P., Ruzzante, D.E., Walde, S.J., Belk, M.C., Cussac, V.E., Gonzalez, J. and Colin, N. (2010) Changes in the distribution of native fishes in response to introduced species and other anthropogenic effects. *Global Ecology and Biogeography* 19: 697-710.

Habit, E. and Parra, O. (2012) Basis and methodological approach for the study of the San Pedro River fish fauna. *Gayana* 76: 1-9.

Hardin, P.J. and Hardin, T.J. (2010) Small-scale remotely piloted vehicles in environmental research. *Geography Compass* 4/9: 1297-1311.

Hardin, P.J. and Jensen, R.R. (2011) Small-scale unmanned aerial vehicles in environmental remote sensing: challenges and opportunities. *GIScience and Remote Sensing* 48 (1): 99-111.

Harwin, S. and Lucieer, A. (2012) Assessing the accuracy of georeferenced point clouds produced via multi-view stereopsis from unmanned aerial vehicle (UAV) imagery. *Remote Sensing* 4: 1573-1599.

Hawkeye UAV (2013) Hawkeye UAV. Available online: <http://www.hawkeyeuav.com> (accessed 01.06.2013).

Heritage, G.L. and Milan, D.J. (2009) Terrestrial laser scanning of grain roughness in a gravel-bed river. *Geomorphology* 113: 4-11.

Hervouet, A., Dunford, R., Piegay, H., Belletti, B. and Tremelo, M-L. (2011) Analysis of post-flood recruitment patterns in braided-channel rivers at multiple scales based on an image series collected by unmanned aerial vehicles, ultra-light aerial vehicles, and satellites. *GIScience and Remote Sensing* 48 (1): 50-73.

Hughenoltz, C., Moorman, B., Riddell, K., and Whitehead, K. (2012) Small unmanned aircraft systems for remote sensing and earth science research. *Eos* 93 (25): 236-7.

Hughenoltz, C., Whitehead, K., Brown, O.W., Barchyn, T.E., Moorman, B.J., LeClair, A., Riddell, K., and Hamilton, T. (2013) Geomorphological mapping with a small unmanned aircraft system (sUAS): Feature detection and accuracy assessment of a photogrammetrically derived digital terrain model. *Geomorphology* 194: 16-24.

Hunt, E.R., Hively, W.D., Fujikawa, S.J., Linden, D.S., Daughtry, C.S.T. and McCarty, G.W. (2010) Acquisition of NIR-green-blue digital photographs from unmanned aircraft for crop monitoring. *Remote Sensing* 2: 290-305.

James, M.R. and Robson, S. (2012) Straightforward reconstruction of 3D surfaces and topography with a camera: accuracy and geosciences application. *Journal of Geophysical Research* 117, F03017, doi: [10.1029/2011JF002289](https://doi.org/10.1029/2011JF002289).

Javernick, L., Brasington, J. and Caruso, B. (2014) Modelling the topography of shallow braided rivers using Structure-from-Motion photogrammetry. *Geomorphology* 213: 166-182.

Kingsford, R.T. (2011) Conservation management of rivers and wetlands under climate change – a synthesis. *Marine and Freshwater Research* 62: 217-222.

Kovalenko, K.E., Thomaz, S.M. and Warfe, D.M. (2012) Habitat complexity: approaches and future directions. *Hydrobiologia* 685: 1-17.

Laliberté, A.S. and Rango, A. (2009) Texture and scale in object-based analysis of subdecimeter resolution unmanned aerial vehicle (UAV) imagery. *IEEE Transactions on Geoscience and Remote Sensing* 47 (3): 761-770.

Laliberté, A.S., Winters, C. and Rango, A. (2011) UAS remote sensing missions for rangeland applications. *Geocarto International* 26 (2): 141-156.

Lane, S.N., Richards, K.S. and Chandler, J.H. (1993) Developments in photogrammetry; the geomorphological potential. *Progress in Physical Geography* 17 (3): 306-328.

Lapointe, M. (2012) River geomorphology and salmonids habitat: some examples illustrating their complex association, from redd to riverscape scales. In Church, M. Biron, P. and Roy, A. (Eds) Gravel-bed Rivers: Processes, Tools, Environments, Wiley-Blackwell, Chichester.

Lejot, J., Delacourt, C., Piegay, H., Fournier, T., Tremelo, M-L. and Allemand, P. (2007) Very high spatial resolution imagery for channel bathymetry and topography from an unmanned mapping controlled platform. *Earth Surface Processes and Landforms* 32: 1705-1725.

Lowe, D.G. (2004) Distinctive image features from scale-invariant keypoints. *International Journal of Computer Vision* 60: 91-110.

MacKenzie, R., Stefanutti, L., Didonfrancesco, G., Amici, S., and Ferlito, L. (2009) Environmental and Earth science using next generation aerial platforms. NERC Scoping Study R8-H10-71.

MacVicar, B.J., Piégay, H., Anderson, A., Oberlin, C., Comiti, F. and Pecorari, E. (2009) Quantifying the temporal dynamics of wood in large rivers: new techniques for wood tracking, monitoring, surveying, and dating. *Earth Surface Processes and Landforms* 34: 2031–2046.

Maddock, I. (1999) The importance of physical habitat assessment for evaluating river health. *Freshwater Biology* 41: 373-391.

Maddock, I., Thoms, M., Jonson, K., Dyer, F. and Lintermans, M. (2004) Identifying the influence of channel morphology on physical habitat availability for native fish: application to the two-spined blackfish (*Gadopsis bispinosus*) in the Cotter River, Australia. *Marine and Freshwater Research* 55: 173-184.

Micheletti, N., Chandler, J.H. and Lane, S.N. (in press) Investigating the geomorphological potential of freely available and accessible structure-from-motion photogrammetry using a smartphone. *Earth Surface Processes and Landforms* doi: 10.1002/esp.3648.

Neitzel, F. and Klonowski, J. (2011) Mobile 3D mapping with a low-cost UAV system. *International Archives of the Photogrammetry, Remote Sensing and Spatial Information Sciences Vol. XXXVIII-I/C22*, Conference on UAVs in Geomatics, Zurich, Switzerland.

Newson, M.D. and Large, A.R.G. (2006) ‘Natural’ rivers, ‘hydromorphological quality’ and river restoration: a challenging new agenda for applied fluvial geomorphology. *Earth Surface Processes and Landforms* 31: 1606-1624.

Newson, M.D. and Newson, C.L. (2000) Geomorphology, ecology and river channel habitat: mesoscale approaches to basin-scale challenges. *Progress in Physical Geography* 24 (2): 195-217.

Niethammer, U., James, M.R., Rothmund, S., Travelletti, J. and Joswig, M. (2012) UAV-based remote sensing of the Super-Suaze landslide: Evaluation and results. *Engineering Geology* 128: 2-11.

Nilsson, C. and Berggren, K. (2000) Alterations of riparian ecosystems caused by river regulation. *BioScience* 50 (9): 783-792.

Orr, H. and Brown, D. (2004) Bassenthwaite Lake Geomorphological Study Findings: Summary Report, Environment Agency Publication Reference ScNW0904BIGO-E-P.

Orr, H.G., Large, A.R.G., Newson, M.D. and Walsh, C.L. (2008) A predictive typology for characterising hydromorphology. *Geomorphology* 100: 32-40.

Petrie, G. (2013) Commercial operation of lightweight UAVs for aerial imaging and mapping. *GeoInformatics* 16 (1): 28-39.

Raven, P.J., Fox, P., Everard, M., Holmes, N.T.H. and Dawson, F.H. (1998) River habitat survey: a new system for classifying rivers according to their habitat quality. In Boon, P.J. and Howell, D.L. (Eds) Freshwater quality: Defining the undefinable Edinburgh HMSO p.215-234.

Rosnell, T. and Honkavaara, E. (2012) Point cloud generation from aerial image data acquired by a quadcopter type micro unmanned aerial vehicle and a digital still camera. *Sensors* 12: 453-480.

Smart Planes (2014) Smart Planes. Available online: www.smartplanes.se (accessed 12.09.2014).

Smith, M.J., Chandler, J. and Rose, J. (2009) High spatial resolution data acquisition for the geosciences: kite aerial photography. *Earth Surface Processes and Landforms* 34: 155-161.

Tamminga, A., Hugenholtz, C., Eaton, B. and Lapointe, M. (2014) Hyperspatial remote sensing of channel reach morphology and hydraulic fish habitat using an unmanned aerial vehicle (UAV): A first assessment in the context of river research and management. *River Research and Applications* doi: 10.1002/rra.2743.

Thorp, J.H., Thoms, M.C. and Delong, M.D. (2006) The riverine ecosystem: biocomplexity in river networks across space and time. *River Research and Applications* 22: 123-147.

Turner, D., Lucieer, A. and Watson, C. (2012) An automated technique for generating georectified mosaics from ultra-high resolution unmanned aerial vehicle (UAV) imagery, based on Structure from Motion (SfM) point clouds. *Remote Sensing* 4: 1392-1410.

United States Geological Survey (2010) UAS Yearbook – UAS: The Global Perspective, 8th Edition, Blyenburgh and Co. Available online: http://uas.usgs.gov/UAS-Yearbook2010/pdf/P161-195_World-UAS-Reference-Section.pdf (accessed 25.09.2014).

Vannote, R.L., Minshall, G.W., Cummins, K.W., Sedell, J.R. and Cushing, C.E. (1980) The river continuum concept. *Canadian Journal of Fisheries and Aquatic Science* 37: 130-137.

Vaughan, I.P., Diamond, M., Gurnell, A.M., Hall, K.A., Jenkins, A., Milner, N.J., Naylor, L.A., Sear, D.A., Woodward, G. and Ormerod, S.J. (2009) Integrating ecology with hydromorphology: a priority for river science and management. *Aquatic Conservation: Marine and Freshwater Ecosystems* 19: 113-125.

Vaughan, A. (2013) WWF plans to use drones to protect wildlife: The green group says by the end of the year it will have deployed 'eyes in the sky' in one country in Africa or Asia. The Guardian Online, Thursday 7th February 2013.

Verhoeven, G. (2012) Getting computer vision airborne – using Structure from Motion for accurate orthophoto production. *RSPSoc Archaeology Special Interest Group Meeting Spring 2012*, p. 4-6.

Verhoeven, G., Doneus, M., Briese, Ch. and Vermuelen, F. (2012) Mapping by matching: a computer vision-based approach to fast and accurate georeferencing of archaeological aerial photographs. *Journal of Archaeological Science* 39: 2060-2070.

Vericat, D., Brasington, J., Wheaton, J. and Cowie, M. (2009) Accuracy assessment of aerial photographs acquired using lighter-than-air blimps: low-cost tools for mapping river corridors. *River Research and Applications* 25 (8): 985-1000.

Vince, G. (2010) Dams for Patagonia. *Science* 329: 382-385.

- Ward, J.V. (1989) The four-dimensional nature of lotic ecosystems. *Journal of the North American Benthological Society* 8 (1): 2-8.
- Ward, J.V. (1998) Riverine landscapes: biodiversity patterns, disturbance regimes and aquatic conservation. *Biological Conservation* 83 (3): 269-278.
- Ward, J.V., Malard, F. and Tockner, K. (2002) Landscape ecology: a framework for integrating pattern and process in river corridors. *Landscape Ecology* 17 (1): 35-45.
- Watts, A.C., Ambrosia, V.G. and Hinkley, E.A. (2012) Unmanned aircraft systems in remote sensing and scientific research: Classification and considerations of use. *Remote Sensing* 4: 1671-1692.
- Westaway, R.M., Lane, S.N. and Hicks, D.M. (2001) Remote sensing of clear-water, shallow, gravel-bed rivers using digital photogrammetry. *Photogrammetric Engineering and Remote Sensing* 67 (11): 1271-1281.
- Westoby, M.J., Brasington, J., Glasser, N.F., Hambrey, M.J. and Reynolds, J.M. (2012) Structure-from-Motion photogrammetry: a low cost, effective tool for geoscience applications. *Geomorphology* 179: 300-314.
- Wiens, J.A. (2002) Riverine landscapes: taking landscape ecology into the water. *Freshwater Biology* 47: 501-515.
- Winterbottom, S.J. and Gilvear, D.J. (1997) Quantification of channel bed morphology in gravel-bed rivers using airborne multispectral imagery and aerial photography. *Regulated Rivers: Research and Management* 13: 489-499.
- Wright, A., Marcus, W.A. and Aspinall, R. (2000) Evaluation of multispectral, fine scale digital imagery as a tool for mapping stream morphology. *Geomorphology* 33: 107-120.
- Wu, C. (2015) Visual SFM: A Visual Structure from Motion System. Available online: <http://ccwu.me/vsfm/> (accessed 11.02.2015).

Chapter 2

Methods

Chapter Overview

A number of the key methods employed within this research are common to the assessment of some or all of the physical river habitat parameters considered within this thesis. These methods include the set-up of the UAS, pre-flight characterisation of the camera, the UAS flying process and image acquisition, the selection of suitable images and the SfM photogrammetric processing. Additionally, data were acquired with a terrestrial laser scanner (TLS) for comparative purposes within Chapters 3 and 4. To avoid repetition, these key methods are described within this chapter. Those methods which are specific to the assessment of each physical river habitat parameter are detailed within the subsequent, respective chapters.

2.1 The Draganflyer X6 UAS

The UAS used within this research is the Draganflyer X6, a radio-controlled, rotary winged UAS (Figure 2.1) manufactured in Canada by Draganfly Innovations Inc. The Draganflyer X6 is a relatively small (91cm x 85cm x 26cm) and lightweight system (1kg), capable of carrying a 0.5kg payload. It features six carbon fibre rotors, each associated with an electric brushless motor. The system is powered by small, rechargeable 14.8V 2700mAh Lithium Polymer (LiPo) batteries which typically provide 5-10 minutes of flying time depending on payload and wind strength. The cost of the Draganflyer X6, including flight training and all accessories was c. £29,500 at the time of purchase in 2010. Since this time, the UAS market has expanded hugely, so that platforms of this specification are now available for the fraction of the price.

The Draganflyer X6 holds eleven on-board sensors, including three gyroscopes, three accelerometers, three magnetometers, a barometric pressure sensor and a GPS receiver. These sensors help to ensure the platform is capable of relatively stable flight. The GPS may be

used to hold position of the platform at a single location, but is not survey-grade and is not used for subsequent georeferencing. With the exception of an automated take-off, flight control and image acquisition are entirely manual using handheld, wireless flight controllers (Figure 2.2). Take-off and landing are vertical and therefore, unlike fixed wing systems, large open areas are not required. This system is capable of flying up to a maximum range of 1km, as determined by the limit of the radio communications.



Figure 2.1. The Draganflyer X6 UAS platform.

Current advice from the UK's Civil Aviation Authority (CAA) states that small UAS, weighing less than 20kg, can be operated without a licence or specific permission for non-commercial purposes, so long as flights are conducted within segregated airspace and within visual line of sight (CAA *pers. comm.*, 2014). Despite the lack of a legal requirement, CAA approved flight training in the form of the Basic National UAS Certificate for Small UAS (BNUC-S™) was nevertheless undertaken in 2012, and the conditions of this permit were adhered to at all times.

Following flight training and initial flying tests, it was found that a two person team was optimal for flying and collecting data using the Draganflyer X6. The first person is responsible solely for manual flight control, including take-off initiation, and the second for navigation and manual triggering of the shutter, tilt and zoom of the camera. This is usually achieved using first person view video goggles (Figure 2.3a), which display real-time imagery from the airborne camera via radio link. A base station was also available for use. This holds a laptop

running the 'Draganview' software allowing the viewing of real-time imagery and telemetry information during flight (Figure 2.4). The base station was rarely used within this research project as its weight and bulky nature made transportation to and around research sites challenging.



Figure 2.2. The Draganflyer X6 handheld controller (Draganfly Innovations Inc. 2013).

The Draganflyer X6 is mounted with a specially modified 10.1 megapixel optical digital camera, a Panasonic Lumix DMC-LX3 (Figure 2.3b). This is a small and lightweight consumer-grade camera which was not designed specifically for the acquisition of aerial imagery. The detailed camera specification is provided in Table 2.1.

Table 2.1. Specification of the Panasonic Lumix DMC-LX3 camera.

Feature	Specification
Dimensions	108.7 x 59.5 x 27.1 mm
Focal length	5.1-12.8 mm (35mm equiv. 24-60mm)
Sensor size	1/1.63 inches (8.07 x 5.56mm)
Sensor type	Charge coupled device (CCD)
Max. resolution	10.1 mega pixels
Lens type	Zoom lens

The procedures and workflows described within this thesis for set-up and use of the Draganflyer X6 are a product of extensive testing and flight experience by the CAA licensed UAS pilots at the University of Worcester. This expertise has been developed during the course of this PhD project and is not extracted from published guidelines or literature. It is noted that

pilot skill and experience is a key factor governing successful data acquisition of high quality imagery using a UAS.

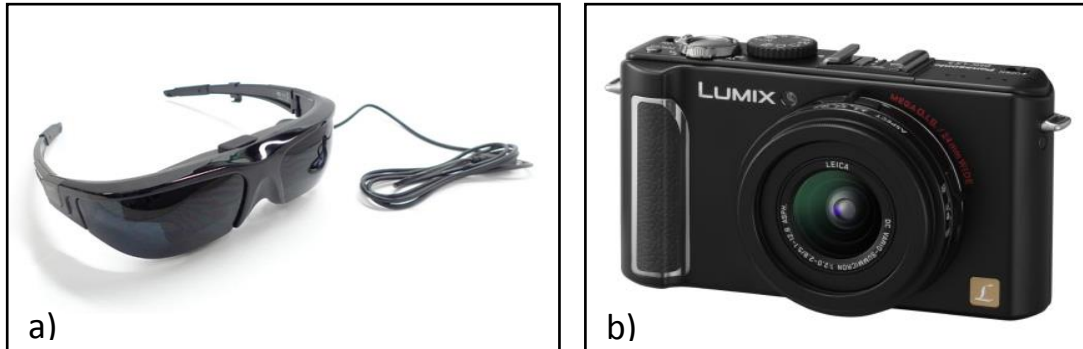


Figure 2.3. a) Video goggles capable of displaying real-time imagery from the camera mounted on the Draganflyer X6 during flight (Draganfly Innovations Inc. 2013),
b) Panasonic Lumix DMC-LX3 (Panasonic 2013)

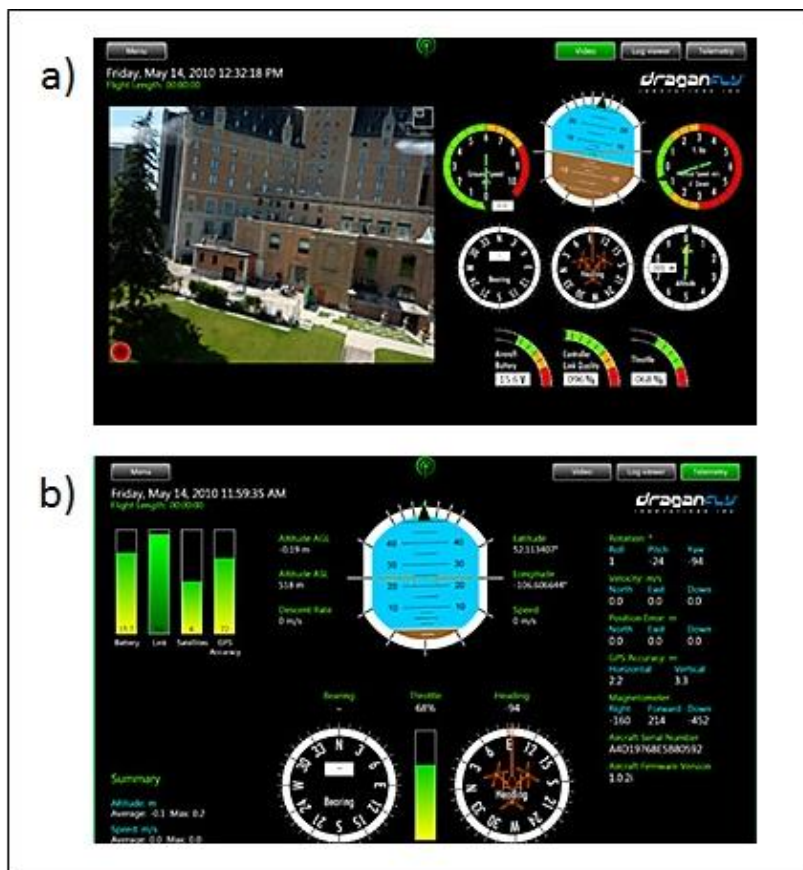


Figure 2.4. Screenshots of the Draganview software showing a) real-time imagery and b) telemetry information (Draganfly Innovations Inc. 2013)

2.2 Pre-flight camera characterisation

Before imagery was acquired using the Draganflyer X6 it was necessary to establish the relationship between flying altitude, image footprint size and pixel size. This relationship is determined by the internal camera optics, and can be estimated by carrying out a simple camera characterisation test, intended to inform flight planning. This test involved setting up a grid of image targets fixed to a wall or flat vertical surface, separated by known distances. The camera was then used to acquire images of the grid of targets, at set distances away from the targets. The set distances are intended to represent flying altitude.

The tests were carried out using the Panasonic Lumix DMC-LX3. The focal length was set manually at 5.1mm, so as to provide the widest angle view. During flight, this maximises ground coverage whilst not compromising spatial resolution. A total of 6 image targets were fixed to the wall of a large sports hall in a 2 by 3 arrangement, as illustrated in Figure 2.5. Targets were separated by 1.5m in the vertical, and 9m in the horizontal, as measured using a hand tape. Images of the targets were acquired over the range 10m to 30m. The distances between targets were then measured on each image, in pixels. This allows an approximation of pixel size, as shown in Equation 1. Where P_s represents pixel size (image resolution or ground sample distance) in metres, D_m is the measured distance between targets in metres and D_p is the distance between targets in pixels.

$$P_s = \frac{D_m}{D_p}$$

Equation (1)

The estimated pixel size can then be used in conjunction with image size to estimate the image footprint size, as demonstrated in Equation 2. Where F represents image footprint size in metres, I represents image size in pixels and w and h indicate the width and height dimensions of the rectangular sensor. The image size of the Panasonic Lumix DMC-LX3 is 3648 x 2736 in pixels.

$$F_{wh} = I_{wh} \times P_s$$

Equation (2)



Figure 2.5. Set-up of the camera characterisation tests, with example artificial target (measuring 20cm x 20cm).

As the distance between the camera and the targets increases (the equivalent of increasing flying altitude) the pixel distance between image targets (Dp) decreases, pixel size (Ps) increases (i.e. spatial resolution becomes coarser) and image footprint size (F) increases (i.e. spatial coverage becomes greater). This relationship can be quantified based on the characterisation testing, and extrapolated in order to estimate the image dimensions (footprint height and width) and image resolution (pixel size) according to flight altitude as shown in Equations 3a, 3b and 3c. Where F_w is image footprint width, F_h is image footprint height, Ps is pixel size and A is the flying altitude. Figures 2.6 and 2.7 indicate the relationships between distance and pixel size, and distance and image dimensions as found for the Panasonic Lumix DMC-LX3 by these tests. These data were used in flight planning to determine the approximate flying altitudes required for each survey.

$$F_w = (1.4174 \times A) - 0.2361$$

Equation (3a)

$$F_h = (1.0631 \times A) - 0.1771$$

Equation (3b)

$$Ps = (0.0004 \times A) - 0.00006$$

Equation (3c)

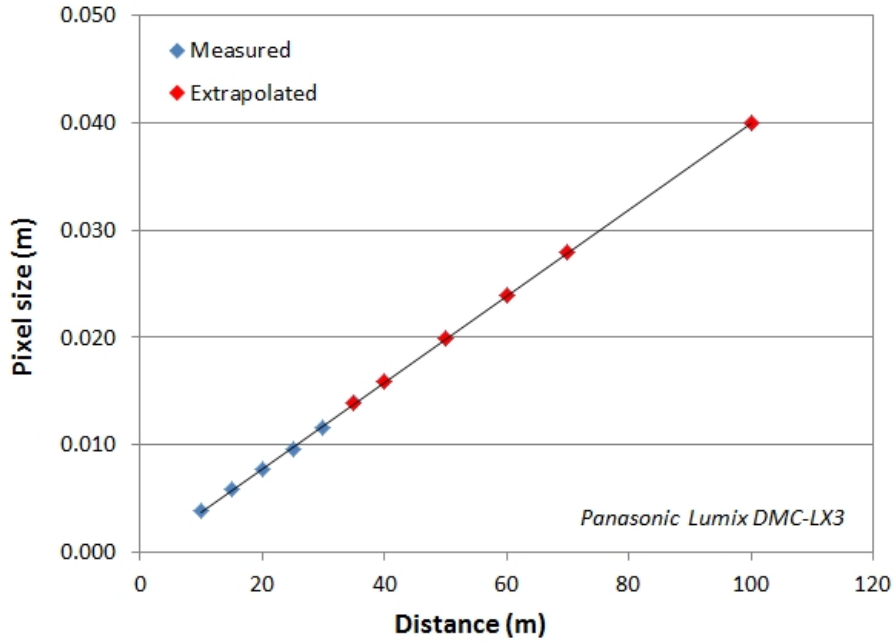


Figure 2.6. Relationship between distance (i.e. flight altitude) and image pixel size, as determined by characterisation of the Panasonic DMC-LX3 camera.

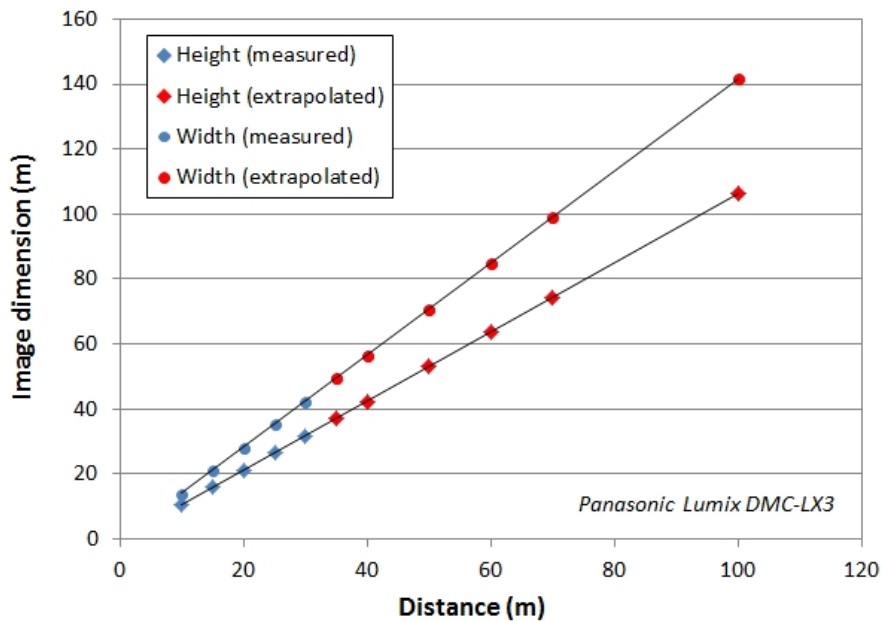


Figure 2.7. Relationship between distance (i.e. flight altitude) and image dimensions, as determined by characterisation of the Panasonic DMC-LX3 camera.

2.3 UAS surveys

2.3.1 Ground control

The majority of sites used within this research are in rural locations which are lacking in fixed, easily identifiable map features such as buildings and roads. As a result, it was necessary to construct and use artificial ground control points during the aerial image surveys for subsequent georectification of the imagery (often known as photo-control points in conventional photogrammetry).

A total of fifty artificial ground control points (GCPs) were constructed prior to data collection from 0.5mm thick black PVC pond liner cut into 20cm x 20cm squares. Two white triangles were spray painted onto each square using white car paint and cardboard templates. Each ground control point was numbered to allow unique identification in the field and during collection of positioning data using a dGPS or total station. Some example GCPs are shown in Figure 2.8. Advice in the construction of these artificial GCPs was taken from Wheaton (2012).

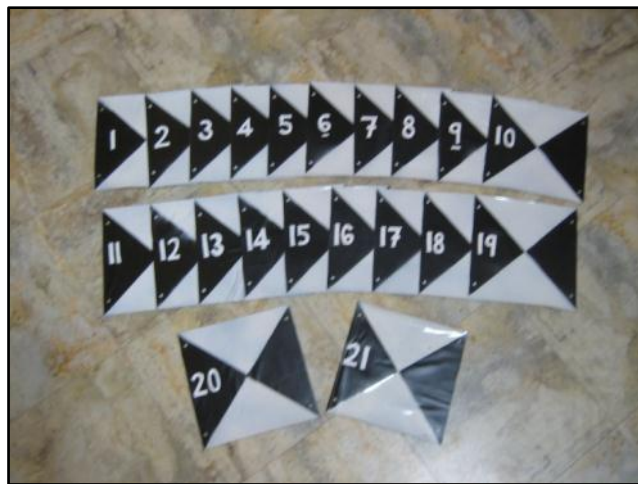


Figure 2.8. The artificial ground control points constructed for use within this research.

The optimum quantity and distribution of GCPs is subject to discussion (e.g. Vericat et al., 2009). The number and locations of GCPs used at each site within this research are presented in Table 2.2 and Figures 2.9 to 2.12. Whilst GCPs configurations vary between research sites,

efforts were made to ensure that GCPs were placed at least every 15m along each bank of the reach in question, and usually at less than 10m intervals. During the survey of the River Arrow in July 2012, a number of GCPs were disturbed or eaten by livestock. As a result, these could not be used in subsequent georeferencing, and the area used for further analyses was adjusted accordingly as indicated in Figure 2.10.

Following image acquisition, the positions of all GCPs were surveyed using a total station or differential global positioning system (dGPS), depending on the availability of satellite signals and equipment. Where a total station was used, all GCP locations were recorded relative to permanent markers of known geographic position as determined by dGPS at another time. Site specific details are provided in Table 2.2.

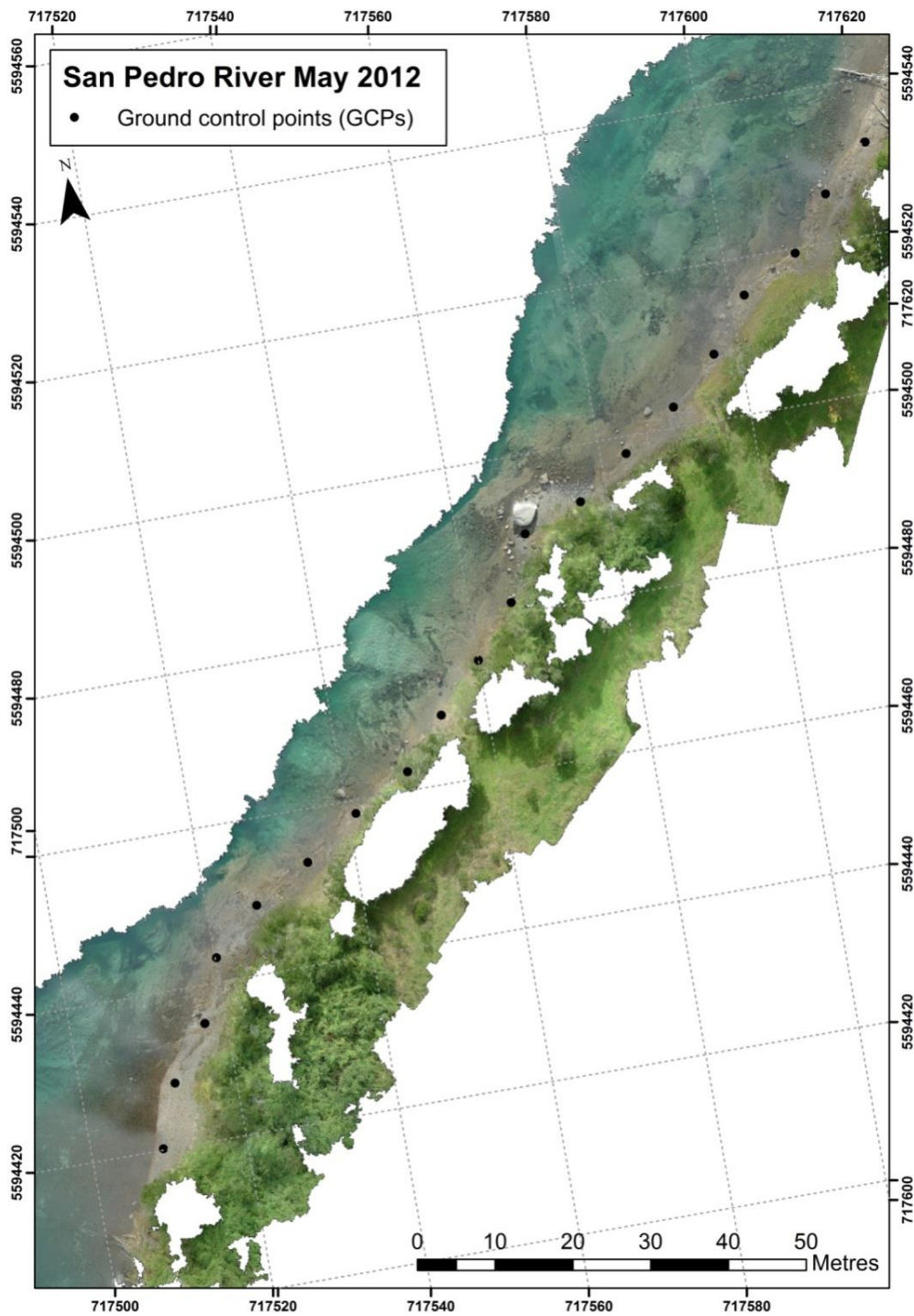


Figure 2.9. Locations of ground control points (GCPs) during the UAS survey of the San Pedro River, May 2012.



Figure 2.10. Locations of ground control points during the UAS survey of the River Arrow, July 2012 (Zone A in Figure 1.6).

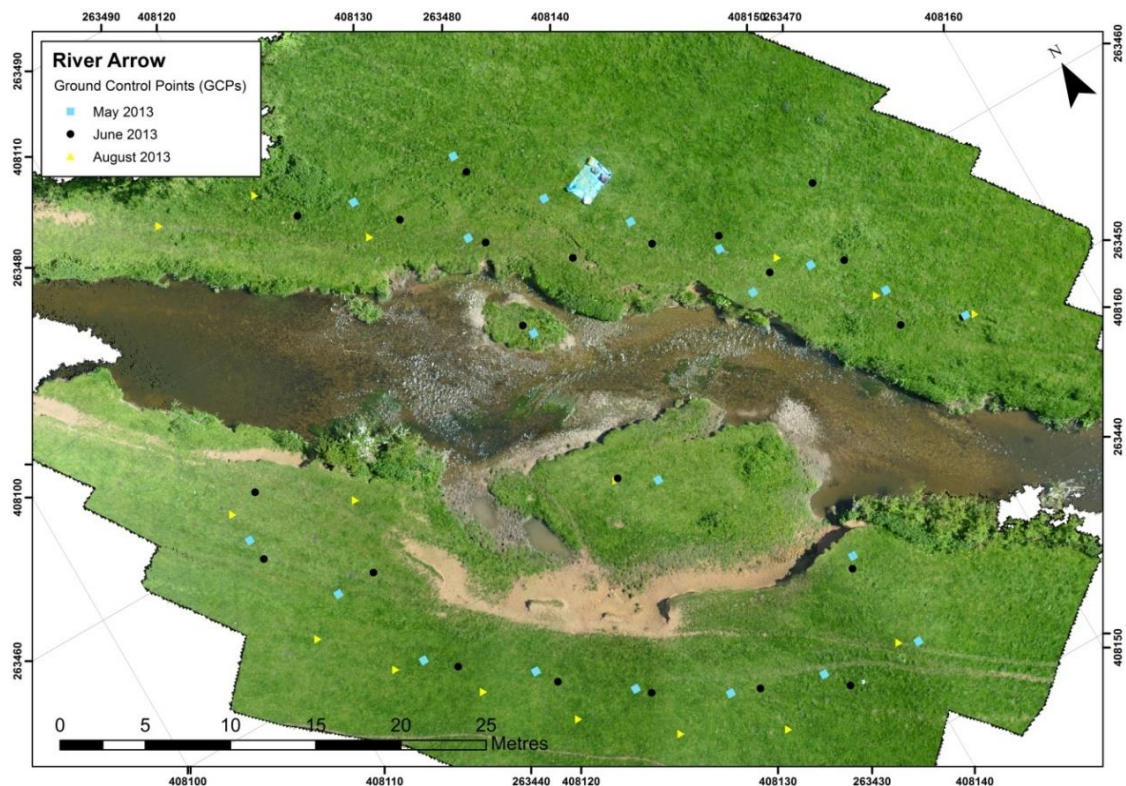


Figure 2.11. Locations of ground control points during the UAS surveys of the River Arrow in May, June and August 2013, shown over the June 2013 orthophoto (modified from Woodget et al., 2015) (Zone B in Figure 1.6).



Figure 2.12. Locations of ground control points during the UAS survey of Coledale Beck, July 2013 (modified from Woodget et al., 2015).

2.3.2 Image acquisition – sports hall

Two UAS surveys were conducted over the floor of a large sports hall at the University of Worcester to assess the ability of the UAS-SfM approach to reproduce a flat surface. The Panasonic DMC-LX3 camera was used on the Draganflyer X6 platform and flown at a height of c. 4m above floor level which permitted an area covering roughly 9m by 7m to be surveyed. Some variation in elevation was introduced by the positioning of objects within the scene. A dense network of ground control points (GCPs) was established across the scene prior to image acquisition, and subsequently surveyed using a Leica Builder 500 total station.

During the first survey, the position of the camera was set to acquire imagery at nadir (looking vertically downwards), whereas during the second survey, the camera was tilted to acquire imagery from an oblique viewing angle. The imagery from each survey was then processed separately using a SfM-photogrammetry workflow within PhotoScan Pro (Agisoft LLC), using the same settings as described for the field sites in section 2.5.

During the georeferencing stage of the SfM workflow, two different GCP arrangements were tested. The first comprised the use of seven GCPs arranged along a roughly central axis within the scene (Figure 2.13a). This arrangement is similar to that used during the San Pedro River UAS survey, where it was only possible to locate GCPs along one bank of the river. The second test used a more even spread of seven GCPs distributed throughout the scene (Figure 2.13b), mimicking the set-up of GCPs at the other field sites. The collection of two different surveys processed using two different GCP arrangements resulted in the output of four different DEMs for the sports hall floor, all of which were of a spatial resolution less than 5mm.

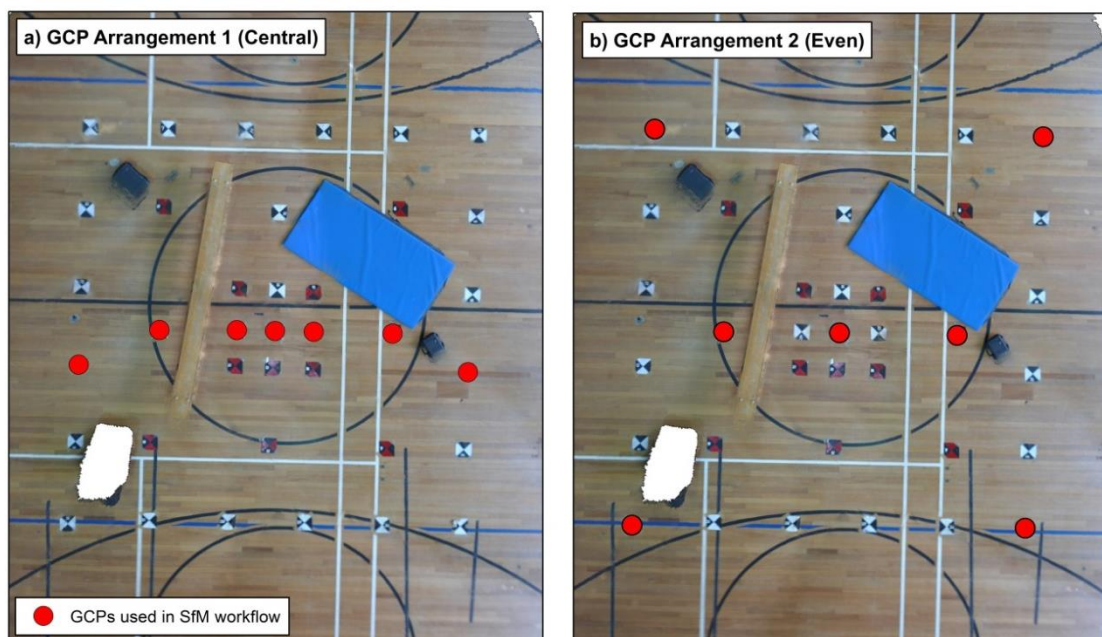


Figure 2.13. Arrangement of GCPs used for the sports hall tests

2.3.3 Image acquisition – field sites

During each field survey, very high resolution (typically <2cm) optical imagery was again collected using the Panasonic Lumix DMC-LX3 mounted on the Draganflyer X6 UAS platform. The Draganflyer X6 was typically flown at a target altitude of 25-30m above ground level (Table 2.2) to ensure spatial resolutions of c. 1cm. The exception was the survey of the River Arrow in July 2012. The original intention of this survey was to acquire a greater reach length of c. 500m which necessitated a slightly higher flying altitude to ensure that image acquisition and associated ground truthing could be conducted within a single day. In practice, only 160m of

this reach was used in subsequent analyses due to the disturbance of a number of GCPs by livestock, and holes in the output orthophoto and DEM relating to the presence of large trees. The handheld controller displays an estimate of flying altitude (based on barometric pressure) in real time, which was monitored throughout each flight to ensure target heights were maintained. However, it should be noted that in practice it is difficult to maintain flight altitude precisely, especially in areas of high topographic diversity.

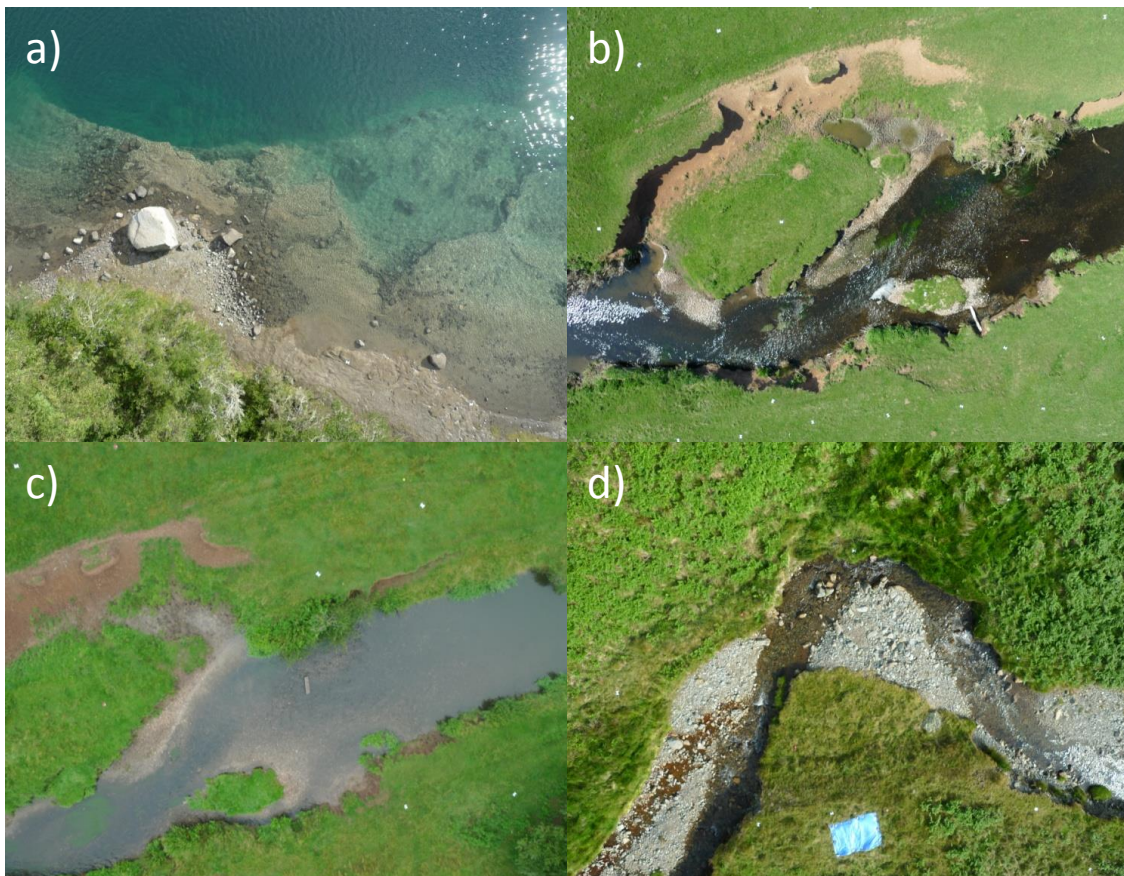


Figure 2.14. Example images acquired using the Panasonic Lumix DMC-LX3 camera mounted on the Draganflyer X6 at a) The San Pedro River, Chile, May 2012, b) The River Arrow May 2013, c) The River Arrow August 2013 and d) Coledale Beck, July 2013.

The camera focal length was manually set at 5.1mm to ensure that at the target altitude all imagery had a pixel size of c.1cm, as established during prior characterisation of the camera. Adequate site coverage was ensured by manual checking of images in between flights. Multiple flights were often required at each site due to limited battery life. The resulting size of each image was 3648 pixels by 2736 pixels, with data collected in the standard visible light

bands of red, green and blue. Some examples are given in Figure 2.14. Resulting image footprint size was approximately 25m x 35m. Images were collected with a high level of overlap (>80%) in order to allow for subsequent image matching and for processing using a SfM approach. The total number of images collected at each site is given in Table 2.2. In practice, these are collected over a number of separate flights due to the limited flight time permitted by each battery (c. 5 minutes). An estimate of the time required for the survey of each site is provided in Table 2.3. Typically, a 40-100m reach takes half a day for GCP set-up, multiple flights and image acquisition and survey of GCP positions. Reaches which are in the region of 200-300m long would usually take about a day.

*Table 2.2. UAS data collection information by survey. *Whilst a c.500m reach of the River Arrow was surveyed in July 2012, only 160m of this reach were used in subsequent analyses. (Some of the data used in this table also appear in Woodget et al., 2015).*

Site Location	San Pedro River	River Arrow				Coledale Beck
Date of survey	May 2012	July 2012	May 2013	June 2013	Aug 2013	July 2013
Approximate reach length (m)	200	500(160)*	50	50	50	120
Total no. of flights	7	4	3	2	2	3
Total no. of images acquired	210	151	93	69	70	88
No. of images used in SfM	128	132	58	41	32	64
No. of GCPs	20	39	21	22	16	25
Instrument used to record GCPs	Spectra Precision EPOCH 50 GNSS (dGPS)	Trimble R8 GNSS RTK GPS	Leica Builder 500 total station	Leica Builder 500 total station	Trimble R8 GNSS RTK GPS	Leica Builder 500 total station
Typical accuracy of instrument used for GCP surveying (m)	<0.010	<0.015	c.0.0015	c.0.0015	<0.015	c.0.0015
Average flying height (metres above ground level)	29.07	37.52	26.89	25.81	27.53	29.39
Co-ordinate system	WGS 1984 UTM Zone 18S	OSGB 1936 – British National Grid				

Table 2.3. Time required for UAS data collection and subsequent SfM processing (some of the data in this table also appear in Woodget et al., 2015).

Site Location	San Pedro River	River Arrow				Coledale Beck
Date of survey	May 2012	July 2012	May 2013	June 2013	Aug 2013	July 2013
Field set-up and image acquisition (inc. use of GCPs)	1 day	1 day	0.5 day	0.5 day	0.5 day	0.5 day
SfM image processing	1 day	1 day	0.5 day	0.5 day	0.5 day	0.5 day

2.4 Image selection

Following image acquisition, the suitability of each image was assessed for further processing. Each image is acquired at a slightly different viewing angle and may be subject to blur. Variation in these attributes between images (including blur) is unavoidable and is related to movement of the platform resulting from manual input and wind conditions. Image selection is therefore important to ensure only high quality images are used in subsequent analyses. Due to a high level of overlap between images, exclusions based on the selection criteria defined below could be made without creating gaps in image coverage. These criteria included;

- Camera tilt angle
- Visual image quality
- Platform roll angle
- Platform pitch angle

Many of these are determined through the use of information stored in a log file created by the Draganflyer X6's internal software during flight. This information is transmitted from the Draganflyer to the handheld controller and recorded on a Micro-SD card. All inputs to and movements of the Draganflyer X6 are recorded, as determined by the on-board sensor system. This is known as the SteadyFlight™ system, and includes three gyroscopes, three accelerometers, three magnetometers, a barometric pressure sensor and a GPS receiver. This information is useful for identifying problems during flight, but is also helpful in subsequent image selection. The log file is ordered in a time sequence which also records when each image was taken and the flight conditions at this exact moment (e.g. flight altitude). An extract from an example log file is shown in Figure 2.15.

	A	B	C	D	E	F	G	H	I	J	K	L	M	N	O	P	Q	R	S
1	System Time	PDOP	Horizontal Accuracy	Vertical Accuracy	GPS Altitude	SV	Hold Mode	Latitude	Longitude	North Velocity	East Velocity	Down Velocity	Right Mag	Forward Mag	Down Mag	Pressure Altitude	Battery Voltage	Throttle	Temperature
352	33421	2.9	2.6	3.4	109	6	0	-39.77172	-72.45949	0	0	-0.2	242	-95	259	5.2	17	0	13
353	33502	2.9	2.6	3.4	109	6	0	-39.77172	-72.45949	0	0	-0.3	241	-77	258	5.2	16	0	13
354	33583	2.9	2.6	3.4	109	6	0	-39.77172	-72.45949	0	0	-0.3	245	-83	259	5.2	17	0	13
355	33664	2.9	2.6	3.4	109	6	0	-39.77172	-72.45949	0	0	-0.3	240	-96	256	5.2	17	0	13
356	33745	2.9	2.6	3.4	109	6	0	-39.77172	-72.45949	0	0	-0.3	239	-94	258	5.2	17	0	13
357	33826	2.9	2.6	3.4	109	6	0	-39.77172	-72.45949	0	-0	-0.3	241	-94	255	5.2	17	0	13
358	33907	2.9	2.6	3.4	109	6	0	-39.77172	-72.45949	0	-0	-0.3	241	-94	255	5.3	17	0	13
359	33988	2.9	2.6	3.4	109	6	0	-39.77172	-72.45949	0	-0	-0.3	241	-94	255	5.3	17	0	13
360	34069	2.9	2.6	3.4	109	6	0	-39.77172	-72.45949	0	0	-0.3	244	-93	259	5.2	17	0	13
361	34150	2.9	2.6	3.4	109	6	0	-39.77172	-72.45949	0	0	-0.3	244	-93	259	5.2	17	0	13
362	34231	2.9	2.6	3.4	110	6	0	-39.77172	-72.45949	0	-0	-0.2	242	-94	256	5.3	17	0	13
363	34312	2.9	2.6	3.4	110	6	0	-39.77172	-72.45949	0	0	-0.2	241	-97	259	5.3	17	0	13

Figure 2.15. Extract from an example log file.

2.4.1 Camera tilt angle

The tilt angle of the camera is controlled manually during flight using a dial on the hand-held controller. This allows imagery to be acquired at any angle from horizontal (camera looking forward) to nadir (camera looking directly downwards). In the planning stages of this research, it was decided that imagery would be acquired at or close to nadir to (a) reduce the amount of geometric distortion within the imagery and (b) minimise the effects of refraction introduced by oblique viewing angles (see Chapter 3). However, since conducting this research it would seem that imagery collected at slightly oblique angles may be important for reducing systematic DEM errors – further discussion is provided in Chapter 3.6.1. It was also important for subsequent SfM processing that the imagery did not contain any view of the sky.

Within the Draganflyer log file, camera tilt angle is recorded using an arbitrary numerical system which ranges from 511 (fully horizontal) to -511 (fully vertical). The log files were used to select only those photos acquired when the camera tilt position was located in the vertical (-511) position.

2.4.2 Visual image quality

Images were assessed visually to ensure images were free from blurring, artefacts and other visible distortions. Given the relatively small numbers of images acquired for each survey, this

manual process did not take long. Images affected by these issues may cause problems during subsequent processing and analysis and therefore were removed. Examples of clear and blurred images collected at the San Pedro River are shown in Figure 2.16.



Figure 2.16. Examples of clear (a - left) and blurred (b - right) imagery.

2.4.3 Platform roll and pitch angles

The movement of an airborne platform in space is usually described in terms of its altitude, roll, pitch and yaw angles – as illustrated in Figure 2.17. Yaw angle relates to the direction in which the platform is facing (in terms of the compass direction) and in this case has no bearing on the quality of image outputs. However, changes in the roll and pitch angle disturb the platform from a level position resulting in tilting of the camera and lead to imagery becoming oblique rather than vertical. Oblique imagery features larger geometric distortions and increases the effects of refraction within submerged areas (see Chapter 3). Whilst the camera gimbal helps to reduce the impact of platform instability on images, experience with flying the Draganflyer indicates that large distortions can still occur.

A compromise must be reached in terms of the range of acceptable roll and pitch angles in order to minimise geometric distortion within the images whilst working within the operational demands of maintaining platform stability during flight. Platform stability is difficult to control manually, and the system is largely reliant on the SteadyFlight™ software to rectify extremes in roll and pitch angle. This becomes more problematic with increasing wind strength, as the platform is forced to sustain a pitched (or rolled) angle in order to maintain a stable position. Following initial test flights, it was thought that pitch and roll angles of +/- 5°

represented an acceptable amount of platform disturbance during flight. With greater flying and image processing experience, it was found that this could be increased to $\pm 12^\circ$ without compromising the quality of the outputs.

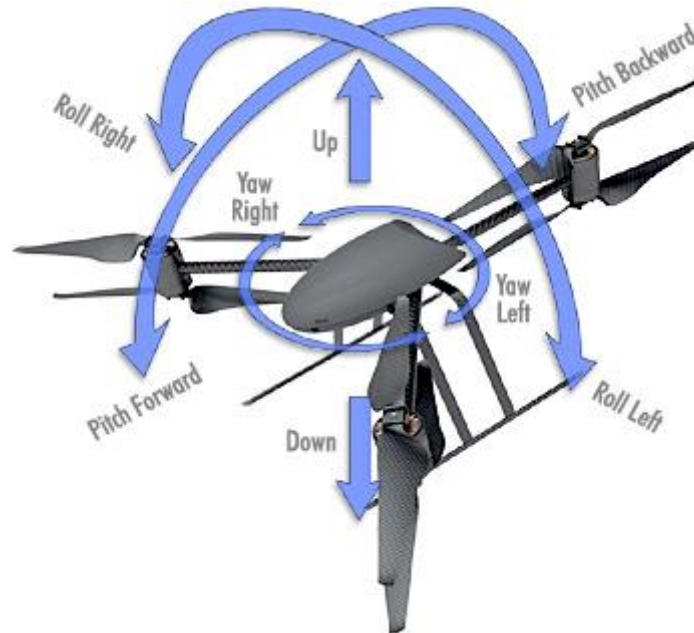


*Figure 2.17. Established measures of aircraft movement – altitude, roll, pitch and yaw
(Draganfly Innovations Inc. 2013).*

2.5 Structure-from-motion processing

The processing of imagery collected at all sites was carried out in PhotoScan Pro version 0.9.1.1714 (Agisoft LLC). This SfM-photogrammetry software package contains the necessary routines required to output rasterised DEMs and fully orthorectified imagery from the raw UAS imagery. The workflow is summarised in Figure 2.18. This section does not provide a detailed mathematical explanation of the SfM process, but instead aims to present an overview of each step and highlight the advantages of the approach for processing imagery acquired from a UAS.

2.5.1 Image import

The process commences with the straightforward uploading of images into the PhotoScan software. Table 2.2 details the number of images used for each survey.

2.5.2 Image alignment

The image alignment phase involves the use of advanced pattern matching algorithms to identify features that are present in a number of overlapping images (i.e. the same real-world features in multiple images). These 'features' are patches of distinctive image textures which are most prominent within the image dataset (James and Robson 2012). The algorithms used in the PhotoScan software to match these image features are thought to be similar to the Scale Invariant Feature Transform (SIFT) proposed by Lowe (2004), but the full details are not publically available. Such algorithms do not rely on the area-based cross-correlation strategies typically used in standard photogrammetry (e.g. Walstra et al., 2007, Lane et al., 2000), which establish conjugate point matches by maximising the correlations between image sub-regions (or templates) and as a result are highly sensitive to differences in scale, orientation and illumination. The use of a template in traditional photogrammetry also leads to a reduction in effective DEM resolution by a factor corresponding to the image template size.

In contrast, the SfM algorithms instead rely on the detection of local image gradients at multiple scales. A hierarchical system is implemented, whereby the image dataset is separated into small groups which are each assessed for successful point matches. The camera parameters, camera orientations and scene geometry are computed for each of these small groups using successive least squares bundle adjustments. The separate groups are then gradually aggregated to create the complete geometric scene. This process allows sub-pixel matching accuracy with invariance to scale, orientation and illumination (Lowe 2004, Snavely et al., 2006, Snavely et al., 2008). Additionally, the advanced feature matching algorithms used in SfM are very computationally efficient meaning that image pre-ordering is not necessary. As a result, the SfM process is, in theory, well suited for use with non-metric UAS imagery.

As with traditional photogrammetry, it is also important to account for image distortions relating to the camera lens (Lane et al., 2000). The PhotoScan software uses the Brown model (Brown 1966, Agisoft LLC 2013) during the image alignment phase, to implement an iterative, auto-calibration approach to estimate and refine extrinsic and intrinsic camera parameters during a bundle block adjustment (Agisoft LLC 2014, *pers. comm.*). This process uses the EXIF header of each image file to calibrate the camera focal length, principal point offset, radial and tangential lens distortion (Agisoft LLC 2013). Further discussion on the importance of camera

lens calibration for accurate outputs from traditional photogrammetry (which is equally applicable to SfM-photogrammetry) is provided by Chandler (1999).

The alignment phase settings used for each survey were as follows;

- *Accuracy: High.*

The 'high' accuracy setting uses the original images to conduct the image alignment. The 'medium' accuracy setting uses images downsampled by a factor of two and lower accuracy settings use even more downsampled images (Agisoft LLC 2014, *pers. comm.*). As a result, the higher the accuracy setting, the greater the processing time, but this results in more accurate camera positioning.

- *Pair preselection: Generic.*

This setting helps to speed up the alignment process by finding overlapping images by matching downsampled images first, and then performing the full scale image alignment using pairs of the original images (Agisoft LLC 2014, *pers. comm.*).

This process results in the positioning and aligning of each image and the generation of a sparse point cloud representing the locations of prominent image features in relative space (i.e. an arbitrary co-ordinate system). The point clouds for each survey were viewed within PhotoScan and manually edited to remove small numbers of obviously erroneous points. Manual editing has clear limitations in terms of user subjectivity and lack of exact repeatability, but provides a rapid approach for the removal of outliers. Recent updates to the PhotoScan software mean it is now possible to also build a dense point cloud at this stage, but this was not an option at the time of processing imagery for this research.

2.5.3 Geometry building

Following image alignment, the edited point cloud is used to generate the topography of the scene, again in a relative co-ordinate system. The process uses a multi-view stereo-reconstruction on the pixel values of the aligned images (Verhoeven 2012) to build the model geometry and generate a dense point cloud. The following settings were used for each dataset;

- *Object type: Height field.*

This option is recommended for planar UAS image sequences, rather the alternative 'arbitrary' setting which may be more useful for modelling 3D objects. It results in the

creation of a 2.5 dimension surface, where the aim is to produce a single elevation (z) value for each planimetric (x, y) location.

- *Geometry type: Sharp.*

This setting is recommended for more faithful scene reconstructions, so that the model would not be subject to interpolation, even in areas where the point cloud is very sparse.

- *Target quality: Medium.*

This quality setting has a similar meaning to the accuracy setting chosen in the image alignment phase. The 'ultra high' setting uses every pixel of the original images to densify the point cloud. Each lower quality step uses a downscaling of the original images by a factor of two (Agisoft LLC 2014, *pers. comm.*). Higher quality settings were initially tested and found to produce large holes in some parts of the scene. The 'medium' quality setting was subsequently chosen to reduce the size of holes and represented a compromise between accuracy and processing speed.

- *Face count: 0.*

This specifies the maximum face count in the output mesh. At the time of processing, the PhotoScan manuals suggested inputting 0 if subsequent decimation of the mesh was not required. The most up-to-date version of the software now gives recommended values of High/Medium/Low depending on the size of the initial point cloud.

- *Filter threshold: 0.5.*

This is the maximum face count of small interconnected components to be removed after the building of the model geometry, as a percentage of the total face count. The default setting is 0.5 and other values were not tested within this research.

- *Hole threshold: 0.1*

This is the maximum size of holes to be interpolated across following the building of model geometry, as a percentage of the total surface area. The default setting is 0.1 and different values were not tested within this research.

The output of this phase is a 3D model which may be viewed as a solid, shaded model, a wireframe mesh or a dense point cloud.

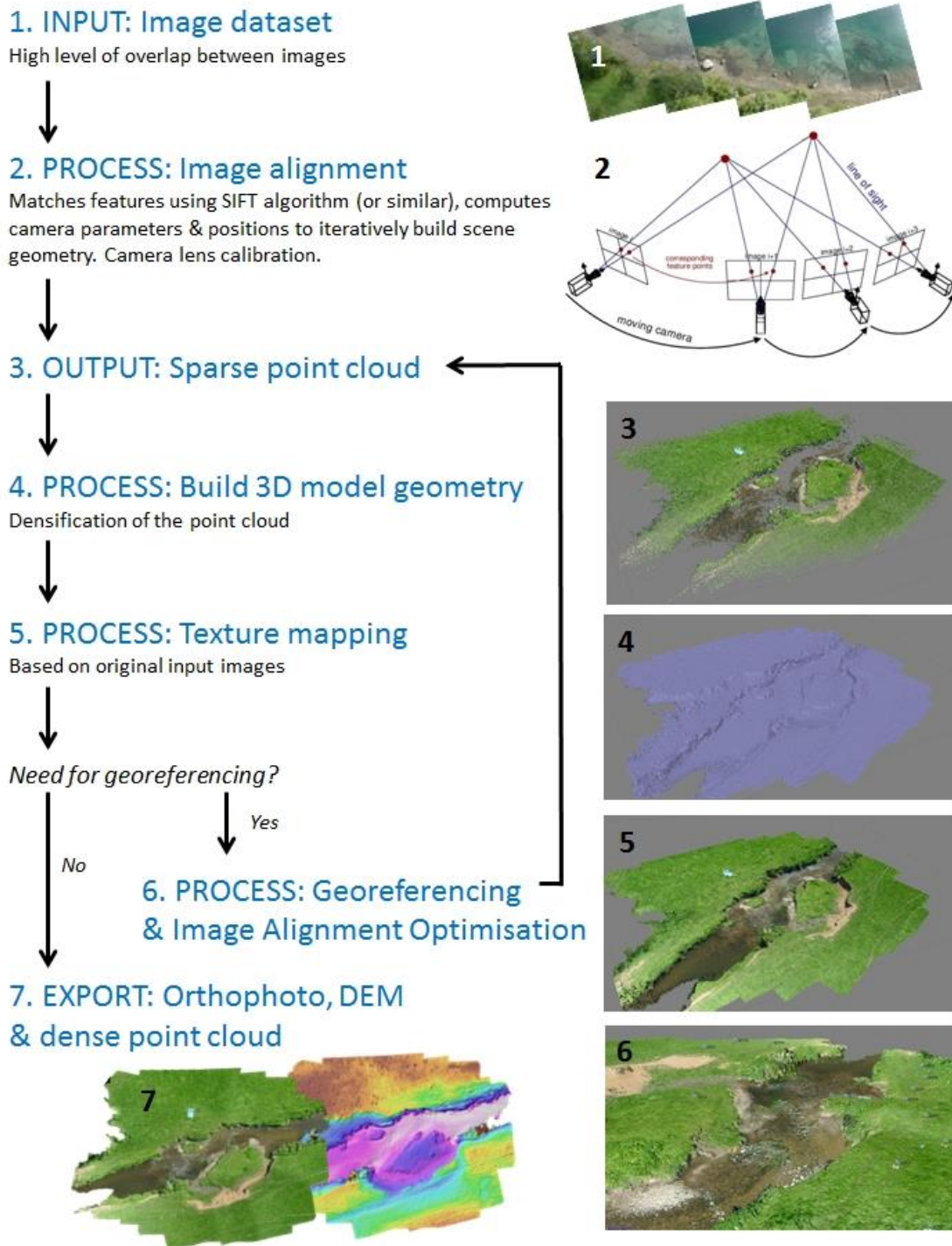


Figure 2.18. Overview of the SfM process, as implemented using the Agisoft PhotoScan Pro software. Image in step 2 sourced from University of Hannover (2013).

2.5.4 Texture building

Following construction of the relative geometry, the 3D model is textured using the raw image pixel values. Essentially, the imagery is draped over the built geometry and fills the gaps in

areas where points do not exist. This step is purely visual and therefore has no influence on the subsequent production of the digital elevation model. The following settings were used for all datasets;

- *Mapping mode: Orthophoto.*
This setting textures the whole surface of the model using an orthographic projection.
- *Blending mode: Mosaic.*
This setting is recommended for orthophoto generation, as it does not mix pixel information from overlapping images like the 'average' mode but instead uses a single image thereby providing a better quality mosaic.
- *Atlas width and height: 10,000.*
This was the default setting and other values were not explored.

2.5.5 Georeferencing

In order to be useful for quantitative geomorphological investigations, the geometric model (and associated point cloud) needs to be scaled, translated and rotated into a relevant geographic co-ordinate system. This was implemented using an indirect approach and used a rigid seven parameter transform, consisting of one scale parameter which applies to all three dimensions, three translation parameters in X, Y and Z and three rotation parameters around the X-axis, Y-axis and Z-axis. These transformation parameters were calculated automatically within the PhotoScan software by relating the positions of the GCPs in the geometric model to their real-world co-ordinates. The locations of GCPs for each survey were identified visually on the textured model and their positions checked on the original input imagery. Then, their associated XYZ co-ordinates (as surveyed in the field) were imported into PhotoScan and used in a least squares sense to derive the relevant transformation parameters and georeference the model. In theory this process requires a minimum of just three GCPs (James and Robson 2012). In practice, more GCPs will produce a better model registration, but it has not yet been firmly established what the optimum number of GCPs is or how they should be distributed for use within a UAS-SfM workflow.

This SfM georeferencing procedure is markedly different from traditional photogrammetry in that the GCPs are not inputted at the start of the photogrammetric process, they are added later, after the image matching has been carried out. The subsequent use of a least squares, rigid-body transformation then provides a linear, affine transformation of the model and does

not remove any higher order, non-linear distortions resulting from the model generation process. The main source of non-linear distortions is the auto-calibration of the camera lens performed during image alignment (James and Robson 2014). As a result, next it is necessary to perform a process which PhotoScan terms 'optimisation' of the initial image alignment.

2.5.6 Optimisation

Following georeferencing, the optimisation procedure implemented in PhotoScan is conducted to refine both the extrinsic and intrinsic camera parameters within the camera lens model. This process is usually based on the weights of the camera, marker and projection accuracy values specified by the user (below) (Agisoft LLC 2014, *pers. comm.*), but may be implemented using the positions of markers (GCPs) alone where camera co-ordinates are not known. The optimisation procedure has the effect of minimising geometric distortions within the 3D model by using the known GCP positions (and camera positions if available) to refine the camera lens model and re-align the images. The following settings were used within the optimisation process for all datasets;

- *Camera accuracy: Not applicable.*
This setting was not implemented by the optimisation process because camera co-ordinates were not known.
- *Marker accuracy: 0.1m.*
This was a conservative estimate based on limited knowledge at the time of processing. Recent updates to the PhotoScan user manual suggest that if GCPs are to be used in the optimisation process (as they are here), then marker accuracy should be set at zero (Agisoft LLC 2013). This setting has also been adopted by recent publications (Javernick et al., 2014) but further testing is required to quantify how this impacts the quality of outputs.
- *Projection accuracy (pixels): 0.1.*
This value provides an estimate of how accurately the markers have been placed on the imagery. At the time of processing a setting of 0.1 was the default option and other settings were not explored within this project.

The built model geometry is cleared by the optimisation process, so a number of earlier steps must be performed again, as specified below. It is possible to carry out the georeferencing on

the sparse point cloud, prior to the first building of geometry and texture mapping. Whilst this would save processing time, it was found that the accurate identification of GCP marker positions was more easily implemented on the textured model than on the sparse point cloud.

2.5.7 Model re-building

Following the optimisation procedure, the geometry of the model is re-built and the texture is recomputed for each survey dataset. The settings specified previously are again used for this process.

2.5.8 Export

At the end of the SfM process, the automated export function within PhotoScan was used to output orthorectified image mosaics and DEMs for each site, referenced to their respective UTM co-ordinate system (Figures A1 to A6 in Appendix A). Further detail concerning the spatial resolution of and residual errors associated with these products is provided in Table 2.4.

Table 2.4. Spatial resolution and residual errors associated with the orthophotos and DEMs produced using UAS imagery within the SfM workflow (some of these data also appear in Woodget et al., 2015).

Site location	San Pedro River	River Arrow				Coledale Beck	
Date of survey	May 2012	July 2012	May 2013	June 2013	August 2013	July 2013	
Spatial resolution of orthophoto (m)	0.007	0.013	0.009	0.009	0.009	0.010	
Spatial resolution of DEM (m)	0.020	0.051	0.018	0.018	0.019	0.020	
Mean of residual errors (m)	X	-0.001	0.006	0.006	-0.028	0.007	0.006
	Y	0.022	-0.011	-0.001	0.008	0.007	-0.007
	Z	-0.013	0.004	0.002	-0.001	-0.015	0.022
St. dev. of residual errors (m)	X	0.072	0.016	0.013	0.162	0.035	0.062
	Y	0.048	0.016	0.014	0.046	0.026	0.043
	Z	0.162	0.031	0.008	0.016	0.019	0.037

The residual errors were calculated by comparing the measured positions of all GCPs against their mapped positions on the orthophoto and DEM. This approach to calculating residual errors would not be acceptable in traditional photogrammetry because the GCPs are specified at an early stage in the process, and the model is built to ensure minimal error at the GCP

locations. In SfM-photogrammetry however, the model is created before the GCPs are added, and then adjusted. As a result, calculating the residual errors in this way is valid, but represents a slightly different method to classic error validation. Table 2.4 shows that the mean of X, Y residual errors is typically less than the spatial resolution of the DEMs. Larger residual errors occur in some places, as indicated by the standard deviation values also given in Table 2.4.

2.6 TLS data acquisition and initial processing

2.6.1 Background

Surveys conducted using a terrestrial laser scanner (TLS) were conducted at Coledale Beck, for comparison with the results of the UAS-SfM approach for quantifying topography (Chapter 3) and substrate size (Chapter 4). This work formed part of a collaboration with colleagues from Bath Spa University (BSU).

Data acquisition and initial processing of the TLS data, including merging scans, georeferencing, clipping data to the area of interest and removal of data spikes, were undertaken by colleagues from BSU (see Appendix A for division of work). The output of this process was a dense point cloud, on which the main analyses were then conducted. The TLS used is a Leica ScanStation C10 (Figure 2.19), a green wavelength (532nm) scanner with a 300m range, 360° by 270° field of view and scan speed of up to 50,000 points per second.

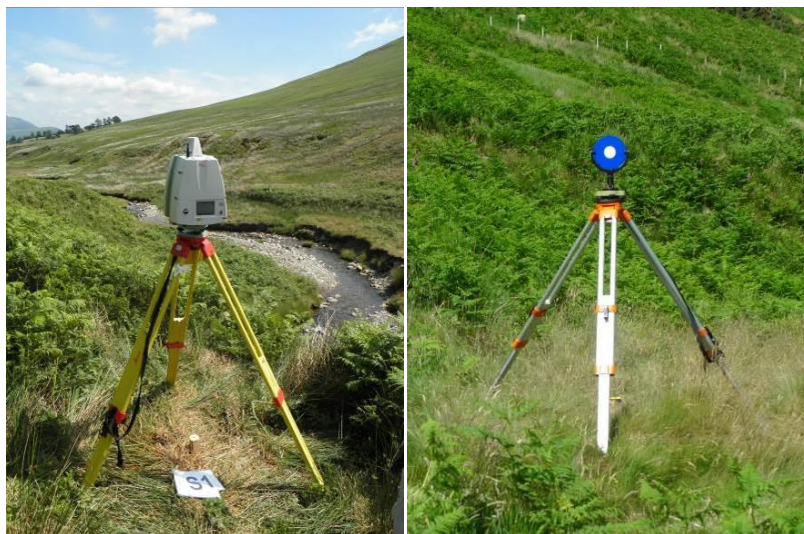


Figure 2.19. Leica ScanStation C10 terrestrial laser scanner (left) and Leica reflective targets (right), in use at Coledale Beck, July 2013.

2.6.2 Field set-up

Prior to data collection, a site assessment was undertaken to establish the optimal locations for scan stations and scan targets to ensure sufficient coverage of the c.120m reach at Coledale Beck. Elevated scan station locations were chosen to ensure higher angles of incidence and to reduce shadowing. Six reflective Leica targets were positioned at visible locations within the area of interest (Figure 2.20) and care was taken to ensure they covered the range of elevations present at the site. Each of these targets is mounted on a tripod (Figure 2.19) which was centred and levelled using an optical plummet. The targets positions were marked with a wooden stake and survey marker (Figure 2.21), and later recorded using a Leica GPS1200 dGPS and post-processed using RINEX data.

2.6.3 Data acquisition

Prior to the scanning process, the tripod-mounted Leica ScanStation C10 laser scanner (Figure 2.19) was centred and levelled at each scan position using a laser plummet, spirit level and dual access compensator. As for the targets, each scan position was marked with a wooden stake and survey marker (Figure 2.21), and later recorded using a Leica GPS1200 dGPS and post-processed using RINEX data. The reflective targets were tilted and rotated relative to the scanner position and their positions recorded by focussed, high resolution scans which were stored in the scanner memory and later used to assist accurate co-registration of the main point clouds. The scanner was then used to acquire high resolution laser scans (defined as 5cm resolution at 100m range) from eight different scan station positions. Each scan took approximately 45 minutes to acquire, with c.10-15 minutes set-up time between scans. In total, the TLS data acquisition took approximately nine hours.

2.6.4 Initial data processing

Initial processing of the dense TLS point cloud was undertaken entirely within the Cyclone software (Leica Geosystems HDS, LLC). This comprised co-registering of the eight separate scans using the known locations of each of the six reflective targets. During this process, those targets producing the greatest errors in the applied registration were removed (T4 and T6 – see TLS error diagnostics in Appendix A). The known positions of the remaining targets and scan stations acquired using dGPS were then used to georeference the merged scan to British National Grid co-ordinates. The full error diagnostics for this registration are provided in

Appendix A. The resulting overall mean absolute error was 0.009m, and average error in the vertical dimension was 0.026m.

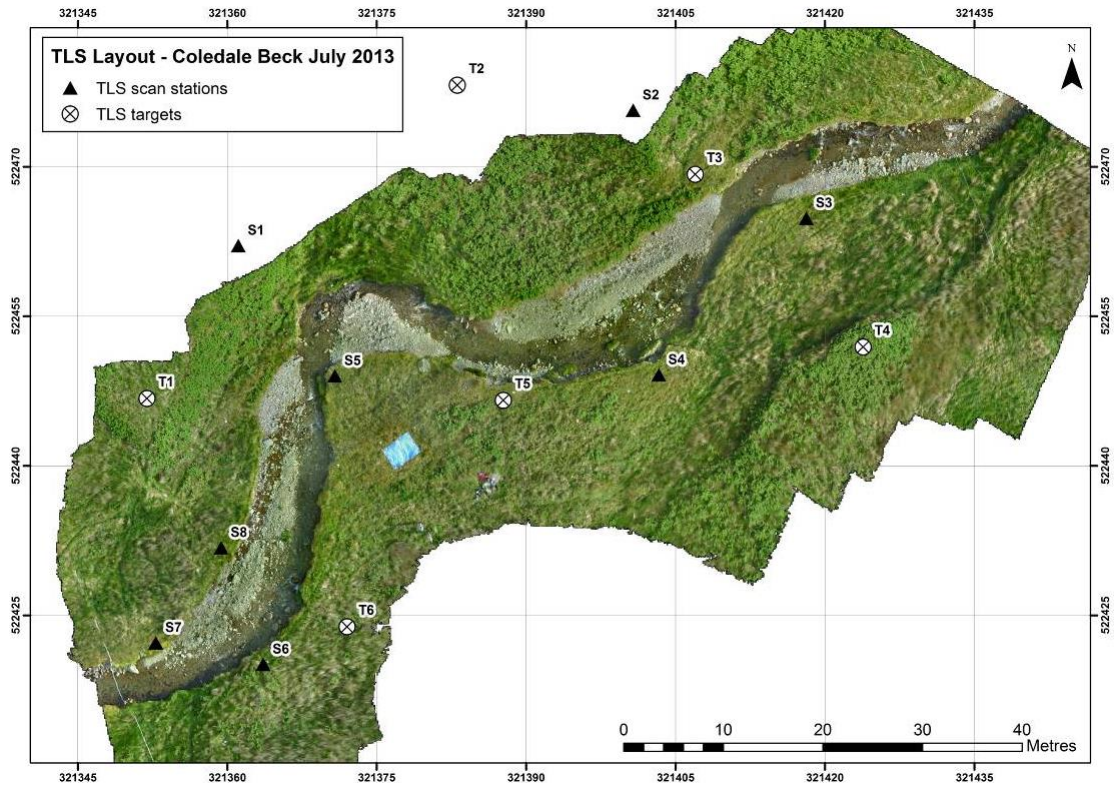


Figure 2.20. Location of TLS targets and scan station positions at Coledale Beck, July 2013.



Figure 2.21. Example of a marker established at Coledale Beck and used as TLS reflective target position markers and TLS scan station position markers.

Manual editing of the TLS point cloud was undertaken to remove clearly erroneous data spikes (due to sensor saturation by sunlight) and then to clip the dataset to match the approximate extent of the UAS survey. The resulting point cloud was exported from Cyclone as a PTS file comprising c. 165 million points with a file size of c. 9GB.

The point cloud was rasterised using code written in-house (R. Austrums 2014). The resulting TLS DEM had a spatial resolution of 0.013m. This pixel size was selected as a compromise between achieving the highest spatial resolution and minimising holes in the DEM in areas of sparser point density. This procedure also included a small amount of interpolation conducted using an iterative gap filling process. This process aims to fill some of the gaps (i.e. empty cells) in the DEM by interpolating the elevation data from those cells which surround the gaps and do contain data. This process is conducted in stages, or 'iterations'. For each iteration (of a total of ten), empty cells were given a value of the mean of all neighbouring cells, where the number of neighbouring cells totalled four or more. Whilst in theory this could result in interpolation over distances of up to 0.13m, in reality this interpolation rarely extended further than 0.05m and was not found to adversely affect subsequent analyses carried out on the TLS DEM. Chapters 3 and 4 describe the subsequent use of the TLS DEM and point cloud for quantifying fluvial topography and substrate size.

2.7 References

- Agisoft LLC. (2013) Agisoft PhotoScan User Manual: Professional Edition, Version 1.0.0.
- Brown, D.C. (1966) Decentering distortion of lenses. *Photogrammetric Engineering* 32 (3): 444-462.
- Chandler, J.H. (1999) Effective application of automated digital photogrammetry for geomorphological research. *Earth Surface Processes and Landforms* 24: 51-63.
- Draganfly Innovations Inc. (2013) Draganflyer X6 Photo Gallery (image). Available online: <http://www.draganfly.com/uav-helicopter/draganflyer-x6/gallery/pictures/picture-23.php> (accessed 10.05.2013).
- James, M.R. and Robson, S. (2012) Straightforward reconstruction of 3D surfaces and topography with a camera: accuracy and geosciences application. *Journal of Geophysical Research* 117, F03017, doi: [10.1029/2011JF002289](https://doi.org/10.1029/2011JF002289).
- James, M.R. and Robson, S. (2014) Mitigating systematic error in topographic models derived from UAV and ground-based image networks. *Earth Surface Processes and Landforms* 39: 1413-1420.

- Javernick, L., Brasington, J. and Caruso, B. (2014) Modelling the topography of shallow braided rivers using Structure-from-Motion photogrammetry. *Geomorphology* 213: 166-182.
- Lane, S.N., James, T.D. and Crowell, M.D. (2000) Application of digital photogrammetry to complex topography for geomorphological research. *Photogrammetric Record* 16 (95): 793-821.
- Lowe, D.G. (2004) Distinctive image features from scale-invariant keypoints. *International Journal of Computer Vision* 60: 91-110.
- Panasonic (2013) Panasonic Lumix DMC-LX3 (image). Available online: www.panasonic.co.uk (accessed 23.03.2013).
- Snavely, N., Seitz, S.M. and Szeliski, R. (2006) Photo tourism: exploring photo collections in 3D. *ACM Transactions on Graphics* 25 (3): 835-846.
- Snavely, N., Seitz, S.M. and Szeliski, R. (2008) Modelling the world from internet photo collections. *International Journal of Computer Vision* 80 (12): 189-210.
- University of Hannover (2013) Structure from Motion (image). Available online: http://www.tnt.uni-hannover.de/project/motionEstimation/triangulation_eng.png (accessed 30.12.2013).
- Verhoeven, G. (2012) 'Getting computer vision airborne – using Structure from Motion for accurate orthophoto production' *RSPSoc Archaeology Special Interest Group Meeting Spring 2012*, p. 4-6.
- Vericat, D., Brasington, J., Wheaton, J. and Cowie, M. (2009) Accuracy assessment of aerial photographs acquired using lighter-than-air blimps: low-cost tools for mapping river corridors. *River Research and Applications* 25 (8): 985-1000.
- Walstra, J., Chandler, J.H., Dixon, N. and Dijkstra, T.A. (2007) Aerial photography and digital photogrammetry for landslide monitoring. In Teeuw, R.M. (Eds) Mapping hazardous terrain using remote sensing. Geological Society, London, p. 53-63.
- Wheaton, J. (2012) Low-Altitude Blimps (Poor Man's Aerial Photography). Available online: <http://www.joewheaton.org/Home/research/tools/low-altitude-blimps-poor-man-s-aerial-photography> (accessed 10.01.2012).
- Woodget, A.S., Carbonneau, P.E., Visser, F. and Maddock, I. (2015) Quantifying submerged fluvial topography using hyperspatial resolution UAS imagery and structure from motion photogrammetry. *Earth Surface Processes and Landforms* 40 (1): 47-64.

Chapter 3

Quantifying fluvial topography using hyperspatial resolution UAS imagery and SfM-photogrammetry

Chapter Overview

The quantification of fluvial topography at high spatial and temporal resolutions is of fundamental importance for a range of river science and management applications, including investigations of flow hydraulics, sediment dynamics and fluvial habitats. Remote sensing has provided a range of approaches for this purpose which offer advantages over traditional topographic surveying. The most challenging region for topographic assessment using remote sensing however, remains the submerged channel, which often necessitates the use of a different technique to that used for exposed parts of the fluvial system. An ideal method would provide a single technique for rapidly quantifying fluvial topography in both exposed and submerged areas, with hyperspatial resolution (<0.1m), continuous coverage at the mesohabitat scale, high accuracy and reasonable cost. Such an approach is yet to be firmly established, even for application to relatively small, shallow streams.

In this chapter, a new approach is tested for filling this gap. Imagery is acquired from a small, rotary-winged unmanned aerial system (UAS) using a consumer grade digital camera and processed using Structure-from-Motion (SfM) photogrammetry to create hyperspatial resolution digital elevation models (DEMs) and orthophotos. The workflow is applied to three contrasting river sites; the River Arrow in Warwickshire, UK, Coledale Beck in Cumbria, UK and the San Pedro River, Chile. Errors resulting from the SfM process are also explored by testing the approach over a flat sports hall floor.

The results demonstrate that mean DEM errors vary within and between sites and are dependent on vegetation coverage, water depth, the spatial configuration of ground control points (GCPs) and the camera viewing angle. Mean errors are found to range from a minimum

of 4mm to a maximum of 44mm in exposed areas and from 17mm (min.) to 89mm (max.) in submerged areas. The use of a simple refraction correction improves errors in submerged areas to between 8mm (min.) and 53mm (max.). The River Arrow site was surveyed multiple times and consistently produces high quality results, indicating the repeatability of the approach. The results from Coledale Beck and the sports hall tests show a slight doming of the DEM, which are thought relate to the self-calibration of the camera lens within the software and the acquisition of imagery predominantly at nadir. GCP configurations were also found to effect final DEM errors significantly, as observed within the San Pedro River and the sports hall datasets. These findings highlight the importance of error assessment and suggest that the visually impressive UAS-SfM outputs are not error free. Comparison of the Coledale Beck DEM and a TLS dataset collected concurrently against an independent ground truth dataset suggests the UAS-SfM approach achieves topographic outputs of equivalent, if not better, accuracy and precision than the TLS. It is possible that a spatial misalignment may be affecting these results however.

Many of the findings reported within this chapter are also presented in Woodget et al., (2015), a copy of which is provided in Appendix B.

3.1. Background and Context

3.1.1 Fluvial topography

The geomorphology of a river system is a key influencing factor on the physical habitat template and has a direct impact on the ecological quality of the fluvial environment (Frissell et al., 1986, Newson and Newson 2000, Frothingham et al., 2002, Wiens 2002, Maddock et al., 2004, Dyer and Thoms 2006, Orr et al., 2008). Fluvial geomorphology comprises the size and shape of the channel, the size and structure of the banks, the size and shape of the material on the channel bed and the inclination or slope angle of the channel with distance downstream (Maddock 1999). This chapter is concerned with topography; a specific element of fluvial geomorphology which may be defined as the size and shape of the channel bed (submerged topography, or bathymetry) and the banks (exposed topography). Within this chapter, the terms 'topography' and 'morphology' are used interchangeably.

This chapter also considers another important physical habitat variable; flow depth. Whilst depth and topography are quite separate variables in terms of their impact on habitat availability and the ecological health of rivers, they are linked. Depth is dependent both on the local topography and the discharge level at a given time. The topography is typically less variable in time than depth, but is altered gradually by the processes of erosion and deposition and more rapidly during high stage flow events or by anthropogenic intervention (e.g. river engineering or restoration works). In studies looking to quantify physical river habitat variables, measurements of depth have been used to infer the underlying channel topography, where the elevation of the water surface is known (e.g. Lane and Carbonneau 2007, Legleiter 2012). The literature concerning the use of remote sensing approaches also tends to group together the characterisation of these two variables (e.g. Lejot et al., 2007). Thus, in order to avoid unnecessary repetition they are considered concurrently within this thesis.

3.1.2 The importance of topography and flow depth

Quantification of fluvial topography and flow depth at high spatial and temporal resolutions is of great importance for a number of applications within both river science and management arenas. This includes geomorphological assessment where three-dimensional data concerning river topography has the potential to enhance understanding of sediment dynamics and morphological change over time (Wheaton et al., 2010, Bangen et al., 2014). Topography and flow depth are also two of the key physical variables which govern the availability and quality of habitats within river systems. Measurement and monitoring of these variables therefore allows an understanding of the spatial distribution of physical habitat and how this might change with bed disturbances, flood events, channel engineering works and or flow regulation (Maddock 1999).

3.1.3 The measurement of topography and flow depth

Chapter 1 reviews a number of key paradigms which have been suggested in recent years for the conceptualisation and understanding of river systems. From this review emerge a series of key requirements, deemed necessary for the characterisation of river systems. These relate primarily to the nature of data collection concerning physical river habitat variables, both geomorphological and hydrological. In short, there is a need for approaches which provide the following:

1. Quantitative datasets collected by objective and repeatable methods, which may be used as baselines from which future change may be measured.
2. Spatially continuous datasets, available in three-dimensions, rather than two-dimensional point or line sampling.
3. Spatially explicit datasets (i.e. fully georeferenced) which can be easily integrated with other spatial datasets.
4. Datasets which cover large spatial areas, with high levels of detail.
5. Datasets which are not difficult to collect in terms of practicality, logistics and cost.

An approach which fulfils these requirements has the potential to characterise the spatial variability of fluvial topography in accordance with the ideals of the 'riverscape' concept (Fausch et al., 2002, Ward et al., 2002, Wiens 2002, Carbonneau et al., 2012). Traditionally, the measurement of channel topography and water depth has been undertaken using a series of fixed cross sections. These are usually located at pre-established locations downstream, and measurements are taken at regular intervals across the channel. Fixed cross sections may be resurveyed over time to monitor changes in topography and/or depth. Such approaches have typically made use of tape measures, a tacheometric staff and levelling equipment. More recently, similar surveys have been carried out using mapping- or survey-grade GPS (global positioning systems) devices and total stations, which offer increased accuracy and precision of measurements, and better geo-positioning.

In relation to the aforementioned key requirements, a number of critical drawbacks of these techniques can be identified (Table 3.1). Ground surveys of this nature are very time consuming and labour intensive, and are therefore often limited in spatial coverage. Typically, the location and spacing of cross sections is often determined by cost and practicality, rather than scientific design, and has been found to result in *"...major inaccuracies in the estimation of morphological change..."* (Lane et al., 1994, p.367). Furthermore, these techniques only offer measurements of topography or depth at specific points, rather than giving continuous coverage. It has been argued that these fundamental limitations restrict the reliable determination of channel morphology using these traditional techniques (Westaway et al., 2001, Westaway et al., 2003, Bangen et al., 2014).

Table 3.1. Assessment of traditional methods for quantifying fluvial topography and depth against the requirements of the ‘riverscape’ concept (Fausch et al., 2002).

Key requirement for characterising physical river habitat variables	Is this requirement met by traditional methods of surveying fluvial topography and depth?
(1) Quantitative datasets collected by objective and repeatable methods	Yes
(2) Spatially continuous datasets, available in three-dimensions	No
(3) Spatially explicit datasets	Sometimes
(4) Datasets which cover large spatial areas, with high levels of detail	No
(5) Datasets which are not difficult to collect in terms of practicality, logistics and cost	No

3.1.4 Quantifying fluvial topography and flow depth using remote sensing

What is ideally required for measuring topography and depth is an affordable, accessible technique which offers high spatial resolution and continuous coverage with high levels of accuracy. For many, the recent advances in remote sensing technologies and techniques have offered a promising alternative here. The aim of this section is to review and evaluate studies which have used remote sensing methods for quantifying fluvial topography.

Spectral-depth relationships

The spectral-depth relationship method is one of the most widely used for quantifying water depth from remote sensing data and has been performed using multispectral, RGB (true colour) and black and white imagery (e.g. Winterbottom and Gilvear 1997, Westaway et al., 2003, Lejot et al., 2007, Feurer et al., 2008, Legleiter 2012). The primary output of this approach is water depth data which is stage dependent, from which the submerged channel topography may also be inferred (e.g. Winterbottom and Gilvear 1997, Westaway et al., 2003, Legleiter 2012).

The successful application of this method makes use of the relatively strong absorption of light by water, which results in an empirical relationship between the water depth at a particular location and the spectral properties (or brightness levels) of an image acquired at that same

location at (approximately) the same time. In theory, shallower submerged areas should produce a brighter response and deeper areas a darker response (Lane and Carbonneau 2007, Marcus 2012). Typically, c. 1000 data points, covering the full range of depths present within the study site, are used to establish a correlation between water depth measurements collected in the field, and the corresponding image spectral properties (Westaway et al., 2003, Carbonneau et al., 2006). The derived relationship is then applied to the remainder of the image to estimate water depths.

The success of this approach is complicated however, by factors other than water depth influencing image brightness. This is formalised by Equation 1;

$$R = R_g + R_w + (R_b - R_w)e^{-Kz}$$

(Equation 1)

From Lejot et al., 2007

Where R is the overall reflectance of the signal, R_g is the reflectance contribution from the water surface, R_w is the reflectance contribution from within the water column (where the water bottom was not reached), R_b is the reflectance from the channel bottom, K is the effective attenuation co-efficient of the water and z is the depth of the water column (Lejot et al., 2007). This equation indicates that the following factors also influence the reflectance patterns shown within an image (Winterbottom and Gilvear 1997, Lejot et al., 2007, Lane and Carbonneau 2007, Bergeron and Carbonneau 2012, Marcus 2012):

- *The nature of the water surface.* Sun glint or high levels of surface roughness result in high levels of reflectance from the water surface which may overwhelm reflectance from the channel bed.
- *The nature of the channel bed, including substrate and submerged vegetation.* Different materials which form, or reside on, the channel bed may have different levels of albedo and therefore reflect different amounts of light from the channel bottom.
- *The conditions within the water column.* High levels of turbidity within the water column severely limit the penetration of light and therefore reduce or prevent reflectance from the channel bed.

- *The atmospheric conditions.* Spatial and temporal variability in levels of scene illumination influence the ingoing and therefore also the outgoing levels of reflectance.

If these factors can be assumed to be homogeneous within an image or within a part of the image, then a direct relationship between water depth and the reflectance signal can be assumed. Yet, this is not always the case, as demonstrated by the examples which follow.

Much of the early work using spectral-depth relationships was applied in coastal and estuarine environments, but since the mid-1990's these techniques have also been tested in a variety of fluvial settings (e.g. Winterbottom and Gilvear 1997, Westaway et al., 2003, Lejot et al., 2007, Feurer et al., 2008, Bergeron and Carbonneau 2012, Legleiter 2012). For example, the work of Winterbottom and Gilvear (1997) explored the potential of using multispectral imagery for mapping water depths within the River Tummel, Scotland. Using 7-band multispectral data, they found a good linear relationship between water depths and spectral properties ($R^2 = 0.67$), up to a depth of 0.60m. This represents the maximum depth estimation that was possible for this site, beyond which the technique could not accurately estimate water depth. The levels of turbidity were low during the image survey and instead it is thought that the high amounts of organic material within the water column were responsible for limiting the depth of light penetration. Accurate depth estimation also proved difficult in areas with high water surface roughness. This was particularly notable in areas of riffles, where the increased surface roughness caused higher levels of surface backscatter which resulted in depths being underestimated. Despite these limitations, Winterbottom and Gilvear (1997) concluded that multispectral imagery had clear potential for depth mapping and could provide a very valuable source of three-dimensional topographic data.

In a recent paper by Legleiter (2012), spectrally based methods were combined with airborne LiDAR for the characterisation of submerged topography. Multispectral image brightness values were correlated against measured water depth values obtained for the Soda Butte Creek and Lamar River within Yellowstone National Park, USA. Legleiter (2012) found similar results to those of Winterbottom and Gilvear (1997) in that it was more difficult to estimate the depth of the deeper parts of the channel. In particular, they found that highly turbid conditions resulted in the under-prediction of pool depths, and a maximum depth estimation of 0.53m was found. This led them to the conclusion that *“Accurate depth estimates can only*

be achieved under a specific, fairly restricted range of conditions, primarily shallow, clear-flowing streams with highly reflective substrates” (Legleiter 2012, p.515).

The spectral-depth method has also been applied to RGB imagery (Westaway et al., 2003, Lejot et al., 2007, Feurer et al., 2008). This is often more widely available and less expensive than multispectral imagery, and may be acquired from lightweight platforms operating at lower altitudes. This allows the collection of higher spatial resolution imagery, and thus also more detailed estimates of flow depth. For example, Lejot et al., (2007) used a UAS platform to acquire high resolution (3.6–14.0 cm) RGB imagery of the Ain and Drôme Rivers in southeast France. In this study, separate empirical spectral-depth relationships were developed for areas of different bed substrate type. This was aimed at accounting for the disparity in reflectance between different substrate types. In areas of aquatic vegetation, depth was best correlated with the green band, to give a co-efficient of determination of 0.90. Alluvial substrate however, was best correlated with the red band with an R^2 value of 0.81. The separate models were applied to the remainder of the image to estimate water depths. These estimates were typically within +/-10cm of the actual depths for areas of alluvial substrate and +/-4cm for areas of aquatic vegetation (Table 3.2).

The work of Lejot et al., (2007) observed large variations in natural illumination conditions between individual UAS images (Figure 3.1) in their application of the spectral-depth approach. An attempt was made to correct for these variations by standardising the image brightness levels before depth values were estimated (using a histogram matching approach). However, variable brightness levels were still found to be disrupting the derived relationships, even after the correction had been applied. This was considered to be a major factor limiting the quality of depth estimation from RGB imagery collected from a UAS.

The work of Carbonneau et al., (2006) also came up against the key issue of variable brightness within datasets containing multiple images. In their study for the Geosalar project, they found large differences in illumination over the 5550 RGB images acquired over an 80km length of the Ste-Marguerite River in Quebec, Canada. They used three individual images to show that these differences could be grouped into three clear parallel relationships between depth and brightness. This indicated that although the overall brightness values were different across the three images, the rate of light attenuation through the water remained the same. This allowed a straight-forward recalibration of image brightness and subsequent application of a single

spectral-depth correlation. Like others, Carbonneau et al., (2006) also note a maximum penetration depth for this approach of <1m.

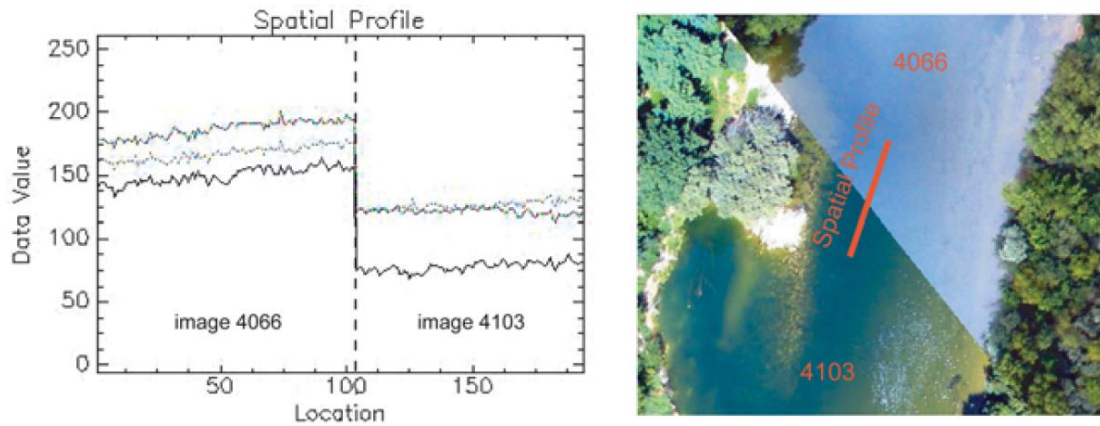


Figure 3.1. Radiometric differences between adjacent images (Lejot et al., 2007).

In summary, it has been shown that the spectral-depth method is capable of producing stage-dependent water depth outputs at spatial resolutions of c. 0.05m and mean errors of c. 0.10m (Table 3.2). It is therefore well suited to mesoscale studies. However, limitations of the method include:

- The method is image specific, so that a relationship developed in one location or at one time cannot be applied elsewhere or at a different time (Westaway et al 2003, Carbonneau et al., 2006, Bergeron and Carbonneau 2012).
- Significant field survey efforts are still required for the collection of depth data on which to base the empirical relationships.
- Maximum penetration depths of c. 1m render this method only really suitable for shallower, clear-flowing rivers (Westaway et al., 2003, Legleiter et al., 2004, Legleiter et al., 2009, Legleiter 2012).
- Variations in scene illumination, turbidity, substrate, cover and water surface roughness can impede accurate depth estimation (Winterbottom and Gilvear 1997, Legleiter et al., 2004, Legleiter et al., 2009).

Photogrammetric approaches

The main advantages of photogrammetry over traditional field sampling of topography are presented by Lane et al., (1993), along with an explanation of the workings of the traditional analogue (hard copy) and more recent analytical (digital) approaches to photogrammetry. A

review of the specific use of photogrammetry for river channel research prior to the year 2000 is provided by Lane (2000). Today, digital photogrammetry is widely used for rapidly generating topographic datasets within fluvial settings (Lane 2000, Westaway et al., 2001, Carbonneau et al., 2003, Lane et al., 2010). Typically, two-dimensional images acquired from a number of different viewing positions are used to reconstruct the three-dimensional geometry of a scene or object shown within the images. These approaches usually require numerous overlapping images which have been acquired in parallel flight lines from manned aircraft, as well as information concerning the altitude and orientation of image acquisition, the camera focal length and a series of ground control points of known positions. Collinearity equations, which relate the 2D co-ordinates within a camera to the 3D co-ordinates of the scene, are then solved, usually using a least-squares bundle adjustment (Lane et al., 1994, Chandler 1999). This process results in the production of continuous topographic datasets, often in the form of digital elevation models (DEMs).

Photogrammetric approaches have a long history for the generation of topographic data, but only since the mid-1990s have they seen significant application to studies of the fluvial environment (e.g. Lane et al., 1994). It is suggested that this is due to the following challenges (Lane 2000, Marcus 2012):

- River channels typically have low relative relief. In order to quantify this in sufficient detail, imagery needs to be acquired at low flying altitudes.
- Overhanging vegetation can obscure fluvial topography and cause problems for matching imagery acquired at different viewing angles.
- Different approaches are needed for exposed and submerged topography, due to the refractive effects of water.

However, despite these challenges, a number of recent publications have highlighted the potential of photogrammetric approaches for mapping both exposed and submerged parts of the fluvial topography (Westaway et al., 2001, Westaway et al., 2003, Lejot et al., 2007, Feurer et al., 2008, Lane et al., 2010).

The work of Westaway et al., (2001, 2003) has been particularly key in this area. This research focussed on the use of through-water digital photogrammetry for the construction of DEMs using black and white aerial imagery of the North Ashburton River, a shallow, clear-flowing, gravel-bed river in New Zealand. Through-water photogrammetry is complicated by two main

factors (1) the refraction of light at the air-water interface and (2) the inability of the camera to ‘see’ the channel bed where water depths are very deep or where it is obscured by high levels of turbidity or surface roughness (Westaway et al., 2001, Feurer et al., 2008, Marcus 2012). The latter issue remains a limiting factor in the application of digital photogrammetry to submerged areas, but procedures may be implemented to ameliorate the former, as described below.

Table 3.2. Comparison of topographic products obtained using the four most popular remote sensing techniques during field tests. Values for submerged areas are shown in italics (Woodget et al., 2015).

Approach	Typical mean error (m)	Typical spatial resolution (m)	Typical mean depth (m)	Typical max. depth (m)	References
Spectral-depth relationship	<i>0.10</i>	<i>0.05 – 4.00</i>	<i><1.00</i>	<i>1.00</i>	Winterbottom and Gilvear 1997, Westaway et al., 2003, Carbonneau et al., 2006, Lejot et al., 2007, Legleiter et al., 2004, 2009, Legleiter 2012, 2013.
Digital photogrammetry	0.05- 0.17 <i>0.10</i>	0.05 – 1.00 <i>0.09</i>	N/a <i><0.60</i>	N/a <i>0.60</i>	Westaway et al., 2001, Westaway et al., 2003, Lejot et al., 2007, Feurer et al., 2008, Lane et al., 2010
Bathymetric LiDAR	<i>0.10- 0.30</i>	<i>1.00</i>	<i><1.00</i>	<i>3.90</i>	Kinzel et al., 2007, Feurer et al., 2008, Bailly et al., 2010, 2012
TLS	0.004- 0.03 <i>0.01- 0.10</i>	<0.05 <i>1.00</i>	N/a <i>0.10</i>	N/a <i>0.50</i>	Heritage and Hetherington 2007, Bangen et al., 2014, Smith and Vericat 2014

The geometry of the refraction of light as it passes through the air-water interface is described by Snell’s Law (Equation 2) and shown in Figure 3.2;

$$\frac{\sin r}{\sin i} = \frac{h}{h_A} = \frac{n_1}{n_2}$$

Equation (2)

Where r is the angle of the refracted light ray above the water surface, i is the angle of the incident light ray originating from below the water surface, h is the true water depth, h_A is the apparent water depth, n_2 is the refractive index of air (which has a value of 1) and n_1 is the refractive index of water. For clear water, n_1 has a value of 1.34, which varies very little for a range of temperature (0 to 30°C) and salinity (0 to 40 ‰) conditions (Jerlov 1976). If uncorrected, this two-media refraction problem results in the overestimation of true bed elevation (i.e. an underestimation of water depth), as shown in Figure 3.2 (Fryer 1983, Fryer and Kneist 1985, Westaway et al., 2001, Butler et al., 2002). However, with the knowledge of apparent water depth (h_A) and the refractive index of water (n_1), the true depth (h) can be estimated using a simple refraction correction, as shown in Equation 3;

$$h = n_1 \times h_A$$

Equation (3)

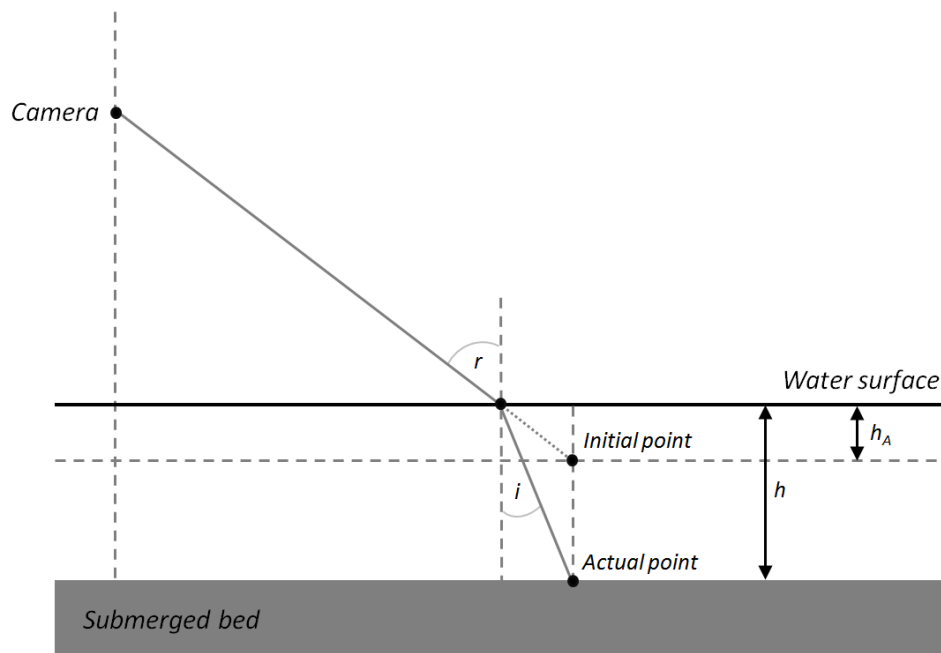


Figure 3.2. The relationship between camera location, water surface elevation, apparent water depth (indicated by the initial point) and actual water depth (indicated by the actual point). Not to scale (after Westaway et al., 2001, Woodget et al., 2015).

This simple correction procedure was first used by Westaway et al., (2000) to adjust digital photogrammetric outputs for submerged parts of the fluvial environment, where the

positioning of the water surface was estimated, the imagery was acquired at vertical view angles and where the submerged bed was visible. The resultant, corrected DEMs produced using this simple method were found to have levels of accuracy and precision commensurate to those produced for exposed topography in areas of shallow water (i.e. depths <0.4m). However, with increasing depth the accuracy and precision of elevation estimates was found to deteriorate, with a systematic bias towards the overestimation of bed elevations (Westaway et al, 2000). A more complex correction procedure was later tested by Westaway et al., (2001), where the exact camera positions were taken into account. However, this more complex method did not significantly improve the quality of results, and yet increased computation times. Both studies noted that clear and relatively shallow waters produced the most accurate results (Westaway et al., 2000, Westaway et al., 2001, Feurer et al., 2008).

In a follow up paper, Westaway et al., (2003) again used digital photogrammetry for estimating fluvial topography from aerial photography, but this time only in exposed areas. They did not choose to apply this method to submerged areas again. Instead, they propose the use of a spectral-depth relationship method for submerged zones due to the higher levels of turbidity present within the water of this particular river. They argue that “...*digital photogrammetry alone is unsuitable for surveying submerged topography where the water is turbid*” (Westaway et al., 2003, p. 804). More recently, Lane et al., (2010) reports that a digital photogrammetry approach is insufficient for quantifying the submerged topography of a sand-bed river due to the lack of image texture. The focus of this study is instead upon using the sparse points generated by the two-media photogrammetry, which alone are insufficient for DEM generation, as calibration data for a spectral-depth approach based on the same imagery. This method therefore has potential for reconstructing the topography of submerged environments from historical imagery, without the need for field-based calibration data.

Following these studies, some recent research efforts in digital photogrammetry have focussed on the use of higher resolution imagery in order to test the ability of this method to produce higher resolution and higher accuracy DEMs of small areas of the fluvial landscape. For this purpose, unmanned aerial systems (UAS) have been proposed as alternative platforms for data collection given their ability for flying at lower altitudes and for rapid, flexible data acquisition (see Chapter 1).

Lejot et al., (2007) tested the use of a motorised paraglider type UAS for collecting aerial imagery of two exposed gravel bars on the Ain and Drôme Rivers in southeast France. This study tested a spectral-depth approach, as described above, as well as digital photogrammetry. The output photogrammetry DEMs from this study had a spatial resolution of 5-10cm and a vertical accuracy of c.10cm. This level of detail is much greater than that obtained previously (using conventional aerial photography) and was found to be sufficient for mapping gravel bar microtopography, including the location and size of medium size pebbles and woody debris (Lejot et al., 2007). It was also acknowledged however, that the limited UAS payload capability currently constrains the calibre of sensor which may be carried and restricts the level of information available concerning external flight parameters. Improvements in both these factors would help to improve the quality of DEMs produced by photogrammetric processing.

Another high spatial resolution study was published by Feurer et al., (2008), exploring the potential of through-water photogrammetry using imagery collected by hand from a low flying aircraft over the Durance River, France. A polarising filter was used in order to try and eliminate unwanted reflection from the water surface and careful processing was necessary to account for the refraction effect. The output DEM resolution was 0.09m, with a mean error of 0.10m and a standard deviation of 0.19m. Despite this high spatial resolution, the levels of turbidity within the water column meant that the detection of individual pebbles was found to be challenging, especially in areas of deeper water (up to 1.6m). The accuracy of the output DEM was also found to be highly sensitive to the accuracy and precision of the GCPs used as input to the photogrammetric process.

Digital photogrammetry is clearly capable of producing DEMs of both the exposed and submerged topography within fluvial environments. The typical values for accuracy and spatial resolution of these DEMs are provided in Table 3.2, and are highly dependent on the following factors:

- *The platform altitude and payload capabilities.* The use of lower altitude platforms typically produces higher resolution imagery, but the lightweight platforms capable of flying low also lack the payload capabilities to carry INS (inertial navigation systems) and dGPS devices. This can limit DEM accuracy and results in the need for a series of highly accurate GCPs (Lejot et al., 2007, Feurer et al., 2008).

- *The depth of the water.* Accuracy and precision of DEMs has been shown to decrease with increasing water depth, as the photogrammetric approach fails to ‘see’ the true location of the river bed (Westaway et al., 2001, Marcus 2012). This relates to the issue of maximum light penetration depth, as also found with the spectral-depth and physically-based model approaches.
- *The water clarity.* Higher levels of turbidity within the water column limit the ability of the photogrammetric approach to accurately estimate submerged bed elevations (Westaway et al., 2003, Feurer et al., 2008, Marcus 2012). This was also found to be an issue in the use of the spectral-depth approach.

Airborne and Bathymetric Laser Scanning

The use of airborne LiDAR (Figure 3.3) for the generation of DEMs in areas of exposed terrain is widespread and has become well established for fluvial applications within the last decade (e.g. Storesund and Minear 2006, Cavalli et al., 2008, Legleiter 2012). Typically, airborne laser scanning systems emit radiation in the eye-safe near-infrared wavelengths (e.g. 1064nm). Whilst this provides highly accurate topographic information for exposed terrain (such as floodplains), the near-infrared radiation is strongly absorbed by water. This results in the majority of laser pulses not returning to the LiDAR sensor, and therefore estimation of topography in submerged areas is usually impossible.

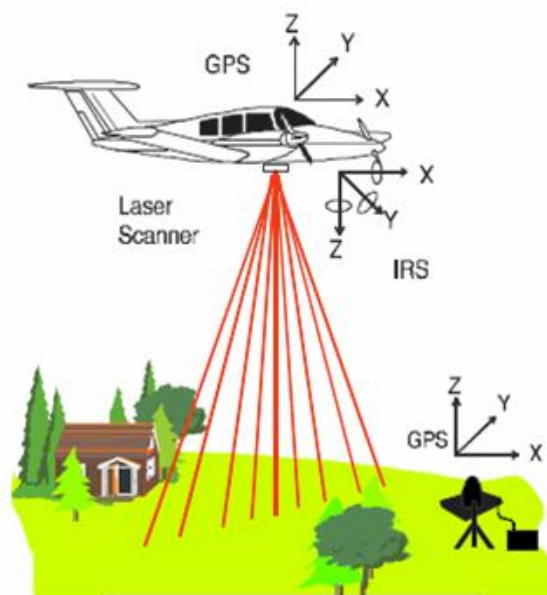


Figure 3.3. Schematic diagram to show the typical set-up of an airborne LiDAR system (Mosaic Mapping Systems Inc, 2001).

Recently, the emergence of blue-green or bathymetric LiDAR systems has provided a new approach for mapping submerged fluvial topography (e.g. Kinzel et al., 2007, McKean et al., 2009, Bailly et al., 2010). These sensors emit radiation with wavelengths typically in the green part of the spectrum (e.g. 532nm), which are capable of penetrating the water surface with limited attenuation (Bailly et al., 2012). Back-scatter to the bathymetric LiDAR sensor is usually received as two peaks, representing reflectance from the water surface and from the channel bed (Bailly et al., 2012, Marcus 2012). Typically, this approach is capable of measuring maximum water depths of up to three times the Secchi depth¹ in clear water, and up to two times in more turbid waters (Feurer et al., 2008, Marcus 2012). This approach also suffers from a lack of reliability in shallow waters however. This occurs because the separation of reflectance signals from the water surface and the channel bed, required to quantify the submerged topography, becomes increasingly challenging at water depths less than c. 0.3m (Bailly et al., 2010, Marcus 2012).

Bathymetric LiDAR systems remain in an early phase of development and application to fluvial environments has only occurred recently. Of the few published studies to date bathymetric LiDAR has been found to be less affected by issues of shadowing, water surface texture, sun angle and glint than typical passive remote sensing approaches to depth and topography mapping (Marcus 2012). Where reported, the maximum penetration depths of this technique are significantly greater than those obtained using the spectral depth or photogrammetric approaches (Bailly et al., 2010, Kinzel et al. 2013) (Table 3.2). At present however, the use of a bathymetric LiDAR approach for mesoscale fluvial topographic assessment is severely limited by high cost, restricted sensor availability and coarse spatial resolution and a lack of reliability in shallower areas. Furthermore, typical accuracies are not as high as those reported for spectral-depth and digital photogrammetry approaches, as demonstrated in Table 3.2 (Kinzel et al., 2007, Feuerer et al., 2008, McKean et al., 2009, Bailly et al., 2010, Bailly et al., 2012, Hicks 2012, Marcus 2012, Kinzel et al., 2013).

Terrestrial laser scanning

Laser scanning techniques have also been employed from ground-based platforms for the characterisation of fluvial topography, where they are typically known as TLS (terrestrial laser scanning/scanners). TLS systems were first developed in the late 1990s, and since then have been

¹ The Secchi depth is the maximum water depth at which a traditional black and white Secchi target disk can be seen from above with the naked eye (Marcus 2012).

used for characterising topography in a variety of settings (e.g. landslides - Dunning et al., 2009, coastal erosion - Rosser et al., 2005). Quantifying topography using TLS typically involves the collection of multiple, oblique scans acquired from a number of different locations or viewing points. This helps to alleviate gaps or occlusions within the data which might otherwise result from shadowing. A series of static reflective targets are distributed throughout the area of interest and used as markers for stitching the individual scans together. Given the close range of this approach, it is known for providing highly detailed topographic data.

Within fluvial settings, TLS has seen increasing use in recent years although has been focussed predominantly on exposed topography. For example, the work of Heritage and Milan (2009) used TLS to create a very high resolution DEM (0.05m) of an exposed point bar on the South Tyne River in Northumberland, UK. The average point spacing within the laser point cloud for this dataset was 0.012m. This density of data allowed the generation of a variety of grain size maps (a subject which is discussed further in Chapter 4). Over a larger area, the work of Heritage and Hetherington (2007) used TLS to generate a high resolution DEM of the exposed areas of an upland reach of the River Wharfe in North Yorkshire, UK. The collection of 21 separate scans allowed the generation of a 0.01m resolution DEM over a 150m x 15m area, with a mean error of 0.004m (Table 3.2) and standard deviation of 0.167m. They reported that 55% of the data was accurate to within 0.02m. This data was sufficiently detailed as to characterise areas of riverbed gravels, bedrock and riparian vegetation.

A number of other studies have also reported the successful use of TLS for characterising the topography of fluvial environments (Hetherington et al., 2005, Milan et al., 2007, Entwistle and Fuller 2009). Due to the use of infrared wavelength TLS systems however these studies have considered only the dry, exposed, exposed element of fluvial topography. Heritage and Hetherington (2007) did note some returns from clear, calm waters within shallow pools and along the channel edges, but the assessment of submerged topography using TLS has been largely unstudied. The exception is recent work by Smith et al., (2012) and Smith and Vericat (2014). These papers have, for the first time, examined the potential of green wavelength (532nm) TLS for through-water topographic assessment. Green wavelengths of light are much less strongly absorbed in water yet the effects of refraction of the laser beam at the air-water interface were found to introduce significant systematic errors, given the strongly oblique viewing angle of the TLS. Whilst these studies have provided important advances in the field

testing of TLS systems and suggest that TLS is capable of providing a single technique for surveying both the exposed and submerged parts of the fluvial environment, further testing of the approach in a variety of field settings is still needed. TLS approaches have not yet been shown to provide centimetre resolution topographic data over mesoscale extents without significant and time consuming field efforts.

TLS approaches are clearly capable of collecting higher resolution and higher accuracy topographic data within fluvial environments than other remote sensing techniques (Table 3.2). However, TLS is not without its drawbacks. For instance, field data collection is time-consuming and labour intensive and multiple scans are usually necessary to ensure sufficient overlap and to avoid holes due to shadowing. TLS DEMs often have limited spatial coverage and atmospheric conditions, such as rain and fog, can lead to spurious results (Heritage and Hetherington 2007). Perhaps most importantly, applications to submerged areas of the fluvial environment are currently very limited, and require further development (Smith et al., 2012, Smith and Vericat 2014).

Other Approaches

The past 20 years or so has also seen the testing of other remote sensing techniques for surveying fluvial topography, including ground penetrating radar (GPR) and range imaging. Studies using GPR have predominantly been spearheaded by research teams at the USGS (United States Geological Survey) and have involved proof-of-concept investigations aimed primarily at quantifying channel geometry and stream discharge using non-contact methods (e.g. Spicer et al., 1997, Costa et al., 2000, Melcher et al., 2002, Figure 3.4). The use of GPR sensors for fluvial topography and depth estimation remains in its infancy and its widespread application is currently severely limited by cost and availability (Marcus 2012). This technique does allow more rapid data coverage than conventional cross-sectional measurements, and has the potential to cover deeper and larger widths of river. However, it does not provide the continuous 3D depth/topography mapping that has been shown possible using other remote sensing methods.

Range imaging is a relatively new form of active remote sensing which is capable of producing 3D point clouds in real-time. It has predominantly been used within indoor lab settings to date, but recent work (Nietsche et al., 2012) has assessed its potential in a fluvial field setting for the

first time. Range imaging also offers a small and lightweight option, however, it has a limited range of c.10m, is highly sensitive to strong ambient light (and therefore works best in shade) and is not yet capable of delivering the resolution or accuracy of TLS-derived elevation outputs (Nietsche et al., 2012). Further field testing and development is necessary before this approach may be considered as a viable option for research and management of fluvial systems.

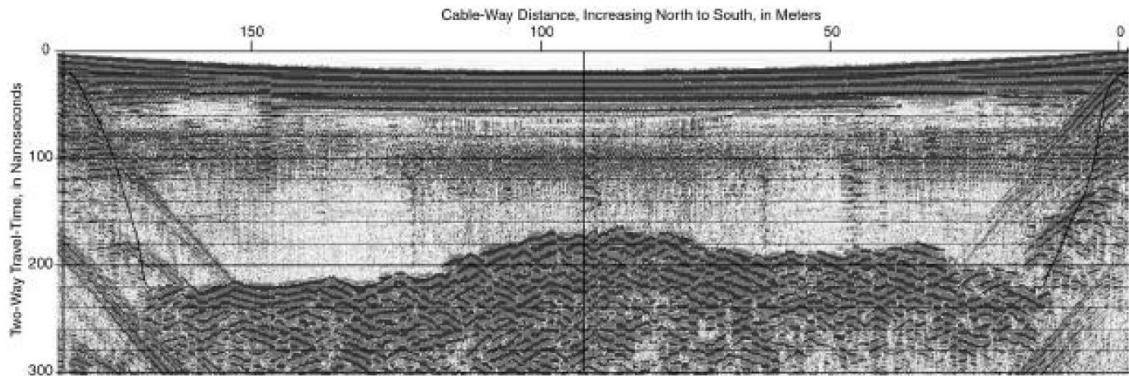


Figure 3.4. An example of a GPR-generated cross section for the Skagit River in Washington, USA (Costa et al., 2000).

Combined Approaches

A number of studies have tried to overcome the limitations of using any one approach for surveying fluvial topography by using a hybrid approach to maximise their capabilities. This may comprise the application of two or more different remote sensing techniques to one dataset (e.g. Westaway et al., 2003, Lane et al., 2010, Javernick et al., 2014), or by combining datasets acquired by different sensors (e.g. Legleiter 2012, Williams et al., 2014). However, this often results in increased cost, greater logistical challenges and or more complicated data processing requirements. The digital photogrammetry approach of Westaway et al., (2000) and the TLS study of Smith and Vericat (2014) are the only known published works which have used a single remote sensing technique over mesoscale lengths of channel to assess both exposed and submerged areas. However, neither of these methods have achieved hyperspatial resolution topographic data (<0.1m) over mesoscale extents.

Emerging Approaches

As discussed in Chapter 1, the recent development of small unmanned aerial systems (UAS) and parallel developments in structure from motion photogrammetry now offer an alternative approach for assessing and quantifying a range of river habitat parameters. A growing number

of published studies have made use of these novel technologies for quantifying topography in a wide range of settings, as reviewed below. However, few published studies have specifically addressed the fluvial environment, and even fewer have attempted to use these techniques to quantify the topography of submerged areas.

Unmanned aerial systems

An early example of UAS research saw the assessment of imagery acquired from a model helicopter for the 3D topographic characterisation of an inaccessible archaeological site in Peru (Eisenbeiss et al., 2005). The helicopter was equipped with a digital camera and a miniature GPS and inertial navigation system (INS) which allowed for stable flight and image acquisition along a predefined flight path. Digital photogrammetry was used to generate a digital surface model (DSM), an orthophoto and visualisation of the site in 3D. The topographic outputs were compared against data collected using terrestrial laser scanning (TLS) as a check on their accuracy. Eisenbeiss et al., (2005) generally found good agreement between the two elevation datasets, with a mean height difference in the order of 0.09m. The DSM created from the UAS approach was of a lower spatial resolution (20cm) than that obtained using TLS (10cm), however significant advantages over traditional surveying techniques (e.g. total station survey) were noted in terms of spatial resolution and acquisition time.

The process of using UAS imagery for characterising topography has also been tested from kite platforms, in the work of Smith et al., (2009). The kite was equipped with a consumer-grade, non-metric camera and tested at three different field sites, including areas of smooth and rough terrain, and on a glacio-fluvial esker landform near Loch Lomond in Scotland. Again a digital photogrammetric approach was used to generate elevation data from a series of overlapping kite images acquired at each site. The use of ground control points (GCPs), surveyed in using a total station was necessary as input to the photogrammetric processing. The mean error of the resulting elevation model was found to be +/- 0.01m, and standard error was typically 0.7m. Smith et al., (2009) concluded that the use of kite imagery provided a quick and cost-effective approach for topographic mapping with good levels of accuracy. The only drawback they note is that the photogrammetric approach was less efficient at identifying matching image features in areas of low image contrast or high homogeneity within the scene.

A digital photogrammetry approach was also employed by Niethammer et al., (2012) in their recent study of the Super-Suaze landslide in southeast France. This study compared the topographic outputs obtained using imagery collected by a mini quad-rotor UAS with that obtained by TLS. The root mean square error of the UAS DEM was 0.31m, although maximum differences were found to be as great as 4.08m in areas of vegetation. Areas of steep terrain also proved more challenging for the UAS-photogrammetry approach given the predominantly nadir view angle, compared with the oblique viewing angle of the TLS. However, Niethammer et al., (2012) conclude that UAS imagery holds much potential for more rapid topographic mapping over larger spatial areas than TLS.

Within fluvial settings, the use of UAS to characterise topography has been relatively limited. As described earlier, the work of Lejot et al., (2007) used a motorised paraglider platform to collect low altitude, high resolution imagery of selected reaches of the Ain and Drôme Rivers in France. This work used a photogrammetric approach to produce elevation data for the exposed parts of the channel, and a spectral-depth relationship approach for submerged areas (as discussed earlier). Topographic outputs had a spatial resolution of 5-10cm and a vertical accuracy of 4-10cm. Whilst this approach provided a valuable means of mapping the microtopography of gravel bars, Lejot et al., (2007) also note limitations in terms of variable image illumination (especially problematic for the spectral-depth approach for submerged topography) and image distortions resulting from the lack of stability of the UAS platform (especially problematic for the photogrammetric approach for exposed topography).

More recently, Tamminga et al., (2014) used a rotary-winged UAS for characterising fluvial morphology of the Elbow River, Canada. Imagery was processed using digital photogrammetry and 5cm resolution DEMs and orthophotos were generated for both exposed and submerged parts of the channel. Two approaches were then tested for correcting the effects of refraction in submerged areas; a simple correction of the DEM based on the refractive index of water and a spectral-depth approach based on the orthophoto. Mean error in exposed areas was 0.032m and in uncorrected submerged areas was 0.144m. The simple refraction correction improved mean error in submerged areas to 0.064m and the spectral-depth approach gave a mean error of 0.007m. The latter approach is therefore advocated for producing more reliable submerged depth estimates. This work emerged after much of the research described in this chapter had been carried out.

A number of key advantages of using UAS platforms emerge from this small, but growing body of research, as summarised in Chapter 1. Data acquisition using a UAS is typically rapid and flexible, and less expensive than using manned aircraft (Eisenbeiss et al., 2005, Lejot et al., 2007, Vericat et al., 2009, Niethammer et al., 2012). Given their ability to fly at low altitudes, the topographic or depth data which may be derived is usually of very high resolution, almost rivalling that provided by TLS (Lejot et al., 2007, Laliberté and Rango 2009, Vericat et al., 2009, Harwin and Lucieer 2012, Niethammer et al., 2012, Rosnell and Honkavaara 2012, Turner et al., 2012, Tamminga et al., 2014). Furthermore, UAS may provide the opportunity to survey otherwise inaccessible areas in a way which is logistically simpler and less time consuming than methods such as TLS (Eisenbeiss et al., 2005).

However, the application of UAS for topographic assessment remains in an early stage of research and a number of current limitations can also be recognised. These relate primarily to the difficulties involved in processing imagery obtained from an unstable platform typically using lightweight, low cost, non-metric sensors (Niethammer et al., 2012). Problems are introduced by the often large illumination differences between images (Dugdale 2007, Lejot et al., 2007, Dunford et al., 2009, Vericat et al., 2009), the geometric distortions introduced by image acquisition off-nadir (Lejot et al., 2007, MacVicar et al., 2009, Smith et al., 2009, Rosnell and Honkavaara 2012) and the limited information available concerning the external flight parameters (Lejot et al., 2007, Rosnell and Honkavaara 2012, Turner et al., 2012). A skilled pilot is also required to obtain adequate imagery from fixed and rotary winged platforms. Fortunately, parallel developments in the fields of computer vision and image analysis mean that a number of these limitations are now starting to be overcome. Structure from motion (SfM) algorithms are now able to cope with imagery of various different scales, view angles, orientations and illumination conditions (Lowe 2004, Snavely et al., 2006, Snavely et al., 2008).

Structure-from-motion photogrammetry

Published examples of the use of imagery processed using SfM for topographic assessments have only started to emerge since 2011, and examples from fluvial settings are currently few in number.

Although focussed on archaeological applications, the work of Verhoeven and others has played a key role in demonstrating the capabilities of the SfM workflow (Verhoeven 2012, Verhoeven et al., 2012). For example, SfM was used to process a series of oblique images of a former Roman settlement which had been collected ten years previously using an uncalibrated consumer-grade compact digital camera from a light aircraft. This allowed the generation of a 3D point cloud, georeferenced to real-world co-ordinates using GCPs identified within the aerial imagery and on a 1:10,000 scale topographic map of the area. The focus within this study was the output of orthophotos, based on the point cloud DEMs, for the identification of archaeological features. No assessment of the accuracy of the topographic outputs is provided, though this perhaps relates to the use of older aerial imagery and the absence of contemporaneous validation data.

James and Robson (2012) demonstrated the use of SfM for a coastal geomorphology application along a 3m high, 50m stretch of cliff at Morecambe Bay in the UK. The images were collected using a handheld DSLR camera at seven time intervals over the course of a year in order to estimate the pattern and magnitude of coastal erosion. Surveys were also collected using TLS for validation purposes. Results show an overall root mean square error of 0.07m, with 68% of the SfM survey falling within 0.21m of the TLS surface. Data collection times using the SfM approach were found to be significantly lower (80%) than for TLS.

Work by Westoby et al., (2012) also assessed the SfM topographic outputs for a coastal cliff by comparison with TLS data. This study used 889 images collected by hand from a consumer-grade digital camera over an area approximately 300m x 300m. The output SfM DEM was subtracted from the TLS DEM to create a DEM of difference for validation purposes. The results indicated that 94% of differences were within +/- 1.0m and 86% were +/- 0.5m. These are larger differences than those reported by James and Robson (2012) and are thought to relate to areas of very steep terrain.

Harwin and Lucieer (2012) provide the first published example of the combined use of UAS imagery and SfM-photogrammetry. A standard DSLR camera was mounted on a rotary-winged OktoKopter system and equipped with an on-board GPS and INS. The UAS was flown at an altitude of 30-50m above ground level and both vertical and oblique imagery was acquired. SfM was performed using the Bundler and PMVS2 software packages to produce dense point

clouds (1 - 3cm point spacings) with high levels of accuracy (2.5-4.0cm). Harwin and Lucieer (2012) found that the accuracy of the georeferencing process was strongly affected by the distribution of artificial GCPs. They recommend an even layout throughout the study site, with a spacing of between one fifth and one tenth of the flying altitude. They conclude that the UAS-SfM approach has the potential to offer “...*affordable hyperspatial and hypertemporal data*”, (Harwin and Lucieer 2012, p. 1594) capable of detecting and monitoring topographic change at the sub-decimetre level.

The use of SfM within fluvial settings however, has yet to see extensive research. Fonstad et al., (2013) provide an overview of the specific advantages of SfM over traditional photogrammetric techniques, and illustrate its use with UAS imagery acquired with a helikite. The study site comprised an exposed bedrock channel and 150m wide floodplain of the Pedernales River, Texas, USA. Freeware software packages including Microsoft PhotoSynth and JAG3D were used to perform the SfM process and indirect georeferencing. A thorough quantitative assessment was not the aim of this study, but initial comparisons were made between the UAS-SfM DEM, an independent GPS survey and an airborne LiDAR dataset. The SfM DEMs provided a much higher spatial resolution and better represented the topographic features at the site than the LiDAR data. The mean difference between the SfM DEM and LiDAR elevation values was found to be 0.6m, although the usefulness of this comparison is questionable given the difference in spatial resolution and time delay of five years between the collection of the two datasets. Comparison with an independent GPS survey is shown by the validation relationship in Figure 3.5, which gives a mean elevation error of 0.07m and standard deviation of 0.15m.

Javernick et al., (2014) assessed the use of SfM combined with spectral-depth relationships for creating high quality DEMs of the topography of a 1.6km x 0.65km stretch of the braided Ahuriri River in New Zealand. Aerial imagery was collected by hand from a light aircraft flown at 600m and 800m above ground level (to produce imagery of spatial resolutions 12cm and 16cm respectively). The imagery was processed using the PhotoScan SfM software (Agisoft LLC) to create a dense point cloud with a typical point spacing of 0.25m. The point cloud was georeferenced using an indirect approach, using the RTK GPS positions of 65 GCPs. Another c. 10,000 RTK GPS topographic positions were also collected for subsequent validation of the SfM topography outputs. The linear georeferencing method was found to produce SfM outputs

with a mean error of 0.42m in areas of bare ground and 1.71m in areas of dense vegetation. These accuracy values were improved to -0.07m (exposed) and 0.41m (vegetated) following an optimisation procedure (defined in Chapter 2, section 2.5.6). A spectral-depth approach was used on the imagery in submerged areas as the SfM process was expected to struggle to make successful point matches here. The results of the spectral depth approach, used on the SfM orthophoto, produced a river bed elevation mean error of -0.06m. Javernick et al., (2014, p. 181) conclude that an SfM approach offers “...non-expert users the ability to effectively produce DEMs of moderately vegetated fluvial environments without high data acquisition costs or exhaustive field labor...”.

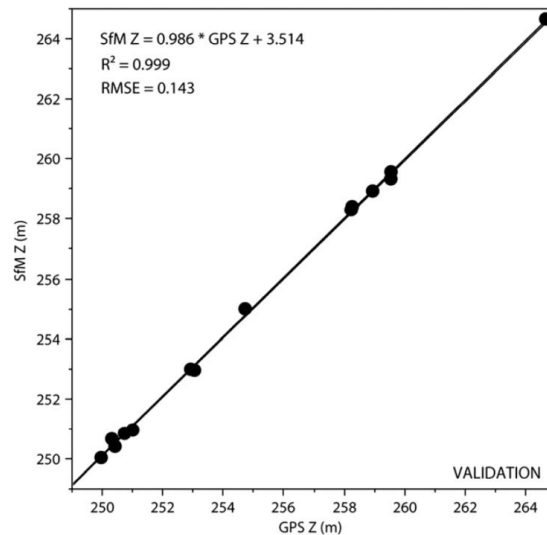


Figure 3.5. Validation plot of the fit between the SfM DEM and GPS observed elevations (Fonstad et al., 2013).

Some limitations to the SfM technique have been noted by these studies. For example, Fonstad et al., (2013) suggest that there is currently no way of removing non-linear distortions within the output point cloud. Furthermore, the technique is reliant on high contrast or texture within the imagery. Where this texture is lacking, point cloud densities are greatly reduced. However, these early studies also suggest that SfM holds great potential for generating topographic data from unstable UAS image acquisitions, in a way which may be capable of providing “...LiDAR-like accuracy and precision or better” (Fonstad et al., 2013, p.6) which has not been possible previously. As stated in Chapter 1, it is early days for deriving topographic datasets using SfM and therefore rigorous comparative studies against existing approaches (such as total station and RTK GPS surveys, and TLS) are urgently required.

3.1.5 Summary

It is clear that remote sensing approaches offer significant advantages for quantifying both exposed and submerged topography over the traditional methods, as indicated in Table 3.3. In particular, remote sensing surveys are less time consuming and labour intensive and offer spatially continuous, spatially explicit, quantitative data in three dimensions.

Table 3.3. Assessment of remote sensing based methods of quantifying fluvial topography and/or water depth against requirements of the 'riverscape' concept (Fausch et al., 2002).

Key requirement for characterising physical river habitat variables	Is this requirement met by remote sensing methods of surveying fluvial topography and depth?						
	Spectral-depth relation-ships	Physically-based models	Digital photo-grammetry	Bathymetric LIDAR	TLS	GPR	UAS & SfM
(1) Quantitative datasets collected by objective and repeatable methods	Yes	Yes	Yes	Yes	Yes	Yes	Potentially, but not widely tested
(2) Spatially continuous datasets, available in three-dimensions	Yes	Yes	Yes	Yes	Yes	No, only used along cross sections at present	Yes
(3) Spatially explicit datasets	Yes	Yes	Yes	Yes	Yes	Yes	Yes
(4) Datasets which cover large spatial areas, with high levels of detail	Yes	?	Yes	Yes, large spatial coverage but limited spatial detail at present	Yes, high detail but coverage over large areas not currently proven	Yes, high detail but coverage over large areas not currently proven	Potentially, but not widely tested
(5) Datasets which are not difficult to collect in terms of practicality, logistics and cost	Mostly, time consuming field data collection needed	?	Yes	No, limited availability & high cost at present	No, high cost at present and time consuming	No, limited availability & logistically difficult at present	Potentially, but not widely tested

Of the reviewed approaches, the passive remote sensing methods have seen most widespread use to date, in particular the spectral-depth relationship method. This approach perhaps represents the best compromise between spatial resolution, spatial coverage, accuracy of results and cost and accessibility of sensors, platforms and processing means. Digital

photogrammetric methods also provide many of the same advantages, but have not seen such widespread use in studies of submerged fluvial topography or depth.

To date and in contrast, active remote sensing approaches, such as bathymetric and terrestrial LiDAR and ground penetrating radar have seen limited use for topography and depth estimation in fluvial settings. This relates primarily to issues of high cost and limited availability, thereby making these approaches largely unfeasible in many research and management scenarios at the present time. However, other limitations include the restricted spatial resolution (bathymetric LiDAR) and coverage (TLS and GPR) of these approaches.

Very recently, the emergence of low altitude small UAS and SfM processing techniques has provided an additional method for characterising topography. Initial research in non-fluvial application areas has demonstrated significant potential for generating very high resolution topographic outputs with high levels of accuracy at mesoscale extents. Data collection and image processing are rapid, flexible and are advocated as providing a cost effective option. However, at the time of commencing this PhD (2011), no published work had assessed the combined use of a UAS-SfM approach for quantifying fluvial topography in both exposed and submerged areas. Recently, the work of Tamminga et al., (2014) has provided some developments in this area, but this study was not accompanied by rigorous quantitative error assessments of the topographic datasets produced. Therefore, there is scope for further evaluation of the products of UAS-SfM approach for providing quantitative fluvial topography and water depth datasets at the mesoscale, and it is here that this chapter aims to contribute.

3.2 Research Questions

The research reported in this chapter aims to provide a thorough, quantitative assessment of computing fluvial topography using hyperspatial resolution data collected from a UAS and processed using SfM-photogrammetry, with a specific focus on obtaining data at the mesoscale. In particular, the following research questions will be addressed:

1. How accurate, precise and replicable are the topographic datasets generated using a UAS-SfM approach? Do these measures vary between different river systems?
2. How does the accuracy and precision of the UAS-SfM DEMs vary between exposed and submerged terrain, and does the application of a simple refraction correction procedure improve the accuracy of topographic products in submerged areas?

3. How does the DEM obtained using the UAS-SfM approach compare with a DEM obtained using TLS?

3.3 Site Locations

The topography and water depth research was conducted at the following four sites. Further detail about these sites is provided in Chapter 1.

- a) **The San Pedro River**, Chile (Figure 3.6a): where a single survey was conducted over the course of two days in May 2012. Lighting and weather conditions during this time were variable, but the water clarity remained very good.
- b) **The River Arrow**, Warwickshire (Figure 3.6b): where surveys were carried out at the following times;
 - a. **May 2013** - This survey was conducted in bright sunny weather with a relatively low flow level and low turbidity.
 - b. **June 2013** - This survey was also conducted in bright sunny weather with a relatively low flow level and low turbidity.
 - c. **August 2013** - This survey was conducted when conditions were overcast and slightly misty. Flow level and turbidity were comparable to the surveys conducted in May and June.
- c) **Coledale Beck**, Cumbria (Figure 3.6c): this survey was conducted in July 2013 during bright and sunny conditions with a low flow level and very clear water.
- d) **Sports hall floor**, University of Worcester (Figure 3.6d): where two UAS surveys were conducted in March 2013. During one of the surveys imagery were acquired only at an oblique angle and during the other, imagery were only acquired at nadir (or as close as possible using the UAS platform). Two different GCP configurations were also tested in the georeferencing of the each survey, as described in Chapter 2.

These sites were selected for the following reasons;

- They provide diverse topographic conditions at the mesoscale, within different landscape settings.
- They were easily accessible and permission from the landowners was granted for UAS flying.

- None are situated in areas of dense vegetation or continuous tree coverage, near major roads or railway lines, power lines or sensitive sites such as airports – factors which might prohibit UAS flying.
- The River Arrow is located close to the University of Worcester so that it could be revisited frequently and at short notice to take advantage of favourable flying conditions for assessing the repeatability of the approach. These repeat surveys allowed an assessment of the success of quantifying topography and flow depth under differing conditions.
- UAS flights acquired using different settings (view angle and GCP alignment) over the floor of a sports hall allowed the ability of the SfM-photogrammetry to reconstruct a flat surface to be tested.

Depending on the availability and quality of data available, these site surveys were used to answer different research questions within this chapter, as detailed in Table 3.4.

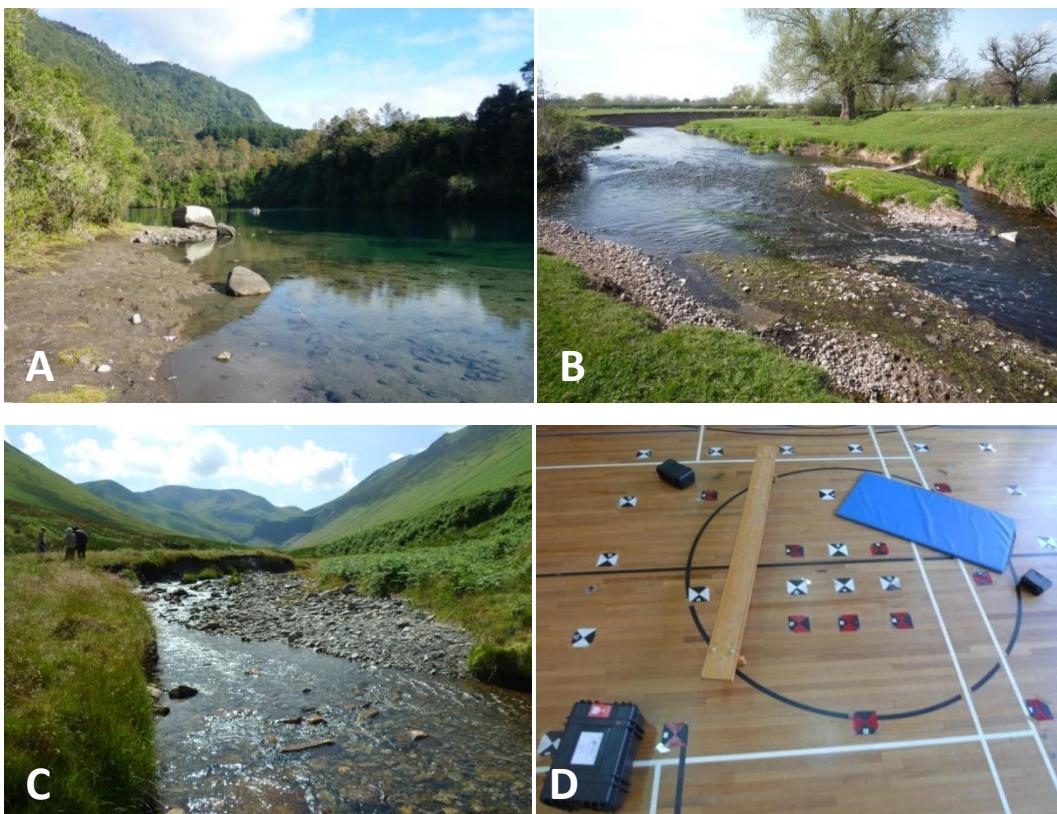


Figure 3.6. Photographs of the sites used for assessing topography and/or flow depth (a) San Pedro River, (b) River Arrow (c) Coledale Beck and (d) Sports hall floor at University of Worcester.

Table 3.4. Datasets used to address each of the research questions.

Site	San Pedro River	River Arrow			Coledale Beck	Sports hall floor
Survey date	May 2012	May 2013	June 2013	August 2013	July 2013	March 2013
RQ 1	✓	✓	✓	✓	✓	✓
RQ 2	✓	✓	✓	✓	✓	
RQ 3					✓	

3.4 Methods

The workflow provided in Figure 3.7 provides an overview of the methods used for quantifying substrate size within this chapter. Those methods which are common to all physical river habitat parameters considered within this thesis are documented in Chapter 2, whereas methods specific to this chapter are detailed here (Table 3.5).

Table 3.5. Overview of methods used within this chapter and where they are described within the thesis.

Stage	Detail	Location
1) Pre-field	Camera characterisation	Chapter 2
2) Data Acquisition	GCP set-up & survey UAS flying & image acquisition	Chapter 2
	TLS data acquisition	Chapter 2
	Independent topographic survey	This chapter 3.4.1
3) Data Processing	Image selection	Chapter 2
	SfM processing in PhotoScan Pro	Chapter 2
	TLS data processing	Chapter 2
4) Data Analysis	Refraction correction	This chapter 3.4.2
	Quantitative DEM validations	This chapter 3.4.3
	Analysis of residual error	Chapter 2
	Comparison of UAS-SfM and TLS DEMs	This chapter 3.4.4

Data Acquisition

The imagery acquired from the UAS surveys for all sites and the TLS data collected at Coledale Beck are used within this chapter and elsewhere. As a result, these methods are described only in Chapter 2 to avoid repetition. The collection and processing of imagery acquired within the sports hall setting is also described in Chapter 2.

3.4.1 Independent topographic survey

Traditional topographic surveying methods were used to collect elevation data as points, for subsequent validation of the topographic data produced using the UAS-SfM approach. This included the use of a differential GPS or total station across both exposed and submerged parts of each site. The numbers of validation points collected at each site are shown in Table 3.6.

San Pedro River

At the San Pedro site, ground validation points were collected in two batches, using a Spectra Precision EPOCH 50 GNSS differential GPS (dGPS) by colleagues at the University of Concepción, Chile. The first were collected in January 2012 (prior to UAS image acquisition and part of another on-going research project) and the second in May 2012 (concurrent with UAS image acquisition). The earlier dataset was confined largely to the submerged areas of the study area, with data collection of the exposed areas and banks carried out during the later survey. The assumption was made that the topography of this site would not have changed significantly between the collection of validation data and the UAS image survey given the lack of potentially erosive, high stage events during the austral late summer. A consistently large offset (>5m) was found within the January batch of the dGPS data, the reason for which was unclear. Given the apparently systematic nature of this elevation offset in relation to the dGPS data collected in May, a simple adjustment factor was applied. Whilst this is not the perfect solution, it provided a viable option given a re-survey of the site was not feasible.

*Table 3.6. Quantity of independent topographic survey points collected at each site. *Denotes that water depth data not collected at this site.*

Site		San Pedro River	River Arrow			Coledale Beck	Sports hall floor
Survey date		May 2012	May 2013	June 2013	August 2013	July 2013	March 2013
No. of independent validation points collected	Exposed areas	701	279	218	57	532	42
	Submerged areas	693*	169	142	113	252	N/a

Quantifying physical river habitat parameters using hyperspatial resolution
UAS imagery and SfM-photogrammetry

1. PRE-FIELD

UAS survey

- a) Camera characterisation to determine relationship between flying altitude and image resolution

2. DATA ACQUISITION

UAS survey

- a) Distribution & survey of GCPs using dGPS or total station
- b) Image acquisition from UAS (multiple flights)

3. DATA PROCESSING

UAS imagery

- a) Manual image selection
- b) SfM processing in Agisoft PhotoScan Pro (see Figure 2.18)
- c) Export georeferenced orthophoto and DEM

TLS survey

- c) Distribution of 6 reflective targets
- d) Scanning at high resolution (5cm at 100m range) from 8 positions
- e) Survey targets & scan station positions using dGPS

TLS data

- d) Co-register scans using targets (Leica Cyclone)
- e) Georeference merged scan to British National Grid co-ordinates using dGPS data
- f) Assess registration accuracy and remove problematic targets as necessary
- g) Clip the merged scan to the area of interest
- h) Manually remove erroneous data spikes
- i) Export dense point cloud as PTS file
- j) Rasterise point cloud to 1.3cm resolution DEM

Ground truthing

- f) Collect independent topographic validation data using dGPS or total station, and water depth measurements

4. ANALYSIS

Refraction correction of UAS-SfM outputs

- a) Map positions of waters edge from orthophoto
- b) Extract DEM values at 0.25m intervals along waters edge
- c) Interpolate between DEM values using TIN model to give estimated water surface elevation
- d) Subtract original DEM from estimated water surface to give estimated water depth
- e) Multiply estimated water depth by refractive index of clear water (1.34)
- f) Compute difference between estimated water depth and refraction corrected water depth
- g) Subtract this difference from original DEM to give refraction corrected DEM in submerged areas
- h) Compute elevation differences between independent validation data and output DEMs (original and refraction corrected)

TLS data

- i) Compute elevation differences between independent validation data and TLS DEM
- j) Compute DEM of difference between non-refraction corrected UAS-SfM and TLS DEMs

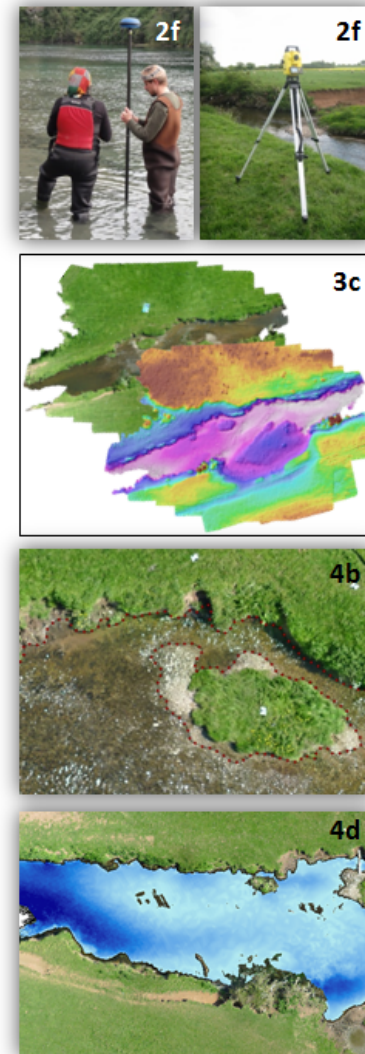


Figure 3.7. Methods workflow for topography chapter.

River Arrow and Coledale Beck

Prior to any data collection at the River Arrow and Coledale Beck sites, a series of four permanent markers were established using wooden stakes and yellow survey markers. All subsequent data were collected using a Leica Builder 500 total station (e.g. locations of GCPs and the independent topographic survey) and referenced to these four permanent markers, which were subsequently surveyed in using a Trimble RTK GPS (River Arrow) or Leica GPS1200 dGPS (Coledale Beck). The dGPS was on loan from Durham University for a very short period of time and therefore could not be used to conduct the wider surveying required by this research. A Trimble R8 RTK GPS was available for use during the fieldwork, but the lack of a consistently good mobile data signal prevented its wider use at either site. The use of permanent markers was particularly important at the River Arrow site where repeat surveys were conducted between May and August 2013.

Following the initial work at the San Pedro site, it was found that an independent water depth validation dataset would assist in the assessment of refraction effects. Therefore, during collection of topographic validation data in submerged areas during the surveys at the River Arrow and Coledale Beck, a measure of water depth to the nearest centimetre was also taken. Unfortunately it was not possible to return to the San Pedro site to collect this independent data, however, refraction corrected water depth was estimated from the DEM itself by extrapolating the channel edge elevations as described in section 3.4.4. This approach does not provide an independent measure of water depth and therefore is not ideal, but it does provide a rough indication in the absence of other data.

Sport hall floor

Although the floor of the sports hall is presumed to be level, an independent topographic survey was nevertheless carried out using a Leica Builder 500 total station. The use of a dGPS device indoors was not possible, so the DEM and independent survey collected using the total station were positioned in relative space rather than in an absolute geographic co-ordinate system.

Data Processing

3.4.2 Refraction correction

Given the passive, optical nature of the SfM-photogrammetry technique, DEM outputs will have been affected by the effects of refraction at the air-water interface. This results in an

overestimation of the true bed elevation, as noted by existing digital photogrammetry studies in submerged areas (Fryer 1983, Fryer and Kneist 1985, Butler et al., 2002, Westaway et al., 2001). UAS imagery were acquired predominantly at nadir to permit the testing of a simple refraction correction procedure for through-water photogrammetry, as described by Westaway et al., (2000). This involves multiplying the apparent water depth by the refractive index of clear water (1.34) to obtain refraction corrected water depths.

To apply this refraction correction it was necessary to model the water surface elevation and estimate water depths within the channel at each site. This was undertaken at the Arrow and Coledale sites by mapping the position of the water's edge from the each orthophoto at a scale of 1:50 in ArcGIS (ESRI Inc.). DEM elevation values were extracted at 0.25m intervals along this mapped line and interpolated using a TIN model to produce a map of estimated water surface elevations. The underlying DEM was then subtracted from this surface to give estimates of water depth (h_A in Figure 3.2) as a raster dataset. The resulting depth values were multiplied by 1.34 to produce maps of refraction corrected water depth (h in Figure 3.2). It was necessary to use the 'set null' tool in ArcGIS in some instances to remove areas of the water depth dataset where erroneous negative water depth values were returned.

Refraction corrected water depth maps are then used to create maps of refraction corrected submerged channel elevations by subtracting the difference in water depth between the non-corrected and corrected datasets from the original DEM. This process assumes a planar water surface, unaffected by waves or surface rippling. Whilst this is unlikely in reality, an assessment of the impact of surface waves on refraction is beyond the scope of this study. Figure 3.8 demonstrates the effects of refraction correction on DEM elevations.

A similar procedure was carried out for the San Pedro site, although the process required modification to account for the presence of only one bank within the imagery. DEM elevation values were extracted every 1m along the water's edge of this larger site and then extrapolated in the across-channel direction. These values were then interpolated (as for the other sites) to generate a TIN of the water surface elevations, and the remainder of the procedure was unchanged. This approach assumes a level water surface in the across-channel direction. Whilst this is unlikely to actually be the case, it represents a possible solution for the lack of information concerning the elevation of the water's edge on the left bank of the San Pedro River.

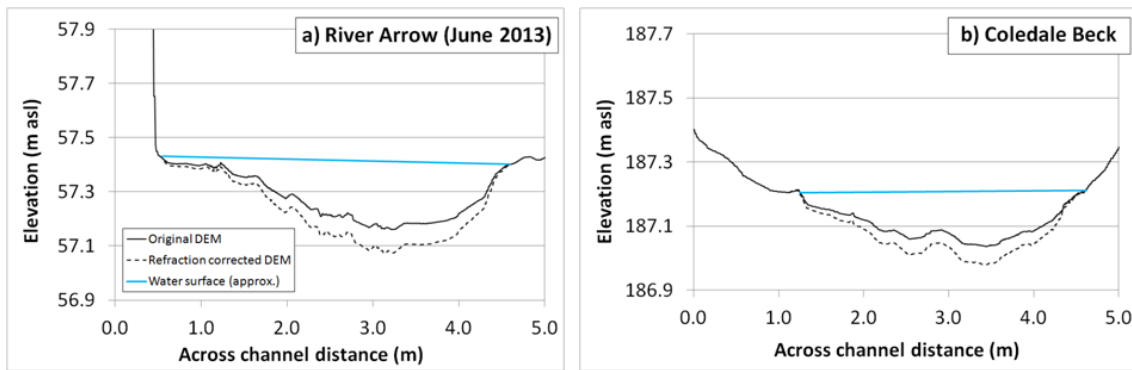


Figure 3.8. Example cross sections demonstrating the effect of refraction correction on DEM elevations in submerged areas a) at the River Arrow and b) at Coledale Beck (Woodget et al., 2015).

Data Analysis

3.4.3 Quantitative DEM validation

A quantitative assessment of the topographic data produced from all UAS-SfM surveys and the TLS approach was undertaken by comparison of each DEM against the independent topographic validation data for each site. This included both the original UAS-SfM DEMs, the refraction corrected UAS-SfM DEMs and the TLS derived DEM.

ArcGIS (ESRI Inc.) was used to overlay the independent validation points on the DEMs. The elevation values from the DEMs at the location of each point were extracted and compared to the independent elevation values in order to calculate the elevation mean error (accuracy) and standard deviation (precision). Precision to flying height and pixel size to precision ratios were calculated for each field survey. The former is defined as the average UAS flying height divided by mean error, and the latter is defined as the mean error divided by DEM resolution (or pixel size).

Linear regression of DEM and independent topographic survey elevations was also undertaken for all datasets (including refraction corrected DEMs). ArcGIS was used to create maps showing the magnitude, direction and spatial distribution of DEM errors for each dataset.

3.4.4 Comparison of UAS-SfM and TLS DEMs

A direct comparison of the DEMs produced from the non-refraction corrected UAS-SfM (section 2.5.8) and TLS approaches (section 2.6.4) conducted at Coledale Beck was undertaken by computing a simple DEM-of-difference. Whilst typically used for geomorphic change

detection using multi-temporal topographic surveys, this calculation also lends itself for assessing differences between DEMs of the same site computed using different methods. The DEMs were loaded into ArcGIS (ESRI Inc.) and the ‘raster calculator’ tool used to subtract one from the other. The output is a raster, indicating the magnitude of difference between the two elevation models.

3.5 Results and Analysis

Research Question 1

How accurate, precise and replicable are the topographic datasets generated using a UAS-SfM approach? Do these measures vary between different river systems?

Research Question 2

How does the accuracy and precision of the UAS-SfM DEMs vary between exposed and submerged terrain, and does the application of a simple refraction correction procedure improve the accuracy of topographic products in submerged areas?

This section first presents the results acquired from the field sites, and then those for the indoor sports hall experiment.

3.5.1 Digital elevation models

The DEMs and associated refraction corrected water depth maps produced for each UAS-SfM survey are shown in Figures 3.9 to 3.13. Table 3.7 details the spatial coverage and resolution of each DEM and Table 3.8 provides the residual errors in all three dimensions.

Table 3.7. Spatial coverage and resolution of UAS-SfM DEMs by site.

Site	San Pedro River	River Arrow			Coledale Beck
Survey date	May 2012	May 2013	June 2013	August 2013	July 2013
Spatial coverage (m ²)	6084.4	2803.9	2563.9	2084.2	4382.0
Exposed areas (% of total coverage)	40.56	83.65	84.18	83.95	90.57
Submerged areas (% of total coverage)	59.44	16.35	15.82	16.05	9.43
DEM spatial resolution (m)	0.020	0.018	0.018	0.019	0.020

Quantifying physical river habitat parameters using hyperspatial resolution
UAS imagery and SfM-photogrammetry

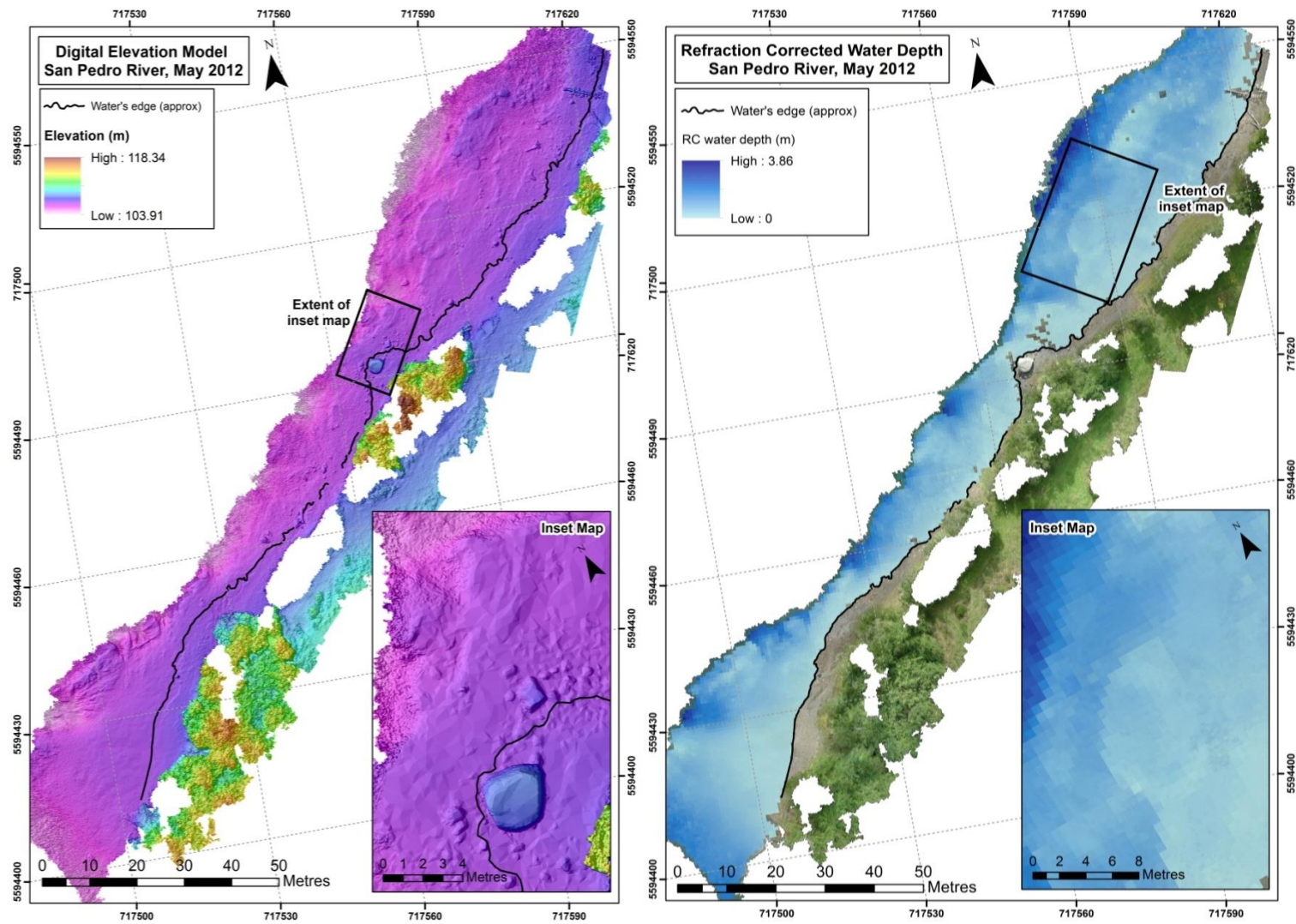


Figure 3.9. Digital elevation model (left) and refraction corrected water depth data (right) computed for the San Pedro River research site.

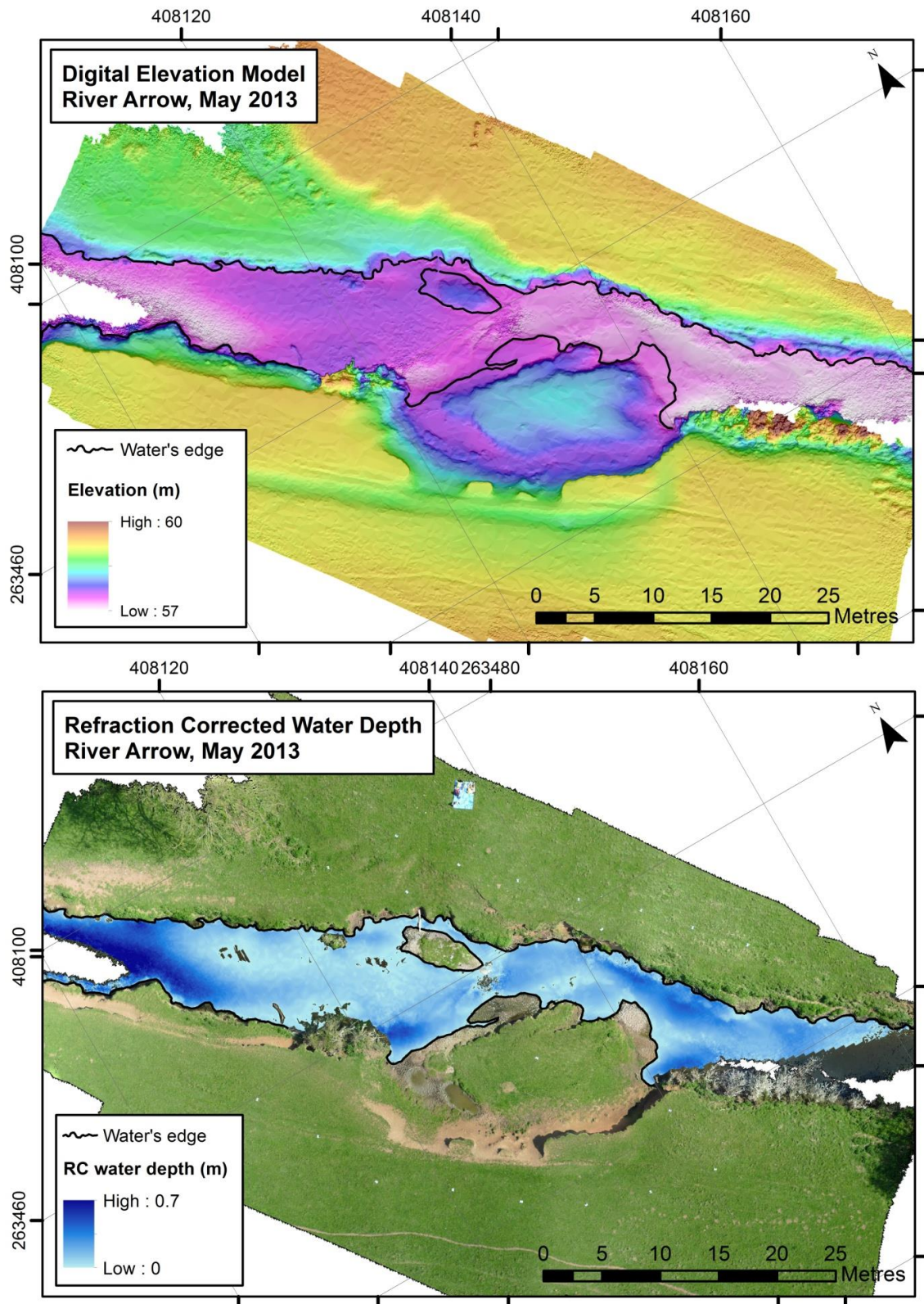


Figure 3.10. Digital elevation model (top) and refraction corrected water depth data (bottom) for the River Arrow survey conducted in May 2013.

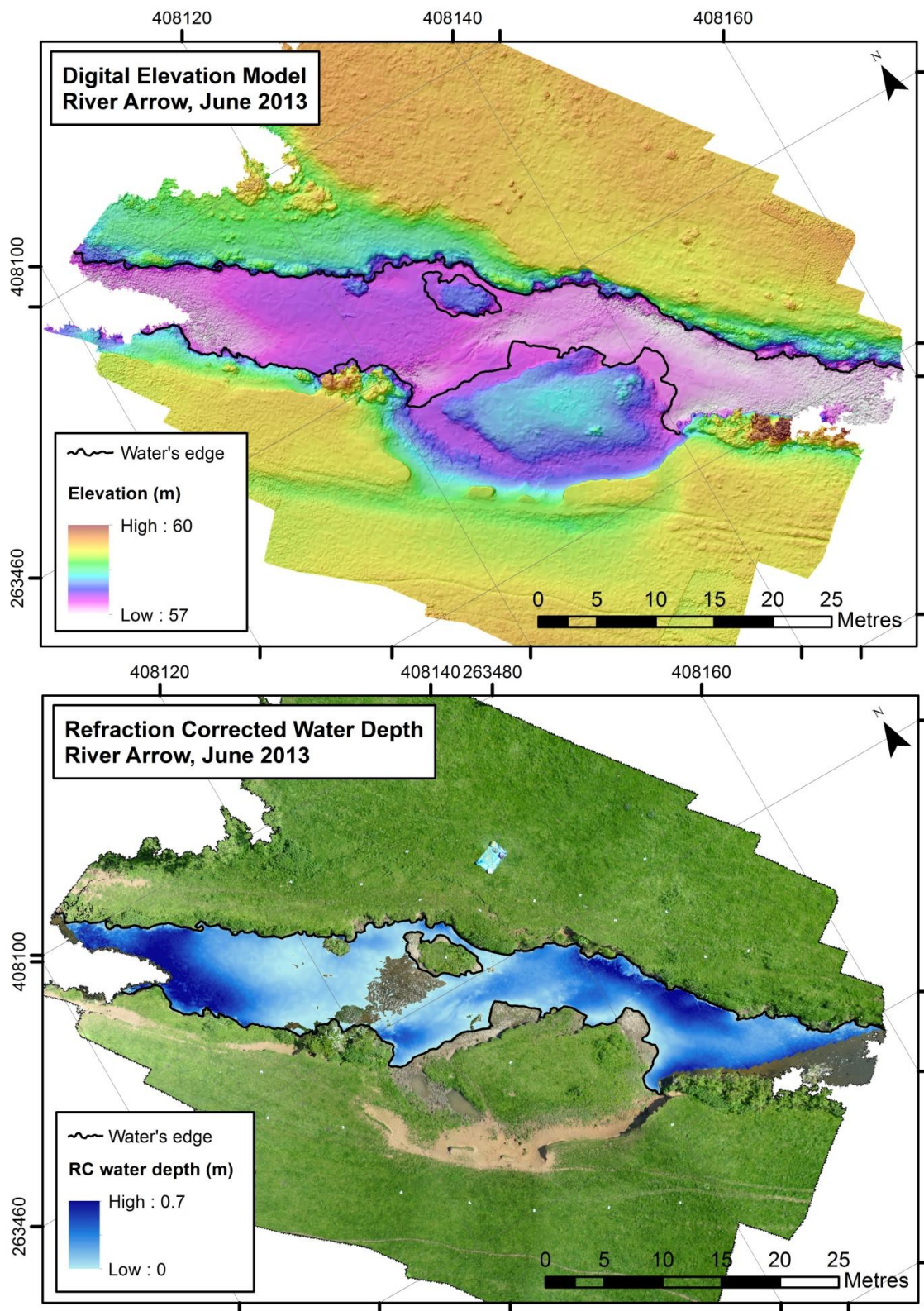


Figure 3.11. Digital elevation model (top) and refraction corrected water depth data (bottom) for the River Arrow survey conducted in June 2013.

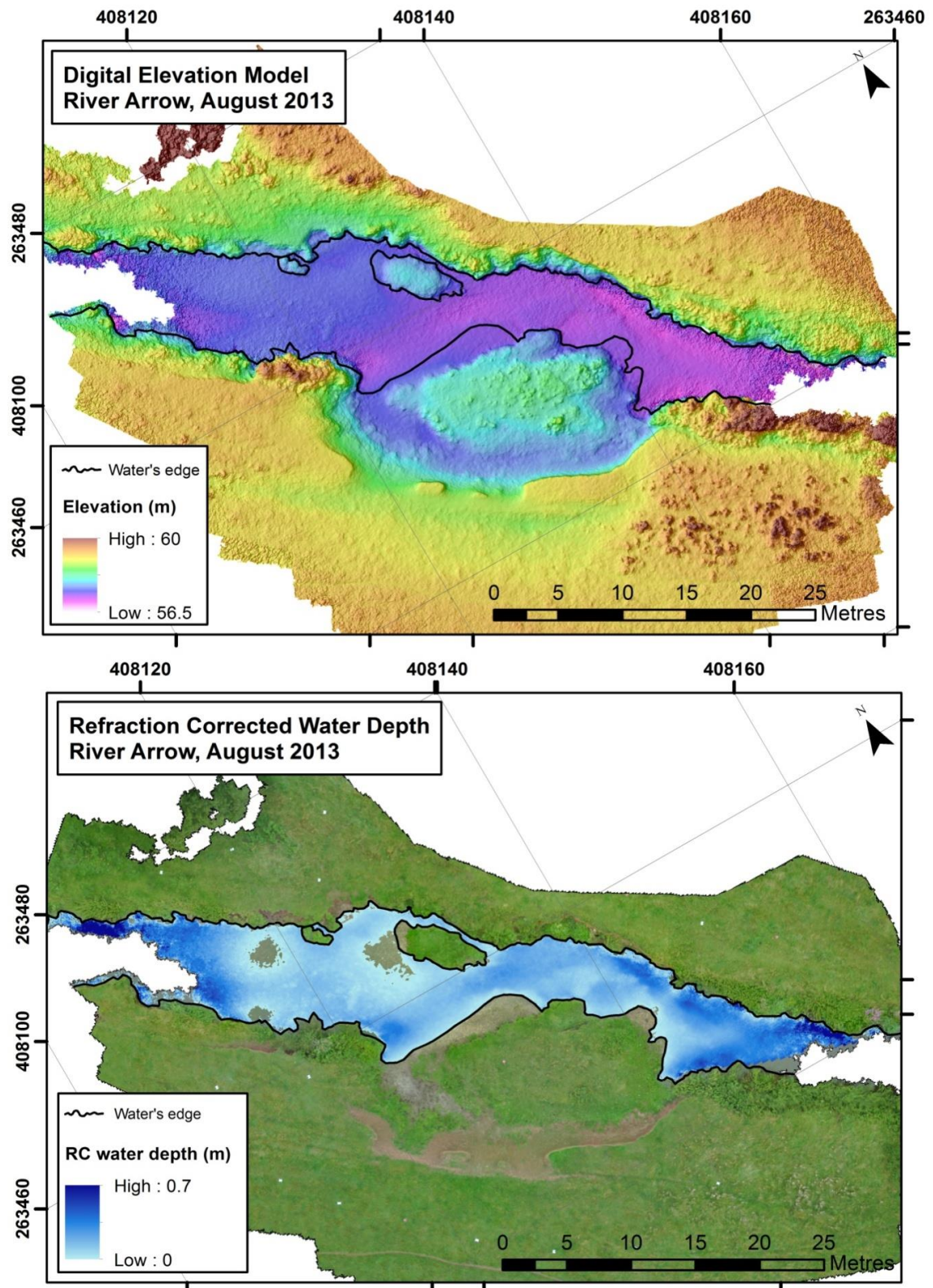


Figure 3.12. Digital elevation model (top) and refraction corrected water depth data (bottom) for the River Arrow survey conducted in August 2013.

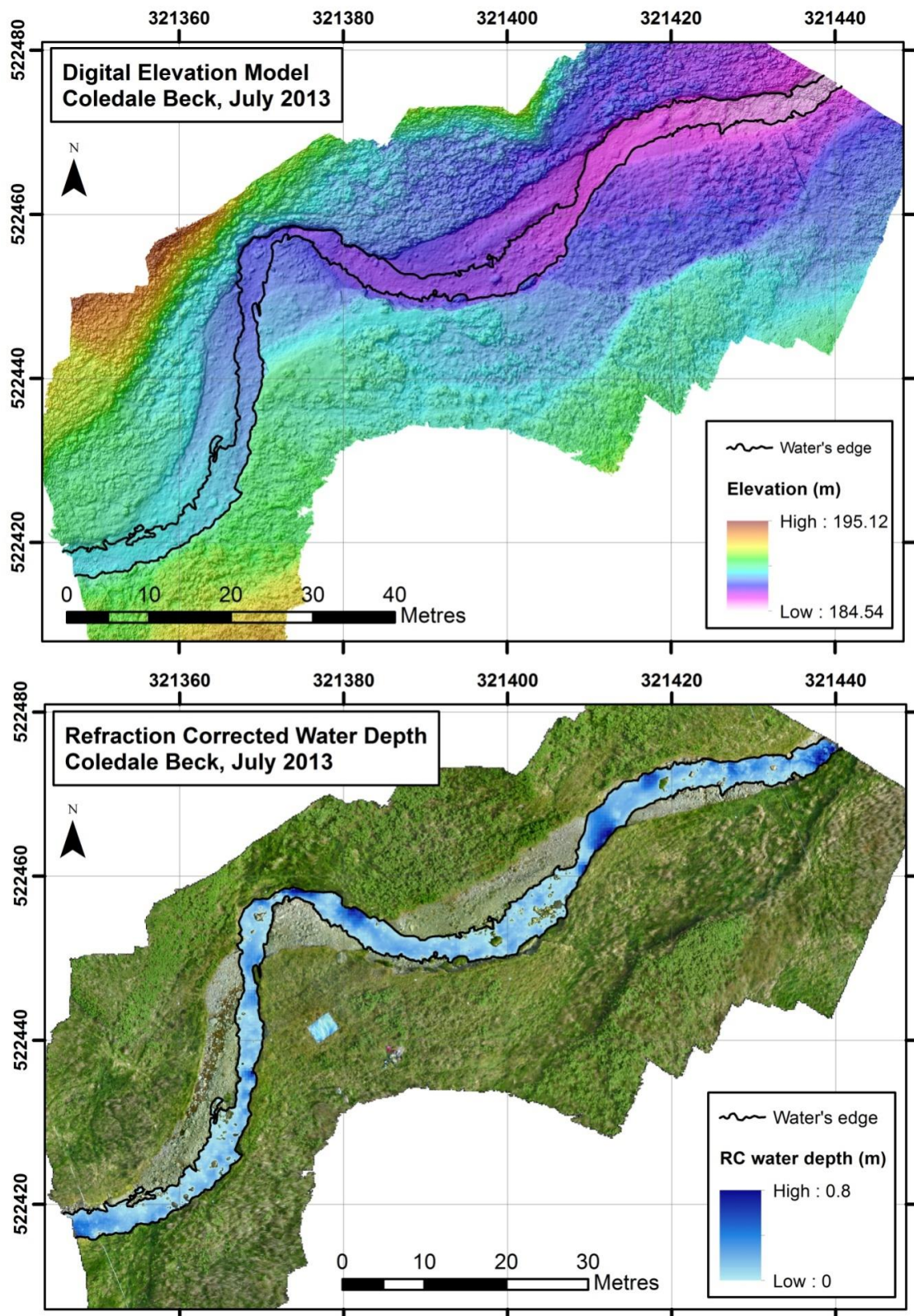


Figure 3.13. Digital elevation model (top) and refraction corrected water depth data (bottom) for the Coledale Beck survey conducted in July 2013.

Residual errors

The data presented in Table 3.8 shows that mean residual errors are nearly always less than 0.01m for all sites. This is less than the pixel size of the DEMs, thereby suggesting the residual planimetric error will have minimal impact on the independent validation of the topographic data. Larger residual errors occur in some places, for example in the Y dimension of the San Pedro River DEM, and in the Z dimension of the Coledale Beck DEM. The standard deviation values also given in Table 3.8 suggest that larger errors are also possible in other surveys. In some cases, these values exceed the pixel size (0.02m) in the planimetric dimension and therefore may start to affect the validation of DEM accuracy in Z.

Table 3.8. Residual errors associated with the UAS-SfM DEM for each survey.

Site		San Pedro River	River Arrow			Coledale Beck
Survey date		May 2012	May 2013	June 2013	August 2013	July 2013
Mean of residual errors (m)	X	-0.001	0.006	-0.028	0.007	0.006
	Y	0.022	-0.001	0.008	0.007	-0.007
	Z	-0.013	0.002	-0.001	-0.015	0.022
Standard deviation of residual errors (m)	X	0.072	0.013	0.162	0.035	0.062
	Y	0.048	0.014	0.046	0.026	0.043
	Z	0.162	0.008	0.016	0.019	0.037

3.5.2 Exposed areas

Accuracy (mean error) and precision (standard deviation) values computed for exposed areas within the DEMs of all field sites are provided in Table 3.9. Mean DEM errors are lowest (i.e. highest accuracy) for the datasets acquired at the River Arrow. Here, mean errors are consistently low and for the May and June surveys these values are 5mm or less. The equivalent values at Coledale Beck are worse (0.11m), caused by the presence of tall, dense bracken and grasses covering much of this site. The removal of validation points collected in these areas leads to an improvement in mean error to -0.04 m. The results obtained at the San Pedro site indicate a significant underprediction of elevations in exposed areas by the UAS-SfM DEM, with a mean error of -0.164 m. Mean error values are used in the calculation of [precision: flying height] and [pixel size: precision] ratios, which therefore reflect these patterns of accuracy between different sites.

Table 3.9 presents a similar pattern of DEM precision for exposed areas. Standard deviation values are lowest (i.e. highest precision) for the River Arrow datasets (c. 0.02–0.07 m), and considerably higher (i.e. lower precision) at Coledale Beck (0.2 m) and the San Pedro River (0.33m). Again, the value for Coledale Beck can be improved (to 0.08m) by exclusion of points in areas of tall vegetation.

Table 3.9. Summary of error assessment of UAS-SfM DEMs for each survey. NC denotes non-refraction corrected, and RC denotes refraction corrected dataset (after Woodget et al., 2015).^a [precision: flying height] ratios are calculated by dividing average flying height by mean error, ^b [pixel size: precision] ratios are calculated by dividing mean error by final DEM resolution.

Site		San Pedro River	River Arrow			Coledale Beck
Survey date		May 2012	May 2013	June 2013	August 2013	July 2013
Mean error (m)	Exposed	-0.164	0.005	0.004	0.044	0.111
	Submerged (NC)	0.026	0.089	0.053	0.063	0.017
	Submerged (RC)	-0.084	0.056	-0.004	0.024	-0.025
Standard deviation (m)	Exposed	0.332	0.019	0.032	0.069	0.203
	Submerged (NC)	0.278	0.076	0.065	0.084	0.074
	Submerged (RC)	0.300	0.080	0.068	0.084	0.078
Precision: Flying height ratio ^a	Exposed	1: 177	1: 5119	1: 6613	1: 627	1: 257
	Submerged (NC)	1: 1118	1: 303	1: 484	1: 433	1: 1729
	Submerged (RC)	1: 346	1: 508	1: 2991	1: 1199	1: 988
Pixel size: Precision ratio ^b	Exposed	1: 8.14	1: 0.28	1: 0.22	1: 2.32	1: 5.55
	Submerged (NC)	1: 1.29	1: 4.94	1: 2.94	1: 3.37	1: 0.80
	Submerged (RC)	1: 4.17	1: 2.94	1: 0.44	1: 1.21	1: 1.45

Prior to the generation of the regression plots shown in Figure 3.14, a test of normality was carried out on the data. All datasets were found to show a roughly normal distribution and so transformation of the data was not conducted. The regression plots in Figure 3.14 indicate the

strength of the relationships between the DEMs and independent validation data. High R^2 values (>0.90) are returned for all sites, with the River Arrow datasets displaying the strongest values (all >0.99). Within the regression line equations, slope values closest to 1 and intercept values closest to 0 represent the best agreement between the DEM and corresponding independent validation data. Again, the best results are observed within the River Arrow datasets (Figure 3.14b-d). The results for Coledale Beck show a large, negative intercept value (Figure 3.14e). The poorest correlation is observed for the San Pedro River, where much greater scatter in the data can be observed (Figure 3.14a). P values of less than 0.01 are observed for all datasets.

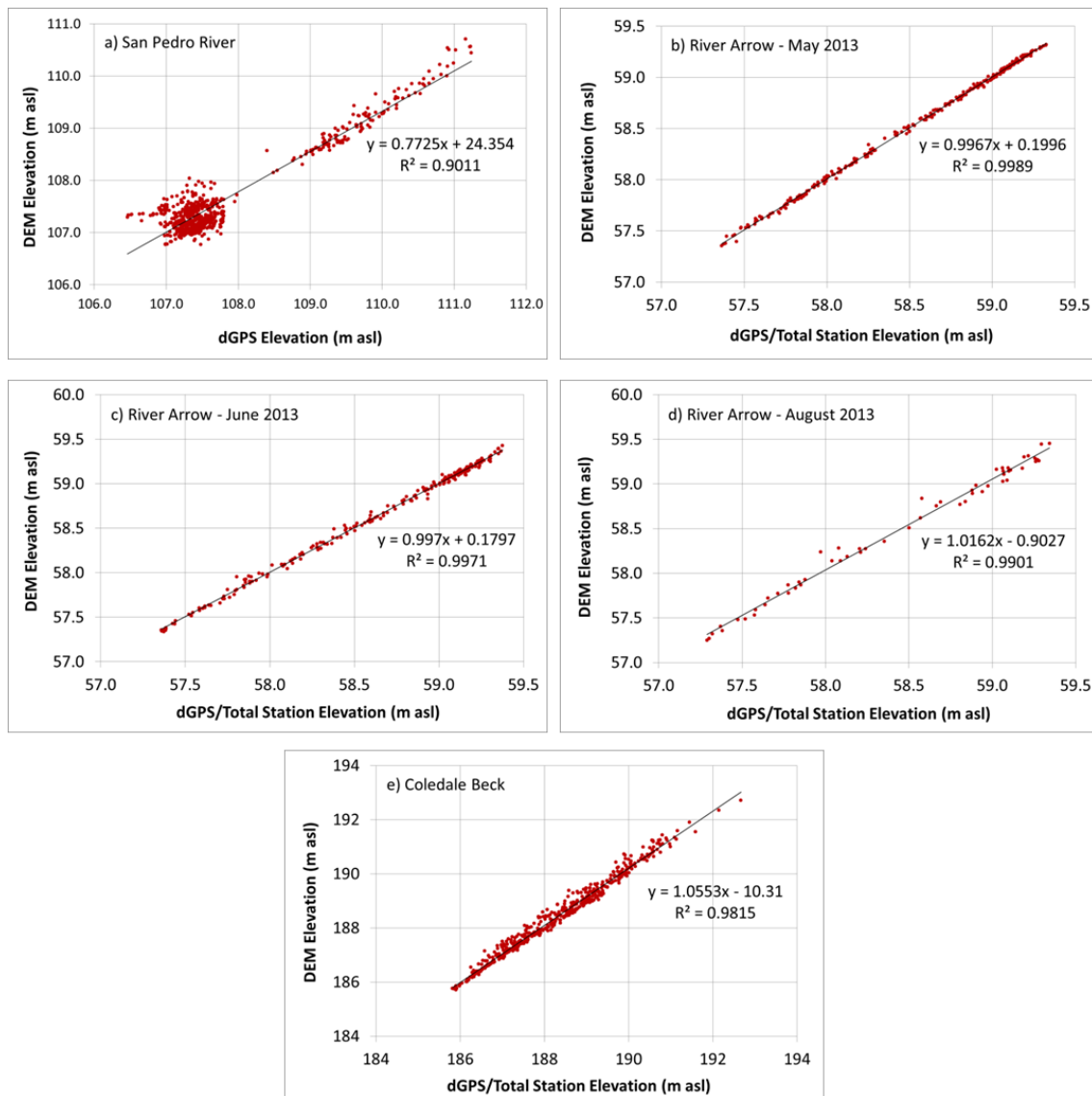


Figure 3.14. DEM elevations plotted against independent topographic survey data for exposed areas of all field sites (after Woodget et al., 2015). P values for all relationships are < 0.01 .

3.5.3 Submerged areas

Prior to refraction correction

Table 3.9 shows that the DEM mean error and standard deviation values are always poorer in submerged areas than in exposed areas for the River Arrow surveys. However, the reverse is observed for the datasets collected at the San Pedro River and Coledale Beck. The lowest mean error within submerged areas is 0.017m, observed for Coledale Beck, and low values are also found for the River Arrow datasets (0.053–0.089m). The standard deviation values for the Coledale and Arrow datasets are similar, in the range of 0.06–0.08m, with a much higher value observed for the San Pedro River (0.278m).

Figures 3.14a-d and 3.15a-d shows that both the San Pedro River and River Arrow datasets show a reduced strength of correlation for submerged areas compared to the equivalent relationships for exposed areas. This is particularly notable for the San Pedro River where the R^2 value has dropped from 0.9011 in exposed areas to 0.1154 in submerged areas. The coefficient of determination for the Coledale data is improved very slightly from 0.9815 (Figure 3.14e) in exposed areas to 0.995 in the submerged zone (Figure 3.15e). The high, positive intercept values observed for the River Arrow and San Pedro datasets is not observed within the Coledale Beck data. P values of less than 0.01, indicating the significance of these relationships, are again observed in all cases.

Water depth and DEM error

Figure 3.16 shows the relationship between water depth and DEM error for all field sites. In the case of the River Arrow and Coledale sites this is an independent measure of water depth (acquired in the field to the nearest centimetre), and for the San Pedro has been computed from the DEM itself. For the Arrow and Coledale datasets DEM error appears to increase with water depth, perhaps resulting from the effects of refraction. This trend is strongest for the Arrow datasets, with R^2 values at about 0.5, and slightly less strong for the Coledale data ($R^2 = 0.4012$). At the San Pedro site the data features a large amount of scatter and no clear relationship between computed water depth and DEM error (Figure 3.16a).

Submerged areas – with refraction correction

The effect of the refraction correction procedure on the accuracy and precision of the DEMs in submerged areas is variable, as shown by Figure 3.15 and Table 3.9. For the River Arrow

datasets, mean error is consistently improved (by c. 0.03–0.06m) following refraction correction. However, this is not observed for the Coledale Beck and San Pedro River datasets, where both mean error and precision are worsened.

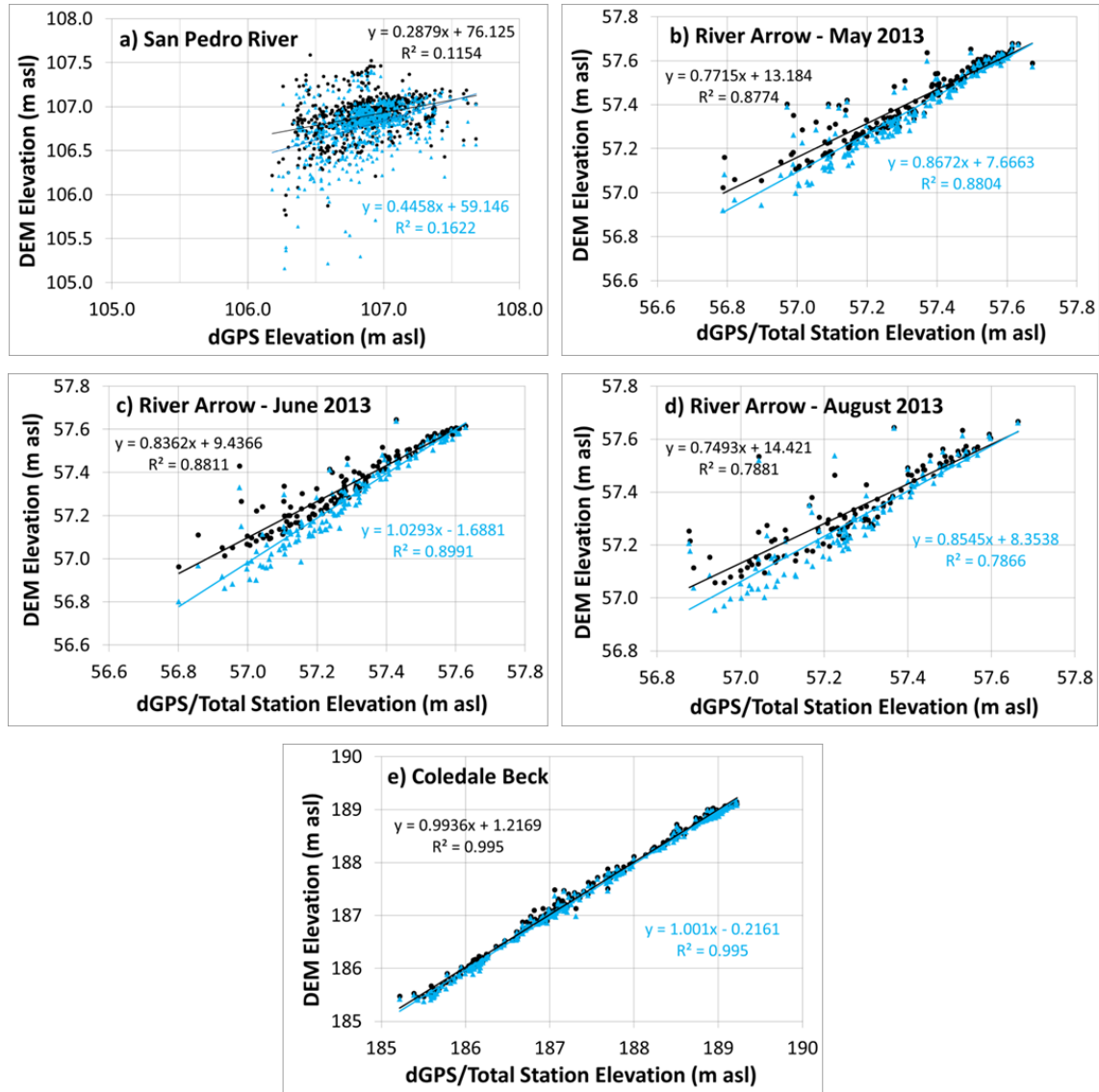


Figure 3.15. DEM elevations plotted against independent topographic survey data for submerged areas of all field sites. Black represents non-corrected data, and blue represents refraction corrected data (after Woodget et al., 2015). P values are all less than 0.01.

The River Arrow and Coledale datasets show no significant changes in DEM precision following refraction correction (Table 3.9), and the co-efficients of determination presented in Figure 3.15 show only a minor increase in strength for the River Arrow datasets and no change for Coledale Beck. However, the nature of the relationship between the DEM and validation data

(as indicated by the regression line equations) is improved in all cases (i.e. the slope is closer to 1 and the intercept closer to 0). The graphs in Figure 3.16 show DEM error plotted against water depth for all surveys both before and after refraction correction. This figure demonstrates that the refraction correction procedure has the effect of reducing the depth dependency of the error for all datasets collected at the River Arrow and at Coledale Beck. At the San Pedro River site, there was no correlation between water depth and DEM error prior to refraction correction (Figure 3.16a). As a result, the application of the correction procedure is perhaps futile and does not lead to an improvement in DEM error.

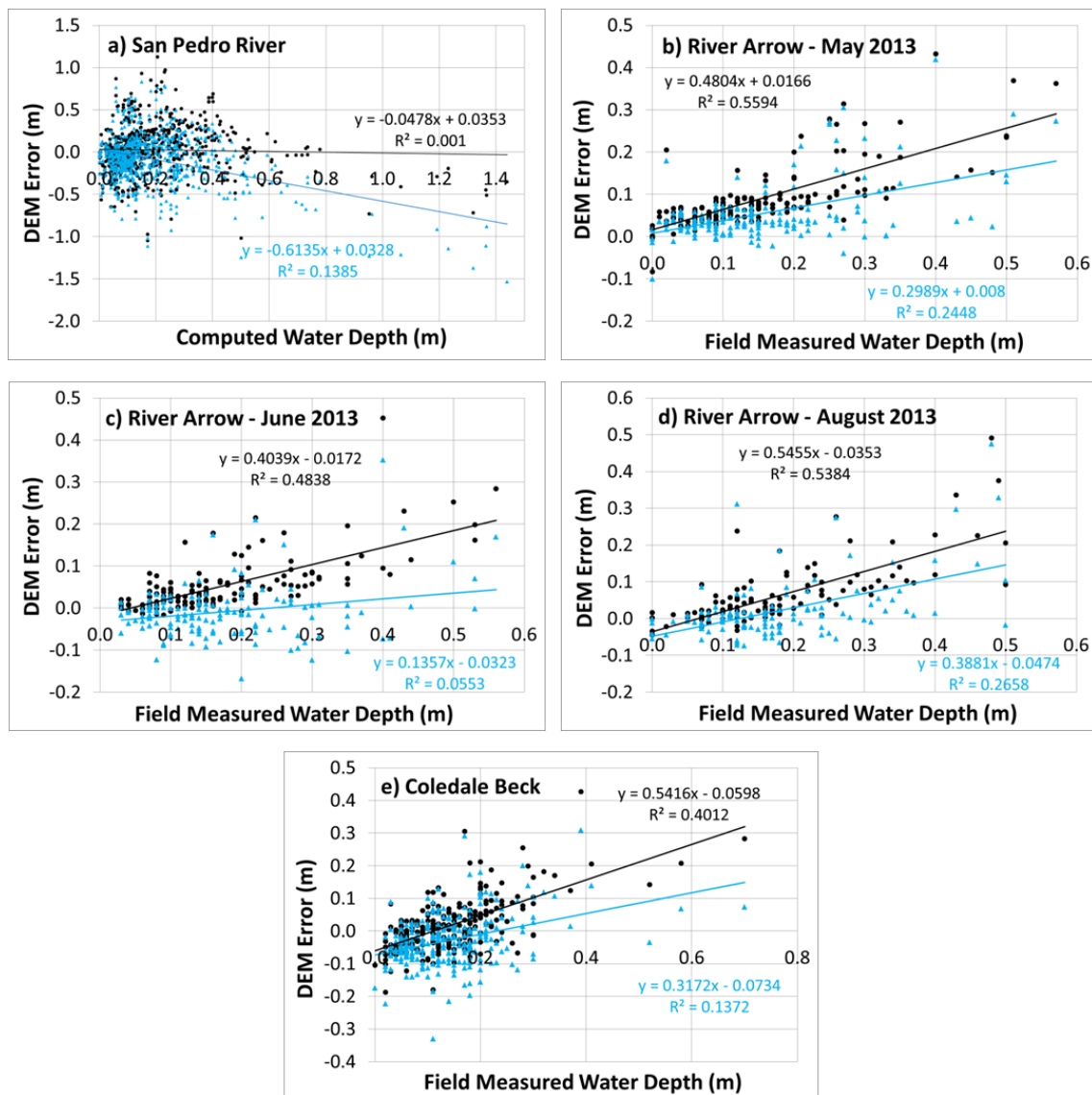


Figure 3.16. DEM error values plotted against field measured water depths for all field sites. Black represents non-corrected data, and blue represents refraction corrected data (after Woodget et al., 2015). P values are all less than 0.01, except a) NC where $p = 0.40$.

3.5.4 Spatial patterns of DEM error

The DEMs produced for the four sports hall floor tests are shown in Figure 3.17. In theory, these DEMs should all represent the same flat surface, yet clear differences are visible between the different DEMs. All DEMs show low mean errors (<0.008m) when validated against the independent elevation data (Table 3.10). The lowest mean error was found for Test 4 which used oblique images and an even distribution of GCPs. Standard deviation values are also generally low (nearly all <0.006m), but with a higher value (lower precision) reported for Test 1, which used vertical imagery (at nadir) and a central alignment of GCPs.

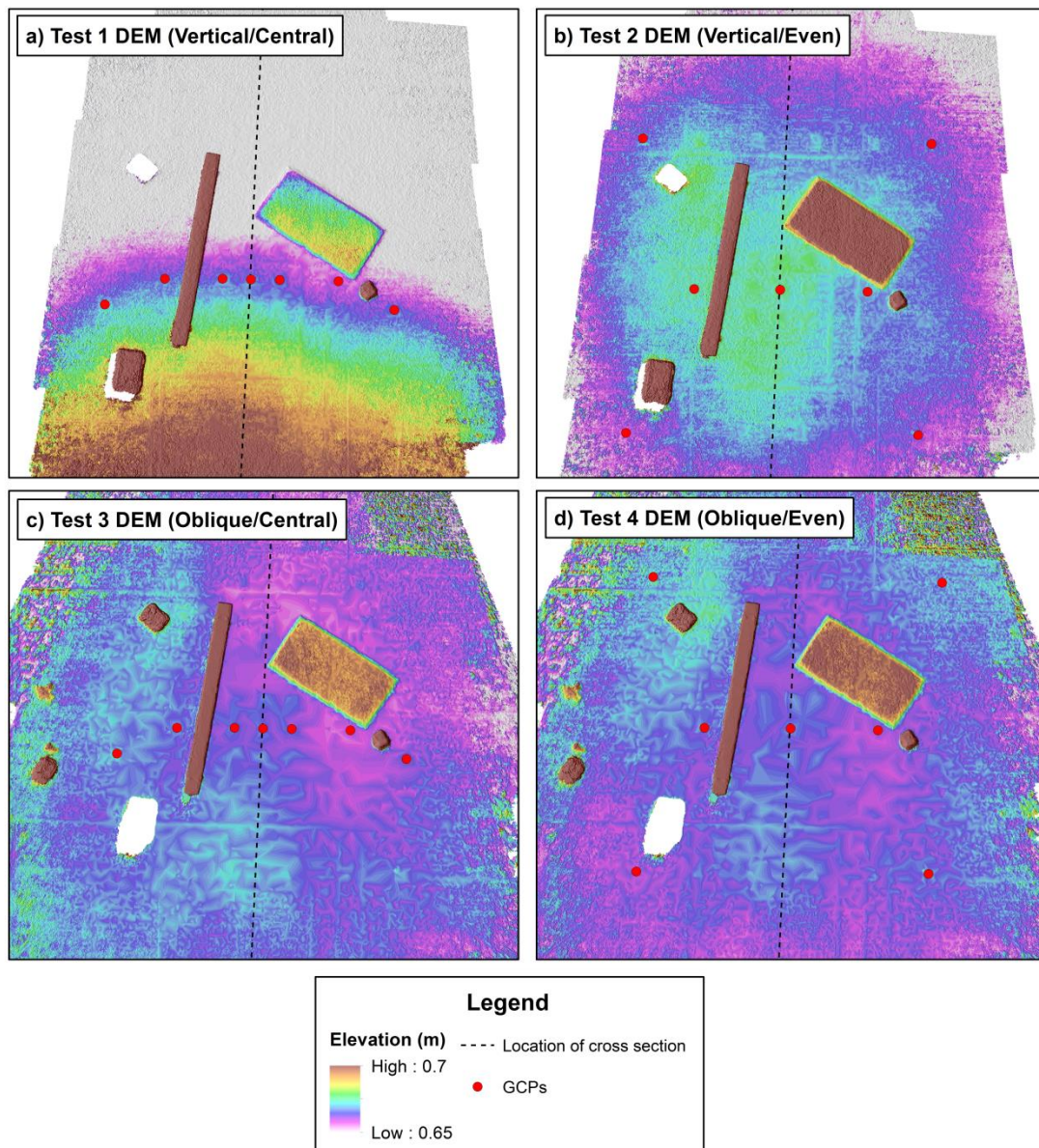


Figure 3.17. Digital elevation models for the four tests carried out for the Sports Hall floor. The dashed line indicates the location of the cross sections used to produce the DEM profiles shown in Figure 3.18.

Figure 3.18 shows a series of cross sections constructed from the DEMs of each sports hall test, compared to the approximate elevation of the sports hall floor. The profile for Test 1 (Vertical/Central) shows a pronounced slant, suggesting a c. 18cm difference in elevation between one side of the sports hall floor and the other, as also shown in Figure 3.17a. The profiles constructed from the DEMs of the other tests appear to follow the true elevation of the sports floor hall more consistently, especially those using imagery acquired at an oblique angle. However, a dome-like deformation is observed for Test 2 (Vertical/Even), with a central peak which is c. 0.02m above the surface. In addition to this deformation, small-scale noise with an amplitude of c. 0.002m is observed within the profiles of all DEMs.

Table 3.10. Spatial resolution, accuracy and precision results for the four Sports Hall tests.

Site	Sports Hall Floor			
Test	1	2	3	4
Camera angle	Vertical	Vertical	Oblique	Oblique
GCP arrangement	Central	Even	Central	Even
DEM spatial resolution (m)	0.0026	0.0026	0.0032	0.0033
Mean error (m)	-0.0075	-0.0022	0.0042	-0.0006
Standard deviation (m)	0.0282	0.0043	0.0058	0.0027

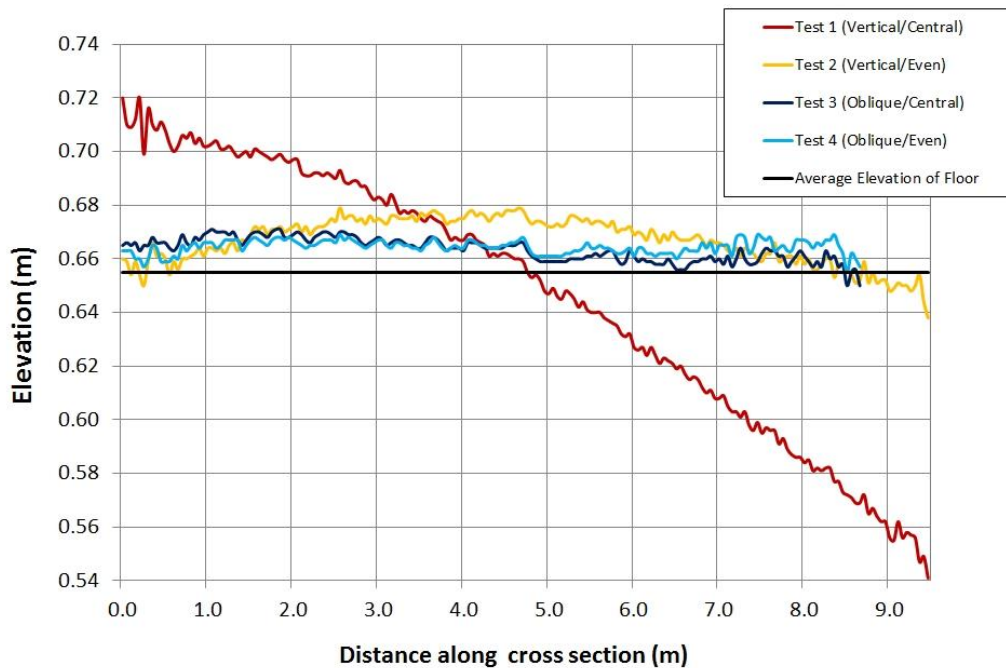


Figure 3.18. Cross section DEM profiles of the four Sports Hall tests (after Woodget et al., 2015).

For the datasets collected in field settings, the spatial patterns of error are shown in Figures 3.20 to 3.24. All figures use non-refraction corrected input DEMs. Figure 3.20 reveals a strong spatial trend in DEM error at the San Pedro River site, where validation points on the landward side of the map show significant under-prediction of elevations (up to 1m). In contrast, validation points falling in deeper submerged areas and at the two extreme ends of the site show a trend towards over-prediction. This pattern of error distribution appears to be hinged around the central alignment of GCPs at this site and is similar to that observed for Test 1 in the sports hall setting, as indicated by the graphs in Figure 3.18 and Figure 3.19.

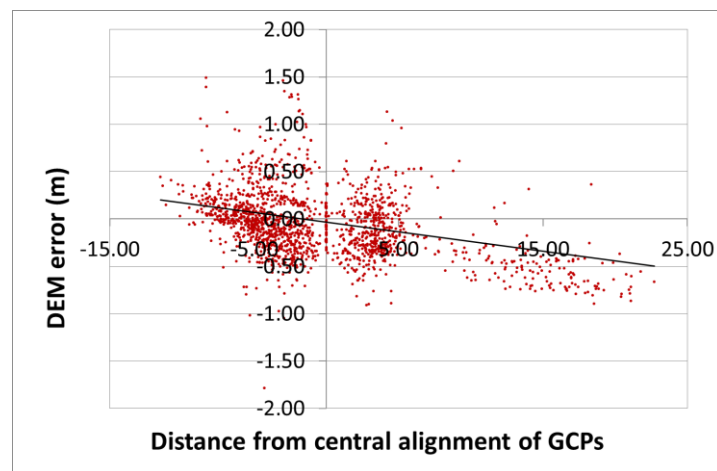


Figure 3.19. DEM errors at the San Pedro River plotted against distance from the central alignment of GCPs.

The three surveys collected at the River Arrow (Figures 3.21 to 3.23) show a consistent over-prediction of elevation within submerged areas and very low errors in exposed areas, as indicated by the data presented in Table 3.9 and Figures 3.14 to 3.15. However, they do not appear to show any other spatial trends in terms of DEM error, such as the DEM tilting observed in Sports Hall Test 1 and at the San Pedro River, or the DEM doming observed in Sports Hall Test 2.

A dome-like deformation is observed in the DEM error data presented for Coledale Beck however, as shown in Figure 3.24, where larger under-predictions occur at the edge of the DEM than in the centre. In this case, the amplitude of the dome-like deformation is c. 0.2 m. This deformation will be affecting the relationship between UAS-SfM DEM elevations and the ground truth data, as presented in Figures 3.14e, 3.15e and 3.16e. Notable over-prediction of elevations is also observed at Coledale in all densely vegetated areas and there is a trend

towards under-prediction of the exposed gravel bars. The over-prediction of elevations in some parts of the submerged areas is also noted at Coledale Beck.

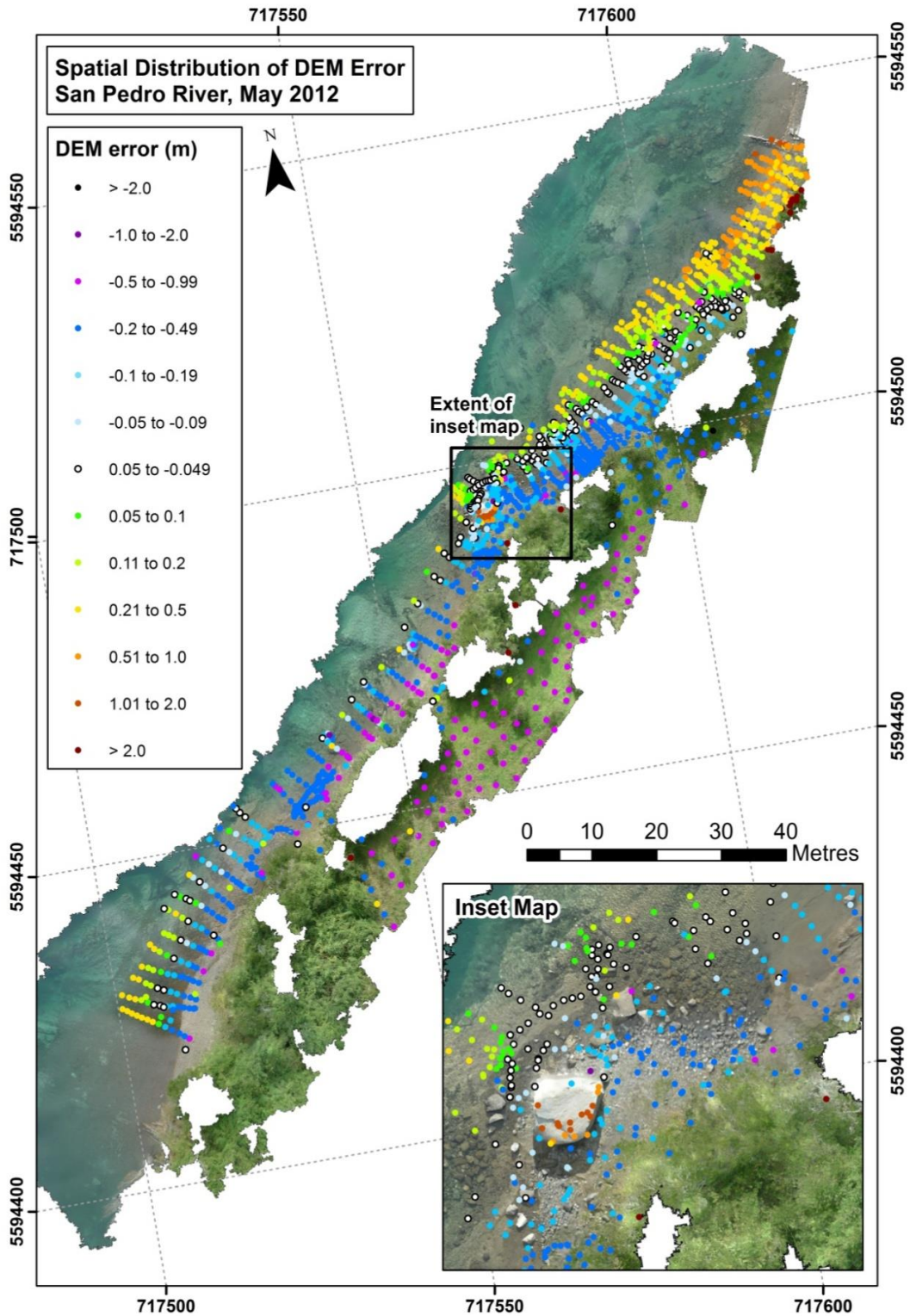


Figure 3.20. Spatial distribution of DEM error for the San Pedro River, May 2012.

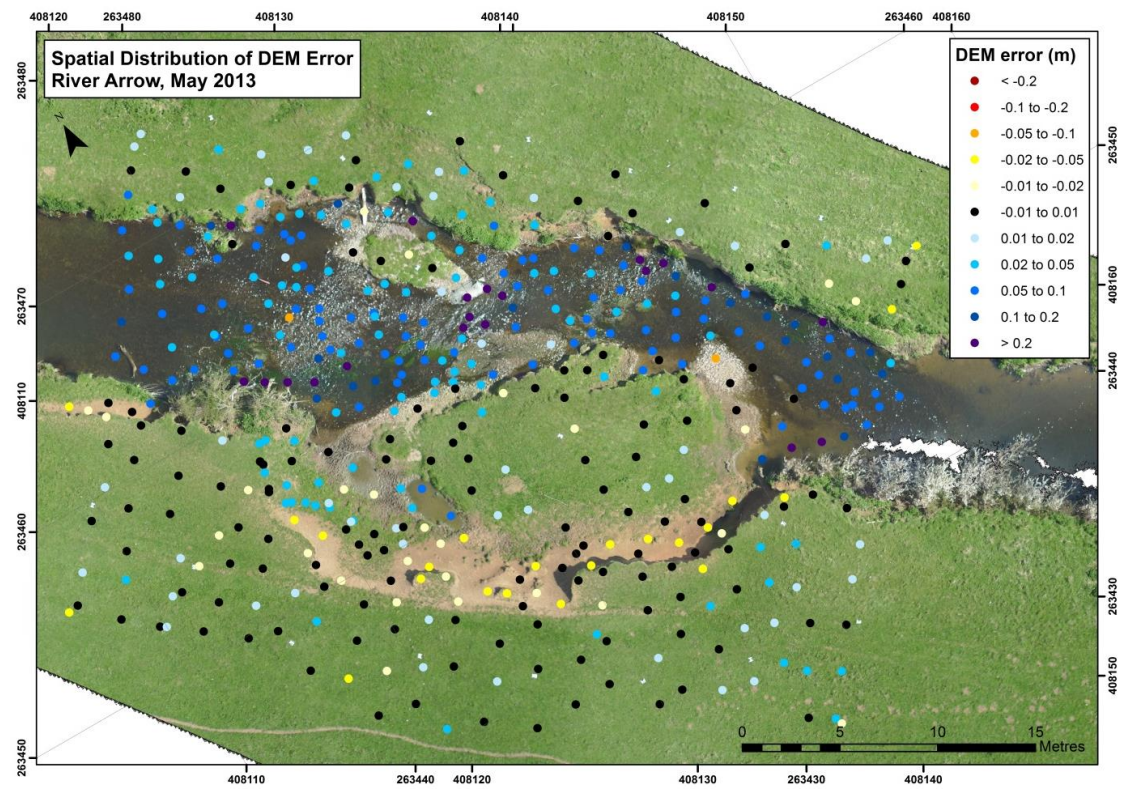


Figure 3.21. Spatial distribution of DEM error for the River Arrow, May 2013.

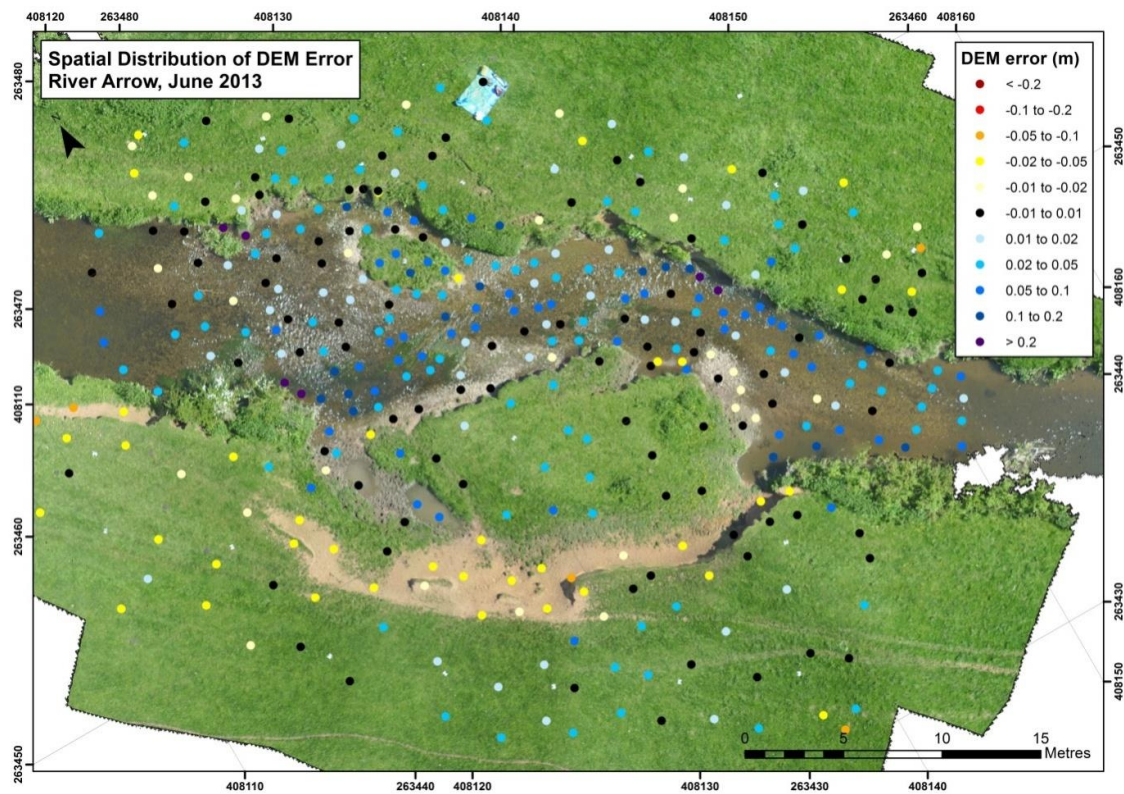


Figure 3.22. Spatial distribution of DEM error for the River Arrow, June 2013
(after Woodget et al., 2015).

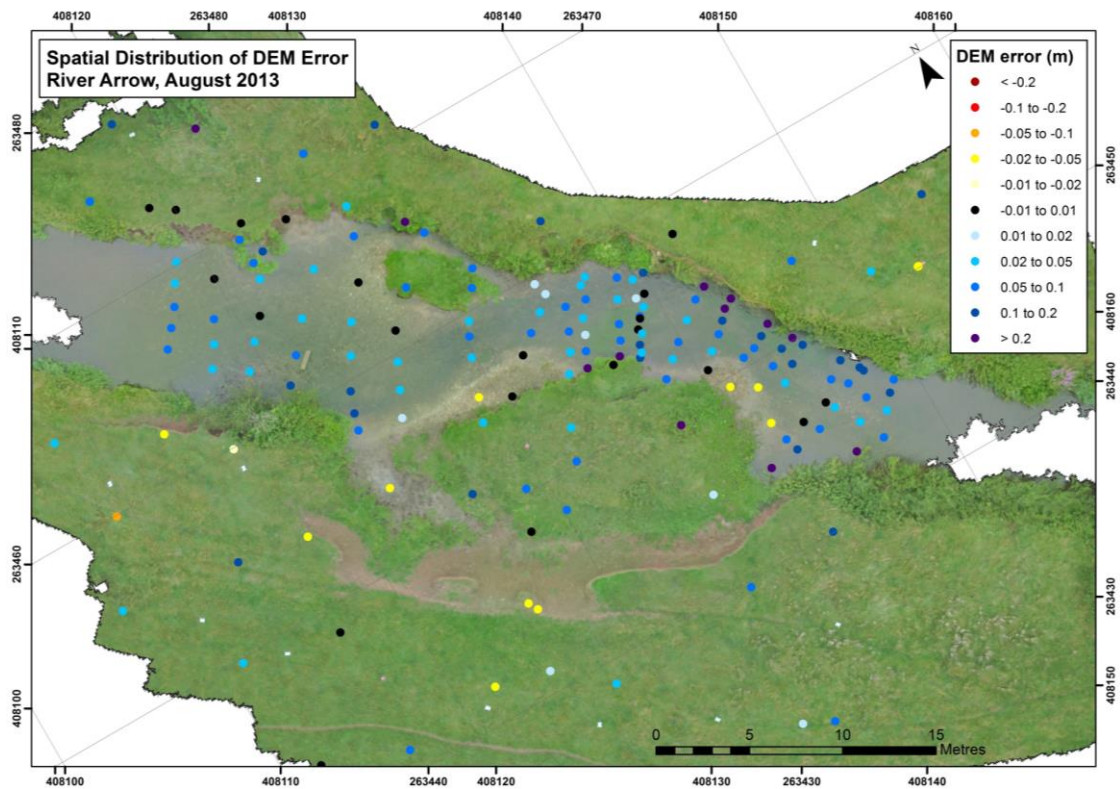


Figure 3.23. Spatial distribution of DEM error for the River Arrow, August 2013.

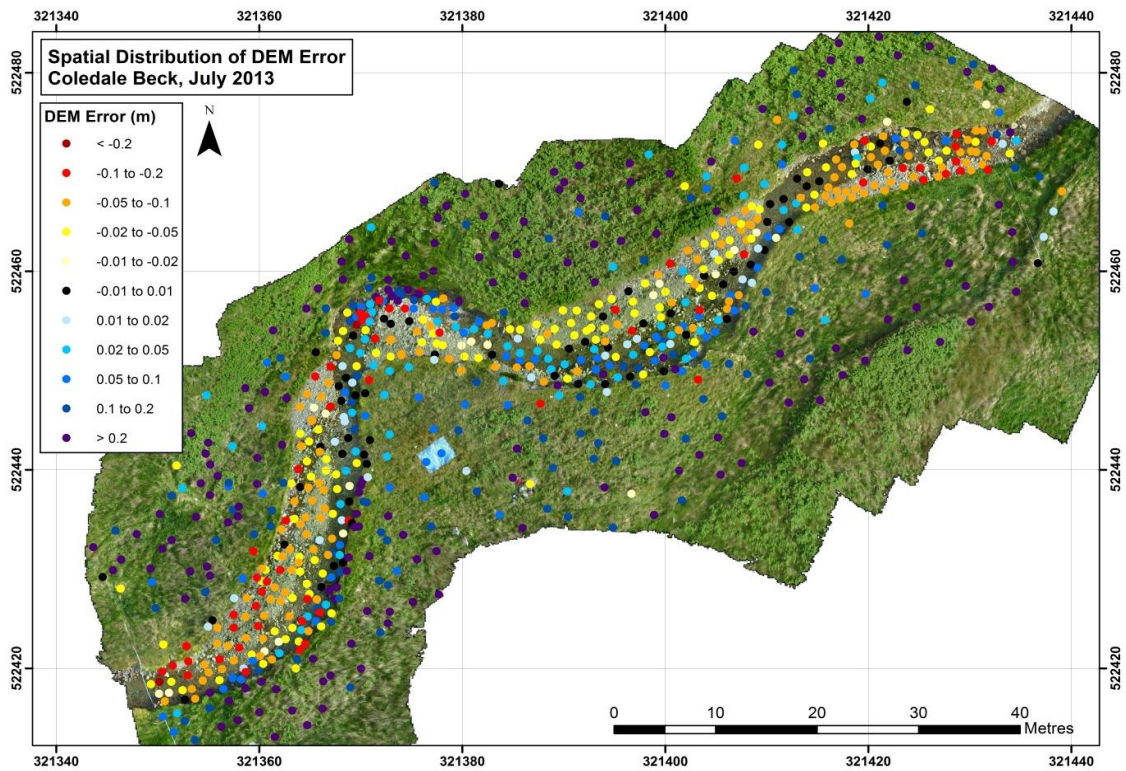


Figure 3.24. Spatial distribution of DEM error for Coledale Beck, July 2013 (after Woodget et al., 2015).

3.5.5 Comparison with TLS

Research Question 3

How does the DEM obtained using the UAS-SfM approach compare
with a DEM obtained using TLS?

The DEM generated from the TLS point cloud is shown in Figure 3.25. The DEM has a spatial resolution of 1.3cm. Despite the use of multiple scans to maximise data coverage, some gaps in the DEM are evident. These are due to the presence of dense vegetation, deeper submerged areas, shadowing and a reduction in points in the vicinity of the scanner positions themselves.

Accuracy and precision

Mean error and standard deviation values indicating the accuracy and precision of the TLS DEM are given in Table 3.11, for direct comparison with the equivalent results from the UAS-SfM data for Coledale Beck. Perhaps surprisingly, DEM accuracy values are higher for the UAS-SfM approach in almost all cases. The exception is exposed areas where validation points falling in densely vegetated areas are excluded. Here the TLS data has a mean error of 0.034m, which is slightly better than the -0.043m reported for the UAS-SfM approach, but is still higher than expected for TLS data. The standard deviation values shown in Table 3.11 indicate that the results from the UAS-SfM approach are also consistently of a higher precision than the equivalent values for the TLS data in all cases.

Spatial distribution of error

The spatial distribution of the TLS DEM error is shown in Figure 3.26. This map shows a trend towards overestimation of elevations in most areas, especially where there is dense vegetation. Within submerged areas no refraction correction has been implemented, and here overestimation is also shown by the majority of validation points. Underestimation occurs much less frequently and is limited to points falling primarily in the region of overhanging banks and occasionally on exposed gravel bars and in submerged areas.

Table 3.11. Summary of error assessment of TLS and UAS-SfM DEM for Coledale Beck. NC denotes non-refraction corrected datasets. Refraction corrected results are not shown for the UAS-SfM data because no equivalent procedure was carried out on the TLS data.

Site		Coledale Beck, July 2013	
Survey type		UAS-SfM	TLS
Mean error (m)	All data	0.082	0.175
	Exposed	0.111	0.213
	Exposed (no dense veg)	-0.043	0.034
	Submerged (NC)	0.017	0.082
Standard deviation (m)	All data	0.186	0.234
	Exposed	0.203	0.257
	Exposed (no dense veg)	0.081	0.117
	Submerged (NC)	0.074	0.086

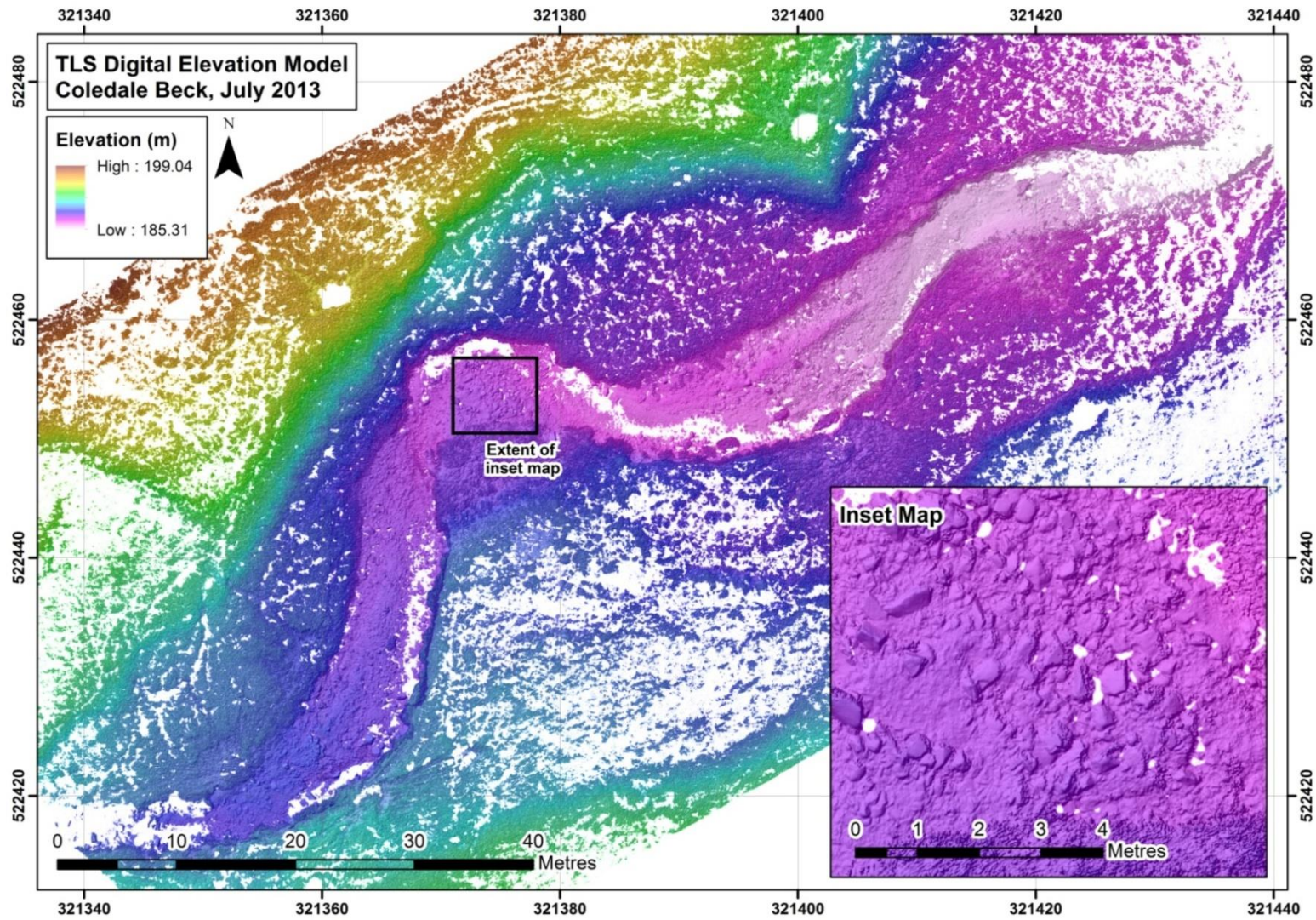


Figure 3.25. Digital elevation model of the Coledale Beck research site, generated from data collected using a TLS, July 2013.

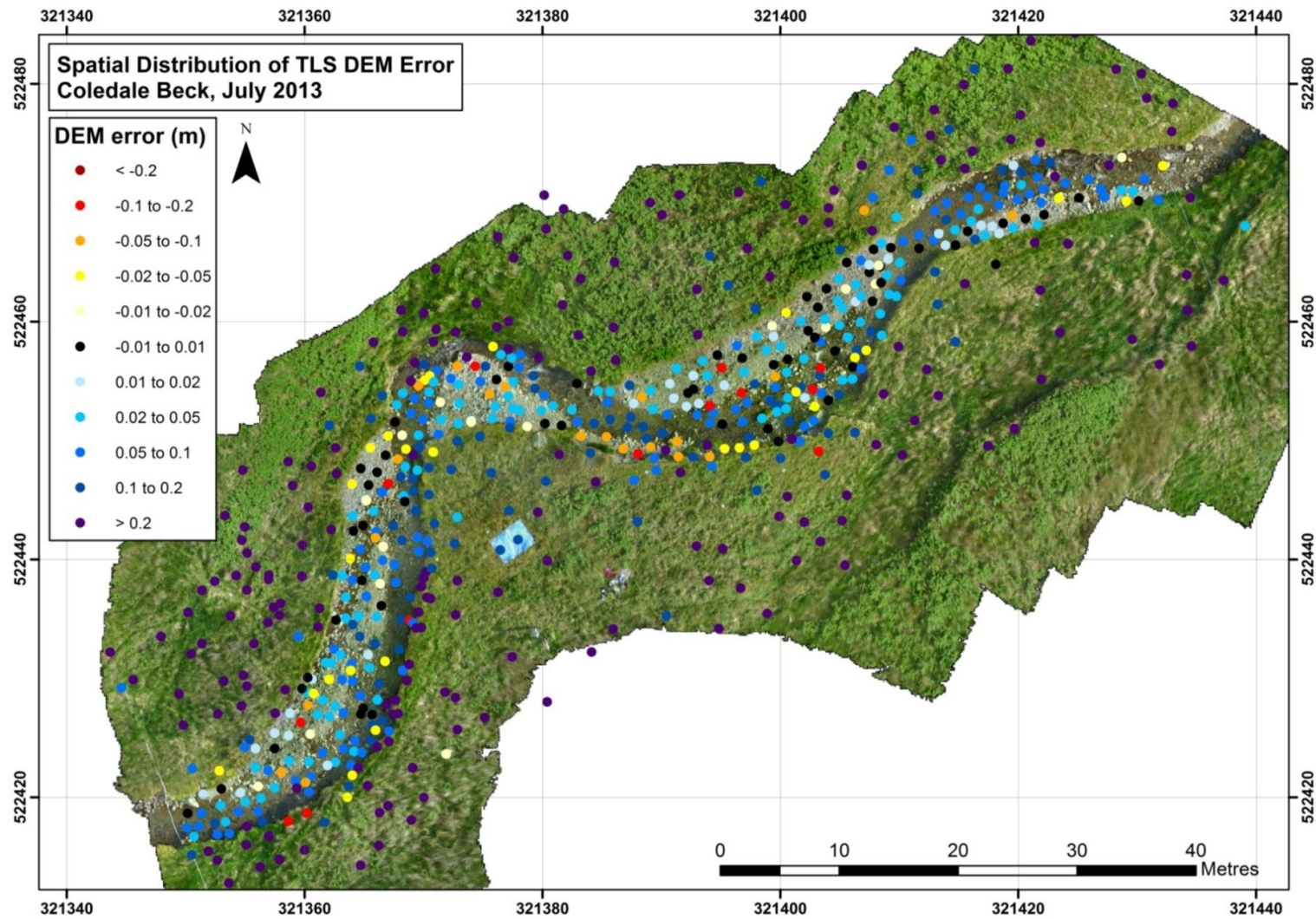


Figure 3.26. Spatial distribution of TLS DEM error for Coledale Beck, July 2013.

DEM of difference

Figure 3.27 shows the difference in elevation between the UAS-SfM and TLS derived DEMs for the Coledale Beck site. Typically, where DEMs of difference are used to assess elevation change over time, it is important to account for the error associated with each dataset as this does not represent real change between the datasets. Whilst change detection is not the focus here, differences of up to 0.048m might be expected as a result of a UAS-SfM mean elevation error of 0.022m and a TLS mean elevation error of 0.026m. The majority of the map in Figure 3.27 indicates that the TLS DEM sits above the UAS-SfM DEM, with large parts of the densely vegetated banks showing greater than 0.2m elevation difference. Along the exposed gravel bars the TLS DEM is typically 0.02-0.05m higher than the UAS-SfM DEM. In contrast, the TLS DEM is lower than the UAS-SfM DEM along the edges of steep, overhanging banks and along other key breaks of slope in vegetated areas.

The inset map within Figure 3.27 appears to show a shadow effect in the area of larger clasts, where the south-westerly sides are exhibiting a higher elevation in the TLS DEM and the north-easterly sides are showing a lower elevation in the TLS DEM (when compared to the UAS-SfM DEM). This suggests that there may be a spatial misalignment between the two datasets. The doming of the Coledale Beck UAS-SfM DEM which is suggested in Figure 3.24 is also observed in Figure 3.27. For example, this is evident along the exposed gravel bars where the TLS DEM appears to be much greater in elevation than the UAS-SfM DEM at the edges of the DEM of difference than it is in the centre.

Quantifying physical river habitat parameters using hyperspatial resolution
UAS imagery and SfM-photogrammetry

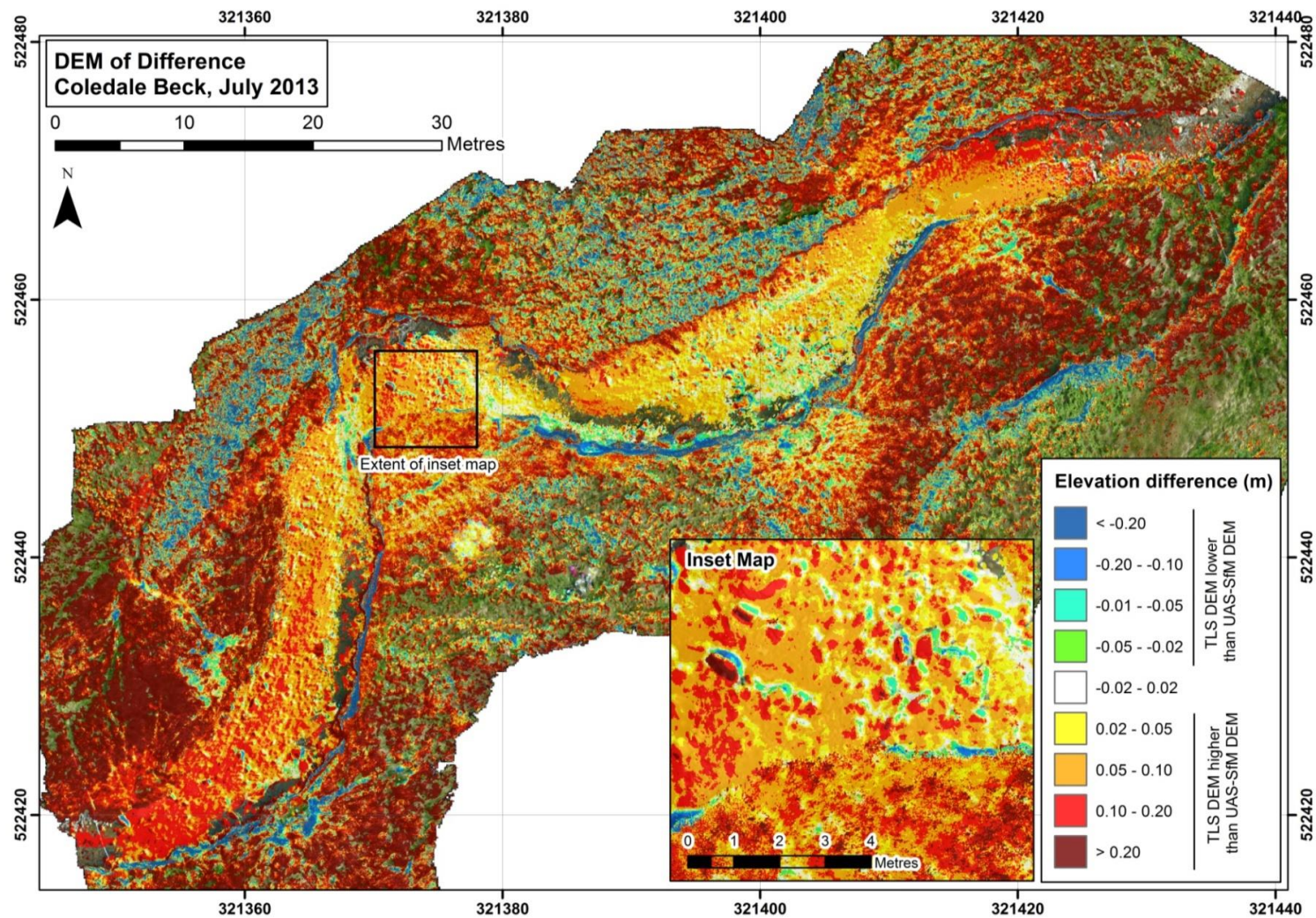


Figure 3.27. DEM of difference map showing the difference in elevation between TLS and UAS-SfM DEMs. Yellows to reds indicate that the TLS DEM has a higher elevation than the UAS-SfM DEM. Greens to blues indicates that the UAS-SfM DEM has a higher elevation than the TLS DEM.

3.6 Discussion

3.6.1 Accuracy, precision and repeatability

Research Question 1

How accurate, precise and replicable are the topographic datasets generated using a UAS-SfM approach? Do these measures vary between different river systems?

Research Question 2

How does the accuracy and precision of the UAS-SfM DEMs vary between exposed and submerged terrain, and does the application of a simple refraction correction procedure improve the accuracy of topographic products in submerged areas?

The quantitative assessment of the UAS-SfM approach presented within this chapter has demonstrated the ability to produce hyperspatial (c. 0.02m), continuous topographic datasets for the fluvial environment.

Exposed areas

The DEMs of the River Arrow and Coledale Beck sites are of high accuracy (0.004-0.04m) and precision (0.02-0.07m) for exposed areas which are non-vegetated or feature only low-level vegetation (such as short grass). These results are comparable with findings reported in the wider literature for the use of UAS and SfM-photogrammetry for quantifying topography in both fluvial and other settings (Lejot et al., 2007, Harwin and Lucieer 2012, James and Robson 2012, Fonstad et al., 2013). The [pixel size: precision] ratios indicate that mean error in exposed areas varies from less than the pixel size (Arrow May and June datasets) to more than five times the pixel size (Coledale Beck) where dense vegetation degrades accuracy measures. Variability is also observed in the [precision: flying height] ratios, which range from 1: 257 to as high as 1: 6613. These results are at best in line with those obtained from traditional photogrammetry (typically 1: 1080-9400), and sometimes below (James and Robson 2012). They are also roughly in line with those results calculated from more recent studies using UAS and/or SfM for exposed areas, as shown in Table 3.12.

Submerged areas

The UAS-SfM DEMs produced in the clear water, submerged areas of the River Arrow and Coledale Beck sites (with refraction correction) have mean errors of 0.004-0.056m and standard deviations of 0.068-0.084m. These datasets are of finer spatial resolutions and higher accuracy than those reported for bathymetric laser scanning, digital photogrammetry and the

spectral-depth method. However, these approaches are often conducted at quite different scales. TLS surveys are more comparable to the UAS-SfM approach in terms of scale of assessment. A direct comparison with TLS data is presented in section 3.6.2.

A comparison of the mean errors, [precision: flying height] and [pixel size: precision] ratios obtained in submerged areas against those obtained by other recent studies is presented in Table 3.12. These data suggest that the spectral-depth approach, applied to hand-held airborne (Javernick et al., 2014) or UAS imagery (Tamminga et al., 2014), provides better results in submerged areas than the refraction correction method presented here and within Tamminga et al., (2014). However, it should be noted that both these studies found it necessary to significantly reduce the image resolution (to 1m in Tamminga et al., 2014 and to 0.5m in Javernick et al., 2014) to account for irregularities in substrate spectral properties and water surface roughness. Whilst this has the apparent effect of improving the [pixel size: precision] ratios, it reduces the attractiveness of the approach for fluvial topography and depth assessments at the mesoscale.

Table 3.12. Comparison of the validation results from recent UAS and SfM approaches. Results from Woodget et al., 2015 are shown in bold and are the same as those reported within this chapter (for the June 2013 survey of the River Arrow). NC and RC denote non-refraction corrected and refraction corrected datasets respectively.

Setting	Reference and Approach	Mean error (m)	Average flying height (m)	Average spatial resolution (m)	Precision: flying height ratio	Pixel size: precision ratio
Exposed areas	Javernick et al., 2014 – SfM only	0.07	700.00	0.14	1: 10000	1: 0.50
	Tamminga et al., 2014 – UAS-SfM	0.032	100.00	0.05	1: 3125	1: 0.64
	Woodget et al., 2015 – UAS-SfM	0.004	25.81	0.02	1: 6613	1: 0.22
Submerged areas (spectral depth)	Javernick et al., 2014 – SfM only	-0.06	700.00	0.5	1: 11667	1: 0.12
	Tamminga et al., 2014 – UAS-SfM	0.007	100.00	1.00	1: 14286	1: 0.01
Submerged areas (DEM - NC)	Tamminga et al., 2014 – UAS-SfM	0.144	100.00	0.05	1: 694	1: 2.88
	Woodget et al., 2015 – UAS-SfM	0.053	25.81	0.02	1: 484	1: 2.94
Submerged areas (DEM - RC)	Tamminga et al., 2014 – UAS-SfM	0.064	100.00	0.05	1: 1563	1: 1.28
	Woodget et al., 2015 – UAS-SfM	-0.004	25.81	0.02	1: 2991	1: 0.44

Repeatability

The three surveys conducted at the River Arrow indicate that the approach is capable of producing consistently high quality orthophotos and DEMs in exposed areas. In submerged areas, all River Arrow surveys produce DEMs with both a mean error and standard deviation less than 0.09m prior to refraction correction and less than 0.06m following refraction correction. Whilst these results suggest a robust and repeatable approach, the accuracy and precision of the topographic datasets is shown to vary between different river systems, and between the exposed and submerged parts of the terrain. A number of key factors can be identified which may each be responsible, in part, for the variable results obtained both within and between sites;

1. The influence of water.

As shown in Table 3.9, submerged parts of the study site typically give reduced levels of accuracy (0.02-0.09m) and precision (0.06-0.09m), and lower [precision: flying height] and [pixel size: precision] ratios compared to exposed areas. The datasets from all sites show a consistent over-prediction of elevation in submerged areas, which increases with water depth (Figure 3.16), suggesting that the DEM error is depth dependent. Comparable results have been found by similar studies and have attributed this overestimation to a combination of refraction effects and the photogrammetric process fixing matches at points within the water column itself (Tewinkel 1963, Fryer 1983, Fryer and Kniest 1985, Westaway et al., 2000, Westaway et al., 2001, Butler et al., 2002, Feurer et al., 2008, Tamminga et al., 2014). In addition, the imagery used here is 8-bit jpeg imagery. This displays radiation intensities in 256 grey levels and results in reduced contrast (or texture) in the deeper, darker parts of the scene. Other studies have found this reduced radiometric resolution in deeper areas to reduce the success of optical bathymetric mapping (Legleiter et al., 2004, Legleiter 2013). The reduced image texture in deeper parts of the channels is likely to reduce the success of the SfM-photogrammetry matching process, and therefore also affect the DEM accuracy in these areas. Future work might explore the success of using higher bit-depth imagery. Although not specifically tested here, it is assumed that increased water turbidity would result in a similar degradation of DEM accuracy, again due to the effect this would have in reducing image texture or obscuring the channel bed altogether.

The simple refraction correction procedure employed here had the effect of reducing the magnitude of, but not entirely eliminating, the DEM overestimation in submerged areas for all surveys except the San Pedro River dataset. The UAS-SfM DEM errors were reduced by c. 50% for River Arrow surveys, as indicated by the [pixel size: precision] ratios in Table 3.9. Refraction correction also led to a significant improvement in mean errors in submerged areas for the River Arrow surveys where there was an existing correlation between DEM error and water depth (Figure 3.16). These improvements were not observed for the Coledale Beck dataset. This may be because the correlation between DEM error and water depth is weaker for Coledale Beck (Figure 3.16e) and the mean error at this site was already very low prior to refraction correction (0.017m). This mean error value is in fact already comparable to those obtained for exposed areas and perhaps suggests that refraction correction is not required for this survey. Westaway et al., (2001) found that at water depths less than 0.2m, the effects of refraction on the results of through-water photogrammetry were negligible thereby deeming correction procedures unnecessary. Coledale Beck is a very shallow stream where 83% of the DEM validation points fall within depths of less than or equal to 0.2m. Therefore, it is suggested that these shallow depths provide an explanation for the limited success of refraction correction at this site. Further research specifically testing this hypothesis would be beneficial.

2. The presence of vegetation.

The UAS-SfM DEMs are based on indirect measures of elevation calculated using image parallax. As a result, only the elevation of surfaces visible within the imagery can be computed. This means that where dense vegetation covers the ground surface, only the elevation of the uppermost 'surface' of the dense vegetation can be obtained. For example, the elevation of the thick brackens and long grasses present at the Coledale Beck site cause the apparent overestimation of elevations in these areas (Figure 3.24). With the removal of validation points in these areas, the mean error and standard deviation are dramatically improved. This effect is also observed within the River Arrow datasets, where the accuracy and precision within exposed areas is notably worse for the August survey when vegetation coverage is at its most dense (Table 3.9). Similar results are found in the SfM work presented by Westoby et al., (2012) and Javernick et al., (2014), and identified as an issue for studies using

traditional photogrammetry (Lane 2000, Lane et al., 2000). For topographic surveying of exposed areas (i.e. non submerged), this limiting factor represents a notable disadvantage in comparison with approaches such as airborne laser scanning, where penetration of vegetation cover is possible in some circumstances (e.g. Kraus and Pfeifer 2001).

3. The configuration of GCPs.

As demonstrated by the test surveys undertaken in the sports hall, the arrangement of GCPs within a scene has a significant impact on the quality of the DEM produced using a UAS-SfM approach. Table 3.10 indicates that the use of a central alignment of GCPs leads to DEMs of lower accuracy (i.e. higher mean errors) and lower precision (i.e. higher standard deviations), than when a more even arrangement of GCPs is used with the same input imagery. Similar findings are reported by Vericat et al., (2009) and Harwin and Lucieer (2012). However, the results from the sports hall test also provide an indication of the spatial distribution of DEM errors resulting from different GCP configurations. In the case of imagery acquired at (or very close to) nadir, the central alignment of GCPs results in a tilting of the DEM, where errors are as great as 10cm. The GCPs used at the San Pedro River site were arranged in a central line due a combination of access constraints and inexperience with the UAS-SfM process. Validation data for this site suggests that a similar tilting of the DEM is being observed here, with resulting errors as great as c. 1m. These findings highlight the importance of a fairly even spread of GCPs which adequately represents the range of elevations within the scene.

4. The viewing angle of the camera.

The test surveys of the sports hall also indicate that the viewing angle of the camera plays an important role in the resultant quality of DEMs produced using a UAS-SfM approach. The use of imagery acquired at (or very close to) nadir using this non-metric, consumer-grade camera produces lower accuracy and lower precision values than equivalent imagery acquired at an oblique viewing angle, when used with the same configuration of GCPs. Furthermore, the use of oblique imagery appears to result in small, random errors within the DEMs, whereas the use of vertical imagery produces larger, systematic error trends. This comprises a tilting of the DEM when vertical

imagery is used with a central alignment of GCPs, and a central doming of the DEM when vertical imagery is used with a more even distribution of GCPs (Figure 3.17 and 3.18). This doming effect is also observed in the DEM produced for Coledale Beck (Figure 3.24), and is particularly evident when the UAS-SfM DEM is compared to the TLS data acquired at this site (Figure 3.27).

Existing studies using traditional photogrammetry have established that the self-calibration of camera lens models can be prone to errors where image datasets are acquired at nadir from consumer-grade digital cameras (Chandler et al., 2003, Chandler et al., 2005, Wackrow and Chandler, 2008). Some have also demonstrated that images acquired at nadir can produce dome-like deformations in the output DEMs, when the radial lens distortion is not adequately modelled (Chandler et al., 2003, Chandler et al., 2005, Wackrow et al., 2007, Wackrow and Chandler 2011). A recent SfM study by Javernick et al., (2014) also found a dome-like pattern of error before the optimisation of the camera lens model in PhotoScan (Figure 3.28). However, similar dome-like deformations are not reported by the recent SfM works of Westoby et al., (2012) or Fonstad et al., (2013). The amplitude of the dome-like deformation seen within the sports hall and Coledale Beck DEMs is moderate. It appears to scale with flying height, with [amplitude: flying height] ratios of 1:200 and 1:300 for the cases of the indoor and outdoor flights respectively. It seems likely that these errors can be deceptively small for small flying heights and therefore may have gone unnoticed in previous literature.

Fortunately, the works of Wackrow and Chandler (2008, 2011) and more recently James and Robson (2014) find that the addition of oblique imagery with convergent view-angles can eliminate the dome-like deformation within output DEMs. It is possible then, that the dome-like deformation is actually not present where image acquisitions comprise sufficient variability around nadir and might explain why it is not observed in some of the DEMs presented within this study and elsewhere (e.g. Westoby et al., 2012, Fonstad et al., 2013). The objective of surveying submerged topography within this thesis dictated the acquisition of imagery from vertical viewing angles. Oblique images would have been affected differently by refraction and thus may have necessitated the use of a more advanced correction procedure. Any

departure from vertical viewing angles within the field surveys presented here results from platform instability during flight rather than survey design. However, the results suggest that in future, greater consideration should be given to image viewing angle during the UAS flight planning phase, when consumer grade digital cameras are being used (Wackrow and Chandler, 2011). Further research is also clearly needed to improve current understanding of the error sources within the SfM-photogrammetry process and users should be aware that the visually stunning outputs are not error-free.

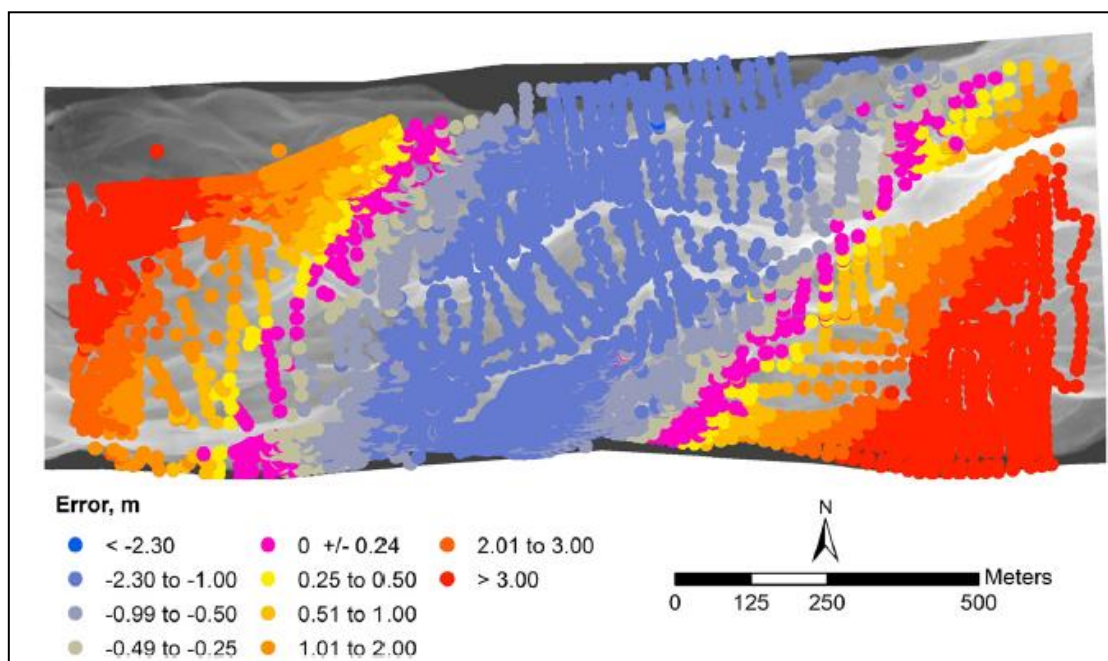


Figure 3.28. Spatial distribution of colour-coded residual elevation errors for all ground truth values (Javernick et al., 2014).

5. The spatial accuracy of the UAS-SfM georeferencing.

The assessment of UAS-SfM DEM accuracy is determined in part by the accuracy of the UAS-SfM georeferencing process. The georeferencing procedure used in SfM-photogrammetry differs significantly from that used within traditional photogrammetry. The GCP locations are not specified at the beginning of the photogrammetric process and it is assumed that the SfM matched points contain less error than surveyed GCPs. In theory, this means that when GCP locations are specified (following the initial image alignment, geometry building and image texturing stages), the use of a least squares, seven-parameter registration solution leads to a more even

propagation of any GCP errors within the DEM, rather than larger errors occurring in localised areas. Whilst this has the advantage that small errors in the GCPs are less disruptive, it also means that errors introduced by the earlier SfM point matching process cannot be removed.

An independent assessment of the spatial errors following the georeferencing process is provided by the residual errors in Table 3.8. These errors can be taken to indicate the likely magnitude of misalignment between the DEM and the independent validation data. Whilst the majority of mean error values presented in Table 3.8 are less than the DEM pixel size (c. 0.02m), the standard deviation values suggest that larger errors do exist in some areas and that the magnitude of errors is not entirely even within each DEM. Therefore, although relatively small, these errors may in part explain the variable accuracy and precision of UAS-SfM DEMs both within and between different research sites.

6. The quality of the input UAS imagery.

The SfM-photogrammetry process computes indirect measures of elevations using parallax, and thus where image quality is poor (e.g. due to blurring) or lacking in texture (e.g. spectrally homogeneous areas) then greater amounts of noise (i.e. erroneous point matches) and larger DEM errors are likely to be observed. Whilst efforts were made to exclude images which were obviously affected by blurring, little can be done to improve texture in spectrally homogenous parts of the image. It is thought that differing scene illumination conditions between surveys and even between flights of the same survey also affect the UAS imagery quality, introducing variable levels of point cloud noise and error within the DEMs. For example, the dull and slightly misty conditions present during the River Arrow August survey may be partly responsible for the observed reduced levels of accuracy and precision in comparison to the May and June surveys of the same site.

7. Errors in the survey positioning data.

Small errors may exist in the total station and dGPS data used as independent topographic data and to survey the position of GCPs used to georeference the UAS-SfM outputs. These errors may be caused by tilting of the survey pole with prism used

to collect total station points (and hence horizontal displacement of positions), or errors inherent to the dGPS data which can result from factors such as poor satellite geometry. In addition, the difference in spatial scale between the survey points and the footprint of the DEM may introduce further error. These two issues are likely to be a particular problem in areas where elevation changes rapidly over short distances. Visual checks sometimes find larger overestimations in the vicinity of steep banks or overhanging vegetation, but this affects only a small proportion of the validation points at all sites.

8. Time lag between UAS survey and collection of validation data.

The independent topographic validation datasets were collected within a day or two of the UAS image acquisition surveys for most sites presented here. Within such time, very little topographic change is expected to have occurred. At the San Pedro River site however, part of the validation data were collected some months before the UAS survey. Little geomorphic change was expected to have occurred within this bedrock channel during this time given the season, however it is possible that some movement of sediment overlying the bedrock occurred. The larger systematic DEM errors introduced by the GCP configuration at this site makes it difficult to reliably identify other sources of error, but the movement of sediment may in part be responsible for the observed distribution of errors at this site (Figure 3.20).

In addition to these factors, a consistent underestimation of c. 4cm of the exposed gravel bars at Coledale Beck is also noted (Figure 3.24). Whilst the magnitude of this underestimation seems to be in part determined by the doming effect discussed previously, it is not clear why it exists in the first instance. Of the 30 GCPs used at this site, only 3 were placed on exposed gravels with the remainder placed at higher elevations of the surrounding banks. This may mean that the range of elevations present within the site were not adequately represented by the GCPs, however further investigation is required to explore this. Similar patterns are not observed within any of the other surveys presented here.

3.6.2 Comparison with TLS

Research Question 3

How does the DEM obtained using the UAS-SfM approach compare with a DEM obtained using TLS?

Comparison with TLS at Coledale Beck

Figure 3.27 shows the DEM of difference for the UAS-SfM and TLS DEMs of Coledale Beck. Whilst this appears to highlight the slight doming present in the UAS-SfM data, its usefulness may be limited by a possible spatial misalignment between the two datasets. This is highlighted in the difference patterns around larger clasts which occurs throughout the scene and therefore is not thought to be related to TLS scan angle. Mean planimetric residual errors are low (<1cm) in both datasets and therefore it is not clear why this apparent offset is observed. Nevertheless, it should be noted that the following observations may have been affected by this spatial misalignment.

A comparison of DEM elevations with the independent topographic validation data suggests that the accuracy and precision of the UAS-SfM DEM is better than the TLS DEM in nearly all parts of the scene (Table 3.11), and the coverage is more continuous and complete. The spatial distribution of TLS DEM error (Figure 3.26) shows a trend towards over-prediction of elevations in nearly all parts of the scene. Given the use of TLS measurements as validation data for UAS-SfM/SfM outputs elsewhere (e.g. Westoby et al., 2012), higher accuracy and precision values might have been expected.

In submerged areas, it is suggested that this overestimation can be largely attributed to the strongly oblique viewing angle of the TLS. This results in a greater angle of refraction at the air-water interface in submerged areas and subsequent over-prediction of channel bed elevations, as also observed in the UAS-SfM data. Refraction correction of TLS surveys in submerged fluvial settings has not been widely used to date, but has recently seen some success in field settings over small areas (Smith et al., 2012, Smith and Vericat 2014), albeit at relatively coarse spatial resolutions (e.g. 1m, Smith and Vericat 2014). However, time, software and data access constraints meant that refraction correction of TLS was not attempted within this study so further comparison is not possible. In deeper parts of the channel (> c. 0.3m), there is a lack of TLS returns altogether resulting in large holes within the DEM. This problem is not observed with the UAS-SfM approach, though it is noted that success of the UAS-SfM approach in these areas is contingent on the presence of clear water and has only been demonstrated up to a maximum depth of c. 0.7m. This is roughly in line with reported maximum depths achieved using digital photogrammetry, bathymetric LiDAR and the spectral-depth method (Table 3.2).

The oblique viewing angle of the TLS also means that in areas of dense vegetation the TLS is more likely to 'see' the upper elevations of vegetation than an approach looking vertically downwards. Thus larger over-predictions are also observed in these areas when compared to the UAS-SfM results. Under-estimations observed along overhanging banks probably also result from the oblique viewing angle of the TLS, allowing it to 'see' beneath the overhang, whilst the independent validation data represents the top of the bank. In contrast, in exposed areas where there is little or no vegetation cover, the TLS survey performs much better. Spatial coverage is improved (i.e. fewer holes in the DEM) and the TLS DEM mean error is not only notably lower than in other parts of the scene, but is slightly better than the equivalent value for the UAS-SfM DEM.

These findings suggest certain advantages of the aerial viewpoint of the UAS-SfM approach over the oblique viewpoint of the TLS. However, they also indicate that where a view of the terrain is not impacted by vegetation or the presence of water, the TLS provides slightly higher resolution and slightly more accurate DEMs. This comparison is not without its trade-offs though. At the current time, TLS systems remain significantly more expensive to acquire (c. £50,000 for a Leica ScanStation C10, Leica Geosystems Ltd 2014, *pers. comm.*) than a UAS-SfM set-up equivalent to the one used here (c. £2000 for a DJI F550 UAS including camera, P. Carbonneau 2014, *pers. comm.*). Furthermore, in the current example, the collection of TLS data took more than double the fieldwork time when compared to the UAS-SfM approach. Future work should look to explore and if possible, reduce the spatial offset between datasets, so that stronger conclusions may be drawn from the comparison of UAS-SfM and TLS DEMs for fluvial topography.

3.6.3 Summary

The choice of a method for quantifying topography, within both fluvial and other settings, will be determined by the specific requirements of the intended application in terms of scale and accuracy, as well as the availability of resources, time and funds. However, the research presented within this chapter has demonstrated the potential of a UAS-SfM approach for quantifying the topography of fluvial environments at the mesoscale with hyperspatial resolutions (0.02m). This approach provides a single surveying technique for generating complete, accurate and precise DEMs for exposed areas of the fluvial environment, and within submerged areas for depths up to 0.7m providing the water is clear, there is limited water

surface roughness (e.g. white water) and refraction correction is implemented. As such, it represents an alternative to hybrid approaches and has potential as a tool for characterising the topographic heterogeneity at the mesoscale within a 'riverscape' style framework (Fausch et al., 2002), albeit within the specified constraints.

Whilst these initial results are encouraging, further targeted research in the following areas would be of benefit:

- **The effects of varying the level of overlap between UAS images.** This has not been addressed within this chapter, but if the level of overlap could be reduced without negatively impacting on data quality, then flight times could be reduced and/or larger areas covered within each flight. Currently flight times are limited by battery life, so any opportunities to expand the amount of data collected per flight would be beneficial.
- **The potential of alternative refraction correction procedures.** This study is one of the first to quantitatively assess the ability of the UAS-SfM approach for producing topographic datasets for shallow submerged fluvial environments. The use of a simple refraction correction procedure has given results which seem to reflect those found in similar studies using digital photogrammetry. However, since the SfM technique builds geometry within submerged areas from multiple images taken from different view angles, it is unclear whether this simple correction procedure represents the most appropriate method for reducing the effects of refraction within data produced from PhotoScan. Further research on this topic would require a greater insight into the largely unknown PhotoScan processing algorithms. Testing of different correction techniques in different fluvial settings would also be of benefit here.
- **Comparison of refraction corrected UAS-SfM DEMs with refraction corrected TLS DEMs for submerged areas.** The results of this research suggest that the TLS DEM suffers strongly from the effects of refraction and lack of returns in deeper waters. However, a direct comparison of the refraction corrected UAS-SfM DEM with an equivalent TLS product was not possible, but should be conducted in future.
- **The ability of repeat surveys for detecting geomorphic change.** Very few studies concerning the use of UAS-SfM surveys for change detection in fluvial settings have been published to date (the exception being Flener et al., 2013). The repeat surveys of the River Arrow presented here were not at sufficient time intervals so as to detect

any meaningful geomorphic change. Therefore, detailed quantitative assessments are required and should consider both the exposed and submerged environments.

- **Use of UAS-SfM point clouds.** Recently, some have suggested a move away from the use of the 2.5D DEM for topographic assessments and a new focus on the analysis of the 3D point clouds themselves (e.g. Lague et al., 2013). The kind of 3D point cloud analysis presented by Lague et al., (2013)'s M3C2 algorithm for TLS data could equally be implemented on UAS-SfM point clouds. Such methods hold clear advantages for geomorphic change detection of complex scenes, including both horizontal and vertical surfaces, such as the steep banks observed at Coledale Beck. Time constraints and limitations in computer processing power prevented the use of the M3C2 algorithm within this research, but future work in this area would be of interest.

3.7 Conclusions

This chapter has provided a quantitative assessment of the use of UAS imagery, processed within a SfM-photogrammetry workflow, to generate hyperspatial resolution topographic datasets at the mesoscale for both the exposed and submerged parts of the fluvial environment. This approach was tested at three contrasting field sites and within a flat sports hall setting with a view to exploring the accuracy, precision and repeatability of the method in contrast to existing remote sensing approaches.

Within exposed areas DEM accuracy values are in the range 4-44mm and approaching those typically obtained using TLS for non-vegetated surfaces. DEM quality was found to be poorer within submerged areas, with an apparent scaling of error with increasing water depth. The use of a simple refraction correction procedure improved mean errors in submerged areas by 8-53mm for sites where there was an existing correlation between error and water depth.

Multiple surveys acquired from the River Arrow site gave consistently high quality results, indicating the repeatability of the approach. Variability in DEM accuracy and precision of differing magnitudes is observed both within and between surveys. However, it is suggested that this variability can be attributed primarily to the presence of water and vegetation, the arrangement of GCPs, view angle of the camera and quality of input UAS imagery. For example, the results from Coledale Beck and the sports hall experiments show a slight central doming of the DEMs, which is thought to relate to the self-calibration of the camera lens model within the SfM software combined with the acquisition of imagery predominantly at

nadir. Results from the San Pedro River and the sports hall tests demonstrate that a central configuration of GCPs can result in a significant tilting of the DEM and introduce large systematic errors. It is also thought that the dense vegetation coverage at Coledale Beck and poor scene illumination conditions during the August 2013 survey of the River Arrow lead to increased DEM errors. Whilst the errors introduced by these factors are typically small in absolute terms and the UAS-SfM outputs often visually impressive, these results highlight the importance of conducting thorough quantitative error assessments, especially where the approach is to be applied for geomorphic change detection.

The selection of an approach for quantifying fluvial topography (and/or flow depth) will ultimately be determined by the specific requirements of a given application. Typically, a compromise will be required in terms of scale, spatial coverage, accuracy, precision, data acquisition and processing times, and cost. This research has demonstrated that a UAS-SfM approach offers a valid alternative to existing remote sensing methods for quantifying the topography of fluvial environments within both exposed and shallow submerged areas simultaneously, albeit within certain constraints. Comparison of results against TLS datasets collected concurrently, and other remote sensing approaches reported within the wider literature, suggests that the approach is well suited to studies of the mesoscale, where hyperspatial resolution datasets covering up to a few hundred metres of channel are required within a day's fieldwork. This is discussed further in Chapter 6.

Key areas which would benefit from further targeted research include; the effects of varying GCP densities; the effects of varying the level of image overlap; the potential of alternative refraction correction procedures; direct comparisons with refraction corrected TLS data in submerged environments; testing the ability of repeat surveys for detecting geomorphic change and; exploring the use of UAS-SfM point clouds rather than 2.5D DEMs.

3.8 References

- Bailly, J-S., Le Coarer, Y., Languille, P., Stigermark, C. and Allouis, T. (2010) Geostatistical estimation of bathymetric LiDAR errors on rivers. *Earth Surface Processes and Landforms* 35: 1199-1210.
- Bailly, J-S., Kinzel, P.J., Allouis, T., Feurer, D. and Le Coarer, Y. (2012) Airborne LiDAR methods applied to riverine environments. In *Fluvial Remote Sensing for Science and Management*, Carbonneau, P.E. and Piegay, H. (Eds) Wiley-Blackwell, Chichester.
- Bangen, S.G., Wheaton, J.M., Bouwes, N., Bouwes, B. and Jordan, C. (2014) A methodological intercomparison of topographic surveying techniques for characterizing wadeable streams and rivers. *Geomorphology* 206: 343-361.
- Bergeron, N. and Carbonneau, P.E. (2012) Geosalar: Innovative remote sensing methods for spatially continuous mapping of fluvial habitat at riverscape scale. In *Fluvial Remote Sensing for Science and Management*, Carbonneau, P.E. and Piegay, H. (Eds) Wiley-Blackwell, Chichester.
- Butler, J.B., Lane, S.N., Chandler, J.H. and Porfiri, E. (2002) Through-water close range digital photogrammetry in flume and field environments. *Photogrammetric Record* 17 (99): 419-439.
- Carbonneau, P.E., Lane, S.N. and Bergeron, N. (2003) Cost-effective non-metric close-range digital photogrammetry and its application to a study of coarse gravel river beds. *International Journal of Remote Sensing* 24: 2837-2854.
- Carbonneau, P.E., Lane, S.N. and Bergeron, N. (2006) Feature based image processing methods applied to bathymetric measurements from airborne remote sensing in fluvial environments. *Earth Surface Processes and Landforms* 31: 1413-1423.
- Carbonneau, P.E., Fonstad, M.A., Marcus, W.A. and Dugdale, S.J. (2012) Making riverscapes real. *Geomorphology* 123: 74-86.
- Cavalli, M., Tarolli, P., Marchi, L. and Fontana, G.D. (2008) The effectiveness of airborne LiDAR data in the recognition of channel-bed morphology. *Catena* 73: 249-260.
- Chandler, J.H. (1999) Effective application of automated digital photogrammetry for geomorphological research. *Earth Surface Processes and Landforms* 24: 51-63.
- Chandler, J.H., Buffin-Bélanger, T., Rice, S., Reid, I. and Graham, D.J. (2003) The accuracy of a river bed moulding/casting system and the effectiveness of a low-cost digital camera for recording river bed fabric. *Photogrammetric Record* 18 (103): 209-223.
- Chandler, J.H., Fryer, J.G. and Jack, A. (2005) Metric capabilities of low-cost digital cameras for close range surface measurement. *The Photogrammetric Record* 20 (109): 12-26.
- Costa, J.E., Spicer, K.R., Cheng, R.T., Haeni, P., Melcher, N.B., Thurman, E.M., Plant, W.J. and Keller, W.C. (2000) Measuring stream discharge by non-contact methods: a proof-of-concept experiment. *Geophysical Research Letters* 27 (4): 553-556.
- Dugdale, S.J. (2007) An evaluation of imagery from an unmanned aerial vehicle (UAV) for the mapping of intertidal macroalgae on Seal Sands, Tees Estuary, UK. Unpublished MSc thesis, Durham University.
- Dunford, R., Michel, K., Gagnage, M., Piegay, H. and Tremelo, M-L. (2009) Potential constraints of unmanned aerial vehicle technology for the characterization of Mediterranean riparian forest. *International Journal of Remote Sensing* 30 (19): 4915-4935.

Dunning, S.A., Massey, C.I. and Rosser, N.J. (2009) Structural and geomorphological features of landslides in the Bhutan Himalaya derived from Terrestrial Laser Scanning. *Geomorphology* 103: 17-29.

Dyer, F.J. and Thoms, M.C. (2006) Managing river flows for hydraulic diversity: an example of an upland regulated gravel-bed river. *River Research and Applications* 22: 257-267.

Eisenbeiss, H., Lambers, K., Sauerbier, M. and Li, Z. (2005) Photogrammetric documentation of an archaeological site (Palpa, Peru) using an autonomous model helicopter. *CIPA 2005 XX International Symposium*, 26 September-1 October, Torino, Italy.

Entwistle, N.S. and Fuller, I.C. (2009) Terrestrial laser scanning to derive the surface grain size facies character of gravel bars. In Heritage, G.L. and Large, A.R.G. (Eds) Laser Scanning for the Environmental Sciences, Wiley-Blackwell, London.

Fausch, K.D., Torgersen, C.E., Baxter, C.V. and Hiram, L.W. (2002) Landscapes to riverscapes: bridging the gap between research and conservation of stream fishes. *BioScience* 52 (6): 483-498.

Feurer, D., Bailly, J.-S., Puech, C., Le Coarer, Y. and Viau, A.A. (2008) Very-high-resolution mapping of river-immersed topography by remote sensing. *Progress in Physical Geography* 32(4): 403-419.

Flener, C., Vaaja, M., Jaakkola, A., Krooks, A., Kaartinen, H., Kukko, A., Kasvi, E., Hyyppä, H., Hyyppä, J. and Alho, P. (2013) Seamless mapping of river channels at high resolution using mobile LiDAR and UAV-photography. *Remote Sensing* 5: 6382-6407.

Fonstad, M.A., Dietrich, J.T., Courville, B.C., Jensen, J.L. and Carbonneau, P.E. (2013) Topographic structure from motion: a new development in photogrammetric measurement. *Earth Surface Processes and Landforms* 38 (4): 421-430.

Frissell, C.A., Liss, W.J., Warren, C.E. and Hurley, M.D. (1986) A hierarchical framework for stream habitat classification: viewing streams in a watershed context. *Environmental Management* 10 (2): 199-214.

Frothingham, K.M., Rhoads, B.L. and Herricks, E.E. (2002) A multiscale conceptual framework for integrated ecogeomorphological research to support stream naturalisation in the agricultural Midwest. *Environmental Management* 29 (1): 16-33.

Fryer, J.G. (1983) A simple system for photogrammetric mapping in shallow water. *Photogrammetric Record* 11 (62): 203-208.

Fryer, J.G. and Kniest, H.T. (1985) Errors in depth determination caused by waves in through-water photogrammetry. *Photogrammetric Record* 11 (66): 745-753.

Harwin, S. and Lucieer, A. (2012) Assessing the accuracy of georeferenced point clouds produced via multi-view stereopsis from unmanned aerial vehicle (UAV) imagery. *Remote Sensing* 4: 1573-1599.

Hetherington, D., Heritage, G.L. and Milan, D.J. (2005) Reach scale sub-bar dynamics elucidated through oblique lidar survey. in *International Association of Hydrological Scientists Red Book Publication*, IAHS Publication 291: 278-284.

Heritage, G. and Hetherington, D. (2007) Towards a protocol for laser scanning in fluvial geomorphology. *Earth Surface Processes and Landforms* 32: 66-74.

Heritage, G.L. and Milan, D.J. (2009) Terrestrial laser scanning of grain roughness in a gravel-bed river. *Geomorphology* 113: 4-11.

Hicks, D.M. (2012) Remotely sensed topographic change in gravel riverbeds with flowing channels. In *Gravel-bed Rivers: Processes, Tools, Environments*, Church, M., Biron, P. and Roy, A. (Eds) Wiley-Blackwell, Chichester.

James, M.R. and Robson, S. (2012) Straightforward reconstruction of 3D surfaces and topography with a camera: accuracy and geoscience application. *Journal of Geophysical Research* 117, F03017, doi: 10.1029/2011JF002289.

James, M.R. and Robson, S. (2014) Mitigating systematic error in topographic models derived from UAV and ground-based image networks. *Earth Surface Processes and Landforms* 39: 1413-1420.

Javernick, L., Brasington, J. and Caruso, B. (2014) Modelling the topography of shallow braided rivers using Structure-from-Motion photogrammetry. *Geomorphology* 213: 166-182.

Jerlov, N.G. (1976) *Marine Optics*. Elsevier, Amsterdam.

Kinzel, P.J., Wright, C.W., Nelson, J.M. and Burman, A.R. (2007) Evaluation of an experimental LiDAR for surveying a shallow, sand-bedded river. *Journal of Hydraulic Engineering* 133 (7): 838-842.

Kinzel, P.J., Legleiter, C.J. and Nelson, J.M. (2013) Mapping river bathymetry with a small footprint green lidar: applications and challenges. *Journal of the American Water Resources Association* 49 (1): 183-204.

Kraus, K. and Pfeifer, N. (2001) Advanced DTM generation from LIDAR data. *The International Archives of the Photogrammetry, Remote Sensing and Spatial Information Sciences XXXIV 3/W4 III Land Surface Mapping and Characterisation using Laser Altimetry Workshop*, 22-24 October 2001, Annapolis, Maryland, USA.

Laliberté, A.S. and Rango, A. (2009) Texture and scale in object-based analysis of subdecimeter resolution unmanned aerial vehicle (UAV) imagery. *IEEE Transactions on Geoscience and Remote Sensing* 47 (3): 761-770.

Lague, D., Brodu, N. and Leroux, J. (2013) Accurate 3D comparison of complex topography with terrestrial laser scanner: Application to the Rangitikei canyon (N-Z). *ISPRS Journal of Photogrammetry and Remote Sensing* 82: 10-26.

Lane, S.N. (2000) The measurement of river channel morphology using digital photogrammetry. *Photogrammetric Record* 16 (96): 937-957.

Lane, S.N., Richards, K.S. and Chandler, J.H. (1993) Developments in photogrammetry; the geomorphological potential. *Progress in Physical Geography* 17 (3): 306-328.

Lane, S.N., Chandler, J.H. and Richards, K.S. (1994) Developments in monitoring and modelling small-scale river bed topography. *Earth Surface Processes and Landforms* 19: 349-368.

Lane, S.N., James, T.D. and Crowell, M.D. (2000) Application of digital photogrammetry to complex topography for geomorphological research. *Photogrammetric Record* 16 (95): 793-821.

Lane, S.N. and Carbonneau, P.E. (2007) High resolution remote sensing for understanding instream habitat' in *Hydroecology and Ecohydrology*, Wood, P.J., Hannah, D.M. and Sadler, J.P. (Eds), John Wiley and Sons, Chichester.

Lane, S.N., Widdison, P.E., Thomas, R.E., Ashworth, P.J., Best, J.L., Lunt, I.A., Sambrook Smith, G.H. and Simpson, C.J., (2010) Quantification of braided river channel change using archival digital image analysis. *Earth Surface Processes and Landforms* 35(8), 971-985.

Legleiter, C.J. (2012) Remote measurement of river morphology via fusion of LiDAR topography and spectrally based bathymetry. *Earth Surface Processes and Landforms* 37: 499-518.

Legleiter, C.J. (2013) Mapping river depth from publicly available aerial images. *River Research and Applications* 29 (6): 760-780.

Legleiter, C.J., Roberts, D.A., Marcus, W.A. and Fonstad, M.A. (2004) Passive optical remote sensing of river channel morphology and instream habitat: physical basis and feasibility. *Remote Sensing of the Environment* 93: 493-510.

Legleiter, C.J., Roberts, D.A. and Lawrence, R.L. (2009) Spectrally based remote sensing of river bathymetry. *Earth Surface Processes and Landforms* 34: 1039-1059.

Lejot, J., Delacourt, C., Piegay, H., Fournier, T., Tremelo, M-L. and Allemand, P. (2007) Very high spatial resolution imagery for channel bathymetry and topography from an unmanned mapping controlled platform. *Earth Surface Processes and Landforms* 32: 1705-1725.

Lowe, D.G. (2004) Distinctive image features from scale-invariant keypoints. *International Journal of Computer Vision* 60: 91-110.

MacVicar, B.J., Piégay, H., Anderson, A., Oberlin, C., Comiti, F. and Pecorari, E. (2009) Quantifying the temporal dynamics of wood in large rivers: new techniques for wood tracking, monitoring, surveying, and dating. *Earth Surface Processes and Landforms* 34: 2031–2046.

Maddock, I. (1999) The importance of physical habitat assessment for evaluating river health. *Freshwater Biology* 41: 373-391.

Maddock, I., Thoms, M., Jonson, K., Dyer, F. and Lintermans, M. (2004) Identifying the influence of channel morphology on physical habitat availability for native fish: application to the two-spined blackfish (*Gadopsis bispinosus*) in the Cotter River, Australia. *Marine and Freshwater Research* 55: 173-184.

McKean, J., Nagel, D., Tonina, D., Bailey, P., Wright, C.W., Bohn, C. and Nayegandhi, A. (2009) Remote sensing of channels and riparian zones with a narrow-beam aquatic-terrestrial LiDAR. *Remote Sensing* 1: 1065-1096.

Marcus, W.A. (2012) Remote sensing of the hydraulic environment in gravel-bed rivers. In *Gravel-bed Rivers: Processes, Tools, Environments*, Church, M., Biron, P. and Roy, A. (Eds) Wiley-Blackwell, Chichester.

Melcher, N.B., Costa, J.E., Haeni, F.P., Cheng, R.T., Thurman, E.M., Buursink, M., Spicer, K.R., Hayes, E., Plant, W.J., Keller, W.C. and Hayes, K. (2002) River discharge measurements by using helicopter-mounted radar. *Geophysical Research Letters* 29 (22) doi: [10.1029/2002GL015525](https://doi.org/10.1029/2002GL015525).

Milan, D.J., Heritage, G.L. and Hetherington, D. (2007) Application of a 3D laser scanner in the assessment of erosion and deposition volumes and channel change in a proglacial river. *Earth Surface Processes and Landforms* 32: 1657-1674.

MOSAIC Mapping Systems Inc. (2001) A White Paper on LIDAR Mapping. Available online: <http://www.ncgc.nrcs.usda.gov/products/datasets/elevation/lidar.html> (accessed 01.12.2006).

Newson, M.D. and Newson, C.L. (2000) Geomorphology, ecology and river channel habitat: mesoscale approaches to basin-scale challenges. *Progress in Physical Geography* 24 (2): 195-217.

- Niethammer, U., James, M.R., Rothmund, S., Travelletti, J. and Joswig, M. (2012) UAV-based remote sensing of the Super-Suaze landslide: Evaluation and results. *Engineering Geology* 128: 2-11.
- Nietsche, M., Turowski, J.M., Badoux, A., Rickenmann, D., Kohoutek, T.K. Pauli, M. and Kirchner, W. (2012) Range imaging: a new method for high-resolution topographic measurements in small- and medium-scale field sites. *Earth Surface Processes and Landforms* 38 (8): 810-825.
- Orr, H.G., Large, A.R.G., Newson, M.D. and Walsh, C.L. (2008) A predictive typology for characterising hydromorphology. *Geomorphology* 100: 32-40.
- Rosnell, T. and Honkavaara, E. (2012) Point cloud generation from aerial image data acquired by a quadcopter type micro unmanned aerial vehicle and a digital still camera. *Sensors* 12: 453-480.
- Rosser, N.J., Petley, D.N., Lim, M., Dunning, S.A. and Allison, R.J. (2005) Terrestrial laser scanning for monitoring the process of hard rock coastal cliff erosion. *Quarterly Journal of Engineering Geology and Hydrogeology* 38 (4): 363-375.
- Smith, M.J., Chandler, J. and Rose, J. (2009) High spatial resolution data acquisition for the geosciences: kite aerial photography. *Earth Surface Processes and Landforms* 34: 155-161.
- Smith, M., Vericat, D. and Gibbins, S. (2012) Through-water terrestrial laser scanning of gravel beds at the patch scale. *Earth Surface Processes and Landforms* 37: 411-421.
- Smith, M.W. and Vericat, D. (2014) Evaluating shallow-water bathymetry from through-water terrestrial laser scanning under a range of hydraulic and physical water quality conditions. *River Research and Applications* 30 (7): 905-924.
- Snavely, N., Seitz, S.M. and Szeliski, R. (2006) Photo tourism: exploring photo collections in 3D. *ACM Transactions on Graphics* 25 (3): 835-846.
- Snavely, N., Seitz, S.M. and Szeliski, R. (2008) Modelling the world from internet photo collections. *International Journal of Computer Vision* 80 (12): 189-210.
- Spicer, K.R., Costa, J.E. and Placzek, G. (1997) Measuring flood discharge in unstable stream channels using ground-penetrating radar. *Geology* 25: 423-426.
- Storesund, R. and Minear, J. (2006) Evaluation of ground-based LiDAR for use in fluvial geomorphology and fluvial restoration. *Eos Transactions AGU Falling Meeting* 87 (52) Abstract G53C-0915.
- Tamminga, A., Hugenholtz, C., Eaton, B. and Lapointe, M. (2014) Hyperspatial remote sensing of channel reach morphology and hydraulic fish habitat using an unmanned aerial vehicle (UAV): A first assessment in the context of river research and management. *River Research and Applications* doi: 10.1002/rra.2743
- Tewinkel, G.C. (1963) Water depths from aerial photographs. *Photogrammetric Engineering* 29 (6): 1037-1042.
- Turner, D., Lucieer, A. and Watson, C. (2012) An automated technique for generating georectified mosaics from ultra-high resolution unmanned aerial vehicle (UAV) imagery, based on Structure from Motion (SfM) point clouds. *Remote Sensing* 4: 1392-1410.
- Verhoeven, G. (2012) Getting computer vision airborne – using Structure from Motion for accurate orthophoto production. *RSPSoc Archaeology Special Interest Group Meeting Spring 2012*, p. 4-6.

Verhoeven, G., Doneus, M., Briese, Ch. and Vermuelen, F. (2012) Mapping by matching: a computer vision-based approach to fast and accurate georeferencing of archaeological aerial photographs. *Journal of Archaeological Science* 39: 2060-2070.

Vericat, D., Brasington, J., Wheaton, J. and Cowie, M. (2009) Accuracy assessment of aerial photographs acquired using lighter-than-air blimps: low-cost tools for mapping river corridors. *River Research and Applications* 25 (8): 985-1000.

Wackrow, R., Chandler, J.H. and Bryan, P. (2007) Geometric consistency and stability of consumer-grade digital cameras for accurate spatial measurement. *The Photogrammetric Record* 22 (118): 121-134.

Wackrow, R. and Chandler, J.H. (2008) A convergent image configuration for DEM extraction that minimises the systematic effects caused by an inaccurate lens model. *Photogrammetric Record* 23 (121): 6-18.

Wackrow, R. and Chandler, J.H. (2011) Minimising systematic error surfaces in digital elevation models using oblique convergent imagery. *Photogrammetric Record* 26 (133): 16-31.

Ward, J.V., Malard, F. and Tockner, K. (2002) Landscape ecology: a framework for integrating pattern and process in river corridors. *Landscape Ecology* 17 (1): 35-45.

Westaway, R.M., Lane, S.N. and Hicks, D.M. (2000) The development of an automated correction procedure for digital photogrammetry for the study of wide, shallow, gravel-bed rivers. *Earth Surface Processes and Landforms* 25: 209-226.

Westaway, R.M., Lane, S.N. and Hicks, D.M. (2001) Remote sensing of clear-water, shallow, gravel-bed rivers using digital photogrammetry. *Photogrammetric Engineering and Remote Sensing* 67 (11): 1271-1281.

Westaway, R.M., Lane, S.N. and Hicks, D.M. (2003) Remote survey of large-scale braided, gravel-bed rivers using digital photogrammetry and image analysis. *International Journal of Remote Sensing* 24 (4): 795-815.

Westoby, M.J., Brasington, J., Glasser, N.F., Hambrey, M.J. and Reynolds, J.M. (2012) Structure-from-Motion photogrammetry: a low cost, effective tool for geoscience applications. *Geomorphology* 179: 300-314.

Wiens, J.A. (2002) Riverine landscapes: taking landscape ecology into the water. *Freshwater Biology* 47: 501-515.

Wheaton, J.M., Brasington, J., Darby, S.E. and Sear, D.A. (2010) Accounting for uncertainty in DEMs from repeat topographic surveys: improved sediment budgets. *Earth Surface Processes and Landforms* 35 (2): 136-156.

Williams, R.D., Brasington, J., Vericat, D. and Hicks, D.M. (2014) Hyperscale terrain modelling of braided rivers: fusing mobile terrestrial laser scanning and optical bathymetric mapping. *Earth Surface Processes and Landforms* 39 (2): 167-183.

Winterbottom, S.J. and Gilvear, D.J. (1997) Quantification of channel bed morphology in gravel-bed rivers using airborne multispectral imagery and aerial photography. *Regulated Rivers: Research and Management* 13: 489-499.

Woodget, A.S., Carbonneau, P.E., Visser, F. and Maddock, I. (2015) Quantifying submerged fluvial topography using hyperspatial resolution UAS imagery and structure from motion photogrammetry. *Earth Surface Processes and Landforms* 40 (1): 47-64.

Chapter 4

Quantifying fluvial substrate size using hyperspatial resolution UAS imagery and SfM-photogrammetry

Chapter Overview

The size and distribution of substrate within fluvial environments plays a fundamental role in the availability of aquatic habitats, yet traditional methods of characterising substrate are time consuming and labour intensive. Remote sensing approaches can provide a rapid and more objective alternative, but to date have tended to provide only coarse grain size outputs (c. 1m) at the catchment scale (up to 80km channel lengths) or very fine resolution outputs (c. 1mm) at the patch scale (c. 1m²). No single approach has yet been shown capable of rapidly providing hyperspatial resolution grain size outputs over river reaches up to a few hundreds of metres in length, in a way which would be of great benefit to habitat assessments at the mesoscale and would fulfil the ideals of the ‘riverscape’ concept.

This chapter assesses the potential of a novel approach which uses imagery acquired from an unmanned aerial system (UAS) and processed using structure-from-motion (SfM) photogrammetry for meeting this requirement. The UAS-SfM method is developed and tested on a c. 120m reach of Coledale Beck in the North West Lake District, England. Issues relating to UAS stability and resulting image blur are known to affect spectrally-based image analysis approaches to grain size quantification. Instead, this work explores the value of the associated point cloud which is produced from the SfM process. A variety of roughness metrics are calculated for the point cloud and correlated against field-measured substrate size. The strongest relationship is observed between the D_{84} of the intermediate axes and the roughness values computed using a 20cm kernel size on the point cloud which has not been detrended, and has been smoothed and filtered. Jack knife analysis shows that the model is

capable of predicting grain sizes with an average residual error of -0.011cm and standard deviation of 1.64cm. An over-prediction of grains less than 5cm in size indicates the lower limit of accurate grain size estimations. Normalised residual errors are found to be as great as -50% and +90% of the grain size. A number of explanations for such large residual errors are suggested.

A comparison of the results with those obtained using a UAS-SfM image texture approach and with a TLS point cloud roughness approach gives variable results. The mean residual error was found to be lowest for the UAS-SfM image texture method yet large residual errors are observed. The precision of grain size estimates and spatial resolution are highest for the UAS-SfM roughness approach. The developed UAS-SfM point cloud roughness method offers a rapid, flexible, high spatial resolution, spatially continuous and spatially explicit approach for quantifying fluvial grain size, and thus meets many of the requirements of the 'riverscape' concept, however higher accuracy results are required. With further testing and on-going developments in the capabilities of UAS and associated SfM software, the method presented here may provide a viable method for quantitative, mesoscale river habitat assessments in the future.

4.1. Background and Context

4.1.1 Fluvial substrate size and its importance

Fluvial geomorphology forms a key part of the physical habitat template (Maddock et al., 2004), and therefore influences directly the ecological quality of the river environment (Frissell et al., 1986, Newson and Newson 2000, Frothingham et al., 2002, Wiens 2002, Maddock et al., 2004, Dyer and Thoms 2006, Orr et al., 2008). Fluvial geomorphology comprises the topography (Chapter 3) and the substrate (Maddock 1999), of which the latter forms the focus of this chapter. The terms 'substrate size', 'grain size' and 'particle size' are used interchangeably here.

The mapping and quantification of fluvial grain sizes has long been recognised as important in the study of river processes, within both science and management applications. Grain size data is often included as a key input parameter to hydraulic models, and is essential for quantifying

sediment entrainment, transfer and deposition within fluvial environments. An understanding of the interactions between the channel substrate and local near-bed flow hydraulics relies on mapped grain size distributions, and the heterogeneity of bed material is also a key determinant of fluvial habitat availability, especially as it provides a spawning substrate for some fish species and the living environment for benthic macroinvertebrates (Wise and Molles 1979, Keeley and Slaney 1996, Evans and Norris 1997).

The inclusion of grain size assessment within the European Union's Water Framework Directive (European Commission 2000) serves to highlight its importance in governing habitat quality. An understanding of grain size distributions as part of the physical river habitat also assists in predicting the ability of fluvial organisms to adapt to extremes in flow level, such as where regulated flow regimes and hydro-peaking operations are in place or are planned, due to dam construction (e.g. Habit et al., 2007, Garcia et al., 2011).

4.1.2 Traditional methods of mapping and quantifying substrate size

Chapter 1 reviewed a number of key paradigms for the conceptualisation and understanding of river systems. From this review, emerged a series of requirements deemed necessary of a data collection technique for characterising river systems. In summary, there is a need for approaches which provide; quantitative datasets collected by objective and repeatable methods; spatially continuous and explicit datasets; datasets which cover large spatial areas, with high levels of detail; and datasets which are not difficult to collect in terms of practicality, logistics and cost.

Traditional studies of fluvial grain size distributions are well established, and include qualitative and quantitative approaches. Qualitative approaches usually comprise a visual assessment of substrate size at set locations and often use the size classes provided by the Wentworth Scale (Wentworth 1922, Table 4.1). For example, the River Habitat Survey (RHS), used routinely to characterise habitat quality in England, uses the Wentworth Scale to record substrate size at spot check locations at 50m intervals along 500m reaches (Environment Agency 2003). Within these surveys, the dominant intermediate or B axis substrate size class within a 1m 'transect' across the channel is determined visually and recorded. The 'Physical Habitat Simulation System' or PHABSIM, devised by the United States Fish and Wildlife Service but now used

more widely, also makes use of these substrate size classes (e.g. Centre for Ecology and Hydrology 2001).

Table 4.1. The Wentworth Scale of particle size definitions (after Wentworth 1922).

Size range		Wentworth Class
Phi (ϕ)	Metric (mm)	
>-8	>256	Boulder
-6 to -8	64-256	Cobble
-5 to -6	32-64	Very coarse gravel
-4 to -5	16-32	Coarse gravel
-3 to -4	8-16	Medium gravel
-2 to -3	4-8	Fine gravel
-1 to -2	2-4	Very fine gravel
0 to -1	1-2	Very coarse sand
1 to 0	0.5-1	Coarse sand
2 to 1	0.25-0.5	Medium sand
3 to 2	0.125-0.25	Fine sand
4 to 3	0.0625-0.125	Very fine sand
8 to 4	0.0039-0.0625	Silt
>8	<0.0039	Clay

Quantitative methods may also adhere to the Wentworth Scale and usually involve the in-situ or laboratory based physical measurement of individual grains. Such approaches may comprise areal sampling, grid or transect sampling or volumetric sampling (Church et al., 1987). Areal sampling usually focuses on small sample patches distributed across the site of interest where measures of the A, B and C axis of every clast are taken. Alternatively, systematic sampling of individual grains may be conducted according to a pre-established grid pattern. For example, the Wolman method suggests the sampling of the intermediate (B) axis of 100 clasts selected from the channel bed at regular intervals determined by pacing or measuring along a transect (Wolman 1954), although the exact number of sample clasts required will be determined by the application at hand (Hey and Thorne 1983, Rice and Church 1996). Wolman reports an attempt to avoid bias by sampling clasts only from “...beneath the tip of the toe of his boot” (Wolman 1954, p. 951), but studies have shown grain samples of certain sizes to be sensitive to operator bias (Hey and Thorne 1983). Laboratory analysis of grain samples is required for volumetric analysis, where weight of the ‘armour layer’ is often sought (Church et al., 1987). Whilst these traditional methods provide quantitative grain size measures, a number of key limitations can be identified. For instance, data collection of this type is never spatially

continuous, only sometimes spatially referenced, and rarely covers large spatial areas with great detail. Furthermore, these approaches can be labour-intensive, time consuming and often make assumptions about the representativeness of the spatially discontinuous selected samples over larger areas (Leopold 1970, Verdú et al., 2005). The finer grain material is often under-sampled by a grid-by number approach (Wolman 1954, Church et al., 1987) and the removal of samples for volumetric analyses in the laboratory can destroy the local patches of habitat that they are aiming to investigate (e.g. freeze coring, Milan 1996).

4.1.3 Quantifying substrate size using remote sensing

Since the 1970s, alternative methods for the characterisation of grain size have been emerging which make use of remote sensing. These developments have been fuelled by the need for less subjective approaches, which are non-invasive, reduce the time and effort spent in the field or laboratory and provide more continuous spatial coverage at larger scales. Ongoing advances in digital photogrammetry, digital image analysis and surveying technologies mean that there is now an evolving body of remote sensing based research for grain size quantification. The majority of these studies make use of optical (RGB) imagery, although there is also a growing use of terrestrial laser scanning systems. This section will review and evaluate the assessment of substrate size using remote sensing methods to date.

Image Based Approaches

Photo-sieving

Photo-sieving approaches make use of high resolution imagery (typically sub-centimetre) acquired from cameras mounted on a tripod or gantry at 1-2m above ground level. Photographs covering c.1m² are used to assess substrate sizes within dry exposed bars, or shallow submerged areas. The resulting imagery is analysed manually or using specialist image processing techniques in order to measure individual grain sizes.

Early work in this field conducted manual measurement of grains from hard-copy photographs and correlated results with size distributions obtained from sieving. Adams (1979) found that both mean grain sizes and grain size distributions could be estimated from imagery, but that estimates were biased. The mean size of grain B axes were reported to be 1.07 times those measured from the photos, with grain size percentiles being c. 7% finer than percentiles calculated from sieving. Similar results were reported by Ibbeken and Schleyer (1986) where

49.8% of samples were predicted as too fine by a manual photo-sieving approach. Furthermore, these largely manual approaches remain time-consuming.

As a result, more recent photo-sieving approaches have developed automated methods of grain delineation. For example, Butler et al., (2001) acquired imagery from a camera positioned 2.2m over a gravel point bar and used grey-scale image thresholding and watershed segmentations to identify individual grains within the high resolution imagery. Sensitivity testing was carried out to identify optimum thresholding and segmentation procedures. A photogrammetric scanner was also utilised for generation of a digital elevation model (DEM), which was used to orthorectify the imagery and correct for geometric distortions. Results indicated that individual grains could be rapidly identified and measured, even using unrectified imagery, but a systematic underestimation of grain size percentiles was observed (Figure 4.1). This relates to packing and imbrication of clasts which cannot be accounted for in grain size estimations from two-dimensional imagery. Sime and Ferguson (2003) also found grain size biases resulting from this issue, with larger discrepancies observed for tail percentiles.

More recently, papers by Graham et al., (2005a, 2005b) have developed the work of Butler et al., (2001), to produce a photo-sieving approach applicable to a range of sedimentary settings and under different sampling conditions (e.g. different lithologies, clast forms and textural characteristics). Field data were collected from three different sites, using a camera mounted 1.5m above ground level. Resulting imagery covered an area of approximately 1.2m² with a pixel size of c.0.7mm. Four different automated image segmentation procedures were developed and evaluated by comparison with manually digitised grains. In comparison to traditional in-situ sampling (Wolman 1954), these methods were found to produce equivalent levels of precision, and took considerably less time to carry out. The mean error of most individual grain size percentiles was often less than 0.05 ϕ , but was found to be larger for coarser grain sizes (c. 0.1 ϕ).

These photo-sieving methods offer a relatively rapid and objective means of quantifying grain size distributions at small scales, compared to traditional field and laboratory methods. Similar studies using close-range photogrammetry have also aimed to quantify such fine-scale variation in elevation (which may be equated to grain size) (Butler et al., 1998, Carbonneau et

al., 2003). Indeed, studies of this nature are of value for microscale (or patch level) habitat assessments but are not well suited for larger scale assessments of grain size distribution as they cannot cover larger areas with ease.

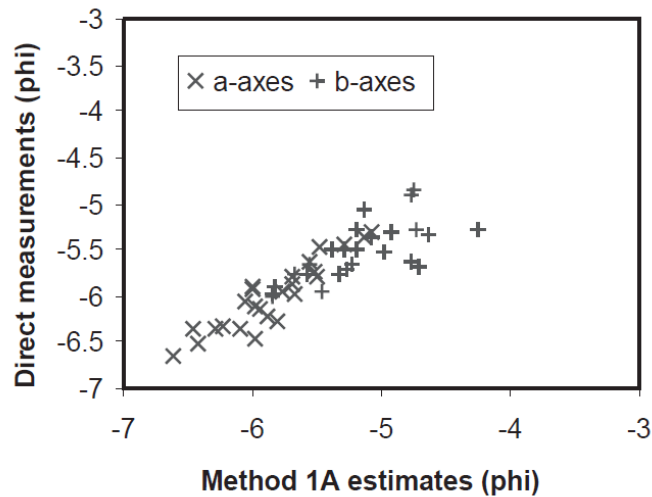


Figure 4.1. Comparison of grain axes measured by direct sampling against those using a fully automated photo-sieving approach (method 1A in Butler et al., 2001).

Statistical Image Analysis

Automated approaches to grain size estimation have also included statistical methods which decompose the two-dimensional spectral signatures of images typically acquired at close-range. Rubin (2004) presented a simple spatial autocorrelation algorithm which allowed the prediction of grain sizes with an average residual error of 0.1mm within a natural beach setting. However, calibration curves (or look up catalogues) for each fraction of the grain size distribution are required, which are representative in terms of shape, colour, mineralogy and packing. Images must be of very high resolution to ensure that the autocorrelation relates to the size of individual grains and not patches of grains, and the scene illumination must be constant between calibration and sample images.

Subsequent research by Buscombe and others has built on these statistical image analyses, to estimate not just mean grain sizes but percentiles of the grain size distribution. Buscombe (2008) again used site-specific calibration 'look-up catalogues' to produce strong observed versus predicted grain size correlations of 0.80 for the 10th percentile (D10) to 0.93 for mean grain size, with mean absolute errors of 0.21-2.99mm. A tendency to underestimate the D90

and D10 percentiles is noted, as shown by comparison against grain sizes derived from both point-counts and sieving. Buscombe and Masselink (2009) tested a number of additional statistical approaches, and again found good correspondence between predicted and sieved grain sizes to within 8-16%. However, until the work of Buscombe et al., (2010) these methods were still limited by the need for extensive, site-specific calibration data.

A new method using a form of spatial two-dimensional autocorrelation was proposed by Buscombe et al., (2010), which made use of the frequency rather than the spatial domain for providing direct statistical estimates of mean intermediate grain size without calibration. Root mean square error (RMSE) of estimates was found to be +/- c. 16%, but with individual errors as a great as -100% and +60%. Recently, it has also been shown that wavelet analysis can be used for grain size predictions with RMSEs within tens of percent for percentiles across the entire grain size distribution. The method presented by Buscombe (2013) is argued to be the first to provide a completely transferable, unmodified approach which again does not require calibration data.

As with photo-sieving, these statistical image analysis methods provide rapid and objective methods of grain size quantification using imagery of very high resolution over very small areas. As such, they are again better suited to patch-scale studies of grain size rather than those at the mesohabitat scale, as sought here.

Image Textural Analysis

Within the last decade, significant contributions to fluvial grain size quantification have been made using another group of image processing methods which rely on the computation of image textural variables, but at a different spatial scale (e.g. Carbonneau et al., 2004, 2005b, Verdú et al., 2005). Such methods typically use imagery with resolutions of c. 3-10cm acquired from airborne platforms over reach or catchment extents, and subsequent correlations of textural variables and field-measured grain sizes.

Carbonneau et al., (2004) used aerial imagery at 3cm and 10cm resolutions for an 80km stretch of the St-Marguerite River in Quebec, Canada. Corresponding field grain size measurements were collected manually and predictive relationships between field-measured median grain size and image textural variables (including semivariance) were then established

for dry, exposed areas, and validated against independent data. The semivariance information obtained from the 3cm imagery was found to be highly sensitive to median grain sizes (Figure 4.2a). Validation of this relationship found a strong relationship between observed and predicted grain sizes (Figure 4.2b), which permitted the automated output of grain size estimations at 1m resolution with a mean error of -0.28cm and standard deviation of 1.39cm. It was recognised that three key factors were necessary for this approach to be successful;

1. The sampling window used to calculate textural and semivariance measures had to be sufficiently large so as to obtain a stable and reliable signal of texture or semivariance.
2. The substrate had to be relatively uniform or at the same spatial scale to the sampling window and to the field calibration sampling area.
3. The smallest detectable grain scaled with the image resolution.

This texture approach has also been successfully applied for the detection of superficial sand coverage in dry, exposed fluvial areas with an overall accuracy of 0.55% and precision of +/-4%. As such, this method is shown to represent significant advantages over grey-level segmentation procedures, which produce accuracy values of 1.4% and precision values of +/-14% (Carbonneau et al., 2005a).

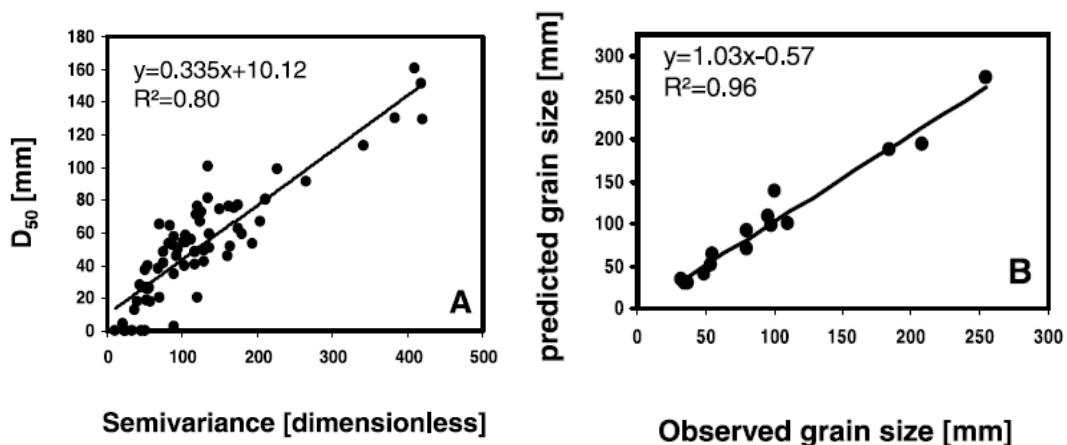


Figure 4.2. Regression plots showing (a) the calibration relationship between median substrate size (D_{50}) and semivariance for exposed substrate and (b) the validation relationship between predicted and observed median substrate size (Carbonneau et al., 2004).

Carbonneau et al., (2005b) built on this earlier work by testing the approach within shallow submerged parts of the river channel. The 3cm optical imagery from the St-Marguerite River was again used in this study, and a predictive relationship established between image semivariance calculated with a sampling window, and field calibration data (Figure 4.3a). The results showed a mean error of -8mm and a standard deviation of +/-29mm. Such data indicate a reduced accuracy and precision and degradation in the strength of the correlation between observed and predicted grain size outputs for shallow submerged areas (Figure 4.3b), compared with those from dry, exposed areas (Figure 4.2b). It is suggested that this relates to various potential error sources including the effects of; water depth, glare patterns from the water surface, particle size, substrate composition and presence of periphytons. Despite these areas for future development, Carbonneau et al., (2005b) demonstrated successfully that grain size information can be obtained from remotely sensed imagery from shallow submerged environments. Furthermore, the methods of Carbonneau et al., (2004, 2005b) have since been employed to demonstrate the utility of the approach for quantifying substrate size distributions within a Fausch et al., (2002) 'riverscape' style framework (Carbonneau et al., 2012).

Verdú et al., (2005) published a similar study which describes an image texture approach for the estimation of grain sizes along a 12km stretch of the Isabena River in northeast Spain. Imagery was collected at 1:1000 and 1:40 scales, and field sampling carried out using a bootstrap transect method. This involved the measurement of 100 clasts for each of the 68 gravel bars considered. Image textural variables were established for discrete grain size ranges, followed by multiple linear regressions to determine the relationship between image texture and field calibration data. Highest correlation values were achieved for median grain size values (D_{50}). These were applied over the 12km reach to give median grain size maps at a resolution of 1.5m. The root mean square error of these estimates was calculated at 26.1%. The authors acknowledge this as a rather high error value, but conclude that this approach remains an important initial step towards the development of accurate tools for grain size estimations over longer river reaches.

These advances by Carbonneau et al., (2004, 2005b) and Verdú et al., (2005) represent an important step in the use of remote sensing techniques for automated grain size mapping over areas much larger than is possible using the traditional in-situ or photo-sieving methods.

However, they still require the collection of field calibration data, which can be time-consuming, labour-intensive, and difficult in more remote areas.

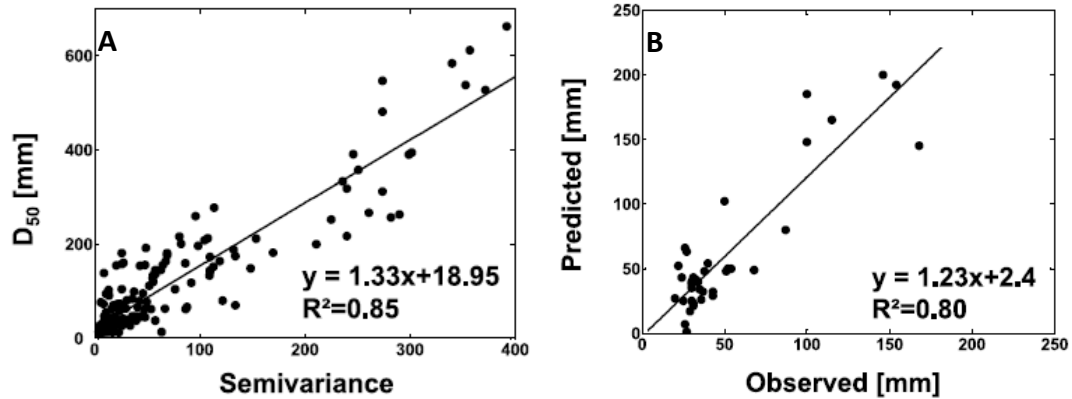


Figure 4.3. Regression plots showing (a) the calibration relationship between median substrate size (D_{50}) and semivariance for submerged substrate and (b) the validation relationship between predicted and observed median substrate size for submerged areas (Carbonneau et al., 2005b).

Dugdale et al., (2010) presented a new method of data calibration with the aim of overcoming some of these limitations. The approach makes use of high resolution (3cm) aerial imagery collected over a test reach (1km long) of the Marshaw Wyre River in Lancashire, UK. This imagery is used to manually measure median grain sizes for a number of selected sample sites of exposed gravels, a method named ‘aerial photo-sieving’. These median grain size measurements are then used for the calibration of image textural information, rather than using grain size data collected in the field. This approach relies on image pixel resolution being an order of magnitude smaller than clast size. Field calibration data were also collected for comparison purposes. Results found that ‘aerial photo-sieving’ methods produced very similar calibration results. However, a systematic bias was identified in the aerial photo-sieving results leading to a consistent over-estimation of median grain size dimensions. It is thought that this relates to the effects of pixel bleeding, where lighter coloured materials, such as clasts, produce a high reflectance value which falsely illuminates adjacent pixels. This results in clasts appearing to be larger than they actually are, and leads to a systematic overestimation of clast sizes. Furthermore, the resolution of the input imagery limits the size of the smallest grains which can be identified using this approach.

Despite this, the work of Dugdale et al., (2010) has demonstrated how aerial photo-sieving may be used as an alternative to field-based data for the calibration of textural information computed for long stretches of exposed river channel deposits. Dugdale et al., (2010) suggest that this approach should now be tested for use on submerged gravels and that the pixel-bleeding issue requires further investigation. Like others before them (Carbonneau et al., 2004, 2005b, Verdú et al., 2005) they also stress the importance of scale, and recommend that future research should ensure that image pixel resolution is suitable for the intended application.

Laser Scanning Based Approaches

Within fluvial settings, terrestrial laser scanning (TLS) has seen increasing use in recent years, including application to grain size quantification in non-submerged areas. The high resolution, high accuracy and high precision elevation data typically provided by TLS can be used to map variations in elevations from the grain scale upwards (Entwistle and Fuller 2009, Hohenthal et al., 2011, Milan and Heritage 2012). To date, the majority of publications on this topic have achieved this by treating TLS point clouds as a random field of elevations, from which various statistical measures of elevation variation can be computed. The premise here is that for a given spatial extent, larger variations in elevation of the point cloud relate to larger grain sizes, whilst smaller variations relate to smaller grain sizes.

Much of this work has been borne out of earlier studies concerned with flow resistance calculations, which explored the relationship between gravel-bed roughness with grain size and bed morphology. These earlier works were predominantly conducted within flume settings using close-range digital photogrammetry or a laser displacement meter to generate the random fields of elevation (e.g. Gomez 1993, Aberle and Smart 2003, Aberle and Nikora 2006). Gravel-bed roughness (or variation in elevation) was found to vary in relation to the surficial grain size, but also in relation to other factors, including particle shape, local topography (i.e. bedforms) and variations in clast packing and burial (Aberle and Nikora 2006).

Heritage and Milan (2009) produced some of the first published work exploring the potential of TLS data for fluvial grain size mapping in this way. A TLS survey of a 180m² gravel point bar on the River South Tyne, near Lambley in Northumberland was acquired using a Riegl LMS Z-210 scanner, to produce a point cloud with an average point spacing of 0.012m. The spatial

variation in elevation (or roughness) within the point cloud was investigated by calculating the standard deviation of point elevations (σ_z) within a moving window. The moving window had a radius of 0.15m, so as to be equivalent in size to the largest visible clast at the Lambley site, and was moved every 5cm in horizontal space across the point cloud. Standard deviation values were multiplied by 2 to give 'effective roughness heights' ($2\sigma_z$) (in accordance with Gomez 1993), which were then gridded at a resolution of 5cm to produce a raster dataset of the surface roughness.

Initial visual comparisons found excellent agreement between the $2\sigma_z$ roughness data and the size of substrate present along the gravel bar at Lambley. Conventional grid-by-number grain size sampling was also carried out for a number of sub-areas for quantitative comparison. Results showed strong linear relationships between grain size and effective roughness height percentiles, with co-efficients of determination typically greater than 0.8 and generally highest for clast C axis length (Figure 4.4). Monte Carlo sampling suggested potential errors in grain size estimation could be as large as +50% and -23%. It is argued that these errors can be explained by variable depths of clast burial by fine materials and clast imbrication angles. Heritage and Milan (2009) conclude by advocating that this approach should replace conventional grid-by-number sampling for quantifying fluvial grain sizes. Testing of this random field approach has also been carried out at other sites (e.g. Entwistle and Fuller 2009), however TLS surveys were not accompanied by conventional grid-by-number sampling and therefore a quantitative assessment was not provided.

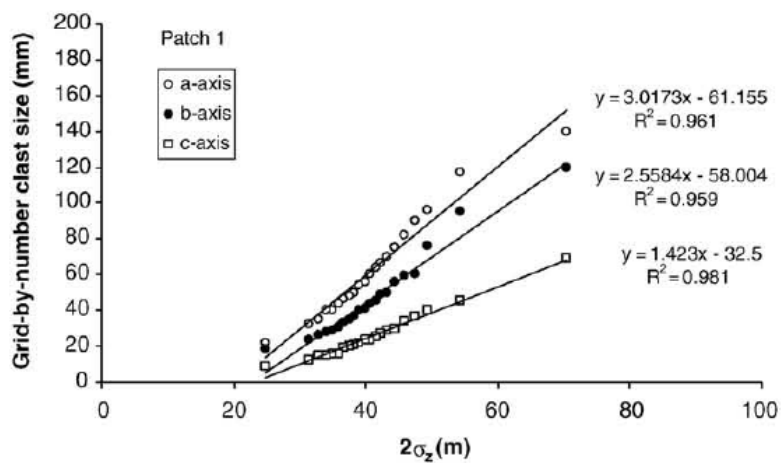


Figure 4.4. Example of the correlation between roughness ($2\sigma_z$) and clast size percentiles for a sample site on a gravel bar on the River South Tyne at Lambley (Heritage and Milan 2009).

More recently, a similar approach was employed by Brasington et al., (2012) to retrieve particle size data for a much larger area (1000m x 300m) of the braided River Feshie, Scotland. This paper presents a geospatial toolkit known as ToPCAT ('Topographic point cloud analysis toolkit'), designed specifically in-house for the analysis of very large TLS datasets. Detrending is undertaken as part of the ToPCAT procedure, which decimates the point cloud and removes the effects of local slope (e.g. resulting from bedforms). This is conducted prior to the calculation of surface roughness with a view that the roughness values will then reflect only variations in grain size, and not a combination of grain size and local topography. Following detrending, the standard deviations of point elevations (σ_z) are calculated for each cell within a regular grid (various different cell sizes are used).

Grid-by-number sampling was also carried out during this study at the River Feshie, for 12 sample plots which varied in size between 1 and 4m² according to the local maximum clast size. Median grain size data (D_{50}) varied between 10mm and 120mm, and was correlated against detrended standard deviation values to give a calibration relationship with a co-efficient of determination of 0.92 (Figure 4.5). This is much stronger than the relationship observed with non-detrended data (Figure 4.5). The relationship was then used to derive substrate size distributions for the whole TLS point cloud (Figure 4.6). Whilst the R^2 value for detrended TLS data presented by Brasington et al., (2012) is encouraging, it is not accompanied by an assessment of error of the resulting grain size predictions. The use of independent ground truth data to determine the mean error and standard deviation of error of grain size estimates would be necessary to determine the value of such an approach for quantitative fluvial research or management applications.

Brasington et al., (2012) identify some challenges involved in the use of TLS for deriving grain size information, including; current difficulties in surveying the submerged parts of the channel, the time taken to acquire TLS data over larger areas and the current limitations of computing systems to process and visualise the unprecedented size of TLS point clouds. However, the results from the River Feshie also demonstrate the feasibility of high resolution, reach-scale mapping of fluvial grain sizes using detrended TLS point clouds.

The work of Rychov et al., (2012) demonstrates further success of this approach, when applied to grain size mapping of the Rees River in New Zealand. Here, detrended standard deviation

data were generated from TLS scans collected before and after a flooding event. This allowed an assessment of the movement of different grain sizes during the flood. Rychov et al., (2012, p. 69) suggest that this approach provides “...the opportunity to create the first hyperscale models of coarse grained braided systems, from the scale of individual grains upwards”.

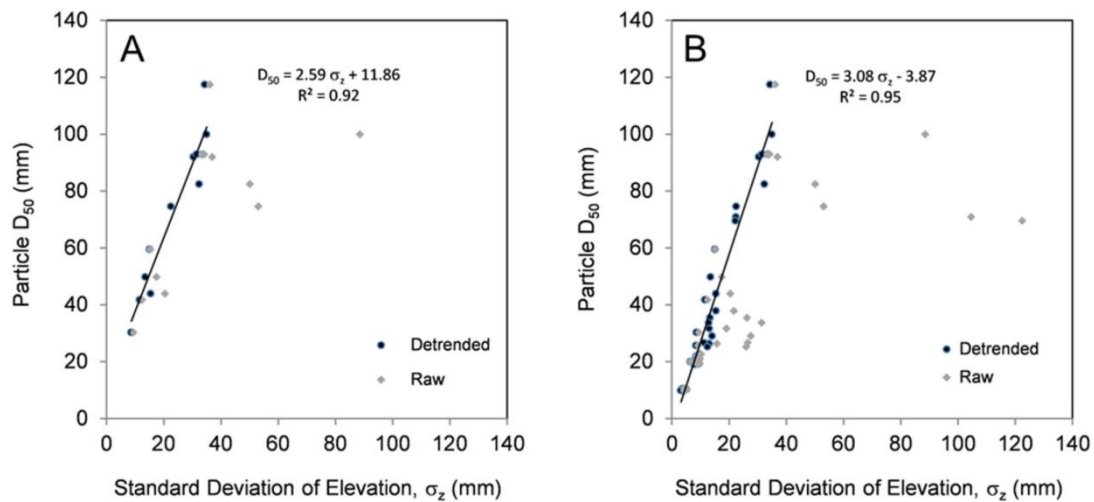


Figure 4.5. Regression plots showing relationship between median substrate size (D_{50}) and standard deviation of local elevation, for both raw and detrended TLS datasets acquired from (a) the River Feshie and (b) with additional data incorporated from the Tan u Bwlch and Rees River (Brasington et al., 2012).

An in-depth assessment of the ability of TLS used at very close range to generate DEMs of gravel surfaces is given by Hodge et al., (2009). Whilst this study presents an interesting strategy for TLS data acquisition and processing, it considers patches of 1m^2 maximum size, and does not go so far as to explicitly quantify grain size distributions. A small number of other studies have also used TLS point cloud roughness measures to assess fluvial gravel surfaces (e.g. Wang et al., 2011, Höfle et al., 2013, Picco et al., 2013, Wang et al., 2013), although most do not make direct quantitative comparisons with grain sizes distributions measured using traditional methods. Recent research has also seen success in applying this approach for grain size estimation in other settings (e.g. Hugenholtz et al., 2013).

TLS approaches are clearly capable of rapidly collecting spatially continuous, accurate, very high resolution data for quantifying fluvial grain size over patch and mesoscale extents. Furthermore, the process is not reliant on indirect measures of elevation through the use of

parallax, as is the case with digital photogrammetry, which can be adversely affected by poor quality imagery and a lack of image texture.

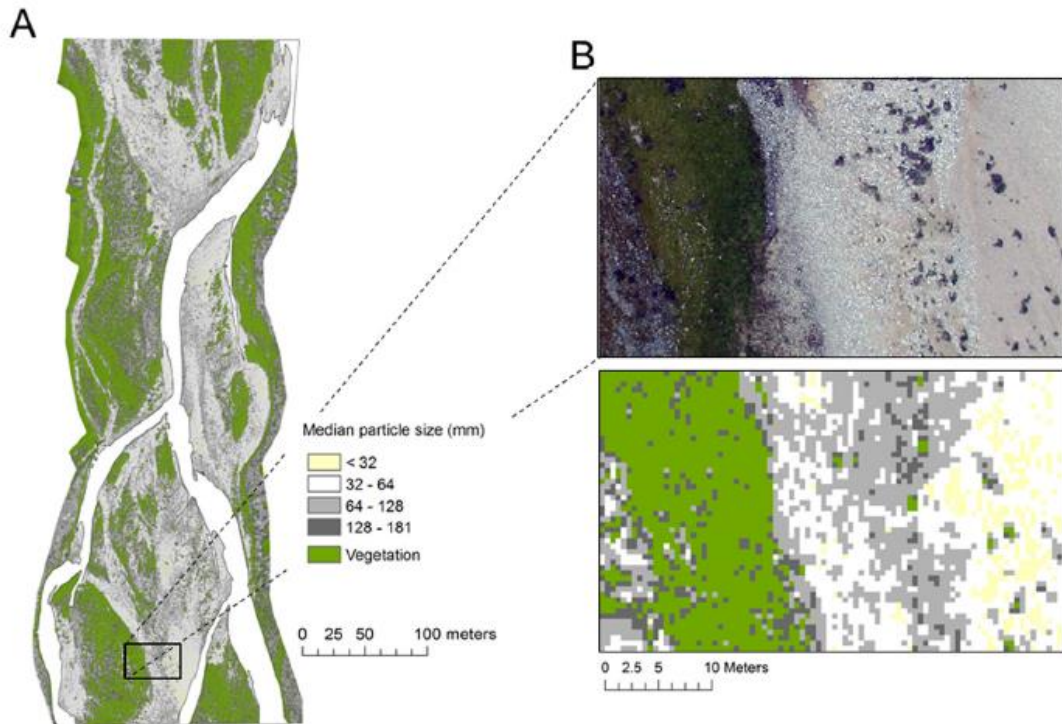


Figure 4.6. Substrate size mapping of the River Feshie derived from TLS point cloud data (Brasington et al., 2012).

However, TLS is not without its drawbacks, including the following:

- Field data collection is time-consuming and labour intensive. Multiple scans are necessary to ensure sufficient overlap between scans and to avoid holes in the data due to shadowing effects (Lane and Carbonneau 2007, Hodge et al., 2009).
- As it is ground based, the results from TLS often have limited spatial coverage compared with other remote sensing approaches which are capable of covering larger areas much more quickly (Brasington et al., 2012).
- Atmospheric conditions, such as rain and fog, can lead to spurious results (Heritage and Hetherington 2007).
- Applications to submerged areas of the fluvial environment are currently limited, and require further development (Entwistle and Fuller 2009, Smith et al., 2012).
- The technique is only able to survey surface material, and thus may be biased as the size of buried or hidden clasts cannot be quantified (Milan and Heritage 2012). Although this is a problem common to all remote sensing approaches.

Emerging Approaches

As discussed in Chapter 1, the recent development of small unmanned aerial systems (UAS) and parallel developments in Structure-from-Motion photogrammetry now offer an alternative approach for assessing and quantifying a range of river habitat parameters. To date however, very few published studies are known to have applied these novel technologies for quantifying fluvial grain size.

Tamminga et al., (2014) acquired 5cm resolution imagery from a small, rotary winged UAS over a 1km stretch of the Elbow River in Canada. Imagery was processed using photogrammetry software EnsoMOSAIC (MosaicMill Ltd, Finland) to create an orthophotograph. The image texture approach similar to that used by Carbonneau et al., (2004) was conducted on this imagery, using a 1m² moving window within which standard deviation was computed. Grain size calibration data were acquired using a close-range photo-sieving style approach, where the B axes of 50 clasts within 30 x 1m² areas were measured automatically using a Matlab routine. The resulting relationship between image texture and grain size is shown in Figure 4.7, where a strong empirical correlation is observed ($R^2 = 0.82$). This relationship was applied to all exposed gravel bars within the orthophoto to produce the grain size map shown in Figure 4.8. Whilst the technique used by Tamminga et al., (2014) makes use of hyperspatial resolution UAS input imagery (5cm) the substrate size predictions are provided at a much coarser 1m spatial resolution. Furthermore, no associated quantitative error assessment of the results is presented. This seriously limits comparisons of the quality of results against more established remote sensing techniques and prevents any assessment of how useful this approach would be for river research or management applications.

As part of a study exploring the evolution of alluvial fan surfaces, de Haas et al., (2014) also applied an image texture approach for quantifying grain size from a UAS-SfM approach. Imagery was collected at a resolution of 4-6cm and processed using the texture approach of Carbonneau et al., (2012) to produce grain size outputs at 0.7m resolution of an area covering 0.745km². Relative motion blur affected the quality of the UAS imagery, and was attributed to a combination of cloudy conditions, which reduced light levels and therefore necessitated increased exposure times, and wind gusts. Blurred parts of the resulting UAS-SfM orthophoto artificially reduced image texture outputs and adversely affected the calibration with grain size. As a result, such areas were excluded from the calibration. Validation of the model using

independent grain size data is not presented by de Haas et al., (2014) which again prohibits an understanding of the accuracy of this texture approach when applied to UAS imagery and limits comparison against other techniques.

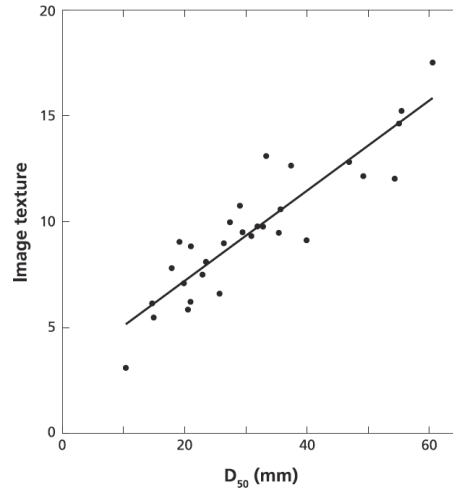


Figure 4.7. Regression plot for the relationship between median substrate size (D_{50}) determined through photo-sieving and UAS orthomosaic image texture computed using a 1m^2 moving window (Tamminga et al., 2014).

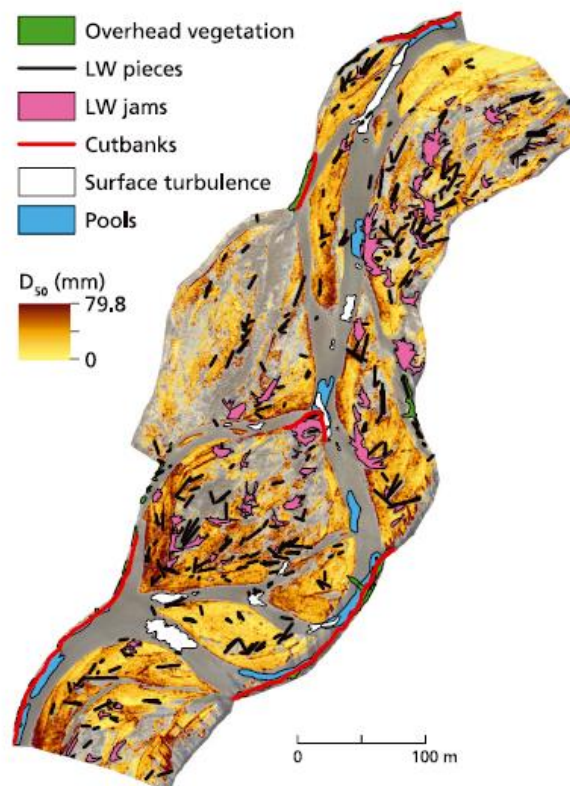


Figure 4.8. Predicted substrate size (D_{50}) and digitised cover features for the area of interest on the Elbow River (Tamminga et al., 2014).

4.1.4 Summary

Remote sensing approaches offer a number of key benefits for quantifying fluvial substrate size over the traditional visual assessment or quantitative sampling approaches, as shown in Table 4.2. All approaches reviewed here are capable of providing quantitative datasets which are spatially continuous and spatially explicit (i.e. fully georeferenced to absolute or relative co-ordinate systems). They are arguably also more objective and repeatable than the traditional measurement of clasts in the field which may be subject to operator bias (Hey and Thorne 1983).

There is an inevitable trade-off between spatial resolution and spatial coverage however. Photo-sieving and TLS approaches are capable of providing spatial resolutions at the millimetre level, but are currently incapable of covering large areas without significant investments of time and effort. In contrast, image texture approaches have been shown to cover large areas with ease, yet have so far only been shown to produce grain size outputs at resolutions of c. 1m². No single technique has yet proved its value for the rapid quantification of substrate size at the mesoscale, with centimetric spatial resolution over channel lengths from c. 50m to a few hundred metres. Yet such outputs would be of great value for contributing to scientific understanding of mesohabitats and their applied management (Frissell et al., 1986, Newson and Newson 2000).

Whilst emerging UAS-SfM technologies may hold potential for assessments at the mesoscale, the limited studies to date have produced only relatively coarse scale grain size outputs (0.7-1m, de Haas et al., 2014, Tamminga et al., 2004) and the image texture approaches used have been adversely affected by the blurred imagery often acquired from relatively unstable UAS platforms (de Haas et al., 2014). As such, the only potential advantages they have been shown to offer over the approaches of Carbonneau et al., (2004, 2005b) are related to increased flexibility of image acquisition using a UAS. However, UAS are not capable of the same spatial coverage. Furthermore, none of the existing studies provide an explicit assessment of the error associated with grain size estimates, which would elucidate a better understanding of their value for habitat assessment at the mesoscale. Given the rapidly growing interest in a UAS-SfM approach for a great variety of environmental applications, there is a need for robust and quantitative testing of grain size estimations produced in this way. In addition, the development and evaluation of alternative UAS-SfM approaches, which do not rely on the

blur-affected image texture approach, would be of potential benefit. For instance, the SfM process also produces a point cloud, the analyses of which have already been conducted for grain size estimation using TLS data (Heritage and Milan 2009, Brasington et al., 2012). This chapter, therefore, aims to develop and evaluate an approach based on the roughness of UAS-SfM point clouds for quantifying fluvial grain size at hyperspatial resolutions over mesoscale channel extents.

Table 4.2. Assessment of remote sensing based methods of quantifying fluvial substrate size against requirements of the ‘riverscape’ concept (Fausch et al., 2002).

Key requirement for characterising physical river habitat variables	Is this requirement met by remote sensing methods of quantifying fluvial substrate size?			
	Photo-sieving	Image analysis	TLS	UAS-SfM
(1) Quantitative datasets collected by objective and repeatable methods	Yes	Yes	Yes	Yes
(2) Spatially continuous datasets, available in three-dimensions	Spatially continuous 2D mapping	Spatially continuous 2D mapping	Yes	Spatially continuous 2D mapping
(3) Spatially explicit datasets	Yes	Yes	Yes	Yes
(4) Datasets which cover large spatial areas, with high levels of detail	High level of detail but only over small areas	Large spatial coverage (c. 80km) at resolutions of c.1m	High level of detail but spatial coverage is limited	Intermediate spatial coverage (c. 1km) at resolutions of c.1m
(5) Datasets which are not difficult to collect in terms of practicality, logistics and cost	Yes	Limited by flight mobilisation from 3 rd party. Cost uncertain.	Currently limited by cost of scanners	Potentially, but not yet specifically tested

4.2 Research Questions

The research reported in this chapter aims to provide an assessment of quantifying fluvial substrate size using hyperspatial resolution data produced using a UAS-SfM approach, with a specific focus on obtaining data at the mesoscale. In particular, the following research questions will be addressed:

1. Can the roughness of the UAS-SfM point cloud be used to quantify fluvial substrate size, and if so, how accurately?

2. How do the results of research question 1 compare with those obtained using existing remote sensing techniques: a) image texture analysis on the UAS imagery and b) TLS point cloud roughness?

4.3 Site Locations

The substrate size research was conducted on a c.120m long reach of Coledale Beck, a gravel-bed river located in Cumbria (Figure 4.9). Further details on the nature of this site are provided in Chapter 1. Data acquisition was undertaken over a week in early July 2013. At this time, weather conditions were bright and sunny, with a low flow level and very clear water.



Figure 4.9. The Coledale Beck research site (July 2013).

This site was selected for the following reasons;

- The presence of large exposed bars, with variable substrate sizes.
- Good accessibility and permission from the landowners (The National Trust) for UAS flying.
- A lack of dense vegetation and tree coverage.
- It is not close to any major roads or railway lines, power lines or sensitive sites such as airports.
- The opportunity to conduct collaborative research with colleagues from the universities of Bath Spa and Durham.

4.4 Methods

The workflow provided in Figure 4.10 details the methods used for quantifying substrate size within this chapter. Those methods which are common to all physical river habitat parameters considered within this thesis are documented in Chapter 2, whereas methods specific to this chapter are detailed here (Table 4.3).

Table 4.3. Overview of methods used within this chapter and where they are described within the thesis.

Stage	Detail	Location
1) Pre-field	Camera characterisation	Chapter 2
2) Data Acquisition	GCP set-up & survey	Chapter 2
	UAS flying & image acquisition	
	TLS data acquisition	Chapter 2
	Ground truthing of substrate size	This chapter 4.4.1
3) Data Processing	Image selection	Chapter 2
	SfM Processing in PhotoScan Pro	Chapter 2
	Processing of UAS-SfM point cloud	This chapter 4.4.2
	Computing image texture	This chapter 4.4.3
	Processing of TLS point cloud	This chapter 4.4.4
4) Data Analysis	Establishing a relationship with substrate size	This chapter 4.4.5
	Accuracy assessment	This chapter 4.4.6

Data Acquisition

Prior to any data collection at Coledale, four permanent markers were established using wooden stakes and yellow survey markers. All subsequent data collected using a Leica Builder 500 total station (e.g. locations of GCPs and ground truth sample plots) were referenced to these four permanent markers, which were subsequently surveyed in using a Leica GPS1200 dGPS on loan from Durham University. The dGPS was on loan for a very short period of time and therefore could not be used to conduct the wider surveying required by this research. A Trimble R8 RTK GPS was also available for use during the fieldwork, but the lack of a consistently good mobile data signal prevented its use at Coledale. The positional accuracy of the Leica GPS1200 dGPS data for the four permanent markers was found to be between 0.013 and 0.027m in x, y and z.

The imagery acquired from the UAS survey and the TLS data collected at Coledale Beck is used both within this chapter and elsewhere. As a result, the flying, data acquisition and SfM processing are described only in Chapter 2 to avoid repetition.

Quantifying physical river habitat parameters using hyperspatial resolution
UAS imagery and SfM-photogrammetry

1. PRE-FIELD

UAS survey

- a) Camera characterisation to determine relationship between flying altitude and image resolution

2. DATA ACQUISITION

UAS survey

- a) Distribution & survey of GCPs using dGPS or total station
- b) Image acquisition from UAS (multiple flights)

TLS survey

- c) Distribution of 6 reflective targets
- d) Scanning at high resolution (5cm at 100m range) from 8 positions
- e) Survey targets & scan station positions using dGPS

Ground truthing

- f) Ground truthing of substrate size – measurement of A and B axis of 25 clasts within each of 25 sample plots
- g) Survey position of sample plots using total station

3. DATA PROCESSING

UAS imagery

- a) Manual image selection
- b) SfM processing in Agisoft PhotoScan Pro – see Figure 2.18

For point cloud roughness

- c) Export dense point cloud as PLY file
- d) Clip point cloud to location of the 25 ground truth sample plots
- e) Test de-trending using Matlab curve fitting toolbox (3rd, 4th and 5th order polynomials)
- f) Test filtering and smoothing using bespoke code written in-house
- g) Test roughness kernel sizes (CloudCompare) & calculate summary statistics for each plot

For image texture

- h) Export orthophotograph
- i) Compute image texture (entropy) using kernel size found to produce strongest correlation in step 4a (Matlab, Carbonneau et al., 2004)
- j) Clip image texture map to the location of the 25 ground truth sample plots
- k) Calculate summary image texture statistics for each plot

TLS data – point cloud roughness

- l) Co-register scans using targets (Leica Cyclone)
- m) Georeference merged scan to British National Grid co-ordinates using dGPS data
- n) Assess registration accuracy and remove problematic targets as necessary
- o) Clip the merged scan to the area of interest
- p) Manually remove erroneous data spikes
- q) Export dense point cloud as PLY file
- r) Clip TLS point cloud to location of ground truth sample plots (CloudCompare/ArcGIS)
- s) Calculate summary roughness statistics for each plot using kernel size found to produce the strongest correlation in step 4a

4. ANALYSIS

UAS-SfM point cloud roughness

- a) Establish roughness and substrate size variables which produce the strongest correlation (Excel)
- b) Calculate roughness for entire point cloud based on strongest measure (CloudCompare)
- c) Use regression equation to compute substrate size from point cloud roughness
- d) Jack knifing analysis to establish accuracy of UAS-SfM roughness substrate size predictions

UAS image texture

- e) Establish image texture and substrate size variables which produce the strongest correlation (Excel)
- f) Use regression equation from strongest correlation to compute substrate size from image texture for whole site
- g) Jack knifing analysis to establish accuracy of image texture substrate size predictions

TLS data

- h) Establish which substrate size variable produces the strongest correlation with TLS roughness (Excel)
- i) Calculate roughness for entire TLS point cloud (CloudCompare)
- j) Use regression equation to compute substrate size from point cloud roughness
- k) Jack knifing analysis to establish accuracy of TLS roughness substrate size predictions

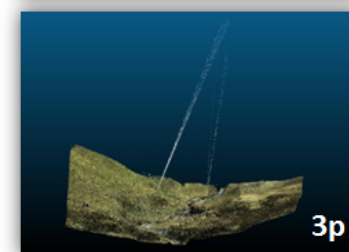
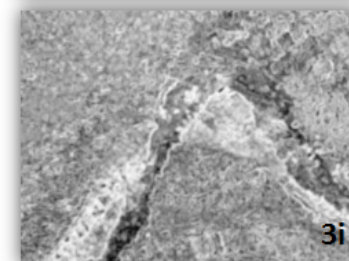
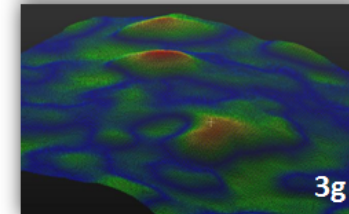


Figure 4.10. Methods workflow for substrate size chapter.

4.4.1 Ground truthing of substrate size

A series of 25 square sample plots were established along the four main exposed bars at Coledale for the purposes of ground truthing. These are labelled bars A to D (Figure 4.11). Each sample plot was measured out using hand tapes to a size of c. 40cm by c. 40cm. This plot size was chosen so as to be sufficiently large as to encompass the size of the larger clasts within the field site, but sufficiently small to ensure substrate size was as uniform as possible within the plot itself. The locations of the four corners of each sample plot were recorded using a Leica Builder 500 total station, relative to the four permanent markers. The XYZ positions of the four corners of each sample plot were used to create a polygon shapefile for each plot. These polygons were subsequently used for clipping out the ground truth plots from the point clouds and imagery.

The locations of the ground truth sample plots are shown in Figure 4.11. An effort was made to distribute the sample plots relatively evenly throughout the area of interest, to encompass the range of grain sizes present at the site and to position each plot in an area of relatively uniform substrate size. In practice, the latter objective was not always easy to achieve given the spatial variability in substrate size at this site, so that some of plots contained greater variation in substrate sizes than others (Figures C1 to C25, Appendix C). Figure 4.12 shows some examples of the sample plots used.

Within each plot, the size of the A and B axes of a sample of c. 25 clasts selected at random were measured by hand using a tape measure. The A axis is the longest axis of each clast, and the B axis is the intermediate axis running perpendicular to the A axis. Given fieldwork time constraints, the shortest clast axes (C axes) were not measured. The ground truth data were used to create substrate size distribution profiles for each plot. A number of summary measures of substrate size were also calculated, including the mean, the D_{50} (grain size of the 50th percentile, or the median) and the D_{84} (grain size of the 84th percentile). In theory, any percentile values could be calculated and used as a measure of plot grain size. The D_{50} and D_{84} were chosen here as they are commonly used (Bunte and Abt 2001).

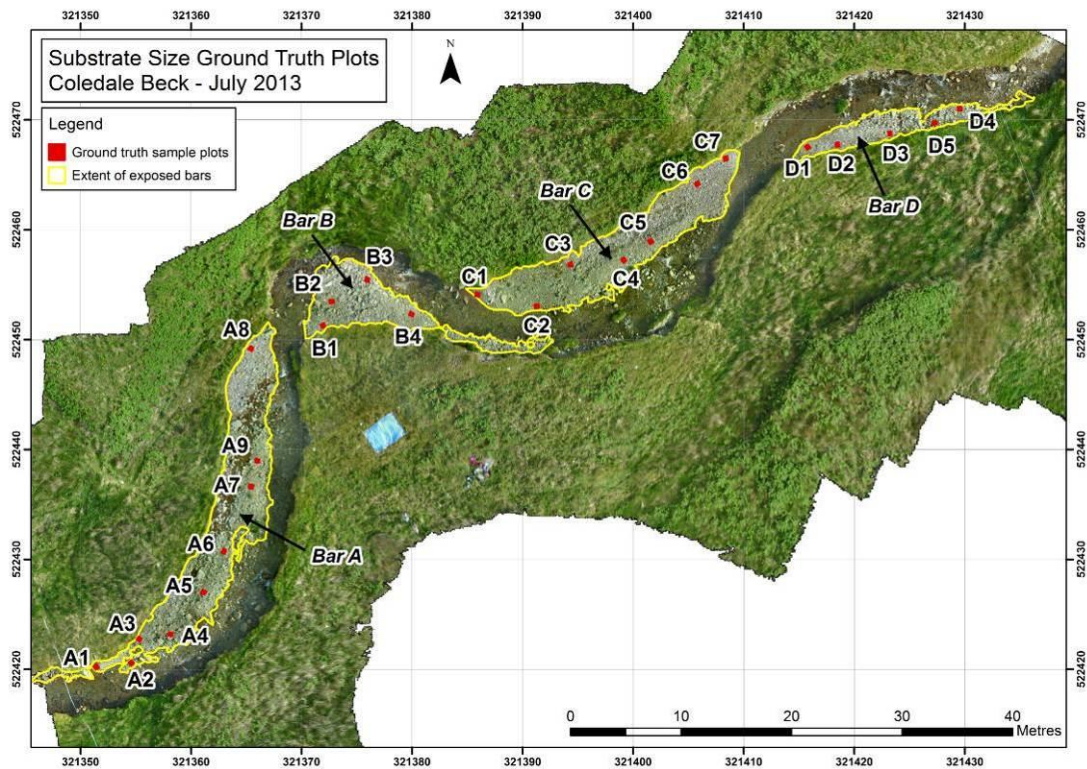


Figure 4.11. Location of ground truth sample plots at Coledale Beck, July 2013.



Figure 4.12. Examples of ground truth sample plots.

Photos show plots A7 (left) and B3 (right).

Data Processing

4.4.2 Processing of UAS-SfM point cloud

Point cloud management

Following the processing of the UAS imagery in a SfM workflow (detailed in Chapter 2), a dense point cloud of the Coledale site was exported from PhotoScan Pro (Agisoft LLC) as an

ASCII text file. This is a large file (c.21 GB) containing approximately 156 million points, with long point co-ordinates stored in the OSGB 1936 British National Grid co-ordinate system. The open source CloudCompare software was chosen for subsequent point cloud processing (www.danielgm.net/cc/). CloudCompare requires a global shift in the point co-ordinates given their size, but the data precision is preserved and the point cloud position is shifted back on export. Opening this large file in CloudCompare takes roughly 15 minutes on an Intel® Core™ i7-2600 16GB 64-bit computer. At this stage the cloud includes areas of vegetated bank and so was manually clipped to the channel extent to make the file size more manageable.

CloudCompare does not feature a tool for clipping out specific areas of interest automatically, which might easily be achieved using the Spatial Analyst tools with ArcGIS (ESRI Inc.). However, ArcGIS (ESRI Inc.) is not designed to cope with such large point cloud files. Therefore, it was necessary to manually clip out parts of the point cloud in CloudCompare which roughly corresponded to the location of the ground truth sample plots. These smaller, more manageable subsets of the original point cloud were saved out as ASCII text files and opened in ArcGIS (ESRI Inc.). The Spatial Analyst 'clip' tool was then used to cut each point cloud to the more precise extent of the ground truth sample plot plus a 50cm buffer. The export tool was then used to save out each dataset as a shapefile and DBF.

The 50cm buffer around each plot is necessary so that subsequent roughness calculations conducted on points at the edge of each plot would take into consideration the surrounding substrate (as demonstrated for the TLS data shown in Figure 4.15). This is important because the measure of roughness used here is a relative measure, describing the fine scale variation in elevation of points relative to each other.

Since carrying out this work, CloudCompare has been updated to incorporate a batch clipping tool and colleagues at the University of Worcester have written a bespoke code for clipping out small parts of large point clouds (*R. Austrums, 2014*). The TLS point cloud used later in this chapter was clipped using the in-house code. In future, the use of these tools should be maximised to save significant amounts of time in data processing.

Detrending

DEM detrending is typically undertaken on point clouds to remove the effects of local slope (e.g. Brasington et al., 2012). If local slope is significant, it may introduce roughness to the point cloud which does not result from grain size. This would then compromise a potential correlation between point cloud roughness and substrate size. The need for detrending was tested by computing both detrended and non-detrended datasets for subsequent analysis.

To detrend the data, the point clouds clipped to the 50cm buffered ground sample plots were imported into Matlab (MathWorks Inc.). Given the nature of the topography at the Coledale site, planar detrending was not considered to be sufficient. Instead, a number of curve fit detrending procedures were tested. The Curve Fitting Toolbox within Matlab (MathWorks Inc.) was used to generate 3rd, 4th and 5th order polynomial curves for each of the plots. The residuals for each of these detrended datasets were exported from Matlab (MathWorks Inc.) and saved out as CSV files. Detrending was always carried out prior to any filtering or smoothing of the data.

Filtering and Smoothing

Visual assessment of the UAS-SfM point cloud reveals some noise, erroneous points and in some areas, 'shadows' of points which sit beneath the main cloud mirroring its pattern (e.g. Figure 4.13). This noise may introduce roughness to the point cloud which does not result directly from grain size. Therefore, a filtering and smoothing procedure was written in-house (*R. Austrums, 2014*) and applied to each buffered sample plot. Point clouds which had not been filtered or smoothed were also tested in subsequent analyses to assess the success of these methods.

The filter considered the elevation of points within the cloud within approximately 6mm x 6mm cells. The mean of the interquartile range in elevation was calculated within each of these cells and outputted as a single point for each cell. This had the effect of removing the vertical noise within the cloud (Figure 4.14).

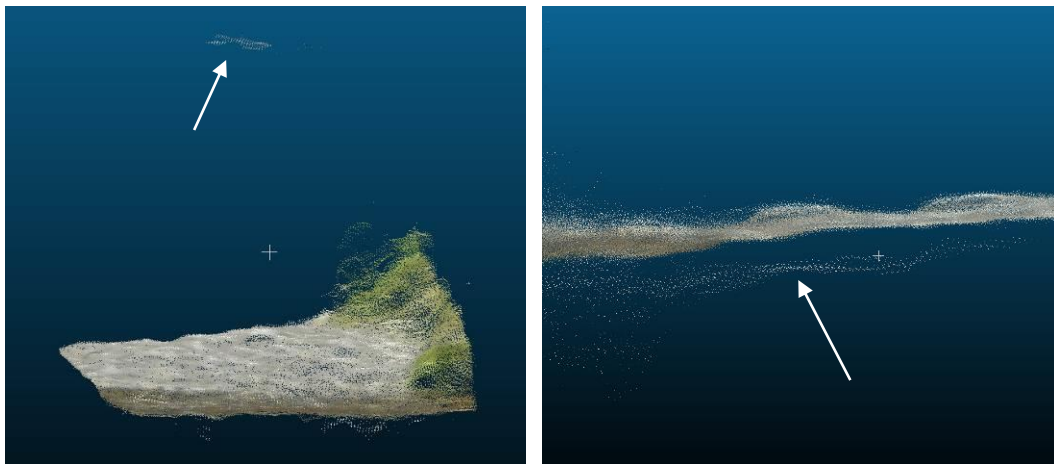


Figure 4.13. Example of erroneous points above the main UAS-SfM cloud (left – plot C7) and ‘shadows’ of points below the main point cloud within the buffered ground truth sample plots (right – plot C2).

Smoothing of each of the filtered plots was then carried out using a 2.5cm radius moving window. This window is passed over each point within the point cloud and assigns each point a new elevation value equal to the average elevation of all points falling within the 2.5cm radius window. A radius of 2.5cm was chosen as it was found to be sufficiently large as to effectively remove noise within the point cloud, and sufficiently small so as to maintain the topographic detail. The filtered and smoothed sample plots (Figure 4.14) were then saved as PTS files for subsequent roughness calculations.

Roughness

PTS files for each buffered ground truth point cloud plot were imported into CloudCompare. This included both detrended and non-detrended datasets, and both filtered/smoothed and non-filtered/smoothed datasets. The roughness tool was then used to compute roughness values for each point within each of these point cloud datasets. Roughness is defined in CloudCompare as the distance between each point in the cloud and the least squares best fitting plane computed on its nearest neighbours within a kernel (sphere) of a specified size. Roughness was computed for a range of kernel sizes from 5cm to 30cm, at 5cm intervals. The upper limit of 30cm was chosen as it adequately encompassed the maximum size of substrate material present at the Coledale site.

Following the roughness computation, each point cloud was exported as an ASCII text file and opened in ArcGIS (ESRI Inc.). The ‘clip’ tool within the Spatial Analyst toolbox was then used to preserve only those points falling within the ground truth plot itself. That is, all

points falling within the wider 50cm buffer were removed. A number of roughness summary statistics were then computed for each dataset, including the mean, maximum, minimum and standard deviation.

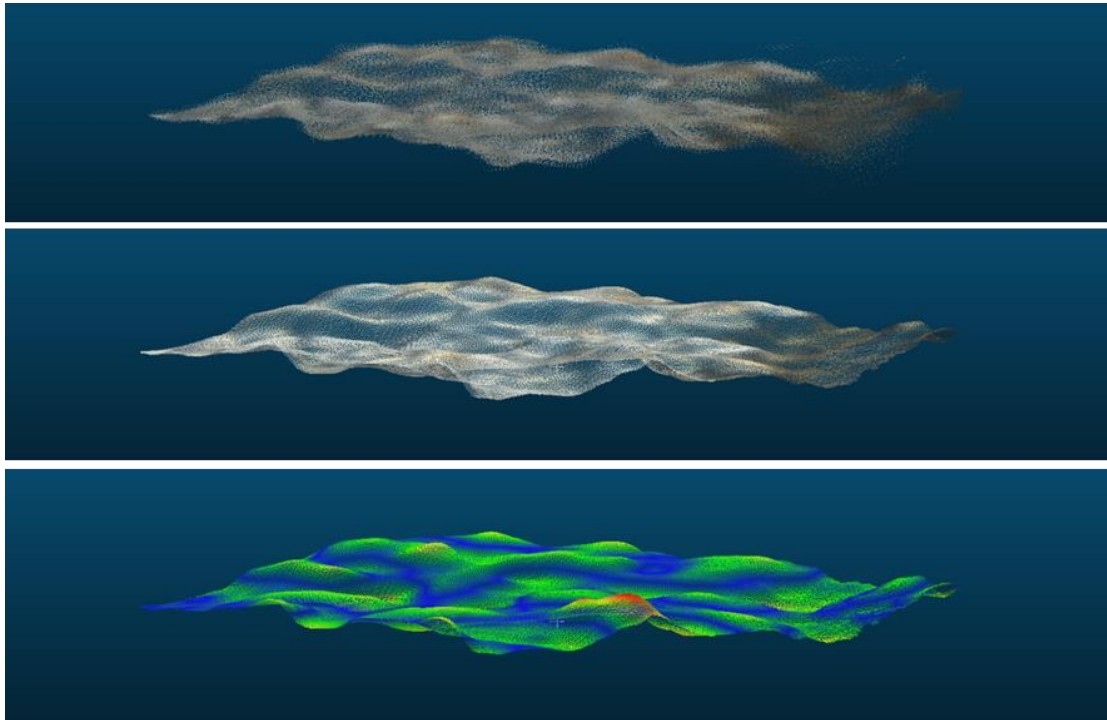


Figure 4.14. Raw, unprocessed UAS-SfM point cloud for ground truth plot B3 (top), filtered and smoothed (middle) and showing roughness computed using a 30cm kernel size (bottom).

4.4.3 Computing UAS-SfM image texture

Following the processing of the UAS imagery in a SfM workflow (detailed in Chapter 2), the hyperspatial resolution RGB orthophotograph of the Coledale site was exported from PhotoScan Pro (Agisoft LLC) as a JPG. This image was then processed by colleagues at the University of Durham according to the technique developed by Carbonneau et al., (2004), to derive a map of image texture. This is an empirical approach which aims to produce output measures of image texture, from which a statistical correlation with substrate size may be established.

The procedure of Carbonneau et al., (2004) is implemented in Matlab (MathWorks Inc.) on only the red band of the imagery, this is an arbitrary choice and the method would also work on other bands. A square moving window with a kernel size of 41 pixels is passed over the

image at intervals of five pixels. A kernel size of 41 pixels is roughly equivalent to a kernel width of 41cm and radius of c. 20cm. This process was conducted after the analysis of the UAS-SfM point cloud, and therefore the kernel size which had been found to produce UAS-SfM roughness values with the strongest correlation to grain size (i.e. 20cm), was used to calculate image texture to ensure a fair comparison. The interval size of five pixels was chosen to reduce processing times and results in texture outputs at 5cm resolution, although these are interpolated to the original image resolution of c. 1cm (P. Carbonneau 2014, *pers. comm*).

Within each kernel step, a measure of image texture is calculated and assigned to the central pixel. In this case, image entropy was calculated. This is a measure of image texture calculated using a grey level co-occurrence matrix (GLCM). These are grey-tone spatial dependence probability distribution matrices which were first advocated by Haralick et al., (1973) as a means of efficiently computing texture measures from imagery. They provide the probabilities of all pairwise (i, j) combinations of pixel grey levels occurring within the specified moving window. The outputs are a function of the angular relationship between a single pixel and its neighbours (V), and the distance between them (the inter-pixel sampling distance, D). Image entropy provides a measure of randomness or the disorder of pixel values and in this instance is calculated according to Equation 4.1;

$$Entropy = \sum_{i,j} P_{i,j} (-\log P_{i,j})$$

Equation 4.1

(after Haralick 1979)

Where $P_{i,j}$ is the co-occurrence matrix of the image within each step of the moving window, based on the number of times that cells with grey levels i and j occur in two pixels separated by set distance D and direction V , divided by the total number of pixel pairs. The output of this process is a map of image entropy for the whole Coledale Beck site. In theory, this is a map of negative entropy given the equation used, but this was conducted so that higher entropy values are returned for more textured or heterogeneous parts of the image and lower values for smoother or more homogeneous areas, and will be referred to as just 'entropy'.

On export from Matlab (MathWorks Inc.), the site-wide image entropy dataset was imported into ArcGIS (ESRI Inc.). The Spatial Analyst 'Clip' tool was used to select the areas of the image corresponding with the location of the ground truth sample plots. The mean, minimum, maximum and standard deviation of image entropy values were then summarised for each plot using the 'Zonal Statistics' tool, and exported to MS Excel.

4.4.4 Processing of TLS point cloud

Following the TLS data acquisition, point cloud registration and editing (detailed in Chapter 2), the following processes were implemented.

Clipping out ground truth plots

The parts of the TLS point cloud falling within each of the ground truth sample plots were clipped out of the main point cloud using bespoke code written in-house (R. Austrums, 2014). The idea here is to create much smaller file sizes (up to c. 30MB) allowing easier file management and reduced data processing times. A 50cm buffer around each plot was included in each clip, so that the subsequent roughness calculations conducted on points at the edge of each plot would take into consideration the surrounding substrate (Figure 4.15). This is important because the measure of roughness used here is a relative measure, describing the fine scale variation in elevation of points relative to each other. A PTS file was exported for each sample plot.

Roughness

Each PTS file was next loaded into the CloudCompare software (examples shown in Figure 4.16) and a measure of roughness calculated using the inbuilt 'roughness' tool. This process was conducted after the analysis of the UAS-SfM point cloud, and therefore the kernel size which had been found to produce UAS-SfM roughness values with the strongest correlation to grain size (i.e. 20cm), was used to calculate roughness of the TLS point cloud. That is, a range of kernel sizes were not explored for calculating roughness of the TLS point cloud plots.

Furthermore, as detrending was not found to improve the correlation of roughness and grain size for the UAS-SfM point cloud, neither was it applied to the TLS cloud. The TLS point

cloud was also found to be significantly less noisy than the UAS-SfM point cloud and therefore neither smoothing nor filtering processes were implemented.

The TLS point cloud plots were exported from CloudCompare as text files, with the roughness values appended to each point. The text files were opened in ArcGIS (ESRI Inc.) and clipped to the extent of the ground truth sample plots (as indicated by the red dashed line given in the example in Figure 4.15) and saved out as a shapefile. The DBF part of each shapefile was subsequently opened in MS Excel and used to compute a variety of roughness statistics for each plot, including mean, maximum, minimum and standard deviation of roughness.

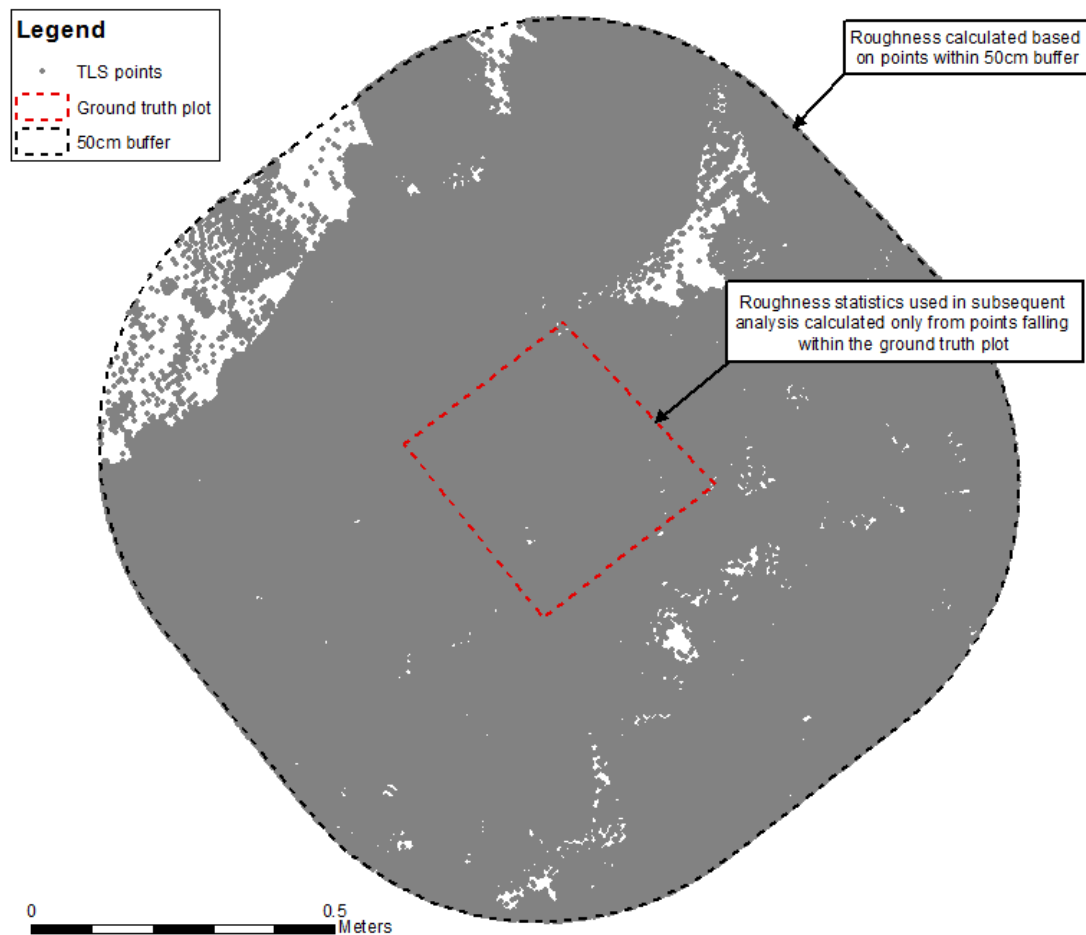


Figure 4.15. Example ground truth and 50cm buffer plots used for calculating point cloud roughness.

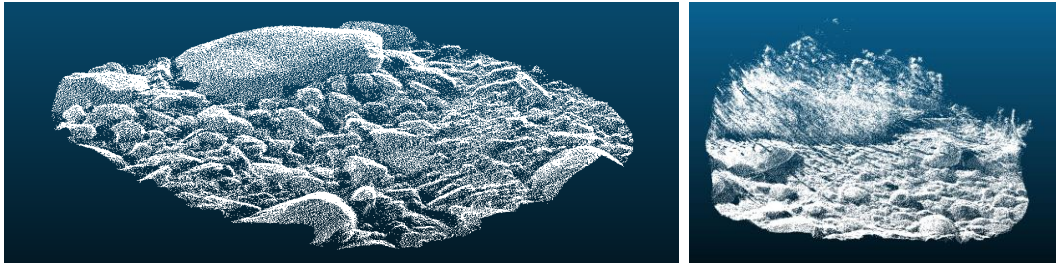


Figure 4.16. Example TLS point clouds for 50cm buffer areas of plots A4 (left) and A3 (right).

Data Analysis

4.4.5 Establishing a relationship with substrate size (model calibration)

Following the computation of UAS-SfM point cloud roughness data for each ground truth sample plot, simple linear regressions were conducted against measures of ground truth substrate size. The process was repeated for each different roughness kernel size, for both detrended and non-detrended datasets and for both smoothed/filtered and non-smoothed/filtered datasets. Different measures of substrate size were also explored, including the mean, D_{50} and D_{84} for both A and B axes, with a view to finding the strongest relationship between UAS-SfM point cloud roughness and substrate size. This results in a total of 288 possible permutations, although in practice not all permutations were considered because the process was conducted in stages. First, all combinations of roughness kernel size, grain size and detrending were compared to determine if the detrending process was necessary. The strongest results were then taken forward and used in combination with smoothed/filtered data to determine the effect of the smoothing and filtering.

Once the strongest linear regression had been identified, any obvious outliers were investigated and excluded from further analysis as appropriate. Plots A1 and C1 were found to be producing much higher roughness values than might be expected from their grain size distributions. It was found that footprints within these plots were the cause of greater point cloud roughness, as shown in Figure 4.17. These plots were therefore excluded from all following analyses, including in the use of TLS point cloud roughness and UAS-SfM image texture.



Figure 4.17. Example of footprints present within ground truth sample plot A1.

The equation describing the relationship between the roughness and substrate size measures was next used as a model to predict substrate size for the whole site. This was achieved by calculating the roughness of the original, unclipped UAS-SfM point cloud in CloudCompare. The data were then exported as a raster grid at 5mm resolution and opened in ArcGIS (ESRI Inc.). Here, the 'raster calculator' tool was used to apply the strongest regression equation to this data to obtain a map of estimated substrate size. In theory, grain size predictions can also be made available for the point cloud itself (rather than a derived raster) and it is these data which are used in the model calibrations and validations reported in this chapter. However, the output of grain size information as a raster layer (as shown in Figures 4.19, 4.24 and 4.29) offers advantages in terms of more meaningful data visualisation and improved data management.

A similar process was also conducted for the TLS roughness and image texture data by linear regression against the substrate size variables to identify those measures producing the strongest correlations. Plots A1 and C1 were again excluded to ensure a fair comparison of results.

The image texture data already existed for the whole site. The TLS point cloud roughness data was computed for the whole site within CloudCompare and exported as a raster grid at 5cm resolution. A finer resolution was not used as it resulted in gaps in the raster. This was due to a lack of data points caused by shadowing. On import of the image texture and TLS roughness data into ArcGIS (ESRI Inc.), the '*raster calculator*' tool was again used to apply the strongest regression equation to these data to obtain maps of estimated substrate size.

4.4.6 Substrate size model validation

The substrate size estimates produced using each of the three predictive models (UAS-SfM point cloud roughness, UAS-SfM image texture and TLS point cloud roughness) were validated using a jack-knife approach (Quenouille 1949, Tukey 1958). This method can be used in the absence of other independent ground truth data, as is the case here. Jack-knifing works iteratively by excluding one ground truth plot at a time, and using the linear regression equation based on the remaining plots to predict substrate size for the excluded plot. These calculations were carried out manually in MS Excel.

The measured grain size for each plot was then compared to the equivalent predicted grain size using a linear regression to assess the strength of the predictive relationship. Measured grain sizes were also subtracted from the predicted grain sizes on a plot by plot basis to obtain a series of residual error values. The average and standard deviation of the residuals for all plots is taken to represent the overall accuracy and precision of grain size estimates.

Residual errors were then normalised in relation to ground truth substrate size measures and expressed as percentages. Average and standard deviations of normalised residual errors were also calculated. These values may be positive or negative, indicating either an over- or under-prediction of the ground truth substrate size. Normalised residual errors were also converted to only positive values and plotted against ground truth substrate size, to investigate the relationship between these two variables.

4.5 Results and Analysis

4.5.1 Ground truth substrate size

The substrate size distribution profiles for each ground truth validation plot and accompanying photographs are shown in Figures C1 to C25 within Appendix C. These profiles show both the A and B axis data. A summary of these data are provided in Table 4.4. Using the Wentworth size class scale and D_{84} of clast B axes as a measure of grain size per plot, plots ranged in size from medium gravels to cobbles, with cobbles being the most frequent (Figure C26 in Appendix C). When all measured clasts are considered individually (and not grouped by plot), grain size (D_{84} of clast B axes) was found to range between very coarse sand and boulders, with most clasts recorded as coarse or very coarse gravels (Figure C27 in Appendix C).

Table 4.4. Overview of ground truth substrate size data per plot.

Ground truth sample plot	Substrate size (cm)					
	A axis			B axis		
	Mean	D_{50}	D_{84}	Mean	D_{50}	D_{84}
A1	1.54	1.1	2	0.9	0.7	1.1
A2	5.5	5	7.9	3.6	3.5	4.5
A3	4.36	4.1	7.9	2.72	2.6	4.2
A4	9.15	7.5	9.9	6.39	5.8	9
A5	4.34	3.6	3.5	2.48	2.3	3
A6	13.66	7.65	20.8	8.88	5.5	15.7
A7	2.62	1.8	2.5	1.85	1.2	2
A8	8.18	8.8	11.6	5.12	4.8	7
A9	4.39	4.4	5.5	3.09	2.7	4.2
B1	5.54	5	5.4	3.44	3	4.5
B2	2.98	2.8	3.4	1.89	1.8	2.6
B3	8.81	7.5	14.5	5.69	4.5	8.4
B4	6.83	5.9	10.7	3.84	3.7	5.6
C1	1.56	1.4	1.5	0.87	0.7	1.3
C2	5.93	4.8	7	3.84	3.5	4.5
C3	8.43	3.45	11.2	5.97	3.2	10.1
C4	7.3	6.6	8.1	4.51	4.2	6.4
C5	7.49	7.5	10.3	5.12	4.9	7.3
C6	8.18	6.3	8.1	5.34	4.2	7.6
C7	6.53	5.7	7.8	3.96	3.6	6.1
D1	2.59	2.1	3.9	1.52	1.3	2.3
D2	4.94	4.6	4.6	3.1	2.9	3.9
D3	8.29	7.5	11	5.28	5	8.5
D4	3.3	2.9	4.4	2.06	1.7	2.3
D5	9.56	6.5	10.2	4.94	4.1	6.5

4.5.2 UAS-SfM point cloud roughness

Research Question 1

Can the roughness of the UAS-SfM point cloud be used to quantify fluvial substrate size, and if so, how accurately?

The roughness values computed from the UAS-SfM point cloud for each plot and each kernel size, and for all detrending and smoothing/filtering scenarios are shown in Tables C1 to C6 Appendix C. Tables 4.5 and 4.6 show the co-efficients of determination for the linear regression of these roughness values against different measures of substrate size.

Detrending

When considering the impacts of detrending, the black box in Table 4.5 indicates that the strongest relationship is found between roughness computed using a 30cm kernel size on a non detrended UAS-SfM point cloud, with the D_{84} of the substrate B axis ($R^2 = 0.4418$, $p < 0.01$). As a result, only non detrended point clouds were used to test the filtering and smoothing procedure, the results of which are shown in Table 4.6. Given the upward trend in R^2 values with increasing roughness kernel size, larger kernel sizes were also tested at this point and the results presented in Table 4.6.

Smoothing and filtering

The black box in Table 4.6 indicates that for non-detrended data, the strongest relationship is observed between roughness computed using a 20cm kernel size on a filtered and smoothed point cloud and the D_{84} of the substrate B axis ($R^2 = 0.6588$, $p < 0.01$). This relationship considers all ground truth sample plots. The exclusion of plots A1 and C1 (due to the effects of footprints) improves the strength of this relationship, to give an R^2 value of 0.7712 ($p < 0.01$).

Despite the apparent upward trend in R^2 values with kernel size observed in Table 4.5 for non-detrended data, this trend is not found to continue beyond a kernel size of 35cm, and does not exceed the higher R^2 values observed for the smoothed and filtered datasets.

Table 4.5. Linear regression results for assessing the impact of detrending. The cells are coloured to show the strength of relationship, with light yellow representing the weaker relationships and dark green representing the stronger. The strongest relationship is highlighted by the black box.

Grain axis	Grain size	Roughness kernel size	Co-efficient of determination for linear regression (R^2)			
			No detrending	3rd order polynomial	4th order polynomial	5th order polynomial
A	Average	5cm	0.0346	0.003	0.0031	0.0037
		10cm	0.0008	0.0038	0.0036	0.0034
		15cm	0.0647	0.0676	0.0661	0.0607
		20cm	0.1789	0.1503	0.1519	0.14
		25cm	0.249	0.1824	0.191	0.173
		30cm	0.2721	0.1746	0.1952	0.1705
	D ₅₀	5cm	0.0073	0.0028	0.0031	0.0027
		10cm	0.0166	0.013	0.0128	0.0128
		15cm	6.00E-05	5.00E-05	2.00E-05	7.00E-07
		20cm	0.0094	0.0051	0.0092	0.0081
		25cm	0.0209	0.0084	0.0167	0.014
		30cm	0.0233	0.0059	0.0176	0.0129
	D ₈₄	5cm	0.0674	0.023	0.023	0.0246
		10cm	0.0184	0.0291	0.028	0.0274
		15cm	0.1366	0.1413	0.1384	0.1305
		20cm	0.2827	0.2494	0.25	0.2363
		25cm	0.3581	0.2836	0.2912	0.2718
		30cm	0.3767	0.2681	0.289	0.2629
B	Average	5cm	0.0324	0.0026	0.0027	0.0033
		10cm	0.001	0.0041	0.0037	0.0035
		15cm	0.0719	0.0729	0.0693	0.0634
		20cm	0.2008	0.1659	0.1617	0.1487
		25cm	0.285	0.207	0.2072	0.1873
		30cm	0.3178	0.2039	0.2147	0.1875
	D ₅₀	5cm	0.0181	0.0005	0.0006	0.0004
		10cm	0.0089	0.0057	0.0059	0.006
		15cm	0.0035	0.0033	0.0037	0.0028
		20cm	0.035	0.0235	0.0266	0.0228
		25cm	0.0629	0.0343	0.0413	0.0338
		30cm	0.0738	0.0318	0.044	0.0325
	D ₈₄	5cm	0.0439	0.0059	0.0062	0.0071
		10cm	0.0073	0.0153	0.0145	0.0139
		15cm	0.1202	0.1239	0.1172	0.1075
		20cm	0.2924	0.2511	0.2407	0.2204
		25cm	0.3991	0.3079	0.2997	0.2699
		30cm	0.4418	0.3086	0.3107	0.2705

Table 4.6. Linear regression results for testing smoothing and filtering. The cells are coloured to show the strength of relationship, with light yellow representing the weaker relationships and dark green representing the stronger. The strongest relationship is highlighted by the black box.

Grain axis	Grain size	Roughness kernel size	Co-efficient of determination for linear regression (R^2)	
			No smoothing or filtering	With smoothing and filtering
A	Average	5cm	0.0346	0.1250
		10cm	0.0008	0.3951
		15cm	0.0647	0.4766
		20cm	0.1789	0.4858
		25cm	0.2490	0.4527
		30cm	0.2721	0.3921
		35cm	0.2685	0.3264
		40cm	0.2543	0.2721
		45cm	0.2376	0.2300
		50cm	0.2161	0.1947
	D50	5cm	0.0073	0.0056
		10cm	0.0166	0.0867
		15cm	0.0001	0.1184
		20cm	0.0094	0.1155
		25cm	0.0209	0.0927
		30cm	0.0233	0.0614
		35cm	0.0198	0.0351
		40cm	0.0153	0.0193
		45cm	0.0121	0.0113
		50cm	0.0096	0.0007
	D84	5cm	0.0674	0.2166
		10cm	0.0184	0.5138
		15cm	0.1366	0.5889
		20cm	0.2827	0.5892
		25cm	0.3581	0.5488
		30cm	0.3767	0.4818
		35cm	0.3667	0.4102
		40cm	0.3484	0.3522
		45cm	0.3309	0.3107
		50cm	0.3091	0.2772
B	Average	5cm	0.0324	0.1227
		10cm	0.0010	0.4022
		15cm	0.0719	0.5002
		20cm	0.2008	0.5311
		25cm	0.2850	0.5050

		30cm	0.3178	0.4510
		35cm	0.3193	0.3859
		40cm	0.3072	0.3297
		45cm	0.2913	0.2845
		50cm	0.2689	0.2445
	D50	5cm	0.0181	0.0169
		10cm	0.0089	0.1416
		15cm	0.0035	0.1910
		20cm	0.0350	0.1970
		25cm	0.0629	0.1760
		30cm	0.0738	0.1389
		35cm	0.0723	0.1017
		40cm	0.0658	0.0748
		45cm	0.0595	0.0569
		50cm	0.0522	0.0436
	D84	5cm	0.0439	0.1895
		10cm	0.0073	0.5150
		15cm	0.1202	0.6260
		20cm	0.2924	0.6588
		25cm	0.3991	0.6435
		30cm	0.4418	0.5927
		35cm	0.4478	0.5284
		40cm	0.4379	0.4709
		45cm	0.4230	0.4220
		50cm	0.3989	0.3755

Computing substrate size from roughness

The equation describing this strongest relationship, between 'y' (D_{84} of the substrate b axis) and 'x' (roughness of filtered and smoothed point cloud calculated using a 20cm kernel size), is shown in Figure 4.18 and has a slope of 1031.1 and intercept of +1.2826.

Figure 4.19a shows the UAS-SfM point cloud roughness for the whole of the Coledale site, calculated using a 20cm kernel size on the non-detrended point cloud following smoothing and filtering. The equation provided in Figure 4.18 was applied to this roughness map to produce the map of predicted substrate sizes shown in Figure 4.19b. The maximum and minimum predicted substrate sizes are 143.32cm and 1.28cm respectively.

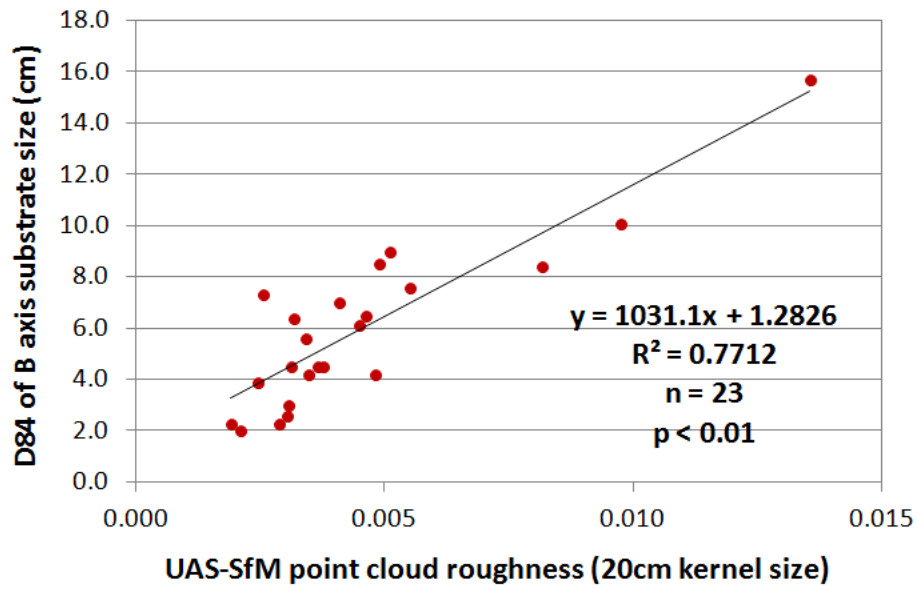


Figure 4.18. Linear regression of UAS-SfM point cloud roughness (no detrending, smoothed and filtered, 20cm roughness kernel size) and ground truth substrate size (D_{84} of B axis). Plots A1 and C1 are not included.

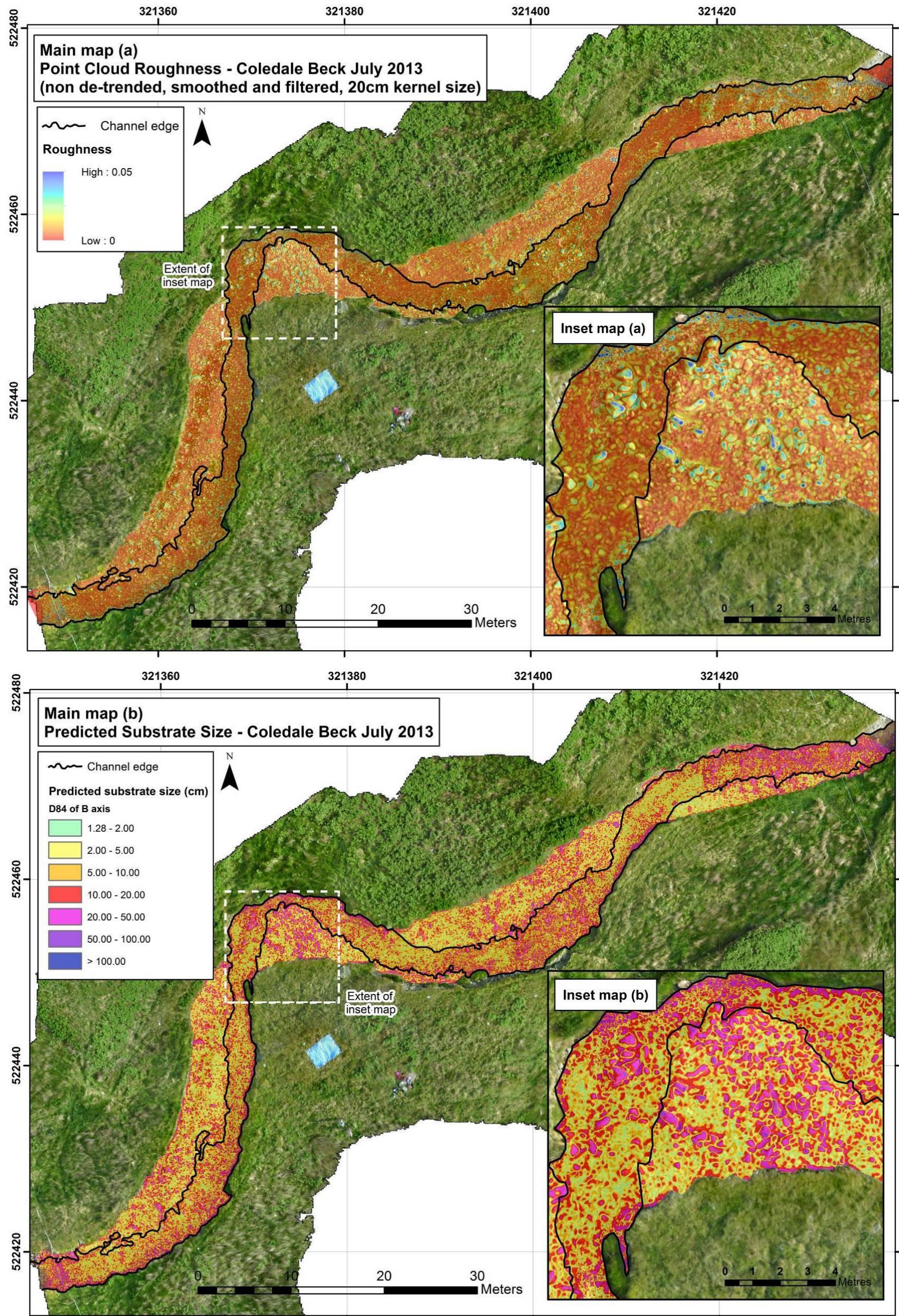


Figure 4.19. a) Point cloud roughness for the Coledale Beck site, computed using a 20cm kernel size on a non detrended, smoothed and filtered point cloud, b) Predicted substrate size for the Coledale Beck, based on the roughness data shown in map (a). Roughness and predicted substrate size layers are displayed with a 30-50% transparency. The black line labelled as 'channel edge' represents the wetted channel at the time of the survey.

Model calibration-validation (using grain size in centimetres)

Table 4.7 presents the results of the calibration-validation of this predictive relationship, carried out using a jack-knife analysis, where grain size is in centimetres. Residual errors range from +2.14cm to -3.62cm, where positive (blue) numbers indicate an over-prediction of grain size by the model and negative (red) numbers indicate an under-prediction of grain size. The mean and standard deviation of residual errors are -0.011cm and 1.641cm respectively.

These residual errors are plotted against ground truth grain size (D_{84} of B axis) in Figure 4.20. This figure shows a strong trend between residual error and grain size. Over-prediction of grain sizes less than c. 5cm is observed and there is some under-prediction of grains larger than c. 5cm in size. The only exceptions to this pattern are plots B3 and C3, where an over-prediction is observed for substrate sizes of 8.4cm and 10.1cm respectively (D_{84} of B axis measures).

*Table 4.7. Model validation results for the UAS-SfM point cloud roughness approach (using grain size in centimetres). The coloured cells highlight positive residual error in blue (i.e. overestimation of grain size) and negative residual error in red (i.e. underestimation). *Normalised residual error is defined as the residual error as a percentage of the ground truth measure of substrate size (D_{84} of B axis).*

Ground truth sample plot	Substrate size (cm) D_{84} of B axis	Roughness 20cm kernel size	Equation when plot is excluded		Predicted grain size (cm)	Residual error (cm)	Residual error normalised by D_{84} of B axis (%)
			Slope	Intercept			
A1	<i>Not included</i>						
A2	4.5	0.0036	1028.10	1.3211	5.07	0.57	12.66
A3	4.2	0.0048	1035.40	1.3565	6.34	2.14	51.06
A4	9	0.0051	1018.00	1.0381	6.22	-2.78	-30.93
A5	3	0.0031	1017.30	1.4114	4.54	1.54	51.19
A6	15.7	0.0135	973.51	1.4978	14.69	-1.01	-6.45
A7	2	0.0021	1007.40	1.4580	3.58	1.58	78.79
A8	7	0.0041	1035.40	1.1945	5.41	-1.59	-22.67
A9	4.2	0.0035	1026.70	1.3325	4.89	0.69	16.33
B1	4.5	0.0038	1027.90	1.3272	5.19	0.69	15.42
B2	2.6	0.0030	1013.40	1.4457	4.52	1.92	73.85
B3	8.4	0.0082	1065.00	1.1942	9.88	1.48	17.56
B4	5.6	0.0034	1036.90	1.2197	4.75	-0.85	-15.10
C1	<i>Not included</i>						
C2	4.5	0.0031	1031.10	1.2831	4.51	0.01	0.13

C3	10.1	0.0097	1083.00	1.1177	11.67	1.57	15.56
C4	6.4	0.0032	1047.20	1.1256	4.46	-1.94	-30.36
C5	7.3	0.0026	1075.20	0.9268	3.68	-3.62	-49.57
C6	7.6	0.0055	1026.90	1.2723	6.92	-0.68	-8.91
C7	6.1	0.0045	1031.20	1.2733	5.89	-0.21	-3.45
D1	2.3	0.0019	1014.20	1.4040	3.34	1.04	45.19
D2	3.9	0.0024	1032.50	1.2719	3.79	-0.11	-2.70
D3	8.5	0.0049	1025.50	1.2087	6.22	-2.28	-26.79
D4	2.3	0.0029	1010.00	1.4679	4.37	2.07	90.08
D5	6.5	0.0046	1030.80	1.2628	6.01	-0.49	-7.51

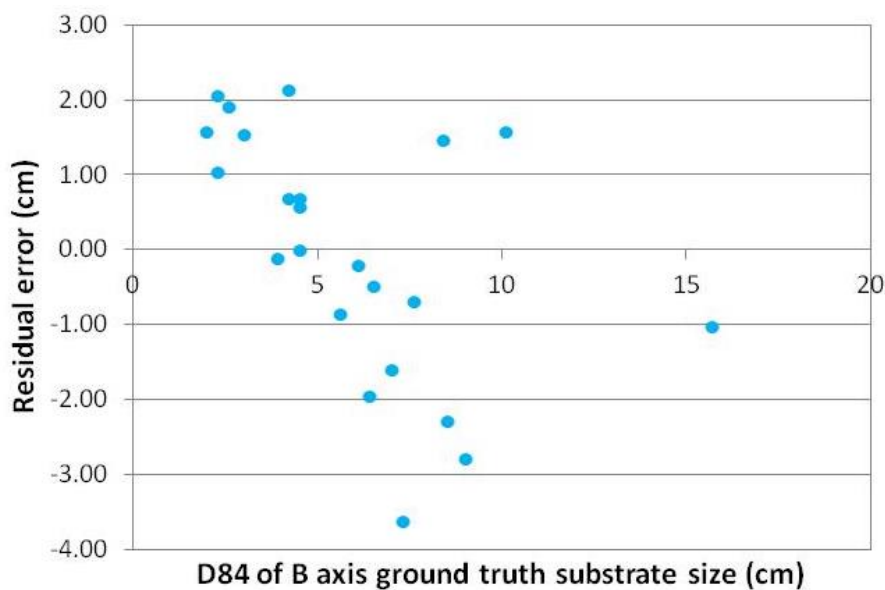


Figure 4.20. Residual error of predicted substrate size from the UAS-SfM point cloud roughness approach plotted against ground truth substrate size.

The residual errors have been normalised by grain size, and are presented as percentages in the final column of Table 4.7. For example, the residual error of 0.57cm for plot A2 represents 12.66% of the ground truth measured substrate size (4.5cm) for that plot. These data indicate that the normalised residual errors can be as small as 0.13% (plot C2) of substrate size, but as large as c. 90% (plot D4). The average normalised residual error is +11.45%, with a precision (standard deviation) of 37.68%. Normalised relative residual errors which have been converted to positive numbers only are plotted against ground truth substrate size data in Figure 4.21. This graph suggests a trend towards larger normalised residual errors at small substrate sizes, where errors are consistently greater than +/-40% for

substrate sizes less than 3cm. As substrate size increases however, normalised residual errors decrease. For substrate sizes greater than 3cm the majority of normalised residual errors are less than +/-30%.

Figure 4.22 shows observed substrate size (D_{84} of B axis ground truth data) plotted against the predicted substrate sizes. The slope value (0.7367) indicates that grain size is typically underestimated by the model, as also indicated by the mean residual error (-0.011cm). The R^2 value (0.7298) indicates that a linear relationship does exist between the data, but this is not particularly strong.

The model calibration-validation was also carried out using grain size measures converted to the phi scale, as presented in Appendix C. This does not help to remove the trend with grain size however, nor does it improve the strength of the observed versus predicted grain size relationship (Table C7, Appendix C)

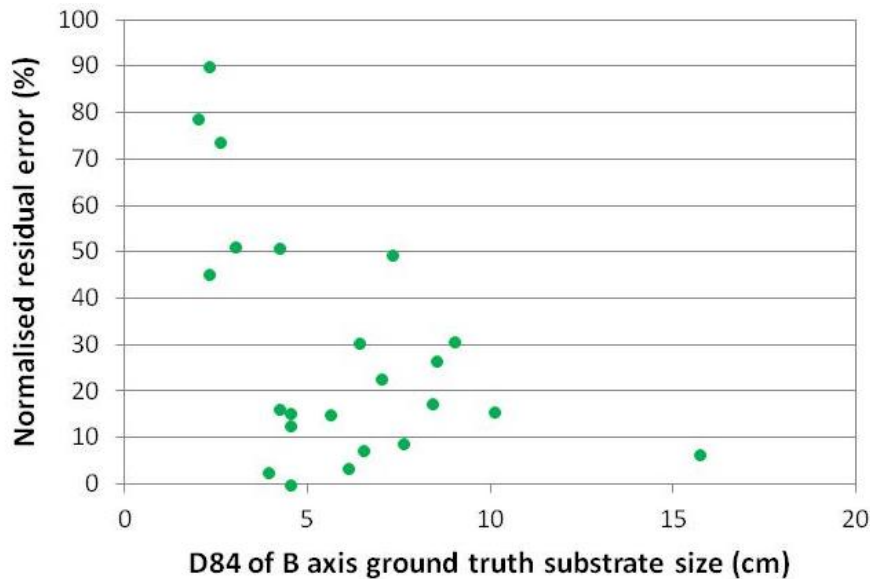


Figure 4.21. Normalised residual error of predicted substrate size from the UAS-SfM point cloud roughness approach plotted against ground truth substrate size.

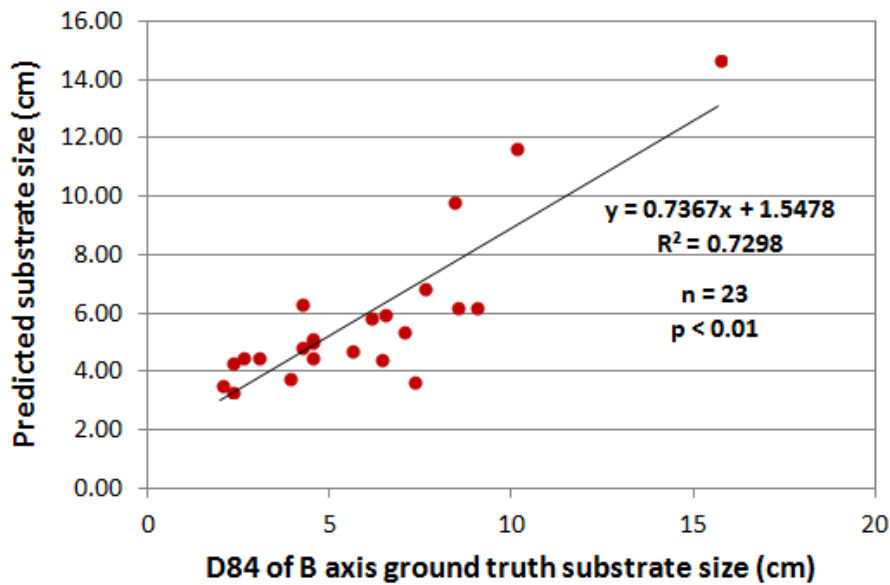


Figure 4.22. Observed ground truth substrate size plotted against predicted substrate size using UAS-SfM point cloud roughness.

4.4.3 UAS-SfM image texture

Research Question 2

How do the results of research question 1 compare with those obtained using existing remote sensing techniques: a) image texture analysis and b) TLS point cloud roughness?

A summary of image entropy values computed from the UAS-SfM ortho-imagery for each plot are shown in Table 4.8. Table 4.9 shows the co-efficients of determination for the linear regression of these entropy values against different measures of ground truth substrate size. The strongest relationship is observed between average A axis substrate size and maximum image entropy values ($R^2 = 0.5077$, $p < 0.01$). With the exclusion of plots A1 and C1 (due to the unwanted effects of footprints), this R^2 value is improved to 0.5595 ($p < 0.01$), as shown in Figure 4.23. Within this graph, points at x,y locations 716, 3.3 (plot D4) and 751, 5.5 (plot A2) might be identified as outliers. The image entropy values for these plots are higher than would be anticipated for their substrate size, based on the regression shown. Possible reasons for this are presented in the discussion, but for the sake of a fair comparison against the other approaches (UAS-SfM and TLS point cloud roughness) these plots are not excluded from further analysis.

Table 4.8. Image entropy statistics computed from the UAS-SfM orthophoto for each ground truth sample plot. Cells have been coloured to highlight those plots showing higher image texture in darker green, and lower image texture in light yellow.

Ground truth sample plot	Image Entropy		
	Mean	Min	Max
A1	675	653	702
A2	732	701	751
A3	620	598	678
A4	661	631	718
A5	656	634	688
A6	739	703	758
A7	577	530	654
A8	702	685	713
A9	635	596	684
B1	635	595	670
B2	607	569	632
B3	712	680	734
B4	632	558	670
C1	638	590	658
C2	647	624	684
C3	685	668	699
C4	655	619	691
C5	669	654	704
C6	718	705	734
C7	665	631	696
D1	620	591	646
D2	654	641	670
D3	702	688	719
D4	676	638	716
D5	756	741	768

Computing substrate size from image entropy

Figure 4.24a shows the UAS-SfM image entropy for the whole of the Coledale site. The equation describing the strongest relationship, between ‘y’ (average of the substrate A axis) and ‘x’ (maximum image entropy), is shown in Figure 4.23 and has a slope of 0.0567 and intercept of -33.164. This equation was applied to the site-wide entropy map to produce the map of predicted substrate sizes shown in Figure 4.24b. The maximum reported substrate size is 10.83cm and negative substrate sizes up to -33.164cm are also produced in submerged areas, indicating that the technique fails to perform in some areas.

Table 4.9. Linear regression results for image entropy and substrate size. The cells are coloured to show the strength of relationship, with light yellow representing the weaker relationships and dark green representing the stronger. The strongest relationship is highlighted by the black box.

Substrate axis	Substrate size measure	Entropy	R ²
A	Average	Average	0.4742
		Min	0.4165
		Max	0.5077
	D ₅₀	Average	0.3324
		Min	0.3041
		Max	0.3681
	D ₈₄	Average	0.408
		Min	0.3259
		Max	0.4403
B	Average	Average	0.4104
		Min	0.3705
		Max	0.4591
	D ₅₀	Average	0.3435
		Min	0.3213
		Max	0.4059
	D ₈₄	Average	0.3703
		Min	0.3251
		Max	0.3938

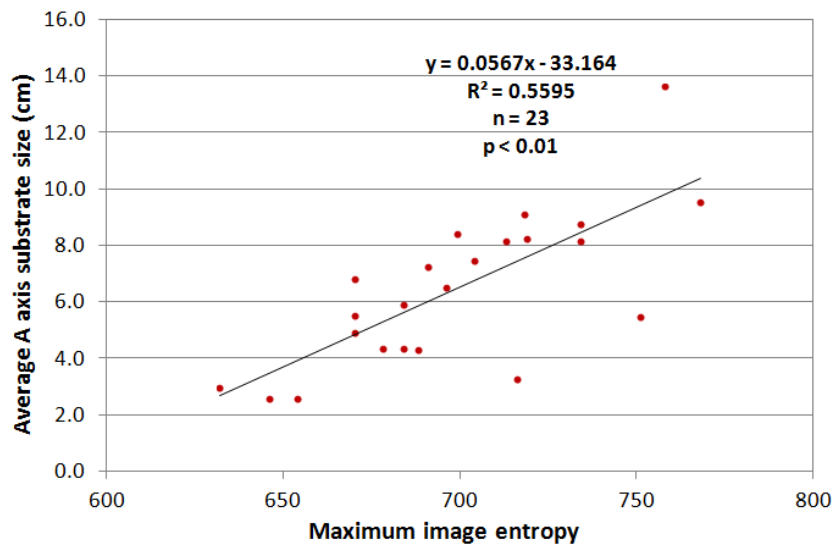


Figure 4.23. Linear regression of UAS-SfM maximum image entropy and ground truth substrate size (average of A axis). Plots A1 and C1 are not included.

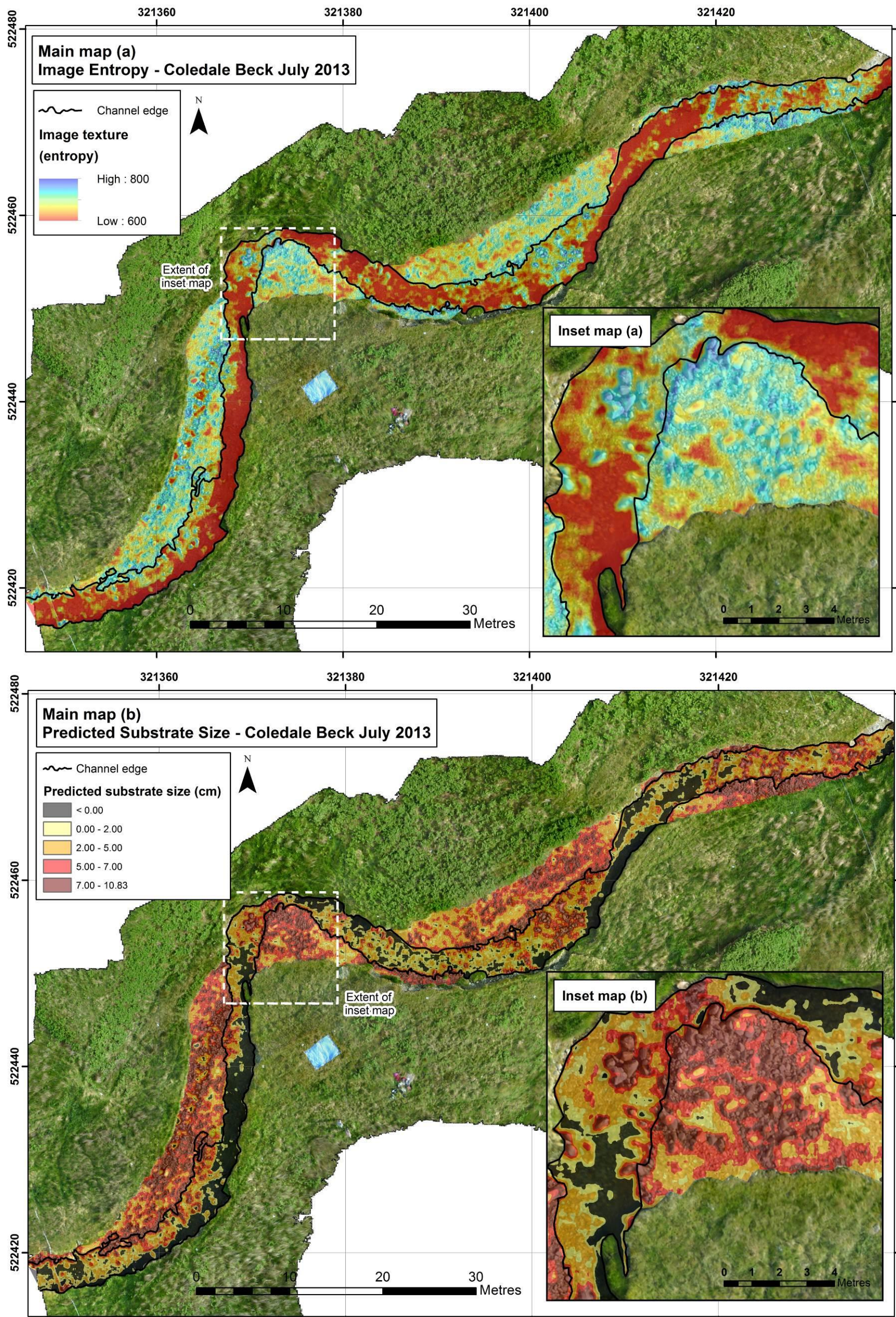


Figure 4.24. a) Image entropy for the Coledale Beck site, computed using a c. 41cm kernel size on the UAS-SfM orthophoto, b) Predicted substrate size for Coledale Beck, based on the image entropy data shown in map (a). Image entropy and predicted grain size layers are displayed with a 50% transparency. The black line labelled as 'channel edge' represents the wetted channel at the time of the survey.

Model calibration-validation (using grain size in centimetres)

Table 4.10 presents the results of the validation of this predictive relationship, carried out using a jack-knife analysis. Residual errors range from +4.56cm to -4.64cm, where positive numbers (blue) indicate an over-prediction of grain size by the model and negative numbers (red) indicate an under-prediction of grain size. The mean and standard deviation of residual errors are 0.003cm and 1.99cm respectively.

*Table 4.10. Model validation results for the UAS-SfM image texture approach. The coloured cells highlight positive residual error in blue (i.e. overestimation of grain size) and negative residual error in red (i.e. underestimation). *Normalised residual error is defined as the residual error as a percentage of the ground truth measure of substrate size (average A axis).*

Ground truth sample plot	Substrate size (cm)	Image entropy	Equation when plot is excluded		Predicted grain size (cm)	Residual error (cm)	Residual error normalised by average of A axis (%)
	Average A axis	Maximum	Slope	Intercept			
A1	<i>Not included</i>						
A2	5.50	751	0.0653	-38.9780	10.06	4.56	82.82
A3	4.36	678	0.0560	-32.6020	5.37	1.00	22.96
A4	9.15	718	0.0555	-32.4240	7.43	-1.72	-18.83
A5	4.34	688	0.0561	-32.6520	5.94	1.61	37.10
A6	13.66	758	0.0468	-26.4510	9.02	-4.64	-33.95
A7	2.62	654	0.0543	-31.4140	4.10	1.48	56.66
A8	8.18	713	0.0562	-32.8660	7.20	-0.98	-11.92
A9	4.39	684	0.0560	-32.6130	5.69	1.30	29.69
B1	5.54	670	0.0575	-33.7580	4.77	-0.77	-13.89
B2	2.98	632	0.0577	-33.8420	2.62	-0.36	-12.05
B3	8.81	734	0.0562	-32.8380	8.41	-0.40	-4.53
B4	6.83	670	0.0590	-34.8470	4.68	-2.15	-31.45
C1	<i>Not included</i>						
C2	5.93	684	0.0569	-33.3020	5.62	-0.31	-5.30
C3	8.43	699	0.0567	-33.2530	6.38	-2.05	-24.31
C4	7.30	691	0.0571	-33.4940	5.96	-1.34	-18.33
C5	7.49	704	0.0566	-33.1010	6.75	-0.74	-9.92
C6	8.18	734	0.0571	-33.4260	8.49	0.31	3.78
C7	6.53	696	0.0397	-21.4960	6.14	-0.40	-6.07
D1	2.59	646	0.0547	-31.7430	3.59	1.00	38.63
D2	4.94	670	0.0568	-33.2600	4.80	-0.15	-2.99
D3	8.29	719	0.0562	-32.8280	7.58	-0.71	-8.59
D4	3.30	716	0.0594	-34.8580	7.67	4.37	132.50
D5	9.56	768	0.0593	-34.9620	10.58	1.02	10.67

These residual errors are plotted against ground truth measures of grain size in Figure 4.25. This figure shows a trend towards over-prediction of grain sizes less than c. 5cm, with most plots of grain size larger than c. 5cm being underpredicted. The only exceptions to this pattern are plots C6 and D5, where slight over-predictions are observed for substrate sizes of 8.18cm and 9.56cm respectively (average A axis measures).

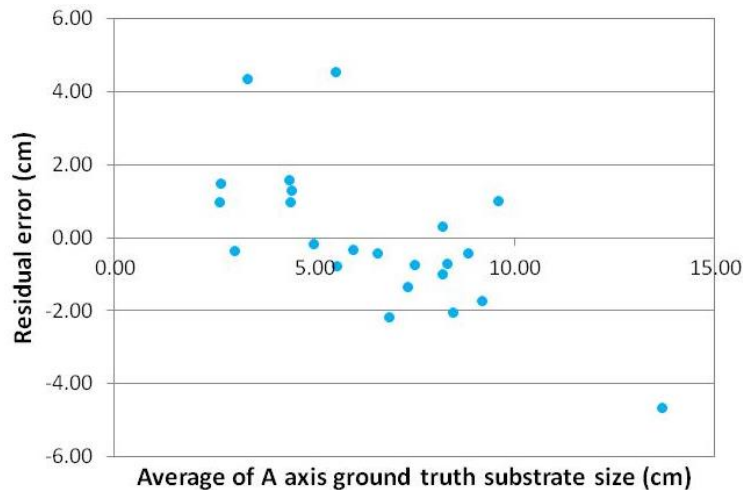


Figure 4.25. Residual error of predicted substrate size from the UAS-SfM image texture approach plotted against ground truth substrate size.

The residual errors are normalised by grain size, as shown by the percentages in the final column of Table 4.10. These data indicate that the normalised residual errors can be as small as c. 3% (plot D2) of substrate size, but as large as c. 133% (plot D4). The average normalised residual error is +9.25%, with a precision (standard deviation) of 39.45%. Normalised relative residual errors which have been converted to positive numbers only are plotted against ground truth substrate size data in Figure 4.26. This graph demonstrates that larger normalised residual errors are found for small substrate sizes, where errors are as great as 133% for substrate sizes less than 3cm. As substrate size increases however, normalised residual errors are typically lower. For substrate sizes greater than c. 6cm the majority of normalised residual errors are less than +/-30%.

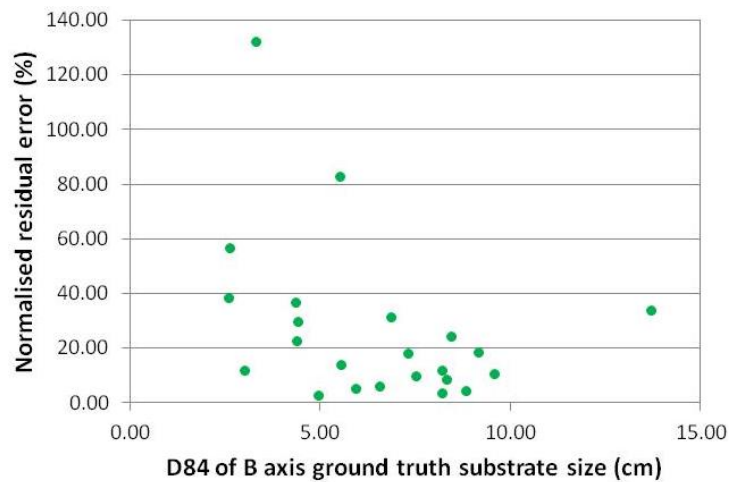


Figure 4.26. Normalised residual error of predicted substrate size from the UAS-SfM image texture approach plotted against ground truth substrate size.

Figure 4.27 shows observed substrate size (average of A axis ground truth data) plotted against the predicted substrate sizes. The slope of 0.5043 suggests that grain size is typically underestimated by the model, and the R^2 value (0.4525) does not suggest a particularly strong linear relationship between these data.

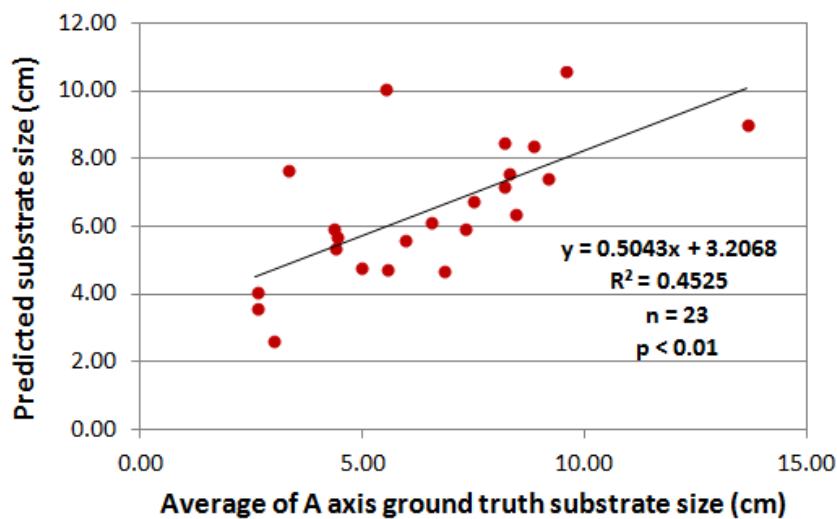


Figure 4.27. Observed ground truth substrate size plotted against predicted substrate size from the UAS-SfM image texture approach.

The model calibration-validation was also conducted using grain sizes on the phi scale. Residual errors calculated from this model (Table C8, Appendix C) still show a trend with

grain size and produce only a very minor improvement in the strength of the observed versus predicted grain size relationship (slope improved to 0.5093, R^2 improved to 0.4696).

4.5.4 TLS point cloud roughness

Research Question 2

How do the results of research question 1 compare with those obtained using existing remote sensing techniques: a) image texture analysis and b) TLS point cloud roughness?

Average TLS point cloud roughness values computed for a 20cm kernel size are shown for each plot in Table 4.11. The highest roughness values were observed for plots A6, C3 and C6, as indicated by the darker green colours in Table 4.11.

Table 4.12 shows the coefficients of determination for the linear regression of these TLS roughness values against different measures of ground truth substrate size. The strongest relationship is observed with the D_{84} of the B axis substrate size ($R^2 = 0.5512$, $p < 0.01$). With the exclusion of plots A1 and C1 (due to the unwanted effects of footprints), this R^2 value is improved to 0.6154, as shown in Figure 4.28. Within this graph, the point at x,y location 0.0279, 7.6 (plot C6) might be identified as an outlier. The TLS roughness for this plot is higher than would be expected for the substrate size, based on the regression shown. Possible reasons for this are presented in the discussion, but for the sake of a fair comparison against the other approaches (UAS-SfM and TLS point cloud roughness) this plots is not excluded from further analysis.

Computing substrate size from roughness

Figure 4.29a shows the TLS point cloud roughness for the whole of the Coledale site. The equation describing the strongest relationship, between 'y' (D_{84} of B axis) and 'x' (TLS point cloud roughness calculated using a 20cm kernel size), is shown in Figure 4.28 and has a slope of 352.48 and intercept of +1.6736. This equation was applied to the site-wide roughness data to produce the map of predicted substrate sizes shown in Figure 4.29b. The maximum and minimum predicted substrate sizes are 59.53cm and 1.67cm respectively.

Table 4.11. Average TLS point cloud roughness values per ground truth plot. The darker green highlights plots of higher roughness, and the lighter yellow highlights plots of lower roughness.

Ground truth sample plot	Roughness (20cm kernel size)	Ground truth sample plot	Roughness (20cm kernel size)
A1	0.0095	C1	0.0117
A2	0.0123	C2	0.0076
A3	0.0057	C3	0.0223
A4	0.0111	C4	0.0121
A5	0.0079	C5	0.0082
A6	0.0313	C6	0.0279
A7	0.0043	C7	0.0073
A8	0.0122	D1	0.0061
A9	0.0052	D2	0.0092
B1	0.0096	D3	0.0133
B2	0.0054	D4	0.0118
B3	0.0134	D5	0.0174
B4	0.0155		

Table 4.12. Linear regression results for TLS point cloud roughness (20cm kernel size) and substrate size measures. The cells are coloured to show the strength of relationship, with light yellow representing the weaker relationships and dark green representing the stronger.

The strongest relationship is highlighted by the black box.

Substrate axis	Substrate size measure	R ²
A	Average	0.5158
	D ₅₀	0.1673
	D ₈₄	0.4411
B	Average	0.4967
	D ₅₀	0.2367
	D ₈₄	0.5512

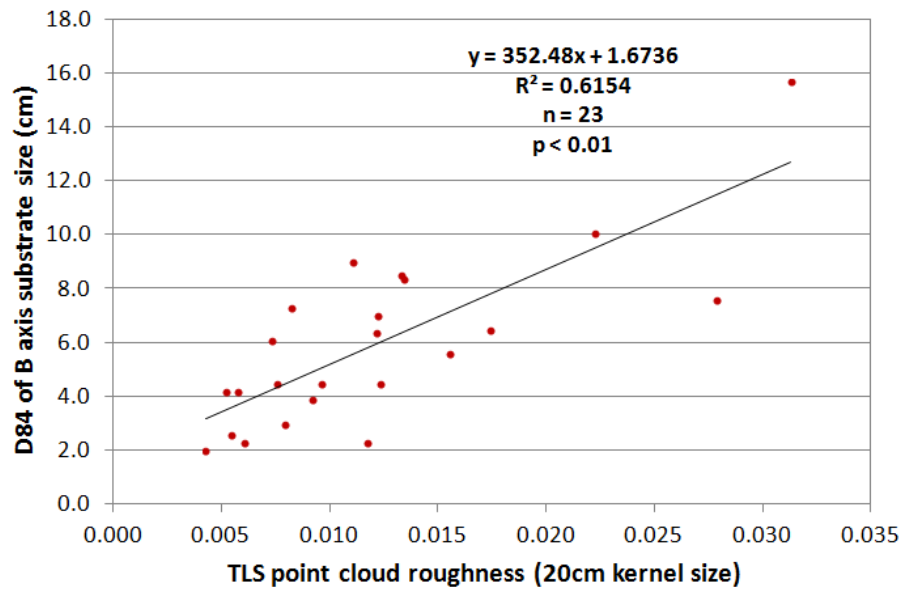


Figure 4.28. Linear regression of TLS point cloud roughness and ground truth substrate size (D_{84} of B axis). Plots A1 and C1 are not included.

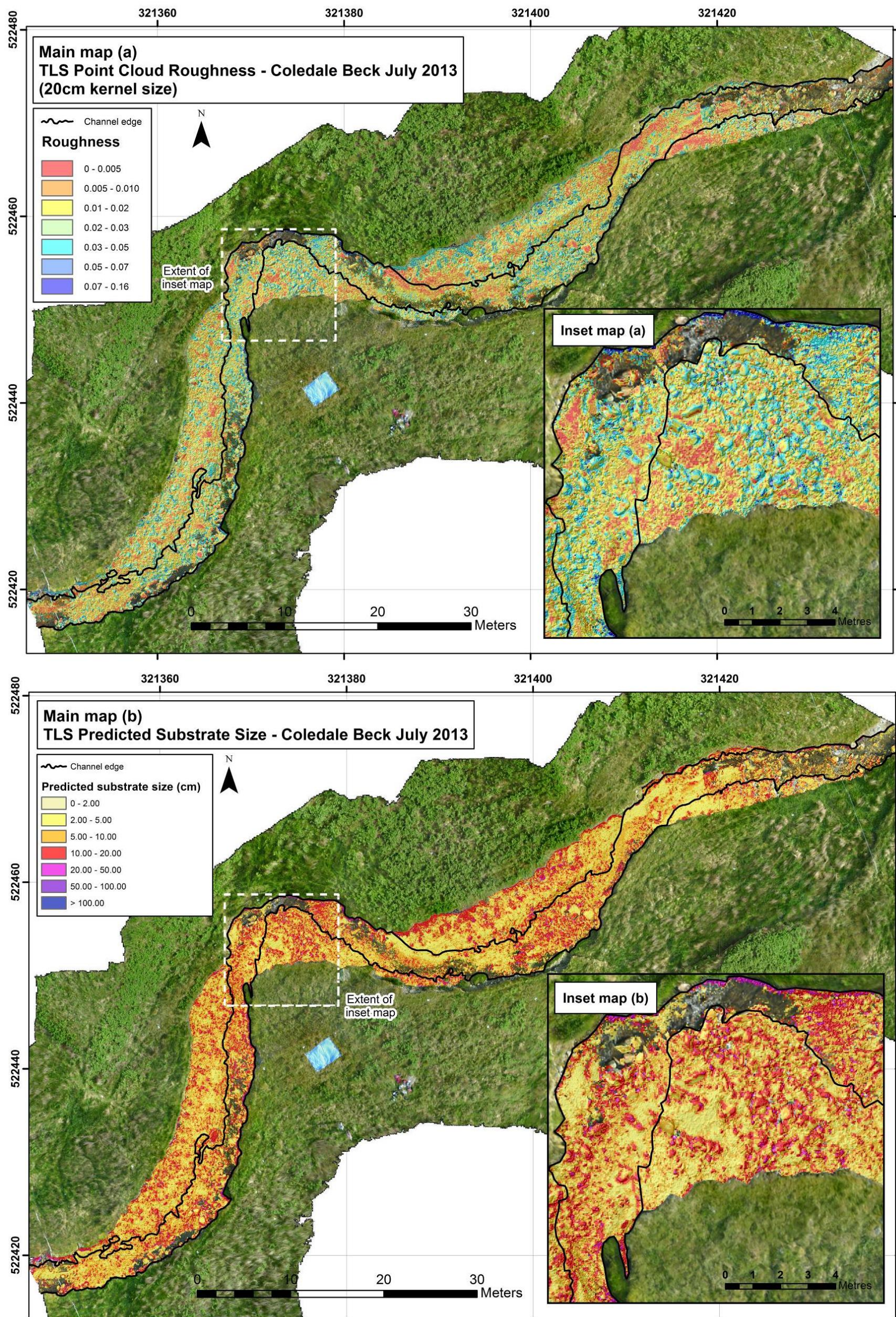


Figure 4.29. a) TLS point cloud roughness for the Coledale Beck site, computed using a 20cm kernel (radius size), b) Predicted substrate size for Coledale Beck, based on the TLS roughness data shown in map (a). Roughness and predicted grain size layers are displayed with a 50% transparency. The black line labelled as 'channel edge' represents the wetted channel at the time of the survey.

Model calibration-validation (using grain size in centimetres)

Table 4.13 presents the results of the validation of this predictive relationship, carried out using a jack-knife analysis. Residual errors range from +5.36m to -4.86cm, where positive numbers (blue) indicate an over-prediction of grain size by the model and negative numbers (red) indicate an under-prediction of grain size. The average residual error is 0.01cm and the standard deviation of residual errors is 2.34cm.

*Table 4.13. Model validation results for the UAS-SfM image texture approach. The coloured cells highlight positive residual error in blue (i.e. overestimation of grain size) and negative residual error in red (i.e. underestimation). *Normalised residual error is defined as the residual error as a percentage of the ground truth measure of substrate size (D_{84} of B axis).*

Ground truth sample plot	Substrate size (cm)	TLS point cloud roughness	Equation when plot is excluded		Predicted grain size (cm)	Residual error (cm)	Residual error normalised by D_{84} of B axis (%)
	D_{84} of B axis	20cm kernel size	Slope	Intercept			
A1	<i>Not included</i>						
A2	4.5	0.0123	352.91	1.74	6.0956	1.60	35.46
A3	4.2	0.0057	355.70	1.61	3.6476	-0.55	-13.15
A4	9	0.0111	355.68	1.48	5.4211	-3.58	-39.77
A5	3	0.0079	346.55	1.81	4.5497	1.55	51.66
A6	15.7	0.0313	266.23	2.50	10.8412	-4.86	-30.95
A7	2	0.0043	343.10	1.84	3.3094	1.31	65.47
A8	7	0.0122	352.29	1.63	5.9432	-1.06	-15.10
A9	4.2	0.0052	357.19	1.58	3.4503	-0.75	-17.85
B1	4.5	0.0096	351.15	1.72	5.0888	0.59	13.08
B2	2.6	0.0054	345.88	1.80	3.6832	1.08	41.66
B3	8.4	0.0134	349.87	1.61	6.3038	-2.10	-24.95
B4	5.6	0.0155	357.68	1.68	7.2314	1.63	29.13
C1	<i>Not included</i>						
C2	4.5	0.0076	353.16	1.66	4.3343	-0.17	-3.68
C3	10.1	0.0223	346.13	1.72	9.4251	-0.67	-6.68
C4	6.4	0.0121	352.44	1.65	5.9350	-0.46	-7.26
C5	7.3	0.0082	362.61	1.43	4.4145	-2.89	-39.53
C6	7.6	0.0279	430.48	0.97	12.9581	5.36	70.50
C7	6.1	0.0073	361.08	1.48	4.1267	-1.97	-32.35
D1	2.3	0.0061	343.45	1.85	3.9370	1.64	71.17
D2	3.9	0.0092	349.66	1.75	4.9592	1.06	27.16
D3	8.5	0.0133	349.85	1.61	6.2724	-2.23	-26.21
D4	2.3	0.0118	351.46	1.85	5.9758	3.68	159.82
D5	6.5	0.0174	369.37	1.65	8.0757	1.58	24.24

These residual errors are plotted against ground truth measures of grain size in Figure 4.30. This figure shows a rough trend towards over-prediction of grain sizes less than c. 5cm, with most plots of grain size larger than c. 5cm being underpredicted. As for the equivalent data for the UAS-SfM point cloud roughness and UAS-SfM image texture (Figures 4.20 and 4.25), the 5-7cm substrate size appears to be a hinge point between over- and under-predicted substrate sizes. The exception to this pattern is plot C6, where a large overprediction (5.36cm) is observed for substrate size 7.6cm (D_{84} of B axis).

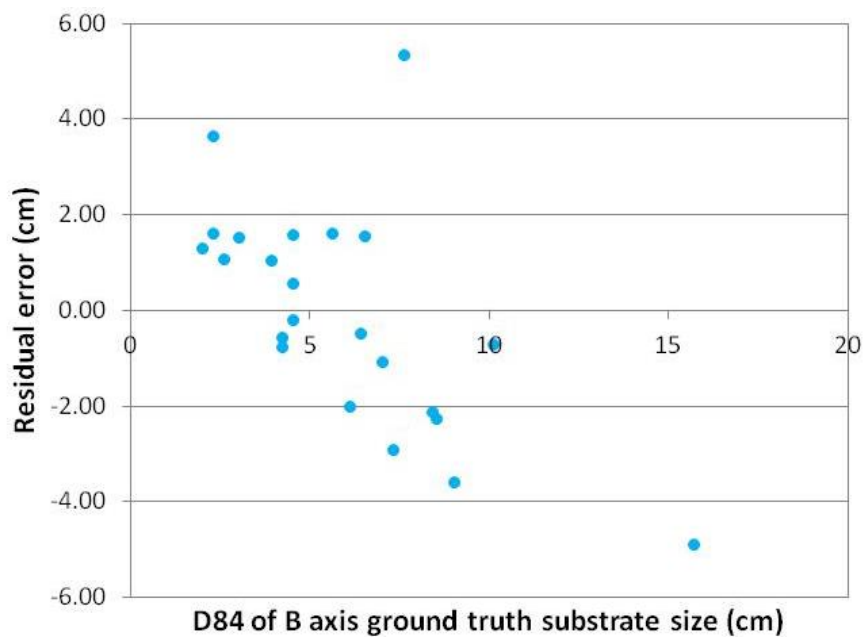


Figure 4.30. Residual error of predicted substrate size from the TLS point cloud roughness approach plotted against ground truth substrate size.

The residual errors which have been normalised by substrate size are shown as percentages in the final column of Table 4.13. These data indicate that the normalised residual errors can be as small as c. -4% (plot C2) of substrate size, but as large as c. +160% (plot D4). The average normalised residual error is +14.43%, with a precision (standard deviation) of 47.85%.

Normalised relative residual errors which have been converted to positive numbers only are plotted against ground truth substrate size data in Figure 4.31. This graph demonstrates that larger normalised residual errors are found for small substrate sizes, where errors are typically greater than +/- 40%, and as great as c. +/-160% for substrate sizes less than or

equal to c. 3cm. As substrate size increases, normalised residual errors are typically lower. For substrate sizes greater than c. 3cm the majority of normalised residual errors are less than +/-40%.

Figure 4.32 shows observed substrate size (D_{84} of B axis ground truth data) plotted against the predicted substrate sizes. The slope (0.5261) suggests that grain size is typically underestimated by the model and the R^2 value (0.4615) does not suggest a strong linear relationship between these data.

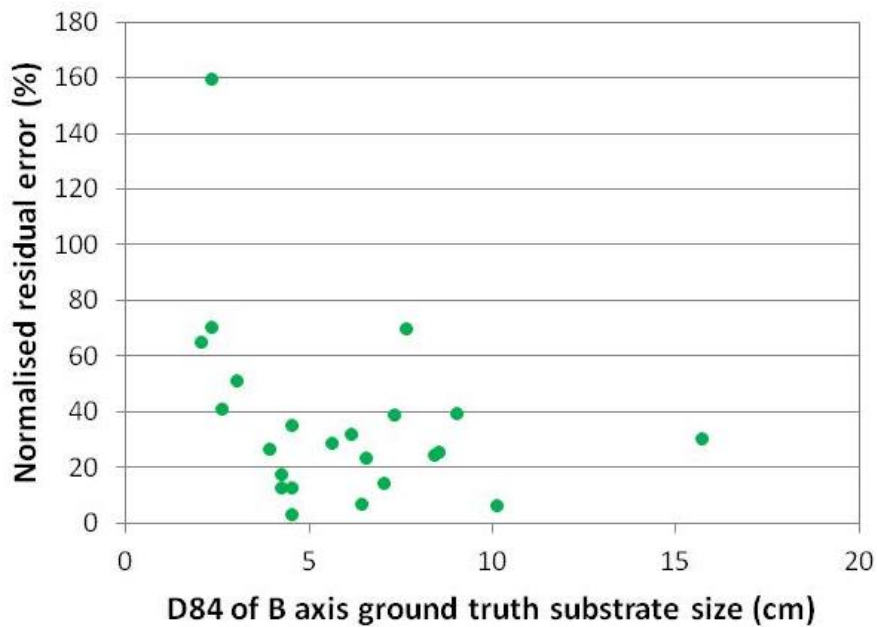


Figure 4.31. Normalised residual error of predicted substrate size from the TLS point cloud roughness approach plotted against ground truth substrate size.

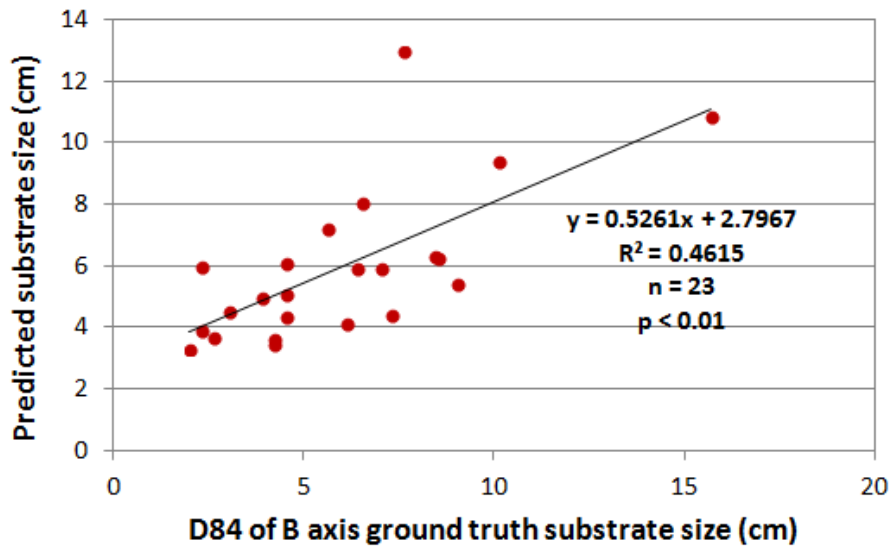


Figure 4.32. Observed ground truth substrate size plotted against predicted substrate size from the TLS point cloud roughness approach. Plots A1 and C1 are excluded.

Calculating the residual errors of this approach using the phi scale (Table C9, Appendix C) does not help to remove the trend with grain size and does not produce an notable improvement in the strength of the observed versus predicted grain size relationship (slope lower slightly to 0.5108, R^2 improved slightly to 0.4961).

4.5.5 Comparison of techniques

Research Question 2

How do the results of research question 1 compare with those obtained using existing remote sensing techniques: a) image texture analysis and b) TLS point cloud roughness?

Table 4.14 and Figures 4.33 to 4.37 provide a quantitative overview of the performance of the three different substrate size estimation techniques. The cells of the table are coloured to show a darker green where the technique performs more favourably relative to the other techniques and yellow where it performs less well. Where applicable, all values are given in centimetres rather than on the phi scale.

As shown in Table 4.14 the lowest mean residual error is achieved using the UAS-SfM image texture approach and the highest using the UAS-SfM point cloud roughness approach,

although mean error is +/- 0.011cm for all approaches. The standard deviation of residual errors is lowest for the UAS-SfM point cloud roughness approach and greatest for the TLS approach. A histogram of these data is presented in Figure 4.33. A similar pattern is observed in the normalised residual errors, where the lowest mean value is observed for the UAS-SfM image texture approach, and the lowest standard deviation is observed for the UAS-SfM point cloud roughness method. A histogram of normalised residual errors is given in Figure 4.34. The UAS-SfM point cloud roughness approach provides the strongest relationship between observed and predicted substrate size, with a slope of 0.7367 and coefficient of determination of 0.7298 at the >99.9% significance level ($p < 0.01$) (Figure 4.35).

Table 4.14. Comparison of key quantitative results for predicting substrate size from different approaches. The cells are coloured to highlight increasingly 'better' results in darker greens (e.g. lowest mean errors, highest observed v. predicted slope, etc).

		UAS-SfM point cloud roughness	UAS-SfM image texture	TLS point cloud roughness
Residual error (cm)	Average	-0.011	-0.003	0.01
	St Dev	1.641	1.998	2.336
Normalised residual error (%)	Average	11.452	9.246	14.429
	St Dev	37.682	39.448	47.849
	Min	-49.57	-33.95	-39.77
	Max	90.08	132.50	159.82
Observed v. predicted substrate size	Slope	0.7367	0.5043	0.5261
	Intercept	1.5479	3.2068	2.7967
	R2	0.7298	0.4525	0.4615
	P value	< 0.01	< 0.01	< 0.01

Figure 4.36 demonstrates that all approaches show a rough trend towards the overestimation of smaller substrate sizes (c. < 5cm), and the under-prediction of larger substrate sizes (> c.5cm). Whilst the magnitude of these under-predictions can be as great as c. 5cm, it is typically less than 3cm.

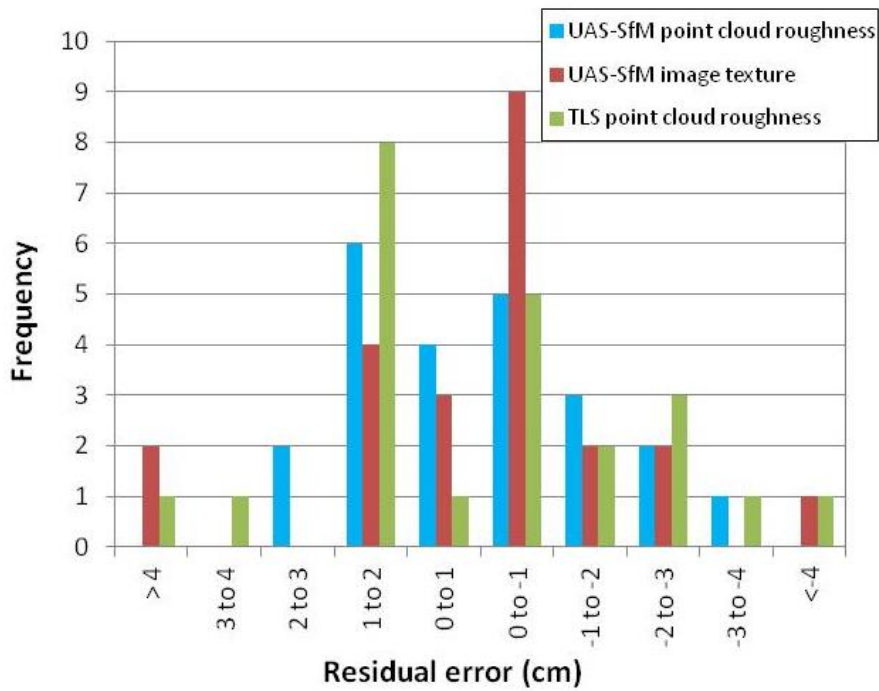


Figure 4.33. Histogram of residual errors, by approach.

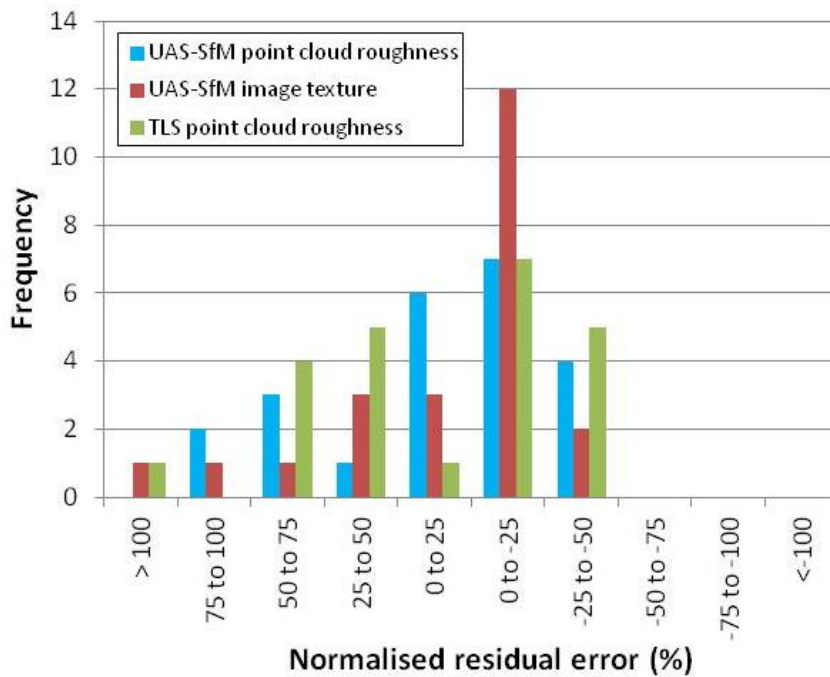


Figure 4.34. Histogram of normalised residual errors, by approach.

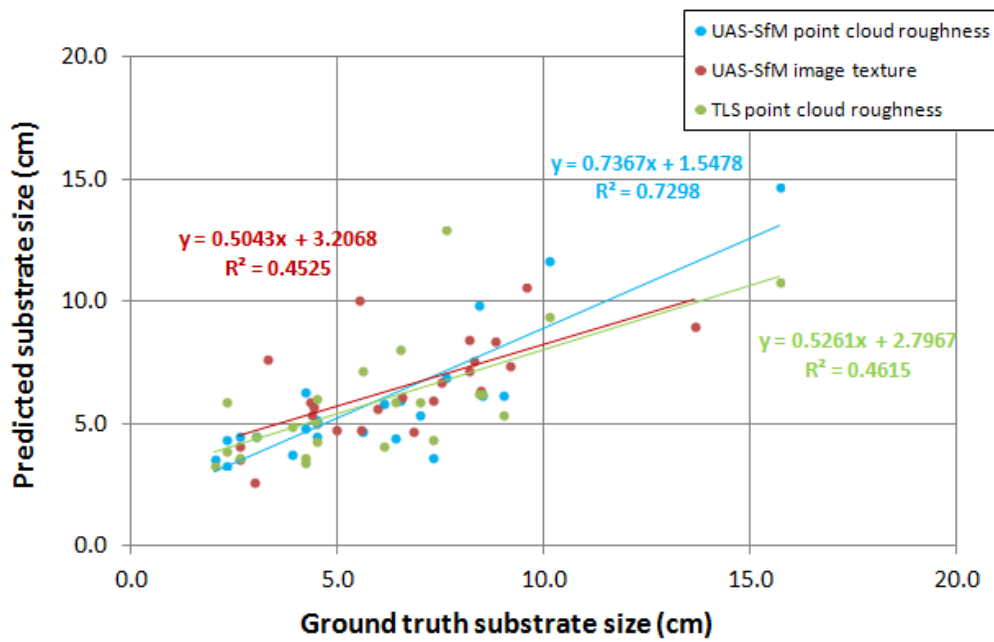


Figure 4.35. Observed ground truth substrate size plotted against predicted substrate size computed using the UAS-SfM point cloud roughness, UAS-SfM image texture and TLS point cloud roughness approaches. P values for all regressions are less than 0.01.

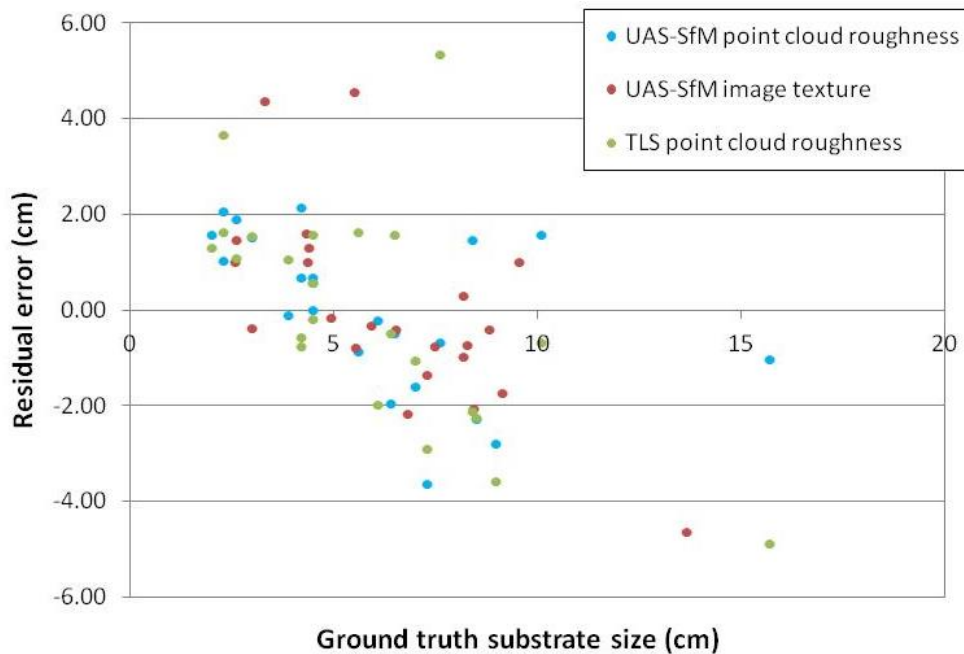


Figure 4.36. Residual error of predicted substrate sizes (from the UAS-SfM point cloud roughness, UAS-SfM image texture and TLS point cloud roughness approaches) plotted against ground truth substrate size.

As shown in Figure 4.37, the magnitude of these residual errors as a proportion of substrate size (normalised residual error) reduces with increasing substrate size for all approaches. Table 4.17 shows that average normalised residual error is lowest for the UAS-SfM image texture approach, yet the standard deviation of normalised residual errors is lowest (i.e. precision is highest) for the UAS-SfM point cloud roughness technique.

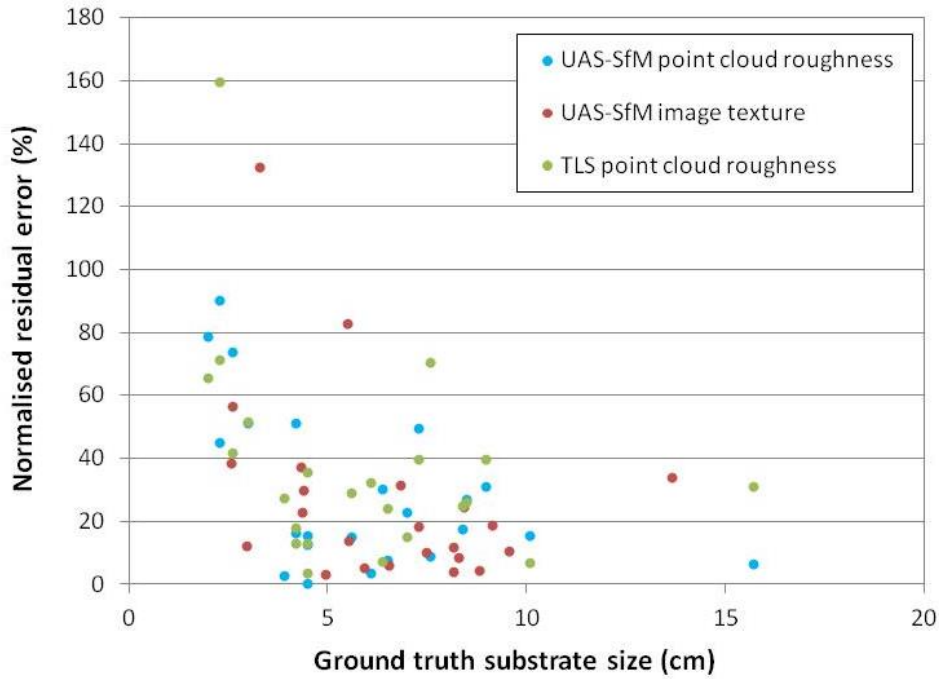


Figure 4.37. Normalised residual error of predicted substrate sizes (from the UAS-SfM point cloud roughness, UAS-SfM image texture and TLS point cloud roughness approaches) plotted against ground truth substrate size.

4.6 Discussion

4.6.1 Quantifying substrate size using UAS-SfM point cloud roughness

Research Question 1

Can the roughness of the UAS-SfM point cloud be used to quantify
fluvial substrate size, and if so, how accurately?

Model calibration

The linear regression of roughness measures computed from the UAS-SfM point cloud against substrate size produced relationships of variable strengths. The strongest correlation ($R^2 = 0.7712$) was found between roughness calculated using a 20cm radius kernel size on a non detrended, filtered and smoothed point cloud, and the D_{84} of substrate B axes. Potential explanations for the relative success of these particular conditions are discussed further below.

Roughness kernel size

The width of the kernel size (i.e. 40cm, which is double the kernel radius of 20cm) used to produce the strongest correlation is roughly equivalent to the maximum clast size recorded at Coledale Beck by the ground truth survey (38.8cm, A axis maximum for plot A6). Other similar studies have reported success using moving window sizes equivalent to the maximum clast size (Heritage and Milan 2009), or equivalent to the size of the ground truth sample plots used for model calibration and validation (Carbonneau et al., 2004). The results reported here appear to corroborate both these earlier findings, given the use of ground truth sample plots of c. 40cm x 40cm in size and success of the 20cm kernel radius.

Detrending

It is thought that the small size of the kernel used for the roughness calculations meant that results were not affected by wider slope trends, and hence why detrending of the data did not help to produce stronger correlations with grain size. Furthermore, by calculating roughness as the distance between each point in the cloud and the least squares best fitting plane computed on its nearest neighbours (within a kernel of a specified size), the process is already providing some compensation for the effects of local topography. Similar explanations for excluding detrending altogether were suggested by Heritage and Milan (2009) in their study of TLS roughness for fluvial substrate size.

Smoothing and filtering

The application of a smoothing and filtering procedure helped to increase the strength of the correlation between roughness and substrate size from $R^2 = 0.4418$ to $R^2 = 0.6588$ (the final value of $R^2 = 0.7712$ was achieved by the removal of two plots adversely affected by footprints). This procedure removes a great deal of the noise from the point cloud (as evidenced in Figure 4.14) so that grain size can become the principal controlling factor in the calculation of roughness. Potential sources of this noise within the point cloud include;

1. **Input imagery is of poor quality or is lacking in texture.** The SfM-photogrammetry process computes indirect measures of elevations using parallax, and thus where image quality is poor (e.g. due to blurring) or lacking in texture (e.g. spectrally homogeneous areas) then greater amounts of noise (i.e. erroneous point matches) are likely to be observed. Whilst efforts were made to exclude images which were obviously affected by blurring, some minor blurring may remain and little can be done to improve texture in spectrally homogenous parts of the image. Blurred imagery has also been found to affect the quality of grain size estimates from UAS imagery using an image texture approach (de Haas et al., 2014). Future work on reducing the causes and effects of blurring in UAS imagery is likely to be of great value for improving grain size estimates from UAS-SfM approaches. On-going work concerned with the filtering of blurred UAS imagery is presented by Sieberth et al., (2013).
2. **The presence of vegetation.** Some of the sample plots used to develop the relationship between roughness and substrate size feature small patches of vegetation within the 50cm buffered area used to compute point roughness values. This includes grasses and small plants which are likely to elevate roughness values when covered by the moving kernel. An example of a plot where roughness is likely to have been affected by vegetation is shown in Figure 4.38.

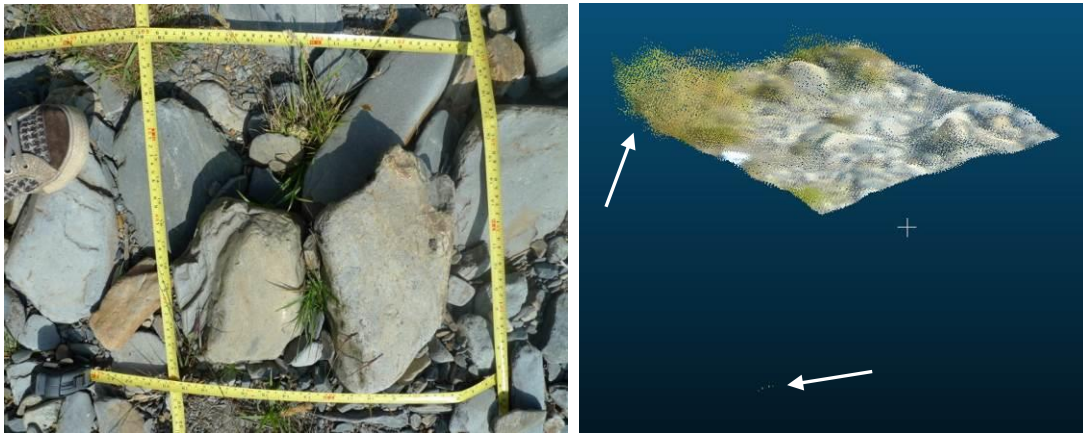


Figure 4.38. Vegetation within and near to ground truth sample plot C3 (left) introducing noise and erroneous points to the UAS-SfM point cloud covering this plot (point cloud shown includes the 50cm buffer zone) (right).

3. **The presence of water.** As also discussed in Chapters 3 and 5, the presence of water reduces the contrast within the UAS imagery. This reduces the success of SfM point matching in submerged areas, an issue which results in greater noise within the point cloud. Whilst such an effect is likely to be most problematic at greater water depths, those ground truth sample plots located close to the water's edge may suffer from increased noise as a result. Specific exclusion of such plots was not conducted here, but care should be taken to address this issue in future.

Accuracy, errors and limitations

Whilst the average residual error of UAS-SfM point cloud roughness grain size predictions is low (-0.01cm), the normalised residual errors show that errors can be as large as c. -50% or c. +90% of the grain size in some instances. Higher accuracies are required if this technique is to be used for reliable grain size predictions. A number of potential error sources and limitations of this method can be identified which may explain the errors observed here and or provide guidance for where the technique may or may not be applicable. These include the following;

1. **The success of the approach is reliant on variation in roughness directly reflecting variation in substrate size. This is not always the case.**

For instance;

- a. Where the quality of the imagery is compromised by blur or lack of image texture, the point cloud becomes more noisy, as previously discussed. The smoothing and filtering procedure is able to reduce the effect of this noise on the roughness measures, but it is likely that the quality of the input imagery is still having some effect on the accuracy of results.

- b. There are places where interstitial spaces between large clasts are occupied by much smaller clasts (all of which are encompassed by the 20cm kernel size). This high variation in local topography means that high roughness values are returned for the smaller clasts, leading to an overestimation of grain size in these localities. Some examples of this problem as shown by circles A-C in Figure 4.39. This effect may be contributing to the trend towards overestimation of smaller grain size plots observed in Figure 4.20. Interestingly, whilst this effect causes problems for accurate grain size estimation it is possible that useful information might also be drawn from these areas. For example, these pockets of smaller substrate size surrounded by larger clasts may provide a unique habitat or refuge for certain species (when submerged). Future work might explore the use of point cloud roughness combined with DEM elevations for mapping these areas and exploring their ecological significance.

- c. A close visual interrogation of the maps in Figure 4.19 reveals that where the upper surfaces of larger grains are relatively flat or subject to packing, burial or imbrication they may, in-part, be predicted as smaller grain sizes. This is an obvious consequence of the reduced variation in elevation over these surfaces (i.e. lack of roughness) but leads to an under-prediction of substrate size in areas where such conditions exist. This issue is illustrated by point A in Figure 4.40, and may also apply to some extent to smaller grains. Similar issues have been widely reported by existing remote sensing studies (Church et al., 1987, Sime and Ferguson 2003, Heritage and Milan 2009, Picco et al., 2013).

- d. High levels of topographic variation over very short distances produce high roughness values and therefore larger predicted substrate sizes. This was observed in ground truth sample plots A1 and C1, where large variations in local topography had been created by footprints in the fine sediment. As a result, erroneously high grain sizes were predicted in these areas, compromising the model calibration. Fortunately these could be easily identified and excluded from the dataset. Whilst a certain amount of topographic variation could be removed by detrending, it would be difficult to remove features such as footprints due to their complexity. Brasington et al., (2012) also acknowledge the difficulty of separating out the roughness signatures of overlapping scales of particles and bed form topographies. Sharp changes in elevation associated with river banks/cliffs will also induce higher roughness values, as observed along the channel banks in Figure 4.19a. It is suggested that the use of smaller kernel sizes helps to minimise the chance of local topography influencing roughness calculations.
- e. The presence of vegetation or submerged areas is likely to increase roughness. As mentioned earlier, increased noise within the point cloud will be observed where vegetation or submerged areas fall within the ground truth sample plot itself, or within a buffer outside it (the buffer being equal in size to the kernel radius). Whilst the filtering and smoothing procedure employed here is thought to reduce the noise resulting from vegetation and submerged areas, this has not been specifically investigated. Future work would benefit from a) greater consideration of the placing of sample plots away from such features, and/or b) specific testing of the magnitude of noise introduced into the point cloud by such features and its subsequent effect on roughness metrics and grain size estimation.

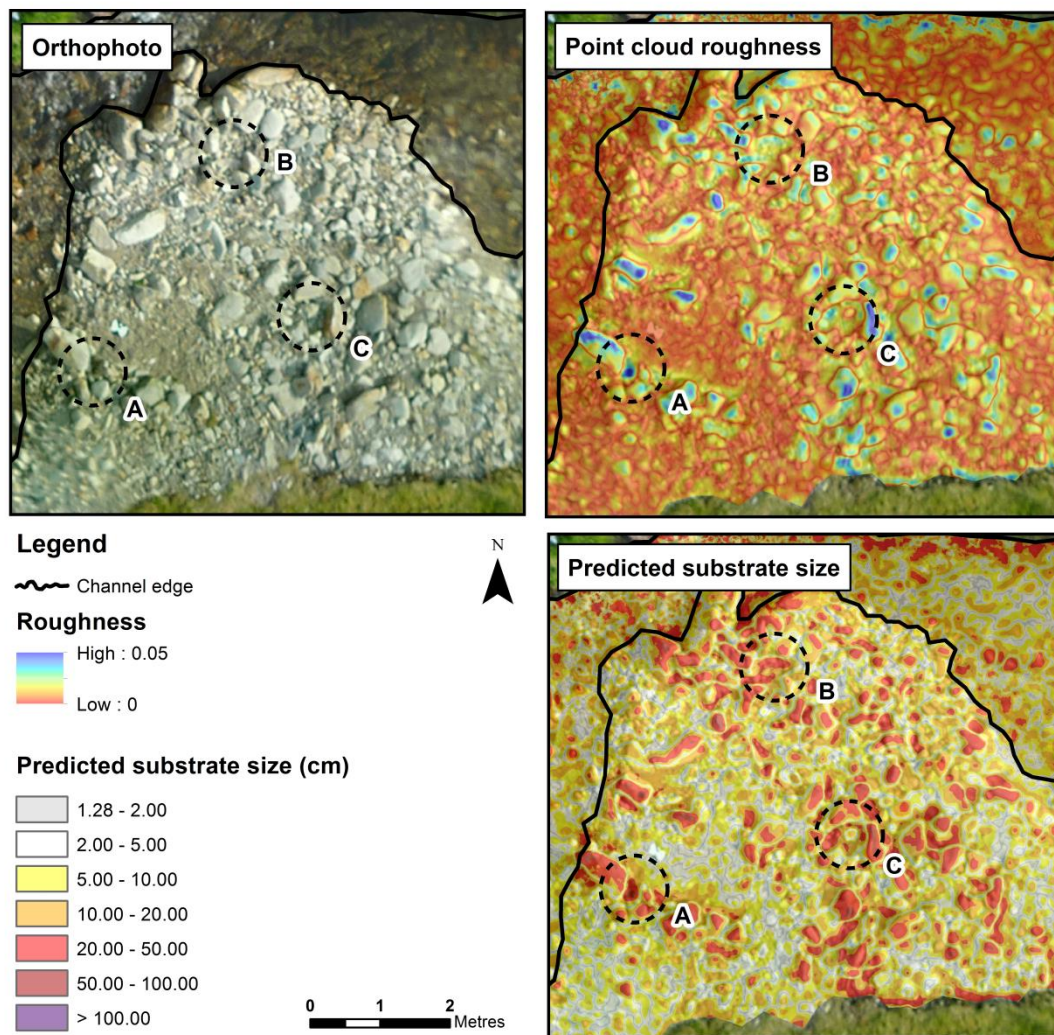


Figure 4.39. Close-up of orthophoto, UAS-SfM point cloud roughness and predicted substrate size, highlighting at points A, B and C the over-prediction of smaller clasts where they are situated in gaps between larger clasts.

2. **There is a limit on the smallest substrate size which can be accurately predicted.**

The roughness and associated substrate size data produced for Coledale Beck is available at a resolution of 5mm. This represents the approximate point spacing within the dense point cloud for this site, which is controlled by the spatial resolution of the UAS imagery (and ultimately by flying altitude). Whilst progress in the estimation of sub-pixel grain sizes has recently been made using an image texture approach (Black et al., 2014), the technique used here is not capable of sub-pixel grain size estimation. Furthermore, the use of a 2.5cm radius smoothing filter means that point elevation is averaged over distances of 5cm. As a result, it is

unlikely that grains smaller than 5cm will be accurately predicted from the UAS-SfM roughness data. This is borne out in Figures 4.20 and 4.21, where particles of this size tend to produce the largest residual and normalised residual errors.

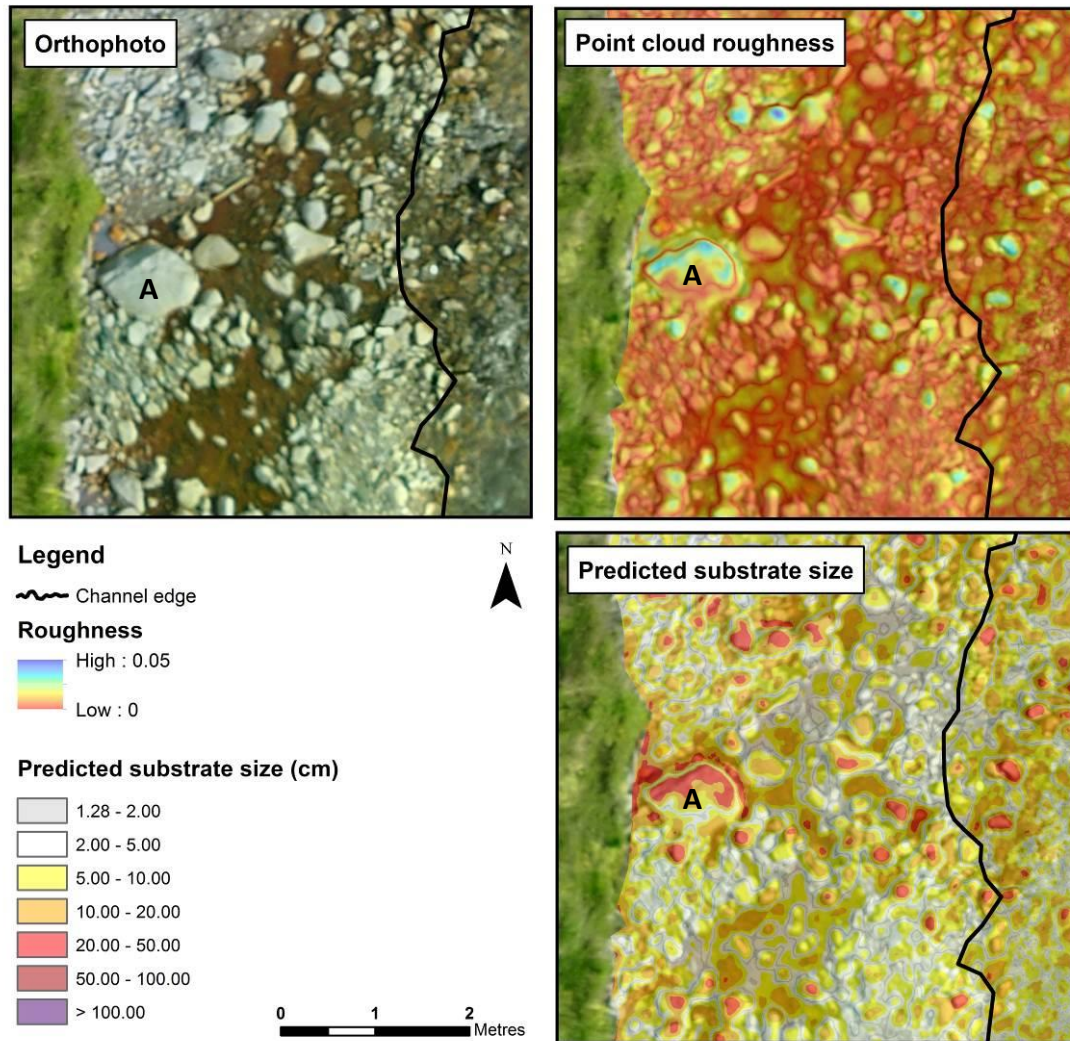


Figure 4.40. Close-up of orthophoto, UAS-SfM point cloud roughness and predicted substrate size, highlighting at point A the underprediction of large, flat grains.

- 3. Non-uniform grain sizes within ground truth sample plots may affect the model.** In theory this should not be a significant issue, because the range of grain sizes should be reflected in the range of roughness values produced for any given plot. This should hold true regardless of whether that range is large or small (i.e. whether grain size is uniform or not). However, where grain size within plots is not very uniform (i.e. there is a large range in sediment size) the success of the method is

reliant on the ground truthing sampling approach adequately representing the range of grain sizes present. Whilst efforts were made to achieve this in the field, it is likely that a bias towards the measurement of larger grain occurs. This issue has been reported elsewhere within the wider literature on grain size measurement (Wolman 1954, Carbonneau et al., 2004, Entwistle and Fuller 2009) and may partly explain the underprediction of substrate size observed for some plots during the jack-knife analysis (Figure 4.20).

4. **Errors in the survey positioning data may affect the model.** Small errors may exist in the total station and dGPS data used to locate the ground truth sample plots and to survey the position of GCPs used to georeference the UAS orthophoto. These may be caused by tilting of the survey pole and prism used to collect total station points (and hence horizontal displacement of positions), or errors inherent to the dGPS data which can result from factors such as poor satellite geometry. The presence of such errors may result in the UAS-SfM point cloud and the location of ground truth sample plots being slightly offset from each other, thereby compromising the quality of the relationship between grain size and roughness. This is likely to be a particular problem in areas where grain size changes rapidly over short distances. Visual checks were undertaken to assess whether the topography of the point cloud matched the expected pattern of substrate size from photos taken in the field. No obvious problems were found, but this does not mean that small spatial misalignments do not exist here, which may be influencing the results in part.

5. **Error inherent to the georeferencing of the UAS imagery may affect the model.** An assessment of the residual error associated with georeferencing undertaken during the SfM-photogrammetry processing is presented in Chapter 2 (section 2.5.8). Mean XY errors are low for the Coledale Beck dataset (0.006m, -0.007m respectively). However, combined with potential positioning errors within the total station and dGPS survey data this may still have a small impact on the quality of results, especially in areas where the grain size changes rapidly over short distances. Furthermore, these residual errors were calculated using GCP positions also used in the georeferencing process and therefore do not represent the classic error assessment typically performed in traditional photogrammetry. Future work should

ensure a surplus of GCPs are available, so that some may be reserved for error assessment only.

6. **The success of substrate size estimation in submerged areas has not been quantified.** This study has not formally addressed the effects of water on substrate size estimation. As shown in Figure 4.19, point cloud roughness data and grain size estimates are available for the entirety of the submerged channel at Coledale Beck. Visual assessment of the maps within Figure 4.19 suggests a good agreement between grain sizes observed within the orthophoto and predicted grain sizes. However, a quantitative assessment of error cannot be undertaken as ground truth data were not acquired within submerged areas. Future work should focus on developing methods of assessing error of substrate size predictions in submerged areas.

7. **The approach is still reliant on ground truth substrate size data to develop a predictive relationship.** As a result, the method presented here still requires an element of fieldwork. The collection of clast size data and the survey of sample plot positions for this research took in the region of a day's worth of time. It is possible that aerial photosieving (as suggested by Dugdale et al., 2010) could be used on the high resolution UAS ortho-imagery as a substitute for grain size data collected in the field, so as to eliminate that element of field work. However, there are also errors associated with aerial photosieving.

Ultimately, the results presented here indicate that the roughness of the UAS-SfM point cloud *can* be used to quantify fluvial substrate size in exposed areas, with low average residual errors. This is an important finding which highlights, for the first time, the value of analysing a UAS-SfM derived point cloud for quantifying fluvial substrate size at the mesoscale. The high resolution, quantitative, objective, spatially continuous, spatially explicit results are easily collected and thus meet many of the requirements specified by the riverscape concept (Fausch et al., 2002). However, it has been shown that individual residual errors can be considerable. As a result, careful consideration of the listed limitations and potential sources of error is of importance, and should be investigated thoroughly if this technique is to be employed more widely. With further work, it is hoped that the substrate

size data produced using this approach will be of value to a range of river habitat research and management applications. Direct measurements of surface roughness may also have potential for input to applications beyond habitat assessment, including studies of flow resistance and hydraulic modelling. The results presented here suggest that such applications might be conducted using UAS-SfM point cloud roughness data in the future.

4.6.2 Comparison with other techniques

Research Question 2

How do the results of research question 1 compare with those obtained using existing remote sensing techniques: a) image texture analysis on the UAS imagery and b) TLS point cloud roughness?

This section provides a comparison of the results of UAS-SfM point cloud roughness approach with the UAS image texture and TLS roughness approaches detailed within this chapter, as well as those from the wider published literature. Table 4.15 provides an overarching comparison of the coverage, resolution and typical accuracies of techniques.

Accuracy, precision and strength of relationship

Average residual errors are <c. 1cm for all methods tested within this research, with the lowest average normalised residual error being reported for the UAS-SfM image texture approach (+9.25%). The equivalent value for the UAS-SfM point cloud roughness method is +11.45%. The precision of grain size estimations is highest for the UAS-SfM point cloud roughness approach than the other two methods, as indicated by the lower standard deviation of average normalised residual errors (+/- c. 37.7%). As shown in Table 4.14, the validation of the models indicates that the strongest relationship for observed versus predicted grain size is achieved for the UAS-SfM point cloud roughness approach. The slope (0.7367) is notably higher than the equivalent results for the UAS-SfM image texture approach (0.5043) and the TLS point cloud roughness approach (0.5261), but is still some way off the ideal 1:1 relationship.

Similar studies within the wider literature frequently provide the slope and co-efficient of determination of model calibrations, yet accompanying model validations providing residual errors and observed versus predicted relationships are not always given. Where possible, a

direct comparison of different approaches is presented in Table 4.15. Despite the occurrence of some high residual errors, the precision (16.4mm) and mean accuracy (c. 1mm) for the UAS-SfM roughness approach grain size estimates are roughly in line with or better than other techniques. The spatial resolution of grain size outputs is also higher than those approaches with similar mean accuracy levels. However, the slope of the observed versus predicted relationship (0.7367) is not as good as those reported by Carbonneau et al., 2004, 2005b (1.03-1.23) for the use of an image texture approach on non-UAS imagery. The latter value also notably out-performs the equivalent slope value for the application of the texture approach to UAS imagery (0.5043). However, this study provides the first application of this approach to UAS imagery where model validation is also conducted. Following the findings of de Haas et al., (2014) it is likely that issues of platform instability and blur are hindering higher accuracy results (de Haas et al., 2014). Future work should aim to quantify the effects of UAS image blur on grain size estimates.

Table 4.15. Comparison of different remote sensing methods for grain size estimation. Typical accuracy is defined as the mean of residual errors and typical precision is defined as the standard deviation of residual errors.

Approach	Typical Spatial Coverage	Typical Spatial Resolution	Typical Accuracy	Typical Precision	Slope (Obs v. Pred)	References
Photo-sieving	c. 1m ²	c. 1mm	<0.25 phi	?	?	<i>Graham et al., 2005b, Sime and Ferguson 2003</i>
Spatial auto-correlation	c. 1m ²	<1mm	<3mm	?	?	<i>Rubin 2004, Buscombe 2008, Buscombe et al., 2010</i>
Image texture	12-80km	c. 1m	3-8mm	13.9-29mm	1.03-1.23	<i>Carbonneau et al., 2004, 2005b, Verdu et al., 2005</i>
TLS point cloud roughness	c. 1km	50mm	c. 1mm	23.4mm	0.5261	<i>Heritage and Milan 2009, Brasington et al., 201, this chapter</i>
UAS image texture	0.1-1km	50 – 100mm	<1mm	19.9mm	0.5043	<i>Tamminga et al., 2014, de Haas et al., 2014, this chapter</i>
UAS point cloud roughness	c. 100m	5mm	c. 1mm	16.4mm	0.7367	<i>This chapter</i>

It might be expected from the strong calibration relationships reported previously (e.g. Heritage and Milan 2009, Brasington et al., 2012, Rychov et al., 2012), that the TLS approach would also produce stronger results in terms of the slope of the observed versus predicted grain size relationship. However, as this study is the first to present a full error assessment of a TLS approach to grain size quantification no direct comparisons with other literature can be made. It is noted that the strength of the calibration relationship presented here (Figure 4.28) is poorer than observed elsewhere.

It is also noted that the results obtained from this study for the UAS-SfM image texture and TLS point cloud roughness approaches may be biased somewhat by the nature of the investigation itself. The settings used for processing the image texture and TLS datasets (kernel size, exclusion of some plots) were determined by the optimum results for the UAS-SfM point cloud roughness. Furthermore, very little experimentation was undertaken to identify the optimum settings for these different approaches. For example, due to time constraints the UAS-SfM image texture approach did not explore different measures of image texture and different kernel sizes or kernel steps. Although the use of a kernel size the same as that used in the UAS-SfM roughness approach does allow a more direct comparison in terms of scale of the results. The TLS point cloud roughness approach used here did not explore the use of detrending, although the results of detrending the UAS-SfM point cloud would suggest it is not required at this site. Again, to enable a direct scale comparison with the UAS-SfM point cloud roughness results, different roughness kernel sizes were not tested on the TLS data. The effects of smoothing and filtering functions were not explored either. This was because the TLS point clouds were significantly less noisy than the equivalent UAS-SfM derived point clouds. However, in the future it would be of benefit to investigate these quantitatively for a more robust comparison of techniques.

Spatial resolution, spatial coverage and scale

The spatial resolution of grain size predictions is higher for the UAS-SfM approach (5mm) than for the UAS-SfM image texture outputs (50mm) and the TLS results (50mm). The resolution of the image texture output is lower because it is limited by the resolution of the input imagery and the kernel step size. The resolution of the TLS raster output is lower because it is conditioned by the need to maintain a balance between data resolution and minimising holes resulting from shadowing (and a lack of returns at all in some deeper,

submerged areas). Compared to other published work, the spatial resolution of grain size outputs provided by the UAS-SfM point cloud roughness approach (5mm) is lower than that typically achieved by photo-sieving and spatial autocorrelation methods (1mm) but higher than that reported for TLS (c. 50mm) and an order of magnitude higher than image texture based approaches (c. 1m) (Table 4.15).

The areal coverage provided by all approaches tested here is for a reach c. 120m long and 5-10m wide (i.e. the channel width including submerged areas). It took approximately 0.5 days to acquire data of this stretch using the UAS and 1 day to acquire data with the TLS. With longer in the field, greater spatial coverage would be possible using both approaches. Such coverage is clearly much greater than the c. 1m² patches typically acquired using ground based photo-sieving and spatial autocorrelation approaches (Table 4.15). However, it is significantly less than the coverage achieved over similar time scales using the image texture approach reported in some studies (e.g. Carbonneau et al., 2004, Table 4.15). Inevitably, there is a trade-off between spatial coverage and spatial resolution. The high spatial resolution and limited spatial coverage of photo-sieving and autocorrelation approaches is well suited to patch scale studies of grain size. Whereas the coarser resolution and much greater spatial coverage of the image texture approach makes it suitable for broader, catchment scale studies of grain size. The UAS-SfM approach has the potential to fill a gap between these two scales, where the high spatial resolution (<1cm) over channel lengths of c. 100m (and greater) makes it well suited to mesoscale studies of substrate size. Whilst the same is theoretically possible using TLS data, the time and effort involved in data acquisition is significantly greater than that required with the UAS with no significant benefits in terms of accuracy or precision yet demonstrated firmly.

The high spatial resolution of the UAS-SfM point cloud roughness grain size predictions actually calls into question the scale at which the model calibration and validation has been undertaken here. Individual grains as small as 10cm can be easily identified visually from the orthophoto and in the subsequent grain size predictions. Therefore, it would perhaps make more sense to develop and validate models at a finer spatial resolution than is currently available using average measures from the 40cm x 40cm ground truth sample plots. Future work might make use of aerial photo-sieving or the size of individual clasts measured in the field and pin-pointed using high accuracy dGPS devices.

Data acquisition and processing

Data acquisition and processing times are not always reported within the wider literature. Of the methods used here, the UAS-SfM based approaches were quickest (1.5 days fieldwork including ground truthing plus 1 days processing each). The TLS data took longer to acquire (2 days fieldwork, including ground truth data collection) and process (c. 2 days) given the larger data volumes.

4.6.3 Summary and future work

Variable results have been obtained from the comparison of the UAS-SfM point cloud roughness approach with the other approaches tested here and within the wider literature. It is clear that further, robust assessment is required for the direct comparison of different methods under a range of different conditions. Future work into the following would be of particular value for extending the findings of this research;

- Testing a wider variety of image texture metrics on the UAS-SfM ortho-imagery.
- Testing the effect of detrending and smoothing and filtering procedures on the results of the TLS point cloud roughness approach.
- Quantifying the effects of UAS image blur on accuracy of grain size estimations using both image texture and point cloud roughness methods.
- Validation of the model results in submerged areas.
- Testing the UAS-SfM point cloud roughness procedure developed here for predicting substrate size within other settings (i.e. testing its repeatability in different environments).
- Collection of ground truth calibration/validation data at a higher resolution.
- Collection of independent ground truth validation data which are not used as part of the initial model calibration.
- Testing the use of ground truth calibration data acquired by aerial photosieving from the high resolution UAS imagery.
- Exploring the use of wavelet analysis or Fourier transforms for spatially decomposing the grain size signal within UAS imagery (as per the suggestion of Brasington et al., 2012 and recent work of Buscombe 2013).

Ultimately, the choice of an appropriate method for quantifying substrate size will be determined by the specific requirements of a given application, and a compromise will be required in terms of scale, spatial coverage, accuracy, precision, data acquisition and processing times, and cost. The aim of this chapter was to investigate the potential for quantifying fluvial substrate size at hyperspatial resolutions over mesoscale lengths of channel using roughness measures derived from the UAS-SfM point cloud, with a view to filling a gap in current capabilities. The results indicate that quantitative substrate size data can be obtained over channel reaches of c. 100m at a spatial resolution of <1cm and with mean accuracies of -0.011cm. Such results are easily achieved with c. 1.5 days fieldwork (the bulk of which is required for ground truth data collection) and c. 1 days subsequent data processing. Per-flight data collection costs are low (when not including initial outlay for the UAS), platform mobilisation is rapid and data acquisition is flexible and straight-forward. As such, with further testing and efforts to improve the precision of results, the UAS-SfM point cloud roughness approach has the potential to fulfil almost all of the requirements for habitat assessment advocated by the 'riverscape' concept and provide an alternative approach for quantifying substrate size at the mesoscale. At the present time, the main drawbacks of this approach are the low precision of grain size estimates (1.64cm) relative to spatial resolution, the cost of acquiring a UAS platform in the first place and limited spatial coverage (as determined by flying altitude and battery life restrictions). With the currently rapid evolution of the UAS market, it is hoped that these factors will not remain as major obstacles for long.

4.7 Conclusions

This chapter has, for the first time, evaluated the potential of using the roughness metrics of a point cloud derived from a UAS-SfM approach for quantifying fluvial substrate size over mesoscale lengths of channel. A c. 120m reach of Coledale Beck in the English Lake District was the site for this research, where UAS imagery was acquired at high resolution and processed using SfM-photogrammetry. A range of different roughness metrics were computed from the resulting point cloud, and the advantages of detrending and smoothing and filtering the point cloud were assessed. Roughness measures calculated using a kernel with a radius of 20cm on a non-detrended, smoothed and filtered point cloud were found to produce the strongest correlation when linearly regressed against ground truth measures of substrate size for a set of 25 sample plots. This calibration relationship was then used to

predict substrate sizes for the wider site. Model validation suggested high accuracy results, with an average residual error of -0.011cm. However, the standard deviation for grain size predictions was poor (1.64cm) and normalised residual errors were found to be as great as -50% and +90% of true grain size. A number of limitations of the approach are recognised and suggested to explain the poor precision of results. These include the influence of factors other than grain size on roughness, a limit on the smallest detectable grain size, potential biases within the ground truth data, errors associated with the survey positioning and georeferencing process, the need for time-consuming field collection of substrate size data for model calibration and validation, and a lack of validation in submerged areas.

A comparison with two other existing remote sensing techniques, UAS-SfM image texture and TLS point cloud roughness, was also undertaken. Average residual errors were found to be fairly low for all methods (<c. 0.01cm), with the highest accuracy reported for the UAS-SfM image texture approach and the highest precision reported for the UAS-SfM point cloud roughness approach. The results indicate a stronger correlation between observed and predicted substrate size for the UAS-SfM point cloud roughness model (slope of 0.7367), than for either of the other two approaches. Spatial resolution of the UAS-SfM point cloud roughness method was higher (0.5cm) than for either of the other approaches, and with reduced data collection times compared to the TLS based approach.

The specific requirements of a given application will determine the choice of method for quantifying fluvial substrate size, and a compromise will usually be necessary in terms of scale, spatial coverage, accuracy, precision, data acquisition and processing times, and cost. This research has demonstrated for the first time that a UAS-SfM point cloud roughness approach can be used for quantifying fluvial substrate size in exposed areas. The approach is rapid and flexible, and produces high spatial resolution results which are both spatially continuous and spatially explicit. As such, the UAS-SfM point cloud roughness approach provides significant advantages over traditional methods of quantifying fluvial substrate size. It also fulfils many of the requirements for habitat assessment advocated by the 'riverscape' concept and if the magnitude of residual errors can be reduced in future, it has potential to provide a highly suitable approach for quantifying substrate size at the mesoscale. With the on-going expansion and maturing of the UAS market alongside parallel developments in computing power and processing software, it is likely that UAS-SfM based approaches of the

type described here will become a viable option for river habitat assessment and monitoring in the future.

In the meantime, further work should be aimed at testing the wider applicability of these results and might include; exploring the success of the technique in other settings, including different river systems and within submerged areas; more in-depth comparison with existing remote sensing techniques; quantifying and reducing the effects of UAS image blur; the use of ground truth data collected at higher spatial resolutions and; the success of model calibration using data acquired by aerial photosieving from the high resolution UAS imagery.

4.8 References

- Aberle, J. and Nikora, V. (2006) Statistical properties of armoured gravel bed surfaces. *Water Resources Research* 42, W11414, doi: 10.1029/2005WR004674.
- Aberle, J. and Smart, G.M. (2003) The influence of roughness structure on flow resistance on steep slopes. *Journal of Hydraulic Research* 41 (3): 259-269.
- Adams, J. (1979) Gravel size analysis from photographs. *Journal of the Hydraulics Division, Proceedings of the American Society of Civil Engineers*, 105, HY10: 1247-1255.
- Black, M., Carbonneau, P., Church, M. and Warburton, J. (2014) Mapping sub-pixel fluvial grain sizes with hyperspatial imagery. *Sedimentology* 61 (3): 691-711.
- Brasington, J., Vericat, D. and Rychov, I. (2012) Modeling river bed morphology, roughness, and surface sedimentology using high resolution terrestrial laser scanning. *Water Resources Research* 48 W11519, doi: 10.1029/2012WR012223.
- Bunte, K. and Abt, S.R. (2001) Sampling surface and subsurface particle-size distributions in wadeable gravel- and cobble-bed streams for analyses in sediment transport, hydraulics and streambed monitoring. General Technical Report RMRS-GTR-74, Fort Collins, CO, *US Dept. of Agriculture, Forest Service, Rocky Mountain Research Station*.
- Buscombe, D. (2008) Estimation of grain size distributions and associated parameters from digital images of sediment. *Sedimentary Geology* 210: 1-10.
- Buscombe, D. (2013) Transferable wavelet method for grain-size distribution from images of sediment surface and thin section, and other natural granular patterns. *Sedimentology* 60 (7): 1709-1732.
- Buscombe, D. and Masselink, G. (2009) Grain-size information from the statistical properties of digital images of sediment. *Sedimentology* 56: 421-438.
- Buscombe, D. Rubin, D.M. and Warrick, J.A. (2010) A universal approximation of grain size from images of noncohesive sediment. *Journal of Geophysical Research* 115 F02014 doi: 10.1029/2009JF001477.
- Butler, J.B., Lane, S.N. and Chandler, J.H. (1998) Assessment of DEM quality for characterizing surface roughness using close range digital photogrammetry. *Photogrammetric Record* 16 (92): 271-291.
- Butler, J.B., Lane, S.N. and Chandler, J.H. (2001) Automated extraction of grain-size data from gravel surfaces using digital image processing. *Journal of Hydraulic Research* 39 (4): 519-529.
- Carbonneau, P.E., Lane, S.N. and Bergeron, N.E. (2003) Cost effective non-metric close-range digital photogrammetry and its application to a study of coarse gravel river beds. *International Journal of Remote Sensing* 24 (14): 2837-2854.
- Carbonneau, P.E., Lane, S.N. and Bergeron, N. (2004) Catchment-scale mapping of surface grain size in gravel bed rivers using airborne digital imagery. *Water Resources Research* 40, W07202, doi:10.1029/2003WR002759.
- Carbonneau, P.E., Bergeron, N.E. and Lane, S.N. (2005a) Texture-based segmentation applied to the quantification of superficial sand in salmonids river gravels. *Earth Surface Processes and Landforms* 30: 121-127.

Carbonneau, P.E., Bergeron, N. and Lane, S.N. (2005b) Automated grain size measurements from airborne remote sensing for long profile measurements of fluvial grain sizes. *Water Resources Research* 41, W11426, doi:10.1029/2005WR003994.

Carbonneau, P.E., Fonstad, M.A., Marcus, W.A., and Dugdale, S.J. (2012) Making riverscapes real. *Geomorphology* 137 (1): 74-86.

Centre for Ecology and Hydrology (2001) Further validation of PHABSIM for the habitat requirements of salmonid fish. *Final project report to Environment Agency (W6-036) and CEH (C00962)*.

Church, M.A. McLean, D.G. and Wolcott, J.F. (1987) River bed gravels: Sampling and Analysis, In Thorne, C.R., Bathurst, J.C. and Hey, R.D. (Eds) *Sediment Transport in Gravel-bed Rivers*, John Wiley and Sons, Chichester.

De Haas, T., Ventra, D., Carbonneau, P. and Kleinhans, M.G. (2014) Debris flow dominance of alluvial fans masked by runoff reworking and weathering. *Geomorphology* 217: 165-181.

Dugdale, S., Carbonneau, P. and Campbell, D. (2010) Aerial photosieving of exposed gravel bars for the rapid calibration of airborne grain size maps. *Earth Surface Processes and Landforms* 35: 627-639.

Dyer, F.J. and Thoms, M.C. (2006) Managing river flows for hydraulic diversity: an example of an upland regulated gravel-bed river. *River Research and Applications* 22: 257-267.

Entwistle, N.S. and Fuller, I.C. (2009) Terrestrial laser scanning to derive the surface grain size facies character of gravel bars. In Heritage, G.L. and Large, A.R.G. (Eds) *Laser Scanning for the Environmental Sciences*, Wiley-Blackwell, London.

Environment Agency (2003) River Habitat Survey in Britain and Ireland: Field Survey Guidance Manual. Available online: https://www.gov.uk/government/uploads/system/uploads/attachment_data/file/311579/LIT_1758.pdf (accessed 11.02.2015).

European Commission (2000) Directive 2000/60/EC of the European Parliament and of the Council of 23rd October 2000: Establishing a framework for Community action in the field of water policy. *Official Journal of the European Communities, Brussels, 22.12.2000, L327: 1-72*.

Evans, L.J. and Norris, R.H. (1997) Prediction of benthic macroinvertebrate composition using microhabitat characteristics derived from stereo photography. *Freshwater Biology* 37: 621-633.

Fausch, K.D., Torgersen, C.E., Baxter, C.V. and Hiram, L.W. (2002) Landscapes to riverscapes: bridging the gap between research and conservation of stream fishes. *BioScience* 52 (6): 483-498.

Frissell, C.A., Liss, W.J., Warren, C.E. and Hurley, M.D. (1986) A hierarchical framework for stream habitat classification: viewing streams in a watershed context. *Environmental Management* 10 (2): 199-214.

Frothingham, K.M., Rhoads, B.L. and Herricks, E.E. (2002) A multiscale conceptual framework for integrated ecogeomorphological research to support stream naturalisation in the agricultural Midwest. *Environmental Management* 29 (1): 16-33.

Garcia, A., Jorde, K., Habit, E., Caamano, D. and Parra, O. (2011) Downstream environmental effects of dam operations: changes in habitat quality for native fish species. *River Research and Applications* 27: 312-327.

Gomez, B. (1993) Roughness of stable, armoured gravel beds. *Water Resources Research* 29 (11): 3631-3642.

- Graham, D.J., Reid, I. and Rice, S.P. (2005a) Automated sizing of coarse-grained sediments: image-processing procedures. *Mathematical Geology* 37(1): 1-28.
- Graham, D.J., Rice, S.P. and Reid, I. (2005b) A transferable method for the automated grain sizing of river gravels. *Water Resources Research* 41, W07020, doi:10.1029/2004WR003868.
- Habit, E., Belk, M.C. and Parra, O. (2007) Response of the riverine fish community to the construction and operation of a diversion hydropower plant in central Chile. *Aquatic Conservation: Marine and Freshwater Ecosystems* 17: 37-49.
- Haralick, R.M., Shanmugam, K. and Dinstein, I. (1973) Textural features for image classification. *IEEE Transactions on Systems, Man and Cybernetics* SMC-3 (6): 610-621.
- Haralick, R.M. (1979) Statistical and structural approaches to texture. *Proceedings of the IEEE* 67 (5): 786-804.
- Heritage, G. and Hetherington, D. (2007) Towards a protocol for laser scanning in fluvial geomorphology. *Earth Surface Processes and Landforms* 32: 66-74.
- Heritage, G.L. and Milan, D.J. (2009) Terrestrial laser scanning of grain roughness in a gravel-bed river. *Geomorphology* 113: 4-11.
- Hey, R.D. and Thorne, C.R. (1983) Accuracy of surface samples from gravel bed materials. *Journal of Hydraulic Engineering* 109 (6): 842-851.
- Hodge, R., Brasington, J. and Richards, K. (2009) In situ characterization of grain-scale fluvial morphology using Terrestrial Laser Scanning. *Earth Surface Processes and Landforms* 34: 954-968.
- Höfle, B., Bechtold, S., Bumiller, D., Ebner, M., Germar, A., Jacke, U.D., Kempf, C., Kraus, B., Lange, J., Link, J., Peters, R., Schauss, A., Schulz, C. and Zimmermann, E. (2013) Acquisition and analysis of laser scanning data in physical geography: HydroChange3 Final Report, Heidelberg University, Institute of Geography.
- Hohenthal, J., Alho, P., Hyyppä, J. and Hyyppä, H. (2011) Laser scanning applications in fluvial studies. *Progress in Physical Geography* 35 (6): 782-809.
- Hugenholtz, C.H., Brown, O.W. and Barchyn, T.E. (2013) Estimating aerodynamic roughness (z_0) from terrestrial laser scanning point cloud data over un-vegetated surfaces. *Aeolian Research* 10: 161-169.
- Ibbeken, H. and Schleyer, R. (1986) Photo-sieving: a method for grain size analysis of coarse-grained, unconsolidated bedding surfaces. *Earth Surface Processes and Landforms* 11: 59-77.
- Keeley, E.R. and Slaney, P.A. (1996) Quantitative measures of rearing and spawning habitat characteristics for stream-dwelling salmonids: guidelines for habitat restoration. Province of British Columbia, Ministry of Environment, Lands and Parks, and Ministry of Forests. Watershed Restoration Project Report 4.
- Lane, S.N. and Carbonneau, P.E. (2007) High resolution remote sensing for understanding instream habitat. In Wood, P.J., Hannah, D.M. and Sadler, J.P. (Eds) *Hydroecology and Ecohydrology*, John Wiley and Sons, Chichester.
- Leopold, L.B. (1970) An improved method for size distribution of stream bed gravel. *Water Resources Research* 6 (5): 1357-1366.

Maddock, I. (1999) The importance of physical habitat assessment for evaluating river health. *Freshwater Biology* 41: 373-391.

Maddock, I., Thoms, M., Jonson, K., Dyer, F. and Lintermans, M. (2004) Identifying the influence of channel morphology on physical habitat availability for native fish: application to the two-spined blackfish (*Gadopsis bispinosus*) in the Cotter River, Australia. *Marine and Freshwater Research* 55: 173-184.

Milan, D.J. (1996) The application of freeze-coring for siltation assessment in a recently regulated stream. *Hydrologie dans les pays celtiques*, Rennes, France 8-11 July 1996. Ed. INRA Paris (Les Colloques 79).

Milan, D.J. and Heritage, G.L. (2012) LiDAR and ADCP use in gravel-bed rivers: Advances since GBR6. In Church, M., Biron, P. and Roy, A. (Eds) *Gravel-bed Rivers: Processes, Tools, Environments*, Wiley-Blackwell, Chichester.

Newson, M.D. and Newson, C.L. (2000) Geomorphology, ecology and river channel habitat: mesoscale approaches to basin-scale challenges. *Progress in Physical Geography* 24 (2): 195-217.

Orr, H.G., Large, A.R.G., Newson, M.D. and Walsh, C.L. (2008) A predictive typology for characterising hydromorphology. *Geomorphology* 100: 32-40.

Picco, L., Mao, L., Cavalli, M., Buzzi, E., Rainato, R. and Lenzi, M.A. (2013) Evaluating short-term morphological changes in a gravel-bed braided river using terrestrial laser scanner. *Geomorphology* 201: 323-334.

Quenouille, M.H. (1949) Approximate tests of correlation in time-series. *Journal of the Royal Statistical Society Series B* 11: 68-84.

Rice, S. and Church, M. (1996) Sampling surficial fluvial gravels: the precision of size distribution percentiles estimates. *Journal of Sedimentary Research* 66 (3): 654-665.

Rubin, D.M. (2004) A simple autocorrelation algorithm for determining grain size from digital images of sediment. *Journal of Sedimentary Research* 74 (1): 160-165.

Rychov, I., Brasington, J. and Vericat, D. (2012) Computational and methodological aspects of terrestrial surface analysis based on point clouds. *Computers and Geosciences* 42: 64-70.

Sieberth, T., Wackrow, R. and Chandler, J.H. (2013) Automation isolation of blurred images from UAV image sequences. *International Archives of Photogrammetry, Remote Sensing and Spatial Information Sciences*, XL-1/W2: 361-366.

Sime, L. C. and Ferguson, R. I. (2003) Information on grain sizes in gravel-bed rivers by automated image analysis. *Journal of Sedimentary Research* 73 (4): 630-636.

Smith, M., Vericat, D. and Gibbins, S. (2012) Through-water terrestrial laser scanning of gravel beds at the patch scale. *Earth Surface Processes and Landforms* 37: 411-421.

Tamminga, A., Hugenholtz, C., Eaton, B. and LaPointe, M. (2014) Hyperspatial remote sensing of channel reach morphology and hydraulic fish habitat using an unmanned aerial vehicle (UAV): A first assessment in the context of river research and management. *River Research and Applications* doi: 10.1002/rra.2743.

Tukey, J.W. (1958) Bias and confidence in not-quite large samples. *Annals of Mathematical Statistics* 29: 614.

Verdú, J.M., Batalla, R.J. and Martínez-Casasnovas, J.A. (2005) High-resolution grain-size characterisation of gravel bars using imagery analysis and geo-statistics. *Geomorphology* 72: 73-93.

Wang, C-K., Wu, F-C., Huang, G-H., and Lee, C-Y. (2011) Mesoscale terrestrial laser scanning of fluvial gravel surfaces. *IEEE Geoscience and Remote Sensing Letters* 8 (6): 1075-1079.

Wang, Y., Liang, X., Flener, C., Kukko, A., Kaartinen, H., Kurkela, M., Vaaji, M. Hyyppä, H and Alho, P. (2013) 3D modelling of coarse fluvial sediments based on mobile laser scanning data. *Remote Sensing* 5: 4571-4592.

Wentworth, C.K. (1922) A scale of grade and class terms for clastic sediments. *Journal of Geology* 30: 377-392.

Wiens, J.A. (2002) Riverine landscapes: taking landscape ecology into the water. *Freshwater Biology* 47: 501-515.

Wise, D.H. and Molles, M.C. (1979) Colonisation of artificial substrate by stream insects: influence of substrate size and diversity. *Hydrobiologia* 65 (1): 69-74.

Wolman, M.G. (1954) A method of sampling coarse river-bed material. *Transactions of the American Geophysical Union* 35 (6): 951-956.

Chapter 5

Mapping surface flow types using hyperspatial resolution UAS imagery and SfM-photogrammetry

Chapter Overview

Surface flow types (SFTs) have been advocated as ecologically relevant hydraulic units, which can be visually mapped from the bankside for rapidly assessing physical habitat availability within small rivers. Mapping SFTs from the river banks is simple, non-invasive and cost-efficient. However, it is also qualitative, highly subjective and plagued by difficulties in accurately recording the spatial extent of SFT units from such a low angle, oblique view. In recent years, remote sensing based approaches have been suggested as an alternate means of SFT mapping, for example using multispectral videography, hyperspectral imagery or terrestrial laser scanning. Yet these studies are few, and even fewer provide a quantitative assessment of SFT mapping error.

In this chapter, the use of hyperspatial resolution imagery collected from a UAS platform combined with an emerging structure from motion (SfM) photogrammetry processing technique is tested for mapping SFTs at the mesoscale, as a proxy for hydraulic habitat heterogeneity. The approach is tested on two different river systems and validated quantitatively against traditional field mapping and an independent ground truth survey. Additionally, quantitative outputs from the SfM process (water depth and point cloud roughness) are explored for differentiating between mapped SFTs using 'Analysis of Similarity' (ANOSIM) tests.

The results indicate that the overall accuracy of SFT mapping can be as good as 75%, but is variable between sites and surveys and is affected by scene illumination, the indistinct nature of SFT boundaries, the vertical camera viewing angle, variable flow level and lack of temporal data. Yet the approach offers a rapid, relatively inexpensive, spatially continuous, spatially

explicit, permanent record of SFTs at an unprecedented spatial resolution. Inclusion of quantitative SfM outputs are not found to improve the separability of SFTs, which may relate to small inaccuracies remaining in water depth measures despite refraction correction and the influence of factors other than water surface patterns (i.e. SFTs) on point cloud roughness, including; image quality, water depth, water clarity and substrate size. It is thought that much finer hydraulic heterogeneity is evident within the point cloud roughness data than is suggested by broad scale SFT mapping, but this cannot be proven at present. The data presented also raises the question of the basic suitability of SFT mapping for inferring hydraulic diversity, which should be addressed further in future.

5.1. Background and Context

5.1.1 Defining surface flow types

Surface flow types (SFTs) are topographic patterns which exist on the water's surface within fluvial systems which are often used as a proxy for in-stream hydraulic habitat units or 'biotopes'. Some have suggested that SFTs exist on a continuum (Figure 5.1), their nature and spatial distribution being determined by local variations in morpho-hydraulic conditions, including substrate size, water depth and flow velocity (Wadeson and Rowntree 1998, Newson and Newson 2000, Dyer and Thoms 2006, Hill et al., 2008, Reid and Thoms 2009). As a result, SFTs are variable in both time and space, and are highly sensitive to changes in discharge (Zavadil et al., 2012). Higher flow levels are generally associated with a lower diversity of SFTs within a particular location, as the smaller units are effectively 'drowned out', whereas lower flows often result in a greater diversity of SFTs (Zavadil et al., 2012, p. 310).

Efforts to characterise the hydraulic character of different SFTs have found that they are usually best differentiated using measures of flow velocity or Froude Number, although what defines a particular SFT at one location may differ significantly from what defines it at another location (Wadeson 1994, Wadeson and Rowntree 1998, Newson and Newson 2000, Reid and Thoms 2008, Hill et al., 2013). Similarly, different combinations of depth and velocity can produce similar Froude Numbers for very different SFTs (Zavadil et al., 2012) and therefore Froude number is not always a reliable distinguisher. However, in general, lower energy SFTs are typically characterised by deeper water, slower velocity and smaller substrate sizes and higher energy SFTs by shallower water with higher velocity and larger substrate sizes (Hill et al., 2013).

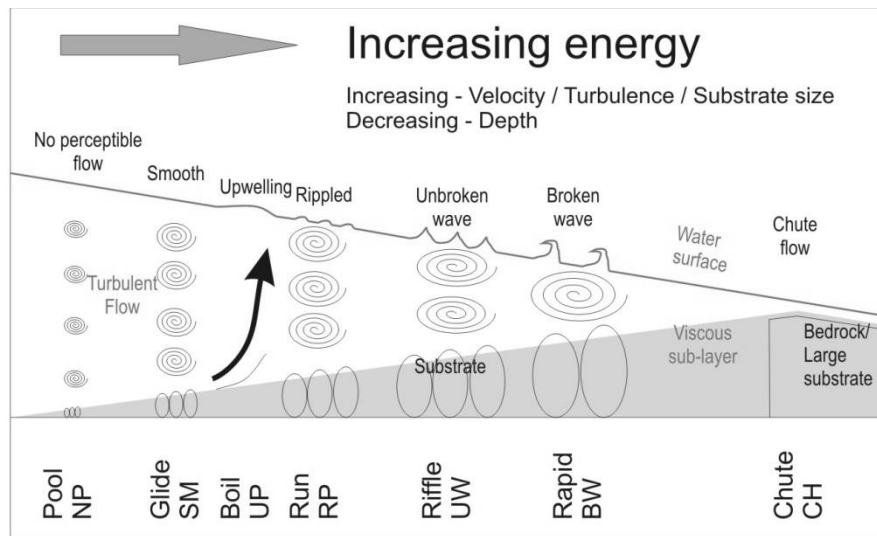


Figure 5.1. The proposed continuum of surface flow types, and their relationship with local morpho-hydraulic conditions (Hill 2011).

A number of classification schemes have been proposed to define the different SFTs or their equivalent biotope units (e.g. Bisson et al., 1982, Wadeson 1994, Montgomery and Buffington 1997, Padmore 1997, Raven et al., 1997, Newson and Newson 2000). Within the UK, perhaps the most well-known of these are the definitions used as part of the River Habitat Survey (RHS) (Environment Agency 2003). The RHS is an approach which enables the rapid characterisation of river habitat conditions over 500m reaches, including SFTs as well as other aspects of physical habitat. It identifies nine different SFTs, as detailed in Table 5.1. A very similar classification is also suggested by Newson and Newson (2000), who identify the associated physical biotopes for each SFT (Table 5.1). Biotopes are defined as “discrete hydraulic conditions within mesoscale units of the channel bed” (Newson and Newson 2000, p. 195), and are sometimes used interchangeably with SFTs.

5.1.2 The importance of surface flow types






“...relationships observed between surface flow types, near-bed hydraulic conditions and substrate character also support the notion that surface flow type mapping is an effective way of characterising the physical habitat template...”





Reid and Thoms 2008, p.1054

The inclusion of SFT mapping within the UK’s national river habitat assessment procedure suggests it holds value as a rapid method for the assessment of hydraulic habitat (Newson and

Newson 2000, Reid and Thoms 2008, Hill et al., 2013) and an efficient alternative to the labour intensive and time consuming point measurements of water depths and flow velocities (Reid and Thoms 2008). The results of the RHS also feed into habitat condition assessments required by the international legislation of the European Union’s Water Framework Directive (European Commission 2000).

Table 5.1. Descriptions of surface flow types and associated biotopes (Environment Agency 2003, and Newson and Newson 2000).

Surface Flow Type	Description	Example photograph	Associated biotope(s) or in-stream habitat unit
Free fall	Where vertically-falling water clearly separates from the ‘back-wall’ of a distinct vertical rock face.		Waterfall
Chute	Low, curving flow with substantial water contact ‘hugging’ the substrate. Where multiple chutes occur over individual boulders or bedrock outcrops, a ‘stepped’ profile is created.		Spill or Cascade
Broken standing waves	Water appears to be trying to flow upstream. A white water tumbling wave must be present for the wave to be described as broken.		Cascade, Rapid or Riffle
Unbroken standing waves	‘Babbling’ water with a disturbed ‘dragon-back’ surface, which has upstream facing wavelets that have not broken. White water may occur as crest waves, not as breaking waves.		Riffle
Chaotic flow	A chaotic mixture of several faster flow types (free fall, chute, broken and unbroken standing waves) in no organised pattern.		

Rippled	Water surface with distinct, symmetrical, small ripples that are generally only a centimetre or so high and moving downstream.		Run
Upwelling	Upwellings are found where strong upward flow movements disturb the surface, creating an appearance of bubbling or boiling water. Typically found on the outside of tight meander bends, behind in-channel structures or below waterfalls, cascade weirs and sluices.		Boil
Smooth	Laminar flow where movement does not produce a disturbed surface.		Glide
No perceptible flow	In ponded reaches, it may be difficult to perceive any surface water movement. Marginal deadwater has no perceptible flow. Also used to record flow in pools where there is obvious rotational surface flow (e.g. eddies), but no obvious net downstream movement of water at the surface.		Pool or Marginal Deadwater

Furthermore, the view of SFTs as hydraulically meaningful and consistent units, and the strong influence of these hydraulic conditions on ecology, means that there is a growing popularity within the field of ‘ecohydraulics’ research for conducting rapid habitat condition surveys using SFTs (Newson and Newson 2000, Dyer and Thoms 2006, Reid and Thoms 2008). Recent research has highlighted the biological relevance of SFTs, given species preferences for certain combinations of depth and velocity (Hill et al., 2008, Reid and Thoms 2008, Hill et al., 2013).

The work of Zavadil et al., (2012) explored the relationship between SFTs and channel geomorphology. Based on their study of SFTs at six field sites in Australia, they note that a greater diversity of SFTs within a given reach generally equates to higher variability of depths and therefore also greater physical habitat heterogeneity. Their findings suggest that the mapping of SFTs can therefore provide meaningful information on channel morphology and depth diversity, as well as hydraulics, within broad-scale river condition assessments.

Overall, the link between SFTs and hydraulics, morphology and ecology is well acknowledged and means that their visual identification can be used to provide rapid baseline assessments and repeat monitoring of physical habitat conditions. They are also often equated with 'biotopes' or in-stream habitat units, which have been championed as the basic units for the assessment of river habitats at the mesoscale (Harvey and Clifford 2009).

5.1.3 Traditional mapping of surface flow types

Chapter 1 reviews a number of key paradigms which have been suggested in recent years for the conceptualisation and understanding of river systems. This review highlights a set of requirements, deemed necessary for the characterisation of river systems in accordance with the 'riverscape' concept (Fausch et al., 2002). This includes the need for; quantitative datasets collected by objective and repeatable methods; spatially continuous datasets, available in three-dimensions; spatially explicit datasets which cover large spatial areas, with high levels of detail; and, datasets which are not difficult to collect in terms of practicality, logistics and cost.

Traditionally, the identification and mapping of SFTs is carried out visually from the bankside. This approach is relatively rapid, non-invasive, and offers an oblique perspective for the identification of the different surface patterns. Given the potential of SFT mapping for characterising flow hydraulics, visual SFT mapping is an efficient alternative to the labour intensive and time consuming point measurement of water depths and flow velocities (Reid and Thoms 2008). For example, within the RHS, SFT mapping is used as a simple, repeatable and cost effective method of assessing hydraulic habitat diversity. This procedure records the predominant flow type (normally occupying at least 50% of the wetted channel) at ten spot check locations every 50m along a 500m reach (Environment Agency 2003).

Within the wider field of research, other SFT mapping approaches have included recording relative proportions of different SFTs within 50m cells (e.g. Dyer and Thoms 2006), estimating the spatial extent of SFTs by mapping onto dGPS surveys of channel outlines shown on large scale channel maps (e.g. Hill et al., 2013) and recording SFTs at specific distances along channel cross sections (e.g. Wadeson and Rowntree 1998).

Table 5.2 highlights a number of limitations associated with typical SFT mapping approaches. Whilst cost effective and easy to conduct, visual SFT mapping from the bankside is qualitative, highly subjective, maybe affected by user bias and is plagued by difficulties in determining the spatial extent of different SFT units (Reid and Thoms 2008, Reid and Thoms 2009, Milan et al., 2010). This results from the indistinct, fuzzy nature of SFT boundaries and the difficulty of producing accurate maps from an oblique viewpoint (Legleiter and Goodchild 2005, Reid and Thoms 2009, Milan et al., 2010).

Table 5.2. Assessment of traditional SFT mapping against requirements of the ‘riverscape’ concept (Fausch et al., 2002).

Key requirement for characterising physical river habitat variables	Is this requirement met by traditional methods of SFT mapping?
(1) Quantitative datasets collected by objective and repeatable methods	No
(2) Spatially continuous datasets, available in three-dimensions	Sometimes spatially continuous, but only in two-dimensions
(3) Spatially explicit datasets	Sometimes
(4) Datasets which cover large spatial areas, with high levels of detail	No
(5) Datasets which are not difficult to collect in terms of practicality, logistics and cost	Yes

5.1.4 Surface flow type mapping using remote sensing

Acknowledging the limitations of traditional methods of SFT mapping, some authors have suggested that “...the rapid survey and proper description of these patterns will benefit from the application of remote-sensing technology... and a GIS approach...” (Newson and Newson 2000, p.196). For other applications, remote sensing has already been shown to provide quantitative and repeatable outputs, to provide spatially continuous and spatially explicit data and to cover relatively large areas with high levels of detail (e.g. for the topographic applications described in Chapter 3). In comparison to the other physical habitat variables considered within this thesis however, relatively little published research has assessed the use of remote sensing for mapping SFTs to date.

Multispectral videography

Some early work exploring the use of remote sensing for delineating mesoscale hydraulic features was described by Hardy et al., (1994). In this study, ground-based multispectral

videography was used to map relative water depths and hydraulic features on the Green River in Utah, USA. These hydraulic features included elements such as runs, pools and riffles, which may be broadly equated with the classifications of biotopes and SFTs used in the UK (Table 5.1). The variability of hydraulic conditions between two different discharges was also assessed. Hydraulic features (i.e. SFTs) were mapped using stills from the video imagery by testing both unsupervised and supervised image classification procedures. These methods were found to produce similar results, and so the faster, unsupervised approach was taken forward. Ground truthing comprised field-based mapping of hydraulic features (SFTs). Extensive cross section data and mesoscale habitat maps created from earlier aerial imagery were also used to assist with validation.

Hardy et al., (1994) found 'excellent' agreement between the spatial extent of hydraulic features mapped from the videography and those mapped as part of the ground truthing process, at both discharge levels. Furthermore, it is suggested that the mapping based on the videography actually represented the spatial arrangement of hydraulic features more accurately than that carried out by eye from the bankside. A detailed quantitative comparison is not provided within this paper though, nor any discussion of the wider applicability of this specific approach. Still, the study concludes that a remote sensing approach such as this *"...could significantly improve the quantification and spatial accuracy of field mapping of hydraulic and habitat features"* (Hardy et al., 1994, p.451).

More recently, Reid and Thoms (2009) also used multispectral videography, this time acquired from a helium balloon suspended 10m above two selected reaches of the Cotter River in Australia. This method was chosen over other remote sensing methods for its cost efficiency and high spatial resolution. Field-based SFT mapping was undertaken concurrently as a means of ground truthing, with SFT extent estimated as a percentage of total surface area within 50m subsections of the larger reach of interest. Still images were extracted from the video imagery, and combined into digital panoramas for each study reach using the SIFT function within the Autostitch software. SFT mapping was then conducted from the imagery within a GIS, for comparison with the field based mapping. The results showed a good overall agreement between ground-based and image-mapped SFTs. However, the accuracy of the SFT coverage estimates varied significantly between different SFTs. For example, higher estimates of rippled flow were found within the ground based mapping and higher estimates of unbroken standing

waves were mapped from the aerial imagery. This observation serves to highlight a well acknowledged difficulty in distinguishing between the similar flow types of rippled flow and unbroken standing waves which was known from field surveys, before the application of remote sensing approaches to SFT mapping. Despite this, Reid and Thoms (2009) conclude that “...the use of aerial imagery to estimate the areal extent of SFTs may prove an effective means to assess spatial and temporal heterogeneity of hydraulic habitat in streams” (Reid and Thoms 2009, p. 66) and suggest the following key advantages of their approach:

- Provides greater precision in the calculation of areal extent of each SFT.
- Provides a permanent record which can be reviewed later or used to monitor change.
- Provides a digital output which can then be used within various spatial analyses to explore the nature of the hydraulic habitat.

Multispectral and hyperspectral imagery

Other studies have used multi- and hyper-spectral imagery for mapping in-stream habitat units with varying levels of success. Whilst these studies focus on classifications of in-stream habitat rather than SFTs, the two are often interchangeable, so that the findings are still of relevance.

Multispectral imagery was used by Wright et al., (2000) for mapping hydrogeomorphic stream units using both supervised and unsupervised image classifications. The best results were in the range 28-80% and made use of an unsupervised, fuzzy classification approach. In addition, they found that larger units were generally more accurately classified than smaller units, and that confusion occurred most often between adjacent units. Many of these observations were argued to result from poor georectification of the imagery, but similar results have been found elsewhere (e.g. Marcus 2002, Marcus et al., 2003) and highlight the difficulties of working with subjective, indistinct units.

Marcus (2002) performed a supervised classification using 1m resolution, 128-band hyperspectral imagery to map habitat types according to a modified version of the Bisson et al., (1982) classification. Overall classification accuracy was reported at 75%, with ‘producer’s accuracies’ varying from 73% for rough water runs to 86% for eddy drop zones. The overall accuracy was improved by a further 10% following the amalgamation of some units. Furthermore, it was found that “...the hyperspectral sensor was detecting spatial heterogeneity within the stream at a finer scale than that mapped by the field teams” (Marcus 2002, p. 122).

This led to apparent ‘inaccuracies’ which were argued to actually represent real hydraulic heterogeneity within the in-stream habitat units.

Similar results were presented by Marcus et al., (2003), again using hyperspectral imagery, with larger ‘inaccuracies’ reported for lower order streams. This is thought to occur because small streams feature smaller habitat units, greater areas of transition zones between units and greater amounts of internal unit variability. The use of exclusion buffers along unit edges was found to improve accuracy values, but some pixel scale heterogeneity was still observed and thought to represent real conditions within the river channel (Marcus et al., 2003).

Other approaches

In recent years, other attempts to map SFTs, in-stream habitat units or to characterise the topography of the water’s surface using passive remote sensing methods have not seen widespread publication. Biron et al., (2002) briefly mention exploratory investigations using stereo-photography of floating balls within different settings to quantify water surface elevations with resolutions of +/-0.01m, but does not link this to SFTs or in-stream habitat. Early-stage research has been on-going at the University of Oregon exploring the use of instantaneous SfM (iSfM) for generating 3D models of water surface topography. This approach uses multiple cameras in different positions to collect images simultaneously and process them using a SfM method. This is advocated to ameliorate the problems associated with the movement of the water surface between the time delayed capture of imagery from a single moving camera. This has been found to be a successful technique for 3D water surface modelling in very small areas where the water is turbid (i.e. not transparent) and where the surface patterns are relatively static (i.e. standing waves). However, ground truthing within studies such as this has not yet been undertaken, and research is currently underway to explore how best to achieve this (Dietrich 2012, *pers. comm.*). This work represents an exciting step forward in the modelling of water surfaces within fluvial systems; however the wider applicability of the technique for habitat assessment at the mesoscale is not yet certain.

Terrestrial laser scanning

The use of active forms of remote sensing for mapping SFTs and characterising the hydraulic conditions within rivers has only appeared within the literature in the last few years, and these have focussed primarily on the use of terrestrial laser scanning (TLS). Early proof-of-concept

work in this field was presented by Large and Heritage (2007). This paper explored the use of TLS for quantifying in-stream hydraulic habitat on a 300m stretch of the South Tyne River in Cumbria, UK. The TLS outputs were processed into a 0.02m grid, from which standard deviation of the water surface elevation was derived. These values give an indication of water surface roughness which is a key determinant of biotope or SFT classification. The data were correlated with field observations of biotope distributions and used to define ranges of surface roughness for each biotope. Whilst this work represented early-stage research, the authors conclude that this new approach has *“...permitted a better spatial quantification of in-stream hydraulic habitat defined by water surface characteristics than has been attempted up to now”* (Large and Heritage 2007, p. 5).

Building on this, Milan et al., (2010) tested the transferability of the TLS approach to a second site at the River Rede, Northumberland. To ensure the scanner was capturing the water surface, an independent survey of water surface elevations was carried out on the same day using a theodolite. Again, field based biotope mapping was undertaken in order to establish the statistical character of the surface roughness of each biotope unit. The results of this study demonstrated that the higher energy biotopes (rapids, cascades) produced greater variations in surface elevation (i.e. greater surface roughness), whereas the lower energy units (pools, glides, marginal deadwater) showed much smoother surfaces which sometimes gave no return signal at all. Surface roughness values for ripples and unbroken standing waves were found to be very similar, and there was also significant overlap in roughness between other biotopes. Variability in surface roughness over time, revealed by thirteen successive laser scans, was found to better distinguish between different biotopes. Overall, these findings serve to confirm the earlier results of Large and Heritage (2007). Further independent testing of the mapping technique produced good success rates ranging from 50% success for an amalgamated rapid/cascade class, to 88% success rate for riffles. The authors conclude that TLS offers a possible method for biotope (or SFT) mapping, and list the key advantages of this technique as; extremely detailed, accurate and objective outputs, rapid survey time, no flight costs, potential for use in cloudy conditions (though not rain or fog) and the potential for rapid mobilisation. However, it is also acknowledged that TLS currently represents a relatively expensive option (Milan et al., 2010).

UAS and SfM

As discussed in Chapter 1, the recent development of small UAS and parallel developments in SfM-photogrammetry now offer an alternative approach for assessing and quantifying a range of river habitat parameters. The work of Reid and Thoms (2009) using 7.5cm resolution imagery acquired from multispectral video camera mounted on a helium balloon provides the only known published example of a UAS-SfM approach to SFT mapping. Mapping accuracy was assessed by comparison with field mapping and was found to vary between SFTs and with changes in discharge. The accuracy and ease of applying this approach to different river systems has not yet been tested and the use of additional quantitative information from the SfM process (e.g. the DEM or point cloud) has also not yet been employed.

5.1.5 Summary

It is clear that remote sensing approaches potentially offer a number of key advantages over traditional visual assessment of SFTs from the bankside. All approaches reviewed here are capable of providing quantitative datasets which are spatially continuous and have the potential to be spatially explicit. They are also more objective, repeatable and spatially accurate than visual bankside mapping and have the potential for covering large areas with high levels of spatial resolution, as indicated in Table 5.3.

The use of multispectral imagery has demonstrated variable levels of success for SFT mapping, with the best results achieved in larger river systems where the proportion of transition zones between SFTs is typically smaller. TLS and iSfM approaches remain somewhat in their infancy for SFT mapping, are costly and logistically challenging, and have not yet been proven for covering larger areas. They also require further rigorous assessment before they might be used routinely for characterising hydraulic habitats. Only one published example of a UAS-SfM approach is known to exist and as a result, more in depth, quantitative assessments are required to establish the value of such emerging approaches for SFT mapping (and as a proxy for hydraulic habitat diversity) on a range of different river systems and under differing data acquisition conditions. In fact, all approaches would benefit from greater quantitative assessment of the accuracy and precision of outputs, although this may always prove challenging given the vague ontological status of SFTs themselves (M. Fonstad 2012, *pers. comm*).

Table 5.3. Assessment of remote sensing based methods of SFT mapping against requirements of the ‘riverscape’ concept (Fausch et al., 2002).

Key requirement for characterising physical river habitat variables	Is this requirement met by remote sensing methods of SFT mapping?			
	Multispectral videography	iSfM	TLS	UAS-SfM
(1) Quantitative datasets collected by objective and repeatable methods	Yes	Yes	Yes	Yes datasets are quantitative, but repeatability has not yet been tested
(2) Spatially continuous datasets, available in three-dimensions	Spatially continuous 2D mapping	Yes	Yes	Yes spatially continuous, but not tested for 3D
(3) Spatially explicit datasets	Yes	Yes, in theory but not currently proven within published work	Yes	Yes
(4) Datasets which cover large spatial areas, with high levels of detail	Yes	Yes, high levels of detail but coverage over large areas not currently proven	Yes, high levels of detail but coverage over large areas not currently proven	Yes
(5) Datasets which are not difficult to collect in terms of practicality, logistics and cost	Yes	No, method involves elaborate set-up of multiple cameras and remains in development at present	Currently limited by cost of scanners	Potentially, but this is yet to be firmly established

5.2 Research Questions

The research reported in this chapter aims to evaluate further the potential benefits of mapping SFTs using hyperspatial resolution data produced using a UAS-SfM approach, building on the initial results of Reid and Thoms (2009). In particular, the following research questions will be addressed:

1. How does the spatial extent and classification of SFT mapping at the mesoscale vary between a) that conducted by eye from a bankside location in the field and b) that mapped directly from the UAS-SfM orthophoto?
2. How accurate and repeatable is the SFT mapping conducted on the UAS-SfM orthophoto and how does the accuracy vary between different SFTs and different surveys?
3. Does the use of quantitative information derived from the UAS-SfM process (i.e. refraction corrected water depth and point cloud roughness) help to differentiate between SFTs?

5.3 Site Locations

The SFT research was conducted at the following two sites. Further detail on these sites is provided in Chapter 1.

- a) **The River Arrow**, Warwickshire (Figure 5.2): where surveys were carried out at the following times;
 - i. **July 2012** – This survey followed a period of heavy rainfall and as a result flow level and turbidity were high. Weather conditions were dull and overcast at the time of image acquisition.
 - ii. **May 2013** – This survey was conducted in bright sunny weather with a relatively low flow level and low turbidity.
 - iii. **June 2013** – This survey was also conducted in bright sunny weather with a relatively low flow level and low turbidity.
 - iv. **August 2013** – This survey was conducted when conditions were overcast and slightly misty. Flow level and turbidity were comparable to the surveys conducted in May and June.

- b) **Coledale Beck**, Cumbria (Figure 5.3): this survey was conducted in July 2013 during bright and sunny conditions with a low flow level and very low turbidity.



Figure 5.2. The River Arrow research site (May 2013).



Figure 5.3. The Coledale Beck research site (July 2013).

These sites were selected for the following reasons;

- Both sites provide a diverse range of SFTs within a relatively short length of channel, allowing assessment of SFT mapping at the mesoscale.

- Both sites are easily accessible and permission from the landowners was granted for UAS flying.
- Neither site is situated in areas of dense vegetation or continuous tree coverage, near major roads or railway lines, power lines or sensitive sites such as airports.
- The River Arrow is located close to the University of Worcester so that it could be revisited frequently and at short notice to take advantage of favourable flying conditions.
- Repeat surveys of the River Arrow allow a comparison of the success of SFT mapping under differing conditions (e.g. flow level, turbidity, illumination conditions).
- Survey of two different sites allows a comparison of the success of the approach under different conditions.

Depending on the availability and quality of data available, these site surveys were used to answer different research questions within this chapter, as detailed in Table 5.4.

Table 5.4. Datasets used to address each of the research questions.

Site	Arrow				Coledale
Survey date	July 2012	May 2013	June 2013	August 2013	July 2013
RQ 1	✓	✓	✓	✓	
RQ 2		✓	✓	✓	
RQ 3		✓	✓	✓	✓

5.4 Methods

The workflow provided in Figure 5.4 details the methods used for mapping and assessing SFTs within this chapter. Those methods which are common to all physical river habitat parameters considered within this thesis are documented in Chapter 2, whereas methods specific to this chapter are detailed here (Table 5.5).

Table 5.5. Overview of methods used within this chapter and where they are described within this thesis.

Stage	Detail	Location
1) Pre-field	Camera characterisation	Chapter 2
2) Data Acquisition	GCP set-up	Chapter 2
	UAS flying & image acquisition	Chapter 2
	GCP survey	Chapter 2
	SFT mapping from the bankside	This chapter 5.4.1
	Ground truthing of SFTs	This chapter 5.4.2
3) Post-Field	Image selection	Chapter 2
4) SfM Processing	Image processing in PhotoScan Pro	Chapter 2
5) Analysis methods	RQ1 - SFT mapping from UAS-SfM orthophoto	This chapter 5.4.3
	RQ1 - Comparing field and UAS-SfM SFT mapping	This chapter 5.4.4
	RQ2- Accuracy assessment of SFT mapping	This chapter 5.4.5
	RQ3 - Deriving quantitative information from the UAS-SfM outputs; i) refraction corrected water depth ii) point cloud roughness iii) depth and roughness of mapped SFTs	This chapter 5.4.6
	RQ3 – Differentiating SFTs using ANOSIM	This chapter 5.4.7

5.4.1 Surface flow type mapping from the bankside

During field campaigns, mapping of the spatial extent of different SFTs was conducted by eye from an oblique viewpoint on the riverbank. The SFT classifications provided by the Environment Agency’s (2003) River Habitat Survey (RHS) were used throughout (Table 5.1). Within the RHS, SFT mapping is usually conducted from the bank, where the dominant SFT is noted at ten 50m spot check locations along a 500m reach. For this research, however, a more spatially explicit mapping approach was required.

SFTs and other key features within the channel were mapped onto hard copy base maps, as detailed in Table 5.6. These base maps varied in scale and comprised OS mapping or existing orthophotos (depending on the highest resolution product available at the time of each survey). This field based SFT mapping was undertaken on the same day as UAS image acquisition. A series of photos were also taken during the SFT field mapping process to provide a permanent record of SFT conditions which could be re-visited later as necessary. The annotated hard copy maps were scanned and geo-referenced using ArcGIS (ESRI Inc.). The field-mapped SFTs were then digitised as polygons (Figures 5.5 to 5.8). Copies of the annotated field maps and a selection of field photos are provided in Figures D1 to D10 in Appendix D.

The base map used at Coledale Beck was derived from aerial imagery acquired by the Natural Environment Research Council (NERC) in 2005. The acquisition of this imagery formed part of an urgency grant awarded to a team from the universities of Durham and Central Lancashire, for the assessment of storm related slope failures (R. Johnson 2014, *pers. comm.*). Unfortunately, it was not possible to acquire more recent imagery of this area. During the process of georeferencing the scanned annotated base maps of Coledale, it was found that the spatially positioning of the imagery was poor. As a result it was not possible to accurately locate the field SFT mapping for this site. Instead, a map of SFTs was created making use of the bankside visual mapping, the UAS-SfM orthophoto and ground truth data (Figure 5.9). This SFT mapping is used later in section 5.4.6.

Table 5.6. Base maps used for SFT mapping in the field, by survey.

SFT Survey	Base Map	Scale of Hard Copy Base Map
Arrow July 2012	OS Mastermap (Digimap 2012)	1:1500
Arrow May 2013	UAS Orthophoto from July 2012 survey	1:150
Arrow June 2013	UAS Orthophoto from May 2013 survey	1:200
Arrow August 2013	UAS Orthophoto from May 2013 survey	1:200
Coledale July 2013	NERC aerial imagery acquired in 2005, orthorectified by Durham University	1:350

1. PRE-FIELD

- a) Camera characterisation to determine relationship between flying altitude and image resolution

2. DATA ACQUISITION

- a) Distribution of GCPs
- b) Image acquisition from UAS platform (multiple flights)
- c) Survey position of GCPs using dGPS or total station
- d) SFT mapping in the field using base maps
- e) Ground truthing of SFTs using dGPS or total station survey, hand tape and EM current meter

3. POST-FIELD

- a) Image selection based on visual quality, view angle and altitude of images

4. SfM PROCESSING

- a) Import images into PhotoScan Pro
- b) Align images – identification of conjugate points to produce a sparse point cloud
- c) Geometry building – densification of the point cloud
- d) Texture building – raw image pixels are draped over the built geometry
- e) Georeferencing – indirect georeferencing using known positions of GCPs (2c)
- f) Optimise image alignment – GCP positions used to refine camera lens model and minimise geometric distortion, sparse point cloud is recomputed
- g) Re-build geometry – densification of recomputed sparse point cloud
- h) Re-build texture – raw images are draped over the re-built geometry
- i) Export georeferenced orthophoto, DEM and dense point cloud

5. ANALYSIS

- a) Manual mapping of SFTs from UAS-SfM orthophoto in ArcGIS
- b) Use *'fishnet'* tool to create regular points for comparison of field and UAS-SfM based SFT mapping using a confusion matrix
- c) Accuracy assessment of UAS-SfM and field based SFT mapping against ground truth using a confusion matrix
- d) Compute refraction corrected water depth from DEM where necessary (see Chapter 3)
- e) Compute point cloud roughness using CloudCompare
- f) Generate roughness profiles for SFTs using full SFT polygons and SFT 'core' areas
- g) Analysis of similarity using PRIMER 6, to test separability of SFTs based on 3 different scenarios of input data :
 - A. UAS-SfM point cloud roughness and refraction corrected depth data only
 - B. Ground truth depth and velocity data only
 - C. Ground truth depth and velocity data and UAS-SfM point cloud roughness

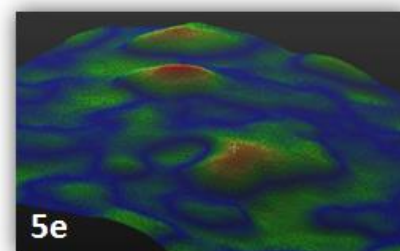
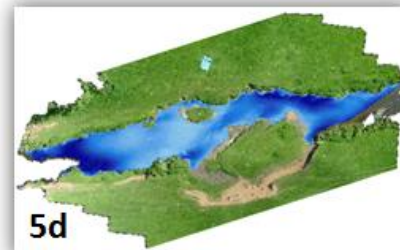


Figure 5.4. Methods workflow for SFTs chapter.

5.4.2 Ground truthing of surface flow types

An independent SFT identification survey was carried out at the time of each field campaign. This comprised a field survey where the SFT was noted at a series of point locations recorded using a Leica Builder 500 total station or Trimble R8 differential GPS, as shown by the black dots in Figures 5.6 to 5.9. This classification process involved looking at the SFT in question from different angles, rather than solely from the bank or in-channel location. This independent survey is taken to represent the 'ground truth' SFT mapping. The accuracy of other SFT mapping datasets is assessed against this survey. At each point within this ground truth survey, a measure of water depth (to the nearest centimetre) was taken using a wading rod and a measure of mean column velocity (m/s) was taken at 0.6 depth using a Valeport EM801 electromagnetic flow meter. These data allow subsequent characterisation of the hydraulic character of SFTs.

During the July 2012 River Arrow survey, high stage flows at the time of data collection prohibited access to the channel. As a result, it was not possible to collect a SFT ground truth survey at this time. At Coledale Beck, it was difficult to identify discrete SFTs both from the bankside and from the UAS imagery. As a result, the ground truth data collected at this site were used to assist a single SFT mapping approach (Figure 5.9) which was used solely for comparison with point cloud roughness and water depth, as detailed in section 5.4.6.

5.4.3 Surface flow type mapping from UAS-SfM imagery

One output of the SfM-photogrammetry processing of the UAS imagery is a hyperspatial resolution orthophotograph (or 'orthophoto'). SFTs were mapped as polygons from these orthophotos within a GIS, at a scale of 1:50. This mapping was conducted manually (rather than using any image classification procedures) and was based only on the visual properties of the water surface. Figures 5.5 to 5.9 show the SFT mapping from the UAS imagery.

The ease of SFT mapping from the orthophotos was found to be affected significantly by the illumination of the scene. For the River Arrow May and June datasets, the mapping was assisted by bright, sunny conditions at the time of the surveys. In contrast, during the August 2013 and July 2012 surveys, conditions were dull and overcast which made differentiation of SFTs much more difficult from the orthophotos alone.

5.4.4 Comparing bankside and UAS-SfM surface flow type mapping

The *Fishnet* tool within ArcGIS was used to create a regular grid of points spaced every 0.5m throughout the study area of each survey. These points were overlain on mapped SFT polygons in the GIS. The ‘*Extract Values to Points*’ tool was used to extract the SFT classification from both the bankside mapping and the UAS-SfM mapping at the location of each point. The resulting data were compiled into a confusion matrix (sometimes called an error matrix) for each survey to compare the SFT mapping from the two different approaches.

5.4.5 Accuracy assessment of surface flow type mapping

The accuracy of both the bankside and the UAS-SfM SFT mapping was assessed against the independent SFT ground truth survey (described in section 5.3.2). The ground truth survey is represented by a series of points which differ in number and location between surveys (Figures 5.6 to 5.8) and are detailed in Table 5.7.

Table 5.7. Number of SFT ground truth points acquired per survey.

Survey	May 2013	June 2013	Aug 2013
No. of ground truth points	107	65	60

The SFT classification of both the bankside and the UAS-SfM mapping was extracted at the location of each ground truth point, using the ‘*Extract Values to Points*’ tool in ArcGIS. The resulting data were compiled into confusion matrices. A confusion matrix is often used to assess the accuracy of an automated image classification (Lillesand and Kiefer 2000), but is also readily applied to a manual classification such as the bankside and UAS-SfM SFT mapping conducted here. The confusion matrices were used to compute the *overall accuracy*, *user’s accuracy*, *producer’s accuracy* and *kappa co-efficient* for each dataset. A summary of the notation used within the equations used to define these accuracy metrics is provided in Table 5.8.

The *overall accuracy* (α) is given as a percentage, representing the total number of correct classifications. This ratio provides an indication of the accuracy of the SFT mapping as a whole,

and is defined in Equation 5.1. In this equation N is the total number of ground truth observations and C_{ii} is the total number of correctly classified observations.

$$\alpha = \left(\frac{1}{N}\right) \sum_{i=1}^m C_{ii}$$

Equation (5.1) – Overall Accuracy

(after Liu and Mason, 2009)

The *user's accuracy* (β) is also given as a percentage. It provides a measure of correctly classified observations within a single mapped SFT category as a proportion of the total number of observations in that category (i.e. the *commission* errors). As such, a different user's accuracy is computed for each SFT as mapped from the bankside or on the UAS-SfM orthophoto. The user's accuracy is defined in Equation 5.2, where C_{ii} is the total number of correctly classified observations in any given SFT category and Nr_i is the total number of observations in that category (as mapped in the field or on the UAS-SfM orthophoto).

$$\beta = \frac{C_{ii}}{Nr_i}$$

Equation (5.2) – User's Accuracy

(after Liu and Mason, 2009)

The *producer's accuracy* (γ) differs from the user's accuracy in that it provides a measure of correctly classified observations within a single ground truth SFT category as a proportion of the total number of observations in that category, rather than within each bankside- or UAS-SfM-mapped SFT category. As such, it represents the *omission* errors within the confusion matrix. The producer's accuracy is computed for each SFT separately and is given as a percentage. It is defined in Equation 5.3, where C_{ii} is the total number of correctly classified observations in any given SFT category and Nc_j is the total number of observations in that ground truth category.

$$\gamma = \frac{C_{ii}}{Nc_j}$$

Equation (5.3) – Producer's Accuracy

(after Liu and Mason, 2009)

In addition to these simple ratios, another measure which can be used for accuracy assessment is the *kappa co-efficient* (or ‘Cohen’s *k*’). The kappa co-efficient (κ) provides a statistical measure of the difference between (a) the observed agreement between the SFT mapping (bankside or UAS-SfM orthophoto based) and the ground truth SFT data, and (b) the chance agreement between the ground truth SFT data and a random theoretical SFT classification. As such it provides an indication of the quality of the SFT mapping as a whole as compared to a random or chance output. A maximum kappa value of 1 would suggest that the SFT mapping is 100% better than one resulting purely by chance and a value of 0 would suggest it is no better. Negative kappa values can also be produced, indicating no agreement between the SFT mapping and the ground truth SFT data. The kappa co-efficient is defined by Equation 5.4.

$$\kappa = \frac{(N \cdot \sum_{i=1}^m C_{ii}) - (\sum_{i=1}^m (Nr_i \cdot Nc_j))}{N^2 - (\sum_{i=1}^m (Nr_i \cdot Nc_j))}$$

Equation (5.4) – Kappa co-efficient

(after Liu and Mason, 2009)

These four accuracy measures are used to assess the agreement between mapped SFTs (bankside or UAS-SfM based) and the ground truth SFTs.

Table 5.8. Summary of notation used in accuracy equations 1-4 (after Liu and Mason, 2009).

Notation	Explanation
N	Total no. of observations (all SFT categories)
C _{ii}	Total no. of correctly classified observations in any given SFT category
Nr _i	Total no. of observations in a given SFT category, as mapped from the bankside or on the UAS-SfM orthophoto
Nc _j	Total no. of observations in a given SFT category with the ground truth SFT dataset

5.4.6 Deriving quantitative information from UAS-SfM outputs

Refraction Corrected Water Depth

Within submerged areas, the DEMs produced by the UAS-SfM process are affected by refraction at the air-water interface, which typically results in an overestimation of the true

bed elevation (Fryer 1983, Fryer and Kneist 1985, Butler et al., 2002, Westaway et al., 2001). Therefore, it is usually necessary to undertake a refraction correction procedure prior to the use of water depth data derived from these DEMs. Chapter 3 provides a detailed description of the methods used here for estimating water depth from the UAS-SfM products and the subsequent correction for refraction. The output of this process is a raster dataset of refraction corrected (RC) water depths.

Despite refraction correction, some errors remain within the DEM. These may be caused by the SfM process fixing point matches which do not represent the true position of the channel bed and therefore depth estimations are inaccurate. A full assessment of RC depth and RC DEM error is presented in Chapter 3, and considered further in the discussion of this chapter. For the purposes of characterising RC depth by SFT, the *Set Null* tool in ArcGIS was used to identify and exclude all pixels with a negative depth value (i.e. where the elevation of the channel bed is erroneously given as higher than the elevation of the water surface). This meant that small areas were lacking RC depth data, but this was considered preferable to including clearly erroneous data within the subsequent SFT analysis.

As identified in Chapter 3, the original DEM for Coledale Beck was of a higher mean accuracy than the equivalent RC DEM. It is thought that the shallower waters at this site mean that refraction correction is not necessary. As a result, the non-RC DEM is used in subsequent analyses for Coledale Beck.

Point Cloud Roughness

One of the outputs from the SfM-photogrammetry process is a dense point cloud. The dense point cloud for each site was loaded into the freeware package CloudCompare (Girardeau-Montaut 2014). The roughness tool within this software was used to calculate the roughness for each point within the dense cloud. This is a measure of fine scale variation in elevation within the point cloud and is defined as the distance between each point and the least squares best fitting plane computed on its nearest neighbours within a sphere (or 'kernel') of a given size. In theory, greater roughness in the point cloud may result from greater roughness of the water surface and therefore variations in point cloud roughness may reveal something about SFT. A sphere radius of 0.2m was chosen for calculating roughness at all sites. This was based

on *a priori* knowledge that the typical size of SFT features at the study sites does not tend to exceed 0.4m.

The per-point roughness data were rasterised and exported from CloudCompare as a TIFF file. It is possible to specify the resolution of each output TIFF. A given resolution was selected for each dataset with a view to preserve as much detail whilst minimising the number of holes within the dataset. As a result, the spatial resolution varied between the different surveys and was related to the UAS flying altitude. The data from the July 2012 survey of the River Arrow were exported at 10cm resolution, whilst all other datasets were exported at 5cm.

5.4.7 Differentiating surface flow types

SFTs are not typically defined by their water depth distributions alone (Newson and Newson 2000). Recent research by Milan et al., (2010) however, suggests that biotopes (which may be equated to SFTs) can be distinguished to some extent by the roughness of TLS point clouds. As a result, point cloud roughness data derived from the SfM process are first analysed in isolation for differentiating SFTs, and then both roughness and depth data derived from the UAS-SfM process are used in an 'analysis of similarity' (ANOSIM) test.

Point cloud roughness was summarised by SFT using the mapping conducted on the UAS-SfM orthophotos, except where the *overall accuracy* of UAS-SfM SFT mapping was less than 50%. In practice this was only the case for the Arrow August 2013 survey, where the bankside mapped SFT units were used instead. Where no overall accuracy measures were available (i.e. Arrow July 2012), the SFT mapping based on the UAS-SfM orthophoto was used so it could be assessed as a single, standalone technique. For Coledale Beck, only one SFT classification was available (based on a combination of bankside, UAS-SfM and ground truth data).

SFT Polygons - The mapped SFTs were in the form of a polygon shapefile for each survey. These polygons were overlain on the roughness raster datasets. A 20cm exclusion buffer was applied along the channel edges, around mid-channel islands and around patches of woody debris. The sharp changes in elevation associated with these features may introduce roughness which is not related to the surface patterns of the SFT itself. This 20cm buffer therefore prevents these features being included in the roughness distributions of the SFTs which are calculated subsequently.

SFT 'Core' Areas - Given that SFTs often have indistinct, fuzzy boundaries, the roughness distributions of the entire mapped extent of SFTs may be affected by neighbouring SFTs. Therefore, circular polygons with a 25cm radius were generated to represent the 'core' of each SFT. These SFT cores were randomly located within the centre of SFTs and at least 20cm away from the channel edges, islands and patches of woody debris, to ensure that roughness induced by such features would not be included.

Zonal Statistics - Basic roughness statistics within each SFT of each survey (both entire polygons and core areas) were summarised using the *Zonal Statistics* tool within ArcGIS. Computed statistics included the minimum, maximum and mean values, as well as the range, standard deviation and sum.

Zonal Histograms - The distribution of roughness values within each SFT of each survey (both entire polygons and core areas) were also characterised, using the *Zonal Histogram* tool in ArcGIS. This tool allows a maximum of 25 separate bins (0 to 24) which must be integers. Therefore it was necessary to use the *raster calculator* to apply an appropriate multiplier to each roughness dataset in order to preserve the detail from the floating point dataset. The multiplier values were determined by dividing the maximum bin value (24) by the highest RC depth or roughness value present within each dataset, and are specified in Table 5.9. The multiplied dataset was then converted to an integer before applying the *Zonal Histogram* tool. The multiplication was reversed in order to summarise the roughness distributions of each SFT.

Table 5.9. Multiplier values using for creating zonal histograms.

Survey	Arrow July 2012	Arrow May 2013	Arrow June 2013	Arrow August 2013	Coledale July 2013
Roughness multiplier	200	297	291	230	213
RC depth multiplier	N/a	21.64	20.92	16.90	20.87

Analysis of Similarity (ANOSIM)

To further address research question three, analysis of similarity (ANOSIM) tests were carried out to explore differences between SFTs. Three ANOSIM tests were conducted for each site survey, each of which used different combinations of data as detailed below. The data were

categorised using the SFTs mapped by the ground truth survey. The three different combinations of data were derived either solely from the UAS-SfM approach, solely from the ground truth survey or a combination of the two for each dataset, and are defined as scenarios A-C in Table 5.10. These different scenarios allow a comparison of the separability of SFTs, based on traditional depth-velocity measures only (Scenario B) versus UAS-SfM quantitative measures only (Scenario A). Scenario C combines these two, to explore whether UAS-SfM derived quantitative measures can be used in addition to traditional field measured depth and velocity readings to improve SFT separability. Each site survey is considered separately.

*Table 5.10. Scenarios used for ANOSIM tests.
With the exception of Coledale, where non-RC depth was used.

Scenario	SFT Mapping	Variable 1	Variable 2	Variable 3
A	Ground truth	RC water depth*	Point cloud roughness	N/a
B	Ground truth	Water depth (ground truth)	Mean column velocity (ground truth)	N/a
C	Ground truth	Water depth (ground truth)	Mean column velocity (ground truth)	Point cloud roughness

The data from each survey and for each scenario were loaded into the PRIMER 6 software (PRIMER-E Ltd, version 6.1.13) as environmental variables. Pairwise scatter plots were created for all imported variables and analysed for skewness and nature of correlation. All data either showed a normal distribution or produced a linear correlation, so that transformation of the data was not necessary. Normalisation of all variables was conducted to ensure they were on comparable scales. Each value was normalised by subtracting the mean and dividing by the standard deviation.

A resemblance matrix was generated in PRIMER 6 for each scenario. This is a triangular matrix which details the differences between all data points (or ‘samples’ as PRIMER calls them), measured in Euclidean distances. At this point the ground truth SFT classifications for each sample were added as a ‘factor’ in PRIMER.

The resemblance matrix is then used to conduct a one-way ANOSIM test. This test is based on the corresponding rank similarities between data points in the resemblance matrix, and not on

actual Euclidean distances (Clarke and Warwick 2001). The outputs of this test include the following:

- **Global R value:** provides a comparative measure of the degree of difference between SFTs and usually falls between 0 and 1. A value of 0 would mean there are no differences between SFTs, and a value of 1 would indicate that all samples within SFTs are more similar to each other than samples from different SFTs.
- **Global significance (p value):** indicates the significance of the relationship, where values less than 0.05 indicate a significance of 95% or more, and are statistically significant.
- **Pair-wise statistics:** R statistic and significance levels (p values) are also given for each pair-wise comparison between SFTs.

5.5 Results and Analysis

5.5.1 Comparing surface flow type mapping

Research Question 1

How does the spatial extent and classification of SFT mapping at the mesoscale vary between a) that conducted by eye from a bankside location in the field and b) that mapped directly from the UAS-SfM orthophoto?

Qualitative Comparison

The spatial extent and classification of SFT units are broadly similar between the bankside and UAS-SfM mapping for the River Arrow May 2013 and June 2013 surveys (Figures 5.6 and 5.7). The bankside SFT mapping for the River Arrow July 2012 survey is less detailed and appears to be more spatially imprecise than the corresponding UAS-SfM SFT mapping (Figure 5.5). This relates to the use of a coarse scale base map (Table 5.6), which may be adversely affecting the accuracy of this bankside SFT mapping (although quantitative data to support this are not available). The UAS-SfM orthophoto SFT mapping for the River Arrow August survey does not correspond well with the equivalent bankside mapping (Figure 5.8). There are notable fewer mapped units, and large parts of the site are mapped as 'smooth'.

Quantitative Comparison

A quantitative comparison of SFT mapping is provided in Table 5.11. The values shown in this table indicate the level of agreement between bankside and UAS-SfM orthophoto mapped

SFTs. That is, for the smooth SFT, this table shows the percentage of points mapped as smooth by the bankside survey that are also mapped as smooth by the corresponding UAS-SfM survey. These data are equivalent to the user’s or producer’s accuracy value often used when comparing classifications to ground truth data. However, the use of these terms is avoided given that the values given in Table 5.11 represent levels of agreement between two classifications, rather than accuracy values.

The greatest, most consistent agreement between bankside and UAS-SfM SFT mapping occurs for the smooth SFT, where the percentage agreement is consistency greater than 76% across all surveys (Table 5.11). The agreement for upwelling is also particularly strong for the Arrow June 2013 and August 2013 surveys, but significantly less so for the earlier surveys. This may relate to the small number of comparison points falling in areas of upwelling and the relative small spatial coverage of this SFT at the River Arrow. Levels of agreement for the other SFTs are highly variable between surveys, especially for no perceptible flow. Typically, higher levels of agreement are observed for the May 2013 and June 2013 surveys than for the July 2012 and August 2013 surveys.

Table 5.11. Level of agreement (%) between bankside and UAS-SfM mapped SFTs by survey and SFT. The higher the percentage, the darker green the cell is coloured.

SFT	River Arrow			
	Jul-12	May-13	Jun-13	Aug-13
Smooth	98.39	77.61	76.05	87.07
USW	42.20	68.22	53.96	32.73
Rippled	21.18	65.17	56.65	30.77
NPF	35.62	65.22	54.22	0.00
Upwelling	0.00	17.86	80.00	100.00

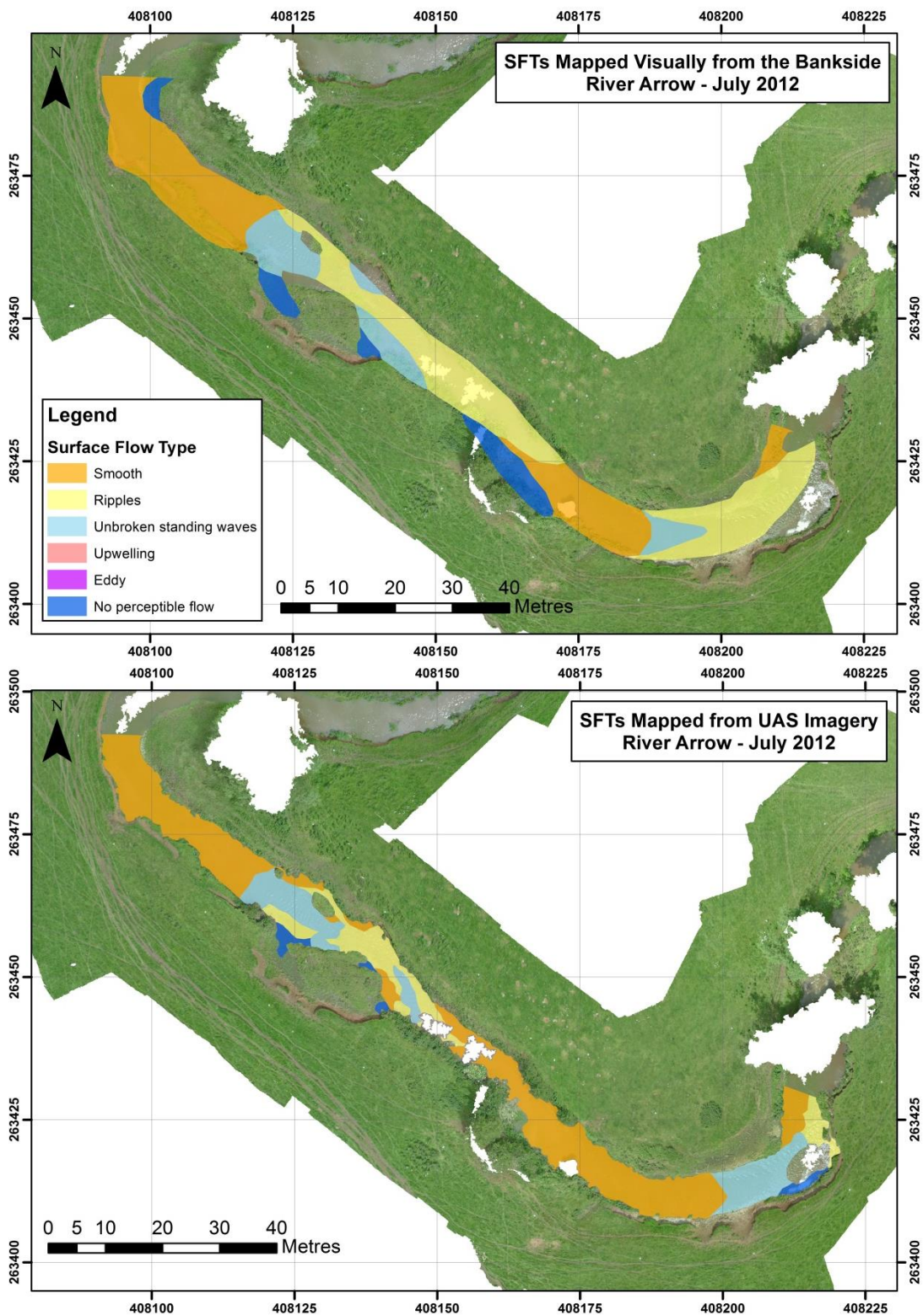


Figure 5.5. SFT mapping conducted visually from the bankside (top) and from the UAS-SfM orthophoto (bottom) for the River Arrow July 2012 survey.

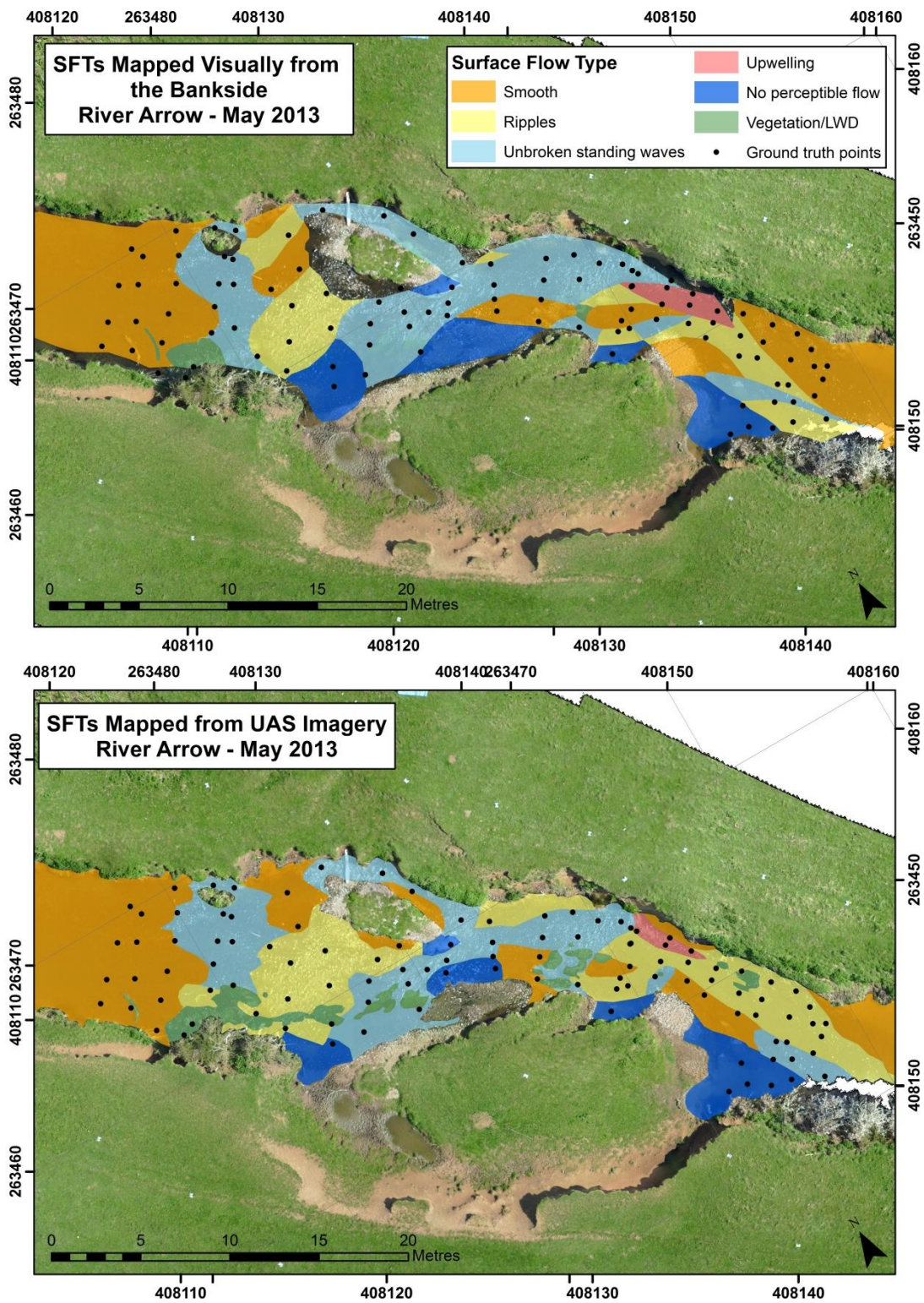


Figure 5.6. SFT mapping conducted visually from the bankside (top) and from the UAS-SfM orthophoto (bottom) for the River Arrow May 2013 survey.

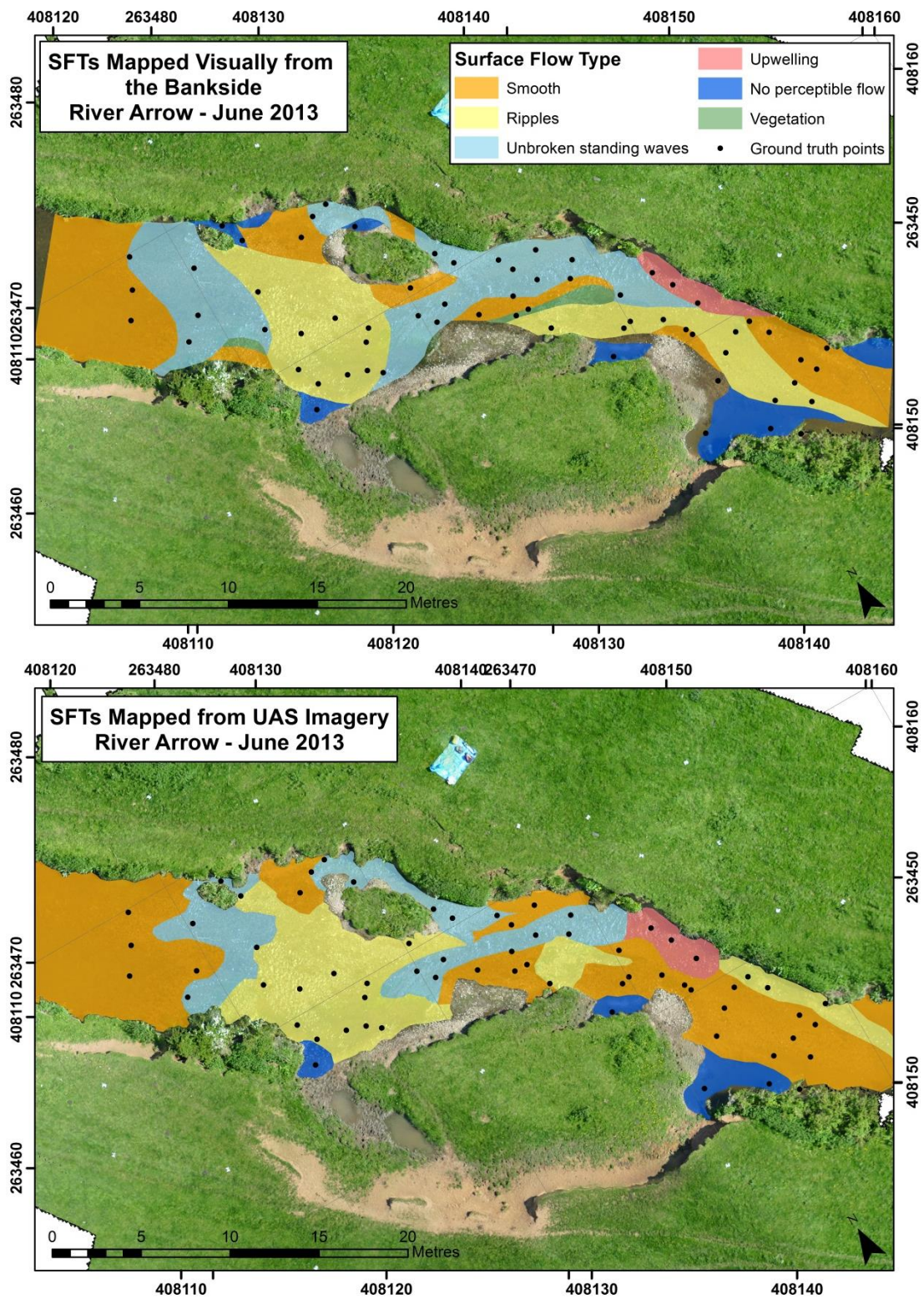


Figure 5.7. SFT mapping conducted visually from the bankside (top) and from the UAS-SfM orthophoto (bottom) for the River Arrow June 2013 survey.

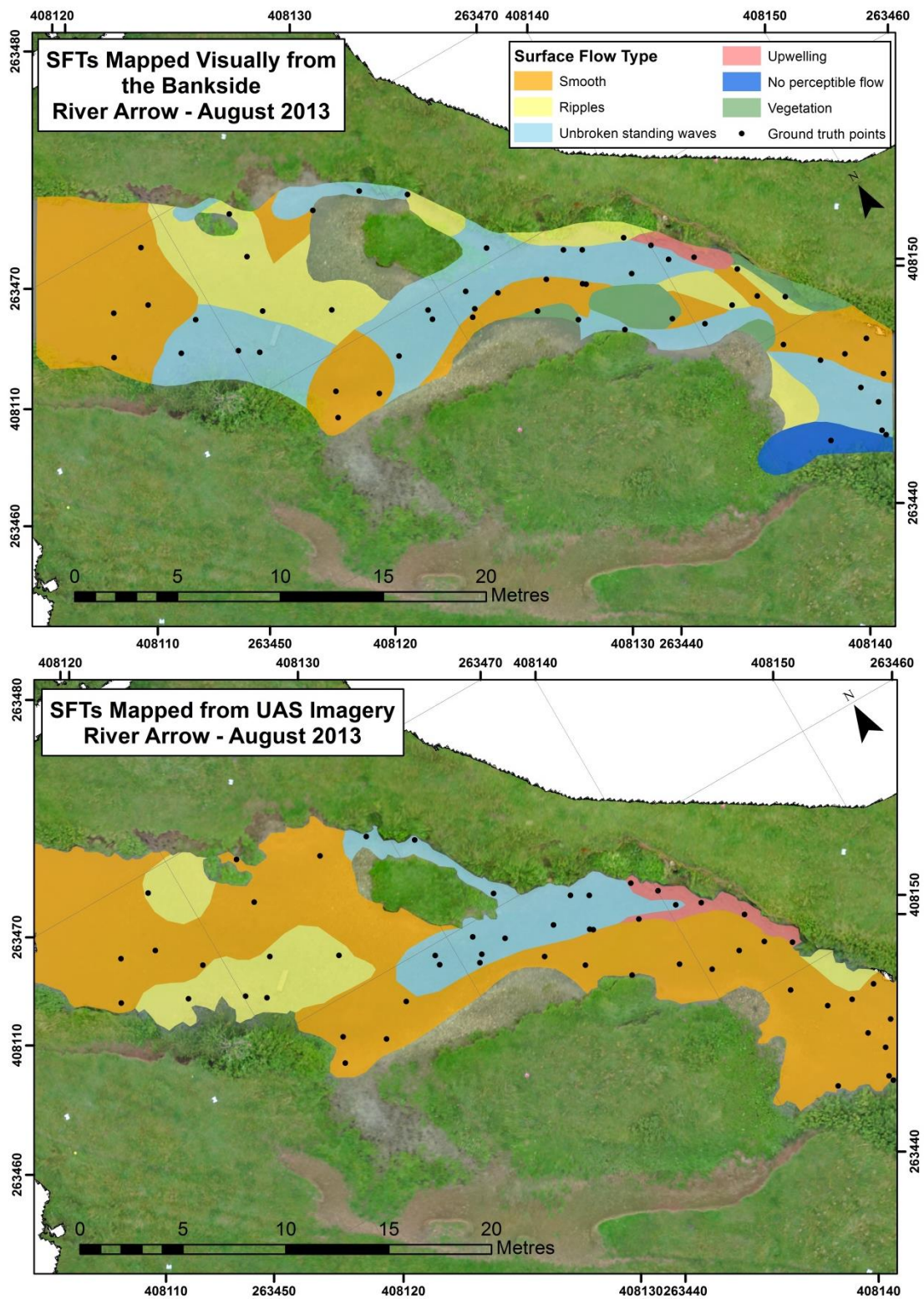


Figure 5.8. SFT mapping conducted visually from the bankside (top) and from the UAS-SfM orthophoto (bottom) for the River Arrow August 2013 survey.

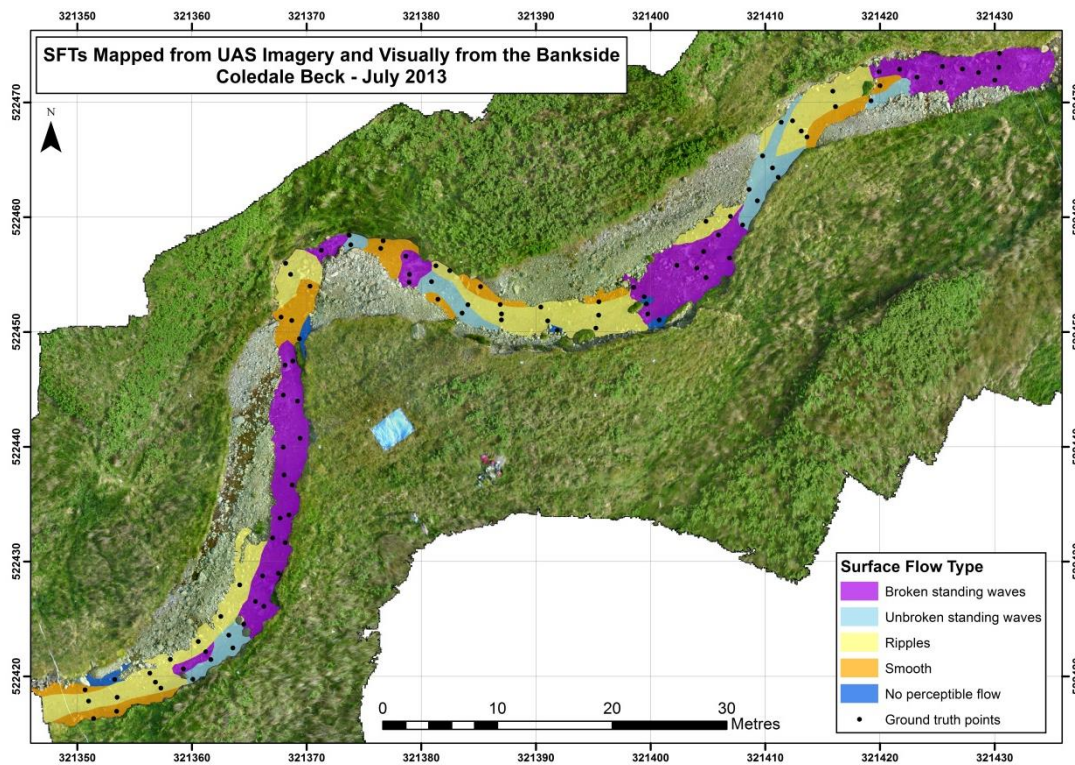


Figure 5.9. SFT mapping conducted from a combination visual mapping from the bankside, mapping from the UAS-SfM orthophoto and ground truth data for Coledale Beck, July 2013.

Table 5.12 provides an indication of how each bankside mapped SFT has been mapped by the equivalent UAS-SfM survey. For example, it shows that for points mapped as unbroken standing waves (USW) by the bankside survey, 42.2% of these are also mapped as unbroken standing waves by the UAS-SfM, as well as 32.51% which are instead mapped as smooth, 21.67% mapped as rippled and 3.61% mapped as NPF. The table indicates which SFTs are often confused between the bankside and UAS mapping.

The agreement for the SFT smooth is high, but is sometimes mapped by the UAS survey as rippled. When not also mapped as USW, these areas are sometimes mapped as smooth or rippled SFTs. Rippled SFTs in the bankside survey seem often confused with smooth SFTs in the UAS mapping and NPF is also often confused with smooth areas. The agreement for upwelling is highly variable between surveys and is sometimes confused with ripples. It should be noted that the differences in areal coverage between the different SFTs will be affecting these results. For example, the area typically mapped as upwelling on the River Arrow surveys is consistently much smaller than that mapped as smooth. As a result, fewer comparison points

fall within this area, and slight spatial differences in the mapped extent of the SFT are therefore likely to produce larger percentage differences shown in Table 5.12.

*Table 5.12. Quantitative comparison of bankside and UAS-SfM mapped SFTs. Values are in percentages. Rows in **bold** highlight where the two SFT classifications are in agreement (e.g. both smooth), all others indicate where the two SFT classifications do not agree (e.g. smooth and rippled). Cells are colour coded to highlight the magnitude of agreement, with higher levels of agreement shown in the darker greens and lower levels of agreement shown in yellow.*

Bankside SFT	UAS-SfM SFT	Arrow			
		Jul-12	May-13	Jun-13	Aug-13
Smooth	Smooth	98.39	77.61	76.05	87.07
	USW	1.54	4.96	3.16	4.75
	Rippled	0.00	16.41	20.79	7.65
	NPF	0.00	1.03	0.00	0.00
	Upwelling	0.00	0.00	0.00	0.00
	Other	0.07	N/a	0.00	0.53
USW	Smooth	32.51	4.96	33.14	44.14
	USW	42.20	68.22	53.96	32.73
	Rippled	21.67	18.95	9.68	19.22
	NPF	3.61	6.41	0.00	0.00
	Upwelling	0.00	1.46	3.23	3.30
	Other	0.00	N/a	0.00	0.60
Rippled	Smooth	45.58	15.92	34.10	59.49
	USW	32.47	11.94	6.94	7.69
	Rippled	21.18	65.17	56.65	30.77
	NPF	0.77	6.97	0.58	0.00
	Upwelling	0.00	0.00	1.73	2.05
	Other	0.00	N/a	0.00	0.00
NPF	Smooth	64.38	2.17	33.73	92.31
	USW	0.00	15.22	8.43	0.00
	Rippled	0.00	17.39	2.41	0.00
	NPF	35.62	65.22	54.22	0.00
	Upwelling	0.00	0.00	0.00	0.00
	Other	0.00	N/a	1.20	7.69
Upwelling	Smooth	28.57	0.00	0.00	0.00
	USW	26.79	0.00	0.00	0.00
	Rippled	19.64	82.14	20.00	0.00
	NPF	25.00	0.00	0.00	0.00
	Upwelling	0.00	17.86	80.00	100.00
	Other	0.00	N/a	0.00	0.00

5.5.2 Accuracy of surface flow type mapping

Research Question 2

How accurate and repeatable is the SFT mapping conducted on the UAS-SfM orthophoto and how does the accuracy vary between different SFTs and different surveys?

Overall Accuracy and Repeatability

An overarching quantitative comparison of ground truth and mapped SFTs is provided in Table 5.13. A comparison of the accuracy of bankside and UAS-SfM SFT mapping gives variable results, with greater consistency being observed for the bankside mapped surveys than for the UAS-SfM mapped surveys. The UAS-SfM mapping has a relatively high overall accuracy for the May 2013 survey (75%), which exceeds the accuracy of the bankside mapping (66%). For the June 2013 and August 2013 surveys however, the bankside mapping gives higher overall accuracy values (74% and 57%) and kappa values (0.59 and 0.30) than the equivalent UAS-SfM mapping (56% and 48%, and 0.40 and 0.27 respectively).

Table 5.13. Summary of overall SFT mapping accuracy by method and date of survey.

		Arrow		
		May-13	Jun-13	Aug-13
Overall Accuracy (%)	UAS	75	56	48
	Bankside	66	74	57
Kappa Coefficient	UAS	0.66	0.40	0.27
	Bankside	0.54	0.59	0.30

Accuracy by SFT

Table 5.14 gives an overview of the variability in the *user's accuracy* between SFTs for the different SFT mapping methods. For the bankside mapping, the highest accuracies are observed for areas of no perceptible flow, although these values vary from c.67% for the May 2013 survey to 100% for the August 2013 survey. Areas of smooth flow give user's accuracies which are consistently greater than 64% and unbroken standing waves greater than 50%, although again there is variability between surveys. The poorest user's accuracies are observed for areas of upwelling during the May 2013 and August 2013 surveys; however, a significantly higher user's accuracy is found for the June 2013 survey.

A similar pattern of accuracy by SFT is observed within the UAS-SfM mapping data. Again the highest and most consistent user’s accuracies are found for the SFTs no perceptible flow and unbroken standing waves, where all values are greater than 73%. The user’s accuracies for smooth and upwelling SFTs are also high for some surveys, but these values are less consistent across the surveys. The poorest user’s accuracies are most often observed for areas of rippled flow.

Table 5.14. Summary of individual SFT user’s accuracies by method and date of survey.

User’s Accuracy (%)	Site Date	Arrow		
		May-13	Jun-13	Aug-13
Bankside SFT Mapping	Smooth	71.0	66.67	64.71
	USW	79.4	85.71	58.33
	Rippled	50.0	61.11	37.50
	NPF	66.7	71.43	100.00
	Upwelling	28.6	100.00	0.00
UAS-SfM SFT Mapping	Smooth	85.7	44.00	48.48
	USW	83.3	76.47	73.33
	Rippled	58.3	33.33	0.00
	NPF	80.0	100.00	N/a
	Upwelling	75.0	100.00	33.33

Incorrectly Mapped SFTs

The stacked bar charts in Figure 5.10 provide further insight into how SFTs are incorrectly mapped by the UAS-SfM survey. For example, the SFT smooth is most commonly mapped as smooth by all the UAS surveys. However, when it is incorrectly mapped, it is most often instead mapped as rippled, with some areas mis-mapped as unbroken standing waves, no perceptible flow or upwelling. Unbroken standing waves are most often mis-mapped as smooth or rippled flow, with a very small percentage also mis-mapped as no perceptible flow. Areas of ripples are frequently incorrectly mapped as unbroken standing waves and sometimes as smooth flow, upwelling or no perceptible flow. No perceptible flow is mapped correctly most of the time, but is occasionally mis-mapped as smooth flow. Areas of upwelling are usually correctly mapped, but have also been confused with unbroken standing waves and areas of rippled flow. Where mis-mapping occurs, SFTs are sometimes confused with those which are adjacent to them on the SFT continuum (Figure 5.1), but this is not a consistent pattern (Figure D11, Appendix D).

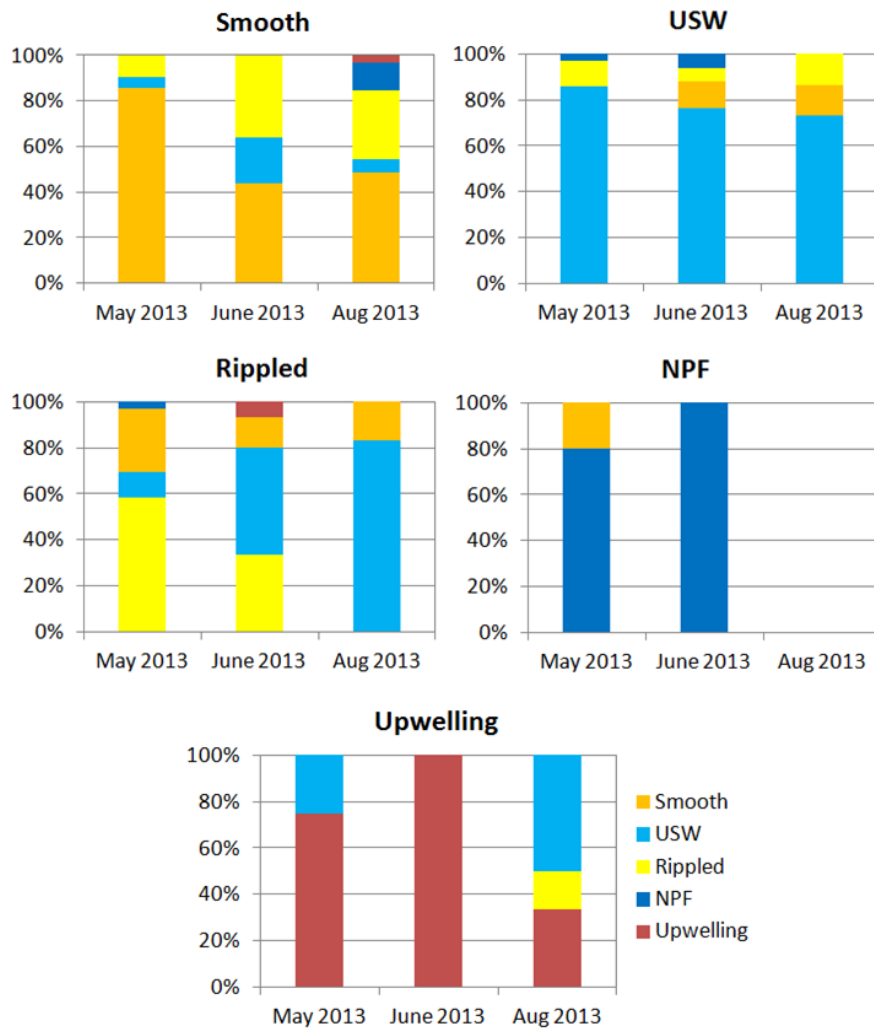


Figure 5.10. Stacked bar charts indicating how ground truth SFTs are mapped by the UAS-SfM survey, by SFT and date of survey.

5.5.3 Differentiating surface flow types using quantitative UAS-SfM outputs

Research Question 3

Does the use of quantitative information derived from the UAS-SfM process (i.e. refraction corrected water depth and point cloud roughness) help to differentiate between SFTs?

Water Depth

The water depth data derived from each UAS-SfM survey is shown in Figures 5.12 to 5.15. Water depth information derived from the UAS-SfM approach is not used alone to test SFT separability but instead used in combination with point cloud roughness within an ANOSIM test (see below).

Given the high flow level and increased turbidity during the River Arrow July 2012 survey, it was not possible to 'see' the channel bed. Therefore, water depth was not computed from the UAS-SfM outputs for this survey. Furthermore, the high flow levels prohibited a ground truth survey being undertaken at this time, meaning that even if water depth were to be computed, an accompanying accuracy assessment would not have been possible. Hence, this dataset is not used in further analysis.

Point Cloud Roughness

The roughness data for each survey is displayed in Figures 5.11 to 5.16. Figure 5.16 shows roughness distribution profiles for the 'core' areas of each SFT for each survey. These graphs provide an indication of how separable the SFTs are in terms of their roughness profiles. Roughness profile graphs were also produced for the whole SFT polygons and show a similar pattern (Figure D12, Appendix D).

It is not easy to differentiate between SFTs based on their point cloud roughness profiles, especially for the survey acquired at the River Arrow in July 2012. However, SFT separation is evident in some situations. For example, smooth and upwelling can be separated for the surveys undertaken at the River Arrow in May and June 2013, but this pattern is less clear for the August 2013 survey at the Arrow and upwelling is not mapped on the July 2012 survey. Where broken standing waves are present at the Coledale Beck site, it may be possible to differentiate these from smooth areas where the roughness tends to be lower.

Figure 5.17 provides a summary of the roughness data by each SFT. This figure allows an assessment of the consistency of roughness within each SFT between the different surveys. For most SFTs there is a lack of consistency within the roughness data as indicated by variable mean roughness values, variable ranges and a variable standard deviation of the roughness. The exceptions are areas of upwelling, which show a mean roughness of c. 0.03 across all three surveys (although range remains variable). A pattern can also be observed for the smooth SFT where mean roughness is greater than 0.02 for the Arrow surveys in July 2012 and August 2013 (when conditions were dull and overcast) and consistently less than 0.01 for all other surveys (when conditions were bright and sunny).

Quantifying physical river habitat parameters using hyperspatial resolution
UAS imagery and SfM-photogrammetry

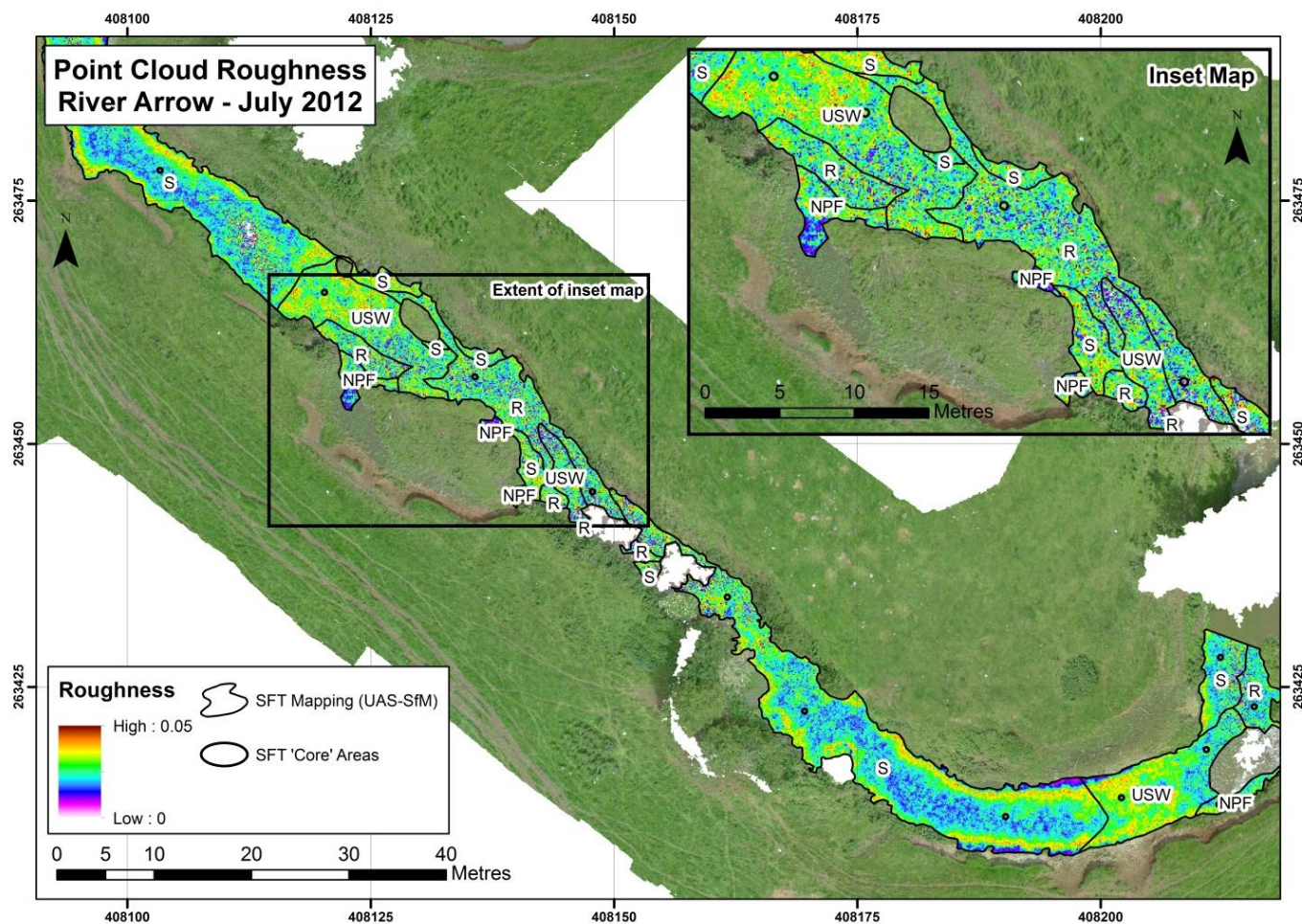


Figure 5.11. Point cloud roughness data derived from the UAS-SfM process for the River Arrow July 2012 dataset. The SFT units mapped from the orthophoto are shown as polygons, and the SFT 'core' areas as small black circles. Code to SFTs: S (smooth), R (rippled), NPF (no perceptible flow), USW (unbroken standing waves), UP (upwelling).

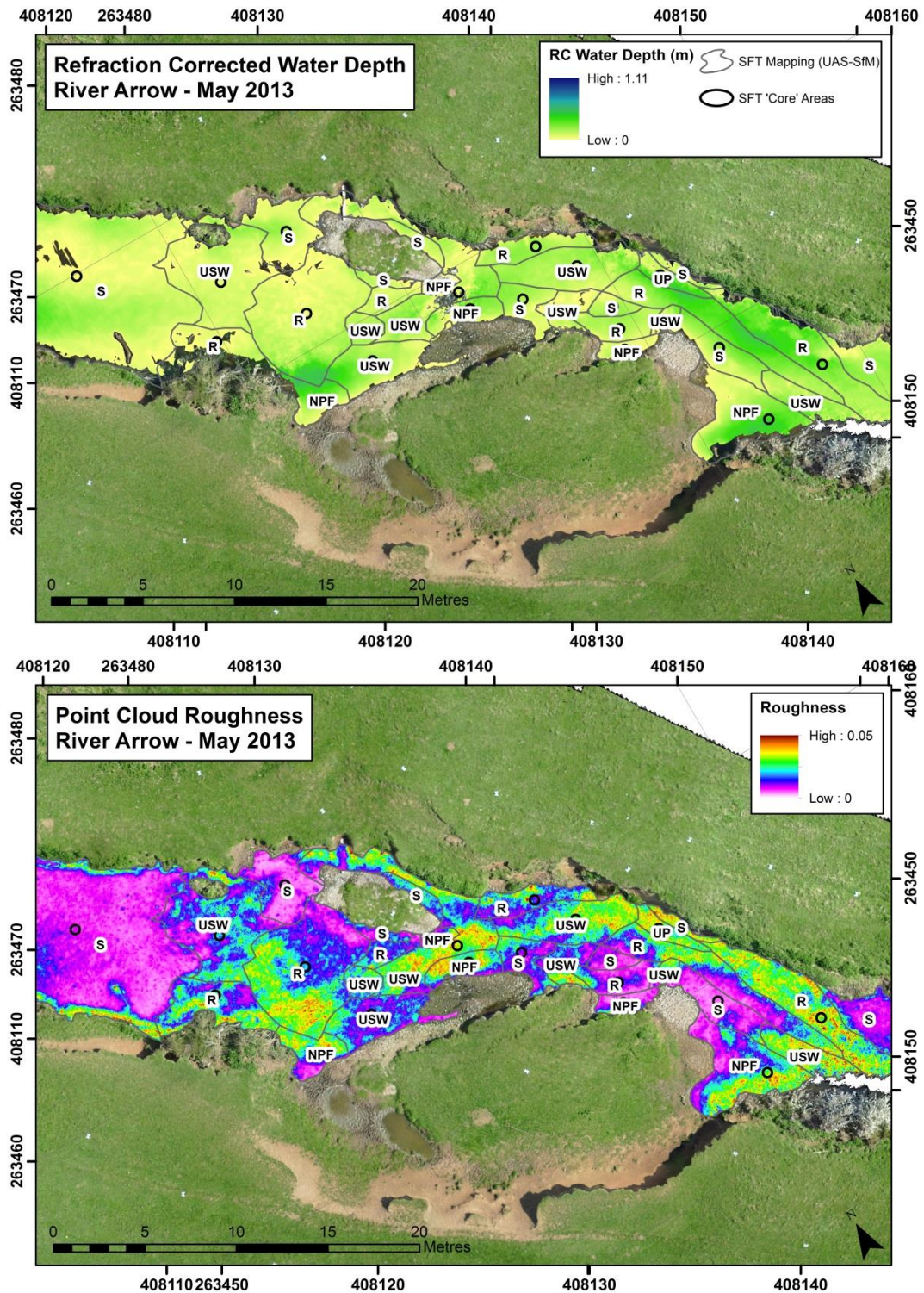


Figure 5.12. Refraction corrected water depth and point cloud roughness data derived from the UAS-SfM process for the River Arrow May 2013 dataset. The SFT units mapped from the orthophoto are shown as polygons, and the SFT 'core' areas as small black circles. Code to SFTs: S (smooth), R (rippled), NPF (no perceptible flow), USW (unbroken standing waves), UP (upwelling).

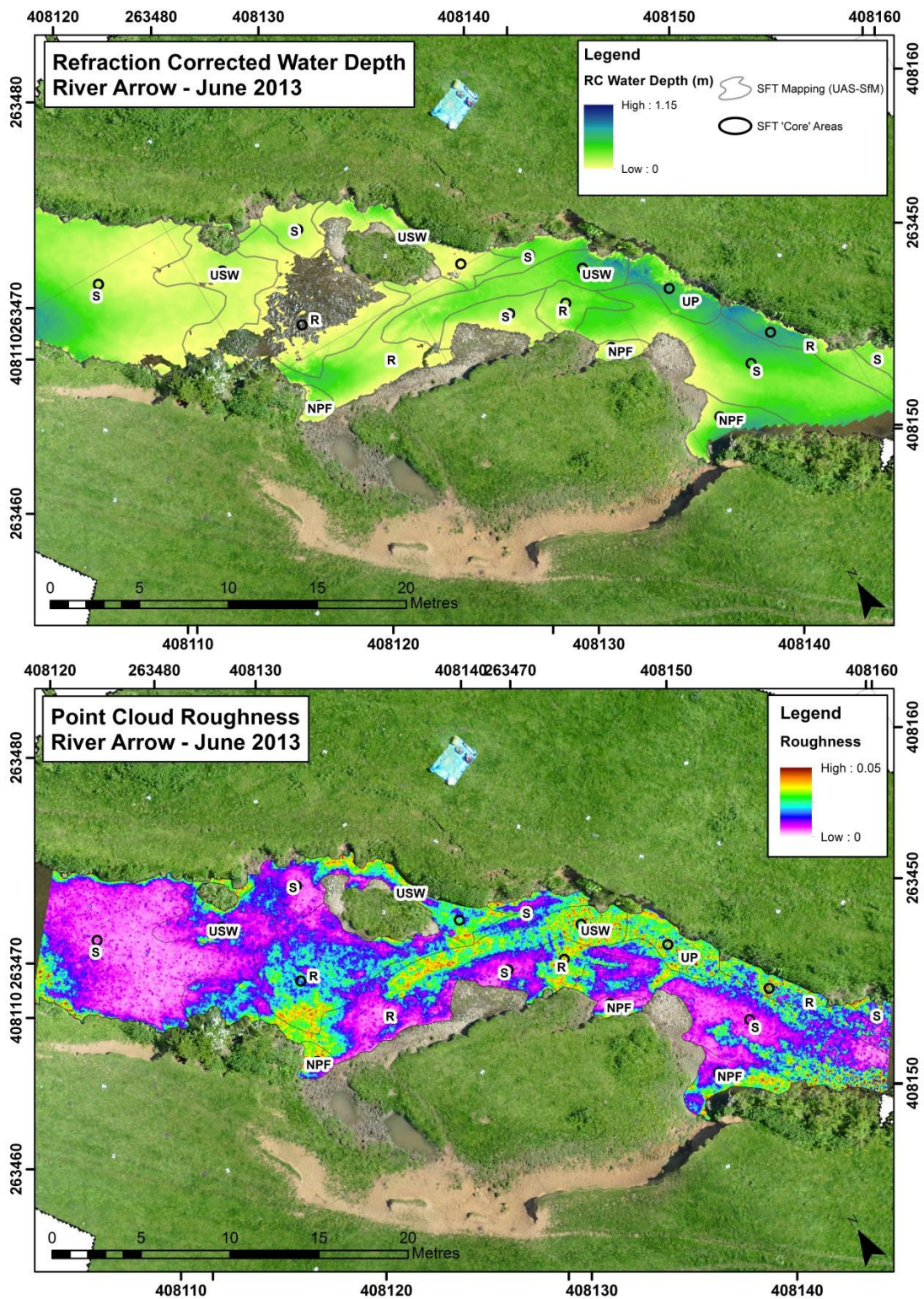


Figure 5.13. Refraction corrected water depth and point cloud roughness data derived from the UAS-SfM process for the River Arrow June 2013 dataset. The SFT units mapped from the orthophoto are shown as polygons, and the SFT 'core' areas as small black circles. Code to SFTs: S (smooth), R (rippled), NPF (no perceptible flow), USW (unbroken standing waves), UP (upwelling).

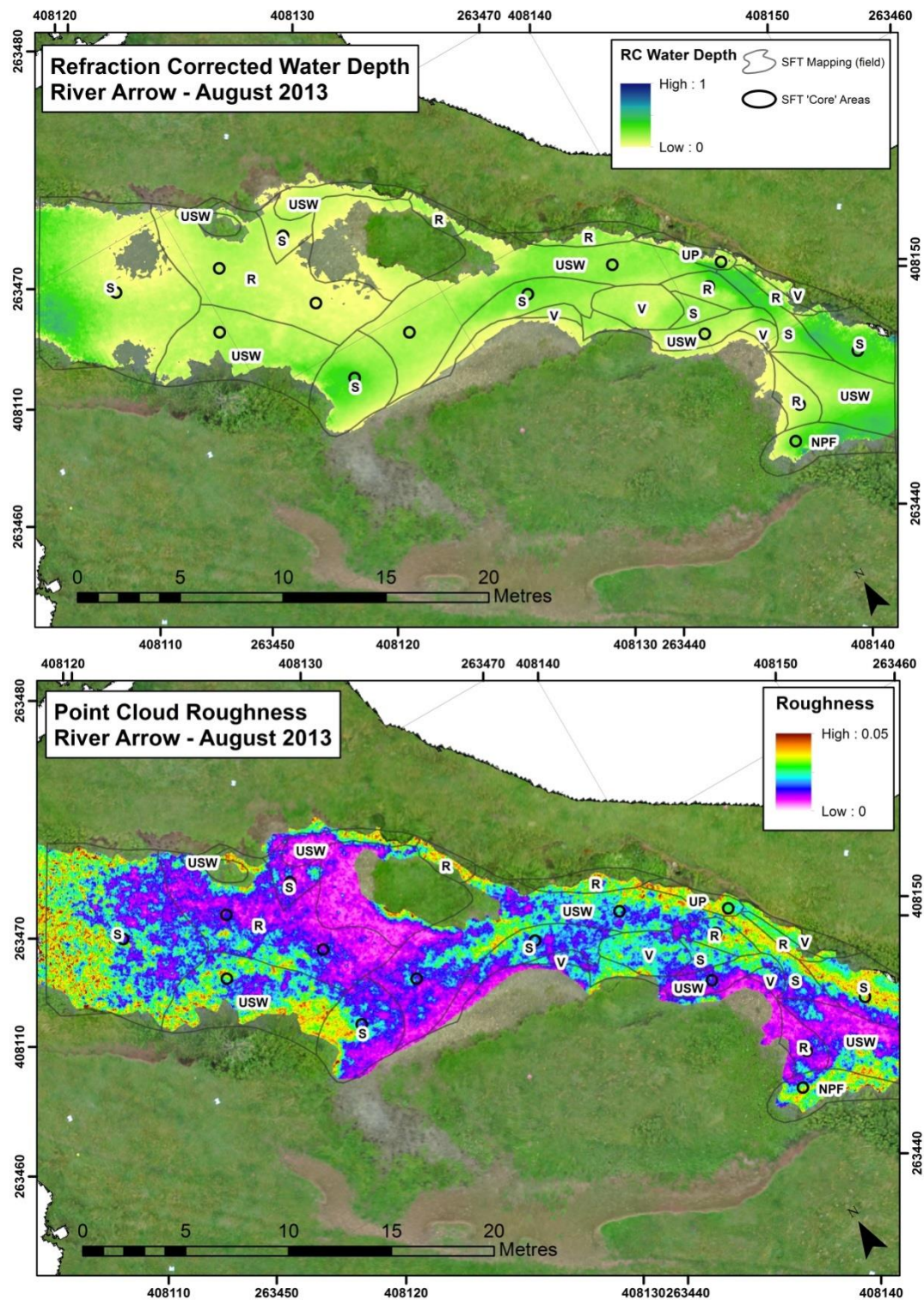


Figure 5.14. Refraction corrected water depth and point cloud roughness data derived from the UAS-SfM process for the River Arrow August 2013 dataset. The SFT units mapped from the orthophoto are shown as polygons, and the SFT 'core' areas as small black circles. Code to SFTs: S (smooth), R (rippled), NPF (no perceptible flow), USW (unbroken standing waves), UP (upwelling). Areas labelled V denote patches of submerged aquatic vegetation.

Quantifying physical river habitat parameters using hyperspatial resolution
UAS imagery and SfM-photogrammetry

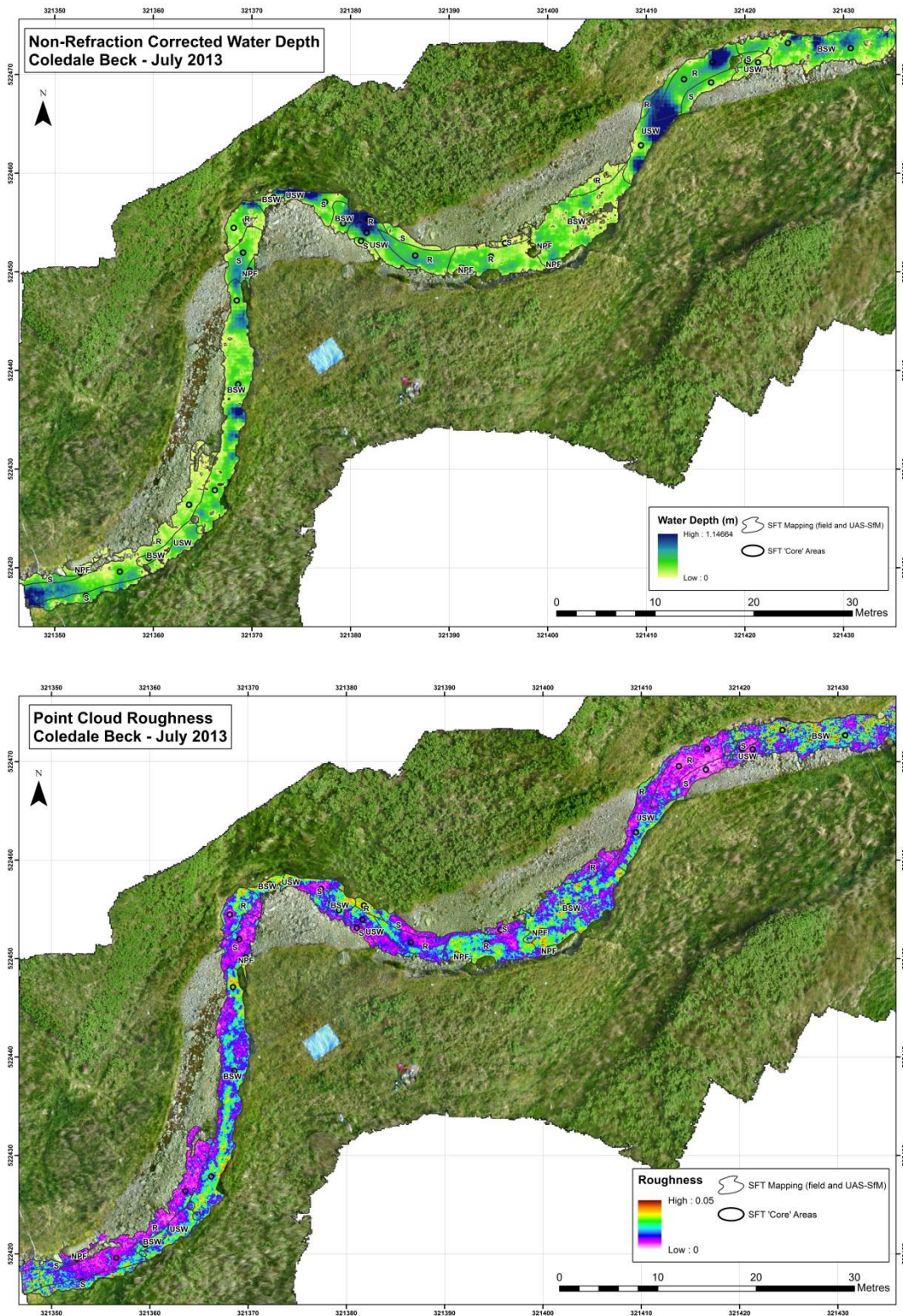


Figure 5.15. Refraction corrected water depth and point cloud roughness data derived from the UAS-SfM process for the Coledale Beck July 2013 dataset. The SFT units mapped from the orthophoto are shown as polygons, and the SFT 'core' areas as small black circles. Code to SFTs: S (smooth), R (rippled), NPF (no perceptible flow), USW (unbroken standing waves), UP (upwelling).

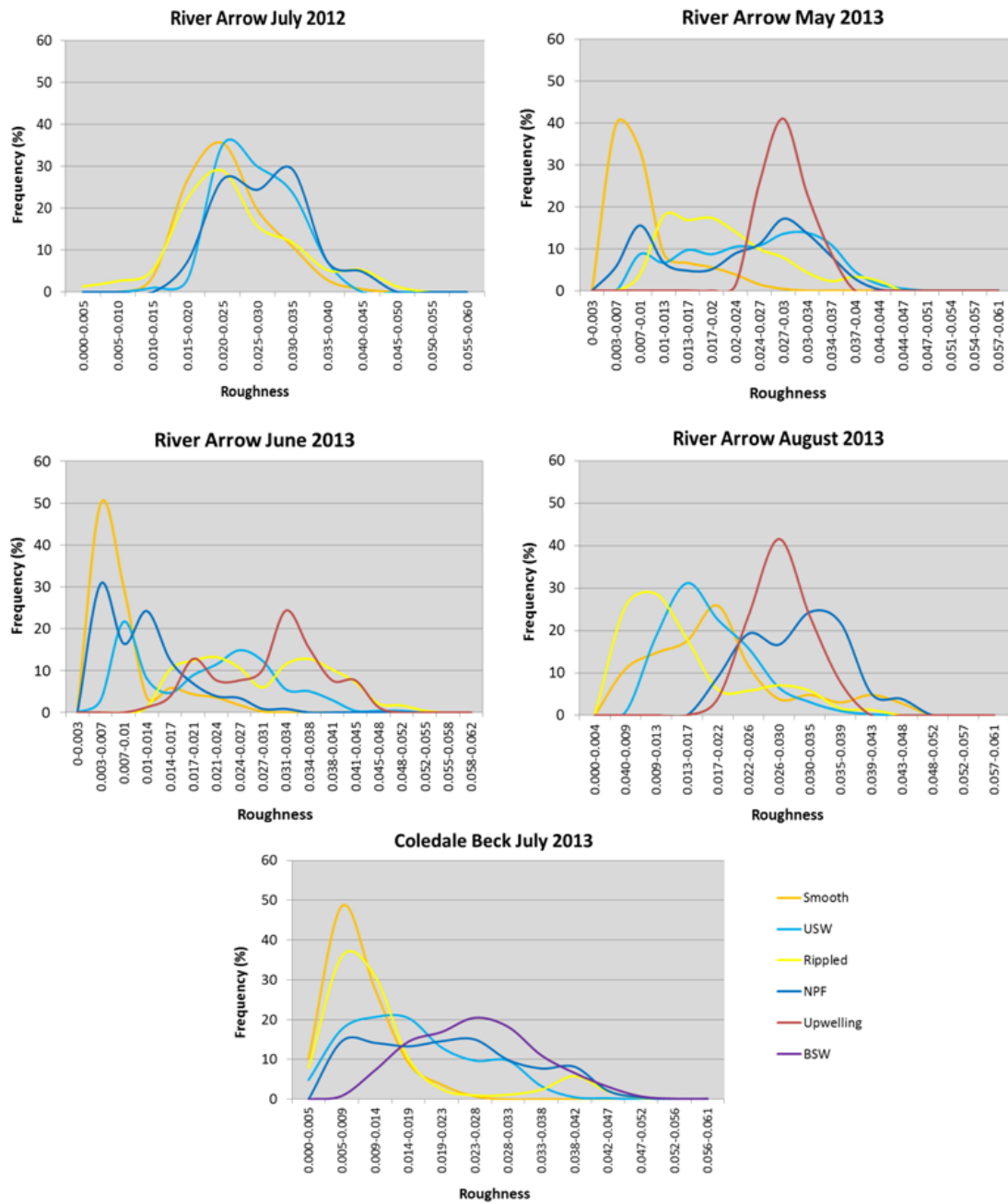


Figure 5.16. Roughness distributions profiles by site and by SFT (for SFT core areas only).

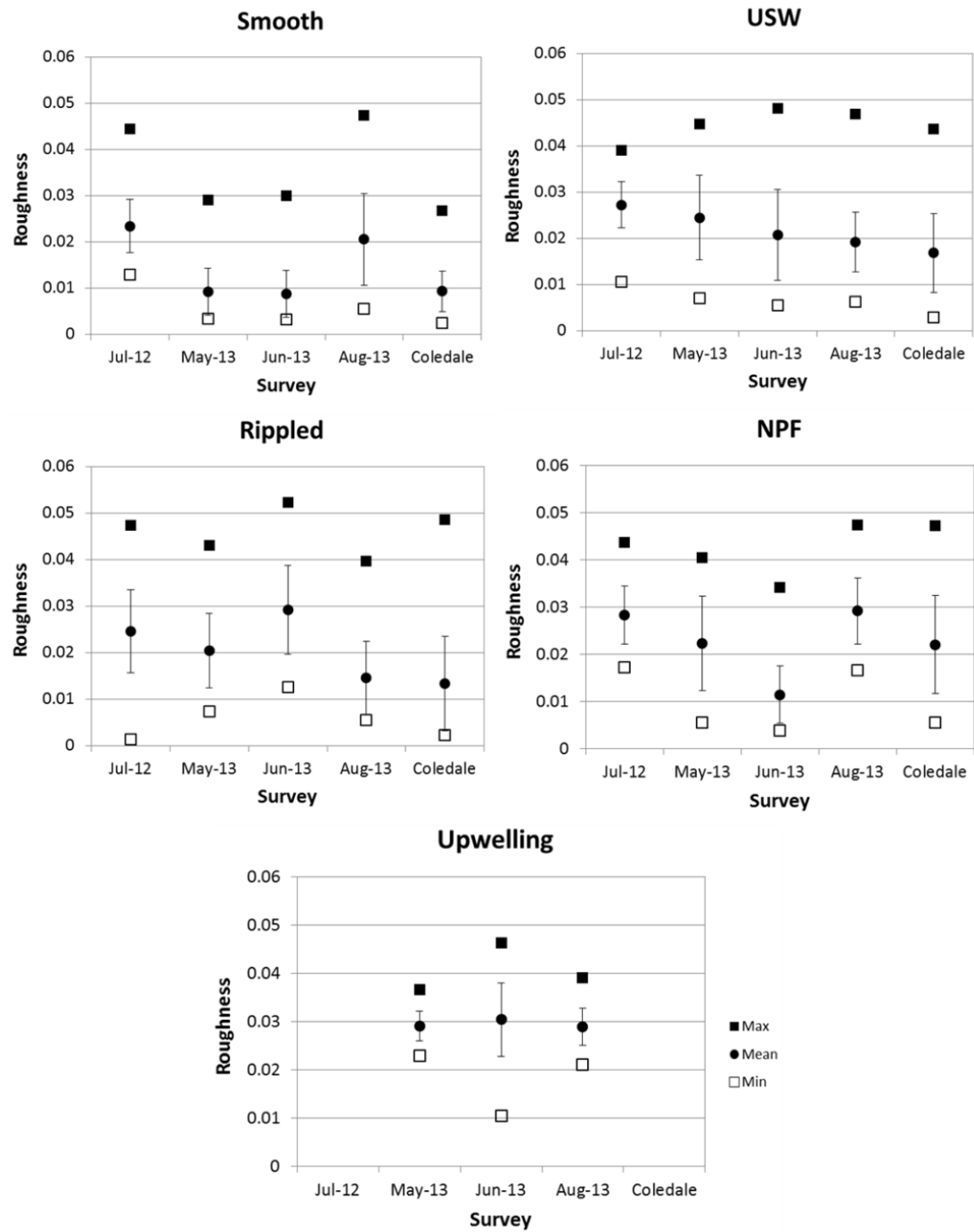


Figure 5.17. Roughness distributions for the core area of each SFT, by survey. The error bars represent one standard deviation of roughness either side of the mean roughness.

Hydraulic Variables

The measures of water depth and mean column velocity acquired during the ground truth survey were plotted against roughness for all applicable surveys (Figures 5.18 to 5.21). These

figures indicate that typically, deeper (> c. 0.35m) and faster flowing (> c. 0.8m/s) waters produce only relatively high roughness values (> c. 0.025). However, such high roughness values are also observed in shallower and slower flowing areas. This suggests that larger water depths and faster flowing water are not the only factors influencing point cloud roughness. Similar results are obtained when roughness is plotted against Froude number (Figures D13 to D16, Appendix D).

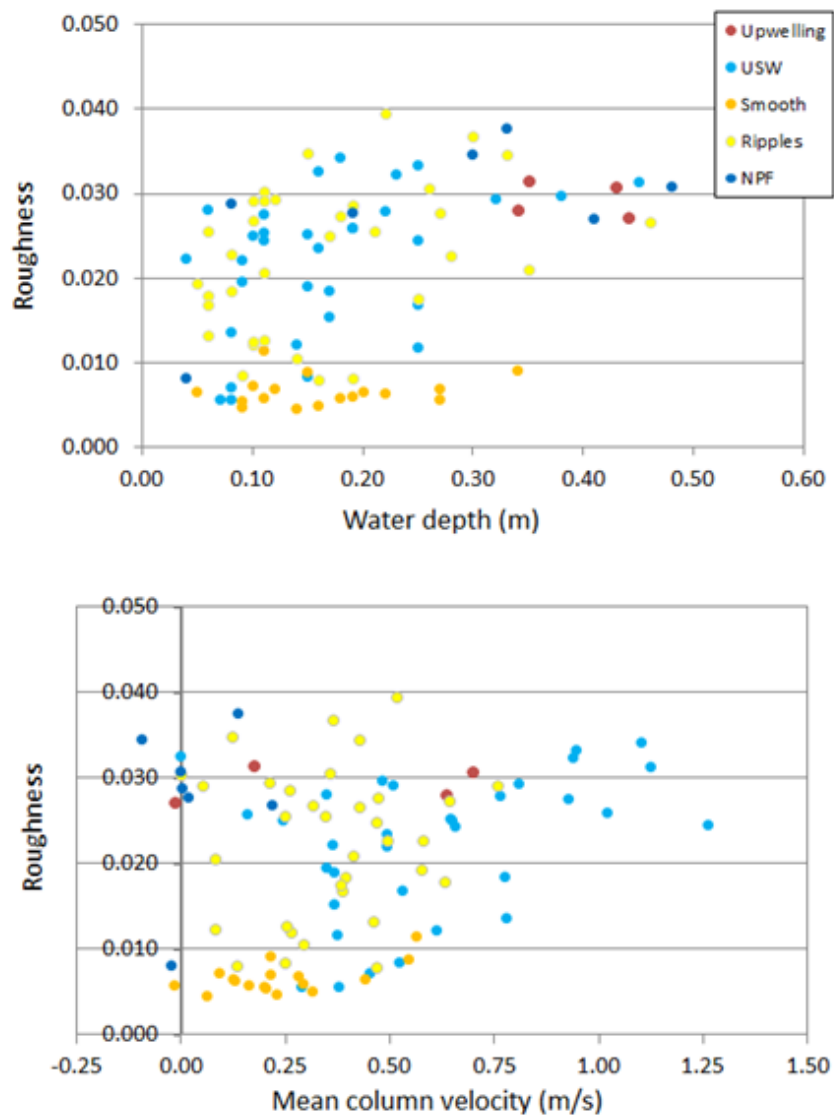


Figure 5.18. Point cloud roughness from the River Arrow May 2013 survey regressed against field-measured hydraulic variables water depth and mean column velocity.

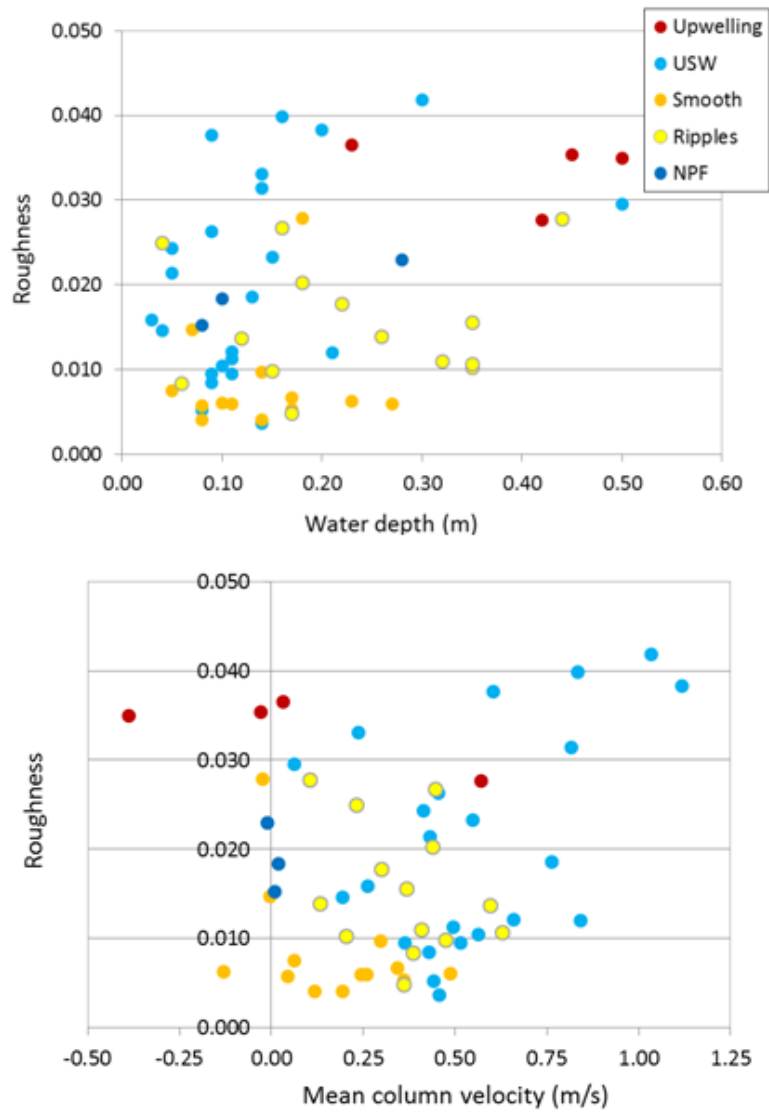


Figure 5.19. Point cloud roughness from the River Arrow June 2013 survey regressed against field-measured hydraulic variables water depth and mean column velocity.

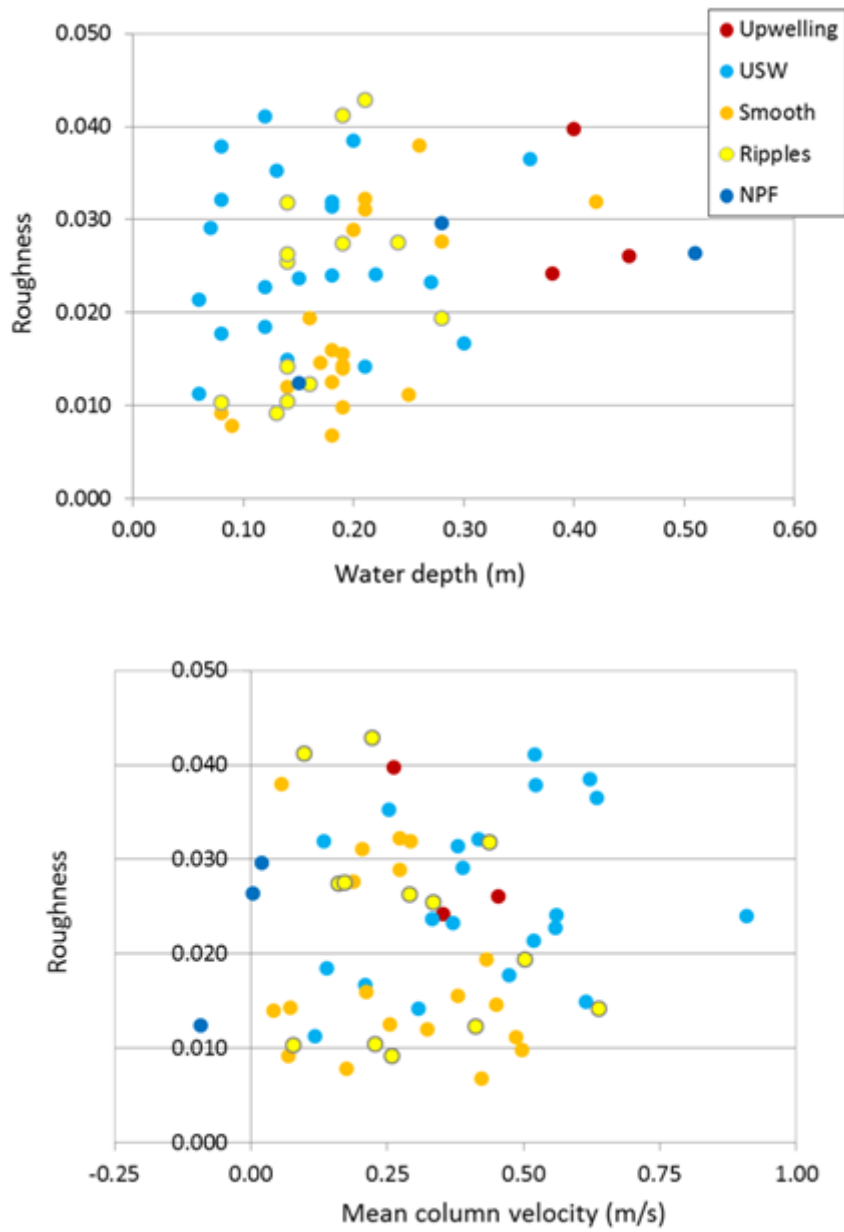


Figure 5.20. Point cloud roughness from the River Arrow August 2013 survey regressed against field-measured hydraulic variables water depth and mean column velocity.

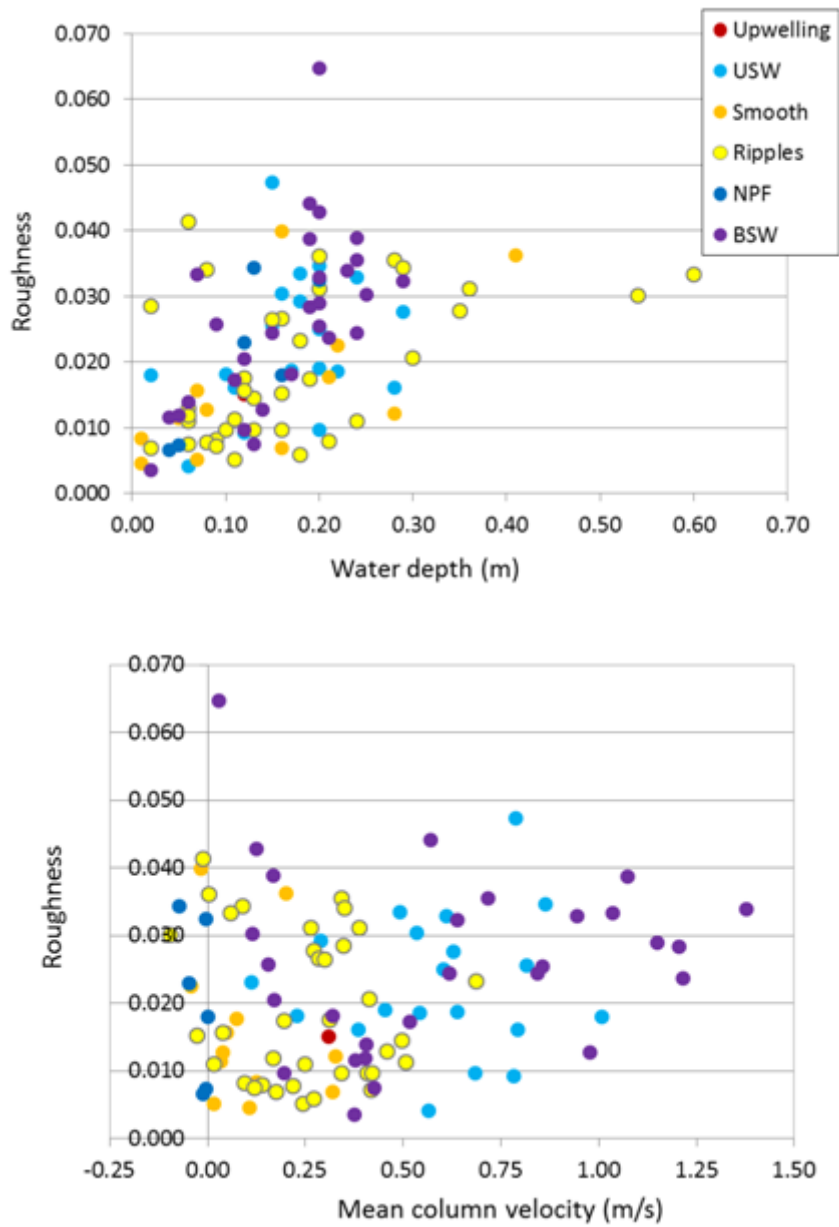


Figure 5.21. Point cloud roughness from the Coledale Beck July 2013 survey regressed against field-measured hydraulic variables water depth and mean column velocity.

Analysis of Similarity (ANOSIM)

Global Comparison

Given the similarity of the SFT roughness profiles within the Arrow July 2012 dataset, these data were not used in the ANOSIM tests. The global R and global significance values (or p values) for all other surveys and scenarios are presented in Table 5.15. The global R statistic values are generally low and vary between 0.12 and 0.32. This suggests that there is some difference between SFTs, but that these differences are not particularly strong. The global R values are typically highest, and therefore the SFTs most differentiable, for Scenario B (ground truth survey data only), with the exception of the River Arrow data acquired in August 2013. Scenario A (UAS-SfM data only) consistently produces the lowest global R values, and in almost all cases the addition of point cloud roughness to the ground truth depth and velocity data (in Scenario C) does not help to differentiate between SFTs. The global significance levels (p values) for almost all surveys and scenarios are below the 5% threshold (i.e. $p < 0.05$), indicating statistically significance differences between SFTs, with the exception of Scenario A at Coledale Beck.

Table 5.15. Global ANOSIM test results by survey and scenario.

Dataset	Scenario	Global R	Global Significance (p value)
Arrow May 2013	A	0.183	0.001
	B	0.279	0.001
	C	0.275	0.001
Arrow June 2013	A	0.221	0.001
	B	0.318	0.001
	C	0.282	0.001
Arrow August 2013	A	0.184	0.002
	B	0.197	0.002
	C	0.207	0.001
Coledale July 2013	A	0.041	0.094
	B	0.144	0.001
	C	0.118	0.001

Pair-wise Comparisons

The pairwise comparisons for all SFTs are shown in Tables 5.16 to 5.19 and Figure 5.22. Pairwise comparisons comprising BSW are not provided for Scenario A for the Arrow May

2013 data because the SfM process failed to produce a reliable refraction-corrected water depth value in the area of BSW. Furthermore, this SFT was not recorded by the ground truth survey or the UAS mapping during the River Arrow June or August campaigns.

Within survey variability

For the River Arrow May 2013 survey (Table 5.16) no statistical differences were observed between SFT pairs NPF/UP and USW/R across all scenarios. The greatest statistically significant differences (as indicated by higher R values and p values of less than 0.05) were observed between SFT pairs USW/UP and S/UP for all scenarios, between USW/NPF and R/UP for scenarios B and C, and for most pairwise combinations featuring BSW.

The River Arrow June 2013 survey (Table 5.16) suggests no statistically significant difference between USW/NPF for scenarios A and C and between S/NPF and R/NPF for all scenarios. All scenarios demonstrate a statistically significant difference between S/UP and USW/UP. Furthermore, scenario A is able to differentiate NPF/UP, scenario B USW/NPF and scenario C R/UP.

All scenarios show a lower degree of separation for SFT pairs S/R and S/USW for the River Arrow August 2013 dataset, as indicated by lower R values. Scenario A also shows that NPF/UP are not separable statistically and scenarios B and C cannot distinguish between USW/R. For all scenarios, a statistically significant difference is observed for USW/NPF, with scenarios B and C providing good separation of S/UP, USW/UP and R/UP.

The results for Coledale Beck generally show a poor degree of separation for pair-wise SFT comparisons, with many comparisons not meeting the 5% significance level (i.e. $p > 0.05$). The exceptions are USW/NPF and S/USW which can be best differentiated under scenarios B or C.

Table 5.16. Pairwise ANOSIM test results for the River Arrow May 2013 survey, by scenario. Values highlighted in bold indicate pairwise combinations where the R value is greater than 0.5 and the significance level is less than the 5% threshold (i.e. $p < 0.05$).

Dataset	River Arrow May 2013					
	Scenario A		Scenario B		Scenario C	
Groups	R Statistic	Sig. level (p value)	R Statistic	Sig. level (p value)	R Statistic	Sig. level (p value)
S, USW	0.19	0.001	0.249	0.001	0.234	0.001
S, R	0.101	0.015	0.114	0.002	0.136	0.003
S, NPF	0.261	0.002	0.428	0.001	0.436	0.001
S, UP	0.444	0.002	0.79	0.001	0.642	0.001
USW, R	0.039	0.111	0.051	0.052	0.025	0.158
USW, NPF	0.395	0.001	0.661	0.001	0.654	0.001
USW, UP	0.73	0.001	0.776	0.001	0.719	0.001
R, NPF	0.191	0.010	0.406	0.001	0.426	0.001
R, UP	0.365	0.001	0.564	0.004	0.507	0.005
NPF, UP	-0.196	0.830	0.174	0.150	0.111	0.252
NPF, BSW	n/a	n/a	0.982	0.091	0.924	0.091
R, BSW	n/a	n/a	0.932	0.036	0.892	0.036
USW, BSW	n/a	n/a	0.881	0.027	0.814	0.027
S, BSW	n/a	n/a	0.999	0.032	0.964	0.032
BSW, UP	n/a	n/a	0.556	0.250	0.556	0.250

Table 5.17. Pairwise ANOSIM test results for the River Arrow June 2013 survey, by scenario. Values highlighted in bold indicate pairwise combinations where the R value is greater than 0.5 and the significance level is less than the 5% threshold (i.e. $p < 0.05$).

Dataset	River Arrow June 2013					
	Scenario A		Scenario B		Scenario C	
Groups	R Statistic	Sig. level (p value)	R Statistic	Sig. level (p value)	R Statistic	Sig. level (p value)
S, USW	0.099	0.057	0.271	0.001	0.217	0.010
S, R	0.22	0.006	0.204	0.004	0.266	0.001
S, NPF	0.288	0.082	0.066	0.302	0.285	0.079
S, UP	0.962	0.002	0.728	0.004	0.956	0.001
USW, R	0.196	0.001	0.198	0.008	0.122	0.050
USW, NPF	-0.189	0.960	0.516	0.017	0.271	0.085
USW, UP	0.565	0.001	0.746	0.002	0.669	0.001
R, NPF	-0.083	0.628	0.335	0.026	0.256	0.076
R, UP	0.504	0.003	0.472	0.004	0.696	0.003
NPF, UP	0.944	0.029	0.259	0.143	0.481	0.057

Table 5.18. Pairwise ANOSIM test results for the River Arrow August 2013 survey, by scenario. Values highlighted in bold indicate pairwise combinations where the R value is greater than 0.5 and the significance level is less than the 5% threshold (i.e. $p < 0.05$).

Dataset	River Arrow August 2013					
	Scenario A		Scenario B		Scenario C	
Groups	R Statistic	Sig. level (p value)	R Statistic	Sig. level (p value)	R Statistic	Sig. level (p value)
S, USW	0.145	0.007	0.093	0.014	0.153	0.001
S, R	0.016	0.311	-0.045	0.802	0.007	0.405
S, NPF	0.249	0.085	0.591	0.009	0.489	0.021
S, UP	0.287	0.076	0.701	0.001	0.593	0.003
USW, R	0.212	0.003	-0.004	0.487	0.019	0.326
USW, NPF	0.627	0.003	0.712	0.001	0.675	0.001
USW, UP	0.373	0.028	0.687	0.001	0.629	0.003
R, NPF	0.017	0.414	0.676	0.004	0.516	0.009
R, UP	0.054	0.345	0.864	0.002	0.651	0.002
NPF, UP	-0.185	0.800	0.556	0.100	0.481	0.100

Table 5.19. Pairwise ANOSIM test results for the Coledale Beck July 2013 survey, by scenario. Values highlighted in bold indicate pairwise combinations where the R value is greater than 0.5 and the significance level is less than the 5% threshold (i.e. $p < 0.05$).

Dataset	Coledale Beck July 2013					
	Scenario A		Scenario B		Scenario C	
Groups	R Statistic	Sig. level (p value)	R Statistic	Sig. level (p value)	R Statistic	Sig. level (p value)
S, USW	0.039	0.239	0.533	0.001	0.447	0.001
S, R	-0.033	0.626	0.047	0.241	0.009	0.396
S, NPF	0.073	0.218	-0.12	0.882	-0.068	0.693
S, UP	-0.187	0.583	-0.136	0.615	-0.255	0.769
USW, R	0.048	0.127	0.189	0.002	0.13	0.015
USW, NPF	-0.093	0.741	0.683	0.001	0.533	0.001
USW, UP	-0.153	0.700	0.065	0.333	-0.045	0.524
R, NPF	-0.012	0.475	0.04	0.354	0.013	0.437
R, UP	-0.145	0.743	-0.33	1.000	-0.368	1.000
NPF, UP	-0.311	1.000	0.6	0.143	0	0.714
NPF, BSW	0.002	0.448	0.235	0.016	0.205	0.025
R, BSW	0.072	0.019	0.149	0.002	0.166	0.001
USW, BSW	0.033	0.201	-0.02	0.681	-0.038	0.861
S, BSW	0.171	0.025	0.219	0.007	0.227	0.004
BSW, UP	-0.102	0.593	-0.194	0.862	-0.183	0.828

Across survey variability

A comparison of the separability of SFT pairs across the different scenarios (based on the global R values) indicates that Scenario A is typically less able to differentiate between SFT pairs than Scenarios B and C, with Scenario B producing the highest R values. Discounting the data from Coledale Beck, which produces consistently poor results, the most consistent separation is observed for S/UP and USW/UP for scenario A. These pairwise combinations produce strong R values for scenarios B and C too. Scenarios B and C also produce fairly consistent high R values for SFT pairs USW/NPF and R/UP, which are almost always statistically significant (the exception is USW/NPF for scenario C of the River Arrow June 2013 survey). The lowest R values are observed for S/USW, S/R, USW/R and R/NPF for Scenario A. Scenarios B and C also produce low R values which are not statistically significant for the SFT pairs S/R and USW/R.

5.6 Discussion

5.6.1 Surface flow type mapping from UAS-SfM orthophotos

Research Question 1

How does the spatial extent and classification of SFT mapping at the mesoscale vary between a) that conducted by eye from a bank-side location in the field and b) that mapped directly from the UAS-SfM orthophoto?

Research Question 2

How accurate and repeatable is the SFT mapping conducted on the UAS-SfM orthophoto and how does the accuracy vary between different SFTs and different surveys?

SFT mapping conducted from the UAS-SfM orthophoto showed a good qualitative agreement with SFT mapping conducted from the bankside as found by other similar studies (Hardy et al., 1994, Reid and Thoms 2009), but a quantitative assessment revealed variable levels of agreement between SFTs from these different mapping approaches. The strongest agreement was found between areas of smooth flow, and in some cases for areas of upwelling (although the latter is based on relatively few data points). Higher levels of agreement were typically observed for the datasets collected at the Arrow in May and June 2013, as opposed to those collected in July 2012 and August 2013. It is thought that this relates to the poor scene illumination conditions during these latter surveys. This results in no sun glint on the water surface which makes the identification of SFTs from the UAS imagery more challenging. Given the paucity of existing research on mapping SFTs, no other studies are known to have commented on the reliance of accurate SFT mapping on adequate scene illumination.

The overall accuracy of the UAS-SfM SFT mapping in comparison with the ground truth data was highly variable by survey and ranged from 48% (Arrow August 2013) to 75% (Arrow May 2013). Again this higher accuracy value was obtained from a survey where illumination conditions were bright and clear. The work of Marcus (2002) presents overall accuracy values of 75% for their mapping of in-stream habitat units using high resolution hyperspectral data, whilst Marcus et al., (2003) find overall accuracy varies from 69% for third order streams to 86% for fifth order streams. As such, it would seem that a UAS-SfM approach is capable of producing SFT mapping with accuracies at or below the level of these existing studies, although it should be noted that differing scales may be playing a role here.

Few other existing studies provide quantitative assessment of the accuracy of SFT mapping from remotely sensed data which can be used for comparison.

For this study, a number of factors can be identified which may be affecting the accuracy of the UAS-SfM SFT mapping (as defined by comparison with both bankside mapped SFTs and ground truthing). These comprise the following;

1. **SFTs have indistinct boundaries.** The delineation of SFTs with crisp boundaries is often difficult and perhaps misleading. Some existing research has made use of transition zones when conducting SFT (or biotope) mapping, to account for or remove these indistinct or fuzzy boundaries between different SFTs (Marcus 2002, Marcus et al., 2003, Legleiter and Goodchild 2005, Milan et al., 2010, Wallis et al., 2010). Within this study, those points used to assess accuracy (or agreement) which are located on or near the SFT boundaries are therefore more likely to be misclassified. Figures 5.22 to 5.24 indicate the location of incorrectly classified points which fall within the vicinity of SFT boundaries (defined as within c. 0.3m). These potential misclassifications account for between 7% and 44% of all 'inaccurate' points, and are likely to have a greater impact on SFTs with smaller spatial extents. In future, an UAS-SfM SFT mapping approach which makes use of fuzzy logic or transition zones might be beneficial for providing a more faithful representation of hydraulic habitat distribution.
2. **The UAS-SfM orthophoto offers a single snapshot in time.** Therefore, the SFT mapping conducted from this imagery struggles to differentiate between those SFTs which are usually defined by temporal variability of their spatial pattern. For example, this might result in areas of ripples being misclassified as USW, and NPF being misclassified as smooth flow. The work of Milan et al., (2010) also found difficulty in differentiating between ripples and USW based on their surface expressions alone. Figures 5.22 to 5.24 demonstrate where this might be occurring within this work. Such potential misclassifications explain between 22% and 35% of the 'inaccurate' points observed in this study. However, this effect does not seem to be consistent across the different surveys and different SFTs. For example, ripples are often misclassified as USW, but USW is much less frequently mis-mapped as

ripples, which may suggest a complex interplay between the factors considered here.

3. **The UAS-SfM orthophoto offers a nadir viewing angle.** The success of SFT mapping from the UAS-SfM approach is affected by the at/near nadir view angle and by illumination conditions at the time of image capture. The at nadir view makes SFT identification more tricky than at an oblique angle, and therefore may reduce accuracy of UAS-SfM mapping relative to the mapping conducted from an oblique angle on the bankside. Furthermore, the greater accuracy observed for the May and June surveys of the River Arrow is also thought to relate, in part, to scene illumination. Sun glint and reflections assist the identification of different SFTs as they highlight differences in the surface patterns. In contrast, the dull conditions experienced during the River Arrow August survey do little to highlight water surface patterns and therefore make it significantly more difficult to map SFTs.

4. **SFTs are highly dependent on flow level.** Recent research has demonstrated that flow level determines the type and spatial distribution of SFTs, with higher flow levels typically associated with a reduced diversity of SFTs (Zavadil et al., 2012). Flow conditions at the rivers studied here are known to change within the space of a few hours in response to rainfall events within the catchment upstream, and therefore SFT distribution is also likely to respond rapidly to these changes. Whilst efforts were made to conduct the SFT ground truthing and bankside mapping as close to the UAS survey as possible, in practice, these datasets were often collected the following day due to weather constraints on UAS flying, and the need to collect other datasets (for use in Chapters 3 and 4). Therefore, apparent classification errors in the UAS-SfM SFT mapping may relate to genuine changes in SFT resulting from changes in flow level.

5. **Ground truth SFT mapping may be inaccurate.** Apparent errors in the UAS-SfM SFT mapping may, in some cases, relate to errors or mistakes in the ground truth data which cannot be easily identified or removed.

Despite these difficulties, a number of key advantages of SFT mapping using a UAS-SfM approach are also evident. The outputs of such an approach are spatially continuous,

spatially explicit, provide a permanent record of site conditions at the time of survey and therefore offer significant advantages over the typical RHS type spot check surveys. Furthermore, the hyperspatial resolution ortho-imagery provides unprecedented levels of detail about SFTs, much greater than that demonstrated by existing studies using hyperspectral imagery for example (Marcus 2002, Marcus et al., 2003). The rapid mobilisation and rapid image acquisition using the UAS platform means that reach-scale lengths of channel (up to a few hundred metres) can easily be covered within half a day's fieldwork with a team of two people. These are larger areas and much quicker data acquisitions than are currently possible using a TLS for example (e.g. Large and Heritage 2007, Milan et al., 2010). Furthermore the rapid UAS mobilisation and use of a relatively inexpensive consumer-grade digital camera provides significant time and cost savings over the commissioning of multi- or hyper-spectral aerial surveys, as conducted by other SFT mapping studies (Marcus 2002, Marcus et al., 2003). Although areal coverage will undoubtedly be reduced using a UAS.

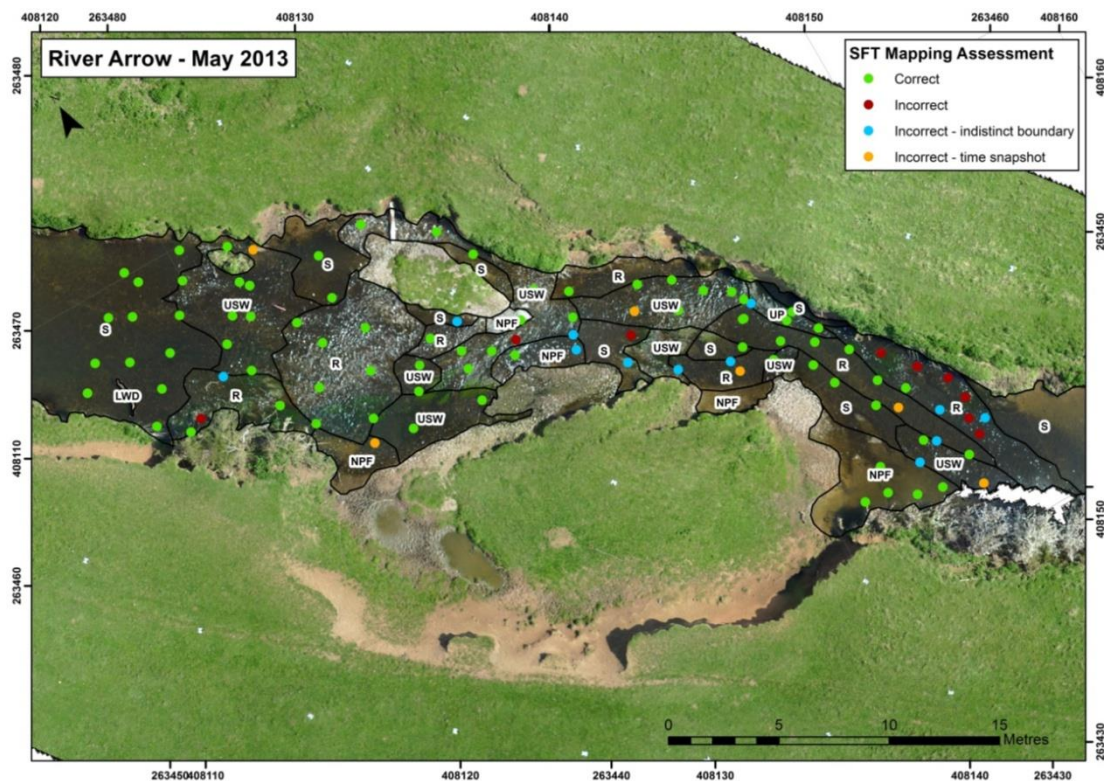


Figure 5.22. Spatial assessment of SFT mapping accuracy for the River Arrow May 2013 survey. Code to SFTs: S (smooth), R (rippled), NPF (no perceptible flow), USW (unbroken standing waves), UP (upwelling) and LWD indicates a piece of large woody debris.

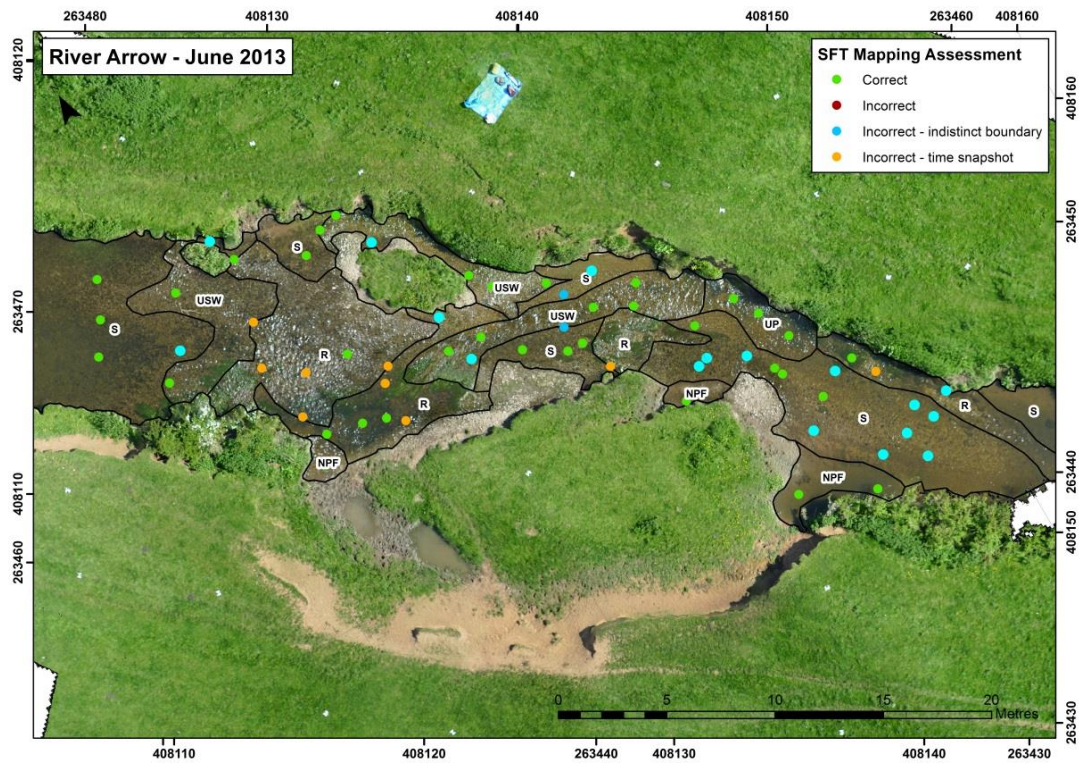


Figure 5.23. Spatial assessment of SFT mapping accuracy for the River Arrow June 2013 survey. Code to SFTs: S (smooth), R (rippled), NPF (no perceptible flow), USW (unbroken standing waves), UP (upwelling).

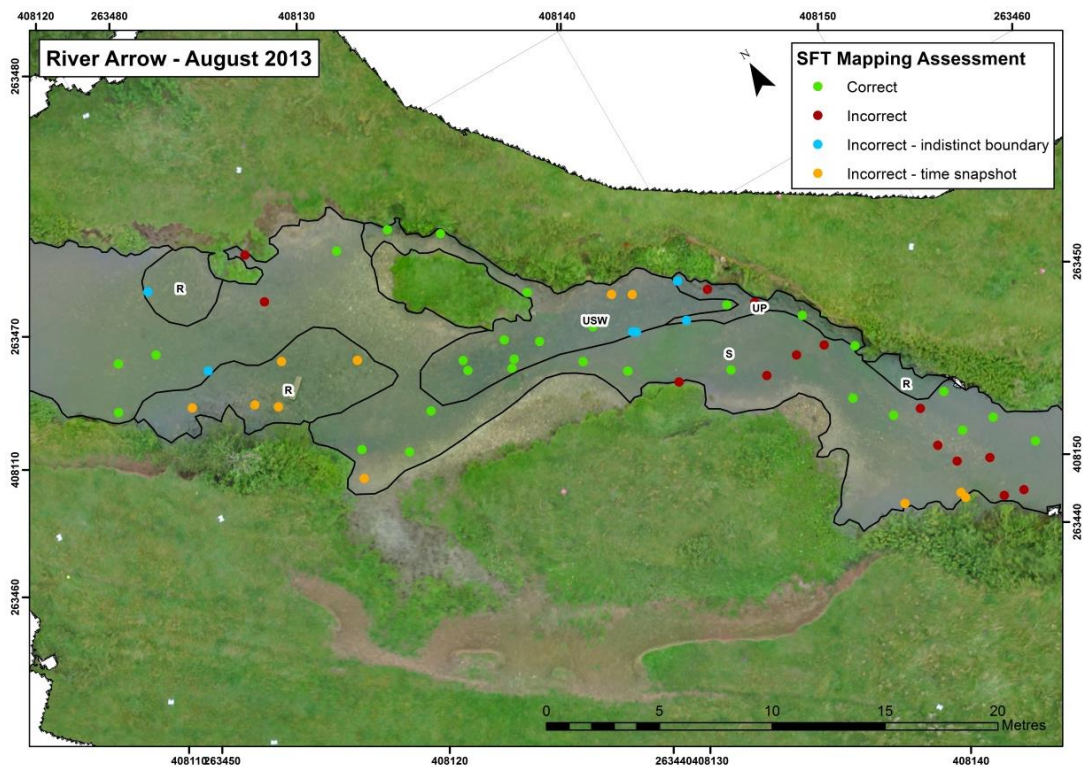


Figure 5.24. Spatial assessment of SFT mapping accuracy for the River Arrow August 2013 survey. Code to SFTs: S (smooth), R (rippled), NPF (no perceptible flow), USW (unbroken standing waves), UP (upwelling).

5.6.2 Differentiating surface flow types using quantitative UAS-SfM outputs

Research Question 3

Does the use of quantitative information derived from the UAS-SfM process (i.e. refraction corrected water depth and point cloud roughness) help to differentiate between SFTs?

SFT Separability

Limited success has been observed in differentiating SFTs based on the quantitative UAS-SfM outputs of depth and roughness. This is true for both the roughness profiles and the combination of depth and roughness used in the one-way ANOSIM tests. The ANOSIM tests consistently demonstrate that SFTs are less separable when defined by UAS-SfM derived depth and roughness (Scenario A) than when they are defined by field measures of water depth and mean column velocity (Scenario B). However, it should also be noted that whilst SFTs are more separable based on these field measures, that the global R values for this scenario (B) still remain fairly low (0.14-0.32).

It is likely that a combination of five key factors is responsible for this observed lack of separability of SFTs. Some or all of these factors will apply to the results from the roughness profiles and the three ANOSIM scenarios, as indicated below;

- 1) Errors in the water depth data derived from the UAS-SfM approach (scenarios A and C).
- 2) Noise in the point cloud roughness derived from the UAS-SfM approach (roughness profiles and scenarios A and C).
- 3) Errors in the SFT mapping (Roughness profiles and all scenarios).
- 4) The scale of assessment and the hydraulic nature of SFTs (roughness profiles and all scenarios).
- 5) SFTs as unreliable proxies for hydraulic heterogeneity (all scenarios).

Water Depth

Where necessary, the water depth data derived from the UAS-SfM process were corrected for the effects of refraction. As detailed in Chapter 3, whilst this has the effect of reducing the magnitude of water depth error it does not eliminate it entirely (Woodget et al., 2015). Furthermore, in some areas the SfM process may erroneously fix matching points within the water column itself, resulting in the areas where the DEM of the channel bed actually appears at a higher elevation than the estimated water surface. This has also been reported

in similar studies using through-water photogrammetry (e.g. Westaway et al., 2000) and results in holes in the water depth maps presented in Figures 5.12 to 5.15. As a result, it is likely that the UAS-SfM derived water depth measures are characterising the hydraulic nature of different SFTs with less success than those depth measures acquired in the field.

Point Cloud Roughness

A visual assessment of the roughness maps based on local site knowledge suggests that patterns of roughness are in some way related to the nature of hydraulic conditions. Figure 5.25 highlights where areas of greater roughness for the River Arrow May survey are associated with deep, fast flowing and/or rough surface waters. Such patterns are also evident for other surveys when conditions were bright and sunny (i.e. the River Arrow June and Coledale Beck datasets). Yet these observations are not borne out in the relationship between roughness and the field measured hydraulic variables of depth and mean column velocity, as shown in Figures 5.18 to 5.21 (or Froude number as shown in Figures D13 to D16 in Appendix D). Whilst greater depths and greater velocities always produce high roughness values, high roughness values are also observed in areas of lower depth and velocity. This suggests that point cloud roughness is being affected by a combination of different factors, the effects of which are likely to vary spatially throughout the scene. Such factors comprise;

1. **The quality of the input UAS imagery.** This is determined by scene illumination and platform stability. Images with some degree of blur are likely to introduce noise into the point cloud resulting in patches of higher roughness. Blur is likely to be spatially variable across the scene thereby introducing greater roughness in some areas.
2. **The depth of the water.** Where water depth is high, roughness is also always high (Figures 5.18 to 5.21). The 8-bit UAS imagery displays radiation intensities in 256 grey levels. This inevitably results in reduced contrast or texture within the darker (and often deeper) parts of the scene. Past studies have found this to reduce the success of optical bathymetric mapping in deeper water (Legleiter et al., 2004, Legleiter 2013). This reduction in contrast is also likely to reduce the success of the SfM point matching process in the darker, deeper parts of the channel. This will result in increased noise within the point cloud (or a lack of matching altogether) which in turn reduces DEM accuracy and increases point cloud roughness. Future work might explore the benefits of using higher bit depth imagery.

Quantifying physical river habitat parameters using hyperspatial resolution
UAS imagery and SfM-photogrammetry

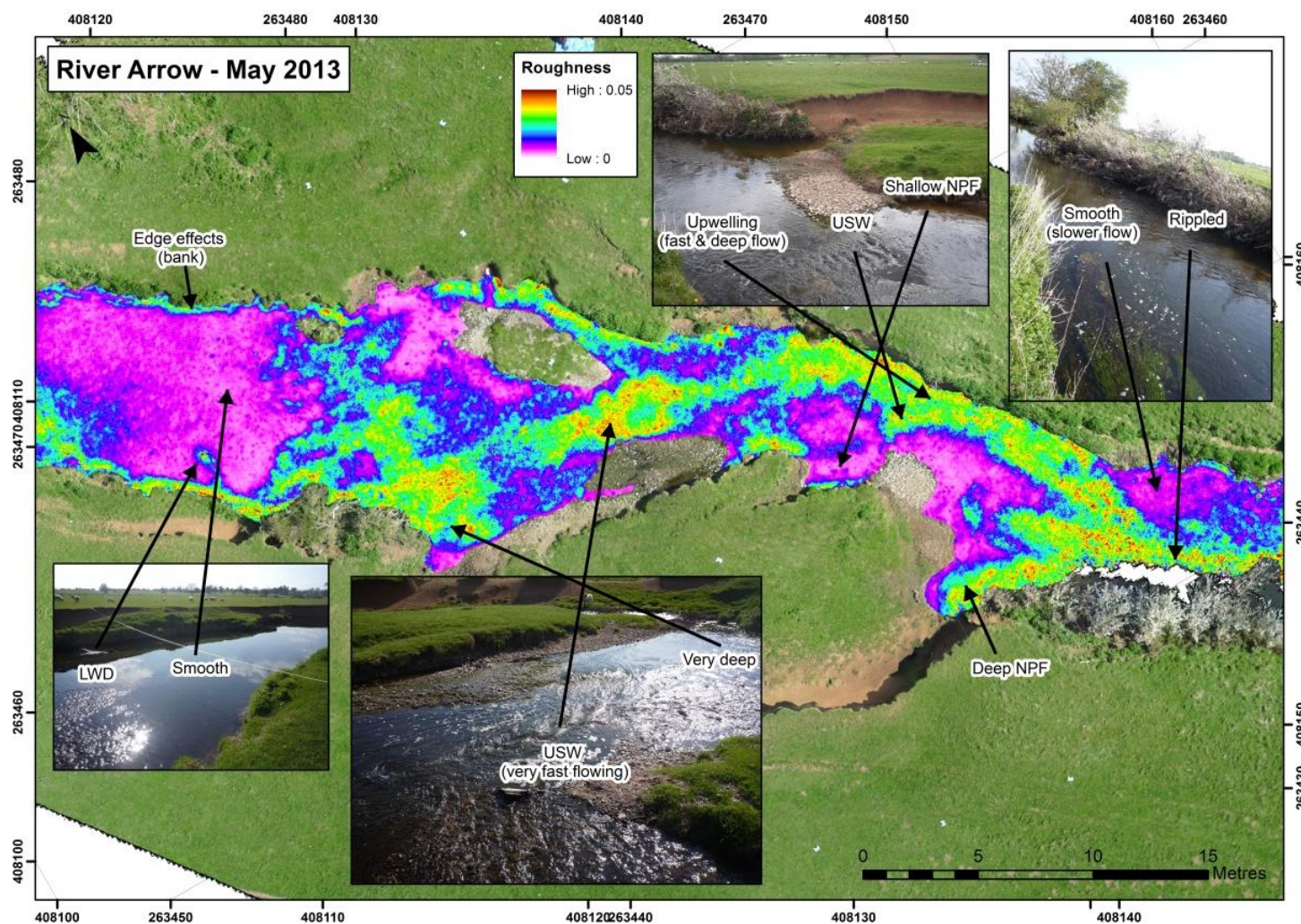


Figure 5.25. Local site observations of the relationship between point cloud roughness and areas of fast flow, deep water or increased water surface roughness.

3. **The water clarity.** An increase in the turbidity of the water causes the material on the channel bed to become obscured (as observed during the River Arrow July 2012 survey). This results in a reduction in image texture. The SfM-photogrammetry process is heavily reliant on texture for accurate point matching. Where texture is lacking, point matching is less successful and either fails completely, or produces a very noisy point cloud. This was observed for the River Arrow July 2012 data where turbidity was high, and resulted in a much poorer differentiation of SFTs based on roughness when compared to the other datasets. In contrast, the clear waters during the River Arrow May and June surveys and the Coledale Beck survey allowed a better view of the textured river bed and consequently have produced a point cloud less affected by noise. Increased turbidity is also recognised as a limiting factor on other habitat mapping approaches which make use of spectral-depth data (Gilvear et al., 1995).
4. **The substrate size.** Where the water is sufficiently clear and the water depth relatively shallow, the shape and size of material on the channel bed can be seen from the orthophotos. As described in Chapter 4, a positive correlation exists between grain size and point cloud roughness. Therefore in some parts of the scene, it is probable that point cloud roughness will be reflecting grain size.

It is suggested that a combination of these factors are responsible for producing the observed patterns of point cloud roughness. Future work might aim to quantify the effects of these factors, test roughness values computed using different kernel sizes or explore the use of other measures of variation derived from the point cloud.

SFT Mapping

The success of differentiating SFTs will also be affected by the accuracy of the mapping used to delineate SFTs in the first place. If the SFT classification is incorrect then attempts to differentiate SFTs based on their roughness and depth will be meaningless.

Factors affecting the accuracy of SFT polygons mapped from the bankside and from the UAS-SfM imagery (used to create the roughness profiles) have been discussed earlier in this chapter. Some of these factors are also likely to affect the accuracy of the *ground truth* SFT classification (used in the ANOSIM tests), namely; the indistinct nature of SFT boundaries, and the time lag between image acquisition (from which the roughness and depth are calculated) and the assignment of ground truth SFTs the following day.

Scale and the hydraulic identity of SFTs

Overall, the results seem to demonstrate that the quantitative outputs from the UAS-SfM process (water depth and point cloud roughness) cannot be used to differentiate reliably between SFTs, as defined within this study. It also follows that the UAS-SfM outputs are thus not a reliable predictor of hydraulic diversity. However, this is based on the assumption that SFTs are themselves a reliable indicator of hydraulic diversity, which may not necessarily be the case.

Scenario B assessed the use of field measured water depth and velocity for differentiating between SFTs. Whilst the global R values computed for Scenario B are greater than those computed for Scenario A (UAS-SfM products), these values are still fairly low (0.14-0.32). Furthermore, the pair-wise ANOSIM comparisons show that some SFTs cannot be easily distinguished from each other using these traditional point wise field measures of water depth and mean column velocity. This suggests that some SFTs do not have a strong hydraulic identity. This is demonstrated in Figures 5.18 to 5.21 where there are large overlaps in hydraulic conditions between different SFTs (e.g. ripples and unbroken standing waves).

Interestingly, where SFTs have more distinctive field-measured depth-velocity combinations they are also more easily distinguished from each other using point cloud roughness. This is demonstrated in Figures 5.18 to 5.20 where smooth areas, which typically feature shallow depths within the Arrow May survey, are characterised by relatively low roughness values, making them distinguishable from areas of upwelling where the water is consistently much deeper and roughness much greater. However, where the hydraulic character of SFTs is less strong, they appear to be less distinguishable using point cloud roughness (Figures 5.18 to 5.21). This might suggest that the roughness data is reflecting the strong hydraulic character which exists within some SFTs and the diversity of hydraulic conditions (or heterogeneity) which exists within others.

Within-SFT hydraulic heterogeneity and overlaps in the hydraulic character of different SFTs (or the equivalent physical biotopes) has been acknowledged by other studies (e.g. Wadson 1994, Marcus 2002, Marcus et al., 2003, Legleiter and Goodchild 2005, Milan et al., 2010). This has been observed as small patches of hydraulic conditions (sometimes expressed as different

surface patterns) which are typically associated with one SFT or biotope being found within another SFT or biotope. The works of Marcus (2002) and Marcus et al., (2003) note the presence of these small, pixel-scale patches on classifications of in-stream habitat units produced from high resolution (1m) hyperspectral imagery. They argue, although cannot prove, that this heterogeneity represents real differences in physical habitat which are often returned as false misclassifications due to the coarser scale of SFT or biotope units mapped in the field. Whilst the use of data extracted only from the SFT 'core' areas attempted to overcome the issues associated with vague SFT boundaries in this study, these were randomly placed, and may still reflect internal hydraulic heterogeneity within single SFT units.

Harvey and Clifford (2009) explored the microscale hydrodynamics of physical biotopes and found that hydraulic heterogeneity not only existed within biotopes but that the magnitude of this heterogeneity varied between biotopes. They argue that this microscale heterogeneity of hydraulics is largely determined by the presence of roughness elements and flow obstructions within the channel. Furthermore, they stress the importance of microscale hydraulic diversity as having a more direct influence on the survival of in-stream biota than hydraulic variability at the mesoscale.

Such findings highlight the importance of scale to the assessment of physical habitat, and raise an interesting point in relation to the approach adopted here. As argued by Fisher (1994, p. 580), *"Interpretation of causation is... scale dependent and the application of results gained at one scale, however carefully done, is often inappropriate (and maybe wrong) at another scale"*. It would seem that the broad scale mapping of SFTs offers an overview of hydraulic diversity which greatly simplifies the continuum of hydraulic conditions that may actually be present within each SFT. In contrast, the hyperspatial resolution outputs from the UAS-SfM process perhaps offer an unprecedented method of quantifying this hydraulic diversity at the microscale. As a result, it might be argued that this mis-match of scales renders unfair an assessment of the usefulness of the UAS-SfM products of depth and roughness against the broad scale, traditional SFT mapping. However, a reliable relationship between quantitative UAS-SfM outputs and field-measured hydraulic variables is yet to be established and so the value of these outputs cannot be proven at present. Further work is required to understand the magnitude of the role that other factors (image quality, water depth, water clarity,

substrate size) play in determining point cloud roughness in submerged areas, and in equating microscale variation in point cloud roughness to microscale variation in hydraulic conditions.

SFTs as a proxy for hydraulic heterogeneity

The analysis of data presented within this chapter might be taken a step further to question the basic validity and reliability of SFTs themselves. Whilst SFT classifications have become widely advocated for inferring fluvial hydraulic diversity and subsequently habitat suitability (e.g. Newson and Newson 2000, Dyer and Thoms 2006, Hill et al., 2008, Zavadil et al., 2012, Hill et al., 2013), there is remarkably little evidence from this research to suggest any robustness in such an approach. As a result, it might be argued that the usefulness of SFT mapping for quantitative assessments of physical river habitat parameters is questionable. An in-depth assessment of the validity of SFTs as a proxy for hydraulic heterogeneity is beyond the scope of this thesis, but should be explored in future.

5.7 Conclusions

Within this chapter, the potential of a UAS-SfM approach for mapping SFTs at the mesoscale has been evaluated. Manual delineation of SFTs can be undertaken directly from the high resolution (c. 1cm) UAS-SfM orthophotos to produce continuous SFT maps over lengths of channel from c.10m to a few hundred metres. Validation against independent ground truth mapping suggests the accuracy of SFT mapping from UAS ortho-imagery is in the region of 48-75%. Key factors thought to be affecting the mapping accuracy include; the indistinct nature of SFT boundaries, the vertical viewing angle of the airborne camera, changes in flow level between the ground truth and UAS surveys and a lack of temporal data to define SFTs. Better results are obtained from datasets acquired during bright, sunny conditions.

The inclusion of quantitative outputs from the UAS-SfM process (water depth and point cloud roughness) were not found to improve separability of SFTs above what can be achieved using traditional field measures of depth and velocity. This may result from small errors in the UAS-SfM water depth data, despite correction for the effects of refraction, and the impact of factors other than water surface patterns on the point cloud roughness. These factors include, but may not be limited to; image quality, water depth, water clarity and substrate size. Most of these factors affect the quality of the point cloud, introducing additional 'noise'. The exception is substrate size, which is directly linked to point cloud roughness, as described in Chapter 4. It is thought that the patterns observed within the maps of point cloud roughness might provide evidence of microscale hydraulic heterogeneity, at a much finer scale than the SFT mapping, but this cannot be proven at present.

The value of this UAS-SfM approach for mapping SFTs and characterising hydraulic diversity will be determined by the scale and accuracy required by the intended application, as well as the availability of resources, time and funds. As summarised by Newson and Large (2006, p.1610), in the context of classifying fluvial habitats for river management applications, *“the administrative choice of appropriate regulatory scales and the ‘tools’ for implementation constitutes... the primary academic challenge to fluvial geomorphology”*. As such, continued research would be of benefit to a UAS-SfM approach for mapping SFTs at an appropriate scale, and for the wider quantification of physical river habitat parameters. Future work should be focussed in the following key areas:

- Better defining the relationship between point cloud roughness and fine scale hydraulic conditions to establish whether valuable information might be available from a UAS-SfM approach at the microscale. This approach might explore the use of an acoustic Doppler current profiler (ADCP) for quantifying hydraulic variables for example.
- Exploring the use of image classification procedures. Both unsupervised and supervised approaches have been previously tested on passive remotely sensed data for mapping in-stream habitat (Hardy et al., 1994, Wright et al., 2002, Marcus 2002). This study has only mapped SFTs manually, however, a rapid assessment of habitat availability may benefit from an automated approach for covering larger areas more quickly.
- The use of fuzzy SFT classification schemes. It is likely that the crisp mapping approach undertaken within this study is responsible for some of the observed mapping error. The use of transition zones or a fuzzy classification should be explored for improving SFT mapping accuracies.

Finally, the data presented here raises the question of the basic suitability of SFT mapping for inferring hydraulic diversity and subsequent assessments of physical river habitat availability. Whilst the data presented here is insufficient to draw any firm conclusions on this matter, future work should be aimed at addressing the validity of this vague classification scheme.

5.8 References

- Biron, P.M., Richer, A., Kirkbride, A.D., Roy, A.G. and Han, S. (2002) Spatial patterns of water surface topography at a river confluence. *Earth Surface Processes and Landforms* 27: 913-928.
- Bisson, P.A., Nielsen, J.L., Palmason, R.A. and Grove, L.E. (1982) 'A system of naming habitat types in small streams, with examples of habitat utilisation by salmonids during low stream flow' In Armandtrout, N.B. (Eds) Acquisition and Utilisation of Aquatic Habitat Information, Western Division of the American Fisheries Society, Portland, Oregon, p. 62-73.
- Butler, J.B., Lane, S.N., Chandler, J.H. and Porfiri, E. (2002) Through-water close range digital photogrammetry in flume and field environments. *Photogrammetric Record* 17 (99): 419-439.
- Clarke, K.R. and Warwick, R.M. (2001) Change in marine communities: An approach to statistical analysis and interpretation. Second Edition, PRIMER-E Ltd, Plymouth.
- Dyer, F.J. and Thoms, M.C. (2006) Managing river flows for hydraulic diversity: an example of an upland regulated gravel-bed river. *River Research and Applications* 22: 257-267.
- Environment Agency (2003) River Habitat Survey in Britain and Ireland: Field Survey Guidance Manual. Available online: https://www.gov.uk/government/uploads/system/uploads/attachment_data/file/311579/LIT_1758.pdf (accessed 11.02.2015).
- European Commission (2000) Directive 2000/60/EC of the European Parliament and of the Council of 23rd October 2000: Establishing a framework for Community action in the field of water policy. *Official Journal of the European Communities, Brussels, 22.12.2000, L327: 1-72.*
- Fausch, K.D., Torgersen, C.E., Baxter, C.V. and Hiram, L.W. (2002) Landscapes to riverscapes: bridging the gap between research and conservation of stream fishes. *BioScience* 52 (6): 483-498.
- Fisher, S.G. (1994) 'Pattern, process and scale in freshwater systems: some unifying thoughts' In Giller, P.S., Hildrew, A.G. and Raffaelli, D.G. (Eds) Aquatic ecology – scale, pattern and process Blackwell, Oxford p. 117-132.
- Fryer, J.G. (1983) A simple system for photogrammetric mapping in shallow water. *Photogrammetric Record* 11 (62): 203-208.
- Fryer, J.G. and Kniest, H.T. (1985) Errors in depth determination caused by waves in through-water photogrammetry. *Photogrammetric Record* 11 (66): 745-753.
- Gilvear, D.J., Waters, T.M. and Milner, A.M. (1995) Image analysis of aerial photography to quantify changes in channel morphology and instream habitat following placer mining in interior Alaska. *Freshwater Biology* 34: 389-398.
- Girardeau-Montaut, D. (2014) CloudCompare Software v.2.5. Available online: <http://www.danielgm.net/cc/> (accessed 05.01.2014).
- Hardy, T.B., Anderson, P.C., Neale, C.M.U., and Stevens, D.K. (1994) 'Application of multispectral videography for the delineation of riverine depths and mesoscale hydraulic features' In Marston, R.A. and Hasfurther, V.R. (Eds) Effects on Human-Induced Changes on Hydrological Systems, *Proceedings of the American Water Resources Association*, Jackson Hole, Wyoming, June 1994, p. 445-454.
- Harvey, G. and Clifford, N. (2009) Microscale hydrodynamics and coherent flow structures in rivers: Implications for the characterisation of physical habitat. *River Research and Applications* 25: 160-180.

- Hill, G. (2011) The relationship of benthic macroinvertebrate assemblages to water surface flow types in British lowland rivers. *Unpublished PhD thesis, Coventry University*.
- Hill, G., Maddock, I. and Bickerton, M. (2008) 'River habitat mapping: are surface flow types biologically distinct?' *British Hydrological Society 10th National Hydrology Symposium*, Exeter.
- Hill, G., Maddock, I. and Bickerton, M. (2013) 'Testing the relationship between surface flow types and benthic macroinvertebrates' In Maddock, I., Harby, A., Kemp, P. and Wood, P. (Eds) *Ecohydraulics: An integrated approach* Wiley, Chichester.
- Large, A. and Heritage, G. (2007) 'Terrestrial laser scanner based instream habitat quantification using a random field approach' *Proceedings of the Remote Sensing and Photogrammetry Society Annual Conference 11-14th September 2007, Newcastle-upon-Tyne, UK*.
- Legleiter, C.J. (2013) Mapping river depth from publicly available aerial images. *River Research and Applications* 29 (6): 760-780.
- Legleiter, C.J., Roberts, D.A., Marcus, W.A. and Fonstad, M.A. (2004) Passive optical remote sensing of river channel morphology and instream habitat: physical basis and feasibility. *Remote Sensing of the Environment* 93: 493-510.
- Legleiter, C.J. and Goodchild, M.F. (2005) Alternative representations of in-stream habitat: Classification using remote sensing, hydraulic modelling and fuzzy logic. *International Journal of Geographical Information Science* 19 (1): 29-50.
- Lillesand, T.M. and Kiefer, R.W. (2000) *Remote sensing and image interpretation* 4th Edition Wiley, New York.
- Liu, J.G. and Mason, P.J. (2009) *Essential image processing and GIS for remote sensing* Wiley-Blackwell, Singapore.
- Marcus, W.A. (2002) Mapping of stream microhabitats with high spatial resolution hyperspectral imagery. *Journal of Geographical Systems* 4: 113-126.
- Marcus, W.A., Legleiter, C.J., Aspinall, R.J., Boardman, J.W. and Crabtree, R.L. (2003) High spatial resolution hyperspectral mapping of in-stream habitats, depths, and woody debris in mountain streams. *Geomorphology* 55: 363-380.
- Milan, D.J., Heritage, G.L., Large, A.R.G. and Entwistle, N.S. (2010) Mapping hydraulic biotopes using terrestrial laser scan data of water surface properties. *Earth Surface Processes and Landforms* 35: 918-931.
- Montgomery, D.R. and Buffington, J.M. (1997) Channel-reach morphology in mountain drainage basins. *Geological Society of America Bulletin* 109 (5): 596-611.
- Newson, M.D. and Newson, C.L. (2000) Geomorphology, ecology and river channel habitat: mesoscale approaches to basin-scale challenges. *Progress in Physical Geography* 24 (2): 195-217.
- Newson, M.D. and Large, A.R.G. (2006) 'Natural' rivers, 'hydromorphological quality' and river restoration: a challenging new agenda for applied fluvial geomorphology. *Earth Surface Processes and Landforms* 31: 1606-1624.

Padmore, C.L. (1997) 'Biotopes and their hydraulics: a method for determining the physical component of freshwater habitat quality' In Boon, P.J. and Howell, D.L. (Eds) Freshwater quality: Defining the undefinable Edinburgh HMSO p.251-257.

Raven, P.J., Fox, P., Everard, M., Holmes, N.T.H. and Dawson, F.H. (1997) 'River habitat survey: a new system for classifying rivers according to their habitat quality' In Boon, P.J. and Howell, D.L. (Eds) Freshwater quality: Defining the undefinable Edinburgh HMSO p.215-234.

Reid, M.A. and Thoms, M.C. (2008) Surface flow types, near-bed hydraulics and the distribution of stream macroinvertebrates. *Biogeosciences* 5: 1043-1055.

Reid, M.A. and Thoms, M.C. (2009) 'Mapping stream surface flow types by balloon: an inexpensive high resolution remote sensing solution to rapid assessment of stream habitat heterogeneity?' In IAHS Publication 328 Ecohydrology of Surface and Groundwater Dependent Systems: Concepts, Methods and Recent Developments, *Proceedings of JS.1 at the Joint IAHS and IAH Convention*, Hyderabad, India, September 2009.

Wadeson, R.A. (1994) A geomorphological approach to the identification and classification of instream flow environments. *South African Journal of Aquatic Science* 20 (1/2): 38-61.

Wadeson, R.A. and Rowntree, K.M. (1998) Application of the hydraulic biotope concept to classification of instream habitats. *Aquatic Ecosystem Health and Management* 1: 143-157.

Wallis, C., Maddock, I., Visser, F. and Acreman, M. (2012) A framework for evaluating the spatial configuration and temporal dynamics of hydraulic patches. *River Research and Applications* 28 (5): 585-593.

Westaway, R.M., Lane, S.N. and Hicks, D.M. (2001) Remote sensing of clear-water, shallow, gravel-bed rivers using digital photogrammetry. *Photogrammetric Engineering and Remote Sensing* 67 (11): 1271-1281.

Woodget, A.S., Carbonneau, P.E., Visser, F. and Maddock, I.P. (2015) Quantifying submerged fluvial topography using hyperspatial resolution UAS imagery and structure from motion photogrammetry. *Earth Surface Processes and Landforms* 40 (1): 47-64.

Wright, A., Marcus, W.A. and Aspinall, R. (2000) Evaluation of multispectral, fine scale digital imagery as a tool for mapping stream morphology. *Geomorphology* 33: 107-120.

Zavadil, E.A., Stewardson, M.J., Turner, M.E. and Ladson, A.R. (2012) An evaluation of surface flow types as a rapid measure of channel morphology for the geomorphic component of river condition assessments. *Geomorphology* 139-140: 303-312.

Chapter 6

Discussion & Conclusion

Chapter Overview

This chapter provides an overview of the initial research aims, as identified in Chapter 1. A summary of the key findings associated with the quantification of each physical river habitat parameter is presented, followed by a broad evaluation of the key advantages and limitations of the UAS-SfM approach. Important areas for future work are highlighted and a number of potential application areas are suggested, with illustrated examples where possible. The chapter closes with a final comment on the use of a UAS-SfM approach in relation to the initial research aims.

6.1 Aims of this research

The overarching aim of this research was to assess the capabilities of a novel approach using unmanned aerial systems (UAS) and structure from motion photogrammetry (SfM) for quantifying a series of three physical river habitat parameters at the mesoscale; topography/depth, substrate size and surface flow types. This research was motivated by a need for rigorous, quantitative assessments of this fledgling approach, which up to now have been lacking amidst the excitement surrounding this novel technology. This thesis has taken a specific focus on the potential of the UAS-SfM approach for fulfilling the ideals of the riverscape concept at the mesohabitat scale, and has included quantitative comparisons with existing remote sensing techniques, in order that the relative advantages and drawbacks of a UAS-SfM approach might be highlighted.

6.2 Summary of key findings

The UAS-SfM approach presented within this thesis has been shown to be capable of quantifying fluvial topography, flow depth and substrate size, and mapping the distribution of

SFTs at the mesoscale, albeit with results of mixed quality and with certain limitations determining where and when it performs best. A summary of the key findings is presented within this section and Figure 6.1, with a focus on the results of a quantitative assessment of accuracy and precision for each of the three physical river habitat parameters.

6.2.1 Fluvial topography (Chapter 3)

The use of a UAS-SfM approach was found capable of producing hyperspatial resolution (c. 2cm) elevation data for a range of different river systems. The DEM error varied both within and between sites, dependent on the density and extent of vegetation cover, water depth, the spatial configuration of GCPs and the image viewing angle. Generally, higher accuracy and precision data were produced for exposed (at best 4mm mean error, 19mm standard deviation of error), as opposed to submerged parts of the system (at best 17mm mean error, 74mm standard deviation of error), where error scales with water depth. The application of a simple refraction correction technique helped to reduce (by c. 50%) but not eliminate error within submerged areas. This correction procedure was only tested in clear waters up to 0.7m, and is likely to be less successful in more turbid or deeper waters.

Whilst the high resolution output DEMs are visually impressive, the potential for systematic doming and tilting errors has been highlighted and observed within field datasets. The magnitude of such errors has been shown to be variable, and is thought to relate to; (1) the self-calibration of the camera lens within the SfM software and insufficient variability around nadir in the image acquisition which can cause a doming effect, as observed in the DEM for Coledale Beck, and; (2) inadequate spatial distribution of GCPs which can causing tilting of the DEM, as observed for the San Pedro River dataset.

Comparison with topographic products from other remote sensing approaches finds similar or slightly lower [precision: flying height] ratios to traditional photogrammetry. Finer resolution DEMs are produced than those typically acquired using bathymetric laser scanning, digital photogrammetry and the spectral-depth approach, due to the very low flying altitude of the UAS. Higher accuracy and precision elevation data than obtained using TLS is observed in nearly all cases (except in unvegetated, exposed areas), however this is largely attributable to the advantages of a vertical (UAS) rather than oblique view angle (TLS).

6.2.2 Substrate size (Chapter 4)

An assessment of the UAS-SfM approach for quantifying fluvial substrate size made use of the dense SfM point cloud, as inspired by previous use of TLS point clouds in this way (e.g. Heritage and Milan 2009, Brasington et al., 2012, Rychov et al., 2012). A relationship was observed between the point cloud roughness (20cm kernel size) and the size of fluvial substrate measured in the field. The strength of this relationship was improved by the reduction of noise within the point cloud using a filtering and smoothing approach. It is thought that this noise is predominantly related to image blur, but may also result from the presence of vegetation and water within the scene.

It was possible to use the established relationship to predict grain size at hyperspatial resolutions (0.5cm). Jack-knife analysis was used to compute an average residual error of grain size estimates of -0.011cm, yet when normalised by grain size, these residual errors were shown to be as much as 90% of grain size. Such error magnitudes are unacceptably large, and would limit the wider applicability of this approach for estimating grain size. The spatial resolution of the input imagery was also found to limit the size of the smallest grains that can be estimated, meaning that the approach is not well suited to sites where predominant grain size is less than 5cm (coarse gravels and smaller).

Comparison of the results with a UAS-SfM image texture and a TLS point cloud roughness approach gave variable results. Higher spatial resolution and a higher precision were found for the UAS-SfM point cloud roughness approach, but a higher mean accuracy of grain size predictions was observed for the UAS-SfM image texture method. Results of all methods are limited by the imbrication and partial burial of grains, as found by many other remote sensing approaches for grain size estimation.

6.2.3 Surface flow types (Chapter 5)

The high resolution UAS-SfM orthoimagery was used for mapping SFTs, the accuracy of which was found to be as good as 75%, but was highly variable between surveys. It is thought that mapping accuracy is adversely affected by poor scene illumination, the vertical image view angle, a lack of temporal data and variations in flow level between the UAS survey and ground truthing which produce genuine changes in SFT distribution.

Quantifying physical river habitat parameters using hyperspatial resolution UAS imagery and SfM-photogrammetry

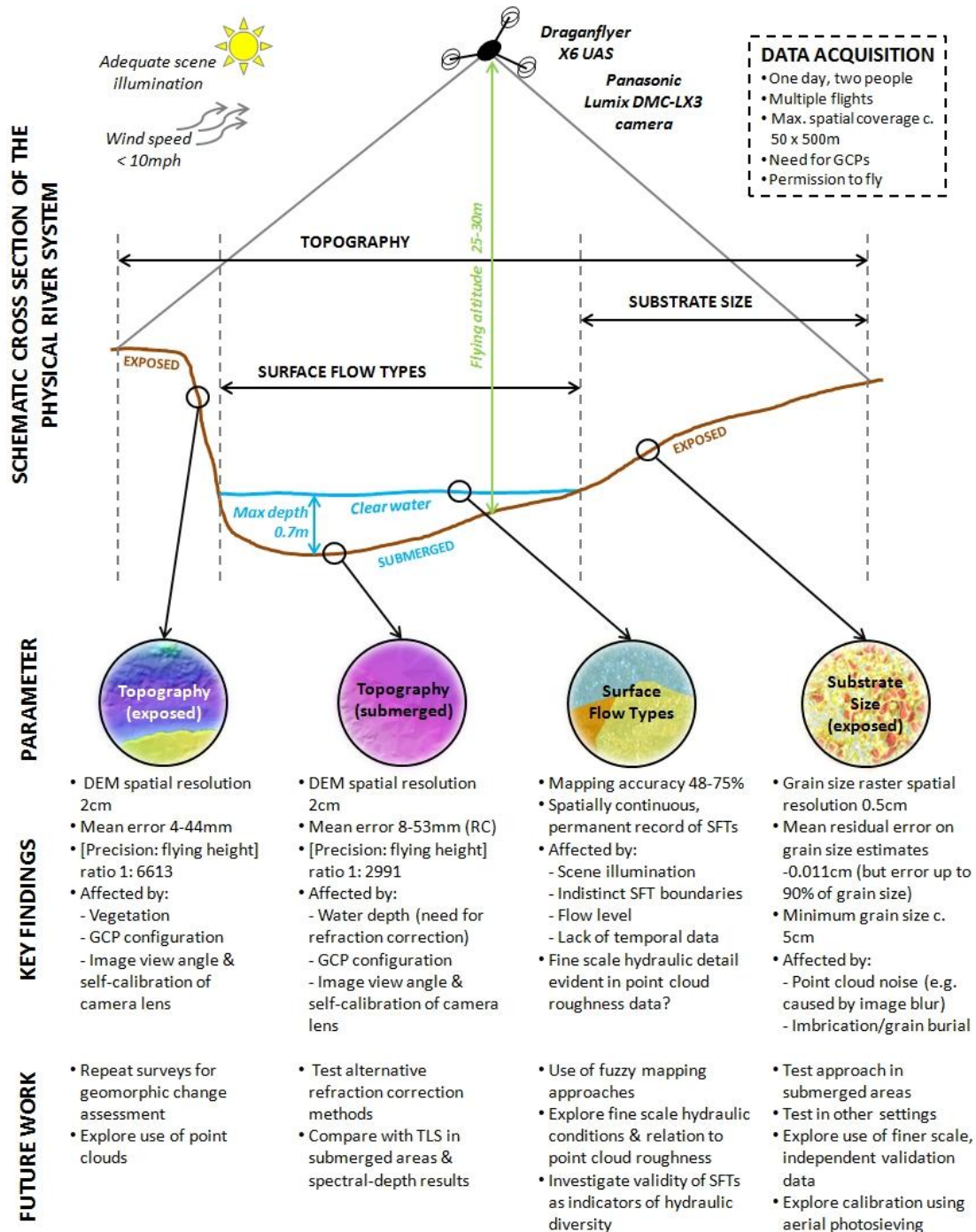


Figure 6.1. Overview of the set-up and key findings of this research, with suggestions for future work. RC denotes refraction corrected results.

Quantitative outputs from the UAS-SfM process included refraction corrected water depth and point cloud roughness which were investigated as factors for defining SFTs as proxies of hydraulic diversity. Despite visual similarities between roughness/depth and local knowledge of hydraulic conditions, these datasets did not help to differentiate between SFTs. The separability of SFTs using established measures of mean column velocity and water depth was also found to be poor. This led to the suggestion of two theories which require further research; (1) that the observed fine scale variability in roughness and depth does reflect hydraulic heterogeneity, but at a scale (i.e. the microscale) not recognised by the broader scale SFT mapping and; (2) that SFTs may not in fact provide a reliable proxy for hydraulic habitat heterogeneity for studies of quantitative hydromorphology or ecology.

Whilst these results indicate that the UAS-SfM approach can be used for quantifying the specified physical river habitat variables, they also present a mixed picture in terms of the accuracy, reliability and usefulness of the outputs. In depth, technical discussions tailored to each physical habitat parameter are provided in Chapters 3-5. A more general evaluation of the approach is presented in the following section.

6.3 Evaluation of the UAS-SfM approach

This section aims to provide an overarching evaluation of the UAS-SfM approach for quantifying physical river habitat parameters at the mesoscale. The key benefits and limitations are discussed, with a focus on the wider, practical applicability of the approach. Some of these findings are also highlighted in Figure 6.1.

6.3.1 Advantages

Compared to traditional field methods

The key findings of this research indicate that the UAS-SfM approach overcomes many of the limitations associated with the traditional field methods for quantifying physical river habitat parameters described in Chapter 1. Perhaps the greatest of these is the high resolution, spatially explicit and spatially continuous data acquisition which can be obtained in a way which is much faster and less laborious. The imagery, DEMs and point clouds also provide a permanent record which may be used as a baseline, to which future surveys may be compared for detailed change detection.

Compared to existing remote sensing approaches

This research has provided one of the first quantitative assessments of the capabilities of the UAS-SfM approach for quantifying a range of physical river habitat parameters at the mesoscale, and compared results against a range of existing remote sensing techniques. Overall, what emerges from this assessment are the following key advantages, which corroborate many of the existing findings introduced in Chapter 1;

- **Exceptionally high spatial and temporal resolution.** The low altitude flying heights (c. 30m) possible using this rotary-winged UAS enable orthophotos with spatial resolutions of c. 1cm and DEMs of c. 2cm. This is significantly greater than the highest resolution LiDAR data, typically available within the UK (0.25-2m, Environment Agency 2014). It is equivalent or slightly coarser than the spatial resolution of TLS and close-range photogrammetry (e.g. Graham et al., 2005, Heritage and Milan 2009), but is found to be capable of covering larger areas more quickly (e.g. Chapter 4). Different UAS, particularly fixed wing platforms, are known to be capable of covering larger areas than those shown here using the Draganflyer X6, although this may come at the expense of spatial resolution and is contingent on suitable areas for UAS launch and landing (e.g. large open areas often needed for skid-landings of fixed wing UAS).
- **Mesoscale coverage.** Within a day, and assuming a field crew of two people, it is possible to obtain imagery over channel widths of up to 50m and channel lengths of a few hundred metres (assuming a UAS set-up equivalent to the one used here). As such, this approach is best suited to small study sites, where high resolution data at the mesoscale is required. The rapidly maturing and expanding UAS market means that greater spatial coverage is increasingly possible however.
- **Rapid and flexible.** Platform mobilisation and data acquisition is rapid compared to the many other remote sensing techniques. For example, at the Coledale Beck study site, the collection of TLS data was found to take more than twice as long as the equivalent acquisition of imagery from the UAS (Chapter 2). Furthermore, the ability to collect data on-demand rather than waiting for a specially commissioned airborne survey represents significant advantages in terms of flexibility and timing.
- **Low cost.** The per-flight costs of operating a UAS are significantly lower than that for a traditional airborne survey. Whilst the Draganflyer X6 platform was costly to acquire (c. £29,500 in 2010), UAS prices have dropped dramatically in recent years, so that an equivalent platform can now be purchased for a fraction of the price (e.g. £2000 for a DJI F550 UAS including camera, P. Carbonneau 2014, *pers. comm.*).

- **Bespoke surveys.** With UAS surveys, data collection and processing is placed into the hands of the user, allowing bespoke surveys of variable scale and coverage, including the mesoscale. Whilst not employed within this research, flight planning software now allows the user to easily pre-programme flight paths and image acquisition sequences which are then implemented by auto-pilot systems.
- **Easily implemented by non-experts.** SfM procedures, such as the one employed within the PhotoScan software (Agisoft LLC) here, are very user-friendly and require less specialist training than traditional photogrammetry packages. Furthermore, the ability of SfM to cope with the unstable viewing geometries of UAS imagery where previous traditional photogrammetry approaches struggle (e.g. Lejot et al., 2007) makes it critical to the success of the UAS for providing outputs suitable for quantitative scientific applications.

6.3.2 Limitations

A number of drawbacks of the UAS-SfM approach have been brought to light by this research. At the current time, these limitations might restrict the wider practical implementation of this approach for physical river habitat assessment. Some of these drawbacks are specific to the UAS platform and software used here whereas others apply more generally to the approach.

Data acquisition

- **Image blur.** The low flying altitude and manual acquisition of imagery during movement of the platform means that a proportion of the imagery will suffer from blur. Severely blurred images can be easily identified visually and removed from small image datasets but the occurrence of some minor blur appears to be inevitable. It is thought that this increases noise within the SfM point cloud which subsequently degrades the quality of both elevation and, critically, substrate size estimations using the methods specified in Chapters 3 and 4. As such, blur is identified as a major limiting factor in this study. Similar findings are reported by de Haas et al., (2014) and suggest the development of methods to identify, reduce or prevent blur within UAS imagery (e.g. Sieberth et al., 2013) should be enhanced in future. For example, the use of UAS carrying medium format, mirror-less cameras mounted using vibration damping gimbals have been found to significantly reduce blur within imagery (P. Carbonneau 2014, *pers. comm.*).

- **Need for GCPs.** For surveys of relatively rural field sites, the use of GCPs providing adequate representation of the site in three dimensions remains essential for accurate spatial positioning and scaling of the output datasets. The positioning and survey of GCPs roughly doubles the time required in the field. Technological developments in miniaturising higher grade GPS systems and increasingly the payload capacity of small UAS may eventually remove the need for GCPs through the use of onboard survey grade GPS data for georeferencing, but adequate progress is yet to be made in this area to date.
- **Consumer-grade sensors.** The small and lightweight nature of the Draganflyer X6 means that its payload capacity is greatly restricted at present. All of the research conducted within this thesis has made use of a consumer-grade RGB camera and the collection of 8-bit imagery. As a result, the radiometric resolution of the image is hindering the restitution of topography in the deeper, darker, submerged parts of the channel due to a reduction in image texture, as mentioned in Chapter 3. It is suggested that the use of higher bit depth imagery be explored, and with the rapid and on-going development of UAS-suitable sensors and greater UAS payload capacities, it is unlikely that this will remain a limitation for long.
- **Scene illumination.** Results from the repeat surveys of the River Arrow between May and August 2013 suggest that poor scene illumination (i.e. dull, overcast conditions) may be responsible for reducing DEM accuracy and precision (Chapter 3) and reduced success in mapping the extent of SFTs (Chapter 5), in comparison to those datasets collected during bright, sunny conditions. Eltner et al., (2013) also report reduced success with SfM for scenes which are less well lit but no research has yet specifically addressed the issue of scene illumination.
- **Wind conditions.** In terms of UAS flying, the Draganflyer platform is small and lightweight and therefore becomes very difficult to operate safely and collect blur-free imagery in wind speeds greater than 10mph. Working predominantly within the UK, wind speeds were found to severely limit the number of days when data acquisition was possible, especially during the winter months. It is noted that newer, heavier, more powerful UAS are likely to be less affected in this way.
- **Pilot experience.** A skilled pilot is critical for ensuring safe flying and for acquiring high quality imagery. Whilst the data collection process itself is rapid, the time taken to gain sufficient flight experience in order to obtain high quality data for quantitative, scientific applications should not be underestimated.

- **Battery life.** Single flight times are limited to c. 5 minutes due to the limited power provided by a single LiPo battery on board the Draganflyer X6. This means that multiple flights are usually necessary to provide adequate coverage of even the smaller sites reported within this thesis. Given this limitation, and the need to maintain visual line-of-sight at all times, it is not possible to collect imagery over much more than a few hundred metres of channel length within a day, assuming a field crew of two people and the need for GCP surveying on the same day. Newer rotary-winged and fixed-winged platforms are reported capable of longer flight durations however, with single flight times of up to 30 minutes. Newer Lithium-Sulphur (Li-S) batteries are also advocated to provide longer flight times. These developments enable faster data acquisition and reduce the number of take-offs and landings, which are typically when most accidents occur.
- **UAS flight regulations.** Unlike in some other countries (e.g. USA), regulatory conditions in the UK are currently favourable for non-commercial research using UAS, providing flights are being undertaken in non-built up areas. This research has not explored the use of UAS in more urban settings where CAA permissions are required, but this might become a limiting factor on the use of UAS surveys for routine monitoring of urban waterways.

Data processing

- **Reliance on image texture.** The SfM process is heavily dependent on image texture. Where this is lacking or variable, the approach is compromised or fails altogether. As a result, within fluvial settings, surveys conducted over large expanses of smooth, opaque water surfaces or where tree coverage obscures parts of the channel (both observed within parts of the River Arrow July 2012 survey) should not be expected to produce useful results for physical river habitat assessments.
- **Geometric restitution is only possible for visible features.** Unlike laser scanning approaches, the SfM technique is only able to reconstruct surfaces that are clearly visible from above. As a result, patches of dense or overhanging vegetation will prevent the approach from 'seeing' underlying features of interest. This is evident in the large overestimations of elevation in the densely vegetated parts of the Coledale Beck survey and has been observed elsewhere (e.g. Westoby et al., 2012, Javernick et al., 2014). Similarly, for the SfM process to work in submerged areas, a clear view of

the channel bed is necessary. This prohibits the use of the approach in particularly deep and turbid waters.

- **Need for high processing power.** The SfM process can be very computationally demanding for large image datasets. For example, for the c. 170m long San Pedro River survey, SfM processing of more than 100 photos took about one working day to complete on an Intel® Core™ i7-2600 16GB RAM 64-bit computer. It is likely that ongoing developments in computer processing power will help to reduce processing times in future however.
- **Unknown error sources within PhotoScan.** The nature of the PhotoScan software means that isolating exact sources of error is impossible. Systematic doming errors present within some output DEMs presented within this research (Chapter 3) and elsewhere (Javernick et al., 2014) are thought to be related to an inadequate self-calibration of the camera lens model within PhotoScan (Chandler et al., 2005, Wackrow and Chandler 2008). Recent research suggests that these errors can be reduced by the addition of imagery acquired at convergent view angles (James and Robson 2014). Further work would be of benefit in order to better understand the error sources within the SfM process.

6.3.3 Applicability to physical river habitat surveying

“The ability to assess habitat variability in time and space may provide valuable new insights into the mechanisms by which populations and communities are regulated”
(Bovee 1996, p. 156)

This research has demonstrated the proof of concept of a UAS-SfM based approach for quantifying physical river habitat variables at the mesoscale, within certain constraints. Significant benefits over existing approaches are offered in terms of high spatial and temporal resolution, rapid and flexible data acquisition and the ability of a single survey to provide both orthoimagery and topographic data. As such, the approach fulfils many of the ideals of the riverscape concept introduced in Chapter 1. The variability in physical river habitat parameters observed within this study, albeit over small river reaches, also lends support to the concept of a spatially heterogeneous ‘riverscape’ system, as advocated by Fausch et al., (2002) and others (Ward et al., 2002, Wiens 2002).

Perhaps the greatest benefit of a UAS-SfM approach is the democratisation of data collection. The low cost, rapid, flexible and bespoke nature of UAS-SfM surveying opens up new possibilities for quantitative sampling of physical river habitat parameters at spatial and temporal frequencies which are currently only paralleled by TLS. In theory, the nature of such sampling permits quantitative, high resolution and high frequency monitoring of geomorphic change and thus may precipitate new understandings of fluvial habitat dynamics and provide valuable data for the calibration and or validation of a variety of simulation models.

In direct comparison to TLS, this research has found the UAS-SfM approach capable of producing topographic products of similar spatial resolutions and accuracies (Chapter 3), providing greater coverage of the submerged topography using a simpler refraction correction approach (Chapter 3, Smith and Vericat 2014), and more accurate and precise estimates of substrate size in exposed areas (Chapter 4). It is suggested then, that the UAS-SfM approach occupies a spatial domain similar to that of TLS, as shown in Figure 6.2. It is also thought that the UAS-SfM approach is capable of characterising the hydraulic heterogeneity of the fluvial environment at similarly high spatial resolutions (Chapter 5, Milan et al., 2010), though this requires further research. Finally, the UAS-SfM approach is significantly less expensive and allows much faster acquisition of data than TLS (Chapter 3).

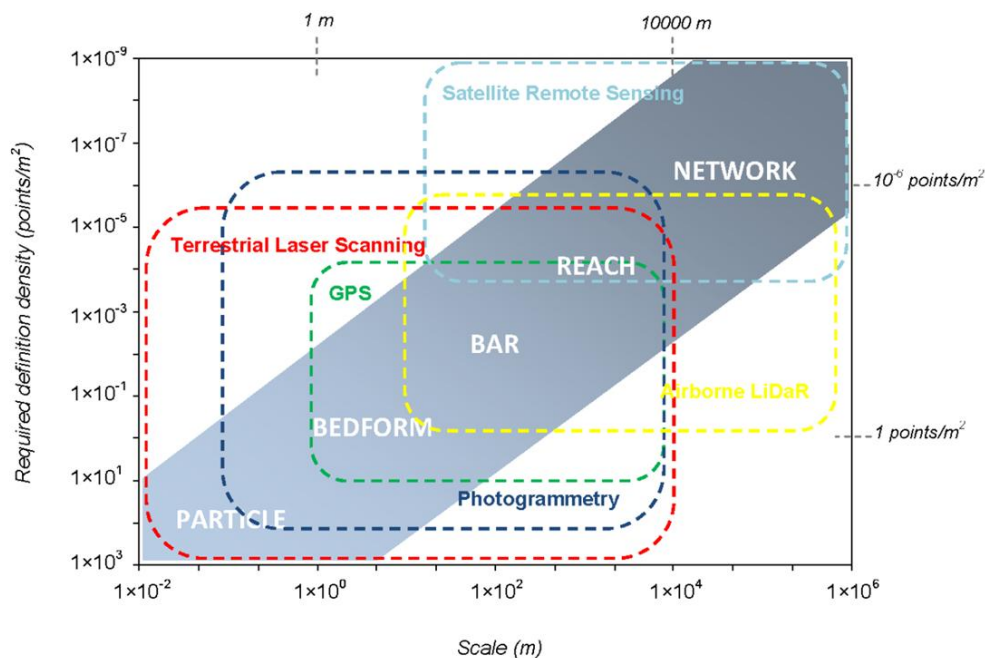


Figure 6.2. The spatial scales of remote sensing and geospatial technologies for mapping fluvial systems (Brasington 2014).

As argued by Newson and Newson (2000, p.199) however, "*Real contributions from research to sustainable management of river systems... need to match a sophistication of concepts with a direct practicality (without which applications are unlikely)*". Whilst the potential benefits of the UAS-SfM approach are clear, significant practical limitations remain. Issues relating to image blur, the need for adequate flying experience and conducive weather conditions represent the most significant barriers to the reliable collection of high quality data at present. Furthermore, greater awareness of the potential for errors resulting from the SfM process is needed, as they are easily overlooked in the excitement of such easy-to-use software and visually impressive outputs. Only if the listed limitations can be addressed in a robust manner will the UAS-SfM approach begin to move beyond a proof of concept stage to provide a viable tool for fluvial habitat assessment.

6.4 Recommendations for future work

It is important that future research efforts are channelled into developing methods for overcoming the limitations of the UAS-SfM approach which have been highlighted by this research. Detailed technical recommendations for future work, specific to the quantification of each physical river habitat variable, are provided in Chapters 3-5 and Figure 6.1. At a higher level, perhaps the most significant areas for future work comprise;

1. **Addressing the challenges of data acquisition.** The rapid development of UAS platforms and similar, albeit slower, advances in associated sensors, provides new opportunities for collecting data at higher radiometric and spectral resolutions. Further research might also explore optimum levels of image overlap, optimum GCP densities and configurations, the results of which would assist in the planning of efficient image acquisition campaigns.

2. **Development of data processing and analysis techniques which exploit efficiently the high spatial and temporal frequency data obtained using a UAS-SfM approach, and allow validation (ground truthing) and comparison against other datasets at appropriate resolutions.** Some progress in this area has been made in recent years, including the increase in availability of open source point cloud management software (e.g. CloudCompare) and processing routines (e.g. M3C2 algorithm by Lague et al., 2013, ToPCAT routine by Brasington et al., 2012). In this vein, an extension of this

research might investigate calibration-validation of the UAS-SfM point cloud roughness approach to substrate size using higher resolution, more spatially explicit ground truth data, the use of advanced methods of decomposing spatial data, such as Fourier or Wavelet analysis for grain size assessment, and exploring the relationship between point cloud roughness in submerged areas with higher resolution, spatially explicit hydraulic data obtained using an acoustic Doppler current profiler (ADCP).

- 3. Testing of the approach for specific applications within river science and management**, as well as quantitative geomorphology more widely. This research has been focussed on the quantification of three physical river habitat parameters. Further work is required however to demonstrate the utility of a UAS-SfM approach for a variety of real-world, practical applications. A number of potential applications arise from this research, some of which have started to be addressed within the wider literature, including geomorphological mapping, geomorphic change detection and habitat suitability mapping (e.g. Flener et al., 2013, Tamminga et al., 2014). Examples from this research are presented in section 6.5. These are intended to be indicative only as progress in overcoming some of the limitations listed in section 6.3 is required before reliable outputs can be achieved.
- 4. Education and training of the next generation of researchers and practitioners.** As the field of UAS-SfM matures, there is a growing need for more formal training in the use of these novel tools and development of the knowledge base in how they can provide valuable, quantitative data for interpreting the (fluvial) environment. This might include integration of UAS and SfM processing (including an appreciation of its origins in photogrammetry) into university degree programmes in geography, geomorphology and remote sensing and where possible, professional development opportunities. The availability of such training is currently limited (Natural Environment Research Council 2014).

6.5 Potential applications

Whilst acknowledging the current limitations of the UAS-SfM approach (section 6.3 and within earlier chapters), the outputs of this research can also be used to highlight potential future

applications. A number of suggestions are presented here. These are intended as examples only and do not comprise an exhaustive list of potential applications.

Geomorphological Mapping

Using an approach based on that advocated by Cooke and Doornkamp (1990), a geomorphological map for the San Pedro River site was created (Figure E1 in Appendix E). Both the UAS-SfM orthophoto and DEM were used to visually identify and manually map different substrate sizes as well as measure slope angles and map key breaks of slope within this shallow, submerged shelf section. Such maps are created and used routinely by a wide range of academic and industrial practitioners for characterising and developing conceptual models of a variety of landscapes (e.g. glacial geomorphology, landslide systems, geohazards) and as decision making tools for directing further investigation (e.g. Smith et al., 2006, Finkl et al., 2008, Halcrow Group Ltd 2009). Maps such as this might also be used for predicting habitat preferences as demonstrated in one of the examples which follows, or for assisting sediment budgets. Unfortunately, the poor GCP configuration and resulting DEM tilting issues observed at the San Pedro site mean this data is only indicative of what might be achieved with higher quality data.

Substrate Size Mapping using the Wentworth Scale

Fluvial habitat studies often make use of grain size information classified according to the Wentworth scale (Wentworth 1922), rather than as absolute sizes (e.g. Bovee et al., 1998, Centre for Ecology and Hydrology 2001, Environment Agency 2003). The grouping of predicted quantitative substrate sizes into these classes is straightforward and can be used to create maps such as that shown in Figure E2 (Appendix E) for Coledale Beck. As discussed in Chapter 4, the accuracy of grain size estimates computed from a UAS-SfM approach requires improvement before these measures might be relied upon for any further applications. This is evident in the bar chart shown in Figure E2 (Appendix E), where only 52% of the ground truth sample plots are assigned the correct Wentworth size class (22% are over-predicted and 26% are unpredicted). If improvements can be made in future, then predictions of substrate size or class might be used for habitat modelling applications.

Fish Habitat Suitability Mapping

The mapped distribution of substrate sizes (Figure E3 in Appendix E) and water depth (Figure 3.9 in Chapter 3) for the San Pedro River site were combined with published data (Garcia et al.,

2011) on the fuzzy habitat preferences for the juvenile and adult life stages of the native Chilean fish species ‘Darter’ (*Percilia irwini*), with an aim to predict habitat availability for this species at the Piedra Blanca site. The predicted habitat suitability maps are presented in Figures E4 and E5 (Appendix E) and should ideally be validated against point sampling of fish abundance. Again, the poor GCP configuration and resulting DEM tilting issues at this site mean that the water depth estimates are not reliable. Therefore, these maps are only indicative of what might be achieved with higher quality data. Nevertheless, such detailed mapping has the potential to make important contributions to native fish habitat assessments within Chilean rivers prior to dam construction, as introduced in Chapter 1.

Similar examples are provided by Carbonneau et al., (2012) for predicting habitat availability for juvenile Atlantic salmon within the River Tromie (Figure 6.3), and Tamminga et al., (2014) for mapping habitat suitability for adult and juvenile brown trout, based on a combined index including UAS derived measures of depth and cover, and velocity computed using a hydrodynamic model (Figure 6.4).

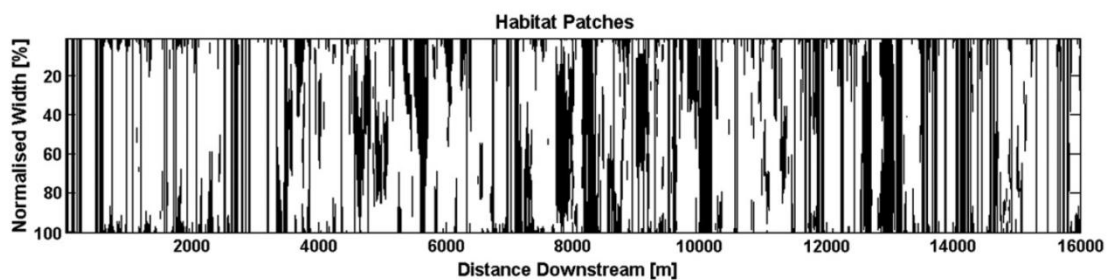


Figure 6.3. Habitat distribution for juvenile Salmon, showing areas in white which meet the depth (0.1-0.6m) and particle size (25-250mm for D50) requirements, and areas in black which do not. The river has been reprojected to a rectangular display so the entire river can be displayed (Carbonneau et al., 2012).

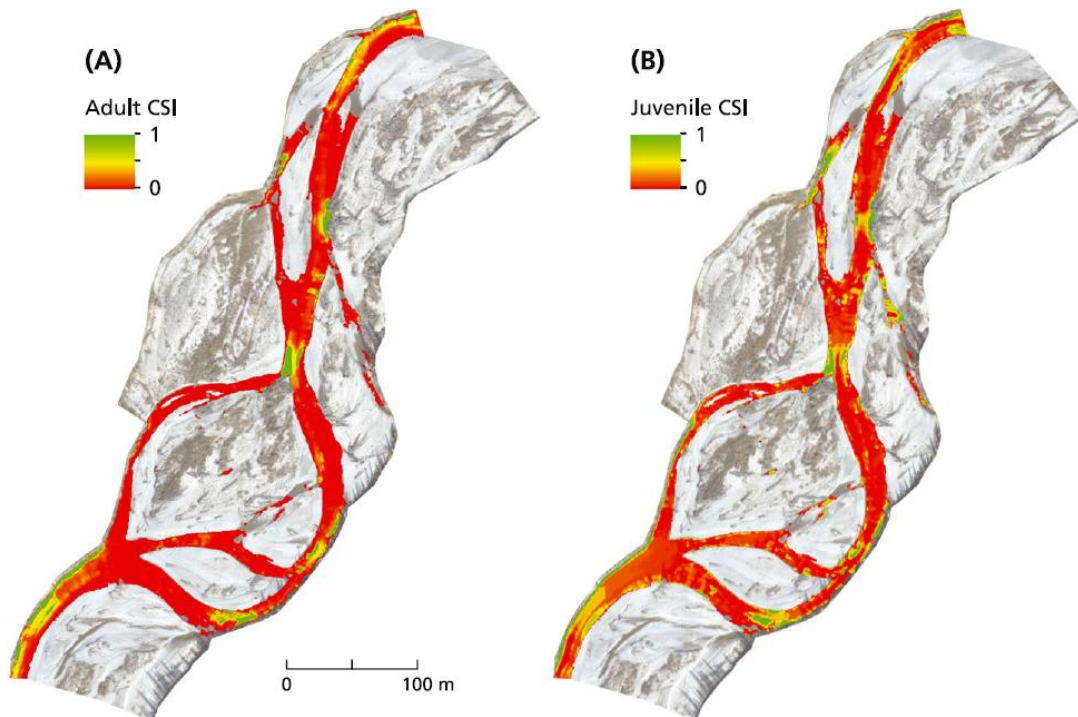


Figure 6.4. Distribution of habitat suitability for (a) adult and (b) juvenile brown trout, based on a composite suitability index (Tamminga et al., 2014).

Geomorphic Change Detection

The repeat surveys at the River Arrow provided an opportunity to conduct geomorphic change detection using the UAS-SfM data. The limited time difference between the May 2013 and August 2013 surveys meant that little geomorphic change was expected to have occurred. The map provided in Figure E6 (Appendix E) accounts for the root mean square error (RMSE) of both datasets ($\pm 0.025\text{m}$) yet appears to show extensive elevation change across the site. This includes erosion of steep banks in places and the growth of bankside vegetation over the summer period. Spatially extensive erosion is also shown within the submerged channel itself, however it is not clear whether this represents real change. An in depth assessment of the ability of the UAS-SfM approach to accurately detect geomorphic change is beyond the scope of this thesis. DEM quality issues relating to, amongst other things, the matching of points in submerged areas and systematic errors resulting from the SfM processing chain require careful consideration however, by comparison with a dedicated ground truthing survey. This should form an important focus for future work, to establish the value of the UAS-SfM quantitative outputs for geomorphic change detection and a range of related applications, such as sediment transport investigations studies similar to the Bassenthwaite Lake Restoration Programme introduced in Chapter 1.

Perhaps due to the immaturity of the approach, very few published studies have yet evaluated multi-temporal UAS-SfM surveys for geomorphic change detection within fluvial settings. The exception is the work of Flener et al., (2013), where DEMs produced using a combination of mobile laser scanning (for exposed areas) and UAS spectral-depth data (for submerged areas) for two consecutive years were compared (Figure 6.5). Figure 6.5 suggests that deposition (in red) of up to 0.7m occurred in parts of the submerged channel, although validation of this data using a level of significant change detection suggests that only 15.4% of the channel area is showing significant change outside of the bounds of error. An indication of the spatial extent of this 15.4% is not provided. This paper therefore highlights the need for more extensive and rigorous assessments of a UAS-SfM approach for detecting fluvial geomorphological change.

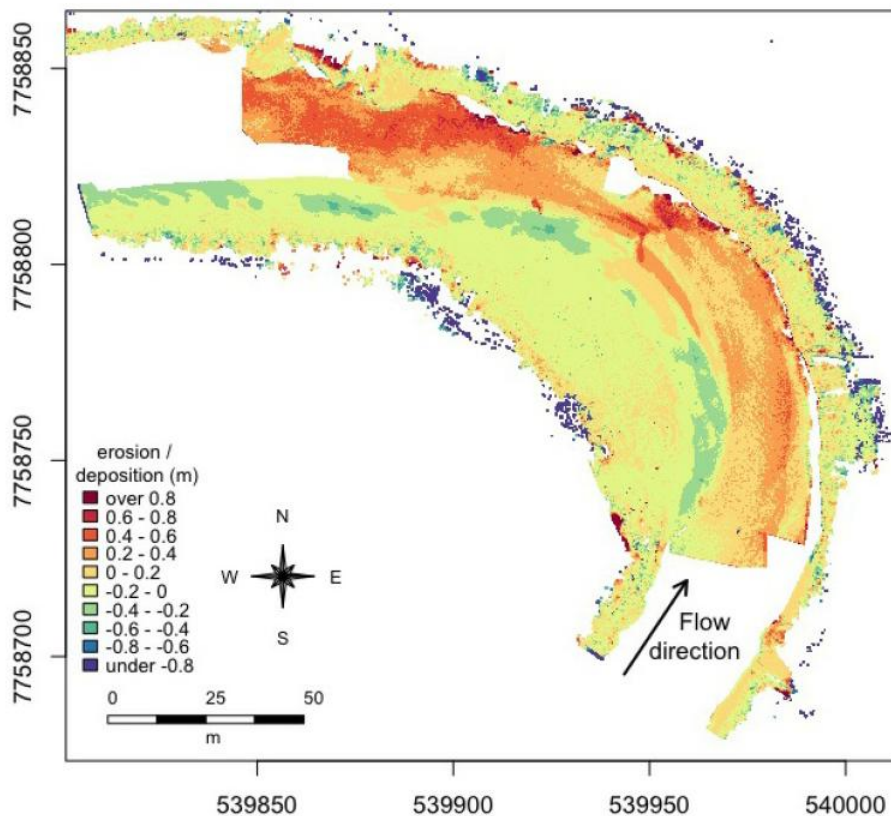


Figure 6.5. Geomorphic change between 2010 and 2011, based on the contiguous DEMs created from UAS and mobile TLS data (Flener et al., 2013).

6.6 Final conclusions

The physical parameters of topography, water depth, substrate size and flow velocity are critical in determining the type, extent and quality of habitat availability within river systems. As a consequence, the measurement and monitoring of these parameters is paramount for maintaining or improving fluvial habitat quality, as required by legislation such as the EU Water Framework Directive. Traditional field-based methods of quantifying physical river habitat parameters are laborious and time consuming, and often fail to represent adequately the fine scale spatial heterogeneity of habitat conditions recognised by a riverscape style framework (Fausch et al., 2002). Remote sensing based approaches have provided many advantages over field based techniques, but few are capable of quantifying simultaneously a number of physical habitat variables using a single dataset whilst also operating within the ideals of a riverscape approach. The research presented within this thesis aimed to assess the capabilities of a relatively novel approach using UAS and SfM-photogrammetric processing for achieving just that. The orthophotos, DEMs and point clouds produced from the UAS-SfM approach were analysed for quantifying the following physical river habitat parameters at the mesoscale; fluvial topography, flow depth, substrate size and SFTs as a proxy for hydraulic conditions.

This research has demonstrated that a UAS-SfM approach can be used to quantify the specified physical river habitat parameters, albeit within certain constraints (Figure 6.1). Significant advantages over traditional fieldwork approaches include the spatially continuous and spatially explicit data coverage which is objective and repeatable, and capable of covering mesoscale extents of channel within a day's fieldwork. The exceptionally high spatial resolution outputs, rapid and on-demand nature of data acquisition and processing also represent advantages over other remote sensing techniques, which are typically conducted from (a) higher flying airborne platforms which tend to provide lower resolution datasets and slower mobilisation speeds, or (b) terrestrial based platforms which are often slower to acquire data, provide more limited spatial coverage and sometimes encounter problems relating to a strongly oblique view point.

Application of the UAS-SfM approach developed within this thesis at three different research sites has enabled the production of c. 2cm resolution DEMs for assessing topography in both exposed and submerged areas, 0.5cm resolution grain size estimates for exposed gravel bars and has allowed detailed mapping of surface flow types from c. 1cm resolution ortho-imagery.

However, the accuracy, precision and reliability of results is shown to be variable within and between different research sites, and the ability to produce consistently high quality outputs for all the specified physical river habitat parameters simultaneously has *not* yet been proven. A number of critical limitations relating to data acquisition (including the effects of image blurring and need for favourable weather conditions) and data processing (systematic errors arising from the SfM processing) have been identified. The recognition of these limitations has highlighted a number of important areas for further work.

Ultimately, the UAS-SfM approach has potential as a valuable tool for providing quantitative information for the assessment of fluvial environments over mesoscale channel extents, and for a wide range of other geomorphological applications. The rapid and on-going developments in the UAS and sensor markets mean that increasingly powerful, more autonomous systems are becoming available, capable of carrying heavier and more complex sensors (e.g. multi-spectral and LiDAR sensors), flying in more challenging conditions and for longer times, enabling coverage of greater areas at hyperspatial resolutions. It is hoped that such improvements in UAS, in conjunction with further rigorous and dedicated quantitative assessments, will facilitate the development of the UAS-SfM approach to a point where it might be used for routine and reliable assessments of the quality and availability of river habitats in future.

6.7 References

- Bovee, K.D. (1996) Perspectives on two-dimensional river habitat models: the PHABSIM experience. In Le Clerc, M., Capra, H., Valentin, S., Boudreault, A., and Cote, Y. (Eds) Ecohydraulique 2000: Proceedings of the 2nd IAHR Symposium on Habitat Hydraulics, Quebec: 150-162.
- Bovee, K.D., Lamb, B.L., Bartholow, J.M., Stalnaker, C.B., Taylor, J. and Henriksen, J. (1998) Stream habitat analysis using the instream flow incremental methodology. *U.S. Geological Survey, Biological Resources Division Information and Technology Report. USGS/BRD-1998-0004*. Viii + 131 pp.
- Brasington, J., Vericat, D. and Rychov, I. (2012) Modeling river bed morphology, roughness, and surface sedimentology using high resolution terrestrial laser scanning. *Water Resources Research* 48 W11519, doi: 10.1029/2012WR012223.
- Brasington, J. (2014) Shining new light on old ground: Novel ways to interpret the Earth. *RSPSoc Wavelength Conference, 14-16 April 2014, Malvern, UK*.
- Carbonneau, P.E., Fonstad, M.A., Marcus, W.A. and Dugdale, S.J. (2012) Making riverscapes real. *Geomorphology* 123: 74-86.
- Centre for Ecology and Hydrology (2001) Further validation of PHABSIM for the habitat requirements of salmonid fish. *Final project report to Environment Agency (W6-036) and CEH (C00962)*.
- Chandler, J.H., Fryer, J.G. and Jack, A. (2005) Metric capabilities of low-cost digital cameras for close range surface measurement. *The Photogrammetric Record* 20 (109): 12-26.
- Cooke, R.U. and Doonkamp, J.C. (1990) Geomorphology in environmental management: a new introduction (2nd Edition), Clarendon Press, Oxford.
- De Haas, T., Ventra, D., Carbonneau, P. and Kleinhans, M.G. (2014) Debris flow dominance of alluvial fans masked by runoff reworking and weathering. *Geomorphology* 217: 165-181.
- Eltner, A., Mulsow, C. and Maas, H-G. (2013) Quantitative measurement of soil erosion from TLS and UAV data. *International Archives of the Photogrammetry, Remote Sensing and Spatial Information Sciences*, Volume XL-1/W2, UAV-g2013, 4-6 September 2013, Rostock, Germany.
- Environment Agency (2003) River Habitat Survey in Britain and Ireland: Field Survey Guidance Manual. Available online: https://www.gov.uk/government/uploads/system/uploads/attachment_data/file/311579/LIT_1758.pdf (accessed 11.02.2015).
- Environment Agency (2014) LiDAR. Available online: www.geomaticsgroup.co.uk/GeoCMS/Products/LIDAR.aspx (accessed 29.09.2014).
- Fausch, K.D., Torgersen, C.E., Baxter, C.V. and Hiram, L.W. (2002) Landscapes to riverscapes: bridging the gap between research and conservation of stream fishes. *BioScience* 52 (6): 483-498.
- Finkl, C.W., Becerra, J.E., Achatz, V. and Andrews, J.L. (2008) Geomorphological mapping along the upper southeast Florida Atlantic continental platform; 1: Mapping units, symbolisation and GIS presentation of interpreted seafloor topography. *Journal of Coastal Research* 24 (6): 1388-1417.
- Flener, C., Vaaja, M., Jaakkola, A., Krooks, A., Kaartinen, H., Kukko, A., Kasvi, E., Hyyppä, H., Hyyppä, J. and Alho, P. (2013) Seamless mapping of river channels at high resolution using mobile LiDAR and UAV-photography. *Remote Sensing* 5: 6382-6407.

Garcia, A., Jorde, K., Habit, E., Caamano, D. and Parra, O. (2011) Downstream environmental effects of dam operations: changes in habitat quality for native fish species. *River Research and Applications* 27: 312-327.

Graham, D.J., Reid, I. and Rice, S.P. (2005) Automated sizing of coarse-grained sediments: image-processing procedures. *Mathematical Geology* 37(1): 1-28.

Halcrow Group Ltd (2009) Cayton Bay Cliff Stability Assessment Ground Investigation and Appraisal of Engineering Stabilisation Options. Report for Scarborough Borough Council.

Heritage, G.L. and Milan, D.J. (2009) Terrestrial laser scanning of grain roughness in a gravel-bed river. *Geomorphology* 113: 4-11.

James, M.R. and Robson, S. (2014) Mitigating systematic error in topographic models derived from UAV and ground-based image networks. *Earth Surface Processes and Landforms* 39: 1413-1420.

Javernick, L., Brasington, J. and Caruso, B. (2014) Modelling the topography of shallow braided rivers using Structure-from-Motion photogrammetry. *Geomorphology* 213: 166-182.

Lague, D., Brodu, N. and Leroux, J. (2013) Accurate 3D comparison of complex topography with terrestrial laser scanner: Application to the Rangitikei canyon (N-Z). *ISPRS Journal of Photogrammetry and Remote Sensing* 82: 10-26.

Lejot, J., Delacourt, C., Piegay, H., Fournier, T., Tremelo, M-L. and Allemand, P. (2007) Very high spatial resolution imagery for channel bathymetry and topography from an unmanned mapping controlled platform. *Earth Surface Processes and Landforms* 32: 1705-1725.

Milan, D.J., Heritage, G.L., Large, A.R.G. and Entwistle, N.S. (2010) Mapping hydraulic biotopes using terrestrial laser scan data of water surface properties. *Earth Surface Processes and Landforms* 35: 918-931.

Natural Environment Research Council (2014) Advanced Training Courses 2014/15. Available online: <http://www.nerc.ac.uk/funding/available/postgrad/advanced/atasc/course-list2014-15.pdf> (accessed 13.02.2015).

Newson, M.D. and Newson, C.L. (2000) Geomorphology, ecology and river channel habitat: mesoscale approaches to basin-scale challenges. *Progress in Physical Geography* 24 (2): 195-217.

Rychov, I., Brasington, J. and Vericat, D. (2012) Computational and methodological aspects of terrestrial surface analysis based on point clouds. *Computers and Geosciences* 42: 64-70.

Sieberth, T., Wackrow, R. and Chandler, J.H. (2013) Automation isolation of blurred images from UAV image sequences. *International Archives of Photogrammetry, Remote Sensing and Spatial Information Sciences*, XL-1/W2: 361-366.

Smith, M.J., Rose, J. and Booth, S. (2006) Geomorphological mapping of glacial landforms from remotely sensed data: An evaluation of the principal data sources and an assessment of their quality. *Geomorphology* 76: 148-165 .

Smith, M.W. and Vericat, D. (2014) Evaluating shallow-water bathymetry from through-water terrestrial laser scanning under a range of hydraulic and physical water quality conditions. *River Research and Applications* 30 (7): 905-924.

Tamminga, A., Hugenholtz, C., Eaton, B. and Lapointe, M. (2014) Hyperspatial remote sensing of channel reach morphology and hydraulic fish habitat using an unmanned aerial vehicle (UAV): A first assessment

in the context of river research and management. *River Research and Applications* doi: 10.1002/rra.2743.

Wackrow, R. and Chandler, J.H. (2008) A convergent image configuration for DEM extraction that minimises the systematic effects caused by an inaccurate lens model. *Photogrammetric Record* 23 (121): 6-18.

Ward, J.V., Malard, F. and Tockner, K. (2002) Landscape ecology: a framework for integrating pattern and process in river corridors. *Landscape Ecology* 17 (1): 35-45.

Wentworth, C.K. (1922) 'A scale of grade and class terms for clastic sediments' *Journal of Geology* 30: 377-392.

Westoby, M.J., Brasington, J., Glasser, N.F., Hambrey, M.J. and Reynolds, J.M. (2012) Structure-from-Motion photogrammetry: a low cost, effective tool for geoscience applications. *Geomorphology* 179: 300-314.

Wiens, J.A. (2002) Riverine landscapes: taking landscape ecology into the water. *Freshwater Biology* 47: 501-515.

Appendix A

Methods

Division of work at Coledale Beck

Participants: Amy Woodget (AW), Richard Johnson (RJ), Andy Skellern (AS), Jeff Warburton (JW), Fleur Visser (FV), James Atkins (JA).

Research concept and design: AW (100%)

Site reconnaissance: AW (50%), RJ (50%)

UAS data collection and processing: AW (100%)

Collection and post-processing of dGPS data: JW (100%)

TLS data collection: RJ, AS (100%)

Co-registering TLS data and error diagnostics: RJ, AS (100%)

Initial editing of TLS point cloud in Leica Cyclone: RJ, AS (100%)

Subsequent analysis of TLS data: AW (100%)

Additional fieldwork assistance from FV, JA and two undergraduates from Bath Spa University is gratefully acknowledged.

Division of work at the San Pedro River

Participants: Amy Woodget (AW), Ian Maddock (IM), Evelyn Habit (EH), Filipe Breton (FB), Caroline Wallis (CW), Alonso Gonzalez-Diaz (AGD)

Research concept: IM (70%), EH (30%)

Research design: AW (100%)

UAS data collection: AW (50%), IM (50%)

Collection of dGPS data: FB (100%)

UAS data processing using SfM: AW (100%)

Subsequent analysis of UAS-SfM data: AW (100%)

Additional fieldwork assistance from CW and AGD is also gratefully acknowledged.

SfM-photogrammetry orthophotos and DEMs

Figure A1. Orthophoto and DEM for the San Pedro River, May 2012.

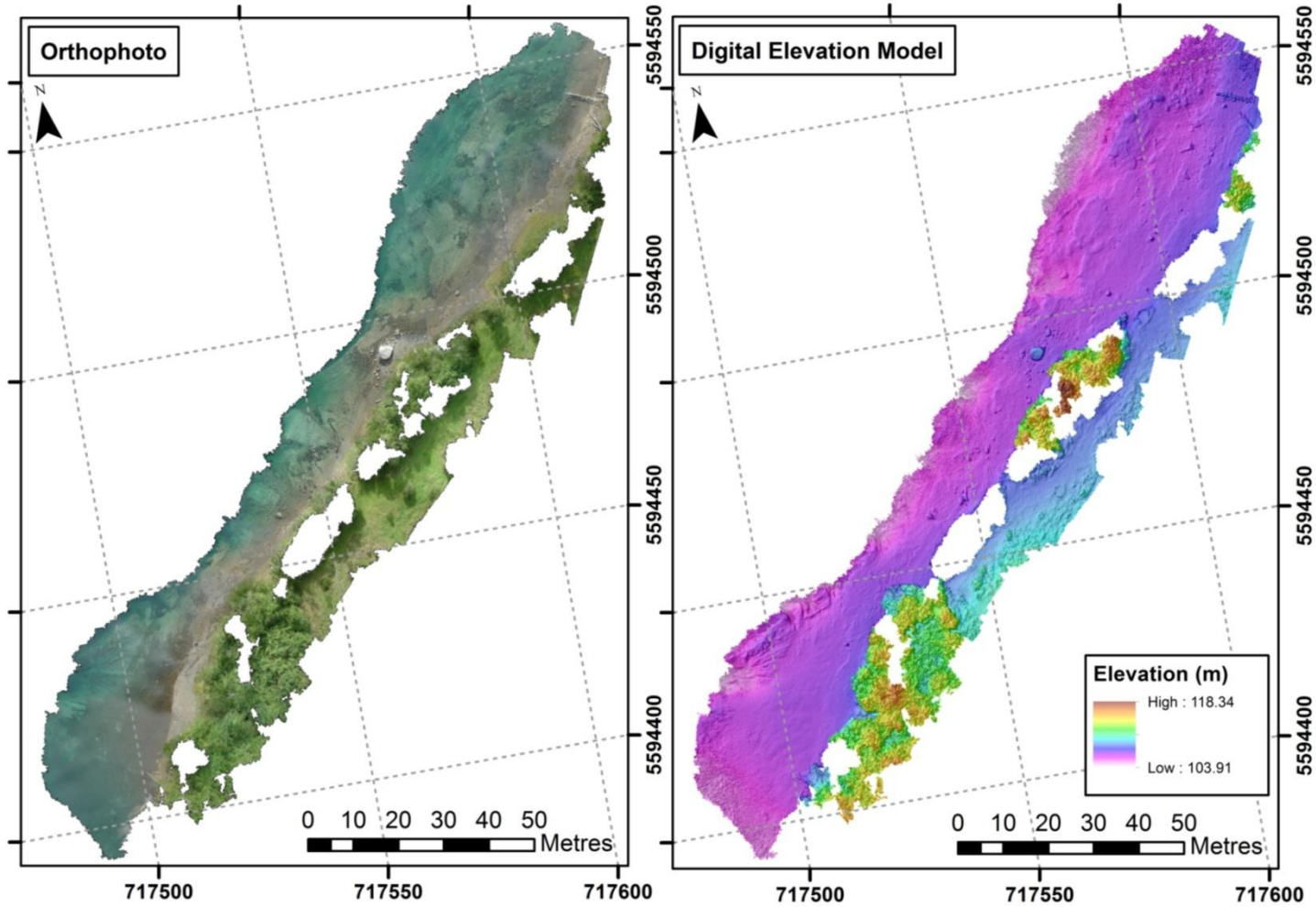


Figure A2. Orthophoto and DEM for the River Arrow, July 2012.

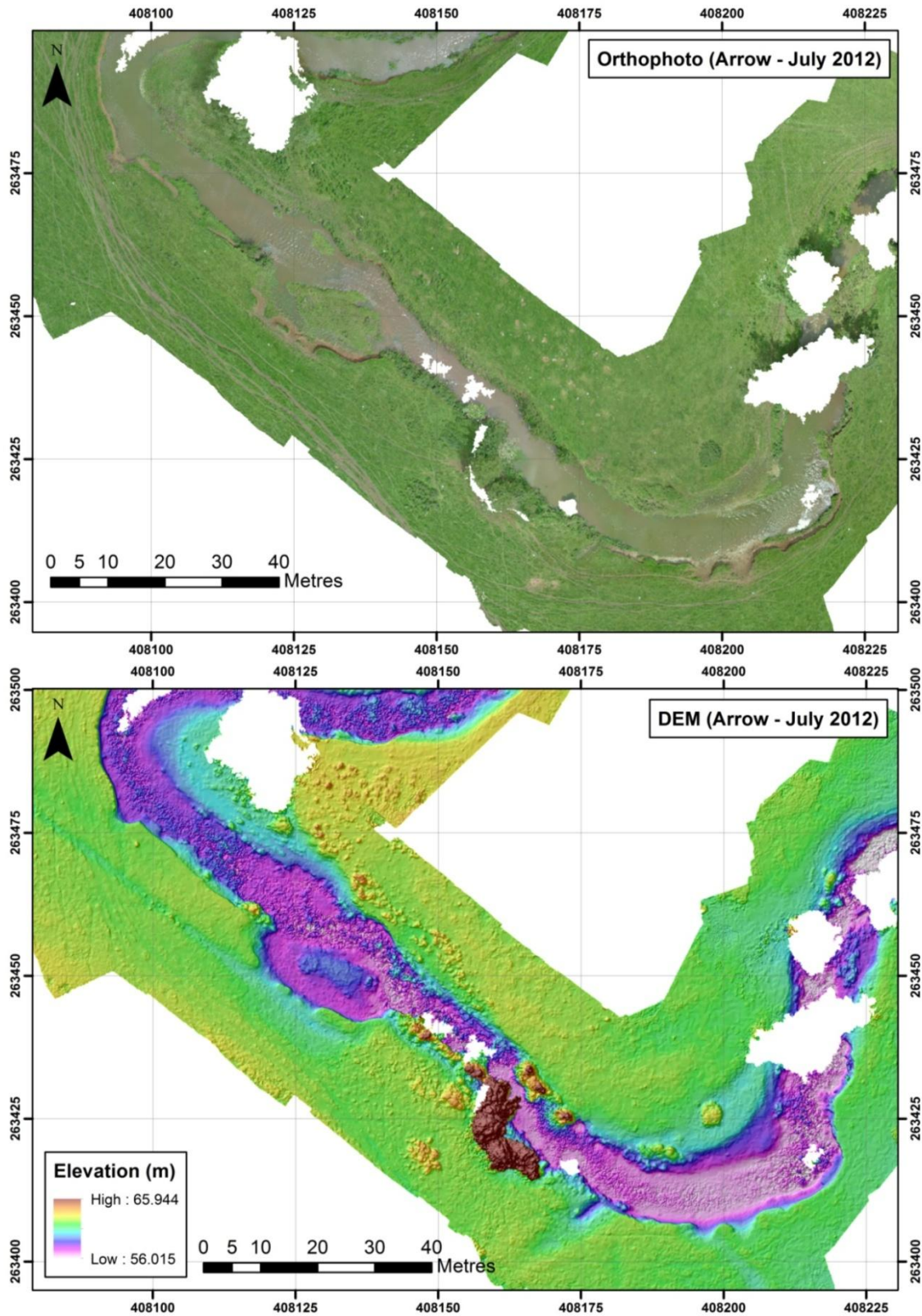


Figure A3. Orthophoto and DEM for the River Arrow, May 2013.

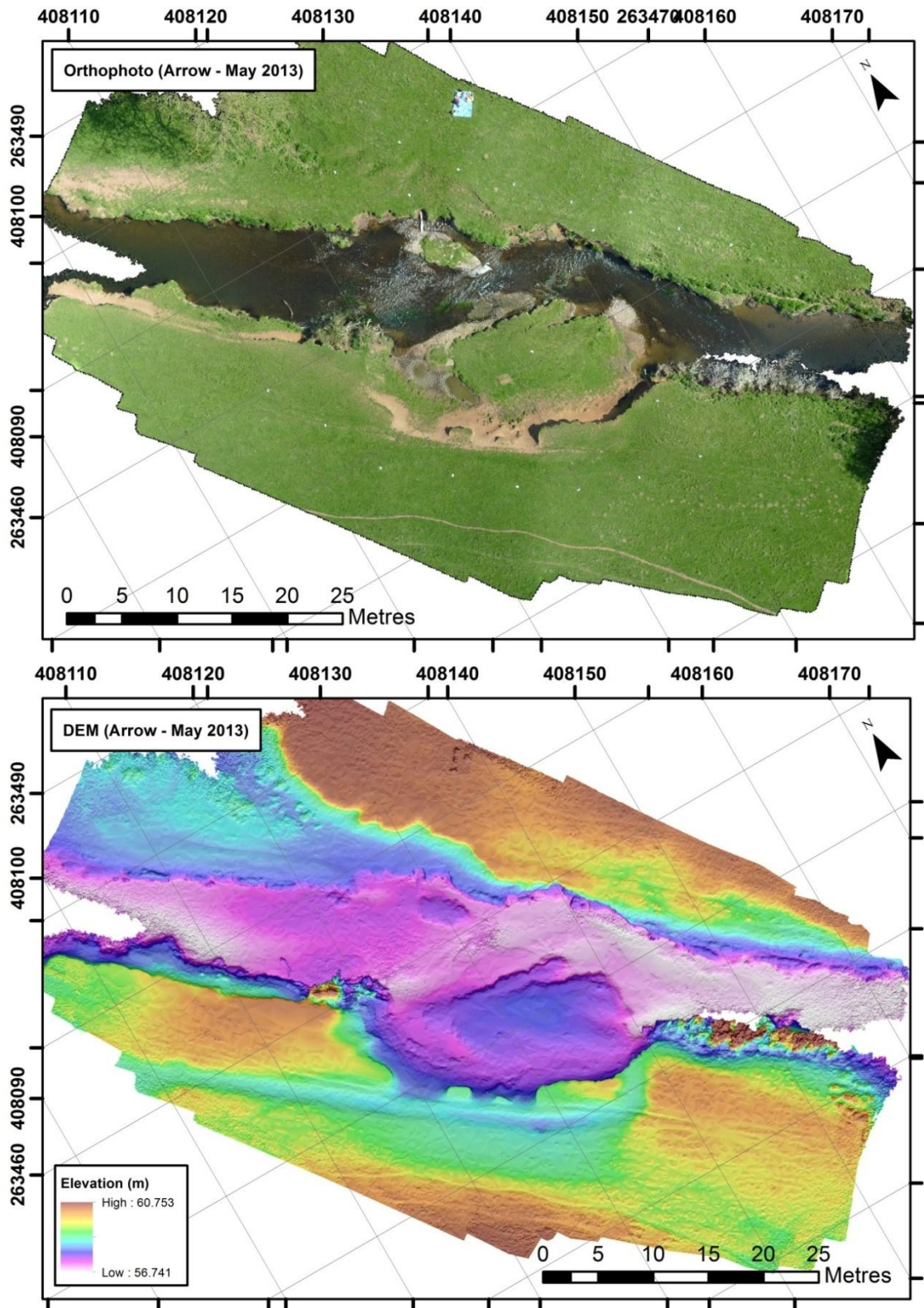


Figure A4. Orthophoto and DEM for the River Arrow, June 2013.

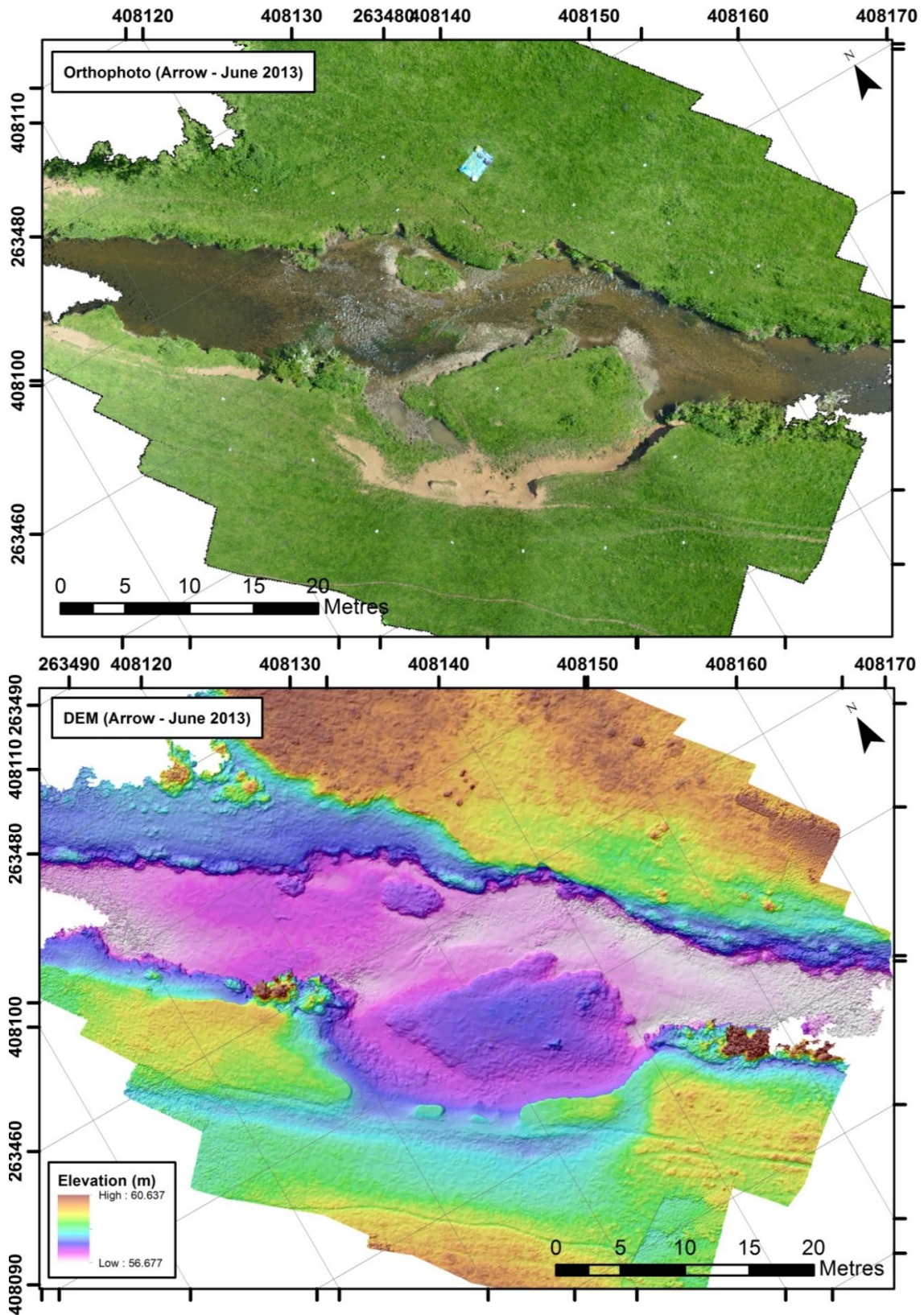


Figure A5. Orthophoto and DEM for the River Arrow, August 2013.

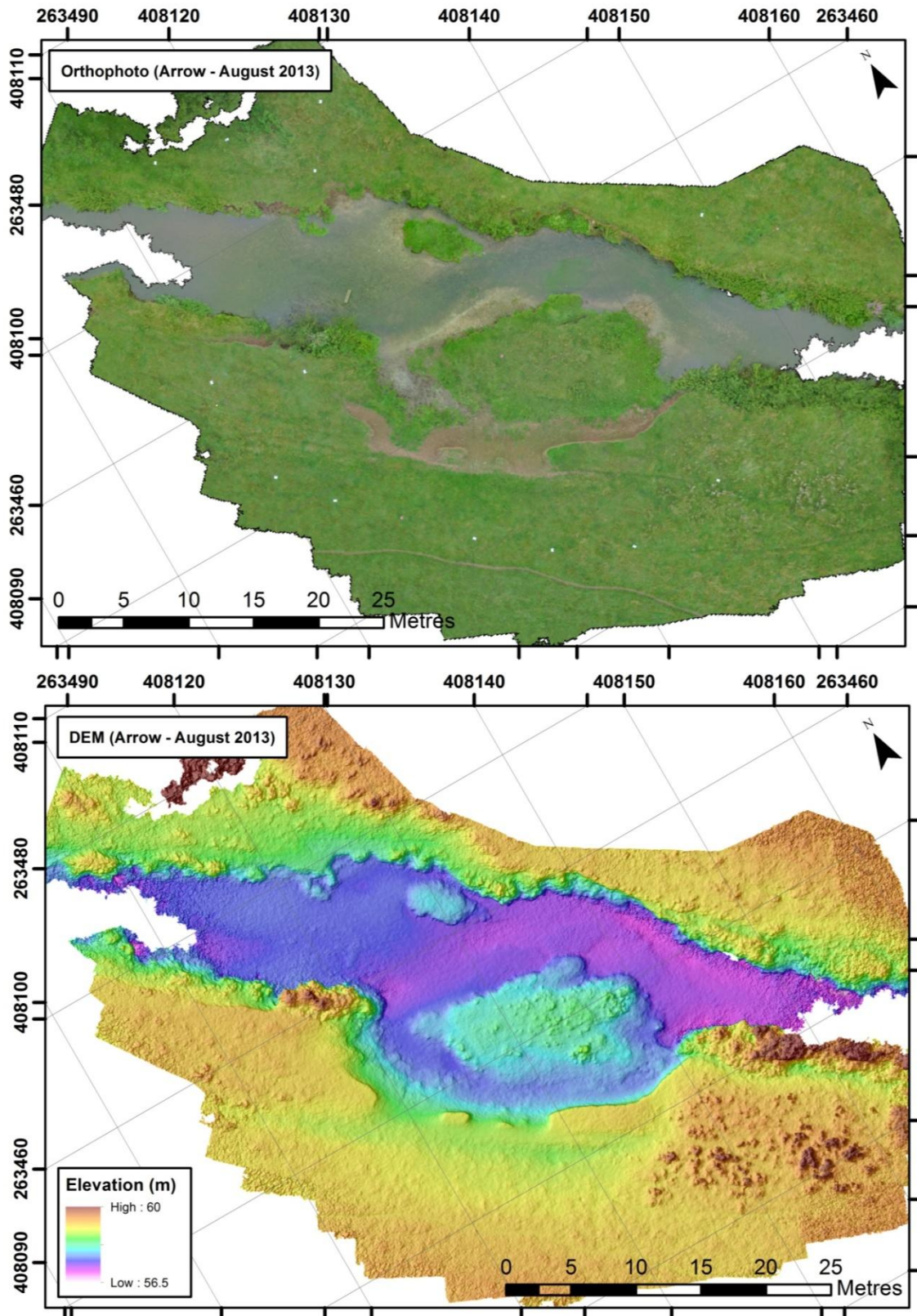
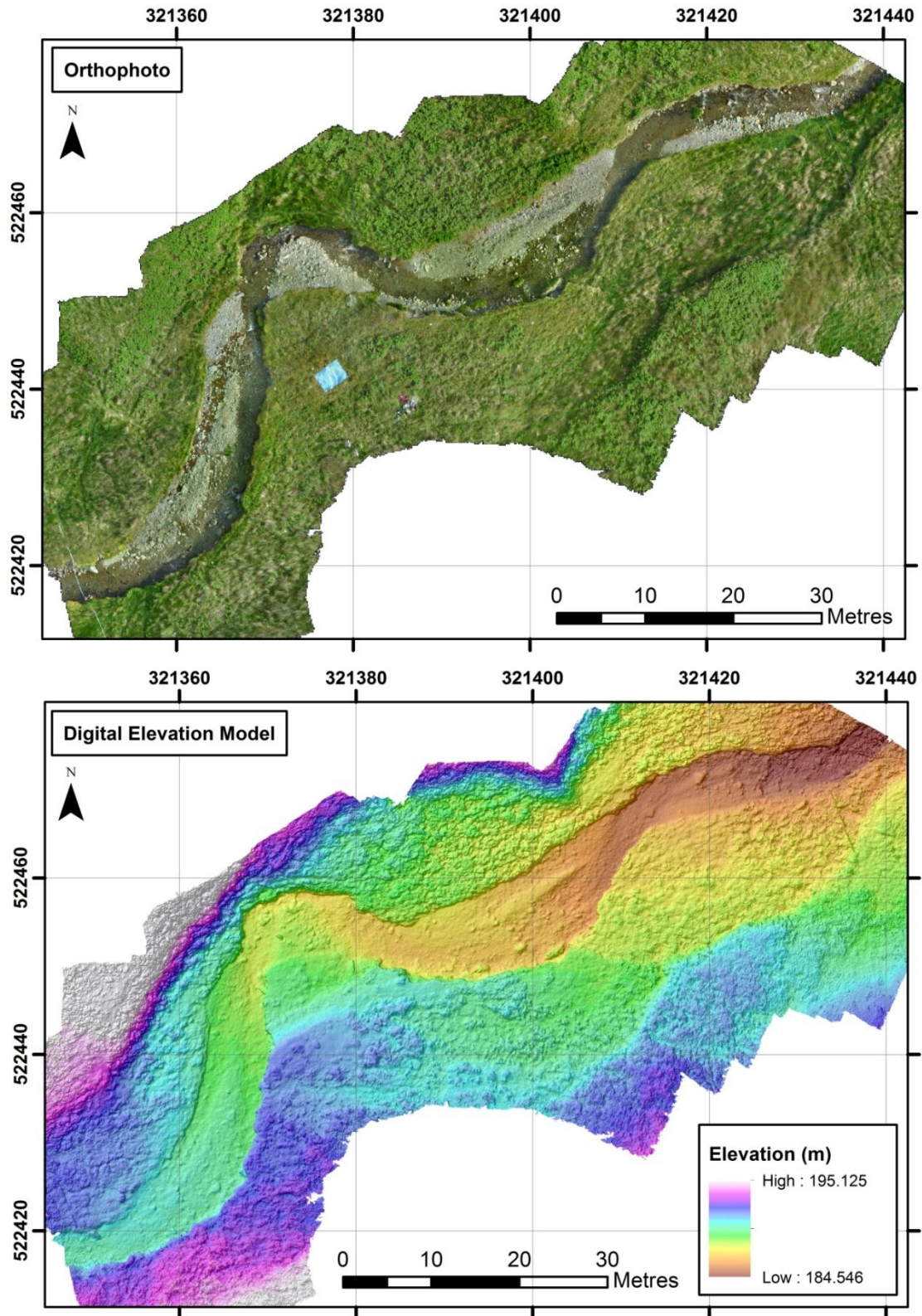


Figure A6. Orthophoto and DEM for the Coledale Beck, July 2013.



TLS Registration Error Diagnostics

Status: VALID Registration

Mean Absolute Error:

for Enabled Constraints = 0.009 m

for Disabled Constraints = 3.059 m

Date: 2014.04.11 12:04:20

Database name : Coledale2013

ScanWorlds

Station-001: SW-001 (Leveled)
Station-002: SW-002 (Leveled)
Station-003: SW-003 (Leveled)
Station-004: SW-004 (Leveled)
Station-005: SW-005 (Leveled)
Station-007: SW-007 (Leveled)
Station-008: SW-008 (Leveled)
Station-006: SW-006 (Leveled)
Coledale090713TargetsRevised.txt (Leveled)

Constraints

ScanWorld Transformations

Station-001: SW-001 (Leveled)
translation: (321361.051, 522462.133, 196.822) m
rotation: (-0.0000, -0.0000, -1.0000):14.247 deg

Coledale090713TargetsRevised.txt (Leveled)
translation: (0.000, 0.000, 0.000) m
rotation: (0.0000, 1.0000, 0.0000):0.000 deg

Station-002: SW-002 (Leveled)
translation: (321400.723, 522475.715, 194.020) m
rotation: (0.0000, 0.0000, 1.0000):85.705 deg

Unused ControlSpace Objects
Station-001: SW-001 (Leveled):
Vertex : unlabeled

Station-003: SW-003 (Leveled)
translation: (321418.190, 522464.852, 188.274) m
rotation: (0.0000, 0.0000, 1.0000):86.089 deg

Station-002: SW-002 (Leveled):
Vertex : unlabeled

Station-004: SW-004 (Leveled)
translation: (321403.434, 522449.029, 189.764) m
rotation: (-0.0000, -0.0000, -1.0000):-117.616 deg

Station-003: SW-003 (Leveled):
Vertex : unlabeled

Station-005: SW-005 (Leveled)
translation: (321370.972, 522448.967, 190.080) m
rotation: (-0.0000, -0.0000, -1.0000):-172.764 deg

Station-004: SW-004 (Leveled):
Vertex : unlabeled

Station-007: SW-007 (Leveled)
translation: (321352.753, 522422.184, 191.205) m
rotation: (0.0000, 0.0000, 1.0000):-176.250 deg

Station-005: SW-005 (Leveled):
Vertex : unlabeled

Station-008: SW-008 (Leveled)
translation: (321359.347, 522431.766, 190.762) m
rotation: (-0.0000, -0.0000, -1.0000):20.785 deg

Station-007: SW-007 (Leveled):
Vertex : unlabeled

Station-006: SW-006 (Leveled)
translation: (321363.658, 522420.068, 191.711) m
rotation: (0.0000, 0.0000, 1.0000):-166.350 deg

Station-008: SW-008 (Leveled):
Vertex : unlabeled

Station-006: SW-006 (Leveled):
Vertex : unlabeled

*Quantifying physical river habitat parameters using hyperspatial resolution
UAS imagery and SfM-photogrammetry*

Table A1. TLS error diagnostics, exported from Leica Cyclone (Leica Geosystems Ltd).

Name	ScanWorld	ScanWorld	Type	On/Off	Weight	Error	Error Vector	Horz	Vert
t1	Station-001: SW-001 (Leveled)	Station-002: SW-002 (Leveled)	Coincident: Vertex - Vertex	On	1	0.003 m	(-0.002, 0.000, 0.001) m	0.002 m	0.001 m
t4	Station-001: SW-001 (Leveled)	Station-002: SW-002 (Leveled)	Coincident: Vertex - Vertex	Off	1	0.002 m	(-0.001, -0.001, 0.002) m	0.001 m	0.002 m
t3a	Station-001: SW-001 (Leveled)	Station-002: SW-002 (Leveled)	Coincident: Vertex - Vertex	On	1	0.002 m	(0.001, 0.001, 0.000) m	0.002 m	0.000 m
t2	Station-001: SW-001 (Leveled)	Station-002: SW-002 (Leveled)	Coincident: Vertex - Vertex	On	1	0.001 m	(0.000, 0.001, 0.000) m	0.001 m	0.000 m
t5	Station-001: SW-001 (Leveled)	Station-002: SW-002 (Leveled)	Coincident: Vertex - Vertex	On	1	0.002 m	(0.001, -0.001, 0.000) m	0.002 m	0.000 m
t6	Station-001: SW-001 (Leveled)	Station-002: SW-002 (Leveled)	Coincident: Vertex - Vertex	Off	1	27.690 m	(15.701, 22.783, -1.076) m	27.669 m	-1.076 m
t1	Station-001: SW-001 (Leveled)	Station-003: SW-003 (Leveled)	Coincident: Vertex - Vertex	On	1	0.005 m	(-0.002, -0.001, -0.004) m	0.002 m	-0.004 m
t4	Station-001: SW-001 (Leveled)	Station-003: SW-003 (Leveled)	Coincident: Vertex - Vertex	Off	1	0.005 m	(-0.002, 0.000, 0.004) m	0.002 m	0.004 m
t3a	Station-001: SW-001 (Leveled)	Station-003: SW-003 (Leveled)	Coincident: Vertex - Vertex	On	1	0.004 m	(0.001, 0.001, 0.004) m	0.001 m	0.004 m
t2	Station-001: SW-001 (Leveled)	Station-003: SW-003 (Leveled)	Coincident: Vertex - Vertex	On	1	0.003 m	(0.000, 0.003, 0.000) m	0.003 m	0.000 m
t5	Station-001: SW-001 (Leveled)	Station-003: SW-003 (Leveled)	Coincident: Vertex - Vertex	On	1	0.003 m	(0.001, -0.003, 0.001) m	0.003 m	0.001 m
t3a	Station-002: SW-002 (Leveled)	Station-003: SW-003 (Leveled)	Coincident: Vertex - Vertex	On	1	0.004 m	(0.000, -0.001, 0.004) m	0.001 m	0.004 m
t4	Station-002: SW-002 (Leveled)	Station-003: SW-003 (Leveled)	Coincident: Vertex - Vertex	Off	1	0.003 m	(-0.001, 0.001, 0.002) m	0.001 m	0.002 m
t5	Station-002: SW-002 (Leveled)	Station-003: SW-003 (Leveled)	Coincident: Vertex - Vertex	On	1	0.002 m	(0.000, -0.001, 0.001) m	0.001 m	0.001 m
t2	Station-002: SW-002 (Leveled)	Station-003: SW-003 (Leveled)	Coincident: Vertex - Vertex	On	1	0.002 m	(0.000, 0.002, 0.000) m	0.002 m	0.000 m
t1	Station-002: SW-002 (Leveled)	Station-003: SW-003 (Leveled)	Coincident: Vertex - Vertex	On	1	0.005 m	(0.000, 0.000, -0.005) m	0.000 m	-0.005 m
t1	Station-001: SW-001 (Leveled)	Station-004: SW-004 (Leveled)	Coincident: Vertex - Vertex	On	1	0.005 m	(-0.002, 0.000, -0.005) m	0.002 m	-0.005 m
t4	Station-001: SW-001 (Leveled)	Station-004: SW-004 (Leveled)	Coincident: Vertex - Vertex	Off	1	0.003 m	(0.000, 0.000, 0.003) m	0.000 m	0.003 m

*Quantifying physical river habitat parameters using hyperspatial resolution
UAS imagery and SfM-photogrammetry*

t3a	Station-001: SW-001 (Leveled)	Station-004: SW-004 (Leveled)	Coincident: Vertex - Vertex	On	1	0.003 m	(0.000, 0.001, 0.003) m	0.001 m	0.003 m
t2	Station-001: SW-001 (Leveled)	Station-004: SW-004 (Leveled)	Coincident: Vertex - Vertex	On	1	0.001 m	(0.000, 0.001, 0.000) m	0.001 m	0.000 m
t5	Station-001: SW-001 (Leveled)	Station-004: SW-004 (Leveled)	Coincident: Vertex - Vertex	On	1	0.002 m	(0.002, -0.001, 0.001) m	0.002 m	0.001 m
t6	Station-001: SW-001 (Leveled)	Station-004: SW-004 (Leveled)	Coincident: Vertex - Vertex	Off	1	0.002 m	(0.000, 0.000, -0.002) m	0.000 m	-0.002 m
t3a	Station-002: SW-002 (Leveled)	Station-004: SW-004 (Leveled)	Coincident: Vertex - Vertex	On	1	0.004 m	(0.000, -0.001, 0.004) m	0.001 m	0.004 m
t4	Station-002: SW-002 (Leveled)	Station-004: SW-004 (Leveled)	Coincident: Vertex - Vertex	Off	1	0.002 m	(0.001, 0.000, 0.001) m	0.001 m	0.001 m
t6	Station-002: SW-002 (Leveled)	Station-004: SW-004 (Leveled)	Coincident: Vertex - Vertex	Off	1	27.690 m	(-15.701, -22.783, 1.074) m	27.670 m	1.074 m
t5	Station-002: SW-002 (Leveled)	Station-004: SW-004 (Leveled)	Coincident: Vertex - Vertex	On	1	0.002 m	(0.000, 0.000, 0.002) m	0.000 m	0.002 m
t2	Station-002: SW-002 (Leveled)	Station-004: SW-004 (Leveled)	Coincident: Vertex - Vertex	On	1	0.001 m	(0.000, 0.001, 0.001) m	0.001 m	0.001 m
t1	Station-002: SW-002 (Leveled)	Station-004: SW-004 (Leveled)	Coincident: Vertex - Vertex	On	1	0.006 m	(0.000, 0.000, -0.006) m	0.000 m	-0.006 m
t1	Station-003: SW-003 (Leveled)	Station-004: SW-004 (Leveled)	Coincident: Vertex - Vertex	On	1	0.001 m	(0.000, 0.000, -0.001) m	0.000 m	-0.001 m
t2	Station-003: SW-003 (Leveled)	Station-004: SW-004 (Leveled)	Coincident: Vertex - Vertex	On	1	0.002 m	(0.000, -0.002, 0.000) m	0.002 m	0.000 m
t3a	Station-003: SW-003 (Leveled)	Station-004: SW-004 (Leveled)	Coincident: Vertex - Vertex	On	1	0.001 m	(0.000, 0.000, -0.001) m	0.000 m	-0.001 m
t4	Station-003: SW-003 (Leveled)	Station-004: SW-004 (Leveled)	Coincident: Vertex - Vertex	Off	1	0.002 m	(0.002, 0.000, -0.001) m	0.002 m	-0.001 m
t5	Station-003: SW-003 (Leveled)	Station-004: SW-004 (Leveled)	Coincident: Vertex - Vertex	On	1	0.002 m	(0.000, 0.001, 0.001) m	0.001 m	0.001 m
t1	Station-001: SW-001 (Leveled)	Station-005: SW-005 (Leveled)	Coincident: Vertex - Vertex	On	1	0.001 m	(0.000, 0.000, -0.001) m	0.001 m	-0.001 m
t4	Station-001: SW-001 (Leveled)	Station-005: SW-005 (Leveled)	Coincident: Vertex - Vertex	Off	1	0.003 m	(0.002, 0.000, -0.003) m	0.002 m	-0.003 m
t3a	Station-001: SW-001 (Leveled)	Station-005: SW-005 (Leveled)	Coincident: Vertex - Vertex	On	1	0.001 m	(0.001, 0.000, 0.000) m	0.001 m	0.000 m
t2	Station-001: SW-001 (Leveled)	Station-005: SW-005 (Leveled)	Coincident: Vertex - Vertex	On	1	0.001 m	(0.000, 0.001, 0.000) m	0.001 m	0.000 m
t5	Station-001: SW-001 (Leveled)	Station-005: SW-005 (Leveled)	Coincident: Vertex - Vertex	On	1	0.001 m	(0.000, -0.001, 0.001) m	0.001 m	0.001 m

*Quantifying physical river habitat parameters using hyperspatial resolution
UAS imagery and SfM-photogrammetry*

t6	Station-001: SW-001 (Leveled)	Station-005: SW-005 (Leveled)	Coincident: Vertex - Vertex	Off	1	0.001 m	(0.001, 0.000, -0.001) m	0.001 m	-0.001 m
t3a	Station-002: SW-002 (Leveled)	Station-005: SW-005 (Leveled)	Coincident: Vertex - Vertex	On	1	0.001 m	(0.000, -0.001, 0.000) m	0.001 m	0.000 m
t4	Station-002: SW-002 (Leveled)	Station-005: SW-005 (Leveled)	Coincident: Vertex - Vertex	Off	1	0.005 m	(0.003, 0.001, -0.005) m	0.003 m	-0.005 m
t6	Station-002: SW-002 (Leveled)	Station-005: SW-005 (Leveled)	Coincident: Vertex - Vertex	Off	1	27.690 m	(-15.701, -22.783, 1.076) m	27.669 m	1.076 m
t5	Station-002: SW-002 (Leveled)	Station-005: SW-005 (Leveled)	Coincident: Vertex - Vertex	On	1	0.002 m	(-0.001, 0.001, 0.001) m	0.002 m	0.001 m
t2	Station-002: SW-002 (Leveled)	Station-005: SW-005 (Leveled)	Coincident: Vertex - Vertex	On	1	0.001 m	(0.000, 0.000, 0.000) m	0.001 m	0.000 m
t1	Station-002: SW-002 (Leveled)	Station-005: SW-005 (Leveled)	Coincident: Vertex - Vertex	On	1	0.003 m	(0.002, 0.000, -0.002) m	0.002 m	-0.002 m
t1	Station-003: SW-003 (Leveled)	Station-005: SW-005 (Leveled)	Coincident: Vertex - Vertex	On	1	0.004 m	(0.002, 0.000, 0.003) m	0.002 m	0.003 m
t2	Station-003: SW-003 (Leveled)	Station-005: SW-005 (Leveled)	Coincident: Vertex - Vertex	On	1	0.002 m	(0.000, -0.002, 0.000) m	0.002 m	0.000 m
t3a	Station-003: SW-003 (Leveled)	Station-005: SW-005 (Leveled)	Coincident: Vertex - Vertex	On	1	0.004 m	(0.000, 0.000, -0.004) m	0.000 m	-0.004 m
t4	Station-003: SW-003 (Leveled)	Station-005: SW-005 (Leveled)	Coincident: Vertex - Vertex	Off	1	0.008 m	(0.004, 0.000, -0.007) m	0.004 m	-0.007 m
t5	Station-003: SW-003 (Leveled)	Station-005: SW-005 (Leveled)	Coincident: Vertex - Vertex	On	1	0.003 m	(-0.002, 0.002, 0.000) m	0.002 m	0.000 m
t6	Station-004: SW-004 (Leveled)	Station-005: SW-005 (Leveled)	Coincident: Vertex - Vertex	Off	1	0.002 m	(0.001, 0.000, 0.002) m	0.001 m	0.002 m
t2	Station-004: SW-004 (Leveled)	Station-005: SW-005 (Leveled)	Coincident: Vertex - Vertex	On	1	0.001 m	(0.000, 0.000, 0.000) m	0.000 m	0.000 m
t1	Station-004: SW-004 (Leveled)	Station-005: SW-005 (Leveled)	Coincident: Vertex - Vertex	On	1	0.004 m	(0.002, 0.000, 0.004) m	0.002 m	0.004 m
t3a	Station-004: SW-004 (Leveled)	Station-005: SW-005 (Leveled)	Coincident: Vertex - Vertex	On	1	0.004 m	(0.000, 0.000, -0.004) m	0.000 m	-0.004 m
t5	Station-004: SW-004 (Leveled)	Station-005: SW-005 (Leveled)	Coincident: Vertex - Vertex	On	1	0.002 m	(-0.002, 0.001, 0.000) m	0.002 m	0.000 m
t4	Station-004: SW-004 (Leveled)	Station-005: SW-005 (Leveled)	Coincident: Vertex - Vertex	Off	1	0.006 m	(0.002, 0.000, -0.006) m	0.002 m	-0.006 m
t1	Station-001: SW-001 (Leveled)	Station-007: SW-007 (Leveled)	Coincident: Vertex - Vertex	On	1	0.002 m	(0.000, -0.001, 0.002) m	0.001 m	0.002 m
t4	Station-001: SW-001 (Leveled)	Station-007: SW-007 (Leveled)	Coincident: Vertex - Vertex	Off	1	0.005 m	(0.000, 0.003, -0.003) m	0.003 m	-0.003 m

*Quantifying physical river habitat parameters using hyperspatial resolution
UAS imagery and SfM-photogrammetry*

t2	Station-001: SW-001 (Leveled)	Station-007: SW-007 (Leveled)	Coincident: Vertex - Vertex	On	1	0.004 m	(0.004, 0.000, -0.001) m	0.004 m	-0.001 m
t5	Station-001: SW-001 (Leveled)	Station-007: SW-007 (Leveled)	Coincident: Vertex - Vertex	On	1	0.001 m	(-0.001, 0.000, 0.001) m	0.001 m	0.001 m
t6	Station-001: SW-001 (Leveled)	Station-007: SW-007 (Leveled)	Coincident: Vertex - Vertex	Off	1	0.004 m	(0.002, 0.001, 0.003) m	0.003 m	0.003 m
t4	Station-002: SW-002 (Leveled)	Station-007: SW-007 (Leveled)	Coincident: Vertex - Vertex	Off	1	0.007 m	(0.000, 0.004, -0.005) m	0.004 m	-0.005 m
t6	Station-002: SW-002 (Leveled)	Station-007: SW-007 (Leveled)	Coincident: Vertex - Vertex	Off	1	27.688 m	(-15.699, -22.782, 1.079) m	27.667 m	1.079 m
t5	Station-002: SW-002 (Leveled)	Station-007: SW-007 (Leveled)	Coincident: Vertex - Vertex	On	1	0.002 m	(-0.002, 0.001, 0.001) m	0.002 m	0.001 m
t2	Station-002: SW-002 (Leveled)	Station-007: SW-007 (Leveled)	Coincident: Vertex - Vertex	On	1	0.003 m	(0.003, 0.000, -0.001) m	0.003 m	-0.001 m
t1	Station-002: SW-002 (Leveled)	Station-007: SW-007 (Leveled)	Coincident: Vertex - Vertex	On	1	0.002 m	(0.002, -0.001, 0.001) m	0.002 m	0.001 m
t1	Station-003: SW-003 (Leveled)	Station-007: SW-007 (Leveled)	Coincident: Vertex - Vertex	On	1	0.006 m	(0.002, 0.000, 0.006) m	0.002 m	0.006 m
t2	Station-003: SW-003 (Leveled)	Station-007: SW-007 (Leveled)	Coincident: Vertex - Vertex	On	1	0.004 m	(0.003, -0.002, -0.001) m	0.004 m	-0.001 m
t4	Station-003: SW-003 (Leveled)	Station-007: SW-007 (Leveled)	Coincident: Vertex - Vertex	Off	1	0.008 m	(0.001, 0.003, -0.008) m	0.004 m	-0.008 m
t5	Station-003: SW-003 (Leveled)	Station-007: SW-007 (Leveled)	Coincident: Vertex - Vertex	On	1	0.003 m	(-0.002, 0.002, 0.000) m	0.003 m	0.000 m
t6	Station-004: SW-004 (Leveled)	Station-007: SW-007 (Leveled)	Coincident: Vertex - Vertex	Off	1	0.006 m	(0.002, 0.001, 0.005) m	0.003 m	0.005 m
t2	Station-004: SW-004 (Leveled)	Station-007: SW-007 (Leveled)	Coincident: Vertex - Vertex	On	1	0.004 m	(0.003, -0.001, -0.001) m	0.003 m	-0.001 m
t1	Station-004: SW-004 (Leveled)	Station-007: SW-007 (Leveled)	Coincident: Vertex - Vertex	On	1	0.007 m	(0.002, -0.001, 0.006) m	0.002 m	0.006 m
t5	Station-004: SW-004 (Leveled)	Station-007: SW-007 (Leveled)	Coincident: Vertex - Vertex	On	1	0.002 m	(-0.002, 0.001, 0.000) m	0.002 m	0.000 m
t4	Station-004: SW-004 (Leveled)	Station-007: SW-007 (Leveled)	Coincident: Vertex - Vertex	Off	1	0.008 m	(0.000, 0.003, -0.007) m	0.003 m	-0.007 m
t2	Station-005: SW-005 (Leveled)	Station-007: SW-007 (Leveled)	Coincident: Vertex - Vertex	On	1	0.004 m	(0.003, -0.001, -0.001) m	0.004 m	-0.001 m
t1	Station-005: SW-005 (Leveled)	Station-007: SW-007 (Leveled)	Coincident: Vertex - Vertex	On	1	0.002 m	(0.000, 0.000, 0.002) m	0.001 m	0.002 m
t6	Station-005: SW-005 (Leveled)	Station-007: SW-007 (Leveled)	Coincident: Vertex - Vertex	Off	1	0.004 m	(0.002, 0.001, 0.004) m	0.002 m	0.004 m

*Quantifying physical river habitat parameters using hyperspatial resolution
UAS imagery and SfM-photogrammetry*

t5	Station-005: SW-005 (Leveled)	Station-007: SW-007 (Leveled)	Coincident: Vertex - Vertex	On	1	0.001 m	(0.000, 0.001, 0.000) m	0.001 m	0.000 m
t4	Station-005: SW-005 (Leveled)	Station-007: SW-007 (Leveled)	Coincident: Vertex - Vertex	Off	1	0.004 m	(-0.002, 0.003, -0.001) m	0.004 m	-0.001 m
t1	Station-001: SW-001 (Leveled)	Station-008: SW-008 (Leveled)	Coincident: Vertex - Vertex	On	1	0.002 m	(-0.001, -0.002, 0.001) m	0.002 m	0.001 m
t4	Station-001: SW-001 (Leveled)	Station-008: SW-008 (Leveled)	Coincident: Vertex - Vertex	Off	1	0.004 m	(0.002, -0.001, -0.004) m	0.002 m	-0.004 m
t3a	Station-001: SW-001 (Leveled)	Station-008: SW-008 (Leveled)	Coincident: Vertex - Vertex	On	1	0.003 m	(0.001, 0.000, -0.002) m	0.001 m	-0.002 m
t2	Station-001: SW-001 (Leveled)	Station-008: SW-008 (Leveled)	Coincident: Vertex - Vertex	On	1	0.003 m	(0.001, 0.001, -0.002) m	0.002 m	-0.002 m
t5	Station-001: SW-001 (Leveled)	Station-008: SW-008 (Leveled)	Coincident: Vertex - Vertex	On	1	0.003 m	(-0.001, 0.000, 0.003) m	0.001 m	0.003 m
t6	Station-001: SW-001 (Leveled)	Station-008: SW-008 (Leveled)	Coincident: Vertex - Vertex	Off	1	0.003 m	(0.002, -0.001, 0.002) m	0.002 m	0.002 m
t3a	Station-002: SW-002 (Leveled)	Station-008: SW-008 (Leveled)	Coincident: Vertex - Vertex	On	1	0.002 m	(0.000, -0.001, -0.002) m	0.001 m	-0.002 m
t4	Station-002: SW-002 (Leveled)	Station-008: SW-008 (Leveled)	Coincident: Vertex - Vertex	Off	1	0.006 m	(0.002, -0.001, -0.006) m	0.002 m	-0.006 m
t6	Station-002: SW-002 (Leveled)	Station-008: SW-008 (Leveled)	Coincident: Vertex - Vertex	Off	1	27.690 m	(-15.699, -22.784, 1.078) m	27.669 m	1.078 m
t5	Station-002: SW-002 (Leveled)	Station-008: SW-008 (Leveled)	Coincident: Vertex - Vertex	On	1	0.004 m	(-0.002, 0.002, 0.003) m	0.002 m	0.003 m
t2	Station-002: SW-002 (Leveled)	Station-008: SW-008 (Leveled)	Coincident: Vertex - Vertex	On	1	0.002 m	(0.000, 0.001, -0.002) m	0.001 m	-0.002 m
t1	Station-002: SW-002 (Leveled)	Station-008: SW-008 (Leveled)	Coincident: Vertex - Vertex	On	1	0.002 m	(0.001, -0.001, 0.000) m	0.002 m	0.000 m
t1	Station-003: SW-003 (Leveled)	Station-008: SW-008 (Leveled)	Coincident: Vertex - Vertex	On	1	0.006 m	(0.001, -0.001, 0.005) m	0.001 m	0.005 m
t2	Station-003: SW-003 (Leveled)	Station-008: SW-008 (Leveled)	Coincident: Vertex - Vertex	On	1	0.003 m	(0.001, -0.001, -0.002) m	0.001 m	-0.002 m
t3a	Station-003: SW-003 (Leveled)	Station-008: SW-008 (Leveled)	Coincident: Vertex - Vertex	On	1	0.006 m	(0.000, -0.001, -0.006) m	0.001 m	-0.006 m
t4	Station-003: SW-003 (Leveled)	Station-008: SW-008 (Leveled)	Coincident: Vertex - Vertex	Off	1	0.009 m	(0.004, -0.001, -0.008) m	0.004 m	-0.008 m
t5	Station-003: SW-003 (Leveled)	Station-008: SW-008 (Leveled)	Coincident: Vertex - Vertex	On	1	0.004 m	(-0.002, 0.003, 0.003) m	0.003 m	0.003 m
t6	Station-004: SW-004 (Leveled)	Station-008: SW-008 (Leveled)	Coincident: Vertex - Vertex	Off	1	0.005 m	(0.002, -0.001, 0.004) m	0.002 m	0.004 m

*Quantifying physical river habitat parameters using hyperspatial resolution
UAS imagery and SfM-photogrammetry*

t2	Station-004: SW-004 (Leveled)	Station-008: SW-008 (Leveled)	Coincident: Vertex - Vertex	On	1	0.003 m	(0.000, 0.000, -0.003) m	0.001 m	-0.003 m
t1	Station-004: SW-004 (Leveled)	Station-008: SW-008 (Leveled)	Coincident: Vertex - Vertex	On	1	0.006 m	(0.001, -0.001, 0.006) m	0.002 m	0.006 m
t3a	Station-004: SW-004 (Leveled)	Station-008: SW-008 (Leveled)	Coincident: Vertex - Vertex	On	1	0.006 m	(0.001, -0.001, -0.006) m	0.001 m	-0.006 m
t5	Station-004: SW-004 (Leveled)	Station-008: SW-008 (Leveled)	Coincident: Vertex - Vertex	On	1	0.003 m	(-0.002, 0.001, 0.002) m	0.003 m	0.002 m
t4	Station-004: SW-004 (Leveled)	Station-008: SW-008 (Leveled)	Coincident: Vertex - Vertex	Off	1	0.007 m	(0.002, -0.001, -0.007) m	0.002 m	-0.007 m
t2	Station-005: SW-005 (Leveled)	Station-008: SW-008 (Leveled)	Coincident: Vertex - Vertex	On	1	0.002 m	(0.001, 0.000, -0.002) m	0.001 m	-0.002 m
t1	Station-005: SW-005 (Leveled)	Station-008: SW-008 (Leveled)	Coincident: Vertex - Vertex	On	1	0.002 m	(-0.001, -0.001, 0.002) m	0.001 m	0.002 m
t6	Station-005: SW-005 (Leveled)	Station-008: SW-008 (Leveled)	Coincident: Vertex - Vertex	Off	1	0.003 m	(0.001, -0.001, 0.003) m	0.002 m	0.003 m
t5	Station-005: SW-005 (Leveled)	Station-008: SW-008 (Leveled)	Coincident: Vertex - Vertex	On	1	0.002 m	(0.000, 0.001, 0.002) m	0.001 m	0.002 m
t4	Station-005: SW-005 (Leveled)	Station-008: SW-008 (Leveled)	Coincident: Vertex - Vertex	Off	1	0.002 m	(0.000, -0.001, -0.001) m	0.001 m	-0.001 m
t3a	Station-005: SW-005 (Leveled)	Station-008: SW-008 (Leveled)	Coincident: Vertex - Vertex	On	1	0.002 m	(0.000, 0.000, -0.002) m	0.001 m	-0.002 m
t6	Station-007: SW-007 (Leveled)	Station-008: SW-008 (Leveled)	Coincident: Vertex - Vertex	Off	1	0.002 m	(-0.001, -0.002, -0.001) m	0.002 m	-0.001 m
t5	Station-007: SW-007 (Leveled)	Station-008: SW-008 (Leveled)	Coincident: Vertex - Vertex	On	1	0.002 m	(0.000, 0.000, 0.002) m	0.000 m	0.002 m
t4	Station-007: SW-007 (Leveled)	Station-008: SW-008 (Leveled)	Coincident: Vertex - Vertex	Off	1	0.005 m	(0.002, -0.005, 0.000) m	0.005 m	0.000 m
t2	Station-007: SW-007 (Leveled)	Station-008: SW-008 (Leveled)	Coincident: Vertex - Vertex	On	1	0.003 m	(-0.003, 0.001, -0.001) m	0.003 m	-0.001 m
t1	Station-007: SW-007 (Leveled)	Station-008: SW-008 (Leveled)	Coincident: Vertex - Vertex	On	1	0.001 m	(-0.001, -0.001, 0.000) m	0.001 m	0.000 m
t1	Station-001: SW-001 (Leveled)	Station-006: SW-006 (Leveled)	Coincident: Vertex - Vertex	On	1	0.004 m	(0.004, 0.001, 0.000) m	0.004 m	0.000 m
t4	Station-001: SW-001 (Leveled)	Station-006: SW-006 (Leveled)	Coincident: Vertex - Vertex	Off	1	0.003 m	(0.000, -0.002, -0.002) m	0.002 m	-0.002 m
t3a	Station-001: SW-001 (Leveled)	Station-006: SW-006 (Leveled)	Coincident: Vertex - Vertex	On	1	0.007 m	(-0.005, 0.003, -0.004) m	0.005 m	-0.004 m
t2	Station-001: SW-001 (Leveled)	Station-006: SW-006 (Leveled)	Coincident: Vertex - Vertex	On	1	0.004 m	(0.003, -0.002, 0.001) m	0.004 m	0.001 m

*Quantifying physical river habitat parameters using hyperspatial resolution
UAS imagery and SfM-photogrammetry*

t5	Station-001: SW-001 (Leveled)	Station-006: SW-006 (Leveled)	Coincident: Vertex - Vertex	On	1	0.004 m	(-0.003, -0.002, 0.002) m	0.004 m	0.002 m
t6	Station-001: SW-001 (Leveled)	Station-006: SW-006 (Leveled)	Coincident: Vertex - Vertex	Off	1	0.005 m	(0.001, -0.002, 0.004) m	0.002 m	0.004 m
t3a	Station-002: SW-002 (Leveled)	Station-006: SW-006 (Leveled)	Coincident: Vertex - Vertex	On	1	0.007 m	(-0.005, 0.002, -0.003) m	0.006 m	-0.003 m
t4	Station-002: SW-002 (Leveled)	Station-006: SW-006 (Leveled)	Coincident: Vertex - Vertex	Off	1	0.004 m	(0.001, -0.001, -0.004) m	0.001 m	-0.004 m
t6	Station-002: SW-002 (Leveled)	Station-006: SW-006 (Leveled)	Coincident: Vertex - Vertex	Off	1	27.692 m	(-15.701, -22.785, 1.081) m	27.671 m	1.081 m
t5	Station-002: SW-002 (Leveled)	Station-006: SW-006 (Leveled)	Coincident: Vertex - Vertex	On	1	0.005 m	(-0.004, -0.001, 0.002) m	0.004 m	0.002 m
t2	Station-002: SW-002 (Leveled)	Station-006: SW-006 (Leveled)	Coincident: Vertex - Vertex	On	1	0.004 m	(0.003, -0.003, 0.001) m	0.004 m	0.001 m
t1	Station-002: SW-002 (Leveled)	Station-006: SW-006 (Leveled)	Coincident: Vertex - Vertex	On	1	0.006 m	(0.006, 0.002, -0.001) m	0.006 m	-0.001 m
t1	Station-003: SW-003 (Leveled)	Station-006: SW-006 (Leveled)	Coincident: Vertex - Vertex	On	1	0.007 m	(0.006, 0.002, 0.004) m	0.006 m	0.004 m
t2	Station-003: SW-003 (Leveled)	Station-006: SW-006 (Leveled)	Coincident: Vertex - Vertex	On	1	0.006 m	(0.003, -0.005, 0.001) m	0.006 m	0.001 m
t3a	Station-003: SW-003 (Leveled)	Station-006: SW-006 (Leveled)	Coincident: Vertex - Vertex	On	1	0.010 m	(-0.005, 0.002, -0.008) m	0.006 m	-0.008 m
t4	Station-003: SW-003 (Leveled)	Station-006: SW-006 (Leveled)	Coincident: Vertex - Vertex	Off	1	0.007 m	(0.002, -0.002, -0.006) m	0.003 m	-0.006 m
t5	Station-003: SW-003 (Leveled)	Station-006: SW-006 (Leveled)	Coincident: Vertex - Vertex	On	1	0.005 m	(-0.004, 0.001, 0.002) m	0.004 m	0.002 m
t6	Station-004: SW-004 (Leveled)	Station-006: SW-006 (Leveled)	Coincident: Vertex - Vertex	Off	1	0.007 m	(0.000, -0.002, 0.006) m	0.002 m	0.006 m
t2	Station-004: SW-004 (Leveled)	Station-006: SW-006 (Leveled)	Coincident: Vertex - Vertex	On	1	0.004 m	(0.003, -0.003, 0.001) m	0.004 m	0.001 m
t1	Station-004: SW-004 (Leveled)	Station-006: SW-006 (Leveled)	Coincident: Vertex - Vertex	On	1	0.008 m	(0.006, 0.002, 0.005) m	0.006 m	0.005 m
t3a	Station-004: SW-004 (Leveled)	Station-006: SW-006 (Leveled)	Coincident: Vertex - Vertex	On	1	0.009 m	(-0.005, 0.002, -0.007) m	0.005 m	-0.007 m
t5	Station-004: SW-004 (Leveled)	Station-006: SW-006 (Leveled)	Coincident: Vertex - Vertex	On	1	0.005 m	(-0.005, -0.001, 0.001) m	0.005 m	0.001 m
t4	Station-004: SW-004 (Leveled)	Station-006: SW-006 (Leveled)	Coincident: Vertex - Vertex	Off	1	0.006 m	(0.000, -0.002, -0.005) m	0.002 m	-0.005 m
t2	Station-005: SW-005 (Leveled)	Station-006: SW-006 (Leveled)	Coincident: Vertex - Vertex	On	1	0.004 m	(0.003, -0.003, 0.001) m	0.004 m	0.001 m

*Quantifying physical river habitat parameters using hyperspatial resolution
UAS imagery and SfM-photogrammetry*

t1	Station-005: SW-005 (Leveled)	Station-006: SW-006 (Leveled)	Coincident: Vertex - Vertex	On	1	0.005 m	(0.004, 0.002, 0.001) m	0.005 m	0.001 m
t6	Station-005: SW-005 (Leveled)	Station-006: SW-006 (Leveled)	Coincident: Vertex - Vertex	Off	1	0.005 m	(0.000, -0.002, 0.005) m	0.002 m	0.005 m
t5	Station-005: SW-005 (Leveled)	Station-006: SW-006 (Leveled)	Coincident: Vertex - Vertex	On	1	0.003 m	(-0.003, -0.001, 0.001) m	0.003 m	0.001 m
t4	Station-005: SW-005 (Leveled)	Station-006: SW-006 (Leveled)	Coincident: Vertex - Vertex	Off	1	0.003 m	(-0.002, -0.002, 0.001) m	0.003 m	0.001 m
t3a	Station-005: SW-005 (Leveled)	Station-006: SW-006 (Leveled)	Coincident: Vertex - Vertex	On	1	0.007 m	(-0.005, 0.003, -0.004) m	0.006 m	-0.004 m
t6	Station-007: SW-007 (Leveled)	Station-006: SW-006 (Leveled)	Coincident: Vertex - Vertex	Off	1	0.003 m	(-0.002, -0.003, 0.001) m	0.003 m	0.001 m
t5	Station-007: SW-007 (Leveled)	Station-006: SW-006 (Leveled)	Coincident: Vertex - Vertex	On	1	0.003 m	(-0.002, -0.002, 0.001) m	0.003 m	0.001 m
t4	Station-007: SW-007 (Leveled)	Station-006: SW-006 (Leveled)	Coincident: Vertex - Vertex	Off	1	0.005 m	(0.001, -0.005, 0.001) m	0.005 m	0.001 m
t2	Station-007: SW-007 (Leveled)	Station-006: SW-006 (Leveled)	Coincident: Vertex - Vertex	On	1	0.003 m	(0.000, -0.002, 0.002) m	0.002 m	0.002 m
t1	Station-007: SW-007 (Leveled)	Station-006: SW-006 (Leveled)	Coincident: Vertex - Vertex	On	1	0.005 m	(0.004, 0.002, -0.002) m	0.005 m	-0.002 m
t6	Station-008: SW-008 (Leveled)	Station-006: SW-006 (Leveled)	Coincident: Vertex - Vertex	Off	1	0.003 m	(-0.001, -0.001, 0.002) m	0.001 m	0.002 m
t5	Station-008: SW-008 (Leveled)	Station-006: SW-006 (Leveled)	Coincident: Vertex - Vertex	On	1	0.003 m	(-0.002, -0.002, -0.001) m	0.003 m	-0.001 m
t4	Station-008: SW-008 (Leveled)	Station-006: SW-006 (Leveled)	Coincident: Vertex - Vertex	Off	1	0.002 m	(-0.002, 0.000, 0.002) m	0.002 m	0.002 m
t1	Station-008: SW-008 (Leveled)	Station-006: SW-006 (Leveled)	Coincident: Vertex - Vertex	On	1	0.006 m	(0.005, 0.003, -0.001) m	0.006 m	-0.001 m
t2	Station-008: SW-008 (Leveled)	Station-006: SW-006 (Leveled)	Coincident: Vertex - Vertex	On	1	0.005 m	(0.002, -0.003, 0.003) m	0.004 m	0.003 m
t3a	Station-008: SW-008 (Leveled)	Station-006: SW-006 (Leveled)	Coincident: Vertex - Vertex	On	1	0.007 m	(-0.006, 0.003, -0.002) m	0.006 m	-0.002 m
t1	Station-001: SW-001 (Leveled)	Coledale090713TargetsRevised.txt (Leveled)	Coincident: Vertex - Vertex	On	1	0.028 m	(0.021, -0.007, 0.017) m	0.022 m	0.017 m
t4	Station-001: SW-001 (Leveled)	Coledale090713TargetsRevised.txt (Leveled)	Coincident: Vertex - Vertex	Off	1	0.165 m	(-0.149, -0.069, -0.011) m	0.164 m	-0.011 m
t3a	Station-001: SW-001 (Leveled)	Coledale090713TargetsRevised.txt (Leveled)	Coincident: Vertex - Vertex	On	1	0.029 m	(-0.024, 0.003, -0.016) m	0.024 m	-0.016 m
t2	Station-001: SW-001 (Leveled)	Coledale090713TargetsRevised.txt (Leveled)	Coincident: Vertex - Vertex	On	1	0.027 m	(0.025, -0.008, 0.002) m	0.026 m	0.002 m

*Quantifying physical river habitat parameters using hyperspatial resolution
UAS imagery and SfM-photogrammetry*

t5	Station-001: SW-001 (Leveled)	Coledale090713TargetsRevised.txt (Leveled)	Coincident: Vertex - Vertex	On	1	0.028 m	(-0.025, 0.012, -0.005) m	0.028 m	-0.005 m
t6	Station-001: SW-001 (Leveled)	Coledale090713TargetsRevised.txt (Leveled)	Coincident: Vertex - Vertex	Off	1	0.081 m	(-0.011, 0.080, -0.005) m	0.081 m	-0.005 m
t3a	Station-002: SW-002 (Leveled)	Coledale090713TargetsRevised.txt (Leveled)	Coincident: Vertex - Vertex	On	1	0.029 m	(-0.025, 0.002, -0.015) m	0.025 m	-0.015 m
t4	Station-002: SW-002 (Leveled)	Coledale090713TargetsRevised.txt (Leveled)	Coincident: Vertex - Vertex	Off	1	0.164 m	(-0.148, -0.069, -0.012) m	0.163 m	-0.012 m
t6	Station-002: SW-002 (Leveled)	Coledale090713TargetsRevised.txt (Leveled)	Coincident: Vertex - Vertex	Off	1	27.630 m	(-15.712, -22.703, 1.071) m	27.610 m	1.071 m
t5	Station-002: SW-002 (Leveled)	Coledale090713TargetsRevised.txt (Leveled)	Coincident: Vertex - Vertex	On	1	0.030 m	(-0.026, 0.013, -0.005) m	0.029 m	-0.005 m
t2	Station-002: SW-002 (Leveled)	Coledale090713TargetsRevised.txt (Leveled)	Coincident: Vertex - Vertex	On	1	0.026 m	(0.025, -0.008, 0.003) m	0.026 m	0.003 m
t1	Station-002: SW-002 (Leveled)	Coledale090713TargetsRevised.txt (Leveled)	Coincident: Vertex - Vertex	On	1	0.029 m	(0.023, -0.006, 0.016) m	0.024 m	0.016 m
t1	Station-003: SW-003 (Leveled)	Coledale090713TargetsRevised.txt (Leveled)	Coincident: Vertex - Vertex	On	1	0.032 m	(0.023, -0.006, 0.021) m	0.024 m	0.021 m
t2	Station-003: SW-003 (Leveled)	Coledale090713TargetsRevised.txt (Leveled)	Coincident: Vertex - Vertex	On	1	0.027 m	(0.025, -0.010, 0.002) m	0.027 m	0.002 m
t3a	Station-003: SW-003 (Leveled)	Coledale090713TargetsRevised.txt (Leveled)	Coincident: Vertex - Vertex	On	1	0.032 m	(-0.025, 0.002, -0.020) m	0.025 m	-0.020 m
t4	Station-003: SW-003 (Leveled)	Coledale090713TargetsRevised.txt (Leveled)	Coincident: Vertex - Vertex	Off	1	0.163 m	(-0.147, -0.070, -0.015) m	0.162 m	-0.015 m
t5	Station-003: SW-003 (Leveled)	Coledale090713TargetsRevised.txt (Leveled)	Coincident: Vertex - Vertex	On	1	0.031 m	(-0.026, 0.015, -0.006) m	0.030 m	-0.006 m
t6	Station-004: SW-004 (Leveled)	Coledale090713TargetsRevised.txt (Leveled)	Coincident: Vertex - Vertex	Off	1	0.081 m	(-0.011, 0.080, -0.003) m	0.081 m	-0.003 m
t2	Station-004: SW-004 (Leveled)	Coledale090713TargetsRevised.txt (Leveled)	Coincident: Vertex - Vertex	On	1	0.027 m	(0.025, -0.009, 0.002) m	0.026 m	0.002 m
t1	Station-004: SW-004 (Leveled)	Coledale090713TargetsRevised.txt (Leveled)	Coincident: Vertex - Vertex	On	1	0.033 m	(0.023, -0.006, 0.022) m	0.024 m	0.022 m
t3a	Station-004: SW-004 (Leveled)	Coledale090713TargetsRevised.txt (Leveled)	Coincident: Vertex - Vertex	On	1	0.031 m	(-0.024, 0.002, -0.019) m	0.024 m	-0.019 m
t5	Station-004: SW-004 (Leveled)	Coledale090713TargetsRevised.txt (Leveled)	Coincident: Vertex - Vertex	On	1	0.031 m	(-0.027, 0.013, -0.007) m	0.030 m	-0.007 m
t4	Station-004: SW-004 (Leveled)	Coledale090713TargetsRevised.txt (Leveled)	Coincident: Vertex - Vertex	Off	1	0.165 m	(-0.149, -0.069, -0.014) m	0.164 m	-0.014 m
t2	Station-005: SW-005 (Leveled)	Coledale090713TargetsRevised.txt (Leveled)	Coincident: Vertex - Vertex	On	1	0.027 m	(0.025, -0.009, 0.002) m	0.027 m	0.002 m

*Quantifying physical river habitat parameters using hyperspatial resolution
UAS imagery and SfM-photogrammetry*

t1	Station-005: SW-005 (Leveled)	Coledale090713TargetsRevised.txt (Leveled)	Coincident: Vertex - Vertex	On	1	0.029 m	(0.022, -0.006, 0.018) m	0.022 m	0.018 m
t6	Station-005: SW-005 (Leveled)	Coledale090713TargetsRevised.txt (Leveled)	Coincident: Vertex - Vertex	Off	1	0.081 m	(-0.011, 0.080, -0.005) m	0.081 m	-0.005 m
t5	Station-005: SW-005 (Leveled)	Coledale090713TargetsRevised.txt (Leveled)	Coincident: Vertex - Vertex	On	1	0.029 m	(-0.025, 0.013, -0.006) m	0.028 m	-0.006 m
t4	Station-005: SW-005 (Leveled)	Coledale090713TargetsRevised.txt (Leveled)	Coincident: Vertex - Vertex	Off	1	0.166 m	(-0.151, -0.069, -0.008) m	0.166 m	-0.008 m
t3a	Station-005: SW-005 (Leveled)	Coledale090713TargetsRevised.txt (Leveled)	Coincident: Vertex - Vertex	On	1	0.029 m	(-0.025, 0.003, -0.015) m	0.025 m	-0.015 m
t6	Station-007: SW-007 (Leveled)	Coledale090713TargetsRevised.txt (Leveled)	Coincident: Vertex - Vertex	Off	1	0.081 m	(-0.013, 0.079, -0.008) m	0.080 m	-0.008 m
t5	Station-007: SW-007 (Leveled)	Coledale090713TargetsRevised.txt (Leveled)	Coincident: Vertex - Vertex	On	1	0.028 m	(-0.025, 0.012, -0.006) m	0.027 m	-0.006 m
t4	Station-007: SW-007 (Leveled)	Coledale090713TargetsRevised.txt (Leveled)	Coincident: Vertex - Vertex	Off	1	0.165 m	(-0.148, -0.073, -0.007) m	0.165 m	-0.007 m
t2	Station-007: SW-007 (Leveled)	Coledale090713TargetsRevised.txt (Leveled)	Coincident: Vertex - Vertex	On	1	0.023 m	(0.022, -0.008, 0.003) m	0.023 m	0.003 m
t1	Station-007: SW-007 (Leveled)	Coledale090713TargetsRevised.txt (Leveled)	Coincident: Vertex - Vertex	On	1	0.027 m	(0.021, -0.006, 0.015) m	0.022 m	0.015 m
t6	Station-008: SW-008 (Leveled)	Coledale090713TargetsRevised.txt (Leveled)	Coincident: Vertex - Vertex	Off	1	0.082 m	(-0.012, 0.081, -0.007) m	0.082 m	-0.007 m
t5	Station-008: SW-008 (Leveled)	Coledale090713TargetsRevised.txt (Leveled)	Coincident: Vertex - Vertex	On	1	0.028 m	(-0.024, 0.012, -0.009) m	0.027 m	-0.009 m
t4	Station-008: SW-008 (Leveled)	Coledale090713TargetsRevised.txt (Leveled)	Coincident: Vertex - Vertex	Off	1	0.165 m	(-0.150, -0.068, -0.007) m	0.165 m	-0.007 m
t1	Station-008: SW-008 (Leveled)	Coledale090713TargetsRevised.txt (Leveled)	Coincident: Vertex - Vertex	On	1	0.028 m	(0.022, -0.005, 0.016) m	0.023 m	0.016 m
t2	Station-008: SW-008 (Leveled)	Coledale090713TargetsRevised.txt (Leveled)	Coincident: Vertex - Vertex	On	1	0.027 m	(0.024, -0.009, 0.005) m	0.026 m	0.005 m
t3a	Station-008: SW-008 (Leveled)	Coledale090713TargetsRevised.txt (Leveled)	Coincident: Vertex - Vertex	On	1	0.029 m	(-0.025, 0.003, -0.013) m	0.025 m	-0.013 m
t2	Station-006: SW-006 (Leveled)	Coledale090713TargetsRevised.txt (Leveled)	Coincident: Vertex - Vertex	On	1	0.023 m	(0.022, -0.006, 0.001) m	0.023 m	0.001 m
t3a	Station-006: SW-006 (Leveled)	Coledale090713TargetsRevised.txt (Leveled)	Coincident: Vertex - Vertex	On	1	0.023 m	(-0.019, 0.000, -0.012) m	0.019 m	-0.012 m
t4	Station-006: SW-006 (Leveled)	Coledale090713TargetsRevised.txt (Leveled)	Coincident: Vertex - Vertex	Off	1	0.164 m	(-0.149, -0.068, -0.009) m	0.164 m	-0.009 m
t6	Station-006: SW-006 (Leveled)	Coledale090713TargetsRevised.txt (Leveled)	Coincident: Vertex - Vertex	Off	1	0.083 m	(-0.011, 0.082, -0.009) m	0.083 m	-0.009 m

*Quantifying physical river habitat parameters using hyperspatial resolution
UAS imagery and SfM-photogrammetry*

t5	Station-006: SW-006 (Leveled)	Coledale090713TargetsRevised.txt (Leveled)	Coincident: Vertex - Vertex	On	1	0.027 m	(-0.022, 0.014, -0.007) m	0.026 m	-0.007 m
t1	Station-006: SW-006 (Leveled)	Coledale090713TargetsRevised.txt (Leveled)	Coincident: Vertex - Vertex	On	1	0.025 m	(0.017, -0.008, 0.017) m	0.019 m	0.017 m

Appendix B

Topography & Water Depth

The original version of this thesis, presented for examination, included a copy of Woodget et al., (2015). For copyright reasons, this paper is no longer included in this copy of the thesis. Please now refer to the published version of this paper:

Woodget, A.S., Carbonneau, P.E., Visser, F. and Maddock, I. (2015) Quantifying submerged fluvial topography using hyperspatial resolution UAS imagery and structure from motion photogrammetry. *Earth Surface Processes and Landforms* 40 (1): 47-64.

Appendix C - Substrate Size

Ground truth substrate size distributions

The following figures present a photo record of each ground truth substrate plot and an associated graph of substrate size distribution. The light blue lines represents the A axes and the dark blue lines represents the B axes.

Figure C1. Plot A1

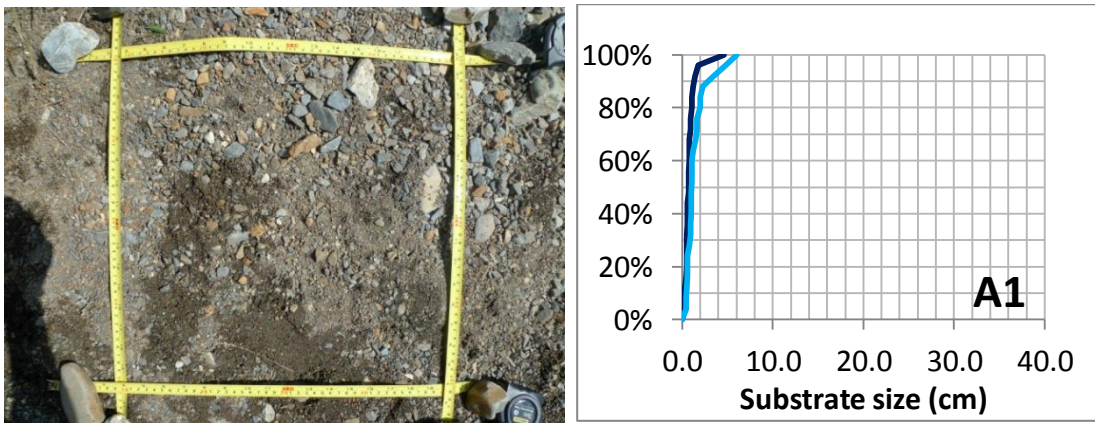


Figure C2. Plot A2

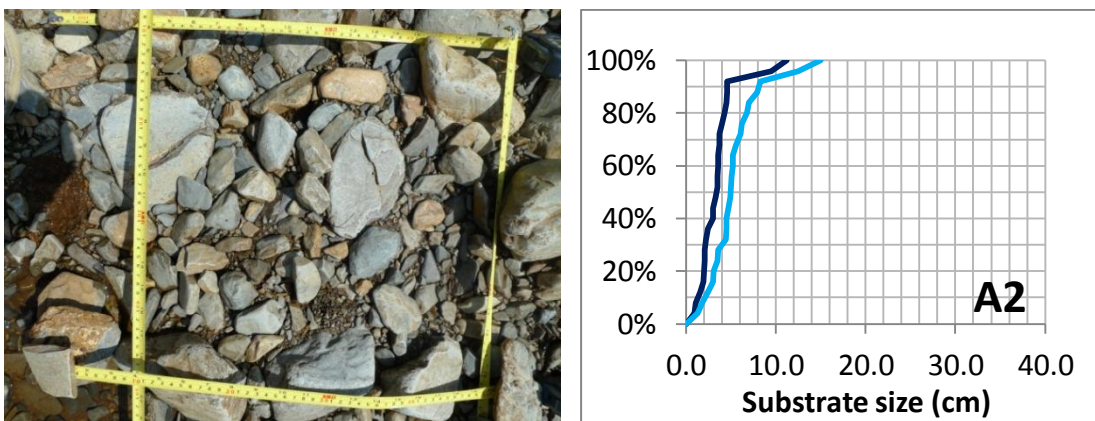


Figure C3. Plot A3

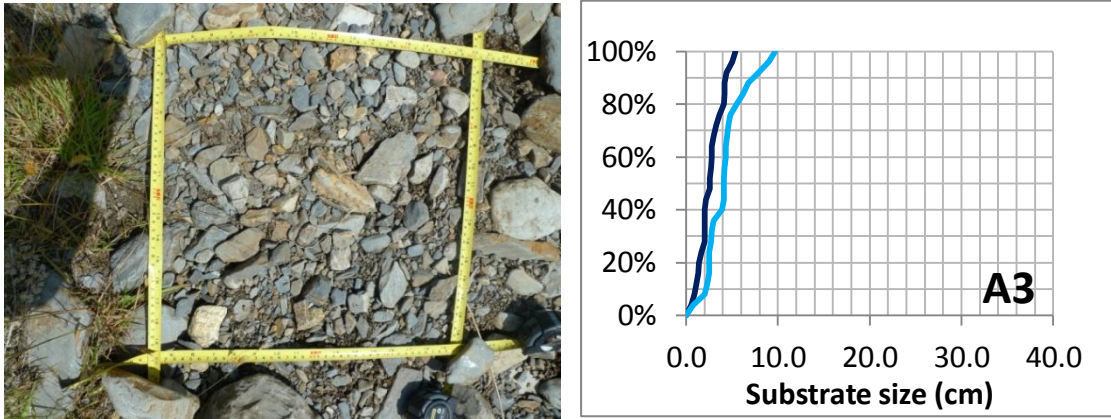


Figure C4. Plot A4

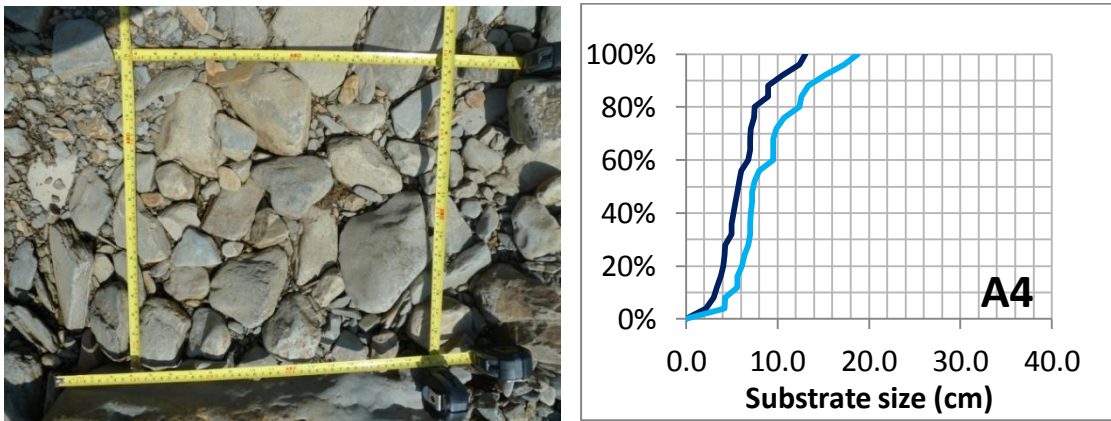


Figure C5. Plot A5

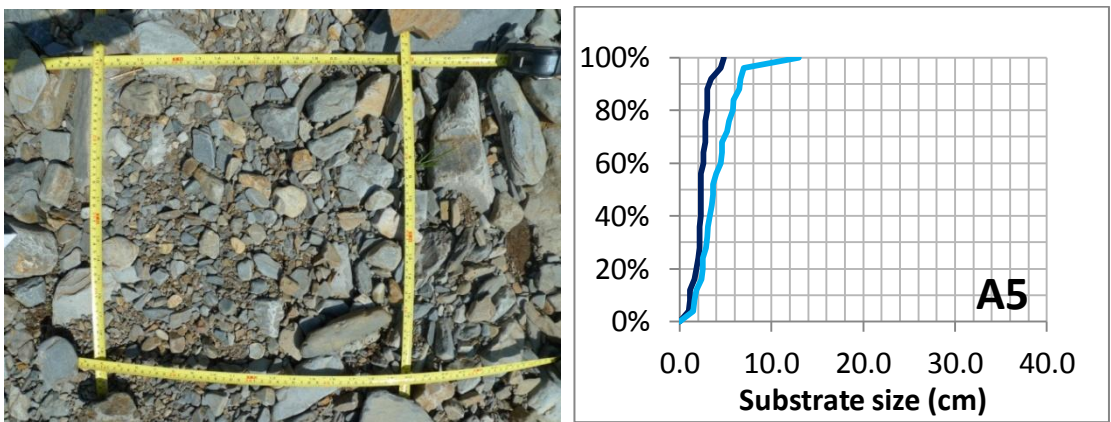


Figure C6. Plot A6

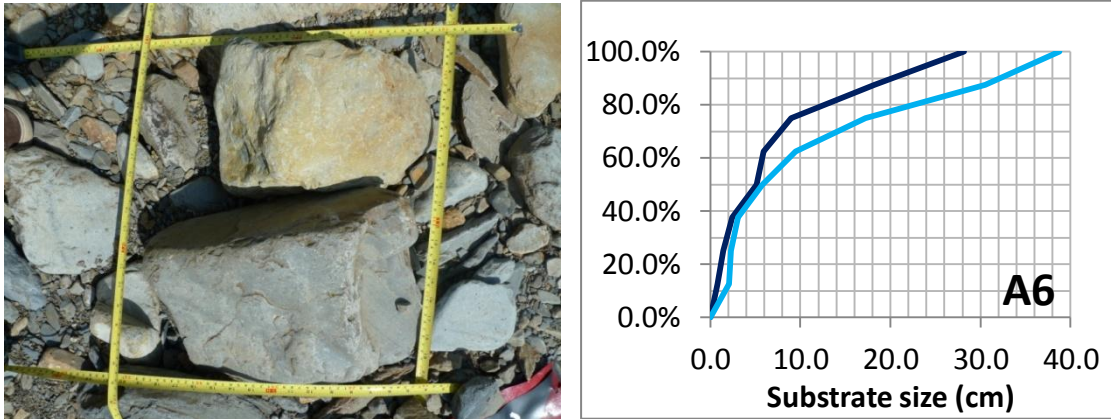


Figure C7. Plot A7

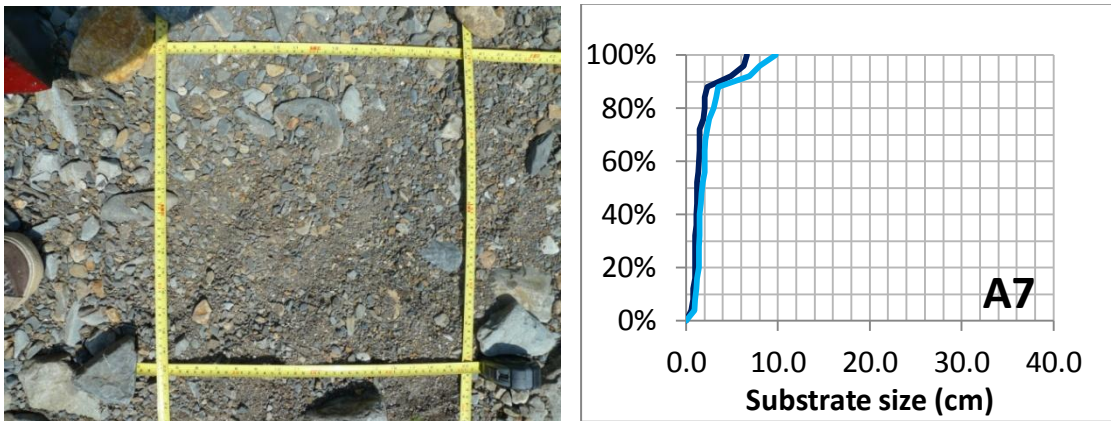


Figure C8. Plot A8

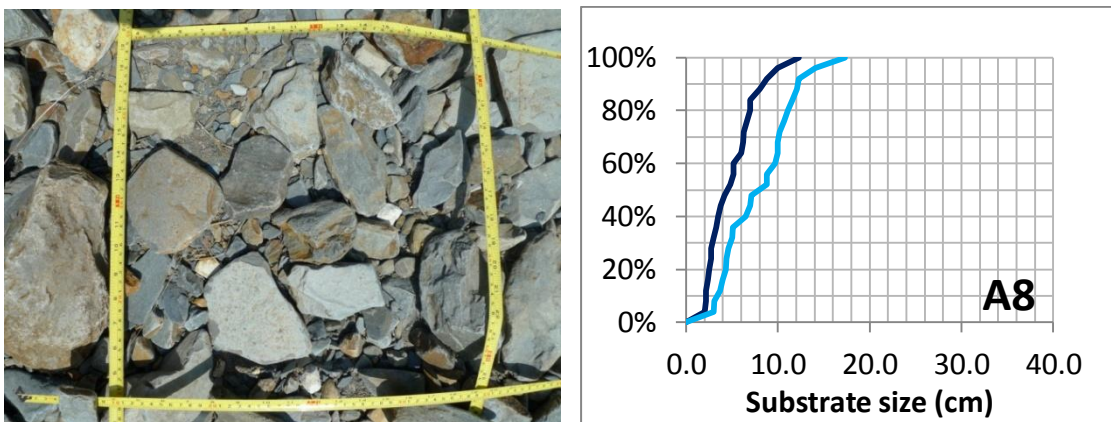


Figure C9. Plot A9

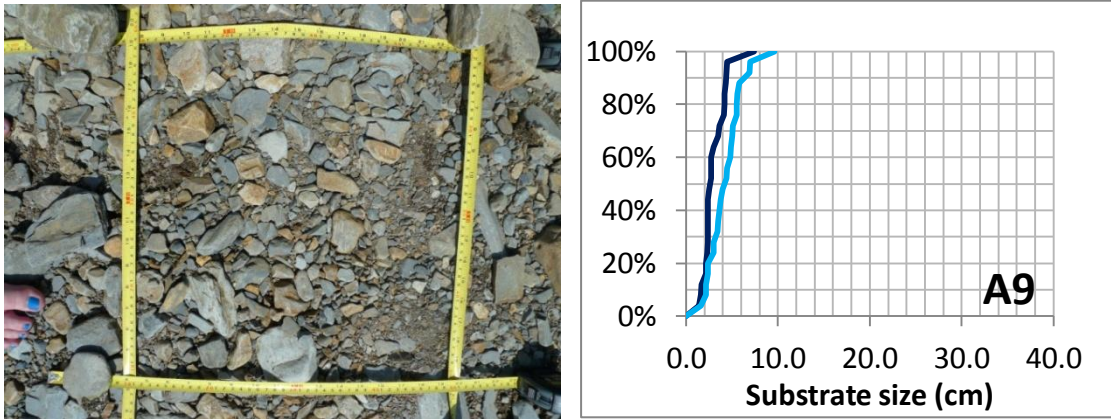


Figure C10. Plot B1

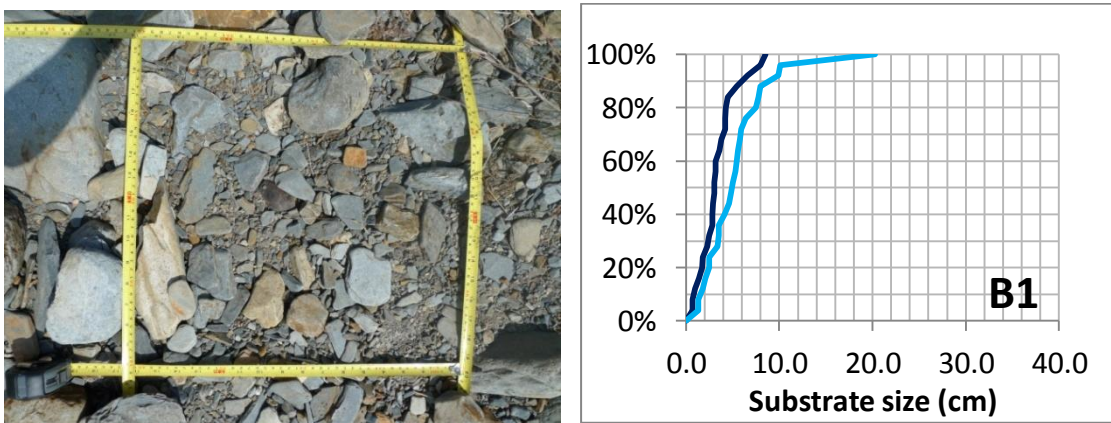


Figure C11. Plot B2

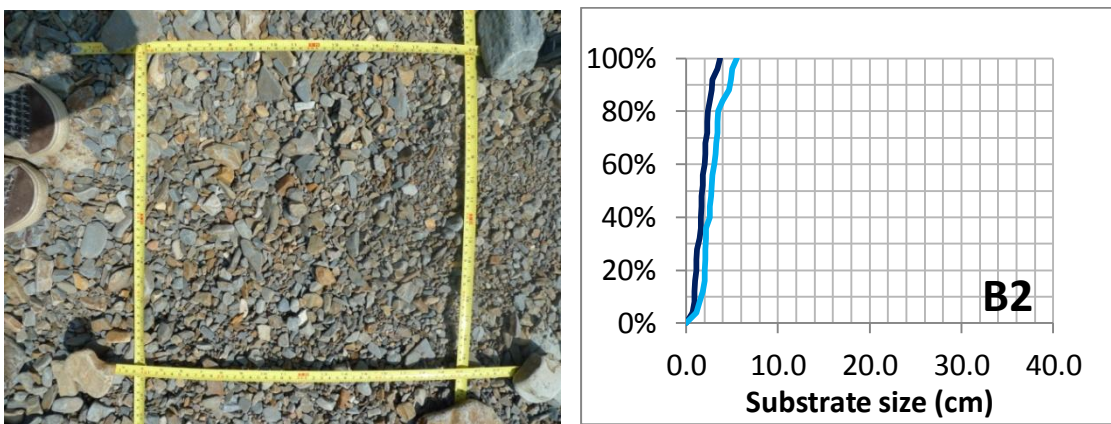


Figure C12. Plot B3

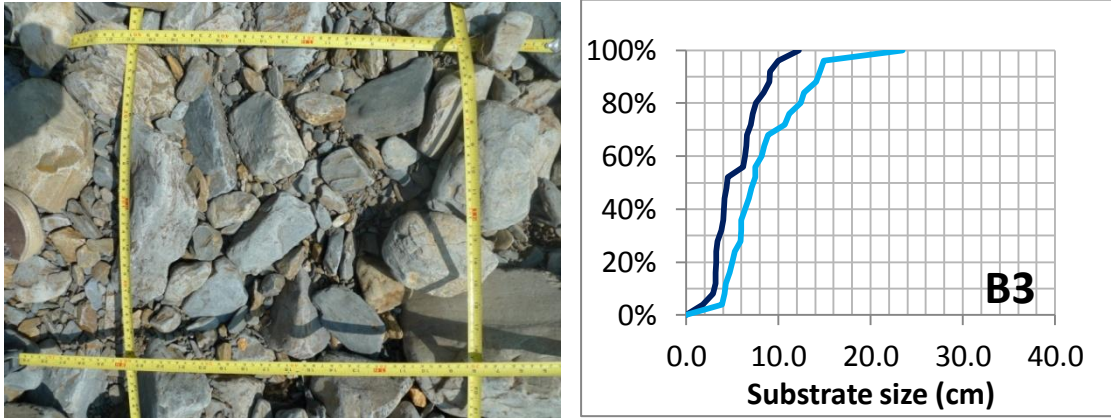


Figure C13. Plot B4

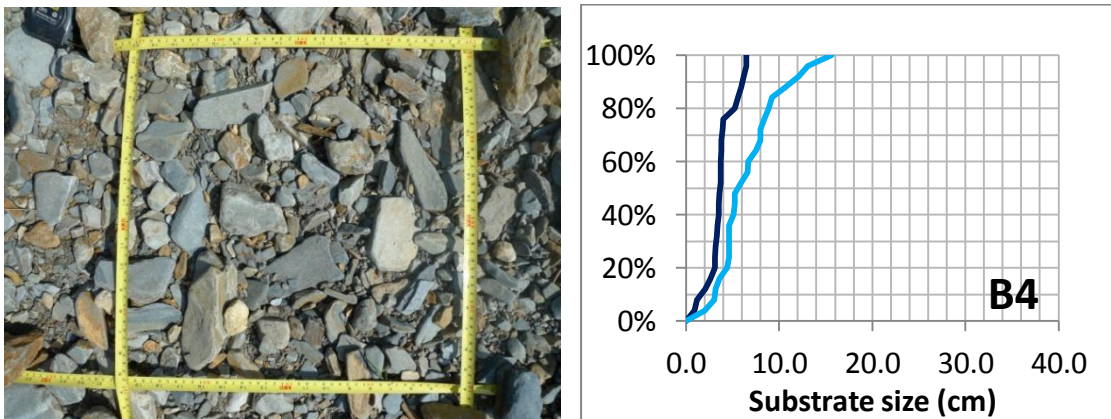


Figure C14. Plot C1

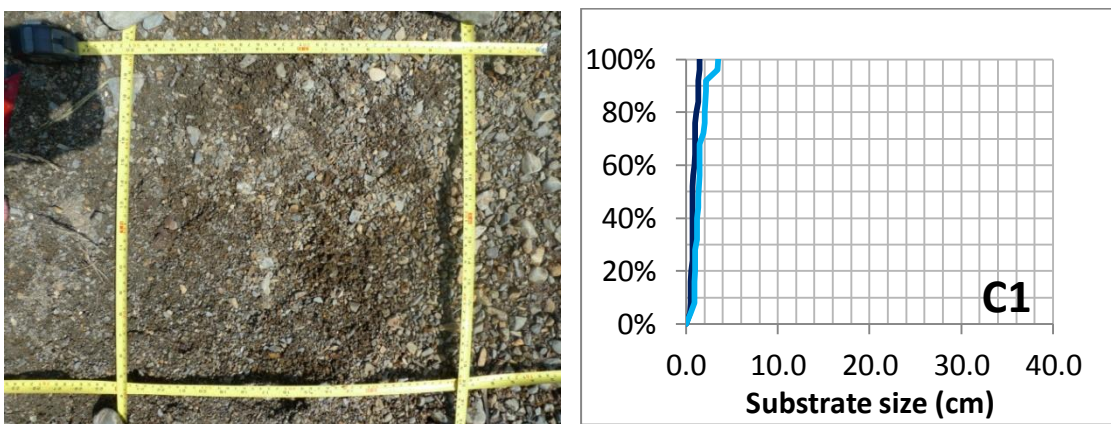


Figure C15. Plot C2

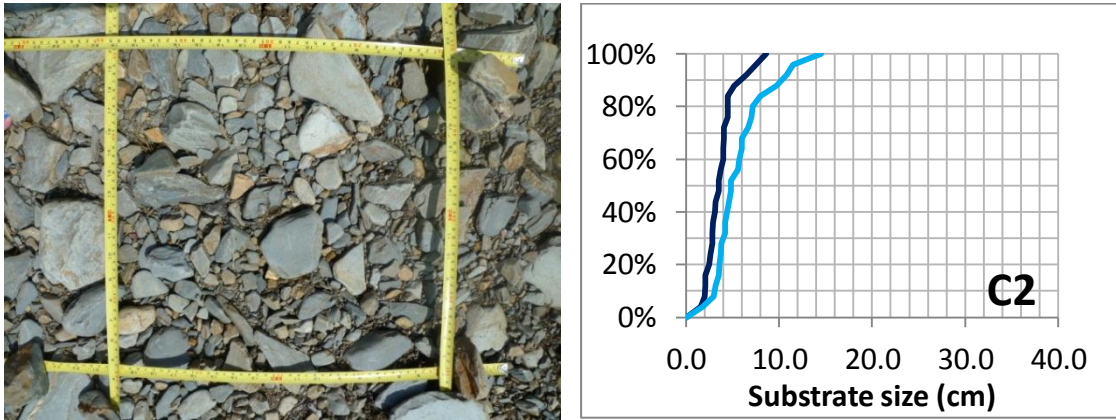


Figure C16. Plot C3

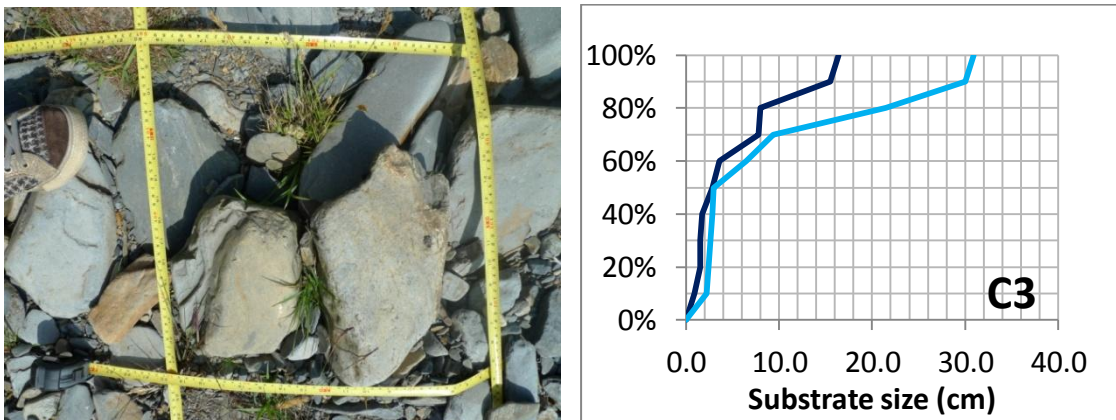


Figure C17. Plot C4

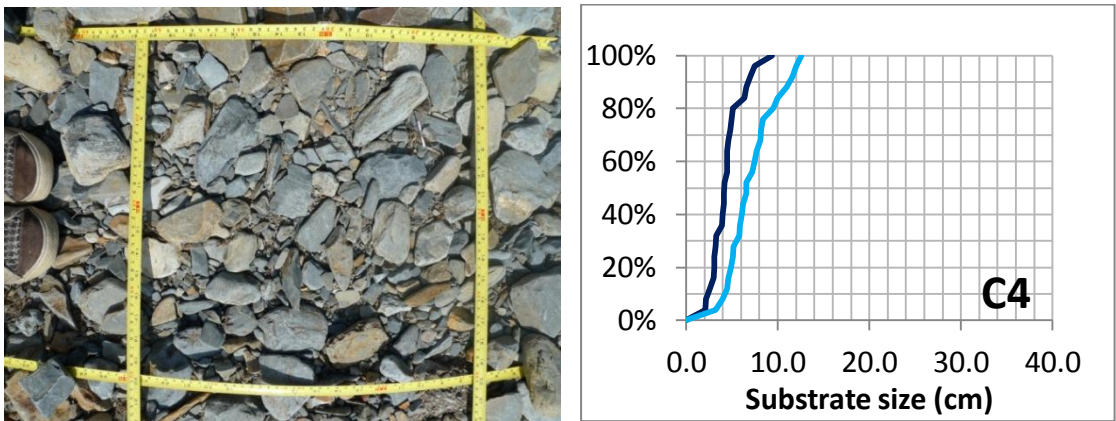


Figure C18. Plot C5

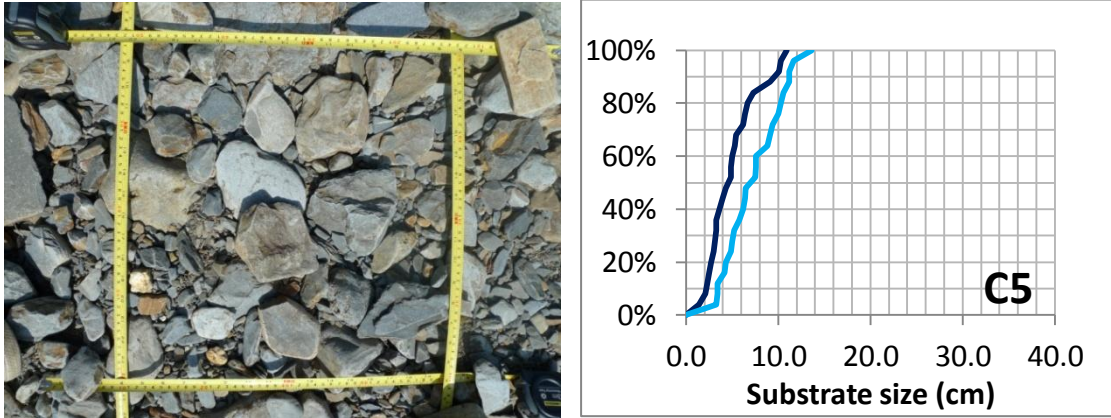


Figure C19. Plot C6

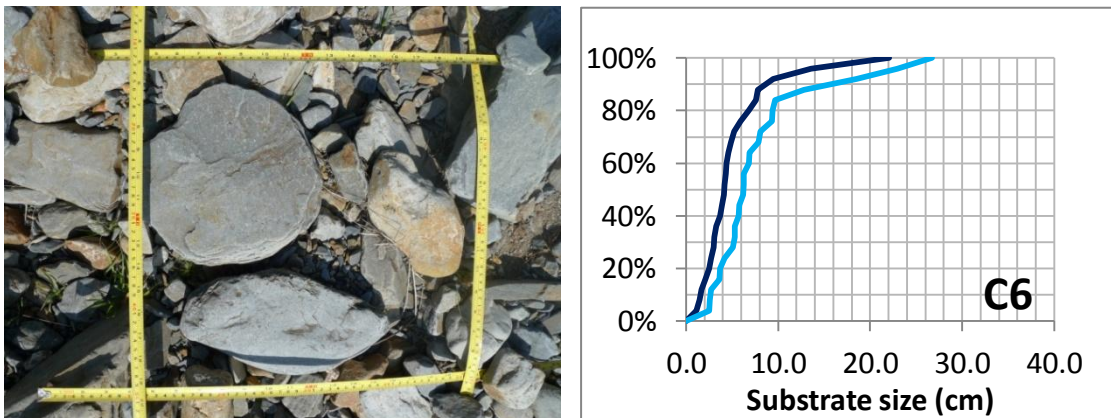


Figure C20. Plot C7

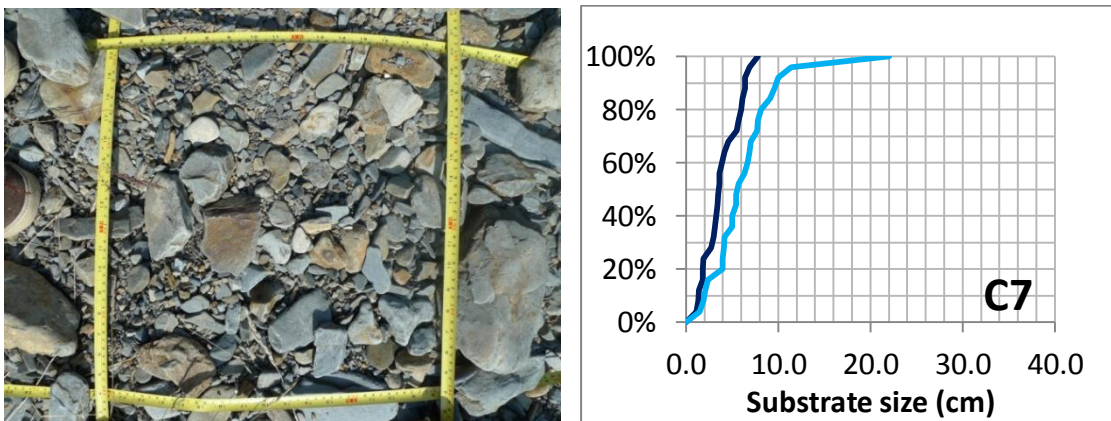


Figure C21. Plot D1

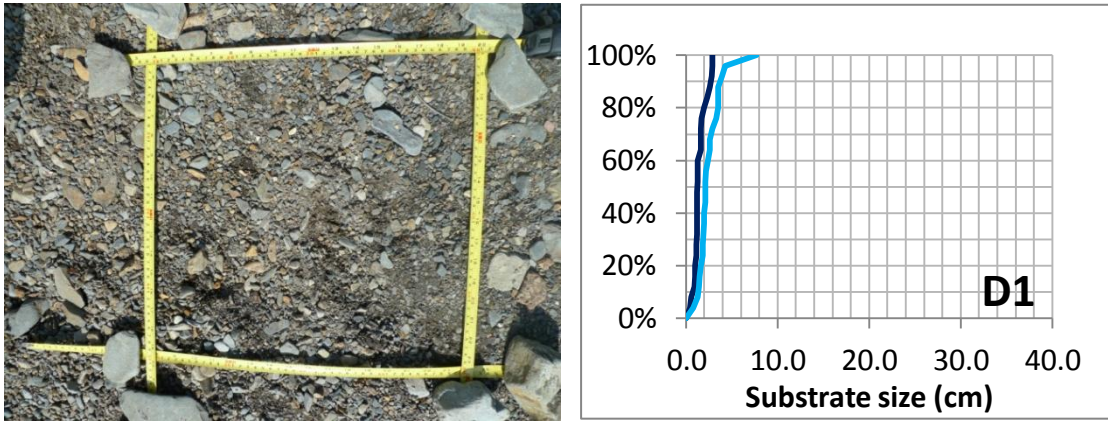


Figure C22. Plot D2

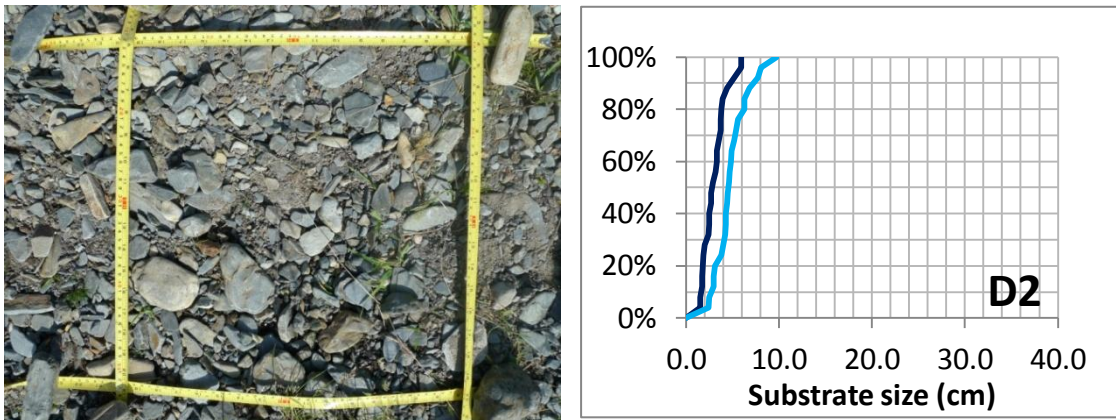


Figure C23. Plot D3

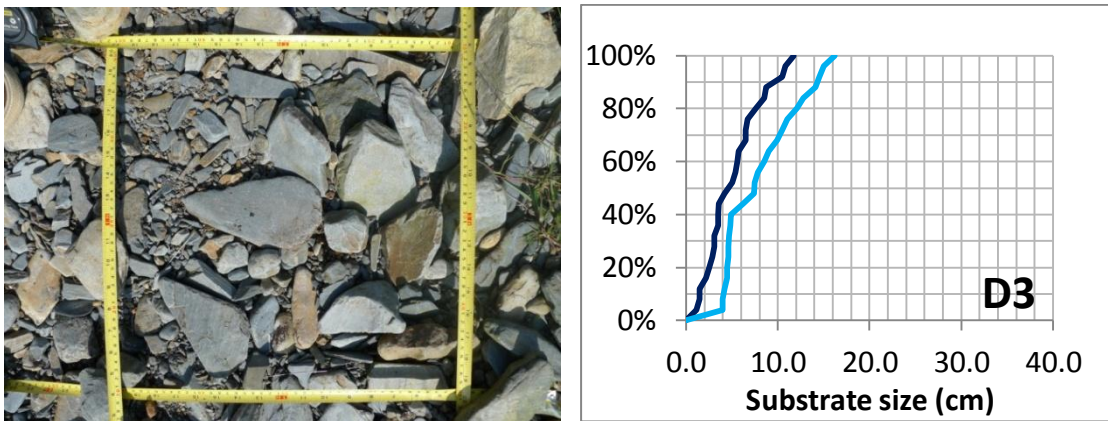


Figure C24. Plot D4

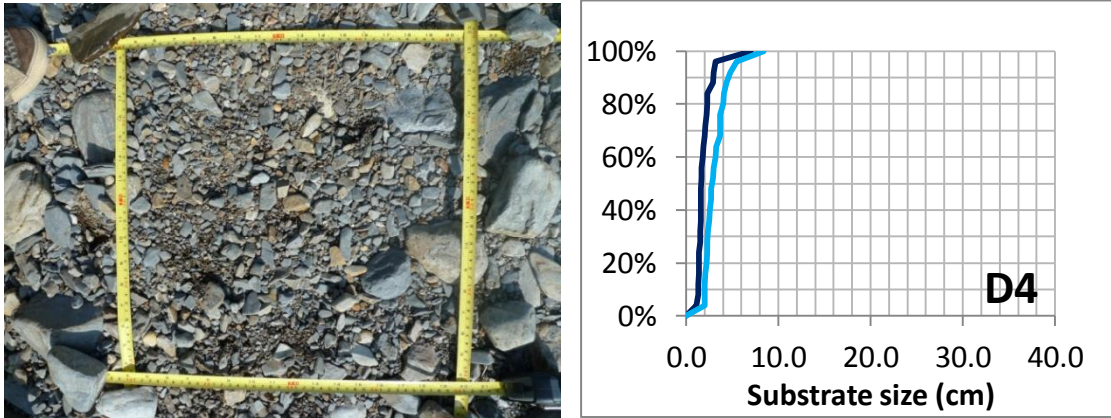


Figure C25. Plot D5

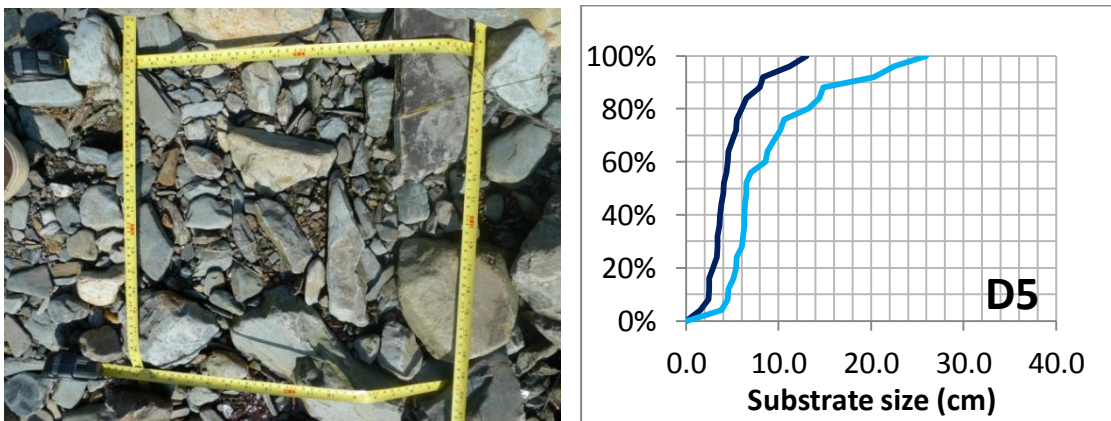
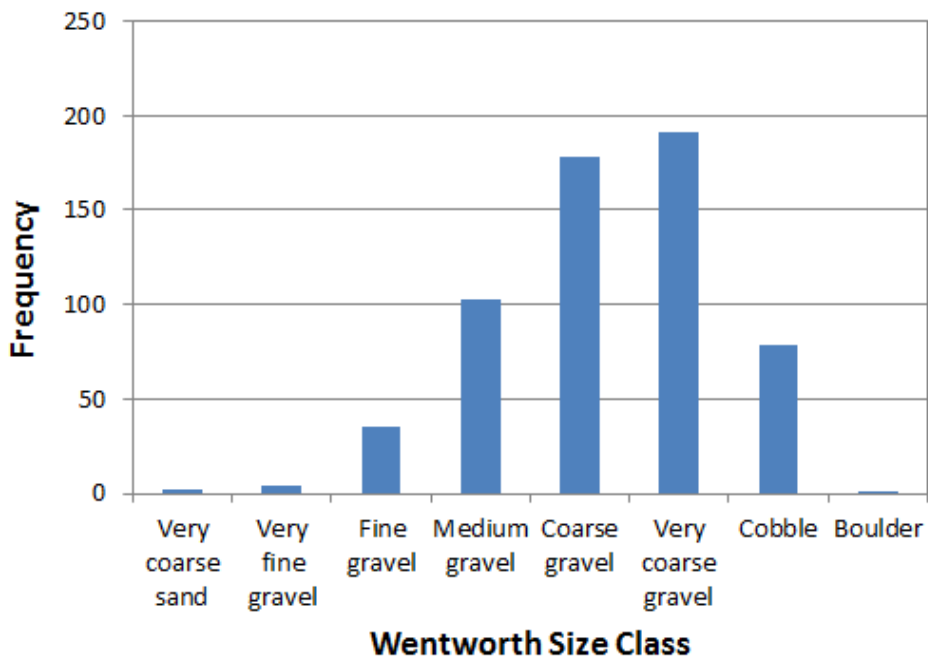


Figure C26. Wentworth size class frequencies of the D84 of the B axis for each sample plot.



Figure C27. Wentworth size class frequencies of the D84 of the B axis for all measured clasts.



UAS-SfM point cloud roughness results

De-trending results

Table C1. Average roughness values per plot computed for different roughness kernel sizes on the non-de-trended UAS-SfM point cloud.

Ground truth sample plot	Average roughness values - No detrending					
	5cm	10cm	15cm	20cm	25cm	30cm
A1	0.00615	0.00773	0.0086	0.00942	0.01034	0.01154
A2	0.00618	0.0068	0.00721	0.00766	0.00806	0.00838
A3	0.00605	0.00687	0.00763	0.00825	0.00886	0.00951
A4	0.00501	0.00557	0.00633	0.00744	0.00888	0.0105
A5	0.00436	0.00481	0.0052	0.00554	0.00604	0.00685
A6	0.00566	0.00746	0.01066	0.01494	0.01955	0.02395
A7	0.00313	0.00336	0.00354	0.00376	0.00404	0.00444
A8	0.00458	0.00514	0.00578	0.00642	0.00687	0.00707
A9	3.31E-03	3.72E-03	4.31E-03	4.99E-03	5.72E-03	6.52E-03
B1	0.00403	0.00473	0.0053	0.00585	0.00625	0.00647
B2	0.00301	0.00343	0.00395	0.00434	0.00454	0.00463
B3	0.00464	0.00578	0.00759	0.00943	0.01085	0.01173
B4	0.004	0.00467	0.00529	0.0058	0.00631	0.00686
C1	0.00584	0.0083	0.00924	0.00992	0.01039	0.01087
C2	0.00455	0.00512	0.006	0.00641	0.00676	0.00717
C3	0.00432	0.00582	0.0082	0.01101	0.01381	0.01643
C4	0.00309	0.00345	0.00402	0.00467	0.00529	0.00598
C5	0.00398	0.00431	0.0046	0.00483	0.00508	0.00555
C6	0.00486	0.00574	0.00672	0.00785	0.00902	0.00997
C7	0.00402	0.00475	0.00556	0.00634	0.00694	0.00744
D1	0.00325	0.00351	0.00375	0.00396	0.00416	0.00439
D2	0.0035	0.00379	0.00406	0.00425	0.00437	0.00446
D3	0.00456	0.00524	0.00606	0.00688	0.00752	0.00801
D4	0.00325	0.00861	0.00881	0.00911	0.00959	0.01024
D5	0.00479	0.00538	0.00608	0.00659	0.00671	0.00663

Table C2. Average roughness values per plot computed for different roughness kernel sizes on the UAS-SfM point cloud which had been de-trended using a 3rd order polynomial function.

Ground truth sample plot	Average roughness values 3rd order polynomial detrending					
	5cm	10cm	15cm	20cm	25cm	30cm
A1	0.00618	0.00781	0.00896	0.01046	0.01244	0.01492
A2	0.00618	0.0068	0.00726	0.00781	0.00832	0.00874
A3	0.0061	0.00696	0.00776	0.00839	0.00899	0.00953
A4	0.00503	0.00556	0.00627	0.00721	0.00835	0.00954
A5	0.00439	0.00484	0.00521	0.0055	0.00586	0.0064
A6	0.00605	0.00805	0.01136	0.01536	0.01926	0.02258
A7	0.00314	0.00337	0.00351	0.0036	0.00367	0.00375
A8	0.00461	0.00516	0.00576	0.0063	0.00662	0.00672
A9	3.31E-03	3.70E-03	4.24E-03	4.85E-03	5.48E-03	6.19E-03
B1	0.00404	0.00477	0.00541	0.00609	0.00669	0.00718
B2	0.00302	0.00346	0.00405	0.00457	0.00503	0.00548
B3	0.00462	0.00574	0.00762	0.00958	0.01106	0.01191
B4	0.00401	0.00467	0.00527	0.00572	0.0061	0.00648
C1	0.00582	0.00835	0.00946	0.01038	0.01136	0.01241
C2	0.00457	0.00513	0.00604	0.00652	0.00694	0.00741
C3	0.00437	0.00585	0.0081	0.01066	0.01307	0.01509
C4	0.0031	0.00348	0.00403	0.0046	0.00503	0.00531
C5	0.00396	0.00431	0.00473	0.00529	0.00608	0.00714
C6	0.00485	0.00574	0.00673	0.00787	0.009	0.00989
C7	0.00405	0.0048	0.00569	0.00674	0.00796	0.0095
D1	0.00327	0.00351	0.00371	0.00384	0.0039	0.00391
D2	0.00352	0.0038	0.00406	0.00423	0.00432	0.00437
D3	0.00457	0.00522	0.00597	0.00666	0.0071	0.00727
D4	0.00741	0.00863	0.00885	0.00912	0.00954	0.01007
D5	0.00483	0.00547	0.00628	0.00693	0.00722	0.00735

Table C3. Average roughness values per plot computed for different roughness kernel sizes on the UAS-SfM point cloud which had been de-trended using a 4th order polynomial function.

Ground truth sample plot	Average roughness values 4th order polynomial detrending					
	5cm	10cm	15cm	20cm	25cm	30cm
A1	0.00622	0.00781	0.00858	0.00916	0.00964	0.01003
A2	0.00618	0.00679	0.00722	0.00771	0.00812	0.0084
A3	0.0061	0.00696	0.00774	0.00834	0.0089	0.00936
A4	0.00503	0.00556	0.00624	0.00714	0.00824	0.00937
A5	0.00438	0.00484	0.00525	0.00562	0.00607	0.00664
A6	0.00607	0.00807	0.01133	0.01516	0.01871	0.02158
A7	0.00314	0.00337	0.00351	0.00361	0.00368	0.00374
A8	0.00459	0.00515	0.00579	0.00643	0.00687	0.00709
A9	3.31E-03	3.69E-03	4.17E-03	4.62E-03	4.92E-03	5.15E-03
B1	0.00404	0.00477	0.00541	0.00608	0.00668	0.00716
B2	0.00301	0.00345	0.00403	0.00455	0.00495	0.00532
B3	0.0046	0.00573	0.00773	0.00987	0.01158	0.01275
B4	0.00401	0.00467	0.00525	0.00565	0.00593	0.00612
C1	0.00582	0.0084	0.00972	0.01106	0.01268	0.01447
C2	0.00457	0.00515	0.00608	0.00656	0.00693	0.00724
C3	0.0044	0.00578	0.00766	0.00966	0.01136	0.01242
C4	0.00312	0.00352	0.00411	0.00472	0.00516	0.00544
C5	0.00397	0.0043	0.0046	0.00486	0.00511	0.0054
C6	0.00486	0.00575	0.00675	0.00787	0.009	0.00987
C7	0.00407	0.0049	0.00578	0.0067	0.00765	0.0086
D1	0.00327	0.0035	0.0037	0.00382	0.00387	0.00387
D2	0.00351	0.00378	0.00403	0.00418	0.00427	0.0043
D3	0.00456	0.00523	0.00601	0.00675	0.00726	0.00754
D4	0.00741	0.00868	0.009	0.00949	0.01022	0.01105
D5	0.00484	0.00547	0.00628	0.00694	0.00726	0.00738

Table C4. Average roughness values per plot computed for different roughness kernel sizes on the UAS-SfM point cloud which had been de-trended using a 5th order polynomial function.

Ground truth sample plot	Average roughness values 5th order polynomial detrending					
	5cm	10cm	15cm	20cm	25cm	30cm
A1	0.00621	0.00783	0.00866	0.0094	0.01016	0.01082
A2	0.00618	0.0068	0.00726	0.00781	0.00828	0.00862
A3	0.0061	0.00696	0.00772	0.00829	0.00878	0.00915
A4	0.00505	0.00554	0.00613	0.00679	0.00749	0.00807
A5	0.00439	0.00484	0.00521	0.00546	0.00573	0.00609
A6	0.00612	0.00801	0.01088	0.01399	0.01649	0.01808
A7	0.00314	0.00337	0.00352	0.00364	0.00374	0.00385
A8	0.0046	0.00518	0.00589	0.00663	0.0072	0.00754
A9	3.31E-03	3.68E-03	4.16E-03	4.59E-03	4.85E-03	5.04E-03
B1	0.00404	0.0048	0.0055	0.00629	0.00705	0.00775
B2	0.00302	0.00346	0.00404	0.00452	0.0048	0.00494
B3	0.0046	0.00574	0.00777	0.00999	0.01171	0.01282
B4	0.004	0.00466	0.00524	0.0056	0.0058	0.00588
C1	0.00581	0.00834	0.00952	0.01065	0.01195	0.01332
C2	0.00457	0.00515	0.00608	0.00656	0.00693	0.00724
C3	0.0044	0.00579	0.00769	0.00974	0.01149	0.0126
C4	0.00312	0.0035	0.00406	0.00461	0.00498	0.00517
C5	0.00397	0.00431	0.00463	0.00492	0.00522	0.00555
C6	0.00486	0.00578	0.00684	0.00803	0.0092	0.01004
C7	0.00409	0.00491	0.00579	0.00665	0.00733	0.00778
D1	0.00327	0.00351	0.00372	0.00388	0.00398	0.004
D2	0.00351	0.00379	0.00406	0.00424	0.00435	0.00441
D3	0.00456	0.00524	0.00605	0.00683	0.00737	0.00765
D4	0.00742	0.00868	0.00896	0.0093	0.00975	0.01028
D5	0.00483	0.00547	0.00631	0.00704	0.00746	0.00771

*Quantifying physical river habitat parameters using hyperspatial resolution
UAS imagery and SfM-photogrammetry*

Smoothing and filtering results

Table C5. Average roughness values per plot computed for different roughness kernel sizes on the UAS-SfM point cloud which had not been de-trended and had not been smoothed and filtered according to the methods specified in Chapter 4. Note that some of this data is therefore reproduced from Table C1.

Ground truth sample plot	Average roughness values - No filtering or smoothing									
	5cm	10cm	15cm	20cm	25cm	30cm	35cm	40cm	45cm	50cm
A1	0.00615	0.00773	0.0086	0.00942	0.01034	0.01154	0.01313	0.015	0.01694	0.01897
A2	0.00618	0.0068	0.00721	0.00766	0.00806	0.00838	0.00867	0.00889	0.00904	0.00914
A3	0.00605	0.00687	0.00763	0.00825	0.00886	0.00951	0.01014	0.01082	0.01173	0.01289
A4	0.00501	0.00557	0.00633	0.00744	0.00888	0.0105	0.01207	0.01343	0.01454	0.01545
A5	0.00436	0.00481	0.0052	0.00554	0.00604	0.00685	0.00792	0.00909	0.01024	0.01137
A6	0.00566	0.00746	0.01066	0.01494	0.01955	0.02395	0.0278	0.0311	0.03395	0.03644
A7	0.00313	0.00336	0.00354	0.00376	0.00404	0.00444	0.00498	0.00564	0.00639	0.00724
A8	0.00458	0.00514	0.00578	0.00642	0.00687	0.00707	0.00715	0.00729	0.00758	0.00803
A9	3.31E-03	3.72E-03	4.31E-03	4.99E-03	5.72E-03	6.52E-03	7.41E-03	8.29E-03	9.11E-03	9.80E-03
B1	0.00403	0.00473	0.0053	0.00585	0.00625	0.00647	0.00657	0.00661	0.00675	0.00713
B2	0.00301	0.00343	0.00395	0.00434	0.00454	0.00463	0.00466	0.00466	0.00471	0.00486
B3	0.00464	0.00578	0.00759	0.00943	0.01085	0.01173	0.01226	0.01284	0.01379	0.01511
B4	0.004	0.00467	0.00529	0.0058	0.00631	0.00686	0.00749	0.00826	0.00914	0.01003
C1	0.00584	0.0083	0.00924	0.00992	0.01039	0.01087	0.01167	0.01298	0.01487	0.01759
C2	0.00455	0.00512	0.006	0.00641	0.00676	0.00717	0.00759	0.00798	0.00832	0.00855
C3	0.00432	0.00582	0.0082	0.01101	0.01381	0.01643	0.01901	0.02172	0.02459	0.02742
C4	0.00309	0.00345	0.00402	0.00467	0.00529	0.00598	0.00694	0.00818	0.00971	0.0114
C5	0.00398	0.00431	0.0046	0.00483	0.00508	0.00555	0.00649	0.00812	0.01068	0.01422
C6	0.00486	0.00574	0.00672	0.00785	0.00902	0.00997	0.01052	0.0108	0.01099	0.01117
C7	0.00402	0.00475	0.00556	0.00634	0.00694	0.00744	0.00804	0.00894	0.01006	0.01126
D1	0.00325	0.00351	0.00375	0.00396	0.00416	0.00439	0.00468	0.00506	0.00551	0.00603
D2	0.0035	0.00379	0.00406	0.00425	0.00437	0.00446	0.00453	0.00463	0.00477	0.00497
D3	0.00456	0.00524	0.00606	0.00688	0.00752	0.00801	0.00842	0.00879	0.0092	0.00971
D4	0.00325	0.00861	0.00881	0.00911	0.00959	0.01024	0.01089	0.0115	0.01201	0.01239
D5	0.00479	0.00538	0.00608	0.00659	0.00671	0.00663	0.00663	0.00682	0.00717	0.00776

*Quantifying physical river habitat parameters using hyperspatial resolution
UAS imagery and SfM-photogrammetry*

Table C6. Average roughness values per plot computed for different roughness kernel sizes on the UAS-SfM point cloud which had not been de-trended but had been smoothed and filtered according to the methods specified in Chapter 4.

Ground truth sample plot	Average roughness values - filtered and smoothed									
	5cm	10cm	15cm	20cm	25cm	30cm	35cm	40cm	45cm	50cm
A1	0.00108	0.00256	0.00395	0.00526	0.00663	0.00827	0.01034	0.01263	0.01501	0.01747
A2	0.00073	0.00165	0.00271	0.00365	0.00425	0.00463	0.00496	0.00536	0.0057	0.00595
A3	0.001	0.0026	0.00389	0.00482	0.00575	0.0067	0.00758	0.00856	0.00986	0.01144
A4	0.00071	0.00189	0.00336	0.00509	0.00707	0.00912	0.01094	0.01247	0.01367	0.01466
A5	0.00069	0.0017	0.00245	0.00307	0.00389	0.00515	0.00667	0.00816	0.00952	0.0108
A6	0.00123	0.00425	0.00857	0.01355	0.01853	0.02313	0.02715	0.03057	0.03352	0.03608
A7	0.00049	0.00117	0.00163	0.0021	0.00266	0.00334	0.00409	0.00489	0.00575	0.00668
A8	0.00077	0.0019	0.00308	0.00407	0.00469	0.00493	0.00502	0.00523	0.0056	0.00616
A9	5.55E-04	1.53E-03	2.54E-03	3.46E-03	4.47E-03	5.50E-03	6.56E-03	7.57E-03	8.46E-03	9.19E-03
B1	0.00066	0.00176	0.00287	0.00376	0.0043	0.00457	0.00467	0.00474	0.00493	0.00536
B2	0.00058	0.00156	0.00247	0.00303	0.00327	0.00338	0.00341	0.00341	0.00349	0.00378
B3	0.00111	0.00341	0.00597	0.00815	0.0097	0.0106	0.011	0.01129	0.01236	0.01425
B4	0.00078	0.00188	0.00272	0.00341	0.00416	0.00499	0.00589	0.00687	0.00794	0.009
C1	0.0011	0.00184	0.00241	0.00313	0.0043	0.00622	0.00879	0.01185	0.0154	0.01943
C2	0.0008	0.00184	0.00256	0.00313	0.00369	0.00421	0.00469	0.00512	0.00557	0.0059
C3	0.00116	0.00362	0.00665	0.00974	0.01269	0.01545	0.01813	0.02095	0.02398	0.02696
C4	0.00055	0.00144	0.00234	0.00318	0.00404	0.005	0.00621	0.00777	0.00957	0.0114
C5	0.00059	0.00144	0.0021	0.00256	0.003	0.00375	0.005	0.00714	0.01029	0.01416
C6	0.0009	0.00239	0.00389	0.0055	0.00716	0.00843	0.00914	0.00946	0.00971	0.00996
C7	0.00081	0.00209	0.00336	0.00448	0.00528	0.00595	0.00675	0.0078	0.00893	0.01005
D1	0.00047	0.00112	0.00161	0.00191	0.00215	0.00245	0.00287	0.00347	0.00416	0.00488
D2	0.00048	0.00131	0.00202	0.00244	0.00264	0.00273	0.0028	0.0029	0.0029	0.0028
D3	0.00082	0.00232	0.00375	0.00489	0.00562	0.00605	0.0065	0.00711	0.00783	0.00861
D4	0.00079	0.00151	0.00214	0.00288	0.00399	0.00543	0.00678	0.00788	0.00869	0.00932
D5	0.00087	0.00243	0.00383	0.00461	0.00478	0.00467	0.00461	0.00483	0.00535	0.00628

Model calibration-validations using the phi scale of grain size

UAS-SfM Point Cloud Roughness

Table C7 presents the results of the calibration-validation model for UAS-SfM point cloud roughness carried out using a jack-knife analysis, with grain size expressed using the phi scale (ϕ). Residual errors range from $+0.797\phi$ to -1.176ϕ , where positive (blue) numbers indicate an over-prediction of grain size by the model and negative (red) numbers indicate an under-prediction of grain size. The mean and standard deviation of residual errors are 0.006ϕ and 0.475ϕ respectively.

Table C7. Model validation results for the UAS-SfM point cloud roughness approach (using phi scale grain sizes shown to 2 d.p.). The coloured cells highlight positive residual error in blue (i.e. overestimation of grain size) and negative residual error in red (i.e. underestimation).

Ground truth sample plot	Substrate size (phi) D84 of B axis	Roughness 20cm kernel size	Equation when plot is excluded (phi - log)		Predicted grain size (phi)	Residual error (phi)
			Slope	Intercept		
A1	<i>Not included</i>					
A2	-5.49	0.0036	-1.325	-13.0240	-5.59	0.094
A3	-5.39	0.0048	-1.349	-13.1810	-5.98	0.591
A4	-6.49	0.0051	-1.302	-12.8710	-6.00	-0.497
A5	-4.91	0.0031	-1.301	-12.9100	-5.38	0.476
A6	-7.29	0.0135	-1.337	-13.0920	-7.34	0.046
A7	-4.32	0.0021	-1.247	-12.6170	-4.93	0.608
A8	-6.13	0.0041	-1.325	-13.0000	-5.71	-0.421
A9	-5.39	0.0035	-1.323	-13.0140	-5.52	0.125
B1	-5.49	0.0038	-1.325	-13.0260	-5.63	0.137
B2	-4.70	0.0030	-1.289	-12.8500	-5.38	0.676
B3	-6.39	0.0082	-1.371	-13.2860	-6.69	0.300
B4	-5.81	0.0034	-1.337	-13.0730	-5.48	-0.330
C1	<i>Not included</i>					
C2	-5.49	0.0031	-1.333	-13.0570	-5.37	-0.124
C3	-6.66	0.0097	-1.379	-13.3320	-6.95	0.288
C4	-6.00	0.0032	-1.356	-13.1630	-5.37	-0.635
C5	-6.19	0.0026	-1.433	-13.5650	-5.01	-1.176
C6	-6.25	0.0055	-1.318	-12.9770	-6.12	-0.128
C7	-5.93	0.0045	-1.325	-13.0150	-5.85	-0.082
D1	-4.52	0.0019	-1.291	-12.8430	-4.76	0.236
D2	-5.29	0.0024	-1.352	-13.1610	-5.03	-0.256
D3	-6.41	0.0049	-1.307	-12.9020	-5.95	-0.461
D4	-4.52	0.0029	-1.273	-12.7700	-5.32	0.797
D5	-6.02	0.0046	-1.322	-13.0010	-5.89	-0.134

UAS-SfM Image Texture

Table C8 presents the results of the calibration-validation model for UAS-SfM image texture approach carried out using a jack-knife analysis, with grain size expressed using the phi scale (ϕ). Residual errors range from +1.149 ϕ to -0.641 ϕ , where positive (blue) numbers indicate an over-prediction of grain size by the model and negative (red) numbers indicate an under-prediction of grain size. The mean and standard deviation of residual errors are 0.012 ϕ and 0.468 ϕ respectively.

Table C8. Model validation results for the UAS-SfM point cloud roughness approach (using phi scale grain sizes shown to 2 d.p.). The coloured cells highlight positive residual error in blue (i.e. overestimation of grain size) and negative residual error in red (i.e. underestimation).

Ground truth sample plot	Substrate size (phi) Average A axis	Image entropy Maximum	Equation when plot is excluded (phi - log)		Predicted grain size (phi)	Residual error (phi)
			Slope	Intercept		
A1	<i>Not included</i>					
A2	-5.78	751	-10.650	63.7980	-6.72	0.94
A3	-5.45	678	-9.359	55.3930	-5.62	0.17
A4	-6.52	718	-9.260	54.7630	-6.14	-0.38
A5	-5.44	688	-9.365	55.4240	-5.76	0.33
A6	-7.09	758	-8.704	51.1290	-6.58	-0.51
A7	-4.71	654	-8.710	51.1180	-5.35	0.64
A8	-6.35	713	-9.346	55.3220	-6.08	-0.28
A9	-5.46	684	-9.358	55.3830	-5.71	0.25
B1	-5.79	670	-9.680	57.5110	-5.48	-0.31
B2	-4.90	632	-9.339	55.2630	-4.96	0.06
B3	-6.46	734	-9.354	55.3690	-6.35	-0.11
B4	-6.09	670	-9.919	59.0920	-5.45	-0.64
C1	<i>Not included</i>					
C2	-5.89	684	-9.525	56.4940	-5.68	-0.21
C3	-6.40	699	-9.439	55.9450	-5.88	-0.52
C4	-6.19	691	-9.527	56.5130	-5.78	-0.41
C5	-6.23	704	-9.410	55.7460	-5.95	-0.27
C6	-6.35	734	-9.459	56.0540	-6.36	0.01
C7	-6.03	696	-9.460	56.0680	-5.85	-0.18
D1	-4.70	646	-8.705	51.0900	-5.24	0.54
D2	-5.63	670	-8.193	47.7240	-5.59	-0.04
D3	-6.37	719	-9.336	55.2560	-6.15	-0.22
D4	-5.04	716	-9.965	59.3130	-6.19	1.15
D5	-6.58	768	-9.901	58.9340	-6.85	0.27

TLS Point Cloud Roughness

Table C9 presents the results of the calibration-validation model for TLS point cloud roughness approach carried out using a jack-knife analysis, with grain size expressed using the phi scale (ϕ). Residual errors range from +1.363 ϕ to -0.791 ϕ , where positive (blue) numbers indicate an over-prediction of grain size by the model and negative (red) numbers indicate an under-prediction of grain size. The mean and standard deviation of residual errors are -0.005 ϕ and 0.543 ϕ respectively.

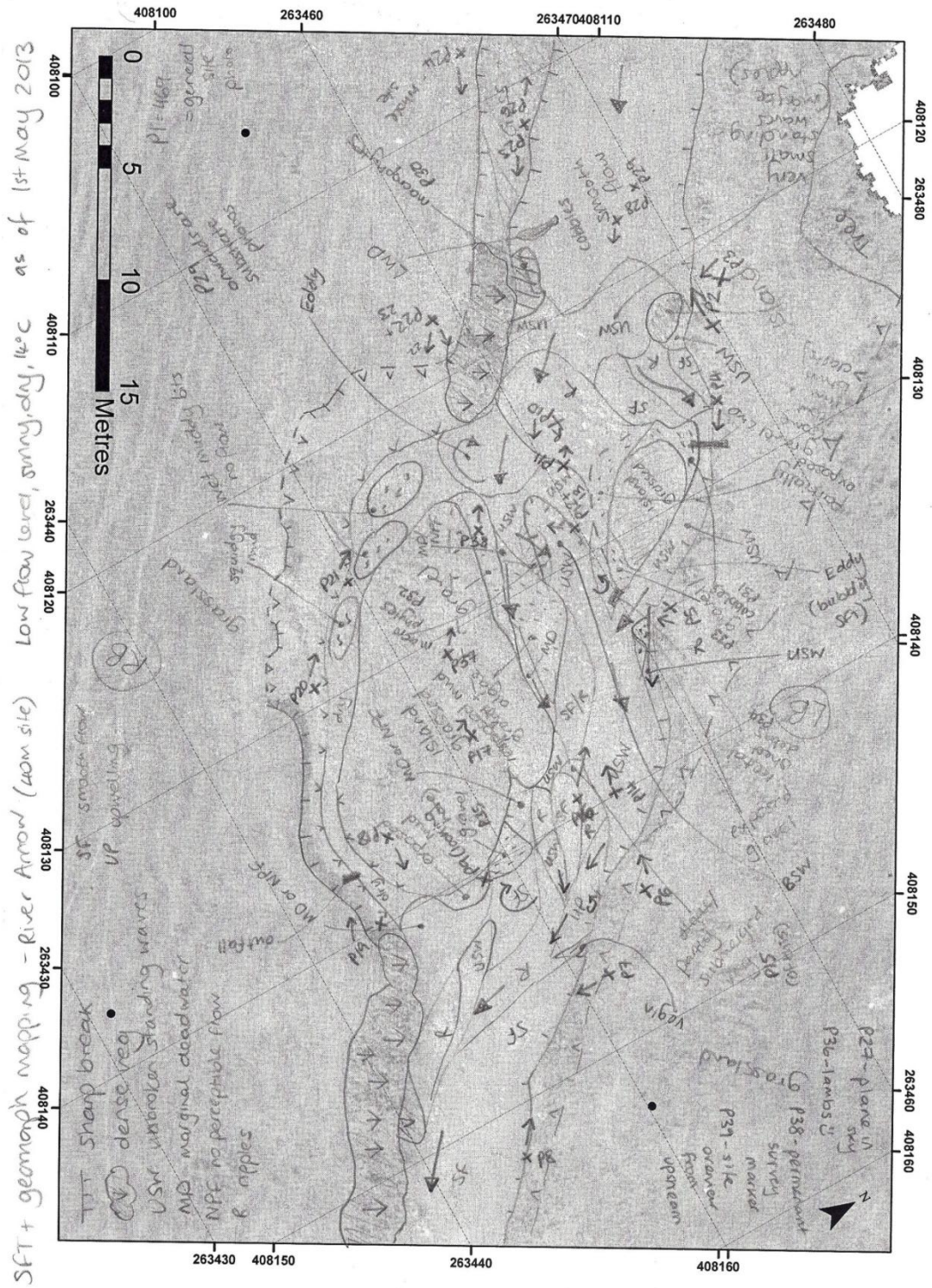
Table C9. Model validation results for the TLS point cloud roughness approach (using phi scale grain sizes shown to 2 d.p.). The coloured cells highlight positive residual error in blue (i.e. overestimation of grain size) and negative residual error in red (i.e. underestimation).

Ground truth sample plot	Substrate size (phi) D84 of B axis	TLS point cloud roughness 20cm kernel size	Equation when plot is excluded (phi - log)		Predicted grain size (phi)	Residual error (phi)
			Slope	Intercept		
A1	<i>Not included</i>					
A2	-5.49	0.0123	-1.095	-10.7080	-5.90	0.40
A3	-5.39	0.0057	-1.123	-10.7990	-5.00	-0.39
A4	-6.49	0.0111	-1.077	-10.5760	-5.73	-0.76
A5	-4.91	0.0079	-1.060	-10.5550	-5.42	0.52
A6	-7.29	0.0313	-0.988	-10.1800	-6.76	-0.54
A7	-4.32	0.0043	-1.012	-10.3350	-4.81	0.49
A8	-6.13	0.0122	-1.077	-10.5970	-5.86	-0.27
A9	-5.39	0.0052	-1.142	-10.8840	-4.88	-0.51
B1	-5.49	0.0096	-1.083	-10.6380	-5.61	0.12
B2	-4.70	0.0054	-1.049	-10.4960	-5.03	0.33
B3	-6.39	0.0134	-1.066	-10.5390	-5.94	-0.45
B4	-5.81	0.0155	-1.106	-10.7550	-6.15	0.34
C1	<i>Not included</i>					
C2	-5.49	0.0076	-1.092	-10.6720	-5.34	-0.15
C3	-6.66	0.0223	-1.064	-10.5410	-6.49	-0.17
C4	-6.00	0.0121	-1.081	-10.6180	-5.85	-0.15
C5	-6.19	0.0082	-1.115	-10.7490	-5.40	-0.79
C6	-6.25	0.0279	-0.946	-10.1170	-6.73	0.48
C7	-5.93	0.0073	-1.123	-10.7900	-5.27	-0.66
D1	-4.52	0.0061	-1.027	-10.4070	-5.16	0.64
D2	-5.29	0.0092	-1.078	-10.6250	-5.57	0.28
D3	-6.41	0.0133	-1.066	-10.5360	-5.93	-0.48
D4	-4.52	0.0118	-1.109	-10.8150	-5.89	1.36
D5	-6.02	0.0174	-1.105	-10.7450	-6.27	0.25

Appendix D

Surface Flow Types

Figure D2. Annotated mapping of SFTs, River Arrow, May 2013



.Figure D3. Annotated mapping of SFTs, River Arrow, June 2013

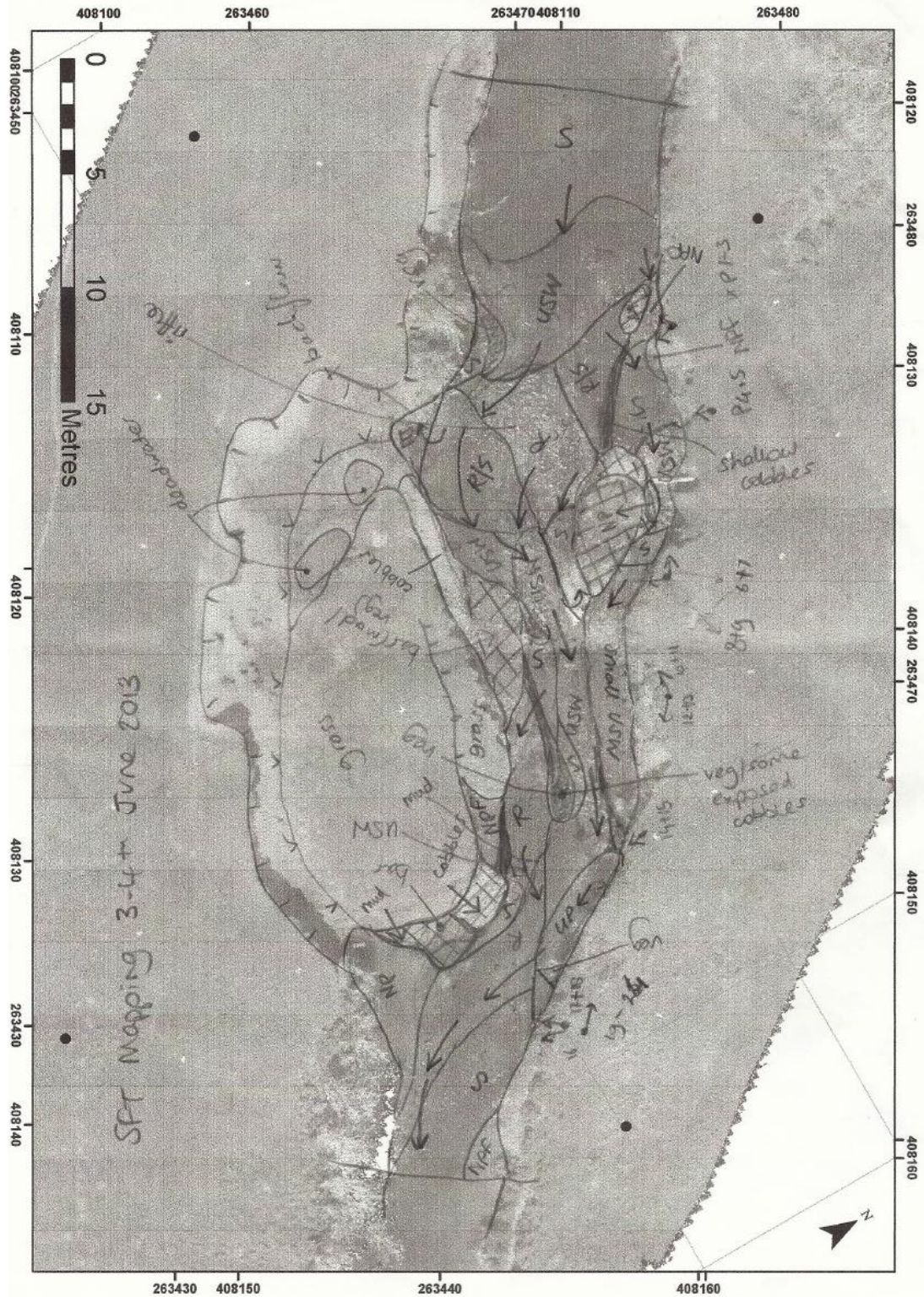


Figure D4. Annotated mapping of SFTs, River Arrow, August 2013.

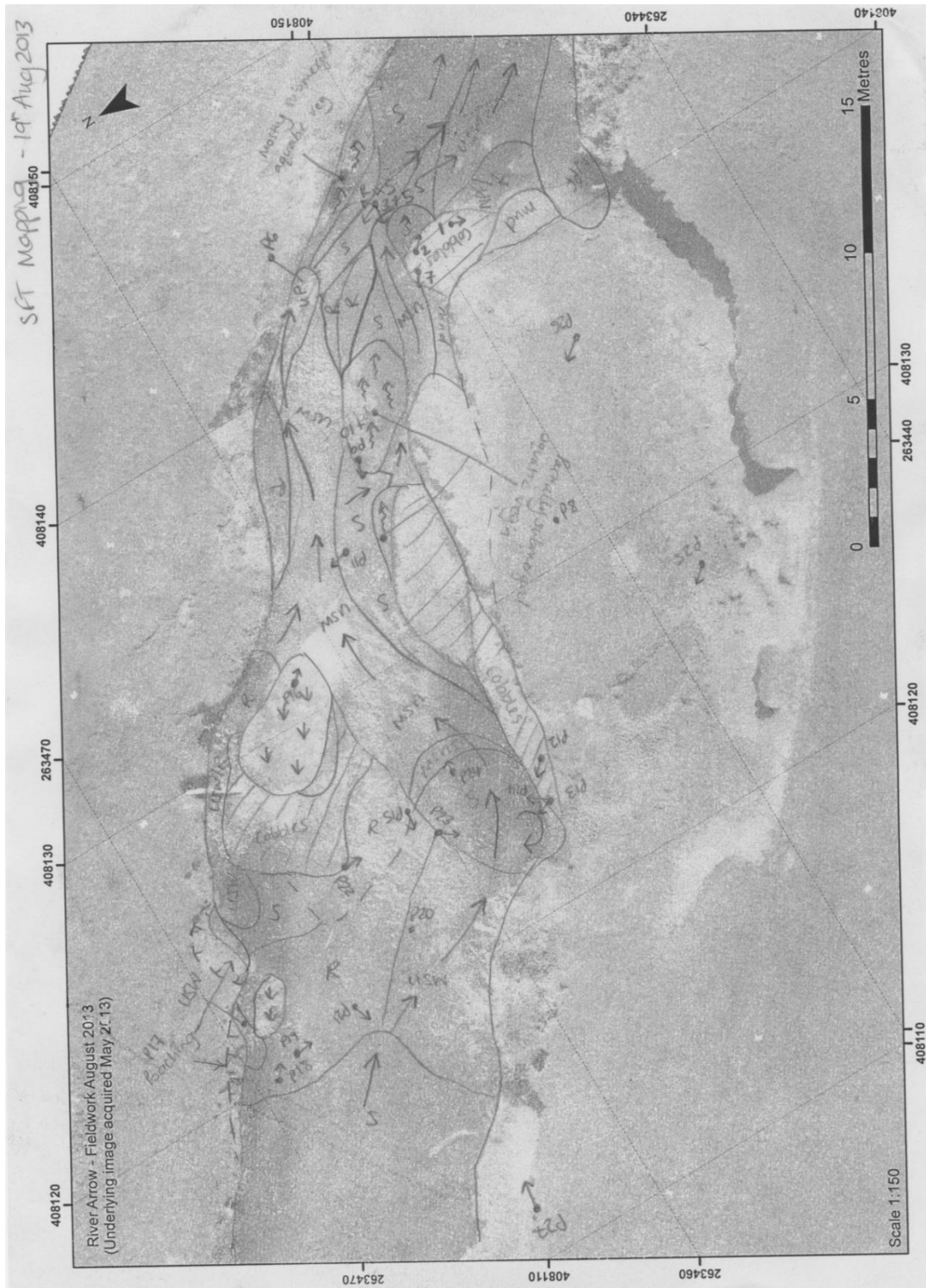


Figure D6. Selected field photos of SFTs, River Arrow, July 2012 (Photos by P. Jurga).

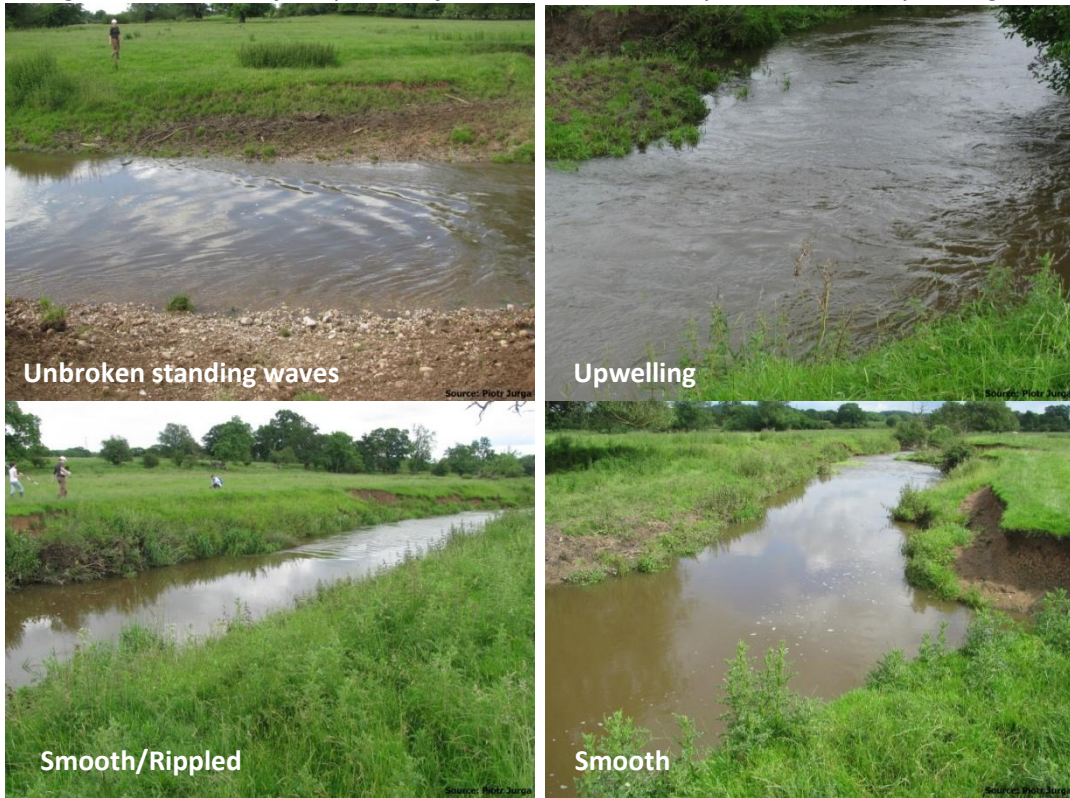


Figure D7. Selected field photos of SFTs, River Arrow, May 2013.



Figure D8. Selected field photos of SFTs, River Arrow, June 2013.



Figure D9. Selected field photos of SFTs, River Arrow, August 2013.



Figure D10. Selected field photos of SFTs, Coledale Beck, July 2013.



Figure D11. Percentage agreement between UAS-SfM mapped SFTs and ground truthing by SFT. Values are averages for the surveys conducted at the River Arrow in May, June and August 2013. The green bars indicate where the surveys are in agreement. SFTs are ordered on the x axis according to the continuum of SFTs proposed by Hill 2011 (Figure 5.1 in Chapter 5).

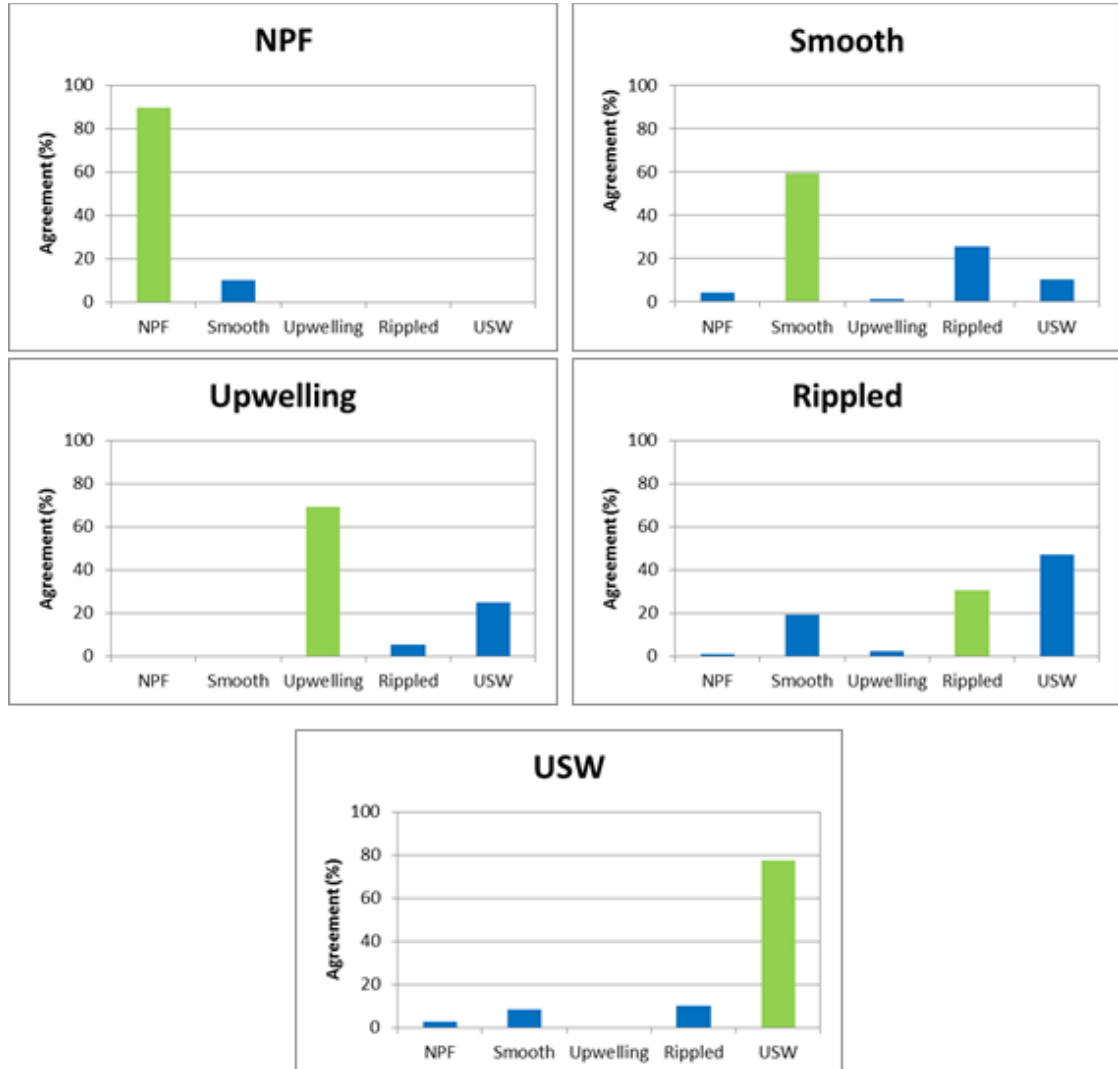


Figure D12. Roughness distributions profiles by site and by SFT (for whole SFT polygons).

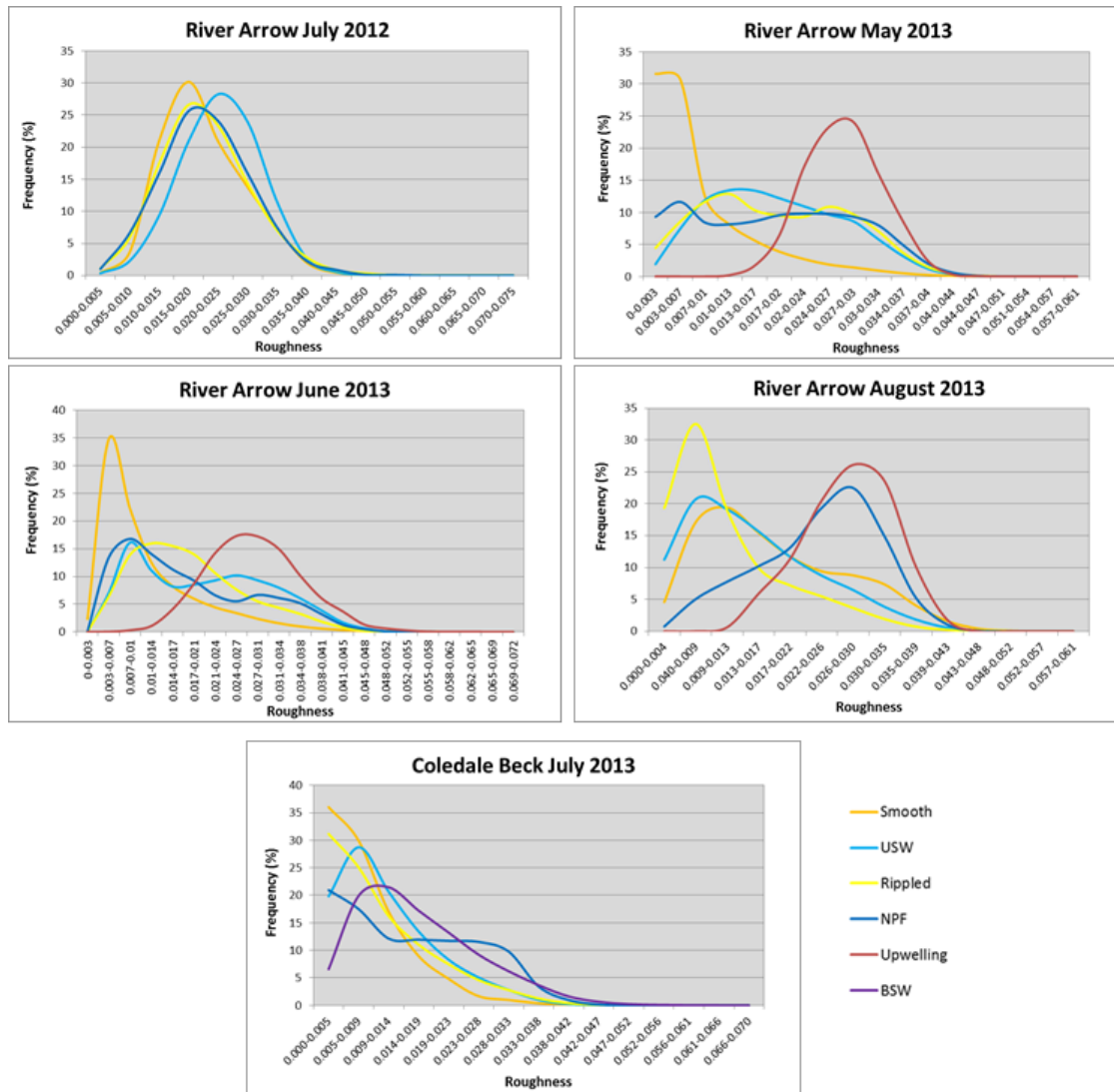


Figure D13. Point cloud roughness from the **River Arrow May 2013** survey regressed against Froude number (calculated using field-measured water depth and mean column velocity).

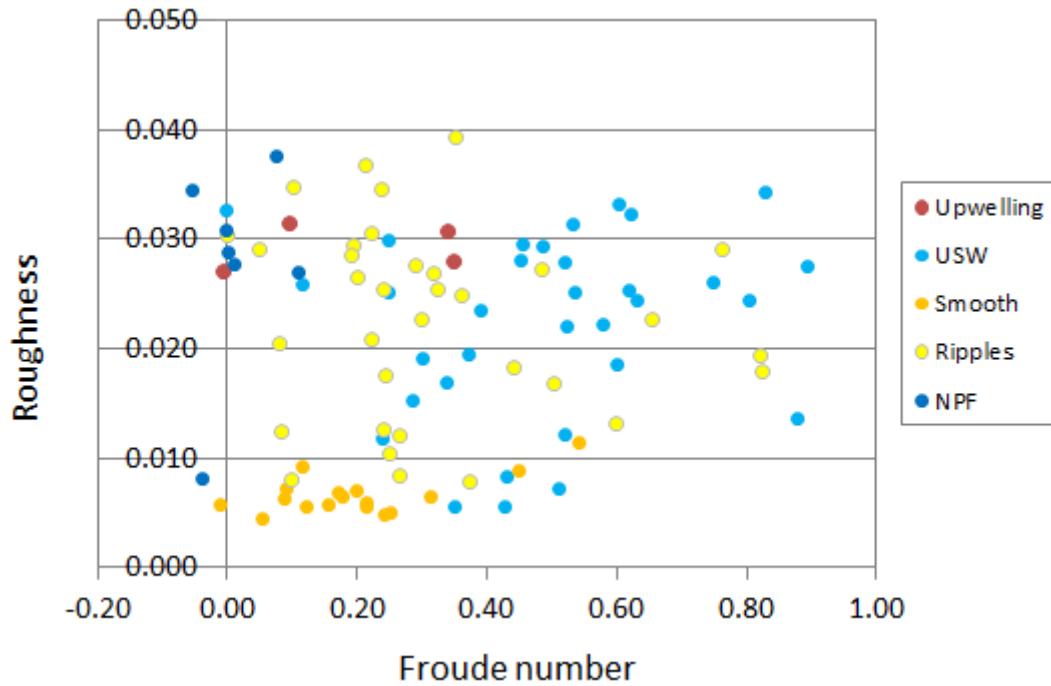


Figure D14. Point cloud roughness from the **River Arrow June 2013** survey regressed against Froude number (calculated using field-measured water depth and mean column velocity).

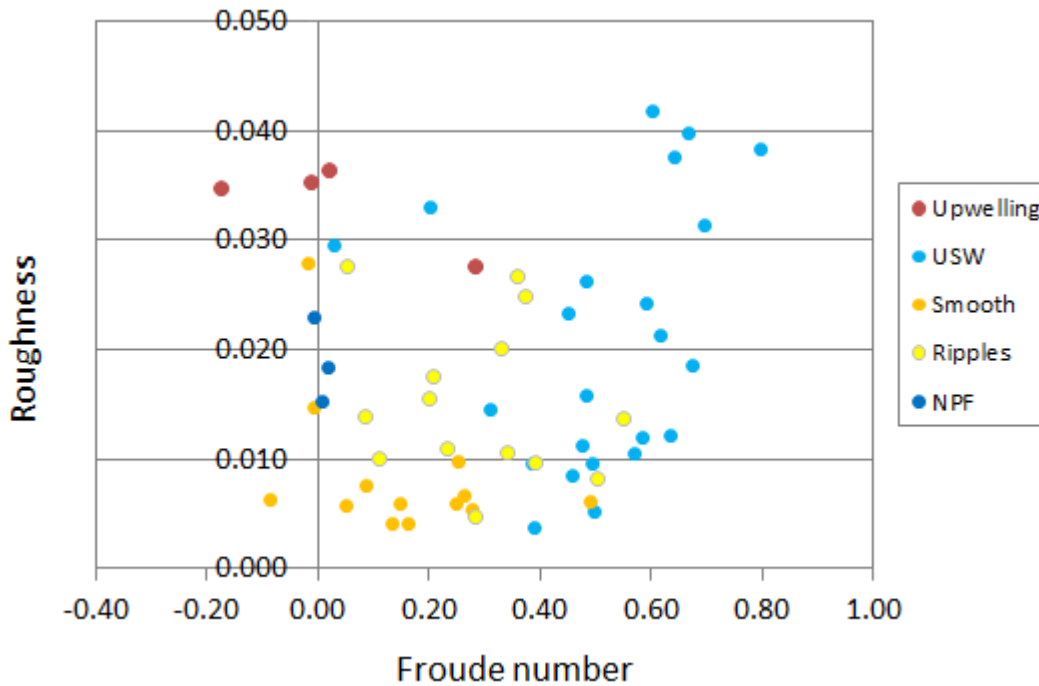


Figure D15. Point cloud roughness from the **River Arrow August 2013** survey regressed against Froude number (calculated using field-measured water depth and mean column velocity).

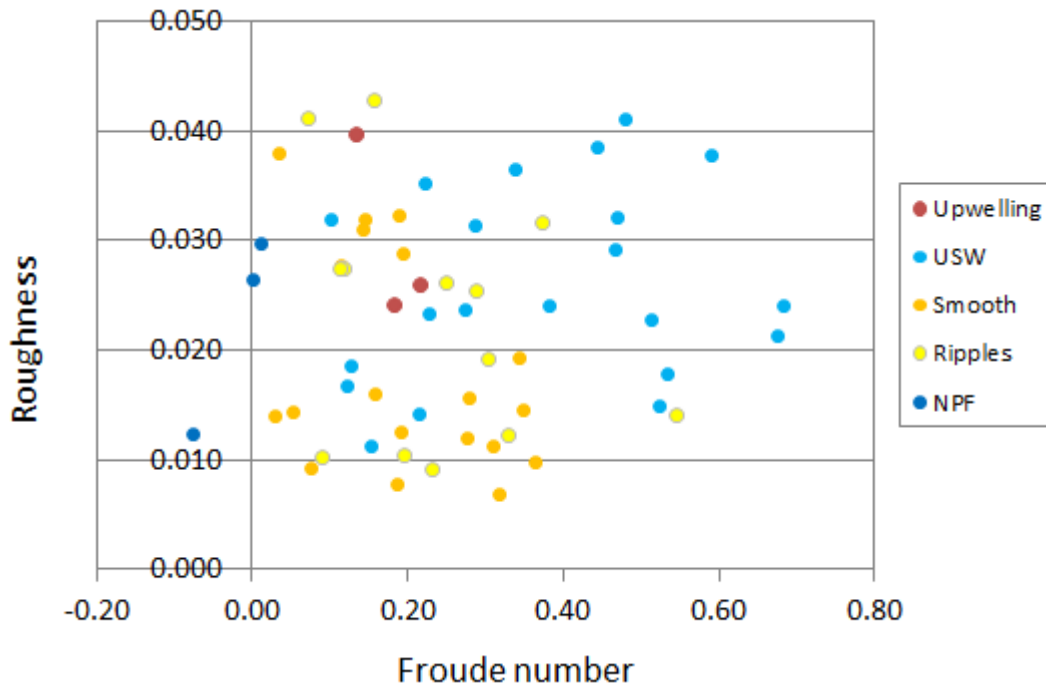
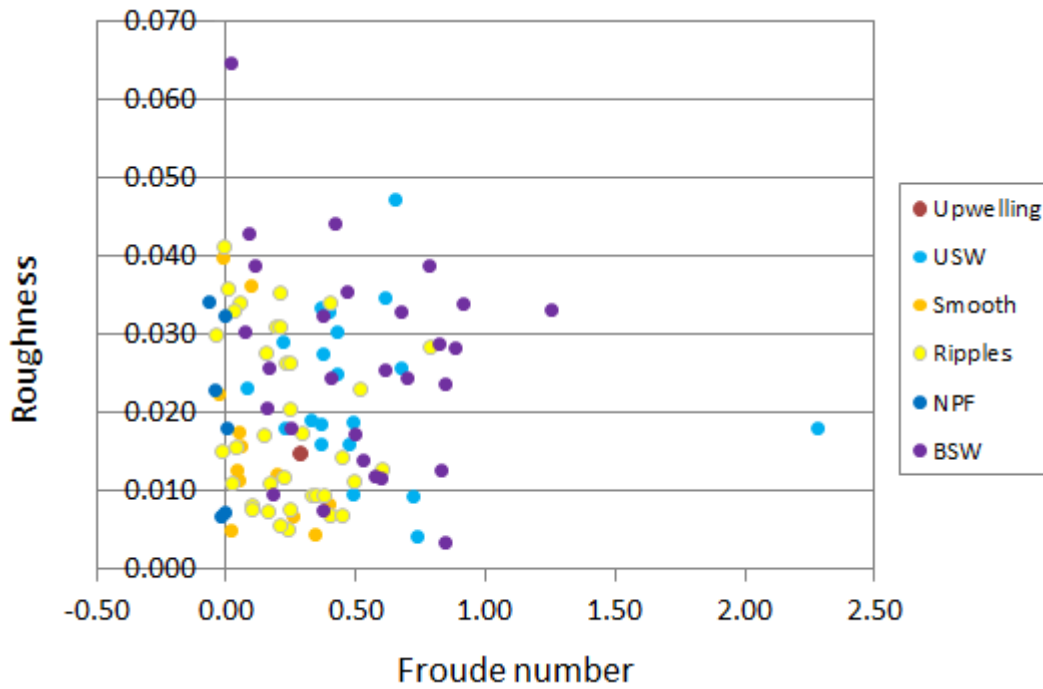


Figure D16. Point cloud roughness from **Coledale Beck July 2013** survey regressed against Froude number (calculated using field-measured water depth and mean column velocity).



Appendix E

Discussion & Conclusion

Quantifying physical river habitat parameters using hyperspatial resolution
UAS imagery and SfM-photogrammetry

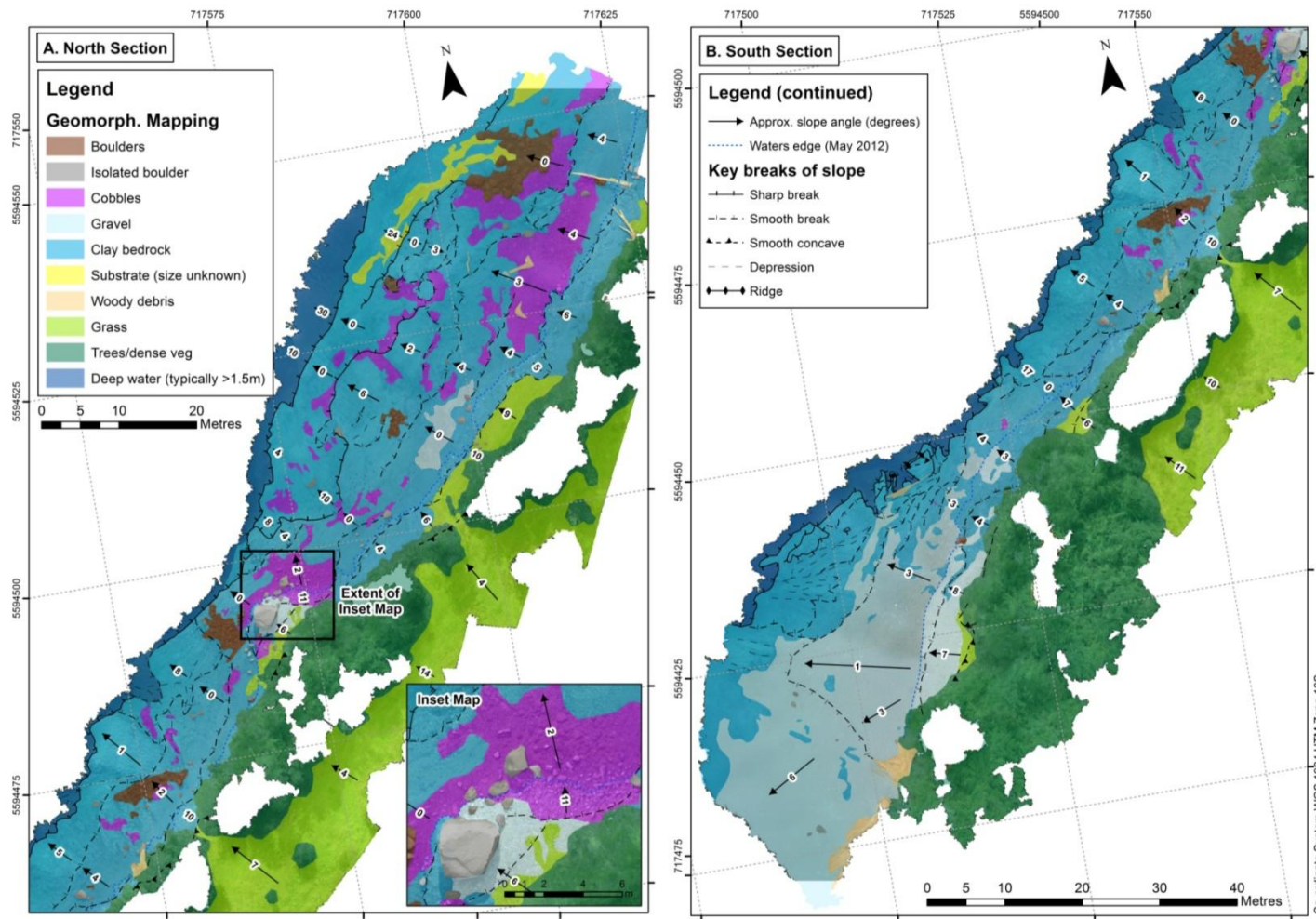


Figure E1. Geomorphological map for the Piedra Blanca research site on the San Pedro River, mapped visually from the UAS-SfM orthophoto and DEM (May 2012).

Quantifying physical river habitat parameters using hyperspatial resolution
 UAS imagery and SfM-photogrammetry

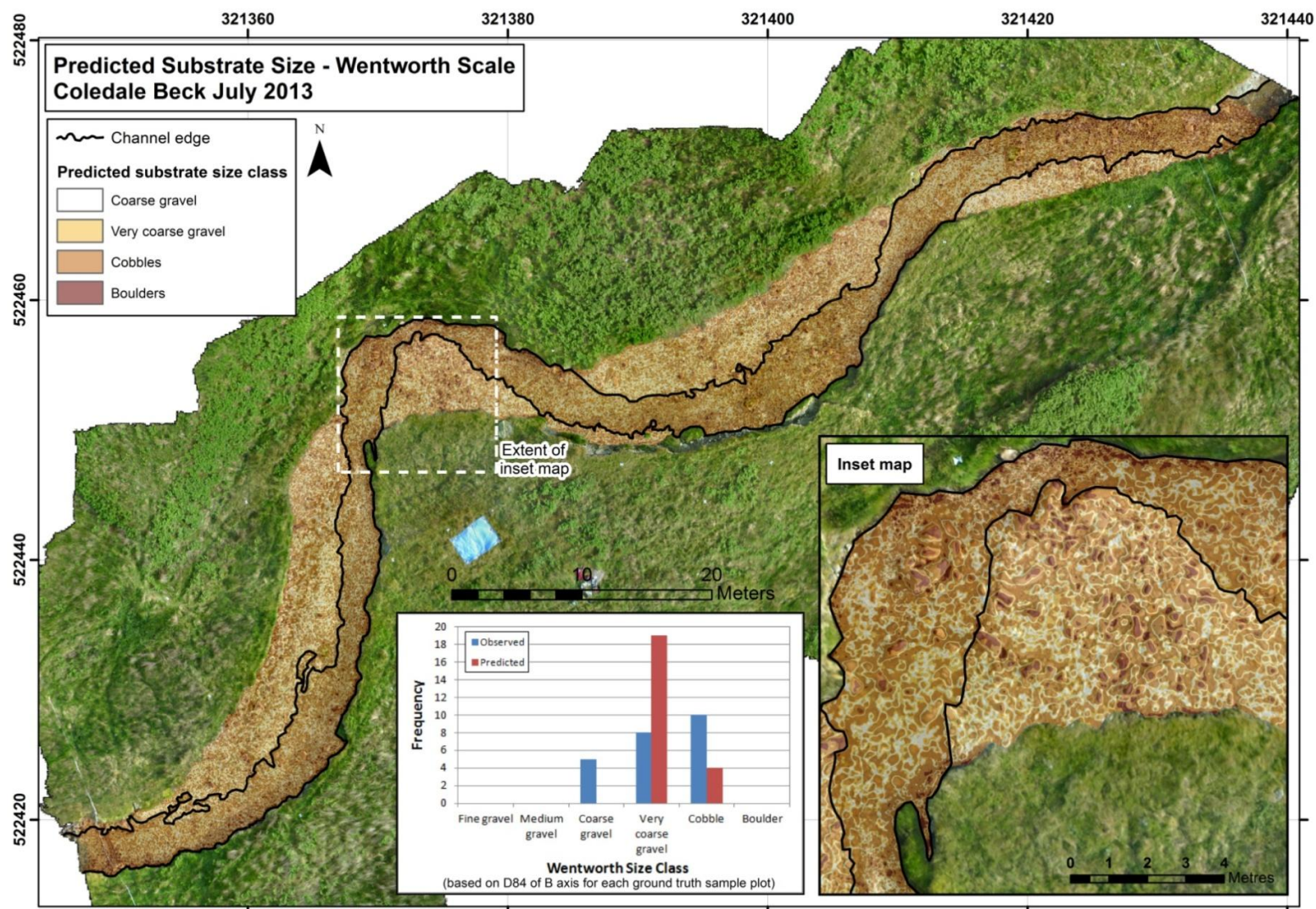


Figure E2. (Previous page) Predicted substrate sizes for Coledale Beck, classified according to the Wentworth Scale (Wentworth 1922). The inset frequency chart shows the difference between observed and predicted ground truth sample plot size classes (excluding plots A1 and C1).

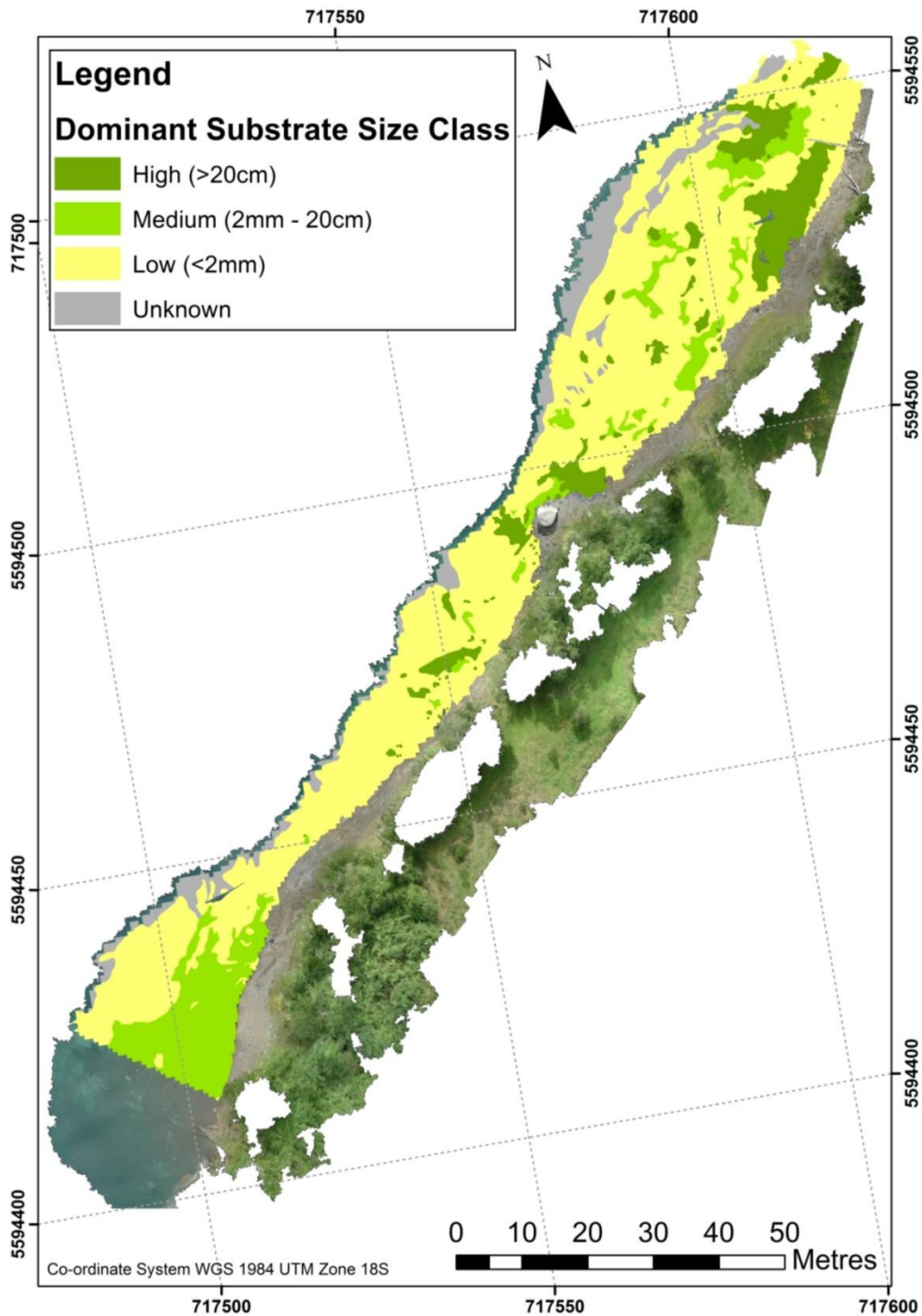


Figure E3. Dominant substrate size classes for the Piedra Blanca research site, mapped visually from the UAS-SfM orthophoto.

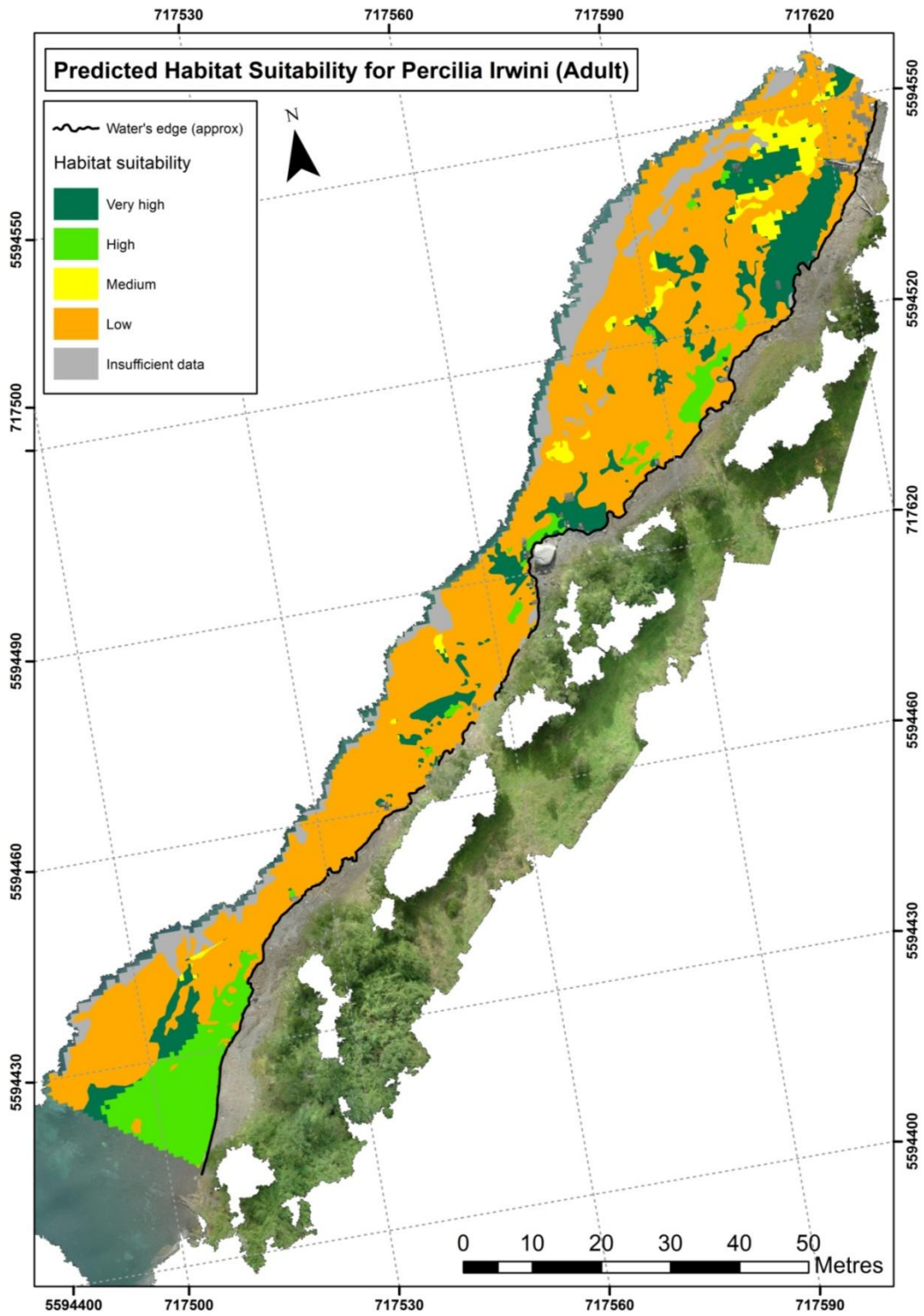


Figure E4. Predicted habitat suitability for the adult life stage of native Chilean fish species *Percilia Irwini* at the Piedra Blanca research site, based on water depth and substrate preferences published by Garcia et al., 2011.

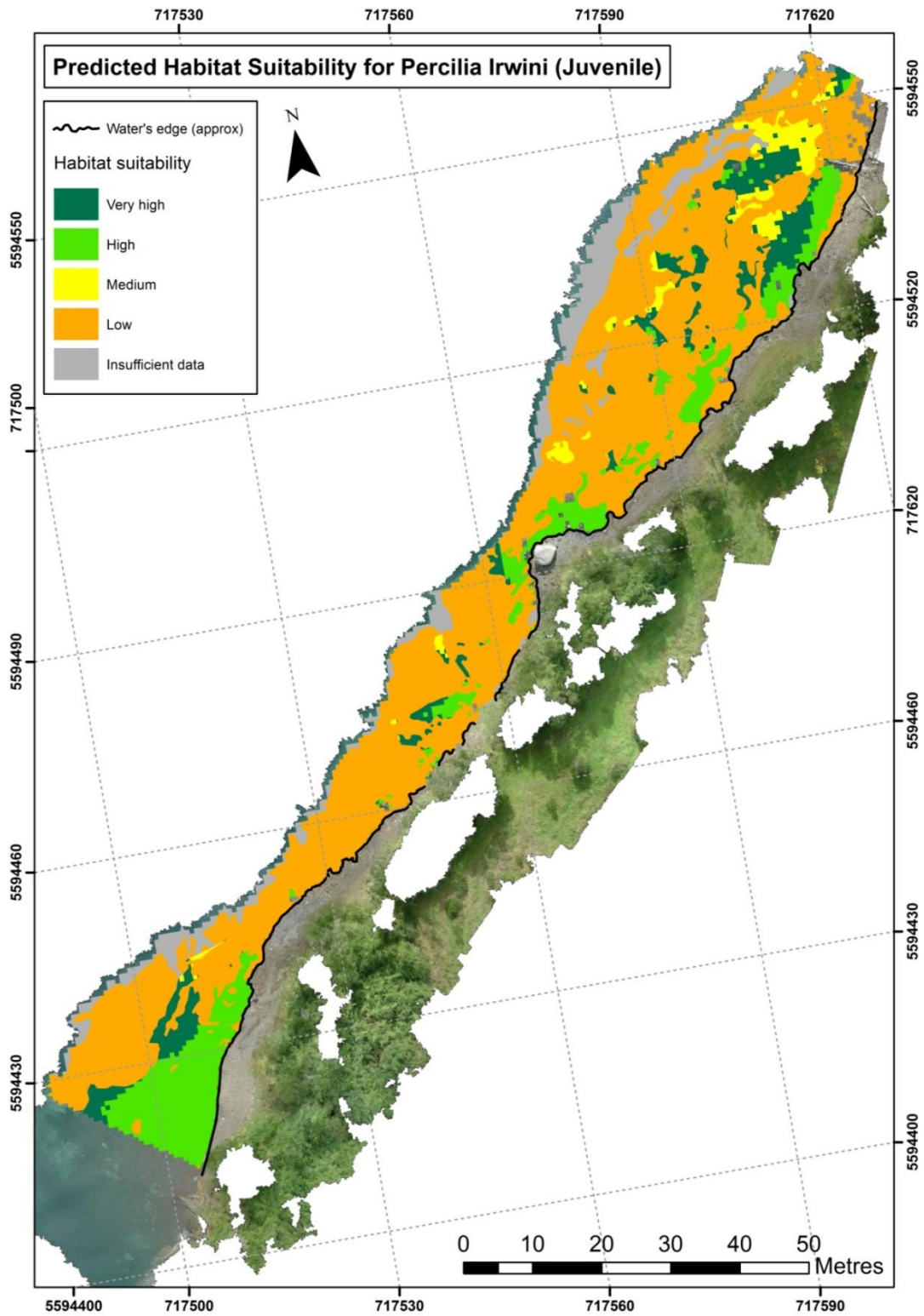


Figure E5. Predicted habitat suitability for the juvenile life stage of native Chilean fish species *Percilia Irwini* at the Piedra Blanca research site, based on water depth and substrate preferences published by Garcia et al., 2011.

Quantifying physical river habitat parameters using hyperspatial resolution
UAS imagery and SfM-photogrammetry

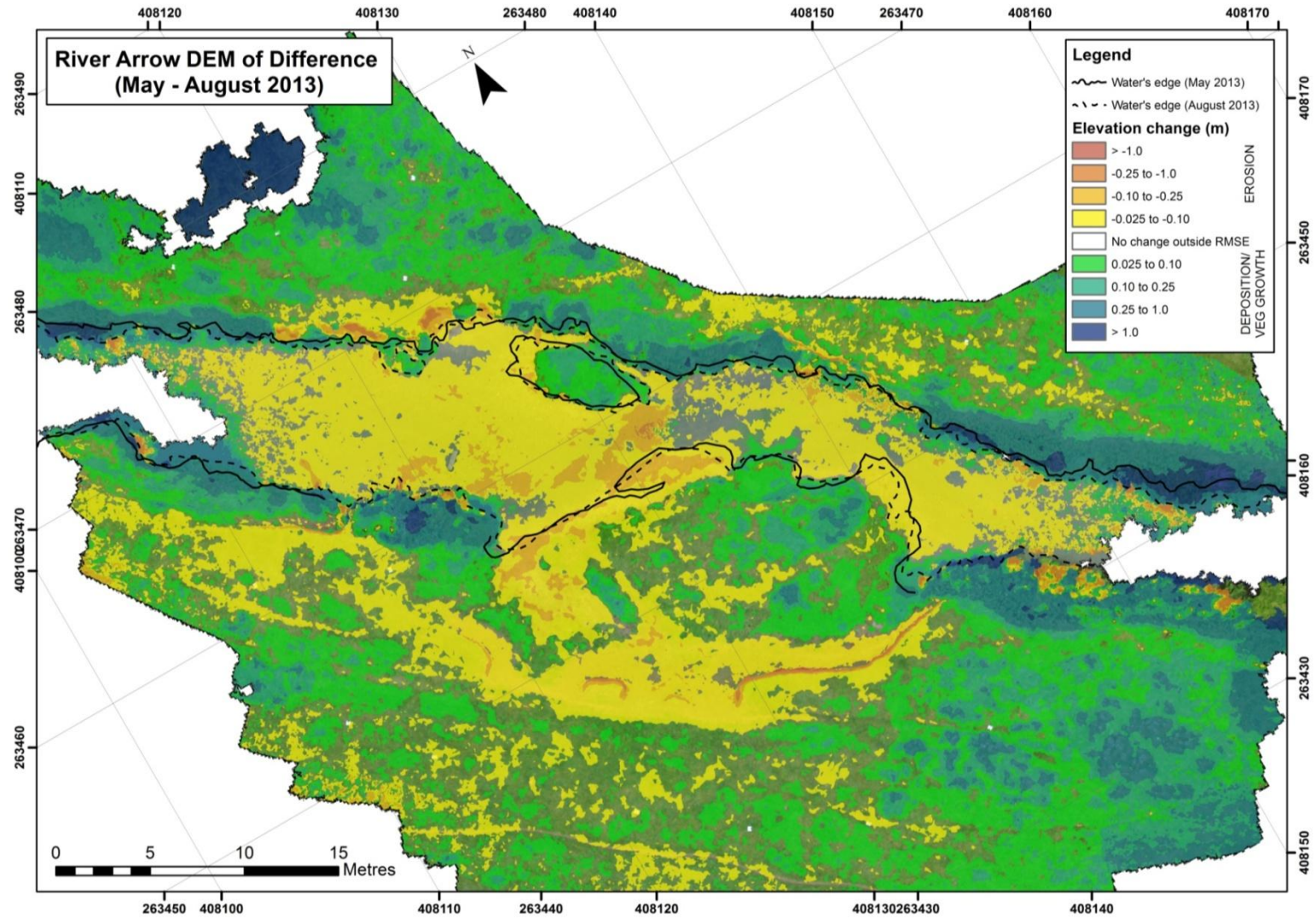


Figure E6. (Previous page) DEM of difference computed using the River Arrow May and August 2013 UAS-SfM DEMs (overlying the August 2013 orthophoto with 30% transparency). Refraction corrected data have not been used in this case, but further work exploring the use of these data should be pursued in future.